frontiers | Research Topics

Thought leaders in analytical science research

Edited by
Huan-Tsung Chang, Elefteria Psillakis, Marianne Fillet, Federico Marini, Ernesto Satoshi Nakayasu, Jason Cheng and John T. Grant

Coordinated by
Chih-Ching Huang and Binesh Unnikrishnan

Published in
Frontiers in Analytical Science

ISSN 1664-8714
ISBN 978-2-8325-6280-2
DOI 10.3389/978-2-8325-6280-2

About Frontiers

Frontiers is more than just an open access publisher of scholarly articles: it is a pioneering approach to the world of academia, radically improving the way scholarly research is managed. The grand vision of Frontiers is a world where all people have an equal opportunity to seek, share and generate knowledge. Frontiers provides immediate and permanent online open access to all its publications, but this alone is not enough to realize our grand goals.

Frontiers journal series

The Frontiers journal series is a multi-tier and interdisciplinary set of open-access, online journals, promising a paradigm shift from the current review, selection and dissemination processes in academic publishing. All Frontiers journals are driven by researchers for researchers; therefore, they constitute a service to the scholarly community. At the same time, the *Frontiers journal series* operates on a revolutionary invention, the tiered publishing system, initially addressing specific communities of scholars, and gradually climbing up to broader public understanding, thus serving the interests of the lay society, too.

Dedication to quality

Each Frontiers article is a landmark of the highest quality, thanks to genuinely collaborative interactions between authors and review editors, who include some of the world's best academicians. Research must be certified by peers before entering a stream of knowledge that may eventually reach the public - and shape society; therefore, Frontiers only applies the most rigorous and unbiased reviews. Frontiers revolutionizes research publishing by freely delivering the most outstanding research, evaluated with no bias from both the academic and social point of view. By applying the most advanced information technologies, Frontiers is catapulting scholarly publishing into a new generation.

What are Frontiers Research Topics?

Frontiers Research Topics are very popular trademarks of the *Frontiers journals series*: they are collections of at least ten articles, all centered on a particular subject. With their unique mix of varied contributions from Original Research to Review Articles, Frontiers Research Topics unify the most influential researchers, the latest key findings and historical advances in a hot research area.

Find out more on how to host your own Frontiers Research Topic or contribute to one as an author by contacting the Frontiers editorial office: frontiersin.org/about/contact

Thought leaders in analytical science research

Topic editors
Huan-Tsung Chang — Chang Gung University, Taiwan
Elefteria Psillakis — Technical University of Crete, Greece
Marianne Fillet — University of Liège, Belgium
Federico Marini — Sapienza University of Rome, Italy
Ernesto Satoshi Nakayasu — Pacific Northwest National Laboratory (DOE), United States
Jason Cheng — University of California, Riverside, United States
John T. Grant — Consultant, Clearwater, United States

Topic coordinators
Chih-Ching Huang — National Taiwan Ocean University, Taiwan
Binesh Unnikrishnan — National Taiwan Ocean University, Taiwan

Citation
Chang, H.-T., Psillakis, E., Fillet, M., Marini, F., Nakayasu, E. S., Cheng, J., Grant, J. T., Huang, C.-C., Unnikrishnan, B., eds. (2025). *Thought leaders in analytical science research*. Lausanne: Frontiers Media SA. doi: 10.3389/978-2-8325-6280-2

Table of contents

05 Editorial: Thought leaders in analytical science research
Binesh Unnikrishnan, Chih-Ching Huang, Huan-Tsung Chang, Elefteria Psillakis, Federico Marini and John T. Grant

07 Maximizing analytical precision: exploring the advantages of ratiometric strategy in fluorescence, Raman, electrochemical, and mass spectrometry detection
Manivannan Madhu, S. Santhoshkumar, Wei-Bin Tseng and Wei-Lung Tseng

21 Simultaneous determination of small molecules and proteins in wastewater-based epidemiology
Yolanda Picó, Antoni Ginebreda, Montserrat Carrascal, Joaquin Abian and Damià Barceló

30 Separation of isobaric phosphorothioate oligonucleotides in capillary electrophoresis: study of the influence of cationic cyclodextrins on chemo and stereoselectivity
Maryam K. Ghassemi, Vincent Hurlet, Jacques Crommen, Anne-Catherine Servais and Marianne Fillet

39 *In vitro* comparative quality assessment of different brands of hydrochlorothiazide tablets marketed in Northeast Ethiopia
Yehualashet Teshome Wondmkun, Haile Kassahun Desta, Yimer Seid Ali, Abate Wondesen Tsige, Kassahun Dires Ayenew, Bedilu Linger Endalifer and Samuel Berihun Dagnew

52 Parallel reaction monitoring targeted mass spectrometry as a fast and sensitive alternative to antibody-based protein detection
Karel Bezstarosti, Lennart Van der Wal, Wouter A. S. Doff and Jeroen A. A. Demmers

63 Novel and rapid analytical platform development enabled by advances in 3D printing
Alexander S. Malinick, Cole P. Ebel, Daniel D. Stuart, Santino N. Valiulis, Victor A. Hanson and Quan Cheng

87 Application of microalgae in wastewater treatment with special reference to emerging contaminants: a step towards sustainability
Pritha Kundu, Nalok Dutta and Sayan Bhattacharya

107 Protein carbamylation and proteomics: from artifacts to elucidation of biological functions
Youngki You, Gina Many and Ernesto S. Nakayasu

115 Protein-templated metal nanoclusters for chemical sensing
Han-Wei Chu, Girum Getachew Demissie, Chih-Ching Huang and Anisha Anand

135 The chemicalome profiling of Zishen Yuzhen Pill *in vivo* and its promoting effect on osteogenic differentiation of MC3T3-E1 cells
Juanjuan Cheng, Xinyue Meng, Daozheng Fang, Yong Zhu, Zhihao Liu, Xinyue Li, Ke Jie, Shiying Huang, Huilin Li, Shangbin Zhang, Jihang Chen and Jianping Chen

151 Multi-energy calibration in plasma emission spectrometry: elemental analysis of animal feeds
Florencia Cora Jofre, Ariane I. Barros, Joaquim A. Nóbrega and Marianela Savio

frontiers | Frontiers in Analytical Science

TYPE Editorial
PUBLISHED 04 April 2025
DOI 10.3389/frans.2025.1596778

OPEN ACCESS

EDITED AND REVIEWED BY
Ernesto Satoshi Nakayasu,
Pacific Northwest National Laboratory (DOE), United States

*CORRESPONDENCE
Huan-Tsung Chang,
changht@ntu.edu.tw

RECEIVED 20 March 2025
ACCEPTED 27 March 2025
PUBLISHED 04 April 2025

CITATION
Unnikrishnan B, Huang C-C, Chang H-T, Psillakis E, Marini F and Grant JT (2025) Editorial: Thought leaders in analytical science research. *Front. Anal. Sci.* 5:1596778.
doi: 10.3389/frans.2025.1596778

Editorial: Thought leaders in analytical science research

Binesh Unnikrishnan[1], Chih-Ching Huang[1], Huan-Tsung Chang[2,3,4,5]*, Elefteria Psillakis[6], Federico Marini[7] and John T. Grant[8]

[1]Department of Bioscience and Biotechnology, National Taiwan Ocean University, Keelung, Taiwan, [2]Department of Biomedical Sciences, Chang Gung University, Taoyuan, Taiwan, [3]Graduate Institute of Biomedical Sciences, Chang Gung University, Taoyuan, Taiwan, [4]Center for Advanced Biomaterials and Technology Innovation, Chang Gung University, Taoyuan, Taiwan, [5]Division of Breast Surgery, Department of General Surgery, Chang Gung Memorial Hospital, Taoyuan, Taiwan, [6]School of Chemical and Environmental Engineering, Technical University of Crete, Chania, Greece, [7]Department of Chemistry, Sapienza University of Rome, Rome, Italy, [8]Surface Analysis Consultant, Clearwater, FL, United States

KEYWORDS

analytical precision, mass spectrometry, wastewater epidemiology, 3D printing, protein nanoclusters

Editorial on the Research Topic
Thought Leaders in Analytical Science Research

Introduction

Analytical science research has received an enormous amount of attention in the last 2 decades and has developed significantly since the COVID-19 pandemic caused a worldwide catastrophe. There were efforts to develop more efficient, rapid, and cost-effective analytical tools and methods over the existing ones. In this context, we started a special issue with the research topic "Thought Leaders in Analytical Science Research", which received good responses from researchers worldwide, and we published eleven articles, encompassing original research, perspectives, and reviews, that embody the innovative methodologies and impactful applications emerging in the modern analytical sciences. These contributions, spanning pharmaceutical quality assessment, novel approaches in mass spectrometry for protein detection, proteomics, separation of isobaric phosphorothioate oligonucleotides in capillary electrophoresis, multi-energy calibration of plasma-based optical emission spectrometry, wastewater-based epidemiology, high-precision ratiometric sensing, 3D printing for instrument fabrication, and protein-templated metal nanoclusters, illustrate the creativity and breadth of analytical scientists confronting today's research challenges. Together, they underscore how thoughtful analytical science underpins advancements in drug safety, disease diagnostics, environmental protection, instrument design, and more. Furthermore, the review articles and perspectives provide an overall update of the developments in analytical science research and future directions.

Overview of contributions

This collection features works that reinforce the critical role of methodical testing, optimization, and validation in analytical science. Wondmkun et al. present a comparative quality assessment of nine hydrochlorothiazide formulations, revealing all of them meet the quality control parameters; however, some of the tablet brands fail in their hardness and friability test, underscoring the need for rigorous *in vitro* equivalence testing. Bezstarosti et al. highlight the advantages of parallel reaction monitoring (PRM) over traditional immunoblotting, demonstrating superior sensitivity and specificity in quantifying complex biomarkers, while Ghassemi et al. explore the potential of cyclodextrin-based additives in capillary electrophoresis to achieve high chemo- and stereoselectivity for the separation of phosphorothioate oligonucleotides. In another study, Jofre et al. introduce multi-energy calibration (MEC) in plasma-based optical emission spectrometry for precise mineral determination in animal feeds, resulting in more accurate feed formulations to ensure optimal livestock nutrition. Cheng et al. employ ultra-high performance liquid chromatography coupled with quadrupole time-of-flight mass spectrometry (UPLC-QTOF-MS) to elucidate the phytochemical composition of Zishen Yuzhen Pill with 152 compounds, 99 metabolites, and 70 prototype components identified in rat tissues after being fed with the pill. The analysis offers a better understanding of the pills in promoting osteogenic differentiation in the pill-treated animals. Additional contributions from perspectives and reviews spotlight new frontiers in proteomics and environmental monitoring. Elucidation of protein carbamylation and its biological function is always challenging because urea, which is used in proteomics procedures, induces carbamylation. You et al. discuss various issues in detail regarding the post-translational modification of proteins and their role in regulating enzymatic activity and disease. The authors provide future directions in proteomic analysis for investigating the effect of post-translational modification of proteins on regulating protein function, activity, localization, interaction, and turnover, with co-purification of acetylated and carbamylated peptides with anti-acetyl-lysine antibodies. Picó et al. provide a clear perspective on wastewater-based epidemiology by determination of small-molecule drug metabolites and proteins to a more inclusive "sewage exposome," through high-resolution MS. Meanwhile, Kundu et al. review the capabilities of microalgae for phytoremediation and the uptake mechanisms, proposing a sustainable, low-cost solution to remove nutrients and emerging contaminants from wastewater, and provide future perspectives.

Several authors emphasize the transformative potential of advanced detection methods and design strategies for improving analytical precision. In this context, Madhu et al. examine how ratiometric approaches offer self-calibrating, high-precision measurements in diverse modes—fluorescence, Raman, electrochemistry, and mass spectrometry—mainly when dealing with complex matrices. Malinick et al. discuss improvement in analytical performances of various techniques using 3D-printed devices that streamline microfluidic, optical, and mechanical components, foreshadowing open-source analytical instrumentation. Lastly, Chu et al. explore protein-templated metal nanoclusters (MNCs), highlighting protein scaffolds' unique luminescent properties and biosensing capabilities, thereby expanding the frontiers of highly sensitive molecular detection. The authors project MNCs as one of the alternatives to conventional dyes to overcome limitations in fluorescence microscopy.

Concluding remarks

Altogether, these eleven articles capture the deep ingenuity and synergistic nature of ongoing analytical research. From robust, cost-effective techniques ensuring pharmaceutical quality to real-time detection of disease biomarkers and toxicants to sophisticated exploitation of quantum and biomaterial phenomena. Each study conveys the pivotal role of advancement of analytical tools and methods in improving precision and solving modern scientific problems. We trust these works, born from close collaborations and well-honed methodological expertise, will continue to inspire innovation among the next-generation of leaders in analytical science research.

Author contributions

BU: Writing – original draft, Writing – review and editing. C-CH: Writing – original draft, Writing – review and editing. H-TC: Writing – original draft, Writing – review and editing. EP: Writing – original draft, Writing – review and editing. FM: Writing – original draft, Writing – review and editing. JG: Writing – original draft, Writing – review and editing.

Funding

The author(s) declare that no financial support was received for the research and/or publication of this article.

Conflict of interest

The authors declare that the research was conducted without any commercial or financial relationships that could be construed as a potential conflict of interest.

The author(s) declared that they were an editorial board member of Frontiers, at the time of submission. This had no impact on the peer review process and the final decision.

Generative AI statement

The author(s) declare that no Generative AI was used in the creation of this manuscript.

Publisher's note

frontiers | Frontiers in Analytical Science

TYPE Review
PUBLISHED 25 September 2023
DOI 10.3389/frans.2023.1258558

OPEN ACCESS

EDITED BY
Huan-Tsung Chang,
Chang Gung University, Taiwan

REVIEWED BY
Scott G. Harroun,
Polytechnique Montréal, Canada
Zhiqin Yuan,
Beijing University of Chemical Technology, China

*CORRESPONDENCE
Wei-Bin Tseng,
tsengwb@mail.dyu.edu.tw
Wei-Lung Tseng,
tsengwl@mail.nsysu.edu.tw

RECEIVED 14 July 2023
ACCEPTED 04 September 2023
PUBLISHED 25 September 2023

CITATION
Madhu M, Santhoshkumar S, Tseng W-B and Tseng W-L (2023), Maximizing analytical precision: exploring the advantages of ratiometric strategy in fluorescence, Raman, electrochemical, and mass spectrometry detection. *Front. Anal. Sci.* 3:1258558. doi: 10.3389/frans.2023.1258558

Maximizing analytical precision: exploring the advantages of ratiometric strategy in fluorescence, Raman, electrochemical, and mass spectrometry detection

Manivannan Madhu[1], S. Santhoshkumar[1], Wei-Bin Tseng[2]* and Wei-Lung Tseng[1,3]*

[1]Department of Chemistry, National Sun Yat-Sen University, Kaohsiung, Taiwan, [2]Department of Environmental Engineering, Da-Yeh University, Changhua, Taiwan, [3]School of Pharmacy, Kaohsiung Medical University, Kaohsiung, Taiwan

Ratiometric strategy are an invaluable method that helps to detect and quantify analytes. This approach relies on measuring changes in the ratio of two or more signals to improve the accuracy and sensitivity of the results. Ratiometric strategies are widely used in a variety of fields including biomedical, environmental monitoring and food safety. It is particularly popular when traditional single-signal based detection methods are not feasible, especially when interfering substances severely affect the detection. In addition, ratiometric methods have the potential to improve the accuracy and reliability of analyte detection, leading to better results in a variety of complex environments. The article provides a comprehensive review of ratiometric strategy, focusing on ratiometric fluorescent nanoprobes for the visual detection of analytes. This paper also discusses the design of ratiometric two-photon fluorescent probes for biomedical imaging, the synthesis of ratiometric surface-enhanced Raman scattering nanoprobes for the imaging of intracellular analytes, the development of ratiometric molecularly imprinted electrochemical sensors for detection of electroactive species, and the use of isotopically-labeled internal standards in matrix-assisted laser desorption/ionization for ratiometric analysis. The article not only discusses each technique in detail, including its principles, advantages, potential applications, and limitations, but also highlights recent advances in each method and possible future directions.

KEYWORDS

ratiometric, fluorescence, Raman, electrochemical, mass spectrometry

1 Introduction

A ratiometric strategy is a "self-calibration" method by measuring the analyte-induced change in the ratio of two or more signals in a sensing element (Huang et al., 2018; Jin et al., 2021; Wei et al., 2022). In contrast to single-signal detection, this method has built-in corrections for fluctuations in instrument operation, interference from the sample matrix, variations in the microenvironment around the probe, and changes in the concentration of

the probe. Due to these advantages, a ratiometric strategy is extensively implemented in a wide range of analytical techniques, including fluorescence, Raman, absorbance, electrochemistry, and mass spectrometry (Ali et al., 2014; Ke et al., 2015; Li et al., 2015; Peng et al., 2016; Chen et al., 2017; Parrilla et al., 2017; Vargas et al., 2019; Vyas et al., 2019; Njoko et al., 2020; Madhu and Tseng, 2021; Spring et al., 2021; Zhu et al., 2021). Two or more fluorescent dyes and nanomaterials are typically integrated into a ratiometric fluorescence sensing analytical platform. Each probe emits a light signal at a unique wavelength to the analyte. The platform measures the intensity ratio of the emitted light to determine the analyte concentration. Similarly, a ratiometric strategy using two independent wavenumbers in Raman spectroscopy can be applied to determine the concentration of an analyte. Absorbance spectroscopy also employs a ratiometric strategy, where the concentration of an analyte is calculated from the ratio of two absorbance readings. Also, amperometry and potentiometry are electrochemical methods that employ a ratiometric strategy to quantify an analyte. As a target analyte is added, more than two currents and potentials are typically monitored. Another analytical method that benefits from a ratiometric strategy is mass spectrometry. In this method, isotopically labeled standards are used as internal references to provide reliable and accurate quantitative measurements of analytes. The researchers can obtain reliable and accurate quantitative results in various analytical fields by employing these ratiometric analytical techniques. A ratiometric strategy has gained a foothold in various analytical fields, especially for quantifying analytes in a complex sample. In environmental monitoring, ratiometric fluorescence sensors are ideally suited for detecting metal ions and organic contaminants in water samples, making them a powerful tool for monitoring and managing water quality. These sensors are quick and easy to use, with results typically available within minutes. In addition, they are cost-effective and can detect a wide range of contaminants with high accuracy and sensitivity (HeeáLee and SeungáKim, 2015). Moreover, *in vivo* and *in vitro* studies, ratiometric phosphorescent sensors are well-developed for monitoring microenvironmental changes and imaging target analytes in living cells and animals. These sensors are also exploited to monitor dynamic events, such as the kinetics of enzyme reactions in living organisms (Jin et al., 2021). In biomedical research, a ratiometric Raman technique integrated with a microscopy-related system is attractive for investigating biomolecular structures at the cellular and sub-cellular levels (Kumar et al., 2016). By adopting the ratiometric Raman technique, researchers can improve the accuracy and precision of measurements compared to quantitative methods based on absolute band Raman intensities. This technique enables the label-free biomolecular fingerprinting of biological samples in their native state. Consequently, a ratiometric strategy has become an indispensable component in a wide range of analytical methods, including fluorescence, Raman, absorbance, electrochemistry, and mass spectrometry, ensuring trustworthy and precise quantitative analysis across different scientific domains.

This review explores a variety of ratiometric measurements in conjunction with various analytical techniques, including precise analytical detection using ratiometric fluorescent nanoprobes and biomedical imaging using two-photon fluorescent probes. Moreover, ratiometric surface-enhanced Raman scattering (SERS) nanoprobes provide Raman-sensitive molecules as a reference signal in the silent cell region, enabling Raman imaging of target analytes in living cells. In the silent region, most intracellular biomolecules are devoid of Raman scattering signals. However, functional groups such as alkyne, azide, and nitrile, as well as substituting C-H for C-D, show characteristic Raman bands in this silent region, which is a fortunate exception. It also highlights how to design ratiometric molecularly imprinted electrochemical sensors and utilize isotope-labeled internal standards to achieve ratiometric analysis in matrix-assisted laser desorption/ionization time-of-flight mass spectrometry (MALDI-TOF-MS). Each technique's advantages and applications are summarized, providing valuable insights for advancing ratiometric sensing across different fields.

2 Merits of ratiometric strategy in analytical chemistry

A ratiometric strategy offers several advantages over other analytical methods: 1) Improved accuracy and precision: A ratiometric strategy eliminates many noise sources, such as variations in instrument response or the influence of the sample matrix, which can affect the absolute value of a single signal. By measuring the ratio of two or more signals, ratio sensing can improve the accuracy and precision of measurements (Bigdeli et al., 2019). 2) Increased sensitivity: A ratiometric strategy can improve the reproducibility of measurements by measuring the ratio of two or more signals, thereby increasing sensitivity and lowering the detection limit (Huang et al., 2018; Wei et al., 2022). 3) Excellent selectivitatiometric strategy achieves selectivity by employing multiple signals with distinct responses to the target analyte. By measuring the ratio of these signals, ratiometric sensing ensures selective detection, even in complex sample matrices (Abbasi-Moayed et al., 2018; Gan et al., 2022; Shan et al., 2022; Zhu et al., 2022). 4) Real-time monitoring: By utilizing multiple signals with distinct responses to the target analyte, a ratiometric sensing enables continuous monitoring without sample processing or time-consuming analysis. This real-time capability allows for swift and dynamic measurements in various research applications (Liu et al., 2019; Qu et al., 2020; Kumaravel et al., 2021; Han et al., 2022). 5) Versatility: Ratiometric methods, incorporating various detection techniques such as fluorescence, absorbance, electrochemistry, Raman scattering, and mass spectrometry, emerge as a powerful tool for achieving accurate and sensitive measurements in diverse research areas. With its broad applicability, a ratiometric sensing proves valuable in a variety of analytical chemistry applications, including environmental monitoring, biomedical analysis, and materials science (Bigdeli et al., 2019; Jin et al., 2021; Wei et al., 2022; Šebela, 2023).

3 Utilizing ratiometric fluorescent nanoprobes for naked-eye detection of analytes

Ratiometric fluorescent nanoprobes contain two or more fluorescent components that emit light at different wavelengths,

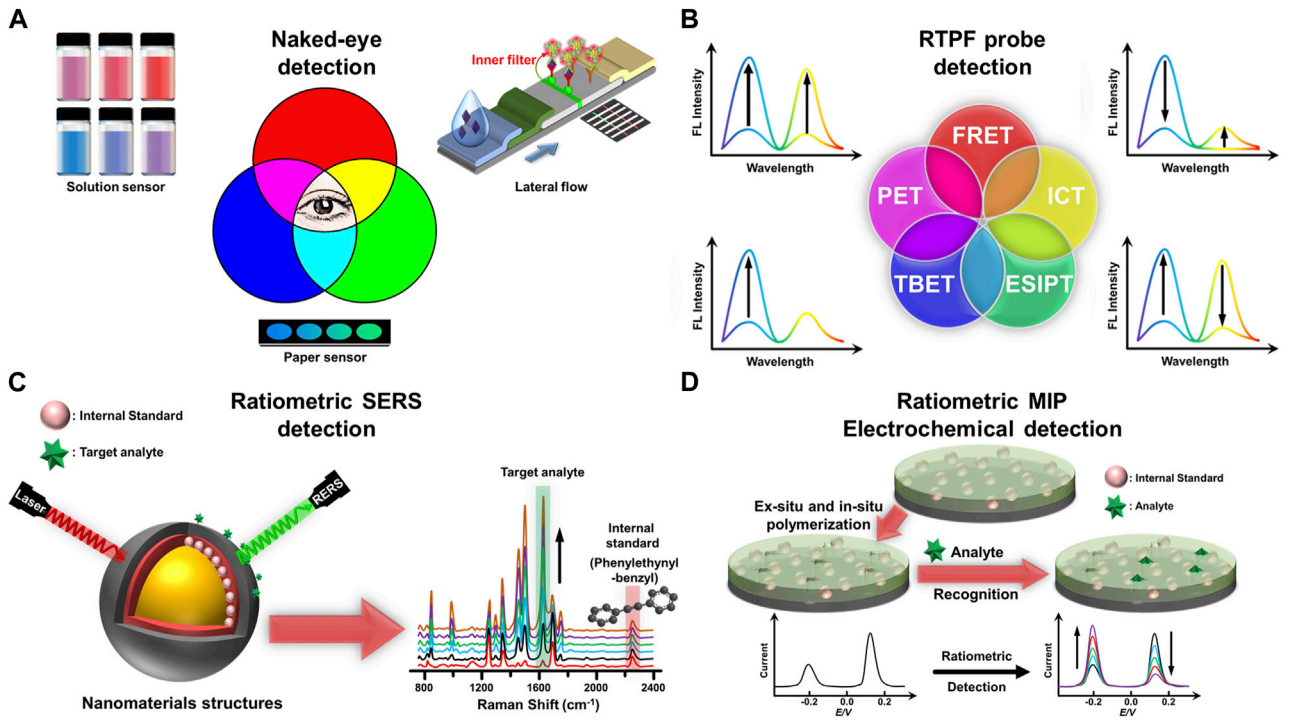

FIGURE 1
(A) Diverse forms of naked-eye detection in fluorescence-based assays. **(B)** Fundamental guidelines for building ratiometric two-photon fluorescent probes based on different ratiometric signal patterns and sensing mechanisms. **(C)** Creation of a ratiometric SERS nanoprobe for detecting target analytes using an internal standard in a region without biomolecule interference. **(D)** Fabrication of the MIP electrochemical sensor with an internal standard for ratiometric detection of target analytes.

allowing ratiometric sensing and imaging. They has become an ideal tool for visualizing, detecting, and quantifying a wide range of analytes, including ions, molecules, and biomolecules (Kumar et al., 2020; Chuang et al., 2022; Tseng et al., 2022; Luo et al., 2023). The design of ratiometric fluorescent nanoprobes involves carefully selecting fluorescent components, including dyes, quantum dots, upconversion nanoparticles, and metal clusters. These components should have different emission spectra and similar excitation spectra to ensure accurate ratiometric sensing. Nanoprobes should also be designed to target specific analytes by chemical modification or using biomolecules, such as antibodies, inducers, or peptides as recognition elements. For naked-eye detection, nanoprobes should have a high contrast between the two emission channels for easy visualization with the naked eye (Kumar et al., 2020; Tseng et al., 2022; Luo et al., 2023). A key aspect of designing ratiometric fluorescent sensors for visual detection is the thoughtful selection of fluorophores with distinct emission spectra. This choice ensures that the emission wavelengths of the two fluorophores are easily distinguishable to the naked eye. The greater the contrast in emission wavelengths, the more pronounced the color change will be, allowing direct differentiation between different states or analyte concentrations. This approach also applies to ratiometric absorption sensors. Firstly, the interaction between the chromophore and the target analyte results in a distinctive spectral wavelength or absorbance change, producing a noticeable color change. This uniqueness is essential for clear visual discrimination between an analyte and possibly interfering compounds. The human naked eye can perceive alterations in a given ratio through noticeable changes in color, intensity, or brightness. These ratios are commonly assessed using various sensing elements, which can be affixed to a solid support, such as lateral flow immunochromatographic assays, loop-mediated isothermal amplification (LAMP) assays, aptamer sensors, smartphone-based assays, and paper sensors. Alternatively, the sensing element can be incorporated into a solution, enabling visual inspection. Naked-eye detection utilizing ratio sensors offers numerous advantages, including simplicity in operation, the convenience of visual endpoint detection, rapidity in obtaining results, specificity in target identification, and cost-effectiveness. Moreover, these sensor-based approaches do not necessitate specialized equipment or highly trained personnel. However, naked-eye testing using ratio sensors lacks precise quantitative information. Although naked eye readings are instinctive, accurate results are not always possible because the interpretation of color changes can be subjective. In addition, the detection limit of this method may not match the detection limit achieved by instrumental techniques, which may limit sensitivity. Among fluorescence-based assays, naked-eye detection can be achieved by solution-based assays, paper-based assays, and lateral flow immunochromatographic assays (LFAs) (Figure 1A). Solution-based assays involve probes with chromophores and fluorophores that cause changes in absorption spectra and fluorescence emission, respectively, upon binding to analytes. On the other hand, paper-based assays use chromatography paper as an analytical detection

platform, where probes attached to chromophores and fluorophores are immobilized on the chromatography paper. After the sample is dispensed, the porous media chromatography paper is able to guide the sample flow through capillary action, and visual detection can be achieved by observing changes in the color of the probes on the paper strip or changes in the fluorescence intensity of the probes. LFAs are designed to detect analytes on paper through immunoassay principles. In the first step, the analyte-specific antibody is attached to the chromophore or fluorophore and then coated onto the conjugate pads. The conjugate pad is then placed on a nitrocellulose membrane containing the test and control lines. The sample flows through the membrane by capillary action. If an analyte is present, it binds to the conjugated antibody or antigen, producing a visible color change on the test line. The secondary antibody on the control line is then connected to the unreacted antibody to ensure correct results.

Here are some examples of how to detect environmental pollutants and biomarkers using the naked eye: in solution, on paper, and through lateral flow immunochromatography. Tseng et al. synthesized gold nanoclusters-loaded lysozyme nanoparticles through the reaction of aggregated lysozyme-stabilized gold nanoclusters with glutaraldehyde. The gold nanoclusters and lysozyme nanoparticles in the nanocomposites emitted blue and red fluorescence, respectively, under a single excited wavelength (Tseng et al., 2022). The presence of cyanide etched gold nanoclusters in the dual-emission nanocomposites, inhibiting their Förster resonance energy transfer (FRET) from lysozyme nanoparticles to gold nanoclusters. As a result, the dual-emission nanocomposites were capable of ratiomatrically detect cyanide within a linear range of 3–100 μM. They demonstrated that the proposed nanocomposites provided exceptional selectivity for cyanide and successfully quantified cyanide levels in tap water and soil samples. Furthermore, the nanocomposites were exploited to monitor the release of hydrogen cyanide from cyanogenic glycoside-containing foods. These findings highlight the probe's potential for diverse environmental analysis and food safety applications.

In addition, a ratiometric fluorescence sensor was developed for the sensitive and selective detection of carbaryl in Iranian apples through 1) the NaOH-mediated hydrolysis of carbaryl to blue-emitting 1-naphthol and 2) the mixing of 1-nanphthol and yellow-emitting cadmium telluride quantum dots (CdTe QDs) (Shahdost-Fard et al., 2021). Using CdTe QDs with yellow fluorescence at 580 nm as a reference, the fluorescence colour changed from yellow to blue as the concentration of carbaryl increased. This ratiometric fluorescent sensor enabled enzyme-free naked-eye detection of carbaryl with a limit of detection (LOD) of 0.12 ng/mL, which is lower than the maximum residue limits (MRLs) specified in the EU Pesticides Database and the USDA Foreign Agricultural Service MRL Database. For example, the MRL for chlorpyrifos in apples is 0.01 mg/kg in the US and 0.05 mg/kg in the EU. The effectiveness of the sensor was confirmed by comparison with high-performance liquid chromatography analysis, demonstrating its potential for rapid and reliable detection of other targets in food safety applications.

Li et al. utilized the mixing of blue- and red-emitting carbon dots for the naked-eye detection of amoxicillin (Li et al., 2023). Hydrogen bonding between amoxicillin and blue-emitting carbon dots led to an increase in the intensity of their blue fluorescence and a change in the color of the solution mixing the two carbon dots from red to blue. A portable hand-held needle sensing device was designed for the direct visual detection of color change of two carbon dot mixtures under UV irradiation in response to amoxicillin stimulation. A smartphone-based illumination device was also fabricated to allow fluorescence imaging of two carbon-dot mixtures after the addition of amoxicillin, which was then quantified based on blue channel/red channel values.

Recently, Miao et al. reported a triple-emission fluorescence sensor consisting of 3-aminophenylboronic acid-derived carbon dots and ovalbumin-stabilized gold nanoclusters for the detection of tetracycline (Miao et al., 2023). The two nanomaterials were hybridized by interacting the cis-diol bond of ovalbumin with the borate group of carbon dots. Tetracycline not only enhanced the red fluorescence of gold nanoclusters through the restriction of their rotational motion but also quenched the blue fluorescence of carbon dots through the inner filter effect process. When the concentration of tetracycline varies between 0.5 and 40 μM, the fluorescence of the sensor changes from blue-violet to yellow-green under UV light; this color change is easy to detect with the naked eye. The proposed hybrid sensor demonstrated the successful determination of tetracycline in real water samples.

Wang et al. described a highly sensitive ratiometric fluorescent lateral flow immunoassay strip for the rapid and accurate detection of cardiac-type fatty acid binding protein, a biomarker associated with acute myocardial infarction (Wang et al., 2021). Fluorescent silica nanoparticles containing gold nanoparticles and red-emitting CdSe/CdS/ZnS quantum dots, along with anti-FABP 10E1 antibodies, were incorporated into the conjugate pad of the testing paper. Simultaneously, green-emitting CdZnSe/CdS/ZnS quantum dots linked to anti-FABP 28 antibodies were affixed in a designated test line of the paper strip. In a positive assay, the above-mentioned quantum dots with fatty acid binding protein in the sample form sandwich-like immunological complex structure at the test line, resulting in the fluorescence color change from green to red. This color change resulted from the target-induced internal filter effect between the loaded gold nanoparticles and green-emitting quantum dots, leading to an enhanced red emission and a reduced green emission. Quantitative detection of heart-type fatty acid binding protein was achieved with a low LOD of 0.21 ng/mL using a custom smartphone-based analytical device and tonality analysis. The ratiometric fluorescent lateral flow immunoassay strip enabled visually distinguishable green-to-red color changes around the threshold concentration of heart-type fatty acid binding protein (6.2 ng/mL), facilitating semi-quantitative diagnosis by the naked eye.

4 Ratiometric two-photon fluorescence probes for cellular and small animal imaging in biomedicine

Fluorescent probes typically require short wavelengths of excitation light, which may interfere with the autofluorescence of cells and tissues, thus limiting their applications (Zhang et al., 2021). The advent of two-photon fluorescent probes coupled to two-photon microscopy overcomes these limitations by utilizing long-wavelength femtosecond laser sources to excite fluorescent probes.

Since Maria Goeppert-Mayer introduced it in the 1930s (Grzybowski and Pietrzak, 2013), this method has been popular for *in vivo* imaging. A two-photon action cross-section is related to the quantitative degree of two-photon absorption capacity, mainly in units of the Goeppert-Mayer abbreviation (1 GM = 1 × 10^{-50} cm^3 s/photon). Ratiometric two-photon fluorescent probes are capable of producing two or more emission peaks of different intensities or wavelengths. The intensity of one or more fluorescence peaks can be varied depending on how the RTPF interacts or reacts with a particular target. By establishing a calibration curve between the fluorescence signal ratio and the analyte standard concentration, the analyte level in the complex matrix can be determined. Four fundamental guidelines exist for building RTPF probes based on different ratiometric signal patterns (Figure 1B): 1) A two-emission probe exhibits the same (simultaneous increasing or decreasing) intensity trend upon analyte reappearance (Jun et al., 2018; Ren et al., 2020); 2) In the presence of analytes, a single-emission probe causes the emergence of a new emission peak and the reduction of the original emission peak (Kim et al., 2013; Park et al., 2018); 3) A two-emission probe consists of a reference signal showing minimal variation and a response signal showing significant variation (Sun et al., 2016; Wang et al., 2019; Reo et al., 2019); 4) The reaction (interaction) of a two-emission probe with a target gives rise to an increase in one emission peak and a reduction in the other emission peak (Divya et al., 2014; Ge et al., 2020). The sensing mechanisms of ratiometric two-photon fluorescence probes include one or more of FRET, through-bond energy transfer (TBET), photo-induced electron transfer (PET), excited state intramolecular proton transfer, intramolecular charge/electron transfer (ICT), and energy dissipation (Luo et al., 2017; Ding et al., 2020). Various reaction types are also involved between RTPF probes and targets in live cells and small animals, such as reduction reaction (Lim et al., 2011), nucleophilic addition (Zhao et al., 2018), and supramolecular assembly (Wang et al., 2018).

The following are examples of *in vitro* and *in vivo* studies using RTPF in recent years. Liang et al. developed a two-photon ratiometric fluorescent probe for real-time imaging and quantification of nitric oxide (NO) based on the coupling of FRET and PET mechanism (Liang et al., 2022). Coumarin and phthalimide-containing naphthalene dicarboximide in the probe acted as fluorescence donor and acceptor, respectively. The probe has two independent fluorescence emissions, high selectivity and good accuracy, with a detection range of 0.1–200 μM and a detection limit of 19.5 nM for NO. The probe successfully monitored and quantified NO in neural stem cells and different brain regions, revealing the role of NO in the activation and quiescent differentiation of neural stem cells, as well as its dose-dependent effect in promoting neuronal differentiation. Furthermore, it was found that NO concentrations were low in the hippocampal DG region of the brains of Alzheimer's disease mice, and that treatment with NO-activated neural stem cells improved the symptoms of Alzheimer's disease mice.

Chen et al. fabricated a two-photon ratiometric fluorescent probe consisting of rhodamine B (energy acceptor), methylhydrazine (recognising element), and quinoline derivatives (energy donor) for sensing Peroxynitrite, with a significant change in fluorescence signal (>200-fold) (S. Chen et al., 2021). Peroxynitrite is a reactive oxygen species (ROS) known to adversely affect physiological processes. The presence of peroxynitrite triggered the oxidation of methylhydrazine in rhodamine B, resulting in a FRET process from quinoline derivatives to rhodamine B. This reaction was completed within 2 min and showed good selectivity for peroxynitrite over other ROS, including hypochlorite. The probe was used to observe fluctuations in peroxynitrite production by arginase 1 *in vivo* and *in vitro*, suggesting that arginase 1 plays a key role in regulating peroxynitrite levels.

Valverde-Pozo et al. prepared a near-infrared fluorescent probe for the detection of dipeptidyl peptidase IV (DPP IV) activity, also known as CD26 (Valverde-Pozo et al., 2023). DPP IV is a transmembrane glycoprotein associated with glucose metabolism and T-cell stimulation. It is overexpressed in certain cancer tissues and can be used as a diagnostic marker for lysosomal storage diseases. This probe consisted of a DPP IV-sensitive dipeptide and a two-photon dicyanodiamine-4H-pyran derivative fluorophore. The dipeptide moiety blocked the internal charge transfer of the two-photon probe, thereby quenching its red emission and enhancing its green emission. Once DPP IV catalyzed the cleavage of the probe, the resultant products without dipeptide moiety produced intense red emission and weak green emission through the restoration of the internal charge transfer process. This two-photon ratiometric probe was suitable for super-resolution fluorescence imaging of DPP IV activity in living cells and tumour tissues when excited by two-photons. Zebrafish experiments show that DPP IV levels increased with developmental stage, suggesting the potential of this probe in cases of DPP IV overexpression such as cancer and diabetes.

Prepared a two-photon near-infrared ratiometric fluorescent nanocomposite via a click reaction between alkyne group-linked fluorescent molecules and azide-modified chitosan, followed by the application to the imaging of hydrogen peroxide (ONOO-) in liver injury (Xie et al., 2022). Liver injury is closely associated with $ONOO^-$, making it an important biomarker for the diagnosis and assessment of liver disease. The small fluorescent molecule comprised a donor–π–acceptor structure of naphthalimide derivative, generating near-infrared emission through the FRET process from a donor to an acceptor. The formed nanocomposites possessed several favorable properties, including good water solubility, low background interference, deep tissue penetration and high imaging resolution. The oxonium functional group of the small fluorescent molecules in the nanocomposites reacted with $ONOO^-$, resulting in the separation of naphthalimide derivative fluorophore and salicylic acid. Due to the cleavage of a donor–π–acceptor structure, the green emission of the nanocomposites intensified with increasing the concentration of $ONOO^-$. The proposed nanoprobe exhibits a short reaction time (~10 s) and a high selectivity and sensitivity for $ONOO^-$ detection with a LOD of 15.3 nM. I Significantly, the developed probe was effectively employed for the detection of ONOO- in viable HepG2 cells, as well as in mouse tissues exhibiting liver injury, and within mouse models.

Zhai et al. designed a viscosity-responsive, lysosome-targeted, two-photon fluorescent probe based on a TBET mechanism (Zhai et al., 2022). During autophagy, cells degrade themselves, keeping the body healthy. The study of autophagy and related diseases requires specific viscosity probes that can accumulate in lysosomes, as the viscosity of lysosomes increases during autophagy. This probe consisted of a viscosity-sensitive styrene

derivative linked to a TBET energy acceptor and a two-photon excited coumarin derivative as an energy donor. An alkyne bond connects these two fluorescent molecules. Under two-photon excitation at 810 nm, the red emission of styrene derivatives in the probe was progressively enhanced with increasing the solution viscosity, while the green emission of coumarin derivatives remained almost unchanged. The integration of a two-photon confocal technique and the proposed probe offered a better signal-to-noise ratio fluorescence image with deeper penetration. The developed probe was applied to visualize autophagy processes under complex physiological conditions, including inflammation and stroke. As a result of the probe's observations, ROS and inflammation may have a causal role in triggering autophagy activation during stroke. These findings demonstrate that the inflammatory-autophagy pathway holds promise for treating cerebrovascular diseases. The examples above confirm that the integration of two-photon excitation and near-infrared fluorescence enhances the imaging capabilities of probes in living cells, tissues, and animal models. It can be expected that as these ratiometric fluorescent probes continue to advance, they have great potential for advancing the understanding of a wide range of biological phenomena and, ultimately, for helping to develop targeted therapeutic interventions for a variety of diseases.

5 Ratiometric SERS nanoprobes in a cellular silent region

A powerful SERS technique can enhance the Raman scattering signal by several orders of magnitude through interactions between molecules and metal nanoparticles or plasmon resonance on rough metal surfaces (Langer et al., 2020; García-Hernández et al., 2023). Electromagnetic enhancement and chemical enhancement that are proposed to contribute to the SERS effect are now generally accepted in the field (Wang et al., 2021; Santhoshkumar et al., 2023; Zhao et al., 2023). Raman scattering signals are enhanced by electromagnetic enhancement when light interacts with metal surfaces, which generates a strong electromagnetic field near the metal nanoparticles. A metallic nanomaterial used in SERS depends on its size, shape, and composition to enhance electromagnetic fields (Santhoshkumar and Murugan, 2021a; Lin et al., 2021; Xianyu et al., 2021). Due to the localized surface plasmon resonance effect, metal nanoparticles with sharp edges or corners, such as gold nanostars, can generate a stronger electromagnetic field (Hao et al., 2007). Silver nanomaterials' higher polarization rate and lower electron density can also lead to stronger electromagnetic enhancement than gold nanomaterials (Chen et al., 2010; Kang et al., 2018). When metal nanomaterials are functionalized with specific molecules or functional groups, their plasmonic properties are altered, and their interactions with analytes are enhanced (Gehan et al., 2010; Santhoshkumar and Murugan, 2021b; Ishida et al., 2021; Lin et al., 2021; Xianyu et al., 2021). Also, semiconductor nanomaterials enhance R The Raman signal can be significantly enhanced by enhancing the charge transfer between the semiconductor and its adsorbed molecules. During charge transfer, electrons are transferred from the molecule to the surface of the semiconductor nanoparticle or *vice versa*, forming a charge transfer complex, which in turn increases the polarizability of the molecule and changes its vibrational modes to significantly enhance the Raman signal. Semiconductor nanomaterials are more affordable and easier to synthesize than those based on precious metals. Various semiconductor nanomaterials, such as silicon (Si), titanium dioxide, zinc oxide, and indium tin oxide, have been used in SERS (Kanehara et al., 2009; Wang et al., 2017; Wang et al., 2019; Zhao et al., 2020; Han et al., 2021; Rajput et al., 2022). In addition, MoS_2 and WS_2 have been shown to have a significant charge transfer mechanism, which is a chemical enhancement in SERS (Masoumi et al., 2022; Santhoshkumar et al., 2023).

The advantages of SERS include high sensitivity and selectivity, the ability to detect molecules at very low concentrations, non-destructive, and can be used for the detection of a wide range of molecules including biomolecules, pharmaceuticals, and environmental contaminants (Cai et al., 2015; Tackman et al., 2018; Geng et al., 2021; Peng et al., 2021; Kamal and Yang, 2022). In addition, SERS can be used for *in situ* and real-time monitoring, making it a valuable tool for a variety of applications, including biosensing, medical diagnostics, and environmental monitoring (Liu et al., 2021; Quan et al., 2021; Xie et al., 2022; Yue et al., 2022). However, one of the main challenges of SERS is the reproducibility and reliability of the measurements, since the intensity of the SERS signal is highly dependent on the preparation of the metal substrate and the specific experimental conditions used. In addition, the high sensitivity of SERS can sometimes lead to false positives or false negatives due to the presence of interfering molecules or lack of specificity of the SERS probe.

To address these challenges, researchers have proposed the ratiometric SERS method to improve the reproducibility of measurements. In ratiometric SERS, two molecules must be selected: a target molecule to be quantified or detected and a reference molecule. The reference molecule is a stable and well-characterized standard for normalizing the Raman signal. By calculating the ratio of the Raman signal intensities of the two molecules, the effects of variables such as laser power fluctuations, sample heterogeneity, and metal substrate variations can be minimized. The reference molecule should have a SERS enhancement factor comparable to that of the analyte molecule but must not be present in the sample. Using a suitable reference molecule ensures normalization of the SERS signal, compensates for variations in experimental conditions, and reduces the effects of SERS substrate variations. This approach is particularly suitable for complex samples or low-concentration samples where the SERS signal may exhibit considerable variability. Choosing an appropriate reference molecule for ratiometric SERS necessitates considering several factors, including the molecule's SERS enhancement factor, chemical stability, and lack of interference with the Raman bands of the analyte. Generally, a suitable reference molecule should have a Raman signal in the spectral range of 1800–2,800 cm^{-1}, where most biological molecules have negligible Raman signals (Figure 1C). Alkynes are a class of organic compounds that contain at least one triple bond between two carbon atoms. Symmetric and asymmetric stretching of C-H bonds in alkynes are detected at approximately 3,400 cm^{-1}, while their C≡C bond display. A single stretching band, typically occurring in the range of 2,100–2,200 cm^{-1}. These vibrational modes occur at higher wavenumbers than those typical of biological molecules, such as proteins, nucleic acids,

and lipids. When two carbon atoms in an alkyne molecule move in the same direction, either toward or away from one another, symmetric stretching takes place. This movement leads to a stretching vibration of the carbon-carbon triple bond, resulting in a Raman signal in a specific band. For example, 4-((4-mercaptophenyl)diazenyl)phenyl 3-((4-(phenyethynyl)benzyl)thio) propanoate exhibited a Raman peak at 2,207 cm^{-1} for the sensing of hypoxia (Qin et al., 2019). Also, N-(12-((4-(phenylethynyl)benzyl) amino)dodecyl) polyethylene glycol with a Raman peak at 2,219 cm^{-1} was exploited to sense alkaline phosphatase (Zhao et al., 2021). Furthermore, a notable illustration is the application of 3-[4-(Phenylethynyl)benzylthio]propanoic acid-modified DNA, which showcased a Raman peak at 2,215 cm^{-1} and served as an endonuclease-responsive probe (Si et al., 2018).

The following are examples of *in vitro* and *in vivo* studies using ratiometric SERS nanoprobes in recent years. Bi et al. synthesized citrate-terminated gold nanoparticles and modified them with the pH-sensitive Raman probe, 4-mercaptopyridine, by forming strong Au-S bonds (Bi et al., 2020). After addition of potassium hexacyanoferrate(II) and ferric chloride, the resulting products were encapsulated into Prussian blue shells. The Prussian blue shell not only exhibited a single C≡N stretch band, which served as a background-free internal standard in living cells, but also had a sub-nanometre porous structure that selectively detected H^+ and OH^- without interference from biomolecules such as biothiol proteins and DNA. The probe uses the ratiometric Raman signal of 4-mercaptopyridine to Prussian blue shell nitrile to measure pH from 4.0 to 9.0 in complex biological environments. They used the probe to monitor a significant decrease in pH when cells were treated with 6-hydroxydopamine, which triggers cellular degradation processes. They also monitored changes in intracellular pH during autophagy induced by nutrient deficiency. This study demonstrated that this ratiometric pH probe was well-suited to observe autophagy by quantifying intracellular pH fluctuations.

Similarly, Shen et al. reported the production of gold nanoparticle-loaded Prussian blue nanocomposites through the two-step process (Shen et al., 2021). Firstly, the seed growth method was used to prepare 60 nm-sized gold nanoparticles, which were then etched with $K_3[Fe(CN)_6]$. This procedure results in the formation of a CN^- molecular layer on the gold nanoparticle surface, which is helpful to form a homogeneous coating of Prussian blue. The subsequent step involved the gradual formation of shell on CN^--coated gold nanoparticles after the addition of $PbCl_2$ or $CuCl_2$ instead of $FeCl_2$ as precursors in the presence of $K_3[Fe(CN)_6]$. Two types of Prussian blue loaded with gold nanoparticles formed from $PbCl_2$ and $CuCl_2$ precursors showed different SERS signals at 2,122 cm^{-1} and 2,176 cm^{-1}, respectively. Modification of ligands targeting epithelial cell adhesion molecules and epidermal growth factor receptor, respectively, on two Raman probes allows for simultaneous determination of the relative expression of these two membrane proteins on the cell surface, thus enabling interference-free ratio detection.

Besides, Zhong et al. used 4-azidobenzenthiol-modified gold nanoparticles as a ratiometric SERS nanoprobe for imaging endogenous H_2S in individual living cells (Zhong et al., 2022). The thiol moiety of 4-azidobenezenthiol attached to the surface of the citrate-capped gold nanoparticles, while its azide moiety showed a strong Rama signal at 2,137 cm^{-1} in the cell silencing zone. In addition, the Raman peak at 1,002 cm^{-1} of 4-azidobenzethiol-modified gold nanoparticles corresponding to C-S stretching was used as an internal standard. The presence of H_2S triggered the reduction of the above azide group to an amino group but did not affect the Raman intensity of the C-S stretching. Therefore, the response of this SERS nanoprobe to H_2S can be generated with a relative standard deviation of 4.9%. Incubation of HeLa cells with the nanoprobe produced significant SERS signals, mainly concentrated in the cytoplasm. Changes in the ratiometric SERS signal were observed when the H_2S scavenger $ZnCl_2$ and S-adenosyl-l-methionine were used to stimulate the cells. This result confirms that this nanoprobe can distinguish between H_2S-rich and H_2S-deficient cells. They suggest that this nanoprobe has the potential to image endogenous H_2S production, differentiate cells based on H_2S levels, and observe H_2S fluctuations in response to external stimuli at single-cell resolution.

Qin et al. synthesized Ag/Au alloy nanoparticle-adsorbed single-wall carbon nanotubes and modified their surface with azo-alkyne derivatives, forming a ratiometric SERS nanoprobe for sensing hypoxia in hepatic ischemia (Qin et al., 2019). The developed nanoprobe exhibited the Raman signals of 2,207 and 2,578 cm^{-1} corresponding to azo-alkyne derivatives and single-wall carbon nanotubes, respectively. In a hypoxic environment, azo-alkyne derivatives underwent a sequential reduction process through different reductase-catalyzed reaction. The reductase-mediated cleavage of the azo bond triggered the removal of the alkyne-groups from the nanoprobe, resulting in the loss of characteristic alkyne Raman bands at 2,207 cm^{-1}. Therefore, the determination of the hypoxia level in different cell lines and rat liver tissue samples (from hepatic ischemia surgery) was successfully achieved by monitoring the ratio of two Raman peak intensities (I_{2578}/I_{2207}). Of notable significance, the application of this innovative SERS nanoprobe revealed that hepatic ischemia induces the emergence of a hypoxic state within the liver. These findings demonstratesthat future developments in ratiometric SERS nanoprobes hold exciting potential. Enhanced sensitivity, multiplexing capabilities, and improved biocompatibility will likely play a pivotal role in advancing these probes for more complex and intricate applications. Integration with imaging techniques such as microscopy could enable real-time monitoring of cellular processes.

6 Ratiometric molecularly imprinted electrochemical sensors

An electrochemical sensor consists of three basic components: a receptor that is adept at binding to the sample, an analyte that initiates a reaction in the sample, and a sensor that is capable of converting the reaction into an electrical signal. One of these, the amperometric sensor, measures the current flowing between the working and reference electrodes when a consistent voltage is applied, and the magnitude of the current reflects the concentration of the desired analyte (Mistry et al., 2014). Potentiometric sensors, on the other hand, measure concentration by analyzing the potential difference between the working and reference electrodes (Bobacka et al., 2008). This difference conforms to the logarithmic relationship specified by

the Nernst equation and is the basis for ion-selective electrodes, which can be used to measure specific ions such as sodium, potassium, and chloride in solution. Impedance sensors, on the other hand, have demonstrated superior performance by using impedance spectroscopy to measure the electrical impedance of a system at different frequencies (He et al., 2020). Shifts in impedance resulting from interactions at the electrode interface or adjustments in the electrolyte's conductivity provide insights into analyte presence and concentration. In addition, photoelectrochemical sensors harness light-induced alterations in electrochemical dynamics (Shu and Tang, 2019). Typically employing semiconductor electrodes, they orchestrate the generation or augmentation of an electrical signal upon exposure to light. These sensors find applications spanning diverse domains, from driving electron transfer processes like solar cells to initiating electrochemical reactions for analyte detection. In these electrochemical sensors, the recognition elements include a variety of different molecules such as antibodies, aptamers, and nucleic acids. Molecularly imprinted polymers (MIPs) are also a recently developed recognition element (Gui et al., 2018; Sajini and Mathew, 2021; Wei et al., 2022). The template molecule is integrated into the polymer matrix during MIP synthesis, and once the template is removed, a specific recognition site is created for that molecule. This feature makes a highly selective polymer sensitive to the target molecule in complex matrices. In addition, they offer a relatively low production cost and scalable production as an alternative to antibodies. Finally, MIPs are renewable and can be reused many times, which reduces overall cost and environmental impact. However, the synthesis of MIPs requires careful selection of monomers and functional groups and is very time-consuming. In addition, the selectivity of MIPs cannot be easily changed after synthesis, limiting their versatility. In addition, MIPs degrade over time and thus lose their recognition properties, and their stability is affected by environmental conditions such as pH and temperature.

MIPs can be fabricated on electrodes by different methods, such as molecular imprinting by surface polymerization (Moreira et al., 2013), molecular imprinting by electropolymerization (Gui et al., 2018; Menon et al., 2018), molecular imprinting using MIP particles embedded in a slurry or ink (Camargo et al., 2022), and molecular imprinting by sol-gel derivatization techniques (Güney and Cebeci, 2015). *In-situ* polymerization reactions produce MIPs using template molecules, functional monomers, and crosslinkers. After removing the embedded template molecules, the MIPs build complementary size and function microcavities. Combined with ratiometric signal output modes, ratiometric MIPs are novel electrochemical sensors. A ratiometric MIP electrochemical detection incorporates an electrochemical signal-producing molecule in addition to the analyte, providing intrinsic calibration of the internal signal. The design of ratiometric signal output with dual-signal output, including on/off and on-off modes, eliminates interferences and improve stability. Ratiometric MIP electrochemical detection can be categorized into three types depending on the source of the signal. In the first type, two signals are detected at the same electrode, one from the target molecule and the other from MIPs or nanomaterials such as Cu^{2+}-linked metal-organic frameworks (Hu et al., 2020), poly (methylene blue) (Liu et al., 2022), and polythionine (Yang et al., 2019). The second type involves a signal from the target molecule and another signal from the electrolyte, such as 3,3′,5,5′-tetramethylbenzidine and $K_3[Fe(CN)_6]$ (Hu et al., 2022a). Thirdly, two electroactive molecules compete for the same binding site at the same electrode, one from the target molecule and the other from its analog as a reference signal (Yi et al., 2019). Ratiometric MIP electrochemical detection shows great potential for a broad range of applications. One of the most important applications is the monitoring of environmental contaminant levels in water and soil samples, such as fluorine-9-bisphenol (Mi et al., 2019). For drug residue monitoring, the ratiometric MIP electrochemical assay can recognize drug residues even in the presence of other interfering compounds and selectively bind to MIP, for example, for the detection of food residues such as chlorpromazine (Liu et al., 2022). In toxin detection, ratiometric MIP electrochemical assays can selectively detect toxins in food, such as mycotoxins (Zhu et al., 2023). In disease screening, ratiometric MIP electrochemical assays can screen for disease markers, such as dopamine in biological fluids (Yang et al., 2019), contributing to the early diagnosis and treatment of the disease. Lastly, pesticide residues in food, including imidacloprid residues, can be effectively detected using the ratiometric MIP electrochemical assay ratio method (Pérez-Fernández et al., 2019).

Examples of recent applications of ratiometric MIP electrochemical detection on real samples are as follows. Wu et al. developed a ratiometric MIP electrochemical sensor for detecting Sunset Yellow based on the integration of Sunset Yellow-selective MIPs with gold nanoparticle-modified indium-tin-oxide electrodes (Wu et al., 2023). In this electrochemical sensor, gold nanoparticles served as a reference signal without interfering with the signal of electroactive sunset yellow. The interesting observation is that the current signal of gold nanoparticles was also enhanced with increasing the Sunset Yellow concentration, referred to as "on-on" mode. Therefore, the MIP-modified electrode not only selectively captured Sunset Yellow from an aqueous solution but also allowed for its precise quantification with a wide detection range (10 nM–100 μM). In addition, the sensor was also demonstrated to detect sunset yellow in food samples with recoveries ranging from 94.0% to 97.0% and relative errors ranging from 5.4% to 8.3%, suggesting that it is promising for practical applications in the detection of sunset yellow.

Hu et al. modified a glassy carbon electrode with electroactive nanocomposites and employed it as a substrate for the formation of ochratoxin A (OTA)-recognised MIPs via the electro-polymerisation of 2,3-toluenediamine in cyclic voltammetry mode (Hu et al., 2022b) (Figure 1D). The nanocomposites, consisting of gold nanoparticles, poly (ionic liquid), flavin mononucleotide-decorated carbon nanotubes, and MoS_2 nanosheets, provided a reference signal for ratiometric sensing of OTA. Under the square wave voltammetry mode, a gradual increase in the OTA concentration resulted in an enhanced peak current of the OTA oxidation products together with a reduced peak current of the nanocomposites. The proposed sensor exhibited a linear response for 0.5–15 μM OTA with a LOD of 14 nM. The excellent sensitivity of the MIP-loaded electrochemical sensors allowed the determination of OTA in food and beverages.

Liu et al. developed a MIP-loaded electrochemical sensor for the sensing of cannabidiol in refined oil and human serum samples (Liu

et al., 2023). They modified the glassy carbon electrode with nitrogen and sulfur elements-doped carbon materials. This modification proficed the active sites for the electrodeposition of Fe^{3+}-coordinated aminophenanthroline and 3,4-ethylenedioxythiophene, forming a MIP film on the electrode. The formed MIP film, in addition to its ability to recognize target molecules and provide a reference signal, also exhibited enzyme-like catalytic activity for the oxidation of cannabidiol. Thus, as the concentration of cannabidiol increased, the resulting electrochemical current associated with cannabidiol also increased. However, notably, the current generated by the MIP film remained relatively constant despite the increasing concentration of cannabidiol. When 5-hydroxytryptophan was used as a template molecule instead of cannabidiol in the synthesis of MIP films, the resultant MIP-loaded electrochemical sensors provided excellent selectivity toward 5-hydroxytryptophan. More importantly, the ratiometric MIP electrochemical sensors improved measurement repeatability and mitigated the effects of variations between batches of electrodes compared to non-ratiometric ones.

Mahmoud et al. designed a Cu^{2+}-linked MIP film on the modified electrode for the ratiometric detection of glutathione in dietary supplements and human serum samples (Mahmoud et al., 2023). The modified electrode consisted of porous carbon doped with nitrogen and sulphur elements as a MIP-loaded substrate and silver nanoparticles as an internal reference signal. Moreover, the formation of a glutathione-sensitive MIP film was conducted via the electropolymerization of pyrrole-3-carboxylic acid and Cu^{2+} in the presence of glutathione. The addition of glutathione led to a decreased signal at 0.18 V due to the glutathione-mediated etching of silver nanoparticles and an increased signal at 0.83 V owing to the oxidation of the Ag(I)-glutathione complex. The proposed MIP specific gravity sensor possessed remarkable features of high measurement reproducibility, wide quantitative range, low LOD and good selectivity. The latest use cases highlight the impressive potential of ratiometric MIP electrochemical sensors. Their ability to combine selective recognition with internal reference signals improves accuracy, repeatability, and adaptability for analyzing real samples. As the field of electrochemical sensing continues to evolve, these innovations pave the way for the development of practical and effective solutions for various analytical challenges.

7 Quantitative MALDI-TOF-MS with isotopic internal standard for precise biomolecule analysis

MALDI-TOF-MS is one of the most advanced and sensitive mass spectrometry techniques, first developed by Tanaka, Karas and Hillenkamp in the 1980s (Mandal et al., 2019). MALDI is a soft ionization technique used to ionize large biological macromolecules, such as proteins, peptides, nucleic acids, carbohydrates, and lipids (Eriksson et al., 2013). Due to its gentle ionization process and reduced fragmentation, MALDI-MS can detect intact molecular ions, making it ideally suited for studying complex biomolecular structures and interactions. The MALDI matrix behaves as an energy transfer agent, efficiently transferring the laser energy to the analyte molecules, triggering their desorption and ionization. The matrix's roles include energy absorption, proton generation, and assisting in analyte ionization. The choice of the matrix depends on the analyte of interest, and commonly used matrices include sinapinic acid for intact proteins, α-cyano-4-hydroxycinnamic acid for peptides, and 2,5-dihydroxybenzoic acid for small molecules. Despite its sensitivity and analytical capabilities, MALDI-TOF MS has historically been considered a non-quantitative technique (Schlosser et al., 2005; Tholey et al., 2006). The main problem with MALDI-TOF MS is the poor reproducibility of the measurements, mainly due to the generation of strong signals in the "sweet spot" regions of the concentration of analyzed molecules (Szaéjli et al., 2008). Due to the unpredictable nature of these spots, achieving consistent detection and quantification in the absence of internal standards is challenging. These spots also hinder automated measurements, limiting the application of MALDI-TOF MS in spatially resolved imaging. The factors responsible for the formation of sweet spots are not fully understood, but the concentration and crystallinity of the matrix appear to play an important role.

To address these challenges and ensure accurate quantitative mass spectrometry results, the relative abundance of molecules in a sample is often assessed using ratiometric MALDI-TOF-MS. Internal standards, especially isotope-labeled analyte analogs, are recognized as effective methods to compensate for fluctuations in the MALDI signal due to variations in ionization efficiency and sample handling. Various stable isotope labeling methods have been developed for accurate and precise quantification of peptides in mass spectrometry-based proteomics (Figure 2). One such method is Isotope-coded affinity tags (ICAT), which employ a chemical labeling approach to attach a specific tag to the thiol group of cysteine residues in proteins (Wdowiak et al., 2021). By selectively labeling proteins or peptides containing cysteine residues with light or heavy isotopes, MALDI-TOF-MS can be used to generate peptide-related mass spectra for quantificative anaysis. Iodoacetamide is commonly used in ICATs for thiol reactivity (Gygi et al., 1999), but it has limitations and side effects, such as poor thiol selectivity and modest adduct formation rates. To address these issues, N-alkylmaleimides (NAMs) have been introduced as an alternative with faster and more selective reactivity (Hansen and Winther, 2009). Recent advances in ICATs led to the successful synthesis of isotope-coded maleimide affinity tags, which react quicker and more specifically to thiols than IAM (Wdowiak et al., 2021). The ICATs also possess a biotin residue at the other end, which facilitates the purification and enrichment of tagged peptides. Two ICAT pairs, which utilized butylene/D8-butylene linkers between maleimide and biotin residues, were found to be effective as MALDI-TOF-MS probes.

Another labeling method, Isobaric tags for relative and absolute quantitation (iTRAQ), employs a similar chemical approach by attaching a N-hydroxysuccinimide (NHS)-derived tag to the N-terminus and lysine residues of peptides (Pierce et al., 2008). The isotopic reporter group, N-methylpiperazine, generates distinct isotopic variants of the iTRAQ tag, which serve as reporter ions during mass spectrometry analysis. This enables the relative and absolute quantitation of peptides or proteins in different samples. Unlike some other labeling methods, iTRAQ tags do not interfere with peptide fragmentation during MS/MS analysis, increasing the signal intensities of native peptides and enhancing fragmentation

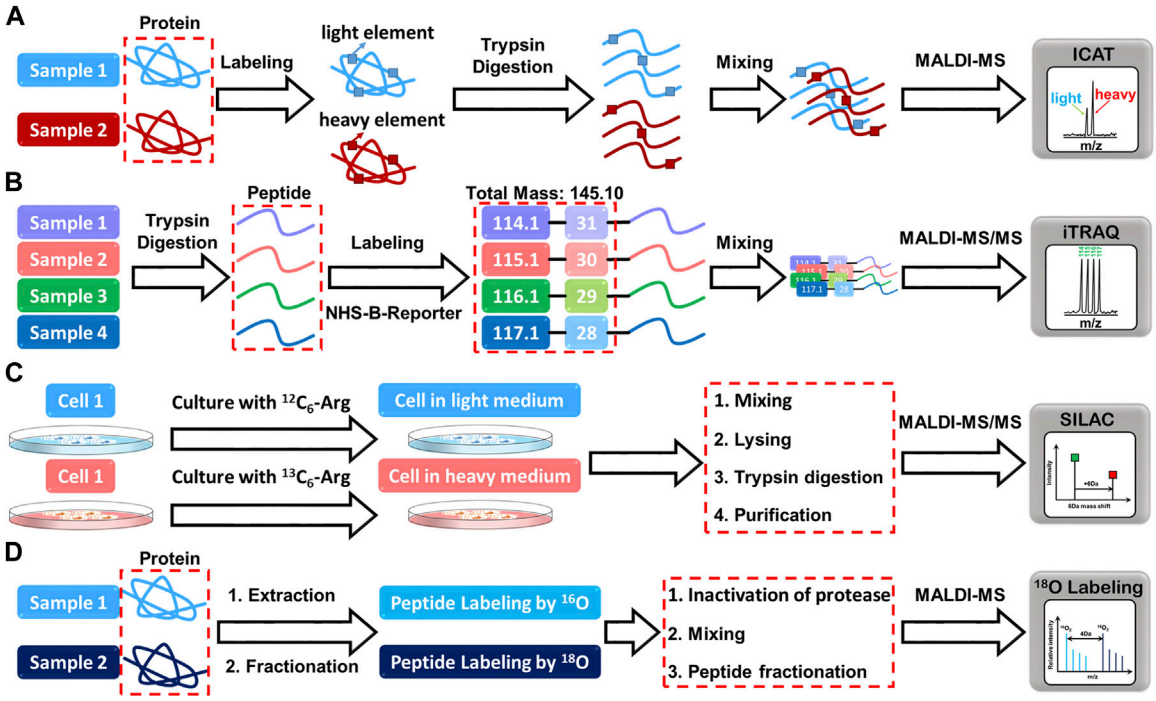

FIGURE 2
The mass spectrometry profiles resulting from the reaction of proteins with **(A)** ICAT, **(B)** iTRAQ, **(C)** SILAC, and **(D)** ^{18}O labeling reagents.

efficiency (Rauniyar and Yates, 2014). This leads to more accurate and reliable quantification of peptide signals. With iTRAQ, researchers can directly read the relative abundance of peptide signals without an internal standard by comparing the relative abundance between different experimental conditions.

Stable isotope-labeled amino acids in cell culture (SILAC) is an another powerful quantitative mass spectrometry that involves incorporating stable isotopes into proteins in living cells (Ong et al., 2002). This is achieved by substituting the normal amino acids with their isotopically marked counterparts. The cells are then cultured in media containing either light or heavy amino acid isotopes, resulting in distinct isotopic labeling of proteins. The differentially labeled proteins are then extracted, digested, and analyzed using mass spectrometry, allowing for the comparison of protein abundance between the light and heavy labeled samples. Besides, SILAC has proven to be a versatile method, particularly in pulse-chase experiments (Beller and Hummon, 2022). This technique entails metabolically incorporating stable isotopes, usually heavy versions of amino acids, into newly synthesized proteins. The heavy amino acids are introduced into cell cultures for a brief duration, facilitating selective labeling of specific proteins or protein populations. By employing pulsed SILAC labeling, researchers can track changes in protein expression over time, providing insights into the dynamics of protein regulation during various biological processes. This temporal analysis in proteomics has opened up new avenues for understanding the complexities of cellular responses. A recent study by Rocha et al. exemplifies the utility of SILAC-based proteomic analysis (Rocha et al., 2020). They investigated metabolic and proteomic changes in osteoarthritic mesenchymal stromal cells during chondrogenesis. Through SILAC, they identified altered protein abundances in metabolic pathways, providing valuable information about the molecular events underlying this cellular process. Additionally, the researchers used matrix-assisted laser desorption/ionization mass spectrometry imaging (MALDI-MSI) for metabolomic analysis, which revealed distinct profiles during the initial stages of differentiation.

Lastly, the ^{18}O labeling entails the introduction of heavy oxygen water to label peptides, causing a 2Da mass shift per oxygen atom (Stewart et al., 2001). This approach involves enzymatic cleavage of the peptide in the presence of ^{18}O-labeled water, with the addition of ^{18}O at the C-terminus, although it has the advantage of eliminating the need for commercial isotope synthesis and high labeling efficiency. However, due to the small difference of only 2 Da between labeled and unlabeled peptide pairs, the mass spectrometry signals will inevitably overlap, thus affecting the accuracy of quantification. In addition, sample complexity and small mass differences complicate data analysis and interpretation. Despite its limitations, ^{18}O labeling remains a valuable technique for specific applications. For example, it has been successfully applied to quantitative proteomics studies of post-translational modifications such as phosphorylation and glycosylation (Ye et al., 2009), providing valuable information on the dynamics of these modifications under different cellular conditions.

Despite their strengths, each quantitative mass spectrometry technique mentioned above has limitations. iTRAQ quantification, while widely used, is limited by the potential for ratio compression or distortion. This can lead to inaccuracies in quantifying changes in protein abundance, especially in complex samples with varying

protein ratios. On the other hand, ICAT is restricted explicitly to cysteine-containing proteins and peptides. While it offers targeted quantification of proteins with cysteine residues, it may not be suitable for analyzing the broader proteome. SILAC, another popular method, incorporates expensive isotope-labeled amino acids into living cells. While it provides reliable and precise quantification in specific experimental setups, the cost of these labeled amino acids may be prohibitive for some researchers. Additionally, SILAC may not be compatible with all cell types or experimental conditions. Similarly, ^{18}O labeling suffers from low labeling efficiency, potentially resulting in incomplete labeling of peptides and affecting quantification accuracy. Moreover, extensive sample purification might be necessary to remove unreacted ^{18}O-labeled water and ensure reliable results. A common challenge across these labeling techniques is the availability and cost of isotope-labeled standards. These standards are often expensive or commercially unavailable, making their use in quantitative studies impractical. Furthermore, synthesizing some isotopically labeled compounds can be extremely difficult or even impossible, limiting the scope of certain analyses. In short, isotope labeling is a powerful technique for quantitative analysis, but due to its limitations, alternative methods must be considered to gain full coverage of a given analytical problem.

8 Conclusion

This article emphasizes the ongoing need for further advancements in ratiometric detection and sensing technologies. Researchers are encouraged to concentrate on designing more precise and sensitive ratiometric fluorescent nanoprobes, enhancing naked-eye detection with improved sensitivity and reproducibility. Exploring new applications for these sensors, such as point-of-care diagnostics and real-time environmental monitoring, holds promise. Integration of ratiometric fluorescent nanoprobe with microfluidic devices could enable high-throughput analysis. The development of novel two-photon probes with enhanced two-photon absorption cross-sections and quantum yields remains a crucial pursuit. Such improvements are pivotal for achieving high sensitivity in ratiometric systems and high-resolution imaging. Notably, ratiometric two-photon fluorescent probes offer potential applications in biomedical therapies, including *in situ* real-time controlled drug release, chemotherapy, immunotherapy, photothermal therapy, photodynamic therapy, and gene therapy. Ratiometric molecularly imprinted electrochemical detection shows potential for overcoming the limitations of conventional electrochemical methods. However, ongoing investigation is necessary to enhance the stability and synthesis process of MIPs. To facilitate real-time monitoring, ratiometric electrochemical sensors can be integrated with microelectromechanical systems. On the ratiometric SERS front, the development of novel Raman-sensitive probes featuring specific recognition elements offers the exciting prospect of simultaneous imaging of distinct organelles within living cells. Furthermore, various extraction methods could be harnessed to enhance SERS sensitivity for analyte detection. Future advancements in MALDI-TOF-MS might focus on refining the accuracy and precision of isotope labeling techniques and exploring more cost-effective strategies for quantitative analysis. Combining ratiometric MALDI-TOF-MS with imaging mass spectrometry could provide spatially resolved analysis of biological samples.

Author contributions

W-BT: Writing–original draft, Writing–review and editing. W-LT: Writing–original draft, Writing–review and editing. MM and SS participated in revising the manuscripts and answering the reviewers' comments, W-BT: contributed to the preparation of the manuscripts and the collection of references for this review article. W-LT: participated in the preparation and modification of the manuscripts. These authors contributed equally to this work.

Funding

The authors declare financial support was received for the research, authorship, and/or publication of this article. We would like to thank the Ministry of Science and Technology (MOST 110-2811-M-110–512) and the NSYSU-KMU Joint Research Project (110-P003), and National Science and Technology Council (NSTC 112-2222-E-212 -002 -MY2) for financial support of this study.

Conflict of interest

The authors declare that the research was conducted in the absence of any commercial or financial relationships that could be construed as a potential conflict of interest.

The authors declared that they were an editorial board member of Frontiers, at the time of submission. This had no impact on the peer review process and the final decision

Publisher's note

References

Abbasi-Moayed, S., Golmohammadi, H., Bigdeli, A., and Hormozi-Nezhad, M. R. (2018). A rainbow ratiometric fluorescent sensor array on bacterial nanocellulose for visual discrimination of biothiols. *Analyst* 143 (14), 3415–3424. doi:10.1039/C8AN00637G

Ali, T. A., Mohamed, G. G., Azzam, E., and Abd-elaal, A. A. (2014). Thiol surfactant assembled on gold nanoparticles ion exchanger for screen-printed electrode fabrication. Potentiometric determination of Ce(III) in environmental polluted samples. *Sens. Actuators B Chem.* 191, 192–203. doi:10.1016/j.snb.2013.09.110

Beller, N. C., and Hummon, A. B. (2022). Advances in stable isotope labeling: dynamic labeling for spatial and temporal proteomic analysis. *Mol. Omics* 18 (7), 579–590. doi:10.1039/D2MO00077F

Bi, Y., Di, H., Zeng, E., Li, Q., Li, W., Yang, J., et al. (2020). Reliable quantification of pH variation in live cells using prussian blue-caged surface-enhanced Raman scattering probes. *Anal. Chem.* 92 (14), 9574–9582. doi:10.1021/acs.analchem.0c00714

Bigdeli, A., Ghasemi, F., Abbasi-Moayed, S., Shahrajabian, M., Fahimi-Kashani, N., Jafarinejad, S., et al. (2019). Ratiometric fluorescent nanoprobes for visual detection: design principles and recent advances-A review. *Anal. Chim. Acta* 1079, 30–58. doi:10.1016/j.aca.2019.06.035

Bobacka, J., Ivaska, A., and Lewenstam, A. (2008). Potentiometric ion sensors. *Chem. Rev.* 108 (2), 329–351. doi:10.1021/cr068100w

Cai, Q., Li, L. H., Yu, Y., Liu, Y., Huang, S., Chen, Y., et al. (2015). Boron nitride nanosheets as improved and reusable substrates for gold nanoparticles enabled surface enhanced Raman spectroscopy. *Phys. Chem. Chem. Phys.* 17 (12), 7761–7766. doi:10.1039/C5CP00532A

Camargo, J. R., Silva, T. A., Rivas, G. A., and Janegitz, B. C. (2022). Novel eco-friendly water-based conductive ink for the preparation of disposable screen-printed electrodes for sensing and biosensing applications. *Electrochim. Acta* 409, 139968. doi:10.1016/j.electacta.2022.139968

Chen, S., Vurusaner, B., Pena, S., Thu, C. T., Mahal, L. K., Fisher, E. A., et al. (2021). Two-photon, ratiometric, quantitative fluorescent probe reveals fluctuation of peroxynitrite regulated by arginase 1. *Anal. Chem.* 93 (29), 10090–10098. doi:10.1021/acs.analchem.1c00911

Chen, X., Wo, F., Chen, J., Tan, J., Wang, T., Liang, X., et al. (2017). Ratiometric mass spectrometry for cell identification and quantitation using intracellular "Dual-Biomarkers". *Sci. Rep.* 7 (1), 17432. doi:10.1038/s41598-017-17812-1

Chen, Y. S., Frey, W., Kim, S., Homan, K., Kruizinga, P., Sokolov, K., et al. (2010). Enhanced thermal stability of silica-coated gold nanorods for photoacoustic imaging and image-guided therapy. *Opt. Exp.* 18 (9), 8867–8878. doi:10.1364/OE.18.008867

Chuang, C. H., Chen, W. Y., Tseng, W. B., Lin, A., Lu, C. Y., and Tseng, W. L. (2022). Microwave-mediated synthesis of near-infrared-emitting silver ion-modified gold nanoclusters for ratiometric sensing of hydrosulfide in environmental water and hydrogen sulfide in live cells. *ACS Sustain. Chem. Eng.* 10 (7), 2461–2472. doi:10.1021/acssuschemeng.1c07440

Ding, H., Yuan, G., Peng, L., Zhou, L., and Lin, Q. (2020). TP-FRET-based fluorescent sensor for ratiometric detection of formaldehyde in real food samples, living cells, tissues, and zebrafish. *J. Agric. Food Chem.* 68 (11), 3670–3677. doi:10.1021/acs.jafc.9b08114

Divya, K. P., Sreejith, S., Ashokkumar, P., Yuzhan, K., Peng, Q., Maji, S. K., et al. (2014). A ratiometric fluorescent molecular probe with enhanced two-photon response upon Zn^{2+} binding for *in vitro* and *in vivo* bioimaging. *Chem. Sci.* 5 (9), 3469–3474. doi:10.1039/C4SC00736K

Eriksson, C., Masaki, N., Yao, I., Hayasaka, T., and Setou, M. (2013). MALDI imaging mass spectrometry—A mini review of methods and recent developments. *Mass Spectrom.* 2, S0022. doi:10.5702/massspectrometry.S0022

Gan, Z., Zhang, T., An, X., Tan, Q., Zhen, S., and Hu, X. (2022). A novel fluorescence-scattering ratiometric sensor based on Fe-NC nanozyme with robust oxidase-like activity. *Sens. Actuators B Chem.* 368, 132181. doi:10.1016/j.snb.2022.132181

García-Hernández, L. A., Martínez-Martínez, E., Pazos-Solís, D., Aguado-Preciado, J., Dutt, A., Chávez-Ramírez, A. U., et al. (2023). Optical detection of cancer cells using lab-on-a-chip. *Biosensors* 13 (4), 439. doi:10.3390/bios13040439

Ge, L., Liu, Z., and Tian, Y. (2020). A novel two-photon ratiometric fluorescent probe for imaging and sensing of BACE1 in different regions of AD mouse brain. *Chem. Sci.* 11 (8), 2215–2224. doi:10.1039/C9SC05256A

Gehan, H. l. n., Fillaud, L., Felidj, N., Aubard, J., Lang, P., Chehimi, M. M., et al. (2010). A general approach combining diazonium salts and click chemistries for gold surface functionalization by nanoparticle assemblies. *Langmuir* 26 (6), 3975–3980. doi:10.1021/la9033436

Geng, Z. Q., Xu, D., Song, Y., Wang, W. P., Li, Y. P., Han, C. Q., et al. (2021). Sensitive label-free detection of bilirubin in blood using boron nitride-modified nanorod arrays as SERS substrates. *Sens. Actuators B Chem.* 334, 129634. doi:10.1016/j.snb.2021.129634

Grzybowski, A., and Pietrzak, K. (2013). Maria goeppert-mayer (1906–1972): two-photon effect on dermatology. *Clin. Dermatol.* 31 (2), 221–225. doi:10.1016/j.clindermatol.2012.06.002

Gui, R., Jin, H., Guo, H., and Wang, Z. (2018). Recent advances and future prospects in molecularly imprinted polymers-based electrochemical biosensors. *Biosens. Bioelectron.* 100, 56–70. doi:10.1016/j.bios.2017.08.058

Güney, S., and Cebeci, F. C. (2015). Selective electrochemical sensor for theophylline based on an electrode modified with imprinted sol–gel film immobilized on carbon nanoparticle layer. *Sensors Actuators B Chem.* 208, 307–314. doi:10.1016/j.snb.2014.10.056

Gygi, S. P., Rist, B., Gerber, S. A., Turecek, F., Gelb, M. H., and Aebersold, R. (1999). Quantitative analysis of complex protein mixtures using isotope-coded affinity tags. *Nat. Biotechnol.* 17 (10), 994–999. doi:10.1038/13690

Han, B., Chen, L., Jin, S., Guo, S., Park, J., Yoo, H. S., et al. (2021). Modulating mechanism of the LSPR and SERS in Ag/ITO film: carrier density effect. *J. Phys. Chem. Lett.* 12 (31), 7612–7618. doi:10.1021/acs.jpclett.1c01727

Han, L., Meng, C., Zhang, D., Liu, H., and Sun, B. (2022). Fabrication of a fluorescence probe via molecularly imprinted polymers on carbazole-based covalent organic frameworks for optosensing of ethyl carbamate in fermented alcoholic beverages. *Anal. Chim. Acta* 1192, 339381. doi:10.1016/j.aca.2021.339381

Hansen, R. E., and Winther, J. R. (2009). An introduction to methods for analyzing thiols and disulfides: reactions, reagents, and practical considerations. *Anal. Biochem.* 394 (2), 147–158. doi:10.1016/j.ab.2009.07.051

Hao, F., Nehl, C. L., Hafner, J. H., and Nordlander, P. (2007). Plasmon resonances of a gold nanostar. *Nano Lett.* 7 (3), 729–732. doi:10.1021/nl062969c

He, S., Yuan, Y., Nag, A., Feng, S., Afsarimanesh, N., Han, T., et al. (2020). A review on the use of impedimetric sensors for the inspection of food quality. *Int. J. Environ. Res. Public Health.* 17 (14), 5220. doi:10.3390/ijerph17145220

HeeáLee, M., SeungáKim, J., and Sessler, J. L. (2015). Small molecule-based ratiometric fluorescence probes for cations, anions, and biomolecules. *Chem. Soc. Rev.* 44 (13), 4185–4191. doi:10.1039/c4cs00280f

Hu, R., Zhang, X., Chi, K. N., Yang, T., and Yang, Y. H. (2020). Bifunctional MOFs-based ratiometric electrochemical sensor for multiplex heavy metal ions. *ACS Appl. Mat. Interfaces* 12 (27), 30770–30778. doi:10.1021/acsami.0c06291

Hu, X., Tang, Y., Xia, Y., Liu, Y., Zhao, F., and Zeng, B. (2022a). Antifouling ionic liquid doped molecularly imprinted polymer-based ratiometric electrochemical sensor for highly stable and selective detection of zearalenone. *Anal. Chim. Acta* 1210, 339884. doi:10.1016/j.aca.2022.339884

Hu, X., Xia, Y., Liu, Y., Chen, Y., and Zeng, B. (2022b). An effective ratiometric electrochemical sensor for highly selective and reproducible detection of ochratoxin A: use of magnetic field improved molecularly imprinted polymer. *Sens. Actuators B Chem.* 359, 131582. doi:10.1016/j.snb.2022.131582

Huang, X., Song, J., Yung, B. C., Huang, X., Xiong, Y., and Chen, X. (2018). Ratiometric optical nanoprobes enable accurate molecular detection and imaging. *Chem. Soc. Rev.* 47 (8), 2873–2920. doi:10.1039/C7CS00612H

Ishida, T., Yanaga, Y., Yamada, S., and Takahashi, Y. (2021). A versatile method for surface functionalization and hydrophobization of gold nanoparticles. *Appl. Surf. Sci.* 546, 148932. doi:10.1016/j.apsusc.2021.148932

Jin, H., Jiang, X., Sun, Z., and Gui, R. (2021). Phosphorescence-based ratiometric probes: design, preparation and applications in sensing, imaging and biomedicine therapy. *Coord. Chem. Rev.* 431, 213694. doi:10.1016/j.ccr.2020.213694

Jun, Y. W., Wang, T., Hwang, S., Kim, D., Ma, D., Kim, K. H., et al. (2018). A ratiometric two-photon fluorescent probe for tracking lysosomal ATP: direct in cellulo observation of lysosomal membrane fusion processes. *Angew. Chem. Int. Ed. Engl.* 130 (32), 10299–10304. doi:10.1002/ange.201804743

Kamal, S., and Yang, T. C. K. (2022). Silver enriched silver phosphate microcubes as an efficient recyclable SERS substrate for the detection of heavy metal ions. *J. Colloid Interface Sci.* 605, 173–181. doi:10.1016/j.jcis.2021.07.084

Kanehara, M., Koike, H., Yoshinaga, T., and Teranishi, T. (2009). Indium tin oxide nanoparticles with compositionally tunable surface plasmon resonance frequencies in the near-IR region. *J. A. Chem. Soc.* 131 (49), 17736–17737. doi:10.1021/ja9064415

Kang, H., Buchman, J. T., Rodriguez, R. S., Ring, H. L., He, J., Bantz, K. C., et al. (2018). Stabilization of silver and gold nanoparticles: preservation and improvement of plasmonic functionalities. *Chem. Rev.* 119 (1), 664–699. doi:10.1021/acs.chemrev.8b00341

Ke, C. Y., Wu, Y. T., and Tseng, W. L. (2015). Fluorescein-5-isothiocyanate-conjugated protein-directed synthesis of gold nanoclusters for fluorescent ratiometric sensing of an enzyme–substrate system. *Biosens. Bioelectron.* 69, 46–53. doi:10.1016/j.bios.2015.02.002

Kim, H. J., Heo, C. H., and Kim, H. M. (2013). Benzimidazole-based ratiometric two-photon fluorescent probes for acidic pH in live cells and tissues. *J. Am. Chem. Soc.* 135 (47), 17969–17977. doi:10.1021/ja409971k

Kumar, A. S. K., Tseng, W. B., Wu, M. J., Huang, Y. Y., and Tseng, W. L. (2020). L-cystine-linked BODIPY-adsorbed monolayer MoS_2 quantum dots for ratiometric fluorescent sensing of biothiols based on the inner filter effect. *Anal. Chim. Acta* 1113, 43–51. doi:10.1016/j.aca.2020.04.006

Kumar, S., Verma, T., Mukherjee, R., Ariese, F., Somasundaram, K., and Umapathy, S. (2016). Raman and infra-red microspectroscopy: towards quantitative evaluation for clinical research by ratiometric analysis. *Chem. Soc. Rev.* 45 (7), 1879–1900. doi:10.1039/c5cs00540j

Kumaravel, S., Wu, S. H., Chen, G. Z., Huang, S. T., Lin, C. M., Lee, Y. C., et al. (2021). Development of ratiometric electrochemical molecular switches to assay endogenous formaldehyde in live cells, whole blood and creatinine in saliva. *Biosens. Bioelectron.* 171, 112720. doi:10.1016/j.bios.2020.112720

Langer, J., Jimenez de Aberasturi, D., Aizpurua, J., Alvarez-Puebla, R. A., Auguié, B., Baumberg, J. J., et al. (2020). Present and future of surface-enhanced Raman scattering. *ACS Nano* 14 (1), 28–117. doi:10.1021/acsnano.9b04224

Li, L., Yang, L., Lin, D., Xu, S., Mei, C., Yu, S., et al. (2023). Hydrogen-bond induced enhanced emission ratiometric fluorescent handy needle for visualization assay of amoxicillin by smartphone sensing platform. *J. Hazard. Mat.* 444, 130403. doi:10.1016/j.jhazmat.2022.130403

Li, Z. Y., Wu, Y. T., and Tseng, W. L. (2015). UV-light-induced improvement of fluorescence quantum yield of DNA-templated gold nanoclusters: application to ratiometric fluorescent sensing of nucleic acids. *ACS Appl. Mat. Interfaces* 7 (42), 23708–23716. doi:10.1021/acsami.5b07766

Liang, M., Liu, Z., Zhang, Z., Mei, Y., and Tian, Y. (2022). A two-photon ratiometric fluorescent probe for real-time imaging and quantification of NO in neural stem cells during activation regulation. *Chem. Sci.* 13 (15), 4303–4312. doi:10.1039/D2SC00326K

Lim, C. S., Masanta, G., Kim, H. J., Han, J. H., Kim, H. M., and Cho, B. R. (2011). Ratiometric detection of mitochondrial thiols with a two-photon fluorescent probe. *J. Am. Chem. Soc.* 133 (29), 11132–11135. doi:10.1021/ja205081s

Lin, S., Cheng, Z., Li, Q., Wang, R., and Yu, F. (2021). Toward sensitive and reliable surface-enhanced Raman scattering imaging: from rational design to biomedical applications. *ACS Sens.* 6 (11), 3912–3932. doi:10.1021/acssensors.1c01858

Liu, J., Jiang, X., Zhang, R., Zhang, Y., Wu, L., Lu, W., et al. (2019). MXene-enabled electrochemical microfluidic biosensor: applications toward multicomponent continuous monitoring in whole blood. *Adv. Funct. Mat.* 29 (6), 1807326. doi:10.1002/adfm.201807326

Liu, R., Jiang, L., Yu, Z., Jing, X., Liang, X., Wang, D., et al. (2021). MXene ($Ti_3C_2T_x$)-Ag nanocomplex as efficient and quantitative SERS biosensor platform by *in-situ* PDDA electrostatic self-assembly synthesis strategy. *Sens. Actuators B Chem.* 333, 129581. doi:10.1016/j.snb.2021.129581

Liu, Y., Hu, X., Xia, Y., Zhao, F., and Zeng, B. (2022). A novel ratiometric electrochemical sensor based on dual-monomer molecularly imprinted polymer and Pt/Co_3O_4 for sensitive detection of chlorpromazine hydrochloride. *Anal. Chim. Acta* 1190, 339245. doi:10.1016/j.aca.2021.339245

Liu, Y., Tang, Y., Cao, J., Zhao, F., and Zeng, B. (2023). A ratiometric electrochemical sensing platform based on multifunctional molecularly imprinted polymer with catalytic activity for the detection of psychoactive substances. *Biosens. Bioelectron.* 220, 114929. doi:10.1016/j.bios.2022.114929

Luo, F., Zhu, M., Liu, Y., Sun, J., and Gao, F. (2023). Ratiometric and visual determination of copper ions with fluorescent nanohybrids of semiconducting polymer nanoparticles and carbon dots. *Spectrochim. Acta A Mol. Biomol. Spectrosc.* 295, 122574. doi:10.1016/j.saa.2023.122574

Luo, W., Jiang, H., Tang, X., and Liu, W. (2017). A reversible ratiometric two-photon lysosome-targeted probe for real-time monitoring of pH changes in living cells. *J. Mat. Chem. B* 5 (24), 4768–4773. doi:10.1039/C7TB00838D

Madhu, M., and Tseng, W. L. (2021). Recent developments in sensing of oversulfated chondroitin sulfate in heparin. A review. *J. Food Drug Anal.* 29 (4), 533–543. doi:10.38212/2224-6614.3379

Mahmoud, A. M., Mahnashi, M. H., and El-Wekil, M. M. (2023). Ratiometric sensing interface for glutathione determination based on electro-polymerized copper-coordinated molecularly imprinted layer supported on silver/porous carbon hybrid. *Anal. Chim. Acta* 1272 (1), 341498. doi:10.1016/j.aca.2023.341498

Mandal, A., Singha, M., Addy, P. S., and Basak, A. (2019). Laser desorption ionization mass spectrometry: recent progress in matrix-free and label-assisted techniques. *Mass Spectrom. Rev.* 38 (1), 3–21. doi:10.1002/mas.21545

Masoumi, Z., Tayebi, M., Kolaei, M., and Lee, B. K. (2022). Efficient and stable core-shell α–Fe_2O_3/WS_2/WO_x photoanode for oxygen evolution reaction to enhance photoelectrochemical water splitting. *Appl. Catal. B Environ.* 313, 121447. doi:10.1016/j.apcatb.2022.121447

Menon, S., Jesny, S., and Kumar, K. G. (2018). A voltammetric sensor for acetaminophen based on electropolymerized-molecularly imprinted poly (*o*-aminophenol) modified gold electrode. *Talanta* 179, 668–675. doi:10.1016/j.talanta.2017.11.074

Mi, P., Zhang, Q. P., Zhang, S. H., Wang, C., Zhang, S. Z., Fang, Y. C., et al. (2019). The effects of fluorene-9-bisphenol on female zebrafish (*Danio rerio*) reproductive and exploratory behaviors. *Chemosphere* 228, 398–411. doi:10.1016/j.chemosphere.2019.04.170

Miao, J., Ji, W., Yu, J., Cheng, J., Huang, Y., Arabi, M., et al. (2023). A triple-emission ratiometric fluorescence sensor based on carbon dots-Au nanoclusters nanocomposite for detection of tetracycline. *Sens. Actuators B Chem.* 384, 133636. doi:10.1016/j.snb.2023.133636

Mistry, K. K., Layek, K., Mahapatra, A., RoyChaudhuri, C., and Saha, H. (2014). A review on amperometric-type immunosensors based on screen-printed electrodes. *Analyst* 139 (10), 2289–2311. doi:10.1039/c3an02050a

Moreira, F. T., Dutra, R. A., Noronha, J. P., and Sales, M. G. F. (2013). Electrochemical biosensor based on biomimetic material for myoglobin detection. *Electrochim. Acta* 107, 481–487. doi:10.1016/j.electacta.2013.06.061

Njoko, N., Louzada, M., Britton, J., Khene, S., Nyokong, T., and Mashazi, P. (2020). Bioelectrocatalysis and surface analysis of gold coated with nickel oxide/hydroxide and glucose oxidase towards detection of glucose. *Colloids Surf. B* 190, 110981. doi:10.1016/j.colsurfb.2020.110981

Ong, S. E., Blagoev, B., Kratchmarova, I., Kristensen, D. B., Steen, H., Pandey, A., et al. (2002). Stable isotope labeling by amino acids in cell culture, SILAC, as a simple and accurate approach to expression proteomics. *Mol. Cell. Proteom.* 1 (5), 376–386. doi:10.1074/mcp.M200025-MCP200

Park, S. J., Kim, Y. J., Kang, J. S., Kim, I. Y., Choi, K. S., and Kim, H. M. (2018). Carboxylesterase-2-selective two-photon ratiometric probe reveals decreased carboxylesterase-2 activity in breast cancer cells. *Anal. Chem.* 90 (15), 9465–9471. doi:10.1021/acs.analchem.8b02101

Parrilla, M., Cánovas, R., and Andrade, F. J. (2017). Paper-based enzymatic electrode with enhanced potentiometric response for monitoring glucose in biological fluids. *Biosens. Bioelectron.* 90, 110–116. doi:10.1016/j.bios.2016.11.034

Peng, R., Si, Y., Deng, T., Zheng, J., Li, J., Yang, R., et al. (2016). A novel SERS nanoprobe for the ratiometric imaging of hydrogen peroxide in living cells. *Chem. Commun.* 52 (55), 8553–8556. doi:10.1039/C6CC03412H

Peng, Y., Lin, C., Long, L., Masaki, T., Tang, M., Yang, L., et al. (2021). Charge-transfer resonance and electromagnetic enhancement synergistically enabling MXenes with excellent SERS sensitivity for SARS-CoV-2 S protein detection. *Nano-Micro Lett.* 13, 52. doi:10.1007/s40820-020-00565-4

Pérez-Fernández, B., Mercader, J. V., Checa-Orrego, B. I., de la Escosura-Muñiz, A., and Costa-García, A. (2019). A monoclonal antibody-based immunosensor for the electrochemical detection of imidacloprid pesticide. *Analyst* 144 (9), 2936–2941. doi:10.1039/C9AN00176J

Pierce, A., Unwin, R. D., Evans, C. A., Griffiths, S., Carney, L., Zhang, L., et al. (2008). Eight-channel iTRAQ enables comparison of the activity of six leukemogenic tyrosine kinases. *Mol. Cell. Proteom.* 7 (5), 853–863. doi:10.1074/mcp.M700251-MCP200

Qin, X., Si, Y., Wang, D., Wu, Z., Li, J., and Yin, Y. (2019). Nanoconjugates of Ag/Au/carbon nanotube for alkyne-meditated ratiometric SERS imaging of hypoxia in hepatic ischemia. *Anal. Chem.* 91 (7), 4529–4536. doi:10.1021/acs.analchem.8b05487

Qu, J., Zhang, X., Liu, Y., Xie, Y., Cai, J., Zha, G., et al. (2020). N, P-co-doped carbon dots as a dual-mode colorimetric/ratiometric fluorescent sensor for formaldehyde and cell imaging via an aminal reaction-induced aggregation process. *Microchim. Acta* 187, 355. doi:10.1007/s00604-020-04337-0

Quan, Y., Su, R., Yang, S., Chen, L., Wei, M., Liu, H., et al. (2021). *In-situ* surface-enhanced Raman scattering based on MTi_{20} nanoflowers: monitoring and degradation of contaminants. *J. Hazard. Mat.* 412 (15), 125209. doi:10.1016/j.jhazmat.2021.125209

Rajput, V., Gupta, R. K., and Prakash, J. (2022). Engineering metal oxide semiconductor nanostructures for enhanced charge transfer: fundamentals and emerging SERS applications. *J. Mat. Chem. C* 10 (1), 73–95. doi:10.1039/D1TC04886D

Rauniyar, N., and Yates, J. R., III (2014). Isobaric labeling-based relative quantification in shotgun proteomics. *J. Proteome Res.* 13 (12), 5293–5309. doi:10.1021/pr500880b

Ren, T. B., Wen, S. Y., Wang, L., Lu, P., Xiong, B., Yuan, L., et al. (2020). Engineering a reversible fluorescent probe for real-time live-cell imaging and quantification of mitochondrial ATP. *Anal. Chem.* 92 (6), 4681–4688. doi:10.1021/acs.analchem.0c00506

Reo, Y. J., Jun, Y. W., Sarkar, S., Dai, M., and Ahn, K. H. (2019). Ratiometric imaging of γ-glutamyl transpeptidase unperturbed by pH, polarity, and viscosity changes: A benzocoumarin-based two-photon fluorescent probe. *Anal. Chem.* 91 (21), 14101–14108. doi:10.1021/acs.analchem.9b03942

Rocha, B., Cillero-Pastor, B., Eijkel, G., Calamia, V., Fernandez-Puente, P., Paine, M. R., et al. (2020). Integrative metabolic pathway analysis reveals novel therapeutic targets in osteoarthritis. *Mol. Cell. Proteom.* 19 (4), 574–588. doi:10.1074/mcp.RA119.001821

Sajini, T., and Mathew, B. (2021). A brief overview of molecularly imprinted polymers: highlighting computational design, nano and photo-responsive imprinting. *Talanta Open* 4, 100072. doi:10.1016/j.talo.2021.100072

Santhoshkumar, S., and Murugan, E. (2021a). Rationally designed SERS AgNPs/GO/g-CN nanohybrids to detect methylene blue and Hg^{2+} ions in aqueous solution. *Appl. Surf. Sci.* 553, 149544. doi:10.1016/j.apsusc.2021.149544

Santhoshkumar, S., and Murugan, E. (2021b). Size controlled silver nanoparticles on β-cyclodextrin/graphitic carbon nitride: an excellent nanohybrid material for SERS and catalytic applications. *Dalton. Trans.* 50 (48), 17988–18000. doi:10.1039/d1dt02809j

Santhoshkumar, S., Wei, W. S., Madhu, M., Tseng, W. B., and Tseng, W. L. (2023). Chemically engineered sulfur vacancies on few-layered molybdenum disulfide nanosheets for remarkable surface-enhanced Raman scattering activity. *J. Phys. Chem. C* 127 (18), 8803–8813. doi:10.1021/acs.jpcc.3c01044

Schlosser, G., Pocsfalvi, G., Huszár, E., Malorni, A., and Hudecz, F. (2005). MALDI-TOF mass spectrometry of a combinatorial peptide library: effect of matrix composition on signal suppression. *J. Mass Spectrom.* 40 (12), 1590–1594. doi:10.1002/jms.937

Šebela, M. (2023). The use of matrix-assisted laser desorption/ionization mass spectrometry in enzyme activity assays and its position in the context of other available methods. *Mass Spectrom. Rev.* 42 (3), 1008–1031. doi:10.1002/mas.21733

Shahdost-Fard, F., Fahimi-Kashani, N., and Hormozi-Nezhad, M. (2021). A ratiometric fluorescence nanoprobe using CdTe QDs for fast detection of carbaryl insecticide in apple. *Talanta* 221, 121467. doi:10.1016/j.talanta.2020.121467

Shan, X., Feng, Q., Yang, J., and Wang, P. (2022). Dual-mode detection and efficient annihilation of pathogenic bacteria based on the construction of a ratiometric

electrochemiluminescent/electrochemical sensor. *Sens. Actuators B Chem.* 372, 132633. doi:10.1016/j.snb.2022.132633

Shen, Y. M., Gao, M. Y., Chen, X., Shen, A. G., and Hu, J. M. (2021). Fine synthesis of Prussian-blue analogue coated gold nanoparticles (Au@ PBA NPs) for sorting specific cancer cell subtypes. *Spectrochim. Acta A Mol. Biomol. Spectrosc.* 252, 119566. doi:10.1016/j.saa.2021.119566

Shu, J., and Tang, D. (2019). Recent advances in photoelectrochemical sensing: from engineered photoactive materials to sensing devices and detection modes. *Anal. Chem.* 92 (1), 363–377. doi:10.1021/acs.analchem.9b04199

Si, Y., Bai, Y., Qin, X., Li, J., Zhong, W., Xiao, Z., et al. (2018). Alkyne–DNA-functionalized alloyed Au/Ag nanospheres for ratiometric surface-enhanced Raman scattering imaging assay of endonuclease activity in live cells. *Anal. Chem.* 90 (6), 3898–3905. doi:10.1021/acs.analchem.7b04735

Spring, S. A., Goggins, S., and Frost, C. G. (2021). Ratiometric electrochemistry: improving the robustness, reproducibility and reliability of biosensors. *Molecules* 26 (8), 2130. doi:10.3390/molecules26082130

Stewart, I. I., Thomson, T., and Figeys, D. (2001). ^{18}O labeling: A tool for proteomics. *Rapid Commun. Mass Spectrom.* 15 (24), 2456–2465. doi:10.1002/rcm.525

Sun, J., Mei, H., Wang, S., and Gao, F. (2016). Two-photon semiconducting polymer dots with dual-emission for ratiometric fluorescent sensing and bioimaging of tyrosinase activity. *Anal. Chem.* 88 (14), 7372–7377. doi:10.1021/acs.analchem.6b01929

Szaejli, E., Feheer, T., and Medzihradszky, K. F. (2008). Investigating the quantitative nature of MALDI-TOF MS. *Mol. Cell. Proteom.* 7 (12), 2410–2418. doi:10.1074/mcp.M800108-MCP200

Tackman, E. C., Trujillo, M. J., Lockwood, T. L. E., Merga, G., Lieberman, M., and Camden, J. P. (2018). Identification of substandard and falsified antimalarial pharmaceuticals chloroquine, doxycycline, and primaquine using surface-enhanced Raman scattering. *Anal. Metthods* 10 (38), 4718–4722. doi:10.1039/C8AY01413B

Tholey, A., Zabet-Moghaddam, M., and Heinzle, E. (2006). Quantification of peptides for the monitoring of protease-catalyzed reactions by matrix-assisted laser desorption/ionization mass spectrometry using ionic liquid matrixes. *Anal. Chem.* 78 (1), 291–297. doi:10.1021/ac0514319

Tseng, W. B., Rau, J. Y., Chiou, H. C., and Tseng, W. L. (2022). Synthesis of gold nanoclusters-loaded lysozyme nanoparticles for ratiometric fluorescent detection of cyanide in tap water, cyanogenic glycoside-containing plants, and soils. *Environ. Res.* 207, 112144. doi:10.1016/j.envres.2021.112144

Valverde-Pozo, J., Paredes, J. M., Widmann, T. J., Griñan-Lison, C., Ceccarelli, G., Gioiello, A., et al. (2023). Ratiometric two-photon near-infrared probe to detect DPP IV in human plasma, living cells, human tissues, and whole organisms using zebrafish. *ACS Sens.* 8 (3), 1064–1075. doi:10.1021/acssensors.2c02025

Vargas, E., Teymourian, H., Tehrani, F., Eksin, E., Sánchez-Tirado, E., Warren, P., et al. (2019). Enzymatic/immunoassay dual-biomarker sensing chip: towards decentralized insulin/glucose detection. *Angew. Chem. Int. Ed.* 58 (19), 6376–6379. doi:10.1002/anie.201902664

Vyas, G., Bhatt, S., and Paul, P. (2019). Synthesis of calixarene-capped silver nanoparticles for colorimetric and amperometric detection of mercury (Hg^{II}, Hg^{0}). *ACS Omega* 4 (2), 3860–3870. doi:10.1021/acsomega.8b03299

Wang, H., He, Z., Yang, Y., Zhang, J., Zhang, W., Zhang, W., et al. (2019a). Ratiometric fluorescence imaging of Golgi H_2O_2 reveals a correlation between Golgi oxidative stress and hypertension. *Chem. Sci.* 10 (47), 10876–10880. doi:10.1039/C9SC04384E

Wang, J., Jiang, C., Jin, J., Huang, L., Yu, W., Su, B., et al. (2021a). Ratiometric fluorescent lateral flow immunoassay for point-of-care testing of acute myocardial infarction. *Angew. Chem. Int. Ed.* 133 (23), 13152–13159. doi:10.1002/ange.202103458

Wang, P., Zhou, F., Zhang, C., Yin, S. Y., Teng, L., Chen, L., et al. (2018). Ultrathin two-dimensional covalent organic framework nanoprobe for interference-resistant two-photon fluorescence bioimaging. *Chem. Sci.* 9 (44), 8402–8408. doi:10.1039/C8SC03393E

Wang, X., Shi, W., Jin, Z., Huang, W., Lin, J., Ma, G., et al. (2017). Remarkable SERS activity observed from amorphous ZnO nanocages. *Angew. Chem. Int. Ed.* 129 (33), 9983–9987. doi:10.1002/ange.201705187

Wang, X., Shi, W., Wang, S., Zhao, H., Lin, J., Yang, Z., et al. (2019b). Two-dimensional amorphous TiO_2 nanosheets enabling high-efficiency photoinduced charge transfer for excellent SERS activity. *J. Am. Chem. Soc.* 141 (14), 5856–5862. doi:10.1021/jacs.9b00029

Wang, Y., Zhang, M., Ma, H., Su, H., Li, A., Ruan, W., et al. (2021b). Surface plasmon resonance from Gallium-doped Zinc oxide nanoparticles and their electromagnetic enhancement contribution to surface-enhanced Raman scattering. *ACS Appl. Mat. Interfaces* 13 (29), 35038–35045. doi:10.1021/acsami.1c05804

Wdowiak, A. P., Duong, M. N., Joyce, R. D., Boyatzis, A. E., Walkey, M. C., Nealon, G. L., et al. (2021). Isotope-coded maleimide affinity tags for proteomics applications. *Bioconjug. Chem.* 32 (8), 1652–1666. doi:10.1021/acs.bioconjchem.1c00206

Wei, J., Liu, C., Wu, T., Zeng, W., Hu, B., Zhou, S., et al. (2022). A review of current status of ratiometric molecularly imprinted electrochemical sensors: from design to applications. *Anal. Chim. Acta* 1230, 340273. doi:10.1016/j.aca.2022.340273

Wu, L., Wu, T., Zeng, W., Zhou, S., Zhang, W., and Ma, J. (2023). A new ratiometric molecularly imprinted electrochemical sensor for the detection of Sunset Yellow based on gold nanoparticles. *Food Chem.* 413, 135600. doi:10.1016/j.foodchem.2023.135600

Xianyu, Y., Lin, Y., Chen, Q., Belessiotis-Richards, A., Stevens, M. M., and Thomas, M. R. (2021). Iodide-mediated rapid and sensitive surface etching of gold nanostars for biosensing. *Angew. Chem. Int. Ed.* 60 (18), 9891–9896. doi:10.1002/anie.202017317

Xie, C., Zhou, Y., Luo, K., Yang, Q., Tan, L., and Zhou, L. (2022a). Activated two-photon near-infrared ratiometric fluorescent nanoprobe for $ONOO^-$ detection and early diagnosis and assessment of liver injury. *Anal. Chem.* 94 (44), 15518–15524. doi:10.1021/acs.analchem.2c04032

Xie, L., Zeng, H., Zhu, J., Zhang, Z., Sun, H. B., Xia, W., et al. (2022b). State of the art in flexible SERS sensors toward label-free and onsite detection:from design to applications. *Nano Res.* 15 (5), 4374–4394. doi:10.1007/s12274-021-4017-4

Yang, J., Hu, Y., and Li, Y. (2019). Molecularly imprinted polymer-decorated signal on-off ratiometric electrochemical sensor for selective and robust dopamine detection. *Biosens. Bioelectron.* 135, 224–230. doi:10.1016/j.bios.2019.03.054

Ye, X., Luke, B., Andresson, T., and Blonder, J. (2009). 18O stable isotope labeling in MS-based proteomics. *Brief. Funct. genomics proteomics* 8 (2), 136–144. doi:10.1093/bfgp/eln055

Yi, Y., Zhang, D., Ma, Y., Wu, X., and Zhu, G. (2019). Dual-signal electrochemical enantiospecific recognition system via competitive supramolecular host–guest interactions: the case of phenylalanine. *Anal. Chem.* 91 (4), 2908–2915. doi:10.1021/acs.analchem.8b05047

Yue, S., Qiao, Z., Wang, X., and Bi, S. (2022). Enzyme-free catalyzed self-assembly of three-dimensional hyperbranched DNA structures for *in situ* SERS imaging and molecular logic operations. *Chem. Eng. J.* 446, 136838. doi:10.1016/j.cej.2022.136838

Zhai, S., Hu, W., Wang, W., Chai, L., An, Q., Li, C., et al. (2022). Tracking autophagy process with a through bond energy transfer-based ratiometric two-photon viscosity probe. *Biosens. Bioelectron.* 213, 114484. doi:10.1016/j.bios.2022.114484

Zhang, D., Wang, D., Xu, Z., Zhang, X., Yang, Y., Guo, J., et al. (2021). Diversiform sensors and sensing systems driven by triboelectric and piezoelectric nanogenerators. *Coord. Chem. Rev.* 427, 213597. doi:10.1016/j.ccr.2020.213597

Zhao, L., Li, T., Xu, X., Xu, Y., Li, D., Song, W., et al. (2023). Polyhedral Au nanoparticle/MoO_x heterojunction-enhanced ultrasensitive dual-mode biosensor for miRNA detection combined with a nonenzymatic cascade DNA amplification circuit. *Anal. Chem.* 95 (24), 9271–9279. doi:10.1021/acs.analchem.3c01062

Zhao, M., Liu, D., Zhou, L., Wu, B., Tian, X., Zhang, Q., et al. (2018). Two water-soluble two-photon fluorescence probes for ratiometric imaging endogenous SO_2 derivatives in mitochondria. *Sens. Actuators B Chem.* 255, 1228–1237. doi:10.1016/j.snb.2017.08.053

Zhao, X., Zhao, S., Song, Z. L., Zhang, X., Zhang, S., Song, W., et al. (2021). Alkyne functionalized graphene-isolated-Au-nanocrystal for the ratiometric SERS sensing of alkaline phosphatase with acetonitrile solvent as an internal standard. *Sens. Actuators B Chem.* 331, 129373. doi:10.1016/j.snb.2020.129373

Zhao, Y., Zhang, Q., Ma, L., Song, P., and Xia, L. (2020). A P/N type silicon semiconductor loaded with silver nanoparticles used as a SERS substrate to selectively drive the coupling reaction induced by surface plasmons. *Nanoscale. Adv.* 2 (8), 3460–3466. doi:10.1039/D0NA00350F

Zhong, Q., Zhang, R., Yang, B., Tian, T., Zhang, K., and Liu, B. (2022). A rational designed bioorthogonal surface-enhanced Raman scattering nanoprobe for quantitatively visualizing endogenous hydrogen sulfide in single living cells. *ACS Sens.* 7 (3), 893–899. doi:10.1021/acssensors.1c02711

Zhu, C., Wang, X., Yang, Y., Chen, L., and Yu, D. (2023). Research progress on ratiometric electrochemical sensing of mycotoxins. *J. ElectroAnal. Chem.* 929 (15), 117115. doi:10.1016/j.jelechem.2022.117115

Zhu, D., Liu, B., and Wei, G. (2021). Two-dimensional material-based colorimetric biosensors: A review. *Biosensors* 11 (8), 259. doi:10.3390/bios11080259

Zhu, X., Han, L., Liu, H., and Sun, B. (2022). A smartphone-based ratiometric fluorescent sensing system for on-site detection of pyrethroids by using blue-green dual-emission carbon dots. *Food Chem.* 379, 132154. doi:10.1016/j.foodchem.2022.132154

frontiers | Frontiers in Analytical Science

TYPE Perspective
PUBLISHED 12 June 2024
DOI 10.3389/frans.2024.1367448

OPEN ACCESS

EDITED BY
Ernesto Satoshi Nakayasu,
Pacific Northwest National Laboratory (DOE), United States

REVIEWED BY
Judith Wong,
National Environment Agency, Singapore

*CORRESPONDENCE
Yolanda Picó,
Yolanda.Pico@uv.es

RECEIVED 08 January 2024
ACCEPTED 21 May 2024
PUBLISHED 12 June 2024

CITATION
Picó Y, Ginebreda A, Carrascal M, Abian J and Barceló D (2024), Simultaneous determination of small molecules and proteins in wastewater-based epidemiology.
Front. Anal. Sci. 4:1367448.
doi: 10.3389/frans.2024.1367448

Simultaneous determination of small molecules and proteins in wastewater-based epidemiology

Yolanda Picó[1]*, Antoni Ginebreda[2], Montserrat Carrascal[3], Joaquin Abian[3] and Damià Barceló[2]

[1]Food and Environmental Research Group of the University of Valencia (SAMA-UV), Research Desertification Centre (CIDE) (CSIC-GV-UV), Moncada, Spain, [2]Department of Environmental Chemistry, Institute of Environmental Assessment and Water Studies, Spanish National Research Council (IDAEA-CSIC), Barcelona, Spain, [3]Proteomics Laboratory CSIC/UAB, Institute of Biomedical Research of Barcelona, Spanish National Research Council (IIBB-CSIC/IDIBAPS), Barcelona, Spain

Wastewater-based epidemiology (WBE) aims to understand a population's consumption habits, exposure to chemicals, and the prevalence of specific diseases or pathogens. This is achieved by the chemical or biological/genomic determination of biomarkers (e.g., excreted metabolic products), which are in urban wastewater generated by that population. WBE has been mostly linked to the determination of small molecules of human origin using liquid-chromatography mass spectrometry (LC-MS). In this Perspective, we provide a state-of-the-art and critical evaluation of further developments in the information achieved by determining small molecules as well as the most promising analytical techniques to enlarge the information obtained. By simultaneously monitoring small and large molecules we can comprehensively trace the population's health by their consumption of prescribed pharmaceuticals and illegal drugs, as well as by the amount of excreted macromolecule biomarkers such as peptides and proteins. Moreover, species-specific protein sequences allow us to monitor animal populations reflecting farming and slaughterhouse activities (poultry, pigs...) or pest occurrences (rats). To this end, the capability of proteomic studies using high-resolution tandem mass spectrometry is highlighted and compared in the context of other advances in the broader field of high-resolution mass spectrometry (HRMS).

KEYWORDS

biomarkers, proteomics, wastewater, high-resolution mass spectrometry (HRMS), metabolites

1 Introduction

Wastewater-based epidemiology (WBE), also known as sewage epidemiology or wastewater epidemiology, is an approach to monitoring public health by analyzing the presence of various substances, including pathogens, chemicals, and drugs, in municipal wastewater (Lorenzo and Picó, 2019; Singer et al., 2023). Figure 1 illustrates the rationale of WBE. Wastewater can be considered as an anonymous pool of feces and urine and in a lesser extent respiratory discharges of the population that is served by the wastewater treatment plant (WWTP) (García-Encina, 2021). Figure 2 summarizes chronologically the main steps in the evolution of WBE. Traditionally, this approach involves identifying microorganisms and analyzing small molecules. Advancements in molecular techniques,

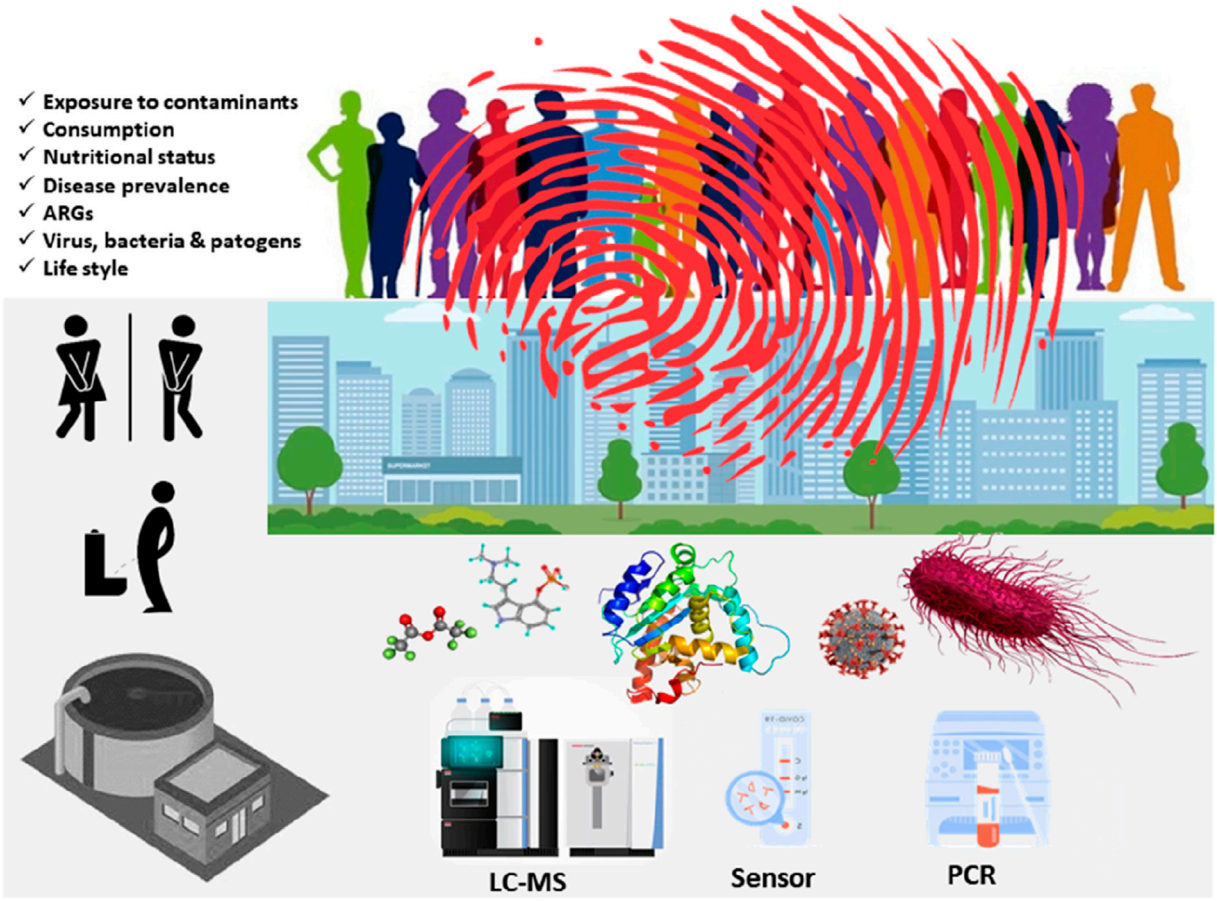

FIGURE 1
Scheme of the WBE.

such as qPCR and sequencing, have enabled the detection of viruses, bacteria, and other potential pathogens. Since 2020, these techniques have become increasingly important due to the need to control the spread of SARS-CoV-2 (Barcellos et al., 2023). As with any research related to SARS-CoV-2, there is an extensive literature on its surveillance in wastewater (Amman and Bergthaler, 2022; Dutta et al., 2022; Gonçalves et al., 2022; Greenbaum et al., 2022; Kumar et al., 2022; Burdorf and Rugulies, 2023; Du Toit, 2023; Gahlot et al., 2023; Hopkins et al., 2023; Oloye et al., 2023; Sodhi and Singh, 2023; Tavazzi et al., 2023). This has resulted in a renaissance of WBE and early warning systems based on pathogen surveillance (O'Brien and Xagoraraki, 2019; Guo et al., 2022a; Guo et al., 2022b; Fitzmorris-Brisolara et al., 2022; Demeter et al., 2023; Hassard et al., 2023; Shaw et al., 2023; Wolfe et al., 2023)

On the other hand, WBE also place significant emphasis on detecting small molecules and/or metabolites excreted by humans. These substances can offer valuable insights into population habits, particularities, and health status serving as biomarkers (Vitale et al., 2021). In this aspect, WBE has been closely linked to the development of liquid-chromatography mass spectrometry (LC-MS) protocols. The recent advent of high-resolution mass spectrometry (HRMS) has opened new insights not only for the determination of target small molecules but also for the application to larger ones (e.g., proteins) as well as for expanding non-targeted "omic" approaches in this field (Rice and Kasprzyk-Hordern, 2019).

In this Perspective article, we will discuss the recent advances of MS-based WBE in the detection and monitoring of the metabolites excreted by living beings in wastewater (including those from licit and illicit drugs consumption), based on the analysis of small molecules and the complementarity and role of proteomics, which is still in a very early stage of development and exploitation.

2 State-of-art of WBE

Firstly, on the detection of small molecules, WBE first gained recognition for monitoring the consumption of illegal drugs within the population (Gao et al., 2023). A scheme of how this consumption is estimated from wastewater analysis is shown in Supplementary Figure S1. Many studies have addressed sampling, sample stability, analytical protocol validation, and back-calculation of drug consumption (Huizer et al., 2021). The examination of these drugs primarily relied on solid-phase extraction (SPE) from wastewater, coupled with subsequent targeted liquid chromatography-tandem mass spectrometry (LC-MS/MS). Passive samplers that provide a more representative sample in time are also applied. Traditionally, the MS/MS analysis involved

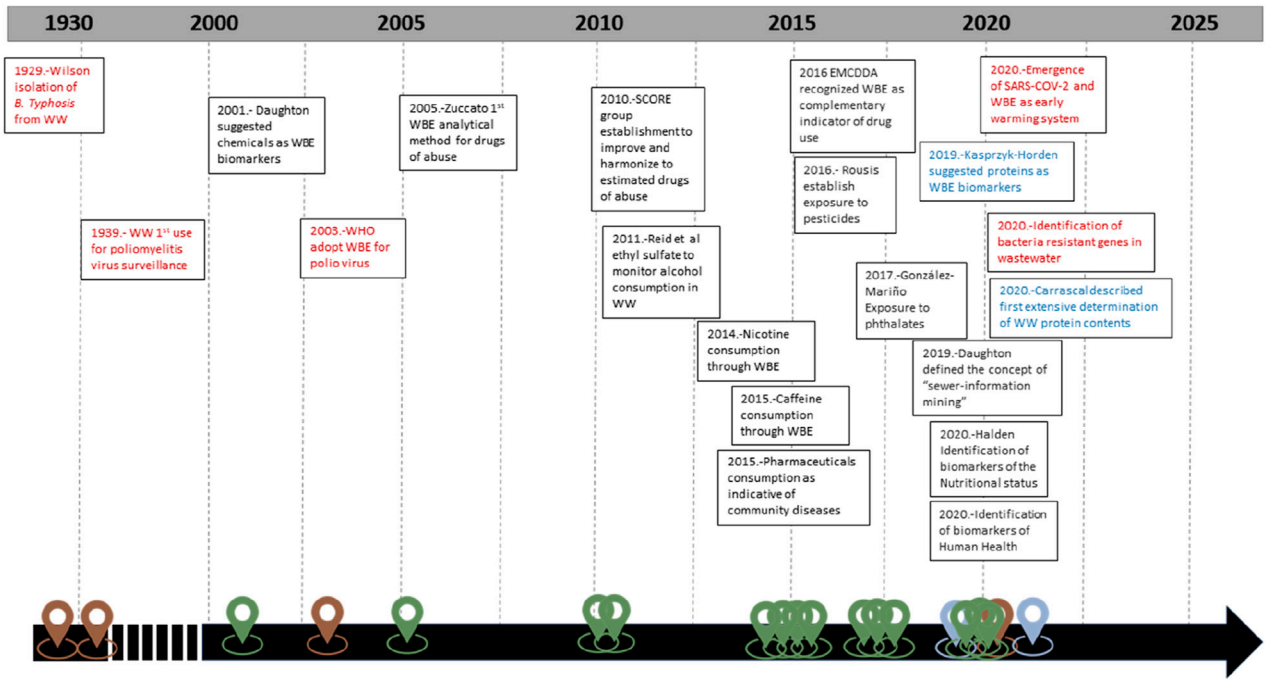

FIGURE 2
Chronological steps of WBE.

triple quadrupoles or linear ion trap configurations; however, contemporary practices have incorporated HRMS systems. Furthermore, enantiomeric separation is particularly crucial in WBE, as metabolism is often enantioselective and racemates could be transformed in one or other enantiomers in the human body (Langa et al., 2021). In any case, the analysis always follows a targeted strategy as needed for the identification of minority compounds. (Rousis et al., 2023). (Bio)sensors were developed to enhance the speed and efficiency of WBE. These sensors play a crucial role in rapidly detecting and measuring specific substances in wastewater, contributing to the overall effectiveness and velocity of WBE processes (Bilge et al., 2022; Kim et al., 2023). Their use enabled quicker and more precise analysis of key biomarkers, enhancing the capabilities of monitoring systems for various substances in wastewater (Pan et al., 2022).

Most studies primarily sample from WWTPs to estimate drug consumption trends in various regions (Shimko et al., 2021; Asadi et al., 2023; Laimou-Geraniou et al., 2023). However, a growing number of studies now employ WBE to monitor substance use in specific communities, focusing on locations such as educational institutions, prisons, music festivals, and sporting events, as well as on special dates, such as, holidays (Verovšek et al., 2020). Advancements in technology and theory have expanded the application of WBE to include surveys on the consumption of legally sold addictive substances like alcohol, nicotine, and caffeine (Gao et al., 2023).

In addition, fewer WBE studies explored other health biomarkers like pharmaceuticals. The significant medical and social implications of pharmaceutical misuse underscore the necessity for comprehensive drug utilization research (Jaunay et al., 2023; Massano et al., 2023). WBE has also been applied to monitor temporal patterns of pharmaceutical use or document interventions such as rescheduling (e.g., changing from over-the-counter to prescription only), sales-restrictions, and educational programs to influence prescription behaviour or consumer choice. WBE can reveal shifts in pharmaceutical consumption patterns during public health crises, like the COVID-19 pandemic (Picó and Barceló, 2023). Although interest in WBE for pharmaceutical monitoring is growing, further background research, including addressing compound-specific uncertainties, is essential to connect WBE data with routine pharmacoepidemiological information and workflows. WBE presents the opportunity to 1) estimate pharmaceutical consumption by analyzing metabolic excretion products in wastewater; 2) continuously and near real-time monitor spatial and temporal consumption patterns of pharmaceuticals; and 3) cross-reference data with other drug utilization research sources to evaluate the impact of strategies or interventions aimed at reducing inappropriate pharmaceutical use (Boogaerts et al., 2021)

Recently, WBE has evolved into a method for creating a city's fingerprint, indicating health, lifestyle habits, and exposure to contaminants in comparison to other cities (Picó and Barceló, 2021a; Singer et al., 2023). This expansion is attributed to identifying human biomarkers and profiling wastewater catchment characteristics that define these conditions.

3 Perspectives and future applications

3.1 Within small molecule biomarkers

WBE shows potential for swiftly assessing the impact of chemical contaminants and dietary nutrients on public health.

Over the last decade, WBE studies have broadened to monitor a wide range of biomarkers and health determinants (HDs), including pharmaceuticals (e.g., antibiotics, benzodiazepines), pesticides, plasticizers, alcohol, tobacco, indicators of oxidative stress (e.g., isoprostanes), and so on (detailed list is outlined in the Supplementary Table S1). WBE has also been proposed for assessing nutritional status in human populations using reported dietary metabolites and known linkages to health effects in human populations (Bowes and Halden, 2019). Analytes examined included 1-methylhistidine (meat intake), isoflavones and lignans (phytoestrogens), allyl isothiocyanates (cruciferous vegetables), and alkyl resorcinols (whole-wheat intake). Results obtained from theory identify WBE as a promising tool for tracking dietary trends in human populations, since it can complement existing tools by providing aggregated quantitative information regarding average consumption.

One key challenge in Public Health is to understand substances which individuals are exposed to in their work places and daily routines. In this sense, Dr. Christopher Wild introduced the term "exposome" in 2005, defining it as "every exposure to which an individual is subjected from conception to death" (Wild, 2005; Wild, 2012). The exposome exhibits significant variability and undergoes evolution throughout one's lifespan. However, comprehending the intricate interplay between environmental exposures such as air pollutants, radiation, chemicals in consumer goods, extreme weather conditions, pathogens, toxic substances, pesticides, heavy metals, dietary factors, physical activity, medications, genetics, epigenetics, and physiology remains a challenge. WBE is well-suited for studying the exposome and its effects. However, discovering biomarkers that reflect different population influences has been challenging and has entailed significant analytical effort. Picó and Barceló (2021a) classified the different methodological schemes into 1) top-down and 2) bottom-up approaches. The top-down approach, the most used in WBE, examines substance metabolism in humans using human biomonitoring (HBM) data, identifying suitable HDs and biomarkers for detection in wastewater. This method involves studying human metabolism, identifying urine-excreted substances, selecting highly representative ones, developing analytical methods for their determination, assessing their stability in wastewater, and ultimately analyzing them in wastewater. The alternative bottom-up approach involves non-targeted analysis of wastewater to identify substances from human sources and evaluate their potential as biomarkers. This method identifies various substances, including biomarkers, transformation products, and other compounds, through the application of non-targeted approaches involving HRMS. The introduction of HRMS has created new avenues for the identification of previously undiscovered chemicals of concern since it can provide the more probable empirical formula and the MS/MS spectrum to aid with structural elucidation (Gil-Solsona et al., 2021). Despite being less utilized than the top-down approach due to wastewater complexity, it holds promise for discovering unknown substances critical to advancing WBE (Henriot et al., 2024). Furthermore, advances in the most recent HRMS instruments equipped with operational commercial or free tools for wide-scope suspect screening and/or automatic annotation of unknowns, have offered an unparalleled opportunity to decipher those molecules that indicate exposure to pollutants (Picó and Barceló, 2021b). These features permit to perform simultaneous wide screening against a target list of compounds and non-target with extensive searching in on-line databases and chemical repositories housing MS/HRMS (such as ChemSpider, Human Metabolism Database (HMDB), Massbank, Metlin, mzCloud, NIST) and are highly promising to discover new biomarkers (Gil-Solsona et al., 2021; Perez-Lopez et al., 2024).

Connecting marker concentrations in wastewater to human exposure levels is challenging due to uncertainties in real sewer system stability and marker excretion rates. Overcoming this challenge involves conducting intensive human biomonitoring using representative specimens alongside well-defined WBE studies in specific catchments. Establishing correlations between concentrations in wastewater and human biological samples can help to forge these crucial links. Notably, Eaton et al. (2022) developed a framework to help public health authorities decide which HDs may be appropriate for WBE and which biomarkers could be used. This framework consists of an assessment tree that summarizes 1) the requirement for individual- or population-level information, 2) alternative methodologies for monitoring the HD, 3) the availability of a suitable biomarker, and 4) the requirement for changes in biomarker levels to be reflective of changes in the prevalence of the HD. This could through light to solve challenges in the future.

WBE has the potential for real-time, tracking of progress in attaining United Nations Sustainable Development Goals (SDGs) globally as a non-expensive method using existing infrastructure. As an example, Rousis et al. (2023) described that WBE approach can be used to monitor the achievement of the SDGs, such as reducing alcohol consumption and reducing the use of tobacco. In addition, it can be applied to monitor total caffeine consumption and assess levels according to the recommended daily safety limit as suggested by the European Food Safety Authority. Furthermore, in a promising effort, Adhikari and Halden (2022) compiled and analyzed existing data to 1) inventory the totality of centralized wastewater infrastructure globally, 2) identify countries featuring and lacking such infrastructure, 3) determine the fraction of the global population that is readily accessible to conventional WBE that leverages centralized sewerage infrastructure, 4) rank countries based on income level (as per UN"s" classification system) and on other factors to identify geographic regions which could benefit most from infrastructure improvements, and 5) compile an initial list of wastewater-borne markers that hold promise for tracking attainment of UN SDGs. Reviewing literature from 2005 to 2021, the authors identified 25 classes of biomarkers, both endogenous and exogenous, that can aid in tracking progress towards achieving the SDGs. These biomarkers encompass hunger and stress hormones, indicators for cardiovascular and pulmonary diseases, cancer, illicit drugs, personal care products, surfactants, hazardous chemicals, drug-resistant pathogens, antimicrobial-resistant genes (ARGs), and psychotropic drugs. These biosignatures offer valuable insights for monitoring SDG attainment.

WBE shows prospects in the growing field of the "One-Health" approach. This approach integrates human, animal, and environmental health efforts, offering a potential avenue to predict and control diseases at the interface of human, animal, and ecosystem interactions. The clearest example of this application within the field of small chemical molecules analysis is to help in the

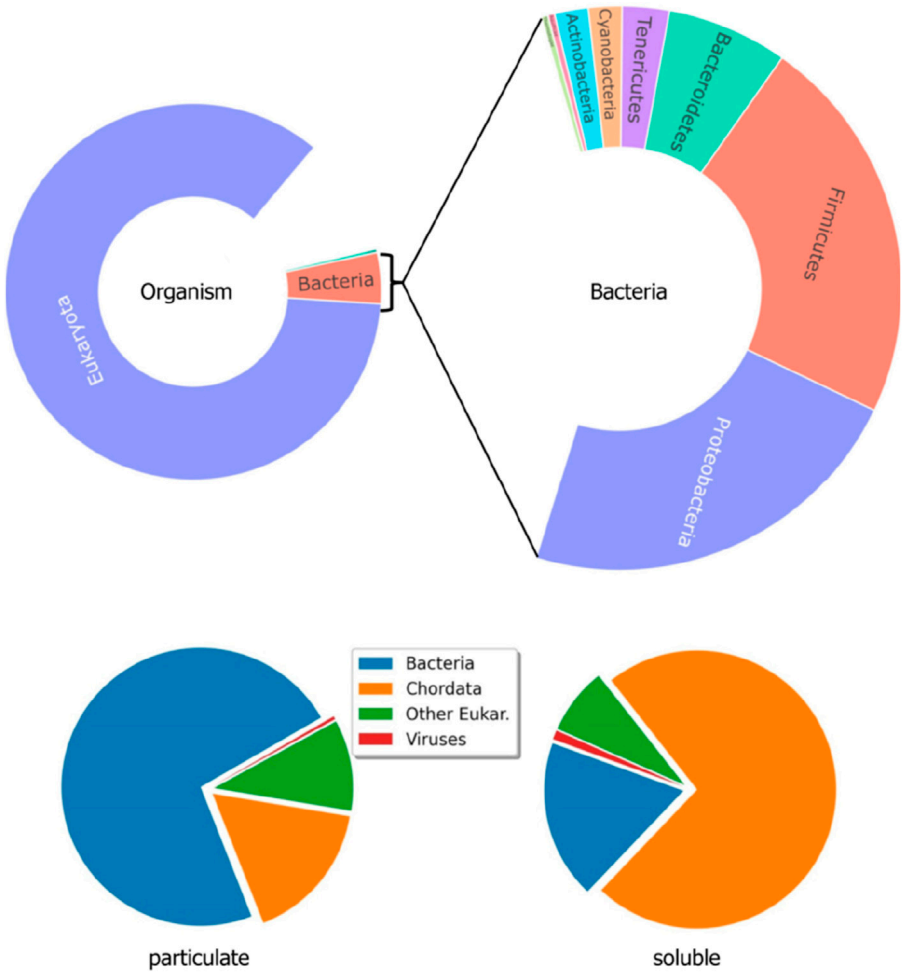

FIGURE 3
Distribution of Bacteria and Eukaryota proteins in the soluble fraction of wastewater and comparison with the particulate fraction (adapted from Carrascal et al., 2023).

study of antibiotic resistance spread in the environment. This is, according to the WHO, a forefront challenge for the future of the human being. Antibiotic residues, antibiotic-resistant bacteria, or ARGs are detectable in wastewater and constitute a study system that provides a wealth of information. In addition to the identification of antimicrobial resistance (AMR) by several microbiological techniques (Sims and Kasprzyk-Hordern, 2020; Chau et al., 2022; Foyle et al., 2023; Larsson et al., 2023; Pandey et al., 2023; Sharma et al., 2023), it is crucial to monitor and assess antibiotic presence in wastewater, and other environmental matrices to address the problem of AMR. WBE is potentially the most reliable approach to estimate antibiotics use (Henriot et al., 2024).

WBE has an environmental safety aspect since many of these small molecules of chemical compounds that humans use or are exposed to directly or indirectly (including potential metabolites and degradation products) are currently considered emerging contaminants of concern (CECs). These molecules are initially collected in sewer systems and, if the treatment in WWTPs is ineffective in removing them, they are subsequently released into the environment, posing associated problems. Interestingly, Zillien et al. (2022) collated the fragmented knowledge and data on in-sewer fate of CECs to develop practical guidelines for water managers on how to deal with in-sewer fate of CECs. To this end, these authors collected experimental half-lives of 96 organic CECs from literature to support environmental modelling efforts and to optimize monitoring campaigns, including field studies in the context of WBE. Furthermore, a pending issue is also hospital wastewater, which is a complex mixture of pharmaceuticals, drugs, and their metabolites as well as different susceptible and antibiotic-resistant microorganisms, including viruses. Many studies pointed out that wastewater from healthcare facilities (including hospital wastewater), significantly contributes to higher loads of CECs in municipal wastewater. Because many pharmaceuticals, drugs, and microorganisms can pass through wastewater treatment plants without any significant change in their structure and toxicity and enter surface waters, treatment technologies need to be improved in terms of efficiency as well as economy (Mackull'ak et al., 2021).

TABLE 1 The 20 most abundant proteins in the wastewater samples based on the normalized number of MS/MS spectra identified (NSCs) (Carrascal et al., 2023). STRCA: Ostrich; FELCA: Cat.

Accession	Protein name	Entry name[a]		Coverage [%]	# NSCs (Thousands)
		Gene	Species		
P04746	Pancreatic alpha-amylase	AMYP	HUMAN	88	10.9
P0DUB6	Alpha-amylase 1A	AMY1A	HUMAN	86	10.5
P19961	Alpha-amylase 2B	AMY2B	HUMAN	88	9.6
P08835	Albumin	ALBU	PIG	93	8.8
P01834	Immunoglobulin kappa constant	IGKC	HUMAN	93	7.7
P01012	Ovalbumin	OVAL	CHICK	75	7.2
P02769	Albumin	ALBU	BOVIN	92	5.5
P01846	Ig lambda chain C region	LAC	PIG	97	4.8
P19121	Albumin	ALBU	CHICK	88	4.4
P02768	Albumin	ALBU	HUMAN	90	4.3
P83053	Pancreatic alpha-amylase	AMYP	STRCA	33	3.0
P00687	Alpha-amylase 1	AMY1	MOUSE	23	2.9
P0DOX7	Immunoglobulin kappa light chain	IGK	HUMAN	60	2.8
P01009	Alpha-1-antitrypsin	A1AT	HUMAN	60	2.7
P00690	Pancreatic alpha-amylase	AMYP	PIG	51	2.6
P14639	Albumin	ALBU	SHEEP	88	2.5
P00689	Pancreatic alpha-amylase	AMYP	RAT	28	2.4
P07478	Trypsin-2	TRY2	HUMAN	63	2.3
P07724	Albumin	ALBU	MOUSE	39	2.2
P49064	Albumin	ALBU	FELCA	32	2.2
P09571	Serotransferrin	TRFE	PIG	94	2.2

[a]UniProtKB/Swiss-Prot entry name. The two terms of the entry name (gene_species) have been separated for convenience.

3.2 Within proteomics field

Since more than 1 decade ago, proteomic studies can be found in the literature as useful tools for the monitoring of changes occurring in the complex microbiomes associated with biotechnological processes such as those used in the treatment of wastewater and sludge (Park et al., 2008; Westgate and Park, 2010; Kuhn et al., 2011; Zhang et al., 2019). This research area is currently active and has found recently specific applications, such as the effects caused by the presence of toxicants in the proteome of the bacterial consortia associated with the anammox process (Zhang et al., 2013; Wang et al., 2021; Kennes-Veiga et al., 2022; Guzmán-Fierro et al., 2024). Owing to these reasons, these proteomic studies are exclusively focused on the prokaryote (i.e., microbial) fraction of the whole wastewater proteome as ultimately responsible for the biological treatment processes. In contrast, the eukaryote higher organisms' proteome (i.e., plants, animals, and humans) has been systematically disregarded, despite being a significant portion of it (the largest in the water phase) (Figure 3).

The use of human proteins occurring in wastewater as potential biomarkers in the assessment of community health was conceptually suggested for the first time by Rice and Kasprzyk-Horden (2019). Later on, Devianto and Sano (2023), reviewed the feasibility of biosensor technology for the real-time analysis of protein-based biomarkers to be used in early warning WBE surveys of human disease. In their study, though a meta-analysis based on 231 articles, they assessed the possible candidate proteins taking into consideration their respective concentration levels in urine and feces, their dilution in wastewater, and available biosensors' detection/quantification limits AMR. These authors suggested up to 64 proteins present either in feces or urine (including, among others, calprotectin and uromodulin), as feasible biomarkers. Altogether, there is a consensus on the requirements for a protein to be utilized as a biomarker in WBE, namely, (a) a well-defined disease–biomarker correlation, (b) its excretion must take place in sufficient amount to allow for its analytical detection and quantification, once it is diluted in wastewater, and (c) its stability both *in vivo* and in the wastewater media must be ensured so that the integrity and representativity of the sample are guaranteed. As for now, the number of potential candidates is scarce and they have not been proven yet.

Despite the interest of proteins for WBE manifested by the above-referred authors, the need (and lack) for experimental research studies addressed to this end is recognized. Advances in liquid chromatography coupled with HR MS non-targeted shotgun proteomic methods have enabled substantial progress in the profiling of wastewater proteome (Picó and Barceló, 2021b) thus allowing to achieve for the first time its comprehensive characterization, encompassing both prokaryotes and eukaryotes (Carrascal et al., 2020; Pérez-López et al., 2021) using passive polymeric devices.

This seminal work paved the way for further research (Carrascal et al., 2023) carried out at the influent collection points of 10 WWTPs using optimized analytical methods for both the soluble and particulate fractions that have been fully described elsewhere (Sánchez-Jiménez et al., 2023). This improved analyses of the wastewater proteome profile and distinguished signals from different groups of organisms. Overall, eukaryotic proteins, primarily from Chordata (i.e., mammals and birds) but also from non-Chordata (plants), were the major proteome components of the liquid phase, followed by bacterial proteins, while the particulate phase shows the opposite trend. Viral proteins were detected in small quantities as well (Figure 3). Over 4,000 peptides, associated with ca. 800 proteins (243 human), were identified through the semiquantitative analysis of the main constituents (Table 1). Despite not being a focused study on human epidemiology, it provided valuable information regarding the presence of endogenous human molecules potentially relevant to WBE. Pancreatic enzymes, dominated by α-amylases, were the most abundant human proteins identified in wastewater, making them the primary markers of human presence. Blood proteins, including albumin, Igs, and complement proteins, and skin-derived proteins, such as keratins, were found in significant amounts as well. A gene ontology analysis (DAVID) (Sherman et al., 2022), highlighted several functional terms that were enriched, such as those associated with the immune response (Igs, calprotectin, lactoferrin, lipocain, and dermcidin) or the anti-inflammatory response (meprin A, orosomucoid, and the serpin family).

A potential application of protein biomarkers of great interest would be the use of rat/mouse pancreatic amylases and immunoglobulins to monitor rodent populations in urban areas (Carrascal et al., 2023). Rat pests not only constitute a human health hazard as potential disease transmitters but also a threat to the integrity of infested infrastructures. Moreover, available rat pest surveillance methods (i.e., live or photo trapping) are costly and typically limited to point (local) monitoring.

The study of the wastewater proteome is currently in its infancy, but their preliminary findings have prompted new and unanticipated scientific inquiries. This is an outcome of our limited understanding of the many aspects that influence protein dynamics and fate during their journey from the emission source to the sampling site, including the actual discharge rates of these proteins over time, hydraulic retention times, stability, and other uncertainties and confounding factors. Still, the exploitation of the potential of proteins as health and environmental biomarkers is deeply recognized as an invaluable source of information about the population's health and lifestyle status.

4 Conclusion

WBE has expanded its potential to become a benchmark for monitoring a population's health and providing information of the population discharges in wastewater. In order to expand the scope of WBE, the effort made in the identification of small molecules is crucial. WBE also has an important future in monitoring the scope of the SDGs and to become a tool within the global "One Health" system bridging the gap between human and veterinary health. The development of faster monitoring systems and advancements in mass spectrometry techniques will make these achievements possible. However, we strongly believe that the simultaneous use of small molecule chemical analysis and proteomic identification is a powerful chemical analytical tool in WBE. This methodology can be even more sophisticated when combined with microbiological and genetic information providing a comprehensive picture of the powerful information that can be extracted from a given wastewater sample.

Data availability statement

The original contributions presented in the study are included in the article/Supplementary Material, further inquiries can be directed to the corresponding author.

Author contributions

YP: Conceptualization, Data curation, Formal Analysis, Funding acquisition, Writing–original draft, Writing–review and editing. AG: Conceptualization, Data curation, Formal Analysis, Funding acquisition, Writing–original draft, Writing–review and editing. MC: Conceptualization, Data curation, Formal Analysis, Funding acquisition, Writing–original draft, Writing–review and editing. JA: Conceptualization, Data curation, Formal Analysis, Funding acquisition, Writing–original draft, Writing–review and editing. DB: Conceptualization, Data curation, Formal Analysis, Funding acquisition, Supervision, Writing–original draft, Writing–review and editing.

Funding

The author(s) declare financial support was received for the research, authorship, and/or publication of this article. This work has been supported by Grants PID 2020-114065RB-C22, PID 2020-114065RB-C21), and PID 2022-138556OB-C22 funded by MCIN/AEI/10.13039/501100011033, by "ERDF A way of making Europe" and by the Grant CIPROM/2021/032 funded by the Conselleria d'Educació, Universitats i Ocupació (Generalitat Valenciana).

Conflict of interest

The authors declare that the research was conducted in the absence of any commercial or financial relationships that could be construed as a potential conflict of interest.

Publisher's note

All claims expressed in this article are solely those of the authors and do not necessarily represent those of their affiliated organizations, or those of the publisher, the editors and the reviewers. Any product that may be evaluated in this article, or claim that may be made by its manufacturer, is not guaranteed or endorsed by the publisher.

Supplementary material

The Supplementary Material for this article can be found online at: https://www.frontiersin.org/articles/10.3389/frans.2024.1367448/full#supplementary-material

References

Adhikari, S., and Halden, R. U. (2022). Opportunities and limits of wastewater-based epidemiology for tracking global health and attainment of UN sustainable development goals. *Environ. Int.* 163, 107217. doi:10.1016/j.envint.2022.107217

Amman, F., and Bergthaler, A. (2022). Wastewater is a robust proxy for monitoring circulating SARS-CoV-2 variants. *Nat. Biotechnol.* 40, 1768–1769. doi:10.1038/s41587-022-01388-x

Asadi, A., Fakhri, Y., Salimi, Y., Daglioglu, N., Tahmasebifard, M., and Aghajarinezhad, M. (2023). Nicotine consumption rate through wastewater-based epidemiology: a systematic review, meta-analysis and probabilistic risk assessment. *Environ. Sci. Pollut. Res.* 30, 63416–63426. doi:10.1007/s11356-023-27017-x

Barcellos, D. S., Barquilha, C. E. R., Oliveira, P. E., Prokopiuk, M., and Etchepare, R. G. (2023). How has the COVID-19 pandemic impacted wastewater-based epidemiology? *Sci. Total Environ.* 892, 164561. doi:10.1016/j.scitotenv.2023.164561

Bilge, S., Dogan-Topal, B., Gürbüz, M. M., Yücel, A., Sınağ, A., and Ozkan, S. A. (2022). Recent advances in electrochemical sensing of cocaine: a review. *TrAC - Trends Anal. Chem.* 157, 116768. doi:10.1016/j.trac.2022.116768

Boogaerts, T., Ahmed, F., Choi, P. M., Tscharke, B., O'brien, J., De Loof, H., et al. (2021). Current and future perspectives for wastewater-based epidemiology as a monitoring tool for pharmaceutical use. *Sci. Total Environ.* 789, 148047. doi:10.1016/j.scitotenv.2021.148047

Bowes, D. A., and Halden, R. U. (2019). Theoretical evaluation of using wastewater-based epidemiology to assess the nutritional status of human populations. *Curr. Opin. Environ. Sci. Health* 9, 58–63. doi:10.1016/j.coesh.2019.05.001

Burdorf, A., and Rugulies, R. (2023). The importance of occupation in the development of the COVID-19 pandemic. *Scand. J. Work, Environ. Health* 49, 231–233. doi:10.5271/sjweh.4094

Carrascal, M., Abian, J., Ginebreda, A., and Barceló, D. (2020). Discovery of large molecules as new biomarkers in wastewater using environmental proteomics and suitable polymer probes. *Sci. Total Environ.* 747, 141145. doi:10.1016/j.scitotenv.2020.141145

Carrascal, M., Sánchez-Jiménez, E., Fang, J., Pérez-López, C., Ginebreda, A., Barceló, D., et al. (2023). Sewage protein information mining: discovery of large biomolecules as biomarkers of population and industrial activities. *Environ. Sci. Technol.* 57, 10929–10939. doi:10.1021/acs.est.3c00535

Chau, K. K., Barker, L., Budgell, E. P., Vihta, K. D., Sims, N., Kasprzyk-Hordern, B., et al. (2022). Systematic review of wastewater surveillance of antimicrobial resistance in human populations. *Environ. Int.* 162, 107171. doi:10.1016/j.envint.2022.107171

Demeter, K., Linke, R., Balleste, E., Reischer, G., Mayer, R. E., Vierheilig, J., et al. (2023). Have genetic targets for faecal pollution diagnostics and source tracking revolutionized water quality analysis yet? *FEMS Microbiol. Rev.* 47, fuad028. doi:10.1093/femsre/fuad028

Devianto, L. A., and Sano, D. (2023). Systematic review and meta-analysis of human health-related protein markers for realizing real-time wastewater-based epidemiology. *Sci. Total Environ.* 897, 165304. doi:10.1016/j.scitotenv.2023.165304

Du Toit, A. (2023). Sewer biofilms and SARS-CoV-2. *Nat. Rev. Microbiol.* 21, 277. doi:10.1038/s41579-023-00882-6

Dutta, H., Kaushik, G., and Dutta, V. (2022). Wastewater-based epidemiology: a new frontier for tracking environmental persistence and community transmission of COVID-19. *Environ. Sci. Pollut. Res.* 29, 85688–85699. doi:10.1007/s11356-021-17419-0

Eaton, C. J., Coxon, S., Pattis, I., Chappell, A., Hewitt, J., and Gilpin, B. J. (2022). A framework for public health authorities to evaluate health determinants for wastewater-based epidemiology. *Environ. Health Perspect.* 130, 125001. doi:10.1289/EHP11115

Fitzmorris-Brisolara, K., Maal-Bared, R., Worley-Morse, T., Danley-Thomson, A., and Sobsey, M. (2022). Monitoring coliphages to reduce waterborne infectious disease transmission in the One Water framework. *Int. J. Hyg. Environ. Health* 240, 113921. doi:10.1016/j.ijheh.2022.113921

Foyle, L., Burnett, M., Creaser, A., Hens, R., Keough, J., Madin, L., et al. (2023). Prevalence and distribution of antimicrobial resistance in effluent wastewater from animal slaughter facilities: a systematic review. *Environ. Pollut.* 318, 120848. doi:10.1016/j.envpol.2022.120848

Gahlot, P., Alley, K. D., Arora, S., Das, S., Nag, A., and Tyagi, V. K. (2023). Wastewater surveillance could serve as a pandemic early warning system for COVID-19 and beyond. *Wiley Interdiscip. Rev. Water* 10, e1650. doi:10.1002/wat2.1650

Gao, Z., Gao, M., Chen, C. H., Zhou, Y., Zhan, Z. H., and Ren, Y. (2023). Knowledge graph of wastewater-based epidemiology development: a data-driven analysis based on research topics and trends. *Environ. Sci. Pollut. Res.* 30, 28373–28382. doi:10.1007/s11356-023-25237-9

García-Encina, P. A. (2021). Wastewater-based epidemiology (WBE). *Water Environ. J.* 35, 1162–1163. doi:10.1111/wej.12761

Gil-Solsona, R., Nika, M.-C., Bustamante, M., Villanueva, C. M., Foraster, M., Cosin-Tomás, M., et al. (2021). The potential of sewage sludge to predict and evaluate the human chemical exposome. *Environ. Sci. Technol. Lett.* 8, 1077–1084. doi:10.1021/acs.estlett.1c00848

Gonçalves, J., Torres-Franco, A., Rodriguéz, E., Diaz, I., Koritnik, T., Silva, P. G. D., et al. (2022). Centralized and decentralized wastewater-based epidemiology to infer COVID-19 transmission – a brief review. *One Health* 15, 100405. doi:10.1016/j.onehlt.2022.100405

Greenbaum, D., Gurwitz, D., and Joly, Y. (2022). Editorial: COVID-19 pandemics: ethical, legal and social issues. *Front. Genet.* 13, 1021865. doi:10.3389/fgene.2022.1021865

Guo, Y., Li, J., O'Brien, J., Sivakumar, M., and Jiang, G. (2022a). Back-estimation of norovirus infections through wastewater-based epidemiology: a systematic review and parameter sensitivity. *Water Res.* 219, 118610. doi:10.1016/j.watres.2022.118610

Guo, Y., Sivakumar, M., and Jiang, G. (2022b). Decay of four enteric pathogens and implications to wastewater-based epidemiology: effects of temperature and wastewater dilutions. *Sci. Total Environ.* 819, 152000. doi:10.1016/j.scitotenv.2021.152000

Guzmán-Fierro, V., Dieguez-Seoane, A., Roeckel, M., Lema, J. M., and Trueba-Santiso, A. (2024). Environmental proteomics as a useful methodology for early-stage detection of stress in anammox engineered systems. *Sci. Total Environ.* 912, 169349. doi:10.1016/j.scitotenv.2023.169349

Hassard, F., Bajón-Fernández, Y., and Castro-Gutierrez, V. (2023). Wastewater-based epidemiology for surveillance of infectious diseases in healthcare settings. *Curr. Opin. Infect. Dis.* 36, 288–295. doi:10.1097/QCO.0000000000000929

Henriot, P., Buelow, E., Petit, F., Ploy, M. C., Dagot, C., and Opatowski, L. (2024). Modeling the impact of urban and hospital eco-exposomes on antibiotic-resistance dynamics in wastewaters. *Sci. Total Environ.* 924, 171643. doi:10.1016/j.scitotenv.2024.171643

Hopkins, L., Ensor, K. B., Stadler, L., Johnson, C. D., Schneider, R., Domakonda, K., et al. (2023). Public health interventions guided by houston's wastewater surveillance program during the COVID-19 pandemic. *Public Health Rep.* 138, 856–861. doi:10.1177/00333549231185625

Huizer, M., Ter Laak, T. L., De Voogt, P., and Van Wezel, A. P. (2021). Wastewater-based epidemiology for illicit drugs: a critical review on global data. *Water Res.* 207, 117789. doi:10.1016/j.watres.2021.117789

Jaunay, E. L., Simpson, B. S., White, J. M., and Gerber, C. (2023). Using wastewater-based epidemiology to evaluate the relative scale of use of opioids. *Sci. Total Environ.* 897, 165148. doi:10.1016/j.scitotenv.2023.165148

Kennes-Veiga, D. M., Trueba-Santiso, A., Gallardo-Garay, V., Balboa, S., Carballa, M., and Lema, J. M. (2022). Sulfamethoxazole enhances specific enzymatic activities under

aerobic heterotrophic conditions: a metaproteomic approach. *Environ. Sci. Technol.* 56, 13152–13159. doi:10.1021/acs.est.2c05001

Kim, K., Stoll, S., Singh, R., Lee, W. H., and Hwang, J. H. (2023). Recent advances in illicit drug detection sensor technology in water. *TrAC - Trends Anal. Chem.* 168, 117295. doi:10.1016/j.trac.2023.117295

Kuhn, R., Benndorf, D., Rapp, E., Reichl, U., Palese, L. L., and Pollice, A. (2011). Metaproteome analysis of sewage sludge from membrane bioreactors. *Proteomics* 11, 2738–2744. doi:10.1002/pmic.201000590

Kumar, M., Vithanage, M., An, A. K., Weber, K. A., and Bhattacharya, P. (2022). Geogenic and pathogenic contamination: issues and innovation in the post-COVID-Anthropocene. *J. Hazard. Mater.* 429, 127501. doi:10.1016/j.jhazmat.2021.127501

Laimou-Geraniou, M., Heath, D., and Heath, E. (2023). Analytical methods for the determination of antidepressants, antipsychotics, benzodiazepines and their metabolites through wastewater-based epidemiology. *Trends Environ. Anal. Chem.* 37, 200192. doi:10.1016/j.teac.2022.e00192

Langa, I., Gonçalves, R., Tiritan, M. E., and Ribeiro, C. (2021). Wastewater analysis of psychoactive drugs: non-enantioselective vs enantioselective methods for estimation of consumption. *Forensic Sci. Int.* 325, 110873. doi:10.1016/j.forsciint.2021.110873

Larsson, D. G. J., Flach, C. F., and Laxminarayan, R. (2023). Sewage surveillance of antibiotic resistance holds both opportunities and challenges. *Nat. Rev. Microbiol.* 21, 213–214. doi:10.1038/s41579-022-00835-5

Lorenzo, M., and Picó, Y. (2019). Wastewater-based epidemiology: current status and future prospects. *Curr. Opin. Environ. Sci. Health* 9, 77–84. doi:10.1016/j.coesh.2019.05.007

Mackull'ak, T., Cverenkárová, K., Staňová, A. V., Fehér, M., Tamáš, M., Škulcová, A. B., et al. (2021). Hospital wastewater—source of specific micropollutants, antibiotic-resistant microorganisms, viruses, and their elimination. *Antibiotics* 10, 1070. doi:10.3390/antibiotics10091070

Massano, M., Salomone, A., Gerace, E., Alladio, E., Vincenti, M., and Minella, M. (2023). Wastewater surveillance of 105 pharmaceutical drugs and metabolites by means of ultra-high-performance liquid-chromatography-tandem high resolution mass spectrometry. *J. Chromatogr. A* 1693, 463896. doi:10.1016/j.chroma.2023.463896

O'Brien, E., and Xagoraraki, I. (2019). A water-focused one-health approach for early detection and prevention of viral outbreaks. *One Health* 7, 100094. doi:10.1016/j.onehlt.2019.100094

Oloye, F. F., Xie, Y., Challis, J. K., Femi-Oloye, O. P., Brinkmann, M., Mcphedran, K. N., et al. (2023). Understanding common population markers for SARS-CoV-2 RNA normalization in wastewater – a review. *Chemosphere* 333, 138682. doi:10.1016/j.chemosphere.2023.138682

Pan, Y., Mao, K., Hui, Q., Wang, B., Cooper, J., and Yang, Z. (2022). Paper-based devices for rapid diagnosis and wastewater surveillance. *TrAC - Trends Anal. Chem.* 157, 116760. doi:10.1016/j.trac.2022.116760

Pandey, R. P., Yousef, A. F., Alsafar, H., and Hasan, S. W. (2023). Surveillance, distribution, and treatment methods of antimicrobial resistance in water: a review. *Sci. Total Environ.* 890, 164360. doi:10.1016/j.scitotenv.2023.164360

Park, C., Novak, J. T., Helm, R. F., Ahn, Y. O., and Esen, A. (2008). Evaluation of the extracellular proteins in full-scale activated sludges. *Water Res.* 42, 3879–3889. doi:10.1016/j.watres.2008.05.014

Perez-Lopez, C., Ginebreda, A., Carrascal, M., Barceló, D., Abian, J., and Tauler, R. (2021). Non-target protein analysis of samples from wastewater treatment plants using the regions of interest-multivariate curve resolution (ROIMCR) chemometrics method. *J. Environ. Chem. Eng.* 9, 105752. doi:10.1016/j.jece.2021.105752

Perez-Lopez, C., Ginebreda, A., Jaumot, J., Yamamoto, F. Y., Barceló, D., and Tauler, R. (2024). MSident: straightforward identification of chemical compounds from MS-resolved spectra. *Chemom. Intelligent Laboratory Syst.* 245, 105063. doi:10.1016/j.chemolab.2024.105063

Picó, Y., and Barceló, D. (2021a). Identification of biomarkers in wastewater-based epidemiology: main approaches and analytical methods. *TrAC - Trends Anal. Chem.* 145, 116465. doi:10.1016/j.trac.2021.116465

Picó, Y., and Barceló, D. (2021b). Mass spectrometry in wastewater-based epidemiology for the determination of small and large molecules as biomarkers of exposure: toward a global view of environment and human health under the COVID-19 outbreak. *ACS Omega* 6, 30865–30872. doi:10.1021/acsomega.1c04362

Picó, Y., and Barceló, D. (2023). Microplastics and other emerging contaminants in the environment after COVID-19 pandemic: the need of global reconnaissance studies. *Curr. Opin. Environ. Sci. Health* 33, 100468. doi:10.1016/j.coesh.2023.100468

Rice, J., and Kasprzyk-Hordern, B. (2019). A new paradigm in public health assessment: water fingerprinting for protein markers of public health using mass spectrometry. *TrAC - Trends Anal. Chem.* 119, 115621. doi:10.1016/j.trac.2019.115621

Rousis, N., Bade, R., and Gracia-Lor, E. (2023). Wastewater-based epidemiology as a surveillance tool to assess human consumption of psychotropic substances: alcohol, nicotine and caffeine as case studies. *TrAC - Trends Anal. Chem.* 167, 117230. doi:10.1016/j.trac.2023.117230

Sánchez-Jiménez, E., Abian, J., Ginebreda, A., Barceló, D., and Carrascal, M. (2023). Shotgun proteomics to characterize wastewater proteins. *MethodsX* 11, 102403. doi:10.1016/j.mex.2023.102403

Sharma, A., Karande, M., and Zumla, A. (2023). Advancing sewage surveillance at mass gathering events for reducing transmission of antimicrobial resistant bacterial pathogens. *Travel Med. Infect. Dis.* 54, 102619. doi:10.1016/j.tmaid.2023.102619

Shaw, A. G., Troman, C., Akello, J. O., O'Reilly, K. M., Gauld, J., Grow, S., et al. (2023). Defining a research agenda for environmental wastewater surveillance of pathogens. *Nat. Med.* 29, 2155–2157. doi:10.1038/s41591-023-02457-7

Sherman, B. T., Hao, M., Qiu, J., Jiao, X., Baseler, M. W., Lane, H. C., et al. (2022). DAVID: a web server for functional enrichment analysis and functional annotation of gene lists (2021 update). *Nucleic Acids Res.* 50, W216–W221. doi:10.1093/nar/gkac194

Shimko, K. M., Piatkowski, T., Thomas, K. V., Speers, N., Brooker, L., Tscharke, B. J., et al. (2021). Performance- and image-enhancing drug use in the community: use prevalence, user demographics and the potential role of wastewater-based epidemiology. *J. Hazard. Mater.* 419, 126340. doi:10.1016/j.jhazmat.2021.126340

Sims, N., and Kasprzyk-Hordern, B. (2020). Future perspectives of wastewater-based epidemiology: monitoring infectious disease spread and resistance to the community level. *Environ. Int.* 139, 105689. doi:10.1016/j.envint.2020.105689

Singer, A. C., Thompson, J. R., Filho, C. R. M., Street, R., Li, X., Castiglioni, S., et al. (2023). A world of wastewater-based epidemiology. *Nat. Water* 1, 408–415. doi:10.1038/s44221-023-00083-8

Sodhi, K. K., and Singh, C. K. (2023). A systematic review on the occurrence, fate, and remediation of SARS-CoV-2 in wastewater. *Int. J. Environ. Sci. Technol.* 20, 8073–8086. doi:10.1007/s13762-022-04326-1

Tavazzi, S., Cacciatori, C., Comero, S., Fatta-Kassinos, D., Karaolia, P., Iakovides, I. C., et al. (2023). Short-term stability of wastewater samples for storage and shipment in the context of the EU Sewage Sentinel System for SARS-CoV-2. *J. Environ. Chem. Eng.* 11, 109623. doi:10.1016/j.jece.2023.109623

Verovšek, T., Krizman-Matasic, I., Heath, D., and Heath, E. (2020). Site- and event-specific wastewater-based epidemiology: current status and future perspectives. *Trends Environ. Anal. Chem.* 28, e00105. doi:10.1016/j.teac.2020.e00105

Vitale, D., Morales Suárez-Varela, M., and Picó, Y. (2021). Wastewater-based epidemiology, a tool to bridge biomarkers of exposure, contaminants, and human health. *Curr. Opin. Environ. Sci. Health* 20, 100229. doi:10.1016/j.coesh.2021.100229

Wang, S., Ishii, K., Yu, H., Shi, X., Smets, B. F., Palomo, A., et al. (2021). Stable nitrogen removal by anammox process after rapid temperature drops: insights from metagenomics and metaproteomics. *Bioresour. Technol.* 320, 124231. doi:10.1016/j.biortech.2020.124231

Westgate, P. J., and Park, C. (2010). Evaluation of proteins and organic nitrogen in wastewater treatment effluents. *Environ. Sci. Technol.* 44, 5352–5357. doi:10.1021/es100244s

Wild, C. P. (2005). Complementing the genome with an "exposome": the outstanding challenge of environmental exposure measurement in molecular epidemiology. *Cancer Epidemiol. Biomarkers Prev.* 14, 1847–1850. doi:10.1158/1055-9965.EPI-05-0456

Wolfe, M. K., Yu, A. T., Duong, D., Rane, M. S., Hughes, B., Chan-Herur, V., et al. (2023). Use of wastewater for mpox outbreak surveillance in California. *N. Engl. J. Med.* 388, 570–572. doi:10.1056/NEJMc2213882

Zhang, P., Zhu, J., Xu, X. Y., Qing, T. P., Dai, Y. Z., and Feng, B. (2019). Identification and function of extracellular protein in wastewater treatment using proteomic approaches: a minireview. *J. Environ. Manage.* 233, 24–29. doi:10.1016/j.jenvman.2018.12.028

Zhang, Y., Fonslow, B. R., Shan, B., Baek, M. C., and Yates, J. R. (2013). Protein analysis by shotgun/bottom-up proteomics. *Chem. Rev.* 113, 2343–2394. doi:10.1021/cr3003533

Zillien, C., Posthuma, L., Roex, E., and Ragas, A. (2022). The role of the sewer system in estimating urban emissions of chemicals of emerging concern. *Rev. Environ. Sci. Biotechnol.* 21, 957–991. doi:10.1007/s11157-022-09638-9

frontiers | Frontiers in Analytical Science

TYPE Original Research
PUBLISHED 13 June 2024
DOI 10.3389/frans.2024.1421463

OPEN ACCESS

EDITED BY
Ann Van Eeckhaut,
Vrije Universiteit Brussel, Belgium

REVIEWED BY
Emmanuelle Lipka,
Lille University, France
Gerhard Scriba,
Friedrich Schiller University Jena, Germany

*CORRESPONDENCE
Marianne Fillet,
✉ Marianne.fillet@uliege.be

RECEIVED 22 April 2024
ACCEPTED 24 May 2024
PUBLISHED 13 June 2024

CITATION
Ghassemi MK, Hurlet V, Crommen J, Servais A-C and Fillet M (2024), Separation of isobaric phosphorothioate oligonucleotides in capillary electrophoresis: study of the influence of cationic cyclodextrins on chemo and stereoselectivity.
Front. Anal. Sci. 4:1421463.
doi: 10.3389/frans.2024.1421463

Separation of isobaric phosphorothioate oligonucleotides in capillary electrophoresis: study of the influence of cationic cyclodextrins on chemo and stereoselectivity

Maryam K. Ghassemi, Vincent Hurlet, Jacques Crommen, Anne-Catherine Servais and Marianne Fillet*

Laboratory for the Analysis of Medicines, Center for Interdisciplinary Research on Medicines (CIRM), University of Liege, Liege, Belgium

Phosphorothioate (PS) oligonucleotides have drawn more and more attention lately due to their great therapeutic potential. The presence of one (or several) phosphorothioate moiety (ies) improves pharmacokinetic properties but at the same time creates an additional chiral center for each phosphorothioate linkage, and thus diastereomers. It is therefore important to develop analytical strategies to monitor individual species to enable more in-depth investigations. In this study, a PVA coated capillary with a background electrolyte made of 100 mM phosphoric acid adjusted to pH 3.0 with triethanolamine was used. A design of experimental approach provides the optimal conditions for the separation of the eight isobaric diastereomers bearing one phosphorothioate linkage (Mix 1), and the separation of the 12 isobaric diastereomers of a mixture made of oligonucleotides with two phosphorothioate linkages (Mix 2). Remarkably, full separation in Mix 1 could be achieved using a combination of a cationic cyclodextrin (2-hydroxy-3-N,N,N-trimethylamino) propyl-γ-CD chloride, and an anionic cyclodextrin (carboxymethyl-β-cyclodextrin sodium salt), while a second cationic cyclodextrin (2-hydroxy-3-N,N,N-trimethylamino) propyl-β-CD chloride) was required for Mix 2, providing additional selectivity.

KEYWORDS

phosphorothioate oligonucleotide, diastereomeric separation, capillary electrophoresis, cyclodextrin, design of experiment

1 Introduction

Capillary electrophoresis (CE) is a powerful analytical technique widely used in various fields of research and industry for the separation of charged molecules based on their electrophoretic mobility in a capillary filled with an electrolyte solution (Schmitt-Kopplin, 2016).

The separation of enantiomers and diastereomers, compounds with identical molecular formulas and structural similarities but distinct three-dimensional spatial

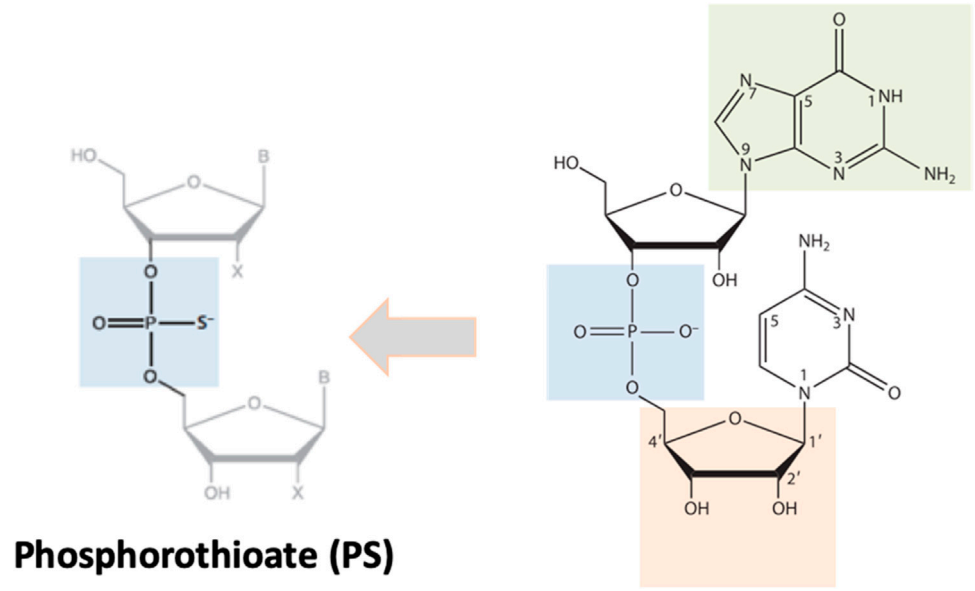

FIGURE 1
Structure of phosphorothioate linkage.

arrangements, has been a longstanding challenge in analytical chemistry and biochemistry. It is essential, especially in pharmacy and molecular biology, where the biological activity of a molecule often depends on its chirality. One breakthrough approach in achieving this separation is the use of CE and cyclodextrins (CDs) in the background electrolyte. CDs, cyclic oligosaccharides composed of glucose units, possess a cavity that can encapsulate molecules, forming inclusion complexes. Over the past few decades, the application of cyclodextrins in CE has revolutionized chiral separation, providing an efficient and high-resolution technique for resolving complex mixtures of chiral compounds (Chankvetadze et al., 1994; Fillet et al., 2000; Rudaz et al., 2000; Fradi et al., 2006; 2012; Marini et al., 2007; Lomsadze et al., 2009).

Phosphorothioate oligonucleotides are structural variants of nucleic acids, in which at least one of the oxygen atoms in the phosphate backbone is replaced with a sulfur atom, creating an additional chiral center for each phosphorothioate (PS) linkage and thus diastereomers (Figure 1). These diastereomers play a crucial role in biotechnology as they can be incorporated into synthetic DNA and RNA sequences, offering enhanced stability and resistance to enzymatic degradation (Iwamoto et al., 2017). Their unique properties have made them valuable tools for various applications, such as antisense oligonucleotide therapeutics and PCR amplification. Understanding the distinct characteristics of phosphorothioate oligonucleotide diastereomers is essential for exploiting their potential in the design of nucleic acid-based technologies and therapies (Genna et al., 2023).

In a recent study, preliminary investigations for the separation of short phosphorothioate oligonucleotide diastereomers with closely related structures were conducted (Demelenne et al., 2020; Ghassemi et al., 2022). We observed that to have a successful separation applying one type of CD is not efficient. An acidic BGE containing a dual CD system containing 25 mM (2-hydroxy-3-N,N,N-trimethylamino) propyl-γ-CD and 10 mM carboxymethyl-β-cyclodextrin was determined as the most appropriate system for the qualitative evaluation of the short oligonucleotides investigated. In the present study, we focused our attention on chemo- and stereoselectivity in two very challenging mixtures containing isomeric phosphorothioate oligonucleotides of identical molecular mass. A Design of Experiment (DoE) approach was used to model the effects of two types of positively charged CD derivatives on the separation.

Full Factorial Design (FFD) is a powerful approach that explores all possible combinations of factors and their levels in a minimum number of experiments. It was applied to investigate the effect of positively charged cyclodextrins, namely, (2-hydroxy-3-N, N, N-trimethylamino) propyl-γ-CD (QA-γ-CD) and (2-hydroxy-3-N, N, N-trimethylamino) propyl-β-CD (QA-β-CD), on the diastereomeric separation of 5-mer oligonucleotide compounds with 1 or 2 phosphorothioate linkages in different positions (Table 1). It provided an understanding of how variables interact with each other and their impact on the number of peaks detected and the resolution of critical pairs, making it a valuable tool for the optimization of diastereomeric separations by CE.

2 Material and methods

2.1 Chemicals

All lyophilized oligonucleotide samples were supplied by Integrated DNA Technologies (Coralville, IA, United States of America). Carboxymethyl-β-cyclodextrin sodium salt (CM-β–CD)

TABLE 1 Composition of oligonucleotide mixtures.

Compound name		Sequence (^{S}= PS link with phosphorous in sp configuration; ^{R}= PS link with phosphorous in Rp configuration)	Number of stereoisomers	Number of stereoisomers in the mixture	MW (g/mol)
Mix 1	**PS 1_1**	5′-T^{S}CGTG-3′ 5′-T^{R}CGTG-3′	2	8	1510.1
	PS 1_2	5′-TC^{S}GTG-3′ 5′-TC^{R}GTG-3′	2		
	PS 1_3	5′-TCG^{S}TG-3′ 5′-TCG^{R}TG-3′	2		
	PS 1_4	5′-TCGT^{S}G-3′ 5′-TCGT^{R}G-3′	2		
Mix 2	**PS 2_1,3**	5′-T^{S}CG^{S}TG-3′ 5′-T^{R}CG^{S}TG-3′ 5′-T^{S}CG^{R}TG-3′ 5′-T^{R}CG^{R}TG-3′	4	12	1526.2
	PS 2_2,3	5′-TC^{S}G^{S}TG-3′ 5′-TC^{R}G^{S}TG-3′ 5′-TC^{S}G^{R}TG-3′ 5′-TC^{R}G^{R}TG-3′	4		
	PS 2_3,4	5′-TCG^{S}T^{S}G-3′ 5′-TCG^{R}T^{S}G-3′ 5′-TCG^{S}T^{R}G-3′ 5′-TCG^{R}T^{R}G-3′	4		

10.3389/frans.2024.1421463

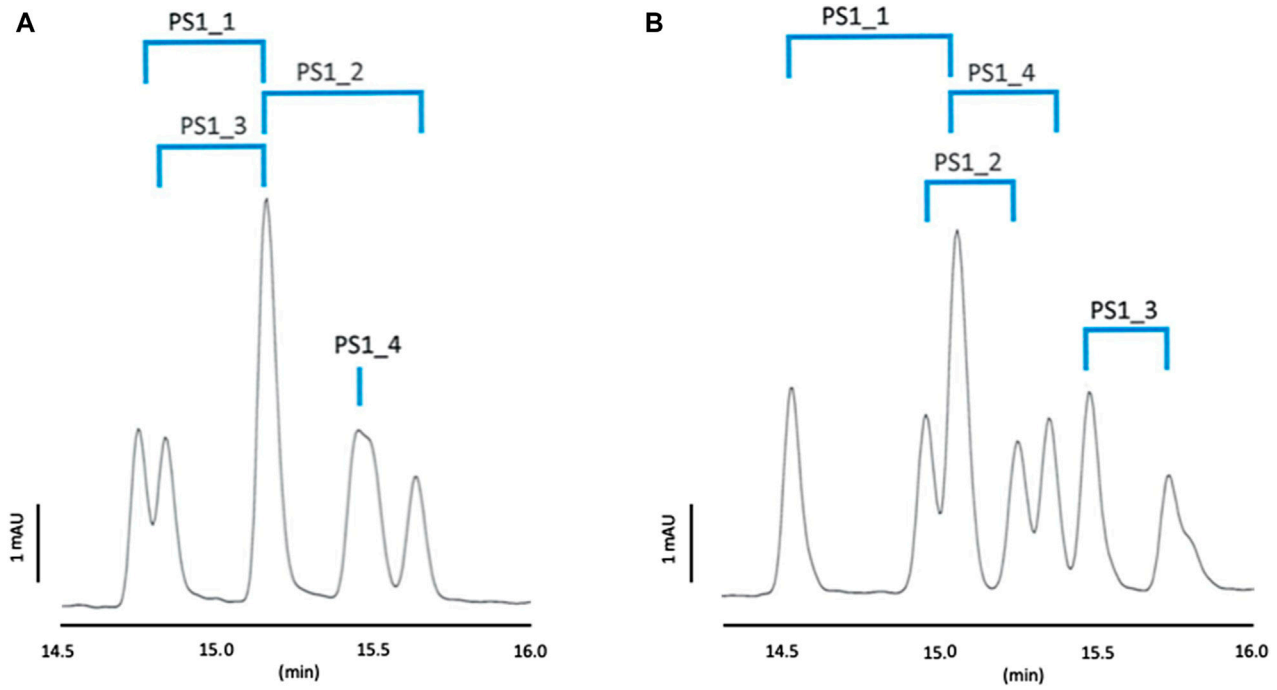

FIGURE 2
Separation profiles of Mix 1. BGE: 100 mM phosphoric acid adjusted with TEA to pH 3.0 containing 10 mM CM-β-CD and 5 mM QA-β-CD **(A)** or 5 mM QA-γ-CD **(B)**, capillary temperature: 25°C, current ~ 75 μA.

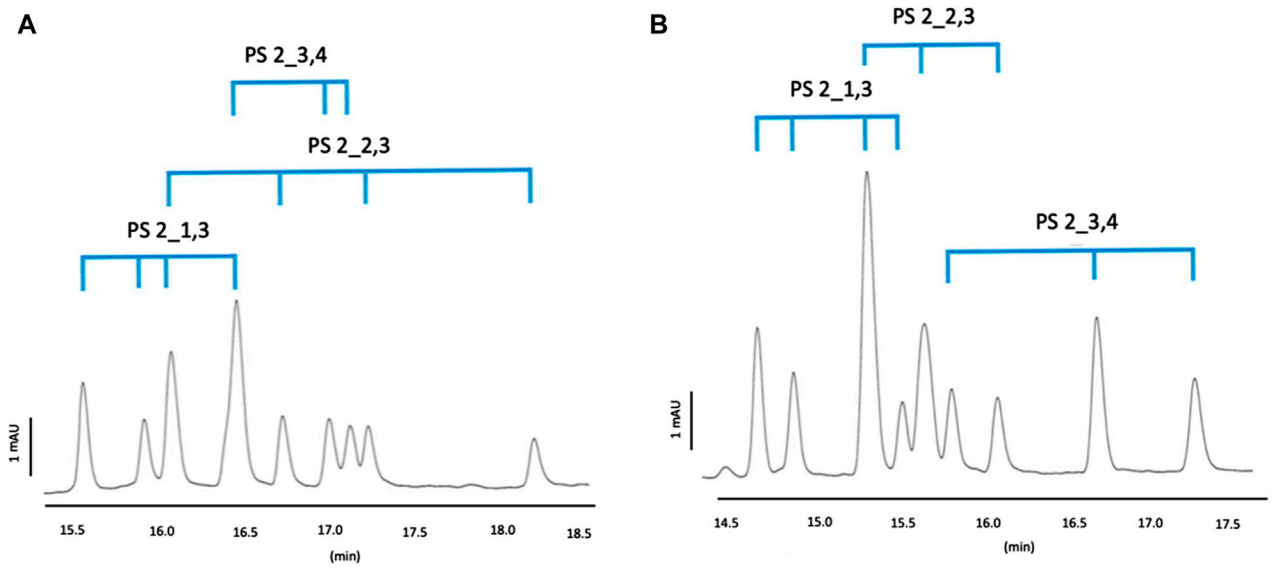

FIGURE 3
Separation profiles of Mix 2, BGE: 100 mM phosphoric acid adjusted by TEA pH 3.0 containing 10 mM CM-β-CD and 5 mM QA-β-CD **(A)** or 5 mM QA-γ-CD **(B)**, capillary temperature: 25°C, current ~ 75 μA.

(DS~3.5) (2-hydroxy-3-N, N, N-trimethylamino) propyl-γ-CD chloride (QA-γ–CD) (DS~3.4), and (2-hydroxy-3-N, N, N-trimethylamino) propyl-*β*-CD chloride (QA-β–CD) (DS~3.4) were provided by Cyclolab (Budapest, Hungary).

Triethanolamine (TEA) and methanol were supplied by Merck (Darmstadt, Germany). Phosphoric acid 85% was purchased from VWR Chemicals (Leuven, Belgium). Ultrapure water was provided by Milli-Q equipment (Millipore, Bedford, MA, United States) and Chromafil syringe filters (0.20 μm) were from Macherey-Nagel (Düren, Germany). All chemicals were of analytical grade and used without further purification.

TABLE 2 Predicted resolution values with the confidence intervals for the critical pairs under the optimum concentrations of each cationic CD for the two oligonucleotide mixtures.

	Rs			No of peaks
	3–4	4–5	6–7	
Mix 1: 10 mM QA-γ-CD	1.4 [0.4–2.4]	2.0 [0.9–3.0]	1.9 [1.0–2.9]	8
	Rs			No of peaks
	2–3	3–4	5–6	6–7	
Mix 2: 10 mM QA-β-CD + 3 mM QA-γ-CD	3.0 [2.3–3.6]	1.7 [1.4–2.0]	1.0 [0.5–1.5]	2.4 [1.1–3.6]	12

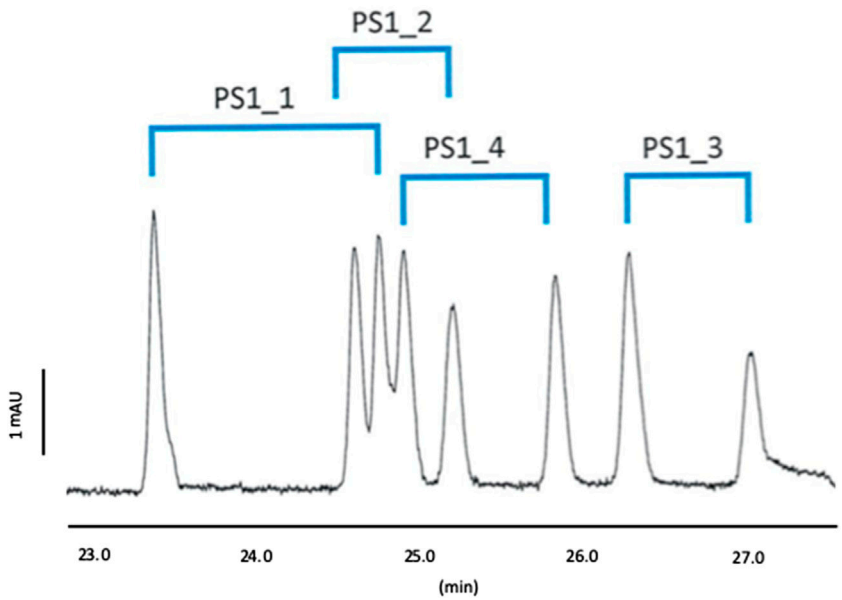

FIGURE 4
Separation profile of Mix 1; BGE: 100 mM phosphoric acid adjusted by TEA pH 3.0 with 7.5% MeOH containing 10 mM CM-β-CD and 10 mM QA-γ-CD; Capillary temperature: 15°C.

2.2 Oligonucleotides

The oligonucleotides investigated had the following sequence: 5′-TCGTG-3'. Variations were related to the amount and position of PS linkages. The individual lyophilized oligonucleotides were reconstituted separately in ultrapure water at 1 mM concentration. Subsequently, all samples were diluted to a final concentration of 50 µM in water. To prepare Mix 1, comprising PS 1_1, PS 1_2, PS 1_3, and PS 1_4 (as detailed in Table 1), these compounds were diluted in water to obtain a concentration of 50 µM for each component. Mix 2, comprising PS 2_1,3, PS 2_2,3 and PS 2_3,4 was prepared using the same approach.

2.3 Equipment

Separations were carried out on a G7100 CE system (Agilent Technologies, Waldbronn, Germany) coupled to a Diode-Array Detector (DAD). A PVA-coated fused-silica capillary of 64.5 cm long (50 µm ID, 56 cm effective length) was used to perform the experiments (Agilent Technologies, Germany). Hydrodynamic injection was used for all samples by applying a pressure of 50 mbar for 6 s, following by an injection of BGE at 50 mbar for 4 s. The separation voltage was set at −30 kV during the experiments. The UV-detection wavelength was set at 254 ± 4 nm. Instrument control and data acquisition were achieved using the Agilent Openlab version 2.7 software.

2.4 CE operating conditions

A new capillary was conditioned first by flushing water, followed by BGE, for 15 min each. At the beginning of each day, the capillary was rinsed with water and then by BGE, both for 10 min. In addition, before each run, water and BGE were successively flushed both for 5 min. The capillary was washed at the end of

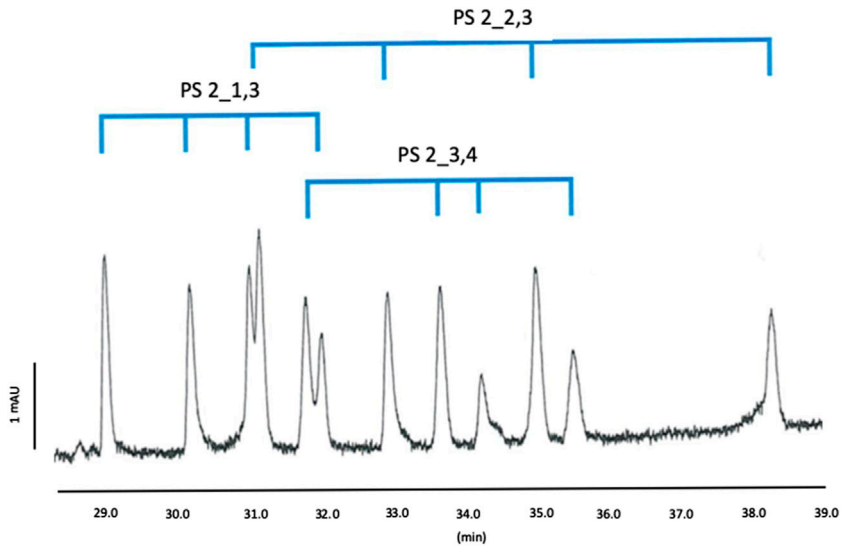

FIGURE 5
Separation profile of Mix 2, BGE: 100 mM phosphoric acid adjusted by TEA pH 3.0 with 7.5% MeOH containing 10 mM CM-β-CD, 10 mM QA-β-CD and 3 mM QA-γ-CD; Capillary temperature: 15°C.

each sequence with water for 30 min and then dried with air for 5 min. Rinses were performed at a pressure of approximately 1 bar. The BGE consisted of 100 mM phosphoric acid adjusted to pH 3.0 ± 0.1 with TEA before CD addition.

2.5 Computation

Experimental design (Supplementary Table S1) and data analysis were performed using JMP software version 17.2.0 (SAS Institute, Inc., Cary, NC, United States).

3 Results and discussion

Several critical parameters play a pivotal role in the CE separation of phosphorothioate oligonucleotide diastereomers using CDs as chiral selectors, such as the choice of BGE, the BGE pH, the capillary length and voltage, and of course, the type and concentration of the CD, possibly used in combination with another one. In our previous article (Ghassemi et al., 2022), various BGEs as well as charged, negatively charged and neutral CDs were investigated for the separation of 5-mer oligonucleotides containing 0, 1, 2, or 3 phosphorothioate linkages. Combining a positively charged cyclodextrin (QA-b-CD or QA-g-CD) with a weakly negatively charged (CM-b-CD) cyclodextrin improved chemo- and enantio-selectivity in a BGE made of 100 mM phosphoric acid adjusted to pH 3.

3.1 Application of previously selected conditions for mix 1 and mix 2

First, we applied the dual CD system conditions selected in a previous study dealing with another mixture of short oligonucleotides (Ghassemi et al., 2022). The BGE was made of a mixture of QA-γ-CD and CM-β-CD or QA-β-CD and CM-β-CD, in 100 mM phosphoric acid-TEA pH 3.0 buffer.

By employing charged CD derivatives, the influence of electrostatic interactions can alter the separation mechanism and profile. Consequently, utilizing chiral selectors possessing an opposite charge to that of the analytes can be highly advantageous for enhancing resolution. Indeed, a wider separation window provides greater flexibility for effectively separating compounds with limited resolution (Blanco et al., 2003).

The combination of 25 mM QA-β-CD or 25 mM QA-γ-CD as a positively charged CD and 10 mM CM-β-CD as a weakly negatively charged CD was first tested (data not shown). By using 25 mM QA-β-CD and 10 mM CM-β-CD, half of the peaks in Mix 1 (4 out of 8) and 9 out of 12 peaks for Mix 2 were observed. A combination of 25 mM of QA-γ-CD and 10 mM CM-β-CD provided better separation of the compounds of Mix 1 (7 out of eight peaks were detected).

To obtain a lower current, shorter migration times and a more stable baseline, a five times lower concentration of the positively charged CDs was tested. The results obtained for Mix 1 and Mix 2 are shown in Figures 2A, B. Each sample was also injected independently in order to assign the peaks.

As can be seen in Figure 2A with QA-β-CD derivative, the PS1_4 diastereomeric pair was not separated and 5 peaks out of eight could be observed, which confirms the poor chemoselectivity provided by this cyclodextrin. On the contrary, all diastereomeric pairs were separated with QA-γ-CD (see Figure 2B), and 7 out of the eight peaks were visible. QA-γ–CD showed thus better chemo- and stereoselectivity, and its concentration should be further optimized for Mix 1. It is also worth mentioning to note that the two studied cationic cyclodextrins do not show the same PS selectivity and profile.

For Mix 2, QA-β-CD could separate the 4 diastereomers of PS2_1,3 and PS2_2,3 but not those of PS2_3,4 (Figure 3A). QA-γ-CD could separate the 4 diastereomers of PS2_1,3 but not those of PS2_2,3 and PS2_3,4 (Figure 3B). In both cases, 9 out of the 12 peaks were observed. As for Mix 1, QA-β-CD and QA-γ-CD do not show the same chemo- and stereoselectivity. QA-β-CD shows the strongest affinity for PS2_2,3, while QA-γ-CD shows the strongest affinity for PS2_3,4. So it could be interesting to test their combination to optimize Mix 2 separation.

Overall, QA-γ-CD showed more promising separation for Mix 1 and inversely, QA-β-CD for Mix 2. Since at lower CD concentrations, an improvement in the resolution of critical pairs and much lower current were observed, it was decided to select the 5 mM concentration for both cationic CDs in further experiments.

3.2 Impact of capillary temperature and methanol on separation

To further investigate the critical experimental parameters, we considered three critical pairs in Mix 1 and four critical pairs in Mix 2 (the critical pair selection was based on full separation profiles obtained in DoE runs, see Section 3.3). Both positional isomers and diastereomers were involved in critical pairs for both mixtures considering that the separation of diastereomers identified as critical pairs was the most complicated.

Temperature can significantly influence the complexation between the chiral selector (CD) and the analytes, impacting both the efficiency and selectivity of the separation. Higher capillary temperatures can enhance analyte mobility, potentially reducing analysis times, but too high temperatures may compromise cyclodextrin complex stability, leading to lower peak resolution. Conversely, lower temperatures can strengthen interactions and improve selectivity at the expense of longer analysis times. Lowering the temperature to 15°C led to a slight improvement in selectivity. Therefore, 15°C was selected for further experiments.

Methanol is often employed to adjust the electrophoretic mobility of analytes, and its concentration in the electrolyte can influence the interactions between the chiral selector and the analytes. An increase in methanol concentration typically leads to reduced viscosity and decreases the electroosmotic flow, which can result in longer analysis times and potentially improved separation efficiency. Methanol contents of 5%–10% were investigated since too high amounts can disrupt the formation of stable complexes between the cyclodextrin and the diastereomers, leading to peak distortion or even loss of resolution. In this study, the addition of methanol did not lead to any increase in resolution but improved the stability of the method, and the methanol content was kept at 7.5%.

3.3 Full factorial design of experiment

In the context of optimizing the CE separation of diastereomers using a combination of cationic and slightly anionic CDs, DoE plays a major role in systematically exploring the intricate interplay of factors that can influence the separation. A full factorial design allows researchers to investigate several factors simultaneously at various levels (Jiju, 2023). These levels refer to specific values or settings at which each factor is tested. According to the abovementioned results, the concentrations of the positively charged CDs were considered the main factors in the elaboration of the FFD at five levels (0, 2.5, 5.0, 7.5, and 10 mM) (Supplementary Table S1). This design comprised 28 runs with three replicates at the central point to evaluate repeatability. All analytes were analysed separately as well as in mixture. Other parameters considered as constant factors were the voltage (−30 kV), the percentage of organic modifier (methanol at 7.5%), the temperature (15°C) and CM-β-CD concentration (10 mM). The concentration of the anionic cyclodextrin was not investigated further, as we had already shown in a previous study (16), and with additional tests (up to 45 mM), concentrations higher than 10 mM only increased viscosity and migration time and had no significant effect on the separation profile.

By choosing the number of peaks and resolution of critical pairs in each mixture as responses (namely, resolution between peaks 3–4, 4-5, and 6-7 in Mix 1 and peaks 2–3, 3–4, 5-6 and 6-7 in Mix 2), we evaluated the data obtained in the 28 runs. The desirability value is a crucial concept to assess the overall quality of a set of experimental conditions with different units or scales, which are combined into a single value. By assigning weights to each response variable to express their relative importance, we used desirability functions to optimize the separation, seeking conditions that maximize the overall desirability value.

Each response was modelled according to the following equation:

$$Y = \beta_0 + \beta_1 X_1 + \beta_2 X_2 + \beta_{12} X_1 X_1 + \varepsilon$$

where β_0 is the intercept, β_1 and β_2 the main effect terms, β_{12} the interaction term, X_1 the QA-β-CD concentration, X_2 the QA-γ-CD concentration and ε the error term.

The coefficients of the model with their statistical significance are presented in Supplementary Table S2. The *p*-value represents the probability of obtaining a result as extreme or more extreme than the observed one, assuming the proposed null hypothesis is true. A factor is considered as significant if its *p*-value is lower than 0.05.

As can be seen in Supplementary Table S2, for Mix 1, QA-γ-CD concentration has a positive impact on the resolution of critical pair 3-4 through its main term, while the interaction between CD concentrations has a significant impact on critical pair 4-5 and the peak number. For Mix 2, significant impacts of QA-β-CD concentration on the separation of critical pairs 2-3 and 3-4 and of QA-γ-CD concentration on critical pairs 2-3 and 6-7 can be observed. The interaction between the two cationic CD concentrations shows a significant effect on all responses, except on critical pairs 6–7. Overall, it can be concluded that the interaction between these two CD concentrations has an impact on the separation of compounds in Mix 2, particularly.

Table 2 presents the predicted R_s values with the confidence intervals for the critical pairs under the optimum concentrations of

each cationic CD for the chemo- and stereo-separation with a desirability of 0.9 in Mix 1 (0.35 mM QA-β-CD and 9.98 mM QA-γ-CD) and a desirability value of 0.75 in Mix 2 (10 mM QA-β-CD and 2.91 mM QA-γ-CD). For practical reasons, we used a BGE made of 10 mM QA-γ-CD for Mix 1 and of 10 mM QA-β-CD and 3 mM QA-γ-CD for Mix 2.

Those conditions were tested experimentally. Figures 4, 5 show the electropherograms under the optimal CD concentrations for Mix 1 and Mix 2.

As the optimal conditions are located at the limits of the experimental domain, CD concentrations higher than 10 mM were tested in order to further increase the resolution values. Nevertheless, no improvement was observed, confirming that the DoE fulfilled its objectives.

Accordingly, we could confirm the prediction of the DoE, allowing the detection of all the expected peaks, i.e. 8 peaks for Mix 1 and 12 peaks for Mix 2, as shown in Figures 4, 5.

4 Conclusion

By combining cyclodextrins with different charge states and testing two different cavity sizes (beta and gamma), it has become possible to exploit a wider spectrum of interactions, in order to achieve better separation selectivity, particularly for mixture 2; bearing in mind that larger cyclodextrin cavities (gammaCD) generally result in longer migration times due to the stronger formation of inclusion complexes. Overall, the interaction between the nature and concentration of cyclodextrins, cavity size and their use in combination is complex and requires careful optimization. By systematically applying the principles of DoE, we have identified the optimum conditions for obtaining better separation of isobaric phosphorothioate oligonucleotides as a function of their chiral centers and overall molecular architectures.

Data availability statement

The raw data supporting the conclusion of this article will be made available by the authors, without undue reservation.

Author contributions

MG: Investigation, Methodology, Writing–original draft. VH: Investigation, Methodology, Writing–review and editing. JC: Writing–review and editing. A-CS: Methodology, Writing–review and editing, Supervision. MF: Conceptualization, Funding acquisition, Investigation, Project administration, Resources, Writing–original draft, Writing–review and editing, Supervision.

Funding

The author(s) declare financial support was received for the research, authorship, and/or publication of this article. The authors thank the University of Liege and the Foundation Léon Frédéricq for the financial support.

Conflict of interest

The authors declare that the research was conducted in the absence of any commercial or financial relationships that could be construed as a potential conflict of interest.

The author(s) declared that they were an editorial board member of Frontiers, at the time of submission. This had no impact on the peer review process and the final decision.

Publisher's note

Supplementary material

The Supplementary Material for this article can be found online at: https://www.frontiersin.org/articles/10.3389/frans.2024.1421463/full#supplementary-material

References

Blanco, M., and Valverde, I. (2003). Choice of chiral selector for enantioseparation by capillary electrophoresis. *TrAC* 22 (7), 428–439. doi:10.1016/S0165-9936(03)00705-2

Chankvetadze, B., Endresz, G., and Blaschke, G. (1994). About some aspects of the use of charged cyclodextrins for capillary electrophoresis enantioseparation. *Electrophoresis* 15 (1), 804–807. doi:10.1002/elps.11501501113

Demelenne, A., Gou, M. J., Nys, G., Parulski, C., Crommen, J., Servais, A. C., et al. (2020). Evaluation of hydrophilic interaction liquid chromatography, capillary zone electrophoresis and drift tube ion-mobility quadrupole time of flight mass spectrometry for the characterization of phosphodiester and phosphorothioate oligonucleotides. *J. Chromatogr. A* 1614, 460716. doi:10.1016/j.chroma.2019.460716

Fillet, M., Hubert, P., and Crommen, J. (2000). Enantiomeric separations of drugs using mixtures of charged and neutral cyclodextrins. *J. Chromatogr. A* 875 (1-2), 123–134. doi:10.1016/s0021-9673(00)00084-4

Fradi, I., Servais, A. C., Lamalle, C., Kallel, M., Abidi, M., Crommen, J., et al. (2012). Chemo-and enantio-selective method for the analysis of amino acids by capillary electrophoresis with in-capillary derivatization. *J. Chromatogr. A* 1267, 121–126. doi:10.1016/j.chroma.2012.05.098

Fradi, I., Servais, A. C., Pedrini, M., Chiap, P., Iványi, R., Crommen, J., et al. (2006). Enantiomeric separation of acidic compounds using single-isomer amino cyclodextrin derivatives in nonaqueous capillary electrophoresis. *Electrophoresis* 27 (17), 3434–3442. doi:10.1002/elps.200500643

Genna, V., Iglesias-Fernández, J., Reyes-Fraile, L., Villegas, N., Guckian, K., Seth, P., et al. (2023). Controlled sulfur-based engineering confers mouldability to phosphorothioate antisense oligonucleotides. *Nucleic Acids Res.* 51 (10), 4713–4725. doi:10.1093/nar/gkad309

Ghassemi, K. M., Demelenne, A., Crommen, J., Servais, A. C., and Fillet, M. (2022). Improvement of chemo- and stereoselectivity for phosphorothioate oligonucleotides in capillary electrophoresis by addition of cyclodextrins. *J. Chromatogr. A* 1676, 463270. doi:10.1016/j.chroma.2022.463270

Iwamoto, N., Butler, D. C. D., Svrzikapa, N., Mohapatra, S., Zlatev, I., Sah, D. W. Y., et al. (2017). Control of phosphorothioate stereochemistry substantially increases the efficacy of antisense oligonucleotides. *Nat. Biotechnol.* 35 (9), 845–851. doi:10.1038/nbt.3948

Jiju, A. (2023) *Design of experiments for engineers and scientists*. 3. Elsevier, 65–87. ISBN 9780443151736. doi:10.1016/B978-0-443-15173-6.00009-3

Lomsadze, K., Martínez-Girón, A. B., Castro-Puyana, M., Chankvetadze, L., Crego, A. L., Salgado, A., et al. (2009). About the role of enantioselective selector-selectand interactions and the mobilities of diastereomeric associates in enantiomer separations using CE. *Electrophoresis* 30 (16), 2803–2811. doi:10.1002/elps.200900076

Marini, R. D., Rozet, E., Vander, H. Y., Ziemons, E., Boulanger, B., Bouklouze, A., et al. (2007). Robustness testing of a chiral NACE method for R-timolol determination in S-timolol maleate and uncertainty assessment from quantitative data. *JPBA* 44 (3), 640–651. doi:10.1016/j.jpba.2006.08.018

Rudaz, S., Cherkaoui, S., Dayer, P., Fanali, S., and Veuthey, J. L. (2000). Simultaneous stereoselective analysis of tramadol and its main phase I metabolites by on-line capillary zone electrophoresis–electrospray ionization mass spectrometry. *J. Chromatogr. A* 868 (2), 295–303. doi:10.1016/S0021-9673(99)01257-1

Schmitt-Kopplin, P. (2016) *Capillary electrophoresis: methods and protocols*. 2. Totowa, United States: Humana Press.

frontiers | Frontiers in Analytical Science

TYPE Original Research
PUBLISHED 30 July 2024
DOI 10.3389/frans.2024.1399843

OPEN ACCESS

EDITED BY
Marianne Fillet,
University of Liège, Belgium

REVIEWED BY
Igor Magalhães,
Federal University of Amazonas, Brazil
Ashok K. Shakya,
Al-Ahliyya Amman University, Jordan

*CORRESPONDENCE
Yehualashet Teshome Wondmkun,
yehualiars@gmail.com

RECEIVED 12 March 2024
ACCEPTED 17 June 2024
PUBLISHED 30 July 2024

CITATION
Wondmkun YT, Desta HK, Ali YS, Tsige AW, Ayenew KD, Endalifer BL and Dagnew SB (2024), *In vitro* comparative quality assessment of different brands of hydrochlorothiazide tablets marketed in Northeast Ethiopia.
Front. Anal. Sci. 4:1399843.
doi: 10.3389/frans.2024.1399843

In vitro comparative quality assessment of different brands of hydrochlorothiazide tablets marketed in Northeast Ethiopia

Yehualashet Teshome Wondmkun[1]*, Haile Kassahun Desta[2], Yimer Seid Ali[2], Abate Wondesen Tsige[3], Kassahun Dires Ayenew[4], Bedilu Linger Endalifer[3] and Samuel Berihun Dagnew[5]

[1]Department of Pharmacy, Pharmaceutical Chemistry Unit, Asrat Woldeyes Health Science Campus, Debre Berhan University, Debre Berhan, Ethiopia, [2]Department of Pharmacy, Pharmaceutical Chemistry Unit, College of Health Sciences, Wollo University, Dessie, Ethiopia, [3]Department of Pharmacy, Clinical Pharmacy Unit, Asrat Woldeyes Health Science Campus, Debre Berhan University, Debre Berhan, Ethiopia, [4]Department of Pharmacy, Pharmacology Unit, Asrat Woldeyes Health Science Campus, Debre Berhan University, Debre Berhan, Ethiopia, [5]Department of Pharmacy, Clinical Pharmacy Unit, Collage of Health Sciences, Debre Tabor University, Debre Tabor, Ethiopia

Background: This study aimed to comparatively evaluate the quality and physicochemical bioequivalence of commercially available brands of hydrochlorothiazide (HCT) tablets in community pharmacies in Dessie town, Northeast Ethiopia.

Methods: Experimental cross-sectional study design was applied using pharmacopeia and non-pharmacopeia methods. The difference (f1) and similarity (f2) factors were calculated to assess the *in vitro* bioequivalence of generic products with the comparator.

Result: The study results revealed that all investigated brands contained the required active pharmaceutical ingredients (APIs). The friability test results were concordant with the United States Pharmacopeia (USP) (<1%) for eight brands; however, brand NF3 (1.36%) failed to pass the specification limit. The hardness levels of the brands NF3 (24.20 ± 7.32 N), NF5 (32.19 ± 4.78 N), and NF9 (35.02 ± 3.12 N) were below the specification limit (39.23 N, USP 2019). The weight variation results of all generic products complied with the USP specification requirement. In the quantitative assay results, the minimum and maximum API contents were 97.4 ± 0.02 (NF6) and 105.8 ± 0.02 (NF8), respectively, which are within the limit specified by the USP (90%–110%). Similarly, all samples met the disintegration time limit (i.e., ≤30 min) and drug-releasing tolerance limit (API released more than 60% within 60 min) requirements. The f2 values were >50, and the f1 values were <15 for all sampled brands.

Conclusion: The majority of the sampled brands of HCT tablets met the quality requirements as per USP official test specifications. From the similarity and difference factor values, all studied brands were shown to be equivalent.

KEYWORDS

hydrochlorothiazide, *in vitro*, quality, weight variation, assay, equivalence

Introduction

Patients often require pharmacological and non-pharmacological treatments for sustained blood pressure reduction. With the development of many antihypertensive drugs, effective management of hypertension has become a reality with minimum side effects. In general, there are five classes of antihypertensive drugs that are used nowadays to decrease blood pressure by minimizing cardiac output or total peripheral vascular resistance. These include beta blockers, diuretics, angiotensin-converting-enzyme inhibitors, angiotensin receptor blockers, and calcium channel blockers (Karmoker et al., 2017).

Hydrochlorothiazide (HCT) is the most prescribed thiazide diuretic with or without other antihypertensive medications to control elevated blood pressure. More than 97% of all HCT prescriptions are based on doses of 12.5–25 mg per day (Pareek et al., 2016). HCT is also an adjuvant medication for treating edematous patients secondary to congestive heart failure, hepatic cirrhosis, as well as corticosteroid and estrogen therapies. It is a white, odorless, and crystalline powder having a slightly bitter taste and a molecular weight of 297.74 g/mol, and its chemical structure is as illustrated in Figure 1 (Pires et al., 2011). The primary target organs of diuretics are the kidneys, and they exert significant activities in the distal convoluted tubules. This produces remarkable diuresis of sodium and chloride ions in equivalent amounts (Pareek et al., 2016). Therefore, the quality of marketed antihypertensive medications should be addressed and assured before reaching the patients. This is one of the reasons for the prevalence of death due to uncontrolled blood pressure, which is increasing every day. For example, studies have shown that 16.5% of the global deaths and 7.0% of global disability-adjusted life years are due to poor control of blood pressure (Lim et al., 2012). A WHO report showed that 31.1% of adults (1.39 billion) worldwide had hypertension (Mills et al., 2020) and that 13% of the global death counts were due to elevated blood pressure (Dreisbach and Batuman, 2013). Ineffective control of blood pressure may be attributed to poor quality of medications used by the patients. For example, approximately 24.3% (202/830) of the generic and 3.5% (11/310) of the branded products for five common antihypertensive medicines (captopril, amlodipine, atenolol, HCT, and furosemide) were found to be substandard in about ten African countries (World Health Organization, 2017).

For effective blood pressure reduction, the medications must be safe and contain therapeutically active formulations with consistent and predictable effects (Noor et al., 2017). Different brands of the same products must have the same quality, strength, purity, and dissolution patterns, or they must be biopharmaceutically and chemically comparable in clinical use (Afifi and Ahmadeen, 2012). Hence, providing high product quality to the community is a sustainable requirement in healthcare systems. However, there are inadequate pharmaceutical industries and quality monitoring policies to deliver sufficient and qualified medicine to the communities across Africa. The quality of pharmaceutical products is assured by the acceptance limits of the active pharmaceutical ingredients (APIs) in the pharmaceutical products. Formulations having APIs above or below the specified levels are considered to be of poor quality. As a result, the two main types of poor-quality medicines are substandard and falsified products (Karmoker et al., 2017).

Substandard manufacturing of legitimate drugs is attributable to a lack of proper quality management procedures during manufacturing (Ozawa et al., 2018). Falsified drugs are a type of poor-quality medicines with hazardous quality or wrong ingredients that are disguised intentionally as genuine medications (Bassat et al., 2016a). Substandard and falsified drug manufacturing is a serious and underreported issue that mainly harms developing countries. The circulation of poor-quality medicines is a critical public health problem in managing different types of communicable and non-communicable diseases (NCDs) common in developing countries (Koczwara and Dressman, 2017); it results in treatment failures with prolonged or more severe sickness with conditions leading to death, development of drug resistance, and adverse drug reactions as well as higher healthcare costs, all of which can negatively affect public trust in the healthcare system (Kovacs et al., 2014).

The use of substandard or falsified medicines causes serious public health issues by increasing the global morbidity and mortality rates (Almuzaini et al., 2013). According to a WHO report, about 10.5% of drugs produced globally are substandard or falsified products. Furthermore, because of inadequate pharmaceutical governance, resources, trained personnel, technological capabilities, and supply-chain management, most of the burden of such products rests on low- and middle-income countries (LMICs) (Rojas-Cortés, 2020). According to the most recent study by the Minimum Development Goal Gap Task Force, up to 80% of mortality from NCDs occurs in LMICs (Yusuf et al., 2014). An assessment of drug quality implemented from 2017 to 2018 in 13 countries of Latin America showed that 236 items were substandard and that 239 drug products were falsified. In sub-Saharan Africa, for example, it is estimated that about 34% of the available drugs are of poor quality with poor pharmacovigilance and drug regulatory structures (Who, 2013). The prevalence of poor-quality drugs is significantly higher for in certain classes of cardiovascular drugs. Around 3,468 cardiovascular drug samples were collected from 10 sub-Saharan countries; out of 1,530 samples, 249 (16.3%) were below the quality standards (Antignac et al., 2017).

According to WHO reports (2017), 42% of the medicines circulating in African countries are either substandard or falsified (World Health Organization, 2017). A study in south Togo showed that the content of APIs in HCT tablets deviated by more than 25% from the declared amounts required by the United States Pharmacopeia (USP) (Antignac et al., 2017). All pharmaceutical products must meet the desired quality standards and must be bioequivalent so that different brands can be prescribed interchangeably. For example, out of five brands of nifedipine marketed in India, one brand failed to meet the specification for uniformity of content and assay (<90%) (Sharma et al., 2006). The factors that critically affect the fabrication, distribution, and use of poor-quality pharmaceuticals as well as severely jeopardize national healthcare systems also impose substantial public health risks with several negative consequences (Schiavetti et al., 2020).

An *in vitro* quality study on seven metformin hydrochloride tablet brands circulated in Ethiopia showed that four were not bioequivalent. Their difference factor (f1) values were below 50 (19, 41, 37, and 39) and similarity factor (f2) values were above 15 (38, 16, 17, and 17 with respect to the f1 values). Such variations may

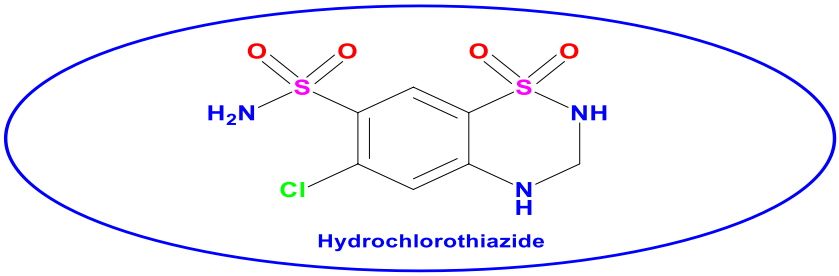

FIGURE 1
hemical structure of hydrochlorothiazide.

TABLE 1 General descriptions of the hydrochlorothiazide 25 mg tablet marketed in the community pharmacies of Dessie town, Northeast Ethiopia.

Code	Brand name	Manufacturer	Country of origin	Batch no.	Manufacture date	Expiry date	Price per tab (Ethiopian birr)
NF 1	HCT-Asthiazide	Madras Pharm	India	ME20B52	Feb-20	Jan-22	3.35
NF 2	HCT-Corzide	Coral Lab Ltd.	India	DCZY2001	Feb-20	Jan-23	1.6
NF 3	HCT-SSP	Sansheng Pharm PLC	Ethiopia	720020010	Feb-20	Jan-22	1.8
NF4	HCT-Cyprus	Limas Sol Industrial	Cyprus-EU	69246	Jul-18	Jul-22	12.1
NF5	HCT-M.Biot	Medicament Biotech	India	NT00074	Apr-20	Mar-23	3.4
NF 6	HCT-Esidrex	Juvise Pharmaceutical	France	F2074	Jun-20	Jun-23	12.7
NF 7	HCT-Novartis	Salutes Pharma GmbH	Germany	KL9471	Jan-20	Dec-21	2.5
NF 8	HCT-Lirplan	Encore Healthcare Pv	India	Ec002	Jun-20	May-23	2.25
NF 9	HCT-Hinozide	Human Well P. PLC	Ethiopia	95210202	Feb-21	Feb-23	0.4

TABLE 2 Peak retention time results of different brands of hydrochlorothiazide 25 mg tablets and the reference standard.

No	Samples tested with the HPLC system	Peak retention time (min)	Telling factor (%)	Peak area (%)
1	Standard	5.783	1.12	0.03
2	NF1	5.69		
3	NF2	5.687		
4	NF3	5.718		
5	NF4	5.683		
6	NF5	5.708		
7	NF6	5.74		
8	NF7	5.658		
9	NF8	5.663		
10	NF9	5.72		

cause treatment failure or resistance to the medication when used interchangeably (Tesfay et al., 2019). Hence, in sub-Saharan countries like Ethiopia, the quality monitoring of pharmaceutical products is not applied strictly across the board, and the prevalence rates of poor-quality medicines are high. For example, a quality analysis study in Ethiopia revealed that 29.2% of samples among 106 combined samples of albendazole, mebendazole, and tinidazole did not meet the pharmacopeia acceptance specifications for assay

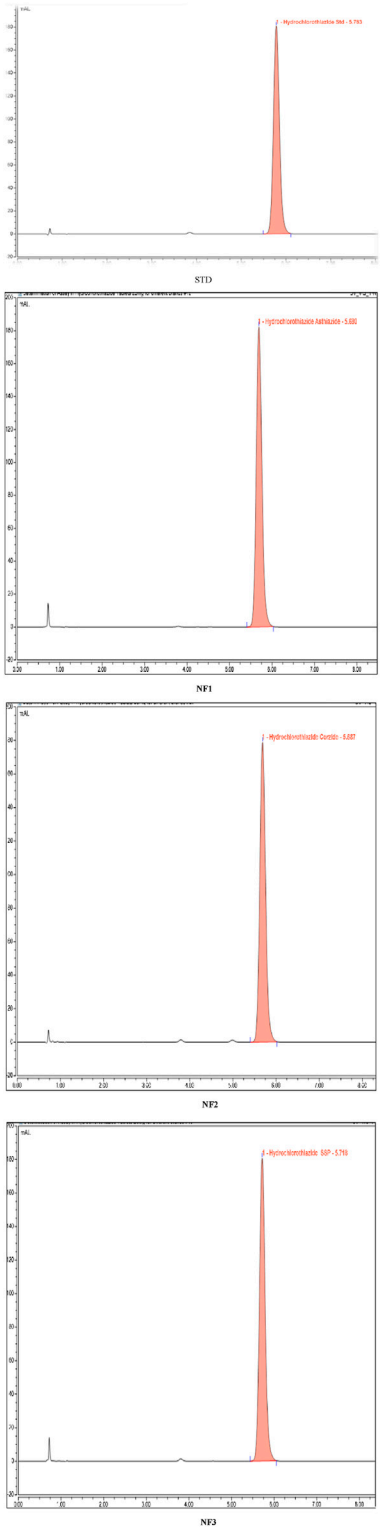

FIGURE 2
(Continued).

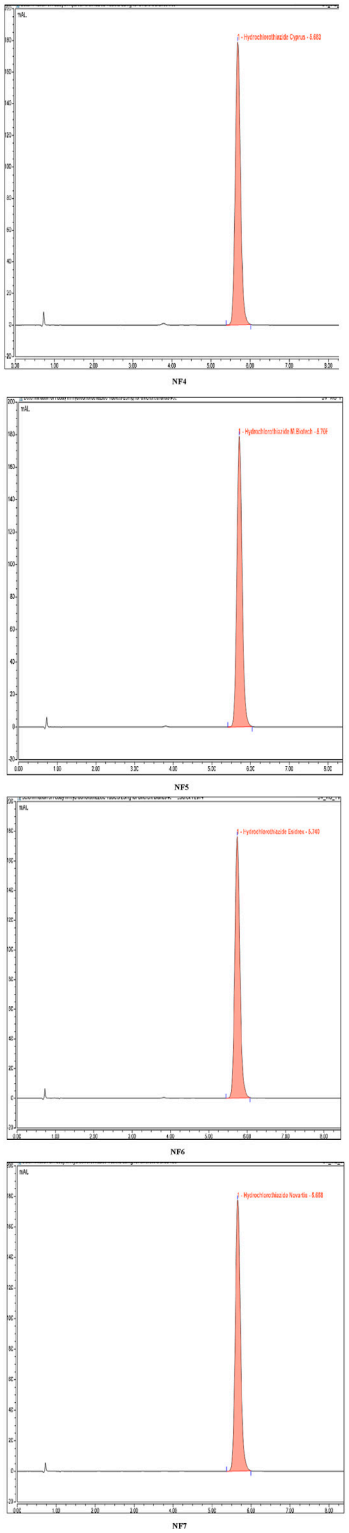

FIGURE 2
(Continued).

and were thus formally grouped under substandard medicines (Wega, 2016). As a result, there may be a chance of access to poor-quality drugs from nearby countries like Djibouti and Somalia in the area of study. The quality of pharmaceuticals supplied in the healthcare system is determined by evaluating the marketed drug product quality. However, there is not enough prior research on the quality of medications in Ethiopia, especially with respect to antihypertensive drugs. In addition, the Ethiopian Food and

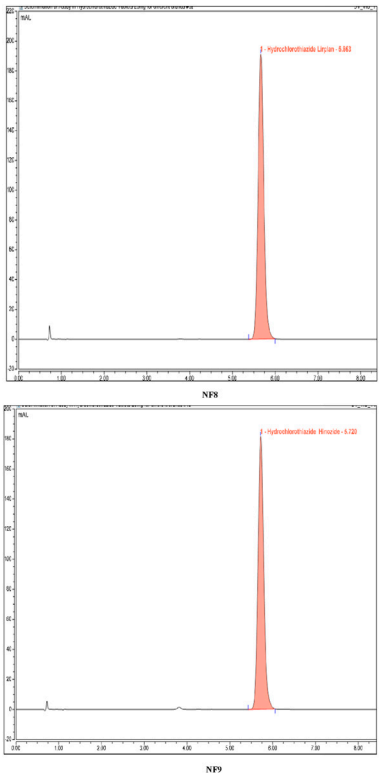

FIGURE 2
(Continued). Representative chromatograms of the standard and nine different brands of hydrochlorothiazide 25 mg.

Drug Administration (EFDA) has recommended researching the quality of select antihypertensive drugs in Ethiopia. Therefore, this study aimed to evaluate the quality of different brands of HCT 25 mg tablets sold in Dessie town, Northeast Ethiopia.

Materials and methods

Materials

Chemicals, solvents, and reagents

The primary standards for HCT were obtained from Human Well Pharmaceuticals. All reagents and solvents used in the experiments were high-performance liquid chromatography (HPLC) grade. These included acetonitrile (Sisco Research Laboratories Pvt. Ltd., India), methanol (Loba Chemie Pvt. Ltd., India), 98% hydrochloric acid (Loba Chemie Pvt. Ltd., India), 98% monobasic potassium phosphate (Lot. No. L331682003, SCR, China), alcohol, and ultrafiltered water.

Instruments and apparatus

The following instruments and apparatus were used for the *in vitro* quality evaluations of different brands of HCT tablets. These included a HPLC column (H605027, Ultimate 3000, United States) of dimensions 4.6 mm × 25 cm packed with L1 made up of C18 (Agilent, California, United State), a single-beam UV-Visible spectrophotometer (Evolution 201, Thermo Fisher, United States), friability tester (FT-2000SE, Tianda-Tianfa, China), ultrasonic shaking incubator (THZ-300, Shanghai-Yiheng, China), dissolution testing apparatus I(ZRS-8G, Tianjin Instrument Factory, China), hardness tester (YD-20KZ, Tianda-Tianfa, China), pH meter (FE-28 standard, Metter Toledo, United States), mortar and pestle, analytical balance (MS205DU, Metter Toledo, United States), disintegration time test apparatus (ZB-1E, Tianda-Tianfa, China), digital calipers (Xin Xing, China), and beakers of different sizes as needed.

Sampled drug products

Nine brands of HCT 25 mg tablets were purchased from a Dessie community pharmacy in Northeast Ethiopia. These brands were coded from NF1 to NF9 for easy identification. All brands were purchased with their original packaging and were within their expiration dates (Table 1). All samples were stored inside a locked cabinet in the quality control laboratory at an ambient temperature of 25°C.

Methods

Study area and study design

An experimental cross-sectional study was conducted from February 2021 to July 2021 in Dessie town, Northeast Ethiopia. Dessie town is 401 km away from the capital f Ethiopia (Addis Ababa); it has two government and three private hospitals, seven health centers, thirty-six community pharmacies, more than twenty wholesalers, thirty-eight drug stores, and more than twelve specialty clinics. The reason for selecting this study area was the presence of many community pharmacies, wholesalers, and government and private health institutions. The town also serves as a referral point for patients from Afar, North Wollo, Kemissie, Kombolcha, and other nearby areas. Thus, most patients would have had access to both prescription and non-prescription (over the counter (OTC)) drugs.

Sampling and sample size determination

The sampling design, sampling, and sample size determination were based on a previous study with slight modifications (Singh and Masuku, 2013; Abebe et al., 2020). First, information about the available brands of HCT 25 mg tablets was gathered from different pharmacy professionals working in the community pharmacies of Dessie town. Thus, nine different brands that were marketed to and used by the community were determined. According to information obtained from the Human Resources of Dessie town health offices, 36 community pharmacies (government and private) were registered legally in the town.

All of these community pharmacies were listed alphabetically and coded. Considering that all these pharmacies provide equal service to their clients and to avoid repeated sampling of the brands,

TABLE 3 Weight variation test results of the hydrochlorothiazide 25 mg tablets (N = 20).

Product code	Mean weight (mg) ± SD	Minimum weight deviation (%)	Maximum weight deviation (%)	Number of tablets out of specifications
NF1	134.85 ± 1.467	−0.11	2.48	None
NF2	303.02 ± 3.941	−0.11	−2.77	None
NF3	90.345 ± 0.905	0.05	2.16	None
NF4	121.775 ± 0.95	0.02	−1.95	None
NF5	140.285 ± 4.608	0	−13.39	1
NF6	141.66 ± 2.009	0	−3.21	None
NF7	160.455 ± 4.538	0.15	−11.38	1
NF8	160.755 ± 2.119	0.09	−3.21	None
NF9	164.85 ± 1.118	0.03	2.15	None

N, number of tablets.

TABLE 4 Thickness (mm), diameter (mm), hardness (N), disintegration time (min), friability (%), and assay (%) test results.

Brand code	Thickness (mm), n = 10	% Deviation of individual tablet thickness	Diameter (mm)	% Deviation of individual tablet diameter	Hardness (N), n = 10	Disintegration time (min), n = 6	Friability (%), n = 20	Assay (%) ±SD
Brands	Mean ± SD	minimum and maximum values	Mean ± SD	minimum and maximum values	Mean ± SD	Mean ± STD		
NF1	2.76 ± 0.02	−1.556 and 0.977	7.28 ± 0.02	−0.453 and 0.508	39.56 ± 3.12	2.92 ± 0.06	0.07	100.5 ± 0.02
NF2	3.22 ± 0.03	−1.516 and 1.889	9.61 ± 0.00	−0.114 and 0.198	49.27 ± 4.22	1.87 ± 0.11	0.03	98.8 ± 0.03
NF3	3.53 ± 0.02	−0.679 and 0.736	6.10 ± 0.03	−0.787 and 0.853	24.23 ± 7.32	0.15 ± 0.04	1.36	99.7 ± 0.05
NF4	2.38 ± 0.01	−0.757 and 0.925	7.12 ± 0.02	−0.295 and 0.548	62.07 ± 1.69	2.56 ± 0.294	0.24	99.1 ± 0.03
NF5	2.92 ± 0.04	−2.497 and 1.95	7.17 ± 0.02	−0.391 and 0.725	32.19 ± 4.78	0.18 ± 0.05	0.21	99.5 ± 0.04
NF6	2.55 ± 0.01	−0.862 and 0.705	7.14 ± 0.01	−0.35 and 0.21	61.44 ± 1.75	4.75 ± 0.17	0.07	97.4 ± 0.02
NF7	2.44 ± 0.01	−0.532 and 1.105	8.16 ± 0.02	−0.392 and 0.588	54.21 ± 3.56	0.31 ± 0.05	0.43	98.1 ± 0.02
NF8	3.25 ± 0.01	−0.338 and 0.277	7.49 ± 0.04	−0.668 and 1.335	42.15 ± 3.72	2.18 ± 0.09	0.12	105.8 ± 0.02
NF9	3.65 ± 0.01	−0.439 and 0.658	7.12 ± 0.15	−1.264 and 5.758	35.02 ± 3.17	0.58 ± 0.41	0.18	100.3 ± 0.03

nine community pharmacies were randomly selected using a lottery method. Then, nine individual prescriptions were prepared for each randomly selected community pharmacy, where HCT 25 mg was prescribed twice a day (BID-based) for 2 months. Finally, single brands with 120 samples (as tablets) were purchased from each community pharmacy for a total of 1,080 samples for the nine brands; the prescriptions were filled from 01/02/2021 to 30/02/2021 using single prescription papers and were coded according to the place of purchase. This means that a brand that was already purchased from one pharmacy was no longer considered from any of the other pharmacies (one unique brand per community pharmacy). Because the prescription was written with brand names and since these were convenient for the study purposes, all available brands were included in the study (Abebe et al., 2020; Eraga et al., 2015). The samples were collected using well-trained pharmacy personnel acting as simulated caregivers to eliminate any suspicion from the medication vendors that their medicines were being acquired for testing. All samples were evaluated by Human Well Pharmaceuticals PLC (quality control department) in the Amhara region, North Shoa, Ethiopia.

In vitro quality control test methods

Nine brands of HCT 25 mg tablets collected from the market were tested for identification, uniformity of dosage unit friability, hardness, disintegration time, dissolution, and assay based on specific monographs in the United States and British pharmacopeia (Usp, 2019; Pharmacopeia, 2009). Ethical approval was not required for this study because it is not an *in vivo* study and

TABLE 5 Data for the standard calibration curve of hydrochlorothiazide.

Concentration (μg/mL)	Absorbance	Percent
6	0.362	50
9	0.571	75
12	0.75	100
15	0.889	125
18	1.114	150
21	1.303	175

TABLE 6 f1 and f2 values of different brands of hydrochlorothiazide against the comparator.

Brands	f1	f2
NF1×NF6	3.6	71.4
NF2×NF6	3.7	70.4
NF3×NF6	8.6	56.1
NF4×NF6	4.5	66.3
NF5×NF6	2.8	78.7
NF7×NF6	4.3	68.5
NF8×NF6	2.4	80.9
NF9×NF6	7.4	59.7

does not include living subjects (like animals or human beings) in the study.

Visual inspection

Visual inspection is a common *in vitro* quality control parameter that helps to evaluate the physical appearance of the tablet. Therefore, the product label was determined using the WHO physical inspection checklist model by randomly selecting 20 tablets from each brand (Tesfay et al., 2019).

Identification test

The authenticity of the product was determined by HPLC (Ultimate 3000, Thermo Fisher, United States) by cross matching the retention time of the major peak of the test sample to the respective chromatogram of the standard solution (Usp, 2019).

Weight variation test

Individual tablets (20 numbers) of each brand were measured using an analytical balance as $W1, W2, W3, \ldots\ldots\ldots, W20$. Then, the mean and percentage deviations of the individual tablets were obtained (Usp, 2019).

$$mean = ((W1 + W2 + W3 \cdots\cdots + W20))/20$$

The formula for percentage deviation is given by

$$\%\, of\ Weight\ variation = \frac{(Individual\ tablet\ weight - average\ weight\ of\ 20\ tablets)}{(average\ weight\ of\ 20\ tablets)} \times 100$$

Hardness test

The strengths of the tablets were measured using a hardness tester (YD-20KZ, Tianda-Tianfa, China) by applying machine-driven force on diametrically placed tablets. The instrument provides the hardness value of each tablet in newton, from which their means and standard deviations were calculated (Afifi and Ahmadeen, 2012; Pharmacopeia, 2009).

Friability test

Twenty tablets were randomly retrieved from each brand and weighed accurately using an electrical beam balance. These tablets were subjected to abrasion using a friability test machine (FT-200SE, Tianda-Tianfa, China) at 25 rpm for 4 min (100 revolutions). After completing the revolutions, the drum was stopped; the tablets were removed from the drum and weighed again. The percentage friability of each brand was calculated based on the following formula (Usp, 2019; Pharmacopeia, 2009).

$$\%\, of\ friability = \frac{(initial\ weight\ of\ 20\ tablets - final\ weight\ after\ rotation)}{(initial\ weight\ of\ 20\ tablets)} \times 100$$

Disintegration time test

Six tablets were randomly retrieved from each brand and transferred to the USP disintegration apparatus (ZB-1E, Tianda-Tianfa, China), which consists of a rigid basket rack assembly holding six cylindrical glass tubes. Each tube moves vertically in the disintegration medium. The disintegration medium was 900 mL of water, and the temperature was maintained at 37°C ± 1°C. The time when no particles remained in the basket was considered as the disintegration time. This time was recorded for each tested tablet, and the mean disintegration time was calculated for each brand (Usp, 2019).

Dissolution test

In vitro dissolution tests were performed using the USP apparatus-I (basket type) as per the monograph of the USP. The test was conducted on six randomly selected tablets from each brand, and the medium used was 900 mL of 0.1 N HCl at a

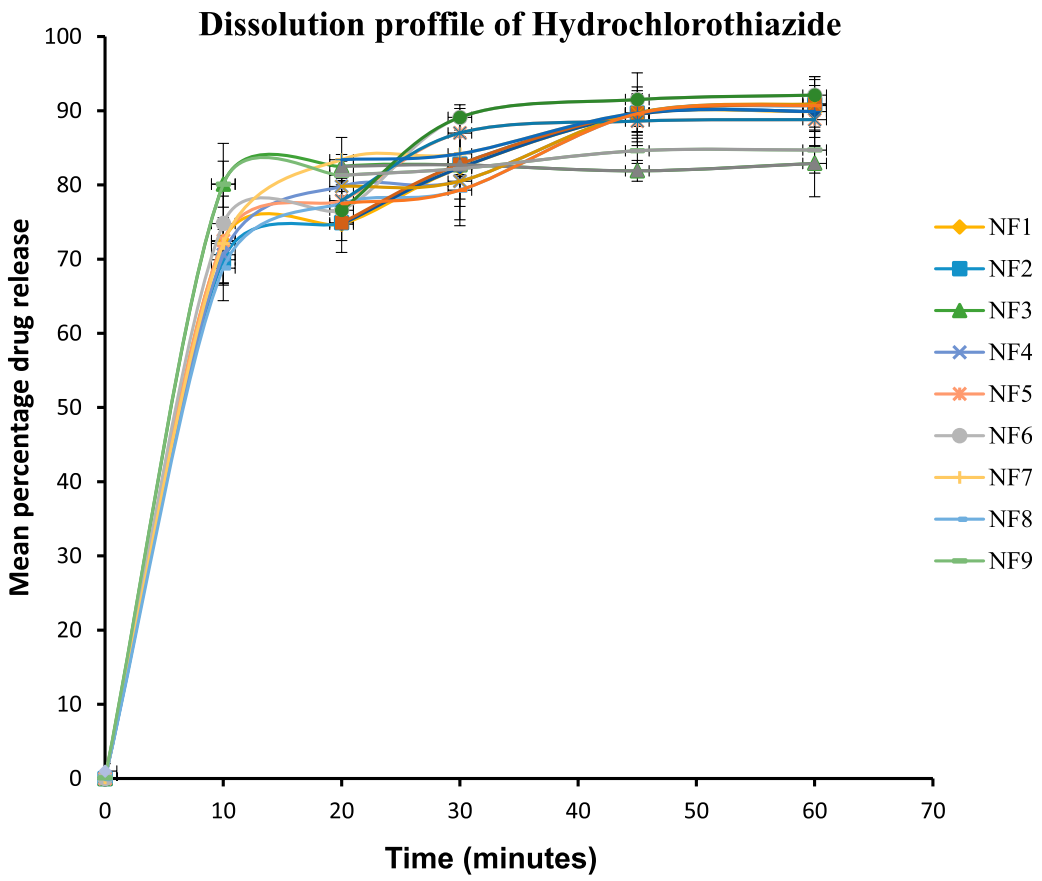

FIGURE 3
Dissolution profiles of the different brands of hydrochlorothiazide tablets.

temperature of 37°C ± 0.5°C. The speed of the apparatus for the experiment was 100 rpm for the individual tests (Usp, 2019).

Preparations of the standard and sample solutions were as follows. First, about 100 mg of the HCT reference standard was accurately weighed and transferred into a 500 mL volumetric flask and dissolved with a medium to a volume limit containing 200 µg/mL. Considering this as the stock solution of the reference standard, six serially diluted standard samples were prepared as described in the procedures. The calibration equation and correlation coefficient were determined by plotting the six serially diluted standard concentrations (6 µg/mL, 9 µg/mL, 12 µg/mL, 15 µg/mL, 18 µg/mL, and 21 µg/mL) on the *x*-axis and their respective absorbance values on the *y*-axis (Moosavi and Ghassabian, 2018). The lowest limit of quantification of the prepared diluted standard sample should be greater than five times the absorbance value of the blank solution (Berthier, 2004).

Six tablets were randomly selected from each brand and transferred to the medium. Then, the sample solution was prepared for UV-visible analysis by retrieving 15 mL from each of the six beakers and transferring into six well-cleaned glass beakers using a 0.45 µm pore size filter at 0, 5, 15, 30, 45, and 60 min. Then, 13.5 mL of the sample solution was drawn from each glass beaker and transferred into individual 25 mL volumetric flasks using a volumetric pipette. Thus, it was deemed that suitable dilution was achieved (adding a diluent to a volume of 25 mL) to obtain the accepted sample concentration of 15 µg/mL (125%) (Othman, 2014); this sample was analyzed using UV-Visible spectroscopy (Evolution 201, Thermo Fisher, United States) at the wavelength of 272 nm to obtain the maximum absorbance (Usp, 2019). The absorbance of each sample was measured thus, and a calibration equation was used to determine the rate of drug release (concentration) over time against a standard solution of known concentration (Sultana and Hosen, 2018). The tolerances were computed as the amounts of APIs released from the tablets, which should not be less than 60% of the stated amount dissolved over 60 min.

Dissolution profile study

The resulting dissolution profiles of different brands of HCT products under the test medium were compared using a model-independent approach of difference factor (f1) and similarity factor (f2). A minimum of more than three sampling points over time is required to characterize the dissolution profile (Use, 2006).

The difference factor is used to determine the percentage difference between two dissolution profiles at each time point, and the relative error between the two profiles is measured (Diaz et al., 2016). The similarity factor is used to indicate the average percentage of sameness between two dissolution profiles. According to the guidelines issued by 14 regulatory authorities, f1 values of up

to 15 (0–15) and f2 values greater than 50 (50–100) ensure the similarity or bioequivalence of two profiles (Diaz et al., 2016).

$$f_1 = \frac{\sum_{t=1}^{n} |R_t - T_t|}{\sum_{t=1}^{n} R_t} \times 100$$

$$f_2 = 50 \times \log_{10}\left[\frac{100}{\sqrt{1 + \frac{\sum_{t=1}^{n} (R_t - T_t)^2}{n}}}\right]$$

where n = number of the dissolution sampling time; R_t and T_t are the individual or mean percentage dissolved at each time point t of the reference product and test dissolution profile, respectively.

Assay test

The assay test for HCT tablets was conducted as per the USP, and the limits are usually expressed with regard to the active moiety or label claim (Usp, 2019). The mobile phase was first prepared as follows. First, 0.1 M monobasic sodium phosphate solution was prepared using ultrafiltered water as the dissolving medium. This solution was mixed with acetonitrile in the ratio of 9:1 and degassed. The pH was adjusted using phosphoric acid to 3.0 ± 0.1 and filtered. The chromatographic system involved the HPLC column (Ultimate 3000, Thermo Fisher, United States) equipped with a 254 nm UV-visible detector. The column was 4.6 mm × 25 cm and packed with L1 made comprising C18 to ensure a reverse-phase system. The column temperature was 30°C, and the data analyzer software used was Chromeleon version 7.2.4.8179. The flow rate was about 2 mL/min with an injection volume of 20 µL. Before injecting the standard and test samples into the HPLC, the column was equilibrated by continuously pumping the mobile phase through the system to ensure that the baseline was straight. Then, chromatograph and peak response of the standard solution was recorded. The relative standard deviation for replicate injection was not more than 1.5% from that of the standard solution.

The standard solution preparation involved accurately measuring 15 mg of the HCT reference standard, which was transferred into a 100-mL volumetric flask. Then, it was dissolved to a certain volume with the mobile phase to obtain a solution having a known concentration of 0.15 mg/mL. The sample solution preparation involved first weighing twenty tablets from each brand and finely powdering them to facilitate solubility of the drug. Then, an accurately weighed portion (equivalent of 30 mg) was retrieved from the fine powder and transferred into a 200-mL volumetric flask. Next, about 100 mL of the mobile phase solution was added to the sample and sonicated for 10 min using a mechanical shaker. This was diluted to a certain volume with the mobile solution and mixed well. Finally, the solution was filtered, and the first 10 mL of the filtrate was discarded.

The analysis procedure involved injecting equal volumes (20 µL) of the standard and the sample solutions separately into the HPLC, and the major peak response was measured from the recorded chromatogram. The percentage of the labeled amount of HCT in a portion of a tablet was calculated using the following formula:

$$(\boldsymbol{Cs}/\boldsymbol{Cu})(\boldsymbol{ru}/\boldsymbol{rs}) \times \mathbf{100}$$

where **Cs** and **Cu** are the concentrations (in mg/mL) of the reference in the standard preparation and nominal concentration of HCT in the sample solution, respectively; **ru** and **rs** are the peak responses of the sample and reference solutions, respectively. For acceptance, the USP asserts that the HCT tablet formulation should contain the API in the range of 90%–110% of the stated amount.

Data analysis

The collected data were evaluated and checked for completeness and consistency before analyses. The data were expressed in terms of mean ± standard deviation (SD). The calibration curve was constructed by plotting the serially diluted standard concentrations along the *x*-axis and their absorbance values along the *y*-axis in Microsoft Excel 2010. The interchangeability and/or bioequivalence were confirmed with one-way ANOVA, followed by multiple comparisons of the Dunnett *t*-test at a 95% confidence interval; $p < 0.05$ was considered to be statistically significant. In addition, the model-independent approach involving f1 and f2 was used.

Results and discussion

Regardless of addressing medical products to the community, there are still unethical commercial practices that influence the service quality, where poor-quality medications are manufactured and distributed in the market (Osei-Asare et al., 2021). Therefore, ensuring the quality of the drugs available in the market is a primary step in controlling disease conditions and decreasing the circulation of poor-quality medications in the supply chain. In addition, encouraging generic medicines from different market sources into the healthcare system regularly reduces healthcare costs, so that patients can easily afford such medications. Of the nine brands of HCT tablets included in this study, two were manufactured locally, while seven were imported from foreign countries. Further, all HCT brands were subjected to several quality control tests to assess their dissolution profiles in line with other quality parameters, including weight variation, friability, hardness, and assay.

Visual inspection

Visually inspection of the tablets offered qualitative information regarding the appearances or product labels of the tablets (screening for the presence or absence of visual quality defects). Hence, among the nine brands, eight were white, while brand NF1 had a yellow color. All brands were round, uncoated, and blister packed with all necessary information printed on the packaging. Moreover, the product strengths were well documented on the blisters. The tablets from all brands evaluated had no scratches, cracks, deformations, unusual colors, discolorations, dirt, foreign matter, mislabeled information, or other defects on the product. An assessment of the physical features, packaging, and labeling revealed no evidence of fake, fraudulently labeled, or falsified products.

Identification test

Unequivocally identifying the API content of different dosage forms is the most important primary test to ensure genuineness of the product before proceeding with further tests (Huang et al., 2020). In this study, the retention time of the HCT standard was 5.783 min, and its peak retention time ranged from 5.658 (NF7) to 5.740 (NF6) min, as shown in Table 2 and Figure 2. All the analyzed samples displayed retention times corresponding to the respective standards; this indicates that all products contained genuine APIs in the dosage forms.

Weight variation test

The weight variation test is a quality parameter that ensure consistency of dose units as per the label claims. The minimum and maximum percentage deviations of the individual brands of HCT 25 mg tablets are shown in Table 3. A negative value indicates that the tablet weight is below the mean (standard) value. The weight variation limits depend on the average weight of the tablets from the corresponding brands. For the individual brands, the mean weights were categorized under ≤130 mg, 130–324 mg, and ≥324 mg, and the percentage deviations of the individual tablets had limits of ±10%, ±7.5%, and ±5%, respectively. It is noted that not more than two tablets were outside these percentage limits, and none of the tablets differed by more than twice their corresponding percentage deviation limits (Usp, 2019). The results from the study showed that the average weights of the brands NF3 and NF4 were less than 130 mg and that none of the tablet percentage deviations were outside the limits of ±10%. The average weights of 20 tablets from the brands NF1, NF2, NF5, NF6, NF8, and NF9 were within the range of 130–324 mg; accordingly, most tablet percentage deviations from the mean values of their corresponding brands were within the limits of ±7.5%. Only one tablet each from the brands NF5 and NF7 had deviations of −13.394% and −11.377%, respectively; however, these values did not exceed twice the corresponding percentage limits (7.5%). Thus, all brands had satisfactory weight uniformity throughout the product. This may be because manufacturing companies strictly adhere to good manufacturing practices during the granulation and compression stages to ensure tablet weight uniformity (Mustapha et al., 2020). This also means that the companies use almost uniform granulation processes and compression forces for tablet production. However, this test is not a confirmatory test for the amount of API and only provides a rough estimation of the formulation.

Hardness test

The mean hardness values of the nine different brands of HCT 25 mg tablets ranged from 24.20 ± 7.32 N (NF3) to 62.07 ± 1.69 N (NF4), as shown in Table 4. A tablet must have a minimum crushing strength of 40 N to withstand mechanical stresses (forces) during the manufacturing, packaging, and shipping processes (Kumar et al., 2018; Alnedhary et al., 2021). Correspondingly, the results of brands NF3 (24.20 ± 7.32 N), NF5 (32.19 ± 4.78 N), and NF9 (35.02 ± 3.12 N) were below the minimum hardness requirement; this may be because of the application of minimum compression force, a lower quantity of binders during manufacturing, or the granulation method used during manufacturing. It has been shown that dry (direct) granulation produces less hardness than wet granulation (Mahant et al., 2020). Tablet hardness for a drug product is a critical parameter that directly affects the bioavailability of the drug by altering its disintegration time, friability, and dissolution profile (Alnedhary et al., 2021). If the tablet is less hard, it will be easily friable and lose the APIs from the formulation. Hence, the amounts of APIs that reach systemic circulation will decrease, diminishing the therapeutic effectiveness. Therefore, tablets must have good mechanical strengths to ensure appropriate hardness-related properties (Ali et al., 2018).

Friability test

As shown in Table 4, the lowest and highest percentage friability results among the different brands of HCT tablets were 0.03% (NF2) and 1.36% (NF3). As described in the USP and British pharmacopeia, the percentage friability of a tablet should be less than 1% (Usp, 2019; Pharmacopeia, 2009). Hence, our results showed that only the brand NF3 (1.36%) failed this friability specification limit (<1%), which could be a result of the lower crushing strength of their tablets (24.23 N). The tablet strength is directly related to the amount and nature of the binder, method of tablet production, and applied amount of compression force during manufacturing. We know that adequate friability is a quality requirement for ensuring a tablet's resistances to abrasion during packaging, handling, and transportation (Onalo et al., 2021). If the tablet is friable, the amount of API present in the formulation will be below the required amount and may cause problems with content uniformity in the product (Othman, 2014). This will also decrease the bioavailability of the drug and customer trust in the product (Isaac et al., 2021). Therefore, the tablet should be manufactured with adequate hardness and reasonable friability to ensure consumer acceptance.

Disintegration time test

The mean disintegration time results of the HCT tablets were in the range of 0.15 ±0.04 min (NF3) to 4.75 ±0.17 min (NF6), as shown in Table 4. The maximum disintegration time for uncoated and film-coated tablets is up to 30 min based on the USP (Usp, 2019). Overall, the mean disintegration times of all tested brands were within the pharmacopeia specification (30 min). In this study, the brands NF3, NF5, NF7, and NF9 had disintegration times of less than 1 min. According to the study by Nigatu et al. (2019), the types and amounts of excipients used in tablet formulations as well as their manufacturing methods are critical factors influencing tablet disintegration times. Accordingly, brands NF3, NF5, and NF9 that had very short disintegration times may have been manufactured using low compression forces because their hardness values were less than the minimum required value (39.23 N). Mainly, the product by NF3 had the lowest disintegration time (0.15 min), which correlated with its lower

hardness and high friability. Brand NF7 also had a short disintegration time possibly owing to the presence of a high amount of disintegrants in the formulation. The disintegration of an orally administered tablet is the primary step through which a physical change occurs after the drug is administered; it helps predict the process of tablet fractionation into smaller pieces and is the rate-determining step in drug dissolution and absorption processes. If the disintegration time is not sufficient, the effectiveness of the drug is not good. The dissolution rate will decrease if the tablet disintegration time is too long; from this, it follows that the expected amount of API will not reach the systemic circulation. Therefore, the type, concentration, and efficiency of the disintegrant affect the dissolution and absorption of orally administered tablet dosage forms to a great extent (Mangal et al., 2012).

Dissolution test

Calibration curves were employed to determine the amounts of APIs released from the tablet dosage forms. A calibration curve, also known as a standard curve in analytical chemistry, is a general technique for measuring the concentration of an analyte in an unknown sample through comparison to a series of known concentrations of the standard solution. Using the results in Table 5, the determination coefficient (R^2) and calibration equation were found to be 0.997 and $y = 61.64x - 0.00$, respectively. This implies a linear relationship between the concentration and absorbance value since R^2 exceeds 0.05. Thus, the calibration equation helps to determine the concentration of the test sample and its percentage release in the dissolution test of the HCT 25 mg tablet. The dissolution of a tablet dosage form is an important quality control parameter that is directly related to the absorption and bioavailability of the drug. The maximum mean percentage of API released at 60 min was from NF6 (92.1 ± 1.0) and the corresponding minimum was from NF3 (82.9 ± 4.8). These results indicate that all studied brands were within the USP dissolution tolerance limits, i.e., the API released was more than 60% within 60 min.

Dissolution profiles of different brands of HCT tablets

The market availability of different brands of medicines can confuse healthcare professionals and patients regarding the choice of brand and possibility of interchangeability among the brands. A bioequivalence study is thus required to ensure that different brands of a drug can be used interchangeably; this was conducted using the model-independent approach based on f1 and f2. The Innovator brand of HCT is not available, so brand NF6 was selected as a comparator according to the principle specified in the decision tree of Annex 11 of WHO 2002 (Preparations, 1999). As shown in Table 6, the f1 and f2 values ranged from 2.4 (NF8) to 8.6 (NF8) and from 56.1 (NF3) to 80.9 (NF8), respectively. In addition, the release patterns of the tablets is expressed graphically in Figure 3, and the findings indicate overlapped dissolution profile curves. The f1 (<15) and f2 (>50) values of all test samples were within the accepted ranges (Diaz et al., 2016). Hence, all test brands were deemed similar or bioequivalent to the comparator drug.

The Dunnett *t*-test statistical analysis results showed that the *p*-values of all brands against the comparator (NF6) ranged from 0.982 to 1.00, and ANOVA resulted in a *p*-value of 0.999. Therefore, there were no statistically significant differences in the percentage releases of APIs between all brands of HCT and the comparator because all of their *p*-values were >0.05. Hence, there is no statistically significant difference in the time-dependent percentage release within and between different brands of HCT products (*p*-value >0.05).

The dissolution rate of a tablet formulation is affected by several factors like the intrinsic properties of the API in the formulation, manufacturing process, dissolution medium used, formulation composition, and characteristics of the excipients (Diaz et al., 2016). Nevertheless, in our study, none of the brands were greatly affected by these factors because the amounts of APIs released from all the brands were above the minimum limit specified by the USP; this may be related to the rates of disintegration of the tablets. The disintegration time results of all brands were below 5 min; such rapid disintegration of the tablet dosage forms implies rapid breakdown of the tablets into smaller particles that will then enhance the dissolution rates of the medications into systemic circulation (Schittny et al., 2020). Therefore, when the dissolution rate increases, the bioavailability and therapeutic effectiveness of the drug will also increase.

Amounts of active pharmaceutical ingredients: system suitability test

As per the Usp (2019), the suitability results of the percentage relative standard deviations (%RSDs) of the peak area response and tailing factor of HCT obtained using the HPLC system were 0.03% (<5%) and 1.12% (<2%), respectively. Therefore, the HPLC system was suitable for the test. The minimum and maximum API percentages of the HCT tablets were 97.4 ± 0.02 (NF6) and 105.8 ± 0.02 (NF8), respectively. Hence, all brands were within the range of the USP specification limits (90%–110%). The detailed assay results of the different brands of HCT tablets used in this study are shown in Table 4.

An assay test of the API content of a dosage form is a critical parameter for ensuring the quality of the pharmaceutical product. Determining the amount of API present in the formulation helps to ensure the potency and efficacy of the drug against the disease condition (Mangal et al., 2012). This means that high-quality pharmaceutical products for HCT can help control hypertension while reducing the mortality and morbidity rates. However, if the API content of the product is below or above the specification limits, it will increase the prevalence of substandard products in the community. If the amount of API is below the specified limit, it will result in poor control over hypertension; however, if the amount of API is above the stated limit, it may lead to a high incidence of adverse reactions and may even decrease the blood pressure below the desired lower limit (Tesfay et al., 2019; Trevisol et al., 2011). As described by McManus and Naughton (2020), poor-quality drugs

can result in treatment failure, mass poisoning, and drug resistance, eventually leading to death. Therefore, all pharmaceutical products must be manufactured using the amended pharmacopeia procedures, and all quality parameters must be evaluated to achieve the desired therapeutic outcomes.

Conclusion

The qualities and physicochemical bioequivalence of nine different brands of HCT tablets were evaluated in this study. The results show that all of the evaluated brands of HCT 25 mg tablets met the quality control parameters as per the pharmacopeia specifications, except for three brands (NF3, NF5, and NF9) that failed the hardness test and one brand that failed the friability test (NF3; 1.36%). The difference factor (f1) and similarity factor (f2) values revealed that all brands were similar to the Innovator brand comparator product. Hence, we showed that these generic brands could be used interchangeably in clinical practice.

Data availability statement

The raw data supporting the conclusions of this article will be made available by the authors without undue reservation.

Author contributions

YW: Conceptualization, Data curation, Formal analysis, Investigation, Methodology, Resources, Supervision, Validation, Visualization, Writing–original draft, Writing–review and editing. HD: Conceptualization, Supervision, Visualization, Methodology, Writing–review and editing. YA: Conceptualization, Supervision, Visualization, Data curation, Writing–review and editing. AT: Data curation, Supervision, Visualization, Formal analysis, Investigation, Writing–review and editing. KA: Supervision, Formal analysis, Visualization, Writing - review and editing. BE: Investigation, Supervision, Visualization, Conceptualization, Formal analysis, Methodology, Writing–review and editing. SD: Conceptualization, Data curation, Software, Validation, Visualization, Formal analysis, Writing–review and editing.

Funding

The author(s) declare that no financial support was received for the research, authorship, and/or publication of this article.

Acknowledgments

The authors extend their sincere thanks to Wollo University and Amhara Regional Health Bureau for supporting this study. The authors also thank Human Well Pharmaceutical Ethiopia PLC and the Ethiopian Food and Drug Administration Authority (EFDA) for the reference standards. The authors thank the team at Research Square as this manuscript was presented as a "Preprint" for comments from the scientific community and researchers.

Conflict of interest

The authors declare that the research was conducted in the absence of any commercial or financial relationships that could be construed as a potential conflict of interest.

Publisher's note

All claims expressed in this article are solely those of the authors and do not necessarily represent those of their affiliated organizations or those of the publisher, editors, and reviewers. Any product that may be evaluated in this article or claim that may be made by its manufacturer is not guaranteed or endorsed by the publisher.

References

Abebe, S., Ketema, G., and Kassahun, H. (2020). *In vitro* comparative quality assessment of different brands of Furosemide tablets marketed in northwest Ethiopia. *Drug Des. Dev. Ther.* 14, 5119–5128. doi:10.2147/DDDT.S280203

Afifi, S. A., and Ahmadeen, S. (2012). A comparative study for evaluation of different brands of metformin hydrochloride 500 mg tablets marketed in Saudi Arabia. *Life Sci. J.* 9 (4), 4260–4266.

Ali, M., et al. (2018). Comparative *in vitro* evaluation of some commercial brands of valsartan tablets marketed in Bangladesh. *Pharma Innovation J.* 7 (4), 1068–1072.

Almuzaini, T., Choonara, I., and Sammons, H. (2013). Substandard and counterfeit medicines: a systematic review of the literature. *BMJ open* 3 (8), e002923. doi:10.1136/bmjopen-2013-002923

Alnedhary, A. A., et al. (2021). A comparative study to assess the quality of different marketed brands of metformin HCl. *Biol. Res.* 6 (3), 84–95.

Antignac, M., Diop, B. I., Macquart de Terline, D., Bernard, M., Do, B., Ikama, S. M., et al. (2017). Fighting fake medicines: first quality evaluation of cardiac drugs in Africa. *Int. J. Cardiol.* 243, 523–528. doi:10.1016/j.ijcard.2017.04.099

Bassat, Q., Tanner, M., Guerin, P. J., Stricker, K., and Hamed, K. (2016a). Combating poor-quality anti-malarial medicines: a call to action. *Malar. J.* 15 (1), 302–312. doi:10.1186/s12936-016-1357-8

Bassat, Q., Tanner, M., Guerin, P. J., Stricker, K., and Hamed, K. (2016b). Combating poor-quality anti-malarial medicines: a call to action. *Malar. J.* 15 (1), 302–312. doi:10.1186/s12936-016-1357-8

Berthier, S. (2004). Validation of bioanalytical methods. *Handb. Anal. Sep.* 5, 113–128. doi:10.1016/s1567-7192(04)80006-8

Bigdeli, M., Peters, D. H., Wagner, A. K., and World Health Organization (2014). *Medicines in health systems: advancing access, affordability and appropriate use.*

Diaz, D. A., Colgan, S. T., Langer, C. S., Bandi, N. T., Likar, M. D., and Van Alstine, L. (2016). Dissolution similarity requirements: how similar or dissimilar are the global regulatory expectations? *AAPS J.* 18 (1), 15–22. doi:10.1208/s12248-015-9830-9

Dreisbach, A. W., and Batuman, V. (2013). Epidemiology of hypertension. *Suppl. JAPI Febr.* 61, 12–13.

Eraga, S. O., Arhewoh, M. I., Chibuogwu, R. N., and Iwuagwu, M. A. (2015). A comparative UV– HPLC analysis of ten brands of ibuprofen tablets. *Asian Pac. J. Trop. Biomed.* 5 (10), 880–884. doi:10.1016/j.apjtb.2015.06.005

Huang, F., Zhang, C., Liu, Q., Zhao, Y., Zhang, Y., Qin, Y., et al. (2020). Identification of amitriptyline HCl, flavin adenine dinucleotide, azacitidine and calcitriol as repurposing drugs for influenza A H5N1 virus-induced lung injury. *PLoS Pathog.* 16 (3), e1008341. doi:10.1371/journal.ppat.1008341

Isaac, J. A., Hayatu, G. I., John, J. E., Ekere, K. E., Daburi, A., Omachoko, S. O., et al. (2021). Quality assessment of brands of prednisolone (5 Mg) tablets marketed in abuja metropolis of Nigeria. *Dissolution Technol.* 28 (1), 24–31. doi:10.14227/dt280121p24

Karmoker, J. R., et al. (2017). Comparative *in vitro* equivalence evaluation of some local Gliclazide brands of Bangladesh. *Pharma Innovation* 6 (3, Part C), 152.

Koczwara, A., and Dressman, J. (2017). Poor-quality and counterfeit drugs: a systematic assessment of prevalence and risks based on data published from 2007 to 2016. *J. Pharm. Sci.* 106 (10), 2921–2929. doi:10.1016/j.xphs.2017.05.018

Kovacs, S., Hawes, S. E., Maley, S. N., Mosites, E., Wong, L., and Stergachis, A. (2014). Technologies for detecting falsified and substandard drugs in low and middle-income countries. *PloS one* 9 (3), e90601. doi:10.1371/journal.pone.0090601

Kumar, M., Tyagi, S., Bhatt, S., Pandurangan, A., Saini, V., Malik, A., et al. (2018). Comparative evaluation of two different marketed brands of enalapril maleate. *J. Drug Deliv. Ther.* 8 (6-s), 265–268. doi:10.22270/jddt.v8i6-s.2127

Lim, S. S., Vos, T., Flaxman, A. D., Danaei, G., Shibuya, K., Adair-Rohani, H., et al. (2012). A comparative risk assessment of burden of disease and injury attributable to 67 risk factors and risk factor clusters in 21 regions, 1990–2010: a systematic analysis for the Global Burden of Disease Study 2010. *lancet* 380 (9859), 2224–2260. doi:10.1016/S0140-6736(12)61766-8

Mahant, S., et al. (2020). Scholars academic. *J. Pharm.*

Mangal, M., et al. (2012). Comparison study between various reported disintegrating methods for fast dissolving tablets. *Afr. J Basic & Appl Sci* 4 (4), 106–109.

McManus, D., and Naughton, B. D. (2020). A systematic review of substandard, falsified, unlicensed and unregistered medicine sampling studies: a focus on context, prevalence, and quality. *BMJ Glob. health* 5 (8), e002393. doi:10.1136/bmjgh-2020-002393

Mills, K. T., Stefanescu, A., and He, J. (2020). The global epidemiology of hypertension. *Nat. Rev. Nephrol.* 16 (4), 223–237. doi:10.1038/s41581-019-0244-2

Moosavi, S. M., and Ghassabian, S. (2018). "Linearity of calibration curves for analytical methods: a review of criteria for assessment of method reliability," in *Calibration and validation of analytical methods: a sampling of current approaches* (London, UK: IntechOpen Limited), 109–127.

Mustapha, K. B., Ekpo, M. D., Galadima, I. H., Kirim, R. A., Odeniran, O. A., and Ache, T. A. (2020). Quality assessment of brands of erythromycin stearate tablets marketed in Abuja, Nigeria. *J. Pharm. Bioresour.* 17 (1), 29–33. doi:10.4314/jpb.v17i1.6

Nigatu, M., Mohammed, F., and Temesgen, A. (2019). *In vitro* comparative study of different brands of pantoprazole sodium enteric coated tablets marketed in addis ababa, Ethiopia. *Asian J. Pharm. Res. Dev.* 7 (1), 13–18. doi:10.22270/ajprd.v7i1.467

Noor, S., et al. (2017). Comparative *in-vitro* quality evaluation of some brands of metronidazole tablet available in Bangladesh. *Int. J. Appl. Res.* 3 (7), 753–758.

Onalo, V. D., Abubakar, D., and Monday Chibuyojo, S. (2021). Quality assessment of some brands of levofloxacin 500mg tablets commercially available in gwagwalada, abuja. *Sch. Acad. J. Pharm.* 3, 43–48. doi:10.36347/sajp.2021.v10i03.002

Osei-Asare, C., Oppong, E. E., Owusu, F. W. A., Apenteng, J. A., Alatu, Y. O., and Sarpong, R. (2021). Comparative quality evaluation of selected brands of cefuroxime axetil tablets marketed in the greater accra region of Ghana. *Sci. World J.* 2021, 6659995. doi:10.1155/2021/6659995

Othman, G. Q. (2014). Comparative analysis of five brands of lisinopril tablets in Yemeni market. *Yemeni J. Med. Sci.* 8, 6.

Ozawa, S., Evans, D. R., Bessias, S., Haynie, D. G., Yemeke, T. T., Laing, S. K., et al. (2018). Prevalence and estimated economic burden of substandard and falsified medicines in low-and middle-income countries: a systematic review and meta-analysis. *JAMA Netw. open* 1 (4), e181662. doi:10.1001/jamanetworkopen.2018.1662

Pareek, A. K., Messerli, F. H., Chandurkar, N. B., Dharmadhikari, S. K., Godbole, A. V., Kshirsagar, P. P., et al. (2016). Efficacy of low-dose chlorthalidone and hydrochlorothiazide as assessed by 24-h ambulatory blood pressure monitoring. *J. Am. Coll. Cardiol.* 67 (4), 379–389. doi:10.1016/j.jacc.2015.10.083

Pharmacopeia, B. (2009). The stationary office:1–4, 2009–10952.

Pires, M. A. S., Souza dos Santos, R. A., and Sinisterra, R. D. (2011). Pharmaceutical composition of hydrochlorothiazide:β-cyclo-dextrin: preparation by three different methods, physico-chemical characterization and *in vivo* diuretic activity evaluation. *Molecules* 16 (6), 4482–4499. doi:10.3390/molecules16064482

Preparations, W. E. C. o. S. f. P. (1999). Annex 11: guidance on the selection of comparator pharmaceutical products for equivalence assessment of interchangeable multisource (generic) products. *Thirty-Fourth Rep.*

Rojas-Cortés, R. (2020). Substandard, falsified and unregistered medicines in Latin America, 2017-2018. *Rev. Panam. Salud Pública* 44, e125. doi:10.26633/RPSP.2020.125

Schiavetti, B., Wynendaele, E., Melotte, V., Van der Elst, J., De Spiegeleer, B., and Ravinetto, R. (2020). A simplified checklist for the visual inspection of finished pharmaceutical products: a way to empower frontline health workers in the fight against poor-quality medicines. *J. Pharm. Policy Pract.* 13 (1), 9–7. doi:10.1186/s40545-020-00211-9

Schittny, A., Huwyler, J., and Puchkov, M. (2020). Mechanisms of increased bioavailability through amorphous solid dispersions: a review. *Drug Deliv.* 27 (1), 110–127. doi:10.1080/10717544.2019.1704940

Sharma, D., et al. (2006). *In vitro* comparative evaluation of different brands of nifedipine capsules. *Asian J. Exp. Sci.* 20 (1), 97–100.

Singh, A. S., and Masuku, M. B. (2013). Fundamentals of applied research and sampling techniques. *Int. J. Med. Appl. Sci.* 2 (4), 124–132.

Sultana, S., and Hosen, M. S. (2018). *In vitro* comparative quality evaluation of different brands of esomeprazole tablets available in selected community pharmacies in Dhaka, Bangladesh. *BMC Res. notes* 11 (1), 1–5.

Tesfay, K., et al. (2019). *In vitro* quality evaluation of metformin hydrochloride tablets marketed in western and North western tigray, Ethiopia. *Austin J. Anal. Pharm. Chem.* 6 (2), 1119.

Trevisol, D. J., Moreira, L. B., Kerkhoff, A., Fuchs, S. C., and Fuchs, F. D. (2011). Health-related quality of life and hypertension: a systematic review and meta-analysis of observational studies. *J. Hypertens.* 29 (2), 179–188. doi:10.1097/HJH.0b013e328340d76f

Use, C. f. M. P. f. H. (2006). *European medicines agency committee for medicinal products for human use (CHMP) guideline on the evaluation of anticancer medicinal products in man.* London, UK: European Medicines Agency.

Usp, U. (2019). *38—NF 33 the United States pharmacopeia and national formulary 2019: main edition plus supplements 1 and 2.* Baltimore, MD, USA: Deutscher Apotheker Verlag.

Wega, S. S. (2016). Quality of selected medicines in Ethiopia: analytical and regulatory contributions. *Ghent Univ.*

Who, W. (2013). A global brief on hypertension: silent killer. *Glob. public health crisis.*

World Health Organization (2017). *WHO Global Surveillance and Monitoring System for substandard and falsified medical products.*

Yusuf, S., Rangarajan, S., Teo, K., Islam, S., Li, W., Liu, L., et al. (2014). Cardiovascular risk and events in 17 low-middle-and high-income countries. *N. Engl. J. Med.* 371 (9), 818–827. doi:10.1056/NEJMoa1311890

frontiers | Frontiers in Analytical Science

TYPE Original Research
PUBLISHED 10 September 2024
DOI 10.3389/frans.2024.1397810

OPEN ACCESS

EDITED BY
Elizabeth Neumann,
University of California, Davis, United States

REVIEWED BY
Mowei Zhou,
Zhejiang University, China
Roman Řemínek,
Institute of Analytical Chemistry (ASCR), Czechia

*CORRESPONDENCE
Jeroen A. A. Demmers,
j.demmers@erasmusmc.nl

†These authors have contributed equally to this work

RECEIVED 08 March 2024
ACCEPTED 14 August 2024
PUBLISHED 10 September 2024

CITATION
Bezstarosti K, Van der Wal L, Doff WAS and Demmers JAA (2024) Parallel reaction monitoring targeted mass spectrometry as a fast and sensitive alternative to antibody-based protein detection.
Front. Anal. Sci. 4:1397810.
doi: 10.3389/frans.2024.1397810

Parallel reaction monitoring targeted mass spectrometry as a fast and sensitive alternative to antibody-based protein detection

Karel Bezstarosti†, Lennart Van der Wal†, Wouter A. S. Doff and Jeroen A. A. Demmers*

Proteomics Center, Erasmus University Medical Center, Rotterdam, Netherlands

The reliable, accurate and quantitative targeted detection of proteins is a key technology in molecular and cell biology and molecular diagnostics. The current golden standard for targeted protein detection in complex mixtures such as complete cell lysates or body fluids is immunoblotting, a technology that was developed in the late 1970s and has not undergone major changes since. Although widespread, this methodology suffers from several disadvantages, such as the inability to detect low-abundant proteins or specific posttranslational modifications, the requirement for highly specific antibodies, the lack of quantitative power and the often-tedious practical procedures. Mass spectrometry (MS) based targeted protein detection is an alternative technology that could circumvent these caveats. Here, we compare immunoblotting with targeted protein mass spectrometry using a parallel reaction monitoring (PRM) regime on the Orbitrap mass spectrometer. We show that PRM based MS has superior sensitivity and quantitative accuracy over immunoblotting. The limit of detection for proteolytic peptides of a purified target protein was found to be in the mid- to low-attomole range and approximately one order of magnitude higher when embedded in a complex biological matrix. The incorporation of synthetic heavy isotope labeled (AQUA) peptides as internal calibrants into the PRM workflow allows for even higher accuracy for both the relative and absolute quantitation of tryptic target peptides. In conclusion, PRM is a versatile and sensitive technology, which can overcome the shortcomings of immunoblotting. We argue that PRM based MS could become the method of choice for the targeted detection of proteins in complex cellular matrices or body fluids and may eventually replace standard methods such as Western blotting and ELISA in biomedical research and in the clinic.

KEYWORDS

parallel reaction monitoring (PRM), targeted mass spectrometry, immunoblotting, limit of detection, GAPDH

Introduction

In molecular biology, biomedical research and clinical diagnostics, the current golden standard of protein detection in complex mixtures such as cell lysates and body fluids is immunoblotting (or: Western blotting). In immunoblotting, a protein sample is first loaded onto a poly-acrylamide electrophoresis (PAGE) gel to separate proteins. Subsequently, proteins are transferred from the gel to a nitrocellulose or polyvinylidene difluoride (PVDF)

solid support membrane using an electric field oriented perpendicular to the surface of the gel, causing proteins to move out of the gel and onto the membrane. Specific (primary) antibodies directed against the target protein of interest then bind to the protein population on the membrane surface and these antibodies are subsequently recognized by other (secondary) antibodies. These secondary antibodies are then visualized through staining, immunofluorescence, or other methods (Towbin et al., 1979; Burnette, 1981; Smith, 1994; Westermeier, 2014). While the basic principles of the technique remain the same since its inception in 1979, there have been advancements in terms of sensitivity, quantification methods, and automation. However, the fundamental steps involved in Western blotting, including protein separation by electrophoresis, transfer to a membrane, antibody binding, and detection, have remained relatively constant.

Though generally considered a robust and inexpensive technique, there are several caveats related to immunoblotting. The specificity of the technique heavily depends on the quality of the antibody that is used. The secondary and tertiary structure of proteins can prevent the binding of antibodies to the relevant epitopes under both denaturing and native conditions, as can the occurrence of post-translational modifications (PTMs). Furthermore, cross-reactivity may cause the antibody to target another, non-related protein than the protein of interest, which happens to have similar gel retention properties (Ghosh et al., 2014). A broad specificity test of commercial antibodies showed that cross reaction with other proteins than the target protein is quite common, with more than 75% of the approximately 6,000 antibodies tested demonstrating a cross reaction or no appreciable binding to its intended target (Weller, 2016). Finally, while the running costs for Western blotting are relatively low, the costs for even limited amounts of antibody can be substantial (typically several 100 s of euros/dollars). Finally, Western blotting is a low-throughput technology: even though several samples may be run in parallel on one SDS-PAGE gel, the number of bands that can be visualised are still limited if different target proteins have similar retention properties (Ghosh et al., 2014).

A more fundamental drawback of Western blotting is the lack of quantitative character. Even when targeting relatively highly abundant cellular proteins, it remains difficult to determine relative quantities of the target protein even in a single experiment (Hammond et al., 2013). While it was recently shown that a newly developed Western blotting-based method can give accurate estimates of protein levels (Deng and Zi, 2022), the requirement of a concentration gradient may impair high-throughput analyses. Furthermore, it assumes that a concentration gradient actually displays a linear relationship in immunoblotting staining intensities, which may not necessarily be true over several orders of magnitude considering previous results [e.g., (Hammond et al., 2013),].

Alternative technologies for the targeted detection of specific proteins may overcome caveats such as the inability to detect low-abundant proteins, specific post-translational modifications and the need for highly specific antibodies, and may thus present superior performance. Here, we focus on mass spectrometry-based methods.

Highly specific methods to detect proteins using mass spectrometry in a targeted fashion are selected reaction monitoring (SRM), multiple reaction monitoring (MRM) or parallel reaction monitoring (PRM). This technology allows for highly selective and accurate proteolytic peptide analysis, since (combinations of) these peptides are assumed to have unique amino acid sequences specific to a particular target protein. SRM was originally developed on triple-quadrupole mass spectrometers, where the first quadrupole is employed as a mass filter that filters the targeted precursor ion, which is subsequently fragmented in the second quadrupole that acts as the collision chamber. The peptide fragment ions are subsequently mass analyzed in the third quadrupole. In SRM, the fragment ions are measured sequentially in distinct scans [reviewed in (Kulyyassov et al., 2021)]. While SRM is monitoring only a single fixed mass window, MRM scans rapidly over multiple narrow mass windows and thus acquires traces of multiple fragment ion masses in parallel (Chambers et al., 2014). So, MRM is the application of SRM to multiple product ions from one or more precursor ions. If the third quadrupole is replaced by a time-of-flight (TOF) or an orbitrap detector that has both a higher mass resolution and higher mass accuracy (Makarov, 2000), all fragment ions can be analyzed simultaneously *and* with high mass accuracy. Hence, this variant is called parallel reaction monitoring (PRM) (Peterson et al., 2012; Shi et al., 2016).

Potentially, targeted mass spectrometry could overcome the caveats described above for immunoassays. In a standard bottom-up proteomics experiment, proteins are first digested into peptides prior to analysis. Hence, multiple proteolytic peptides per target protein can be selected for targeted detection, whereas antibodies generally recognize only one epitope of a protein. In addition, isoform specific peptide sequences or post-translationally modified peptides can be targeted. Since mass spectrometric detection does not require the use of an antibody, the amino acid sequence information is usually sufficient to select the peptide precursors of interest. Peptide fragmentation patterns can be experimentally determined or predicted using AI Based algorithms such as PROSIT (Gessulat et al., 2019) to select the optimal set of fragment ions. Although in many studies targeted mass spectrometry and immunoblotting techniques for protein detection and relative quantitation have been applied and compared (Bluemlein and Ralser, 2011; Lau et al., 2011; Martínez-Márquez et al., 2013; Tsuchiya et al., 2013; Yang et al., 2013; 2014; Prasad and Unadkat, 2014; Parsons and Heazlewood, 2015; Sowers et al., 2015; Jayasena et al., 2016; Thorsen et al., 2023), a systematic assessment of the limits of detection, both for pure proteins and of proteins in complex biological matrices, has not been done. Also, many comparative studies it highlights the latest, sensitive Orbitrap technology for targeted detection as opposed to more widespread and discussed triple quadrupole mass spectrometry.

Here, we set out to make a head-to-head comparison between immunoblotting and PRM in a systematic manner, using a commercially available target protein – antibody combination (glyceraldehyde-3-phosphate dehydrogenase, GAPDH), both in pure form and spiked into a complex biological matrix. First, we determined the limit of detection (LOD) of immunoblotting using a dilution series. Subsequently, we digested GAPDH using trypsin and performed PRM on a selection of GAPDH proteolytic peptides. Peptides could be detected in the low femtogram (i.e., low- to mid-attomole range), presenting over five orders of magnitude higher sensitivity over immunoblotting. Also, the dose-response

relationship was linear over a wide concentration range, spanning several orders of magnitude. Next, target peptides were absolutely quantified using known quantities of synthesized heavy isotope labelled (AQUA) peptides as internal calibrants. Furthermore, we show that using PRM, GAPDH proteolytic peptides could be detected and relatively quantified in a complex biological matrix (i.e., a yeast complete lysate). Finally, we present several suggestions for improvement of sample preparation protocols for targeted proteomics, which could even further enhance the sensitivity and quality of such measurements.

Materials and methods

Reagents

Rabbit-GAPDH was purchased from Sigma (G5262-1VL). *Saccharomyces cerevisiae* extract was purchased from Promega (V6941). Heavy isotope labeled VIPELGNK ($^{13}C_6$, $^{15}N_2$-Lys) peptide was custom made by Thermo Scientific.

Immunoblotting

Lysates were diluted into 4X Laemmli buffer, boiled and sonicated for 5 min. Lysates were then separated on 10% SDS-PAGE acrylamide gel and transferred to 0.2 µm PVDF (Merck Milipore). Membranes were blocked in 5% skim milk in PBS-0.1% Tween for 1 h, incubated overnight for primary antibodies, and incubated for 1.5 h for the secondary antibody. Bands were visualized using ECL imaging on the Amersham Imager. HRP-Goat-α-Mouse (Sigma, cat # AP308P, used in 1:5,000 dilution) and HRP-Goat-α-Rabbit (Sigma, cat # AP307P, used in 1:5,000 dilution) were used as a secondary antibody to allow for ECL visualization. Primary antibodies used were Mouse-α-GAPDH (Abcam, cat # ab8245, used in 1:5,000 dilution) and Rabbit-α-*Drosophila* GAPDH (homemade, 1:500).

Mass spectrometry sample preparation

Samples were prepared as described earlier (van der Wal et al., 2018). For absolute peptide quantitation, synthesized heavy stable isotope (ThermoFisher Scientific) labeled VIPELGNK peptide was added to the sample in known quantities before tryptic digestion. A stock solution of 20 fmol/µL was used to spike in 500 pg of the labeled VIPELGNK peptide into a yeast background.

Targeted mass spectrometry

A tryptic digest of purified GAPDH was analyzed using a data dependent acquisition (DDA) regime to select the appropriate proteotypic peptides for PRM. Proteolytic peptides were analyzed by nanoflow liquid chromatography tandem mass spectrometry (nLC-MS/MS) on an EASY-nLC coupled to an Orbitrap Lumos Tribrid mass spectrometer (ThermoFisher Scientific), operating in positive mode and running Tune version 3.3. Peptides were trapped on a 2 cm × 100 µm Pepmap C18 column (Thermo Fisher 164,564) and then separated on an in-house packed 25 cm × 75 µm capillary column with 1.9 µm Reprosil-Pur C18 beads (Dr Maisch) at a flow rate of 250 nL/min, using a linear gradient of 0%–32% acetonitrile in 0.1% formic acid during 90 min. The eluate was directly sprayed into the electrospray ionization (ESI) source of the mass spectrometer. Spectra were acquired in continuum mode in the Orbitrap at 120,000 resolution for MS1 and 30,000 resolution for MS2 in profile mode and with standard AGC target settings. Fragmentation of the peptides was performed by HCD.

For targeted proteomics, a parallel reaction monitoring regime (PRM) was used to select for a set of previously defined peptides on an Orbitrap Tribrid Fusion Lumos mass spectrometer (ThermoFisher Scientific) operating in positive mode. Precursors were selected in the quadrupole with an isolation width of 0.7 m/*z* and fragmented with HCD using 30% collision energy (CE). MS1 and MS2 spectra were recorded in the orbitrap at 30,000 resolution in profile mode and with standard AGC target settings. The injection time mode was set to dynamic with a minimum of 9 points across the peak. The sequence of sampling was blanks first and then in order of increasing peptide input amounts to avoid any contamination of previous samples.

Data analysis

Analysis of PRM data was performed using Skyline (v 22) (MacLean et al., 2010) and in-house software. Regression analysis was performed using Graphpad Prism (v 5.02).

Data deposition

All raw mass spectrometry data have been deposited to the ProteomeXchange Consortium via the PRIDE partner repository with the dataset identifier PXD050407.

Results

Parallel reaction monitoring (PRM) is a sensitive and specific mass spectrometry technology to target proteolytic peptides of interest in a sample. PRM differs from regular bottom-up data dependent acquisition (DDA) mass spectrometry (Figure 1) in a number of ways. In DDA MS, MS1 spectra are recorded and based on the relative mass spectral intensities of peptide precursors, several are selected for fragmentation. Typically, the Top*N* most intense precursor peaks are selected in each duty cycle (consisting of MS1 + *x* MS2 spectra), with a dynamic exclusion time that prevents multiple selection events of the same precursor. This exclusion time ensures the sampling of the highest number of precursor peptides and, thus, the deepest coverage of the proteome. The peptide fragments are subsequently analyzed in the Orbitrap at high mass accuracy and high resolution. Next, fragmentation spectra are matched with *in silico* generated spectra of tryptic peptides resulting in identification of the peptide. Based on the MS1 and/or MS2 spectral intensities, semi-quantitative analysis of peptides is possible. There is a stochastic element in the DDA protocol,

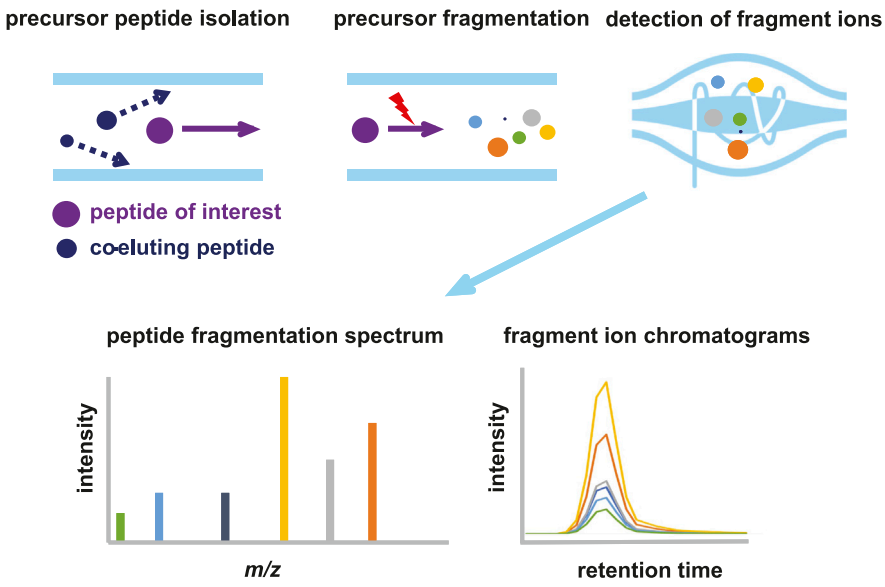

FIGURE 1
Schematic representation of parallel reaction monitoring (PRM) mass spectrometry. In PRM, the quadrupole is used to select and isolate ions of a predetermined *m/z* value. Precursor ions are then fragmented by CID or HCD to generate fragment ions, which are analyzed at high resolution and mass accuracy in the orbitrap. Quantitation is achieved by measuring the abundances (peak area under the curve or intensity) of the fragment ions derived from the target peptide. The summed abundances are then used to relatively quantify the peptide in different samples.

resulting in lower abundant peptides being eluted and detected in the MS1 spectrum, but not selected for fragmentation. These peptides will therefore not be identified in the database matching procedure.

In PRM, the mass spectrometer is configured in such a way that only *a priori* selected peptide precursors are isolated and fragmented. All available time can thus be allocated to the fragmentation and analysis of a limited selection of peptides, resulting in enhanced detection sensitivity. The first quadrupole in the Orbitrap act merely as a filter and allows only predetermined ions to pass, which are selected based on their highly accurate *m/z* and retention time (RT) window. All precursor ions that fulfill the selection criteria are continuously selected and fragmented, as long as the corresponding peptide elutes from the LC column. The selection of peptides of interest and their properties (i.e., *m/z* and RT) is based either on recorded spectra in earlier experiments, peptide libraries or AI based prediction models such as PROSIT (Gessulat et al., 2019). Fragmentation of the precursor leads to several fragment ions (called "transitions"), which have both highly specific *m/z* values and relative spectral intensities. Even using relatively short LC gradients, several 100 s proteolytic peptides can be targeted in a single LC-MS run.

We set out to compare the sensitivity and specificity of immunoblotting versus PRM. Rabbit glyceraldehyde 3-phosphate dehydrogenase (GAPDH) was chosen as the target protein of interest, since both the purified protein and highly specific antibodies were commercially available. First, we estimated the LOD for SDS-PAGE and Western blotting in a dilution series ranging from 100 ng to 1 pg. Using colloidal Coomassie blue (CBB) staining (Figure 2A) the visual LOD was about 100 ng of protein input, which is in accordance with the CBB manufacturer's indication that it can be used to visualize quantities of protein in the ng range. Using silver staining, the band representing GAPDH at 50 ng input material was still visible by the eye, while lower amounts were below the visual detection limit ((Figure 2B).

We then performed Western blotting with HRP-antibody conjugates on a similar dilution series. We used enhanced chemiluminescence (ECL) pico solution to simulate acquisition. With ECL pico, input amounts of down to 10 ng could still be detected (Figure 2C). While a band is visible in the 5 ng input amount long exposure channel, the intensity of the band does not correspond with the expected linear decrease in staining intensity and is thus most likely a background signal. We were not able to visualize protein amounts in the sub-nanogram range. Verification with another protein – antibody pair, *i.e.*, GST tagged *Drosophila* GAPDH and an in-house generated antibody against *Drosophila* GAPDH, did not result in the detection of quantities in the sub-nanogram range either (Supplementary Figure S1).

Now that we established the baseline detection of GAPDH using SDS-PAGE based immunoblotting methods, we set out to check the detection of GAPDH using PRM. We used a bottom-up mass spectrometry approach to first determine which tryptic peptides display the highest response in a DDA LC-MS analysis. We focused on three proteotypic peptides, *i.e.*, VIPELNGK, TVDGPSGK and QASEGPLK. GAPDH was digested with trypsin in a dilution series from 10 ng down to 10 pg and PRM was performed on the three target peptides. The MS/MS spectrum and extracted fragment ion chromatograms for peptide VIPELGNK are shown in Figures 3A, B; Supplementary Figure S2A, B. Starting from input amounts of 500 fg and lower, the number of detected transitions is reduced, although even at 10 fg one transition could still be clearly observed. In order to determine the limit of detection (LOD) and the dose-response correlation, we performed regression analysis on a dilution series, which revealed an R^2 of 0.9960 (Figure 3C). Similar assays for the

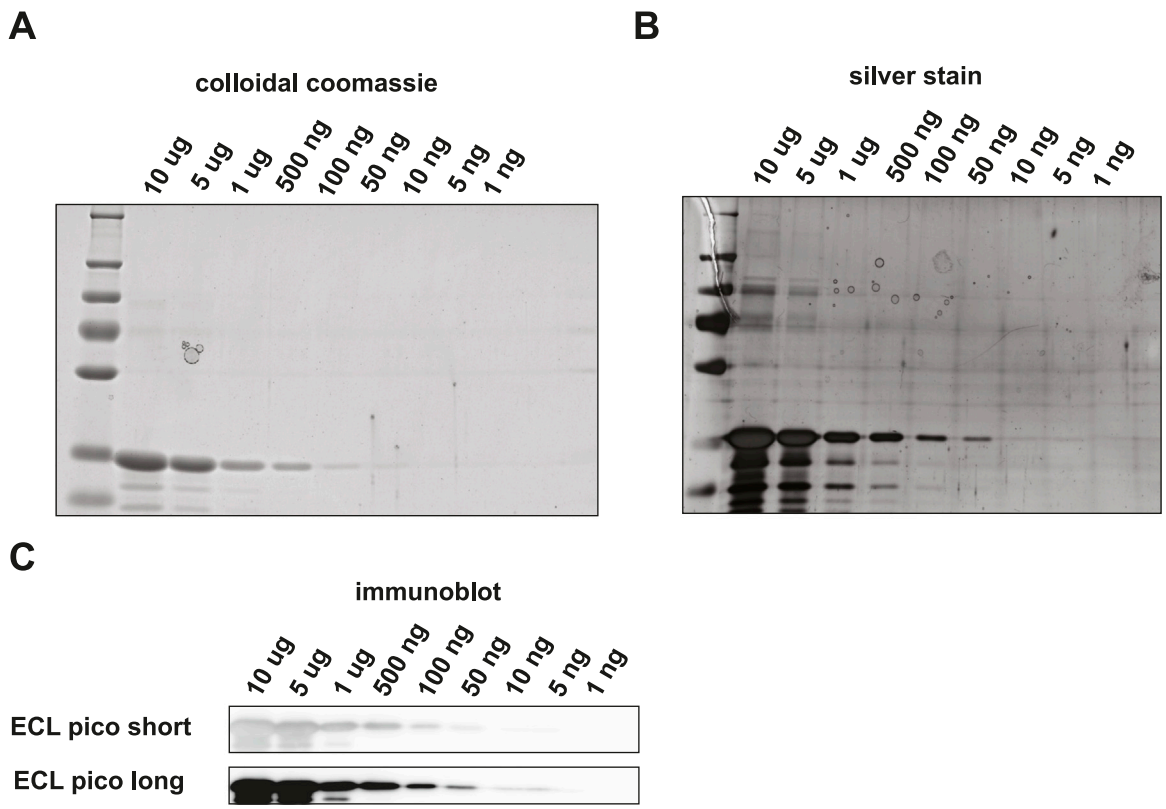

FIGURE 2
Detection of GAPDH loaded onto an SDS-PAGE gel and subsequent visualization using **(A)** colloidal coomassie, **(B)** silver stain **(C)** or Western blot followed by HRP-antibody binding and ECL Pico visualization.

two other GAPDH tryptic peptides, *i.e.*, TVDGPSGK and QASEGPLK, produced R^2 values of 0.9982 and 0.9984, respectively (Supplementary Figures S2C, S2F). Thus, there is a linear relationship between peptide input amount and observed spectral intensities of its specific fragment ions over at least 4 orders of magnitude. Most likely, this linear relationship spans even more order of magnitude, but we did not include higher amounts than 10 ng on column in the dilution series. At this stage, we did not include replicate experiments. Although the individual dilution series were all measured several times, this was done on different LC-MS setups and on different days. Given the variation in the absolute signals because of this, we therefore decided not to treat these as pure replicates.

Although the targeted detection of proteolytic peptides from a pure protein digest is a valid benchmark test to determine the assay sensitivity, the real power of such an assay would be reflected by the capability of detecting target proteins embedded in a complex biological matrix. Therefore, we set out to investigate the sensitivity of this method by targeting the same selection of tryptic peptides mixed into a complex protein matrix. To avoid cross species reactivity issues, we used an *S. cerevisiae* lysate as the background matrix. The amino acid sequences of the three target peptides under investigation were unique to rabbit GAPDH. First, GAPDH was spiked into 5 µg of a yeast whole cell lysate according to the dilution scheme used before (Figure 4). We then performed Western blotting and subsequent visualization via HRP-conjugated antibodies using two different ECL solutions. No apparent background signal was observed in the Western blotting samples in the MW range where GAPDH was expected. Using ECL pico visualization GAPDH could still be detected at 50 ng total input (Figures 4B, C).

Next, we performed PRM on digests of various amounts of GAPDH spiked into 200 ng of *S. cerevisiae* lysate. The same selection of target tryptic peptides as before were used (Figure 5A; Supplementary Figure S4). Highly accurate transitions were detected at input quantities >500 fg GAPDH, but with lower input amounts the background interference masked the specific signals. Transitions were scored based on the dotP value reported by Skyline and the output data were converted to bar graphs (Figure 5B; Supplementary Figures S4B, S4E). Regression analysis for the peptides VIPELNGK, TVDGPSGK and QASEGPLK produced R^2 values of the peptides as 0.9986, 0.9980 and 0.9980 respectively (Figure 5C; Supplementary Figures S4C, S4F), while the LODs were 5 pg, 1 pg and 10 pg, respectively. At this stage, we did not include replicate experiments. Although the individual dilution series were all measured several times, this was done on different LC-MS setups and on different days. Given the variation in the absolute signals because of this, we therefore decided not to treat these as pure replicates. In conclusion, the detection of very low amounts of peptide embedded in a complex background matrix was more challenging, and the LODs were roughly one order of magnitude higher than for the purified protein.

Under ideal digestion conditions, 50 fg (1.4 amol) GAPDH should produce 1.4 amol of each tryptic peptide. We determined the

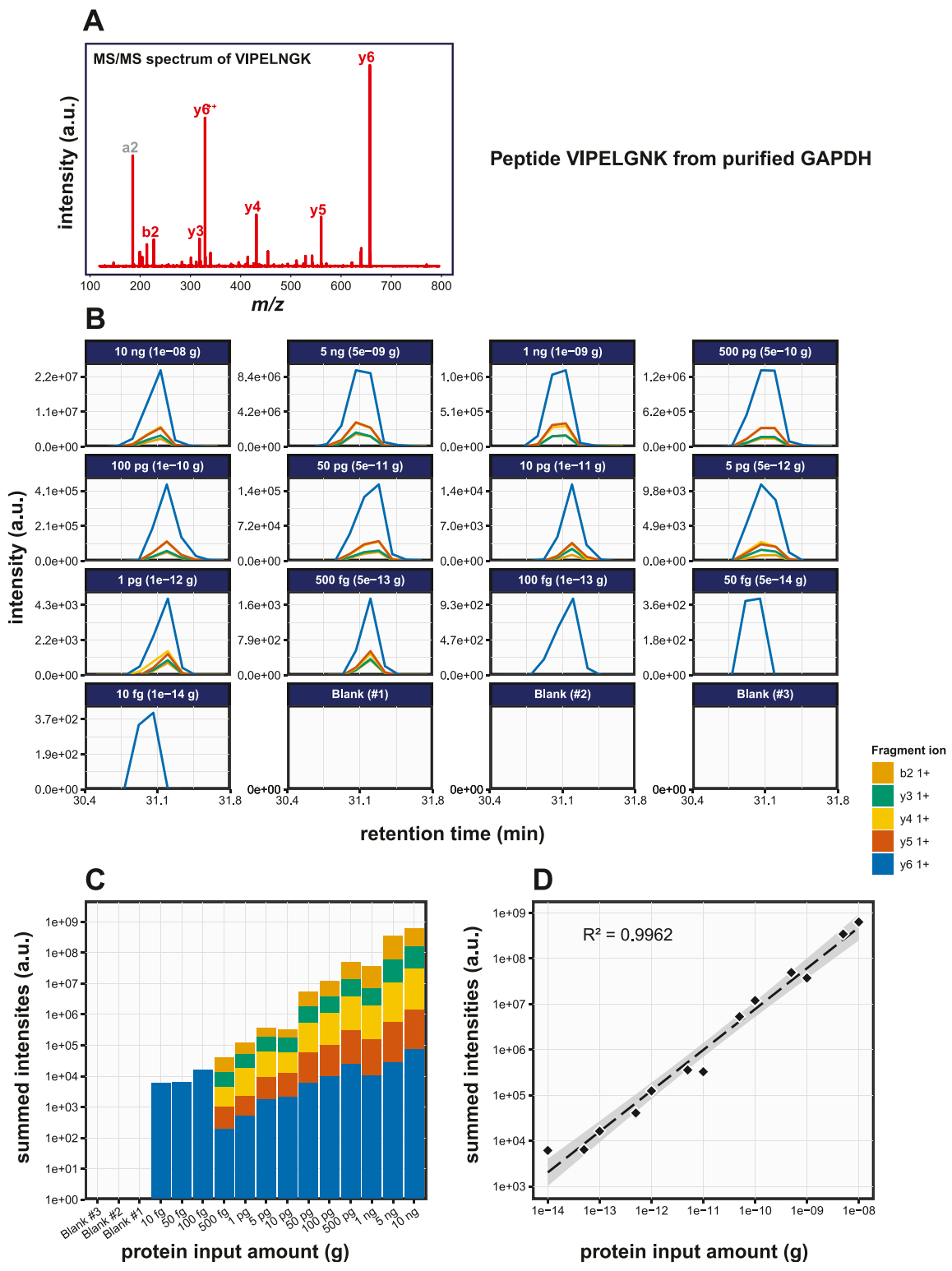

FIGURE 3
Detection of the GAPDH derived tryptic peptide VIPELGNK using PRM. **(A)** MS/MS spectrum of the VIPELGNK peptide. **(B)** Fragment ion chromatograms of VIPELGNK, exported from Skyline. **(C)** Area under the curve (AUC) plot of the fragment ion chromatograms shown in **(B)**. **(D)** Regression analysis of the data shown in **(C)** with the best fit line drawn in striped black.

trypsin digestion efficiency by spiking a known amount of a heavy isotope labeled variant of peptide VIPELNGK (VIPELNGK(+8)) into the sample to absolutely quantitate the peptide. The heavy isotope labeled lysine residue ensures that it can be distinguished from endogenous, non-labeled VIPELNGK peptide by its higher *m/z* value, while keeping similar biophysical properties such as

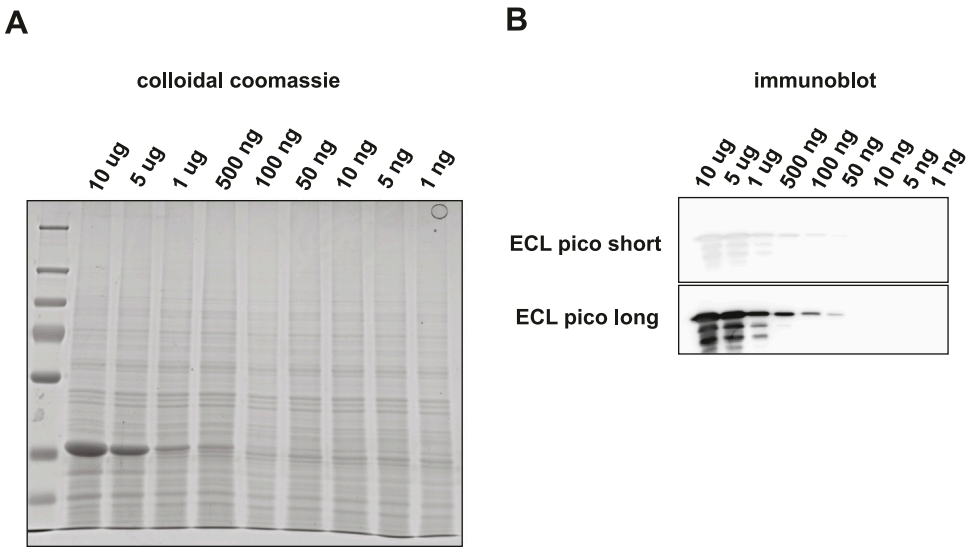

FIGURE 4
Detection of GAPDH embedded in a 200 ng yeast total lysate background matrix using SDS-PAGE and subsequent visualization by **(A)** colloidal coomassie staining or by **(B)** Western blot followed by HRP-antibody binding and ECL Pico visualization.

electrospray ioinization responsiveness and retention time unchanged. As such, mass spectral intensity ratios can be used for absolute quantitation.

Known amounts of AQUA peptide were spiked into both the purified GAPDH sample and the GAPDH mixed with yeast lysate sample. 500 pg (14 fmol) of GAPDH was digested under standard conditions and then mixed with 10 fmol of VIPELNGK (+8). The resulting mixed sample was then added to 200 ng yeast lysate. The results of the PRM assay on these samples are shown in Figures 6A, B. The overall intensities for the transitions of the endogenous peptide were 2.74 ± 0.05 x lower than those of the heavy peptide (Figure 6B). Precision is generally expressed as coefficient of variation (CV) and the repeatability in a triplicate analysis was very good as evidenced by the low standard deviations and CV values for both the endogenous and the spiked-in AQUA target peptides in both the purified GAPDH sample and the GAPDH mixed in a complex biological matrix sample (Figure 6C). The latter represents a more realistic biological situation and although high levels of contaminating proteins might disturb the detection of the target peptide, these data show that the target peptide can still be detected at very low levels, illustrating the robustness of the methodology. All CV's were far below 20%, which is considered a good precision in a PRM assay (see, e.g., (Gallien et al., 2015)). The use of an AQUA peptide spike-in allows the absolute quantitation of target peptides. If the digestion efficiency were 100%, the mass spectral intensities for the endogenous peptide are expected to be 1.4 x higher than for the AQUA peptide. In contrast, since the total area fragment signal of the endogenous peptide is 3.84 x lower, this indicates that only 3.65 fmol of the endogenous peptide was present in the sample, suggesting a digestion efficiency of only 27%. From this, we conclude that the genuine LOD is in fact approximately four times lower than was calculated from the initial experiment without the presence of AQUA peptide.

Discussion

Targeted detection of specific proteins in complex matrices is a cornerstone in molecular biology and reliable detection and quantitation of protein levels over a large input range and in a robust manner is of utmost importance. Traditionally, immunoassays have been used since several decades and although several minor improvements have been made since these methodologies still suffer from severe limitations. Here, we investigate the advantages of targeted mass spectrometry based on parallel reaction monitoring (PRM) over immuno-based methods. PRM is presented as a superior alternative for targeted detection of proteins and is able to overcome at least some of the limitations posed by immunoblotting.

One of the major limitations of immunoassays is the dependence on highly specific antibodies targeting the protein of interest. It is not uncommon for an antibody to have off-target effects, *i.e.*, target the wrong epitope and, thus, protein. Such off-target effects obviously hamper a correct interpretation of the results. Targeted mass spectrometry does not require the use of antibodies. The specificity of the methodology is fully embedded in the unique character of the amino acid sequence of the target peptide. Fragmentation of a peptide results in a unique combination of fragment ion *m/z* values (referred to as transitions) and intensities and often also retention time when LC-MS based methods are used. Even when no experimental peptide fragmentation spectra are available to serve as library spectrum for comparison purposes, *in silico* digestion in combination with AI based approaches [*e.g.*, (Gessulat et al., 2019; Searle et al., 2020),] can result in reliable transition predictions. In addition, large repositories of high-resolution DDA peptide fragmentation mass spectrometry data contain millions of spectra that can be used as transition libraries for PRM acquisition experiments. To increase the reliability even further, multiple tryptic peptides per protein can be targeted in one

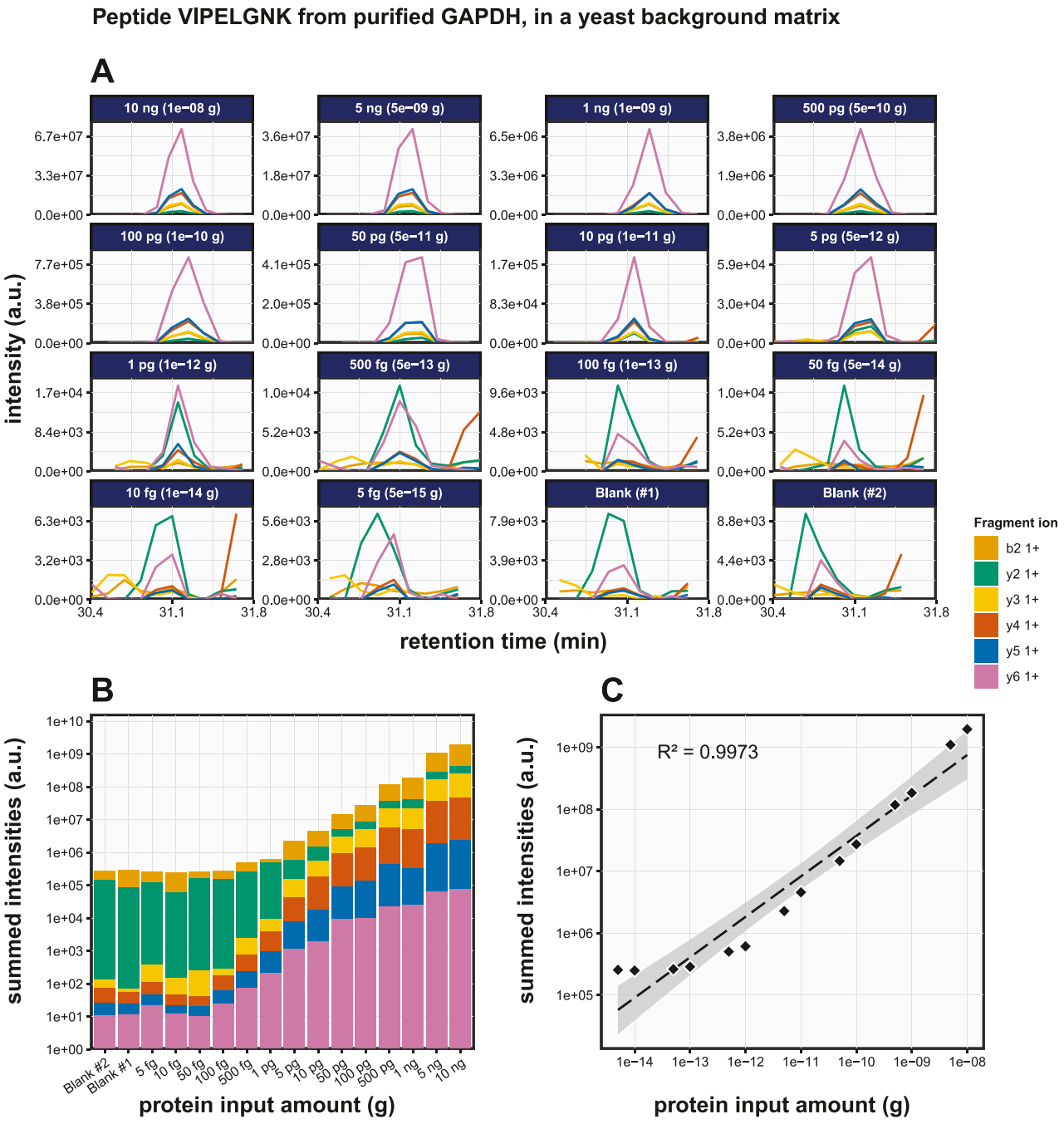

FIGURE 5
Detection of the GAPDH derived tryptic peptide VIPELGNK in a yeast total lysate background matrix using PRM. **(A)** Fragment ion chromatograms of peptide VIPELGNK in a yeast background (200 ng per sample), exported from Skyline. **(B)** AUC bar graphs of the fragment ion chromatograms shown in **(B)**. **(C)** Regression analysis of the data shown in **(B)** with the best fit line drawn in in striped black.

assay and multiple proteins (several 10 or even 100 s) can thus be targeted in a single LC-MS run. Importantly, we show here that PRM shows a linear dose-dependent intensity correlation over an extended range of input values that spans at least five orders of magnitude and probably more. In addition, for absolute quantitation of peptides we also show here that heavy isotope labeled AQUA peptides can be used as a spike-in or calibrants. To increase the sensitivity of PRM, prior fractionation of the digested protein sample into multiple peptide fractions by HILIC, high pH reversed phase (RP) or any other fractionation method, could be included in the workflow. We have shown before that this methodology can be used to detect and relatively quantify SARS-CoV-2 Nucleocapsid derived tryptic peptides both in research samples as well as in clinical specimens (van der Wal et al., 2018), illustrating that the technology can indeed be used for diagnostic purposes.

The reliable quantitation of proteins using Western blotting is challenging. Although one advantage of immunoblotting is

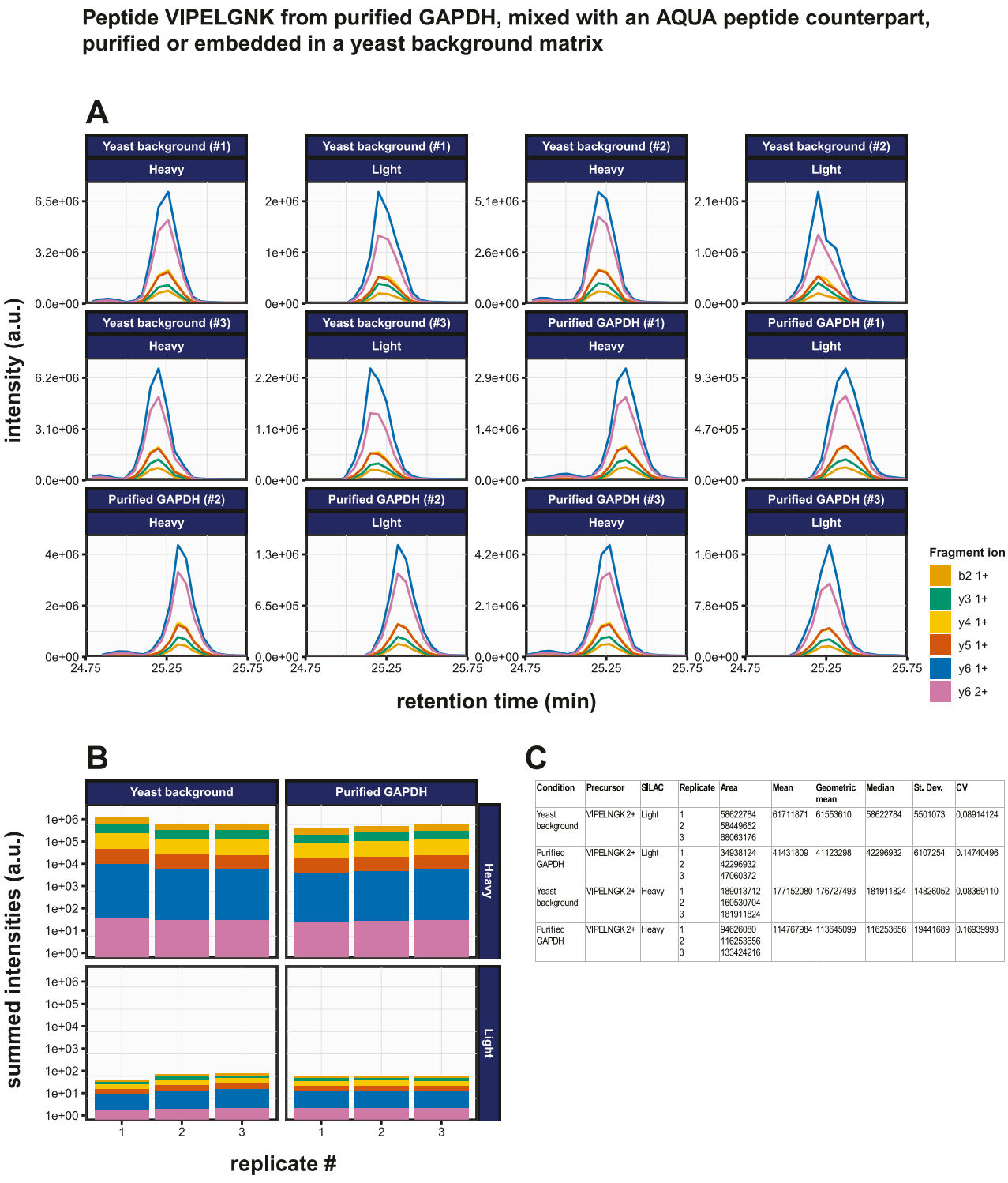

Condition	Precursor	SILAC	Replicate	Area	Mean	Geometric mean	Median	St. Dev.	CV
Yeast background	VIPELNGK 2+	Light	1 2 3	58622784 58449652 68063176	61711871	61553610	58622784	5501073	0.08914124
Purified GAPDH	VIPELNGK 2+	Light	1 2 3	34938124 42296932 47060372	41431809	41123298	42296932	6107254	0.14740496
Yeast background	VIPELNGK 2+	Heavy	1 2 3	189013712 160530704 181911824	177152080	176727493	181911824	14826052	0.08369110
Purified GAPDH	VIPELNGK 2+	Heavy	1 2 3	94626080 116253656 133424216	114767984	113645099	116253656	19441689	0.16939993

FIGURE 6
Absolute quantification of the GAPDH derived tryptic peptide VIPELGNK using PRM. **(A)** Fragment ion chromatograms exported from Skyline of the endogenous peptide VIPELGNK (light) and of the isotopically labeled AQUA peptide VIPELGNK(+8) (heavy). Ten fmol of the AQUA peptide was spiked into the sample. Results from purified GAPDH as well as from GAPDH embedded in a 200 ng yeast total lysate background matrix are shown. **(B)** AUC bar graphs of light and heavy VIPELGNK peptide based on data in **(A)**. **(C)** Statistical and variability analysis of data in **(B)**.

fractionation of proteins by SDS-PAGE electrophoresis prior to transferring the proteins to the Western blot membrane, differences in protein expression can be only relatively quantified and also the expression levels under different conditions should not differ too much. Large differences in expression levels cannot be accurately quantified because the dynamic range is only limited, while more subtle differences present additional challenges. A twofold increase of protein input amount often does not result in a likewise increase

of the staining intensities (Hammond et al., 2013), even though Western blot quantitation is often intensity based. Therefore, the staining intensities on an immunoblot may not accurately represent the absolute protein differences. The staining intensity on an immunoblot depends on several factors, such as the readout method that is used, the concentration of antibody, the absolute amount of protein, the exposure time, etc.

The time investment required to perform SDS-PAGE based protein detection and Western blotting is reasonable low. The whole procedure can be completed in half a day, with some waiting time. The time investment in PRM is about half a day to a day, including sample prep and input of the necessary information for the mass spectrometer to detect the necessary precursor ions. However, in this time frame, a much higher number of proteins can be detected, with negligible extra mass spectrometry time or sample preparation required. Thus, although in speed Western blotting may outperform PRM, this is completely compensated for by the much higher power to multiplex the PRM assay without substantial extra time investment [see, e.g., (Sijm et al., 2022)]. In terms of costs, assuming that a high-resolution mass spectrometer is available, the running costs are relatively low as no expensive antibodies are needed.

In conclusion, in terms of detection sensitivity, specificity and multiplexing targeted proteomics-based methods like PRM are superior over immunoblotting assays. We advocate the use of PRM as an alternative to Western blotting and ELISA assays in molecular biology, biomedical research and clinical and diagnostic assays.

Data availability statement

The datasets presented in this study can be found in online repositories. The names of the repository/repositories and accession number(s) can be found in the article/Supplementary Material.

Author contributions

KB: Conceptualization, Data curation, Formal Analysis, Funding acquisition, Investigation, Methodology, Project administration, Resources, Software, Supervision, Validation, Visualization, Writing–review and editing. LV: Data curation, Methodology, Project administration, Visualization, Writing–review and editing. WD: Data curation, Formal Analysis, Methodology, Software, Visualization, Writing–review and editing. JD: Conceptualization, Data curation, Formal Analysis, Funding acquisition, Investigation, Methodology, Project administration, Resources, Software, Supervision, Validation, Visualization, Writing–original draft, Writing–review and editing.

Funding

The author(s) declare that no financial support was received for the research, authorship, and/or publication of this article.

Conflict of interest

The authors declare that the research was conducted in the absence of any commercial or financial relationships that could be construed as a potential conflict of interest.

The author(s) declared that they were an editorial board member of Frontiers, at the time of submission. This had no impact on the peer review process and the final decision.

Publisher's note

Supplementary material

The Supplementary Material for this article can be found online at: https://www.frontiersin.org/articles/10.3389/frans.2024.1397810/full#supplementary-material

References

Bluemlein, K., and Ralser, M. (2011). Monitoring protein expression in whole-cell extracts by targeted label- and standard-free LC-MS/MS. *Nat. Protoc.* 6, 859–869. doi:10.1038/nprot.2011.333

Burnette, W. N. (1981). "Western blotting": electrophoretic transfer of proteins from sodium dodecyl sulfate--polyacrylamide gels to unmodified nitrocellulose and radiographic detection with antibody and radioiodinated protein A. *Anal. Biochem.* 112, 195–203. doi:10.1016/0003-2697(81)90281-5

Chambers, A. G., Percy, A. J., Simon, R., and Borchers, C. H. (2014). MRM for the verification of cancer biomarker proteins: recent applications to human plasma and serum. *Expert Rev. Proteomics* 11, 137–148. doi:10.1586/14789450.2014.877346

Deng, D., and Zi, Z. (2022). "Absolute quantification of TGF-β signaling proteins using quantitative western blot," in *Methods in molecular biology*, 1–12.

Gallien, S., Kim, S. Y., and Domon, B. (2015). Large-scale targeted proteomics using internal standard triggered-parallel reaction monitoring (IS-PRM). *Mol. Cell. Proteomics* 14, 1630–1644. doi:10.1074/mcp.O114.043968

Gessulat, S., Schmidt, T., Zolg, D. P., Samaras, P., Schnatbaum, K., Zerweck, J., et al. (2019). Prosit: proteome-wide prediction of peptide tandem mass spectra by deep learning. *Nat. Methods* 16 (16), 509–518. doi:10.1038/s41592-019-0426-7

Ghosh, R., Gilda, J. E., and Gomes, A. V. (2014). The necessity of and strategies for improving confidence in the accuracy of western blots. *Expert Rev. Proteomics* 11, 549–560. doi:10.1586/14789450.2014.939635

Hammond, M., Kohn, J., Oh, K., and Liu, N. (2013). A method for greater reliability in western blot loading controls: stain-free total protein quantitation. *Biorad Bull.* 6360.

Jayasena, T., Poljak, A., Braidy, N., Zhong, L., Rowlands, B., Muenchhoff, J., et al. (2016). Application of targeted mass spectrometry for the quantification of sirtuins in the central nervous system. *Sci. Rep.* 6, 35391. doi:10.1038/srep35391

Kulyyassov, A., Fresnais, M., and Longuespée, R. (2021). Targeted liquid chromatography-tandem mass spectrometry analysis of proteins: basic principles, applications, and perspectives. *Proteomics* 21, 2100153. doi:10.1002/PMIC.202100153

Lau, T. Y. K., Collins, B. C., Stone, P., Tang, N., Gallagher, W. M., and Pennington, S. R. (2011). Absolute quantification of toxicological biomarkers by multiple reaction monitoring. *Methods Mol. Biol.* 691, 417–427. doi:10.1007/978-1-60761-849-2_25

MacLean, B., Tomazela, D. M., Shulman, N., Chambers, M., Finney, G. L., Frewen, B., et al. (2010). Skyline: an open source document editor for creating and analyzing targeted proteomics experiments. *Bioinformatics* 26, 966–968. doi:10.1093/bioinformatics/btq054

Makarov, A. (2000). Electrostatic axially harmonic orbital trapping: a high-performance technique of mass analysis. *Anal. Chem.* 72, 1156–1162. doi:10.1021/AC991131P

Martínez-Márquez, A., Morante-Carriel, J., Sellés-Marchart, S., Martínez-Esteso, M. J., Pineda-Lucas, J. L., Luque, I., et al. (2013). Development and validation of MRM methods to quantify protein isoforms of polyphenol oxidase in loquat fruits. *J. Proteome Res.* 12, 5709–5722. doi:10.1021/pr4006712

Parsons, H. T., and Heazlewood, J. L. (2015). Beyond the Western front: targeted proteomics and organelle abundance profiling. *Front. Plant Sci.* 6, 301. doi:10.3389/fpls.2015.00301

Peterson, A. C., Russell, J. D., Bailey, D. J., Westphall, M. S., and Coon, J. J. (2012). Parallel reaction monitoring for high resolution and high mass accuracy quantitative, targeted proteomics. *Mol. and Cell. Proteomics* 11, 1475–1488. doi:10.1074/MCP.O112.020131

Prasad, B., and Unadkat, J. D. (2014). Optimized approaches for quantification of drug transporters in tissues and cells by MRM proteomics. *AAPS J.* 16, 634–648. doi:10.1208/s12248-014-9602-y

Searle, B. C., Swearingen, K. E., Barnes, C. A., Schmidt, T., Gessulat, S., Küster, B., et al. (2020). Generating high quality libraries for DIA MS with empirically corrected peptide predictions. *Nat. Commun.* 11, 1548–1610. doi:10.1038/s41467-020-15346-1

Shi, T., Song, E., Nie, S., Rodland, K. D., Liu, T., Qian, W. J., et al. (2016). Advances in targeted proteomics and applications to biomedical research. *Proteomics* 16, 2160–2182. doi:10.1002/pmic.201500449

Sijm, A., Atlasi, Y., Knaap, J. A. V. D., Meer, J. W. V. D., Chalkley, G. E., Bezstarosti, K., et al. (2022). USP7 regulates the ncPRC1 Polycomb axis to stimulate genomic H2AK119ub1 deposition uncoupled from H3K27me3. *Sci. Adv.* 2. doi:10.1126/sciadv.abq7598

Smith, B. J. (1994). "SDS polyacrylamide gel electrophoresis of proteins," in *Basic protein and peptide protocols* (New Jersey: Humana Press), 23–34. doi:10.1385/0-89603-268-X:23

Sowers, J. L., Mirfattah, B., Xu, P., Tang, H., Park, I. Y., Walker, C., et al. (2015). Quantification of histone modifications by parallel-reaction monitoring: a method validation. *Anal. Chem.* 87, 10006–10014. doi:10.1021/acs.analchem.5b02615

Thorsen, A. S. F., Riber, L. P. S., Rasmussen, L. M., and Overgaard, M. (2023). A targeted multiplex mass spectrometry method for quantitation of abundant matrix and cellular proteins in formalin-fixed paraffin embedded arterial tissue. *J. Proteomics* 272, 104775. doi:10.1016/j.jprot.2022.104775

Towbin, H., Staehelin, T., and Gordon, J. (1979). Electrophoretic transfer of proteins from polyacrylamide gels to nitrocellulose sheets: procedure and some applications. *Proc. Natl. Acad. Sci. U. S. A.* 76, 4350–4354. doi:10.1073/PNAS.76.9.4350

Tsuchiya, H., Tanaka, K., and Saeki, Y. (2013). The parallel reaction monitoring method contributes to a highly sensitive polyubiquitin chain quantification. *Biochem. Biophys. Res. Commun.* 436, 223–229. doi:10.1016/j.bbrc.2013.05.080

van der Wal, L., Bezstarosti, K., Sap, K. A., Dekkers, D. H. W., Rijkers, E., Mientjes, E., et al. (2018). Improvement of ubiquitylation site detection by Orbitrap mass spectrometry. *J. Proteomics* 172, 49–56. doi:10.1016/j.jprot.2017.10.014

Weller, M. G. (2016). Quality issues of research antibodies. *Anal. Chem. Insights* 2016, 21–27. doi:10.4137/Aci.s31614

Westermeier, R. (2014). Looking at proteins from two dimensions: a review on five decades of 2D electrophoresis. *Arch. Physiol. Biochem.* 120, 168–172. doi:10.3109/13813455.2014.945188

Yang, T., Xu, F., Xu, J., Fang, D., Yu, Y., and Chen, Y. (2013). Comparison of liquid chromatography-tandem mass spectrometry-based targeted proteomics and conventional analytical methods for the determination of P-glycoprotein in human breast cancer cells. *J. Chromatogr. B Anal. Technol. Biomed. Life Sci.* 936, 18–24. doi:10.1016/j.jchromb.2013.07.023

Yang, T., Xu, F., Zhao, Y., Wang, S., Yang, M., and Chen, Y. (2014). A liquid chromatography-tandem mass spectrometry-based targeted proteomics approach for the assessment of transferrin receptor levels in breast cancer. *Proteomics Clin. Appl.* 8, 773–782. doi:10.1002/prca.201300109

frontiers | Frontiers in Analytical Science

TYPE Review
PUBLISHED 06 December 2024
DOI 10.3389/frans.2024.1505510

OPEN ACCESS

EDITED BY
Zhanjun Yang,
Yangzhou University, China

REVIEWED BY
Ying Liu,
Nanjing University, China
José Alberto Fracassi da Silva,
State University of Campinas, Brazil
Chen Zong,
China Pharmaceutical University, China

*CORRESPONDENCE
Quan Cheng,
quan.cheng@ucr.edu

†These authors have contributed equally to this work and share first authorship

RECEIVED 03 October 2024
ACCEPTED 22 November 2024
PUBLISHED 06 December 2024

CITATION
Malinick AS, Ebel CP, Stuart DD, Valiulis SN, Hanson VA and Cheng Q (2024) Novel and rapid analytical platform development enabled by advances in 3D printing.
Front. Anal. Sci. 4:1505510.
doi: 10.3389/frans.2024.1505510

Novel and rapid analytical platform development enabled by advances in 3D printing

Alexander S. Malinick†, Cole P. Ebel†, Daniel D. Stuart, Santino N. Valiulis, Victor A. Hanson and Quan Cheng*

Department of Chemistry, University of California, Riverside, Riverside, CA, United States

3-Dimensional (3D) printing technology has greatly facilitated the recent advancements in science and engineering that benefit many aspects of scientific investigation, with examples including disease diagnostics, dentistry, aerospace, and fundamental research. For analytical chemistry, many advancements can be directly linked to achievements associated with 3D printing of optics, flow systems, mechanical/structural components, and parts related to detection/measurement, which before the advent of 3D printing were limited by complicated, cumbersome, expensive, and material-limited production. More importantly, the totality of these advances has made the possibility of 3D printing the majority of an analytical system an achievable reality. In this review, we highlight the recent achievements and advancements reported in literature that will facilitate the development of the next-generation analytical instrumentation through the use of 3D printing technology. A great deal of attention is given to those in the context of bioanalytical platforms and novel biosensing strategies. Limited by space, we will explicitly focus the discussion on the following areas: improvement/utilization of new printing materials, methods towards higher resolution, fabrication and production of optical components, novel microfluidic flow systems, and printed structural components for instrumentation.

KEYWORDS

3D printing, analytical instrumentation, optics, fluidics, scaffolds

1 Introduction

3D printing, also known as additive manufacturing, is a rapidly evolving field that has revolutionized the workflow of a number of diverse disciplines (Shahrubudin et al., 2019; Su X. et al., 2021; Dawood et al., 2015; Lambert et al., 2018; Cardoso et al., 2020; Su, 2021; Grajewski et al., 2021). The widespread adoption of 3D printing can be attributed to three key factors. First, the ease of generation and modification of 3D printed objects, which relies on user-friendly computer aided design (CAD) software (Junk and Kuen, 2016). Second, 3D printing is relatively inexpensive and allows access to a large range of printable materials (Shahrubudin et al., 2019), including polymers, organics, glass, ceramics, and metals, the vast majority of which are commercially available (Lee et al., 2017). Third, rapid improvements in print resolution, have facilitated the creation of defined features both on and within the printed object that were previously impossible, enabling new applications (Shahrubudin et al., 2019; Lee et al., 2017). These features have made the process of going from concept to prototype more efficient and reliable. While many 3D printing techniques exist and offer different degrees of power and capability, the most widely used ones, include

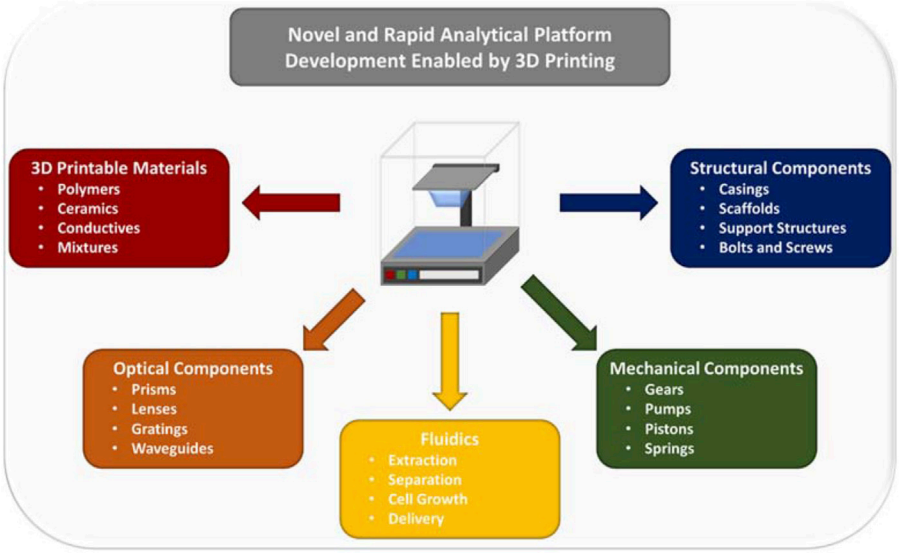

GRAPHICAL ABSTRACT

fused deposition modeling (FDM) (Mohamed et al., 2015), VAT polymerization stereolithography (SLA) (Ng et al., 2020), digital light processing (DLP) (Amini et al., 2023), polyjet printing (PJT) (Layani et al., 2018), selective laser sintering (SLS) (Kruth et al., 2003), and two photon printing (T-PP) (Xing et al., 2015). A summary of the general advantages and disadvantages of each technique is shown in Table 1.

FDM involves the layer-by-layer extrusion of semi-liquid material through a heated nozzle (Mohamed et al., 2015). The materials come in the form of long thermoplastic filaments, such as polylactic acid (PLA) and acrylonitrile butadiene styrene (ABS), or biocompatible and highly chemical resistant chemicals such as polyetheretherketone (PEEK), fluoropolymers, polyetherimide (PEI), as well as various composite materials (Shanmugam et al., 2021). FDM based 3D printers tend to be quite affordable and can quickly produce macrostructures, making them an attractive option for applications in which high print precision is not necessary. Additionally, many of these devices are compatible with multi-material printing by exchanging the material being extruded, thereby expanding the applicability of FDM-based 3D printers by allowing for configurations of unique physio-chemical properties (Mohamed et al., 2015). Another key advantage associated with FDM-based 3D printing is that it requires little to no post-processing after deposition, thereby further reducing both expense and production time. However, FDM has some major limitations including low resolution, high surface roughness, and poor mechanical robustness due to lack of strong bonding between layers.

While both SLA and DLP are vat polymerization 3D printing methods (Quan et al., 2020), they have slightly different operating workflows. DLP relies on a conventional stationary light source, such as an arc lamp that triggers the polymerization process of the liquid monomer, usually an epoxy or acrylic-based resin (Quan et al., 2020). The 3D object is built layer-by-layer by hardening the photopolymer on a movable solid platform. SLA uses a UV laser to harden the polymer in both the X and Y coordinates tracing a cross section of the mold spot-to-spot until the layer is completed (Quan et al., 2020). In DLP the operator can control the intensity of the light source thus changing the consistency of the 3D print, which contrasts with the laser used in SLA that cannot be adjusted (Maines et al., 2021). SLA offers better curing (hardening) of the 3D print through the layer-by-layer process, thus potentially improving the surface quality of the print when compared to DLP (Jiang et al., 2022). In terms of printing speed, DLP is generally faster than SLA, as it polymerizes the entire layer at once (Maines et al., 2021). When compared to FDM, both SLA and DLP show significantly reduced surface roughness, lower porosity, and higher resolution at the expense of a higher cost (Quan et al., 2020). While commercial vat polymerization printers currently do not support multi material printing recently Fernandes et al. (2023) have developed a DLP printer that replaced the resin within the vat enabling multi material printing to be achieved.

PJT printers use photocurable liquid resins similar to those employed in VAT polymerization strategies (SLA/DLP), while carrying the added benefit of multi-material printing (Su, 2021). While SLA/DLP rely on the photopolymer as the support for the print, PJT uses a wax filling material as the support during the print (Su, 2021). PJT systems achieve this by employing inkjet heads in conjunction with photopolymers polymerized by a UV light to produce 3D printed structures where different materials can be introduced through a set of inkjet heads. Generally, PJT is used for the production of multi-material parts with complex structures that require smooth surface quality/low porosity such as microfluidics and membranes, though PJT is limited in its ability to produce small, closed channels due to the need to remove support material. The substantially higher expense when compared to vat-polymerization and FDM is also a potential major drawback (Carrasco-Correa et al., 2021). In addition to high cost, another drawback of PJT is the long post-processing of the print, particularly with regards to highly complex designs, which makes this method less attractive for some scientific applications (Carrasco-Correa et al., 2021).

SLS operates by fusing cross sections of a powdered material deposited on a solid support using a high-powered laser (Gross et al.,

TABLE 1 Overview of advantages and disadvantages of some of the major 3D printing techniques for development of bioanalytical instrumentation.

Print type	Advantages	Disadvantages	Compatible materials	Common analytical applications	References
Fused Deposition Modeling (FDM)	No post-processing Wide variety of printable materials Multi-material printing Very affordable High throughput	Final print is not smooth Low resolution in the X, Y, and Z-axes Poor bonding between layers Generally, requires structural supports/waste material	Thermoplastics Ceramic Composites Metal Composites	Mechanical Components Structural Components Electrochemical Components Casings	Mohamed et al. (2015), Shanmugam et al. (2021), Kalinke et al. (2020)
Vat Polymerization (SLA/DLP)	Smooth surface quality Transparent options Decent resolution in Z-axis High resolution in X and Y-axes Strong bonding between layers Affordable	Post processing required Commercial printers are incompatible with multi-materials Many materials are proprietary Generally, requires structural supports/waste material	Photopolymers	Optical Components Mechanical Components Fluidics/Microfluidics	Ng et al. (2020), Quan et al. (2020), Maines et al. (2021), Jiang et al. (2022), Fernandes et al. (2023), Milton et al. (2023)
Selective Laser Sintering (SLS)	High precision in X, Y, and Z-axes Very strong final material Metal and ceramic printing compatible No structural supports required	Post-processing required for smooth surface Very expensive	Polymers Metals Ceramics	Electrochemical Components	Kruth et al (2003), Gross et al. (2017), Zhang et al. (2021a), Jonušauskas et al. (2018), Gadagi and Lekurwale (2021), Ngo et al., (2018), Ni et al. (2019)
Two-Photon Printing (T-PP)	High Precision in X, Y, and Z-axes Highest resolution for features Lowest surface roughness Biocompatible options Transparent options Support structures not required	Very low throughput Expensive	Photopolymers Hydrogels	Small Optical Components Microfluidics	Xing et al. (2015), Carlotti and Mattoli (2019), Agrawaal and Thompson (2021), He et al. (2018), Purtov et al. (2019)
Polyjet Printing (PJT)	Decent resolution in Z-axis Smooth surface quality Multi-material printing	Low resolution in X and Y-axes Generally, requires structural supports/waste material Post-processing can be extensive Poorer mechanical strength than FDM Expensive	Photopolymers	Fluidics/Microfluidics	Su (2021), Layani et al. (2018), Carrasco-Correa et al. (2021), Gupta and Paull (2021), Keshan Balavandy et al. (2021)

2017). The solid support is moved after each cross section is completed, more powder is applied, and the process is repeated until the 3D printed structure is finished (Zhang D. et al., 2021). Because the unfused powder remains to support the structure as it is constructed, unique geometries can be facilitated that are not possible with some of the previously discussed methods (Jonušauskas et al., 2018). Using SLS additionally allows for the use of a wider range of materials such as ceramics, metals, organic polymers, and glass. While this process allows for high precision, the complex cleaning process and the use of high-powered laser make SLS expensive and largely inaccessible for hobbyists and researchers alike (Shahrubudin et al., 2019; Vanaei et al., 2021).

The final major 3D printing modality that will be discussed in this review is T-PP (Carlotti and Mattoli, 2019). T-PP operates through a pulsed laser that polymerizes photoactive material at single points within the bulk polymer with high precision (Xing et al., 2015). Due to the polymerization process of T-PP, exceptionally small feature structures can be generated that are well outside the capabilities of other 3D printing techniques (Agrawaal and Thompson, 2021). This quality has made T-PP an extremely valuable tool for applications that require high precision, such as tissue engineering, drug delivery, and optical component development (Carlotti and Mattoli, 2019). However, T-PP comes with a major limitation in print speed due to the point-by-point nature of the printing method. Hence, its usage is generally limited to very small objects.

While many areas of study are using 3D printing in a plethora of unique ways, the presented review will focus on the advancements and utilization of the aforementioned 3D printing methods in the context of bioanalytical sciences, particularly regarding the instrumentation used in those studies. To date, researchers in the field of bioanalytical sciences have used 3D printing for the fabrication of various components for analytical instruments, including but not limited to moving components, casings, optics, flow systems and sensing platforms (Carrasco-Correa et al., 2021; Ambrosi and Bonanni, 2021; Bishop et al., 2016). This has dramatically expanded the capabilities and accessibility of various analytical instruments, as well as reducing the long-term operation

cost of the instruments (Carrasco-Correa et al., 2021). With the ever-increasing reliability and technical capabilities of 3D printing, the question of whether a complete analytical system/instrument can be 3D printed and mass produced has arisen (Bishop et al., 2016). From the recent advancements in areas such as new materials, higher resolution methods, and increased print speed, it has become increasingly clear that the answer to this question is a resounding yes. This review will cover some of the recent developments and achievements that have a strong linkage to creating analytical platforms with printing technology and the works that can serve as a resource for implementing 3D printing strategies into the construction of analytical instruments.

While several reviews in the past have covered 3D printing topics in great detail ranging from materials, optical components, microfluidic systems, and more. The presented review attempts to give a new perspective on recent advances in the field of 3D printing related to analytical instrumentation, and to then present an outline on how one could effectively 3D print the bulk of an instrument. For the purposes of this work, the designation of analytical instrument will apply to an instrument that quantitatively measures the presence, properties, interactions, and/or composition of and analyte or solution of interest. While a great deal of publications are widely available related to the 3D printing of various analytical instrumentation components we attempt to outline the process by which one using various materials and methods could generate a 3D printed instrument composed of structural components, moving parts (gears and pumps), optical pieces (prisms and lenses), flow/separation systems (microfluidics and chromatography columns), and/or sensors.

2 3D printing materials

While the 3D printing strategies mentioned above have provided avenues to construct increasingly detailed and functional structures, many of their current capabilities are due to advances in the materials available. These materials are fundamental to the functioning of 3D printing techniques and therefore can enable improvements in a variety of areas, such as print speed (Khosravani and Reinicke, 2020), cost (Carrasco-Correa et al., 2021), resolution (Mao et al., 2017; Wen et al., 2021), surface roughness (Hartcher-O'Brien et al., 2019; Vaidya and Solgaard, 2018a; Al-Dulaijan et al., 2022), biocompatibility (Sta. Agueda et al., 2021; Guttridge et al., 2022), resistance to degradation (Chen et al., 2018; Upadhyay et al., 2020; Khalfa et al., 2021), solvent resistance (Heikkinen et al., 2018; Erokhin et al., 2019), transparency (Nguyen et al., 2017; Odent et al., 2017; Cecil et al., 2020), conductivity (Cardoso et al., 2020; Su, 2021), as well as other diverse properties, such as flexibility (Balakrishnan et al., 2021; Lin et al., 2022). Due to the importance of the material used in additive manufacturing, understanding which materials are available and their applicability is key to the utilization of 3D printing to its fullest potential. For information about the specifics of 3D printing materials, Ranjan et al. (2022) recently provided an in-depth review. As such we will touch only on currently available and recently demonstrated materials that fall under four key categories: polymers, ceramics, metals/conductive materials, and additives to 3D printing materials. Each material possesses its own unique applications to sensor and instrument development, which will be discussed in later sections.

2.1 Polymers

Polymers constitute the most commonly utilized 3D printing materials due to the ability to rapidly and precisely initiate the liquid to solid phase transition. For a more in-depth discussion of the subject Ligon et al. (2017) provide a relatively recent review. Because many polymeric compounds have relatively low melting points and can be heated to extrude small quantities on demand, their use is vital to FDM printing. While pre-polymerized material is used in FDM, monomers can be precisely crosslinked under a UV light source as is done in SLA, DLP, PJT, and T-PP 3D printing. There are many commercially available 3D printing polymers for use in each of these techniques, with PLA, acrylonitrile styrene acrylate, polyethylene terephthalate, polyethylene terephthalate glycol (PETG), polycarbonate (PC), polypropylene, PEEK, polyetherketoneketone, and PEI making up the vast major of commercially available materials with slight variations due to additives (Tümer and Erbil, 2021; Pakkanen et al., 2017; Rett et al., 2021; Dizon et al., 2021; Spoerk et al., 2020; Oladapo et al., 2021; Norani et al., 2021). However, many of the commercial materials often lack integral chemical information due to their proprietary nature (Grajewski et al., 2021). As such, it is required to identify the ideal material for the application before a particular commercial material is chosen. For example, Musgrove et al. (2022) compared three clear polymer resins in the properties of viscosity, heat stability, biocompatibility, and optical clarity. A guide was created on how to systematically test, select, and improve polymer resin printing for optimal integration into a select case. With the extensive list of available polymers for 3D printing it has become a major undertaking to identify the ideal material for each print.

2.2 Ceramic materials

Ceramic materials have become widely used 3D printable materials due to a number of highly desirable properties. Notable features of ceramics include hardness, chemical inertness, resistance to wear/corrosion, and mechanical properties significantly different from other 3D printable materials. Ceramics have found use in sensing applications predominantly through the 3D printing of glass or similar materials for optical components, which will be discussed in more detail later in this review. Notably, analytical use of 3D printed ceramics also includes the fabrication of piezoelectric substrates as recently demonstrated by Liu et al. (2022) The authors investigated three ceramic resins: barium titanate, lead zirconate titanate, and aluminum nitrate, for the fabrication of piezoelectric structures that were then monitored for their applicability to wearable motion sensors. A review by Romanczuk-Ruszuk et al. on 3D printable ceramics Romanczuk-Ruszuk et al. (2023) provides a more complete overview of the field for those interested, but outside of optical components, they see scarce application to analytical instrumentation.

2.3 Metals and conductive materials

3D printing of metals is a niche area due to the added difficulty of controlled melting while maintaining both structural integrity and chemical stability for the print. It relies on either SLS or similar processes known as selective laser melting (SLM) (Gadagi and Lekurwale, 2021). Each of these techniques comes with specific materials they are capable of printing, as well as differing material characteristics. Notably, SLS metal prints are highly porous and brittle (Ngo et al., 2018). SLM has therefore been the popular technique for recent work due to higher fidelity and ability to print metal combinations (Ni et al., 2019). A wide variety of metals are available to be used in these processes, including aluminum, copper, nickel, steel, and titanium, as well as a number of metal alloys (Ni et al., 2019). Alternative methods to deposit metals have also been developed to allow for a wider adoption of metals in additive manufacturing (Ni et al., 2019). For example, 3D printing of copper has been demonstrated with nanometer scale resolution through precise electrochemical reduction of a copper solution onto the substrate. However, this requires a conductive surface be present and the presence of a working electrode (Hengsteler et al., 2021). In addition, several other 3D printing methods can be used for the incorporation of metals into additive manufacturing, such as those demonstrated by Wei et al. (2015) with a graphene electrode and a custom-made resin on FDM.

Conductive 3D printing materials are often produced through addition of inexpensive conductive materials such as carbon black (Stefano et al., 2022) and graphene (Guo et al., 2019). Recently Kalinke et al. (2020) compared the two most popular FDM-PLA conductive 3D printing materials: graphene-PLA by Black Magic and PLA-carbon black by Proto Pasta. They showed that the electrodes made from graphene had superior electrochemical and structural performance relative to those made from carbon black. In contrast, a custom electrode resin developed by Stefano et al. (2022), produced by refluxing PLA and graphite, showed better electrochemical response than commercial graphene or carbon black. Intrinsically conductive polymer mixtures like PEDOT:PSS (Yuk et al., 2020) have also found use in 3D printing. These discoveries lead to the question of what other properties can be achieved via additives and what effects these additives have on printability.

2.4 Material additives

Each of the aforementioned materials is effective alone, but through the combination of the printing materials or addition of other materials, new properties can be achieved. For example, the formation of polymer composites has been a major area of 3D printing material additive research and has been reviewed by Singh et al. (2020) For sensing applications, integration of nanoparticles into 3D printing resins has been demonstrated, and the approach is attractive to many due to the presence of novel functionality. Specifically, conductivity, magnetism, and piezoelectricity can be tuned through the incorporation of nanoparticles (Shafranek et al., 2019). However, these addition can cause major complications, such as loss in structural integrity and/or resolution of the final product (Cardoso et al., 2020). This has been shown to be caused by variable mechanisms dependent on the nanoparticle themselves (Muñoz and Pumera, 2020). For example, plasmonic nanoparticles affect the structure through thermal heating in the process of stereolithography, leading to thermal degradation of the organic polymer. Semiconducting and plasmonic polymers, on the other hand, act as radical quenchers and reduce the amount of radical activated polymerization (Su, 2021).

In a similar fashion to plasmonically active nanoparticles, dyes can be used as additives to facilitate visible light as a cure in SLA resins. Exact control of the optical absorption of the resin is required in all directions during the curing phase to ensure fine resolution is maintained (Quan et al., 2020). As the absorption of the resin increases, the resolution improves as there is less dispersion of the light through the uncured medium (Ahn et al., 2020). In addition to their role as curing catalysts, dyes are also used to introduce functionality to the polymers, such as indicators to changes of pH, physical pressure, light and temperature. The advantages of these additives allow for fine tuning of the polymer to the specific purpose necessary in the application (Gastaldi et al., 2020).

3 Mechanical and structural components

The ability of 3D printers to quickly generate various geometrical designs with sufficient structural stability has made this technology attractive for production of components that enable the sensing apparatus through component alignment, movement, and protection. A great deal of work has been conducted towards 3D printed structural and mechanical parts that are essential to the development and assembly of an analytical instrument. 3D printing of these components has allowed researchers to quickly design and produce unique setups with greatly reduced difficulty. Publications related to formation of gears, cell scaffolds, and outer casings, as well as those demonstrate their application to sensing platforms will be discussed and reviewed in the following section. While not particularly complicated and not directly involved in the sensing, these are components crucial to making 3D printed instruments a reality.

3.1 Moving parts

The use of 3D printed gears and pumps has been reported in various studies including uses for robotics, domestic applications, and in analytical instrumentation (Zhang et al., 2020a; Arena et al., 2023; Vasilescu, 2019; Zatopa et al., 2018; Zolfagharian et al., 2016; Naz et al., 2023). The main benefits of using the parts generated from additive manufacturing include sufficent surface quality, broad availability from both metallic and non-metallic materials, high flexibility in design modifications, and less waste as compared to other strategies (Del Rosario et al., 2022). These features are associated with the material used when printing gears, the most common of which include nylon, ABS, PLA, and PETG (Zolfagharian et al., 2016; Del Rosario et al., 2022; Subramaniyan et al., 2022). One of the major concerns for the printed gears and pumps is limited operational life expectancy, specifically in terms of

wear and thermal behavior over prolonged uses. Recent studies have focused on understanding how misalignments, temperature, and heavy use can affect 3D moving parts, and approaches to optimize the system to improve longevity (Zhang et al., 2020a; Subramaniyan et al., 2022; Zhang et al., 2020b; Kotkar et al., 2018; Buj-Corral and Zayas-Figueras, 2023).

The most common types of gears for scientific investigations include spur gears, helical gears, bevel gears, worm gears, and planetary gears (Subramaniyan et al., 2022). Spur gears are defined by having straight protrusions that are parallel to the axis of rotation. Due to their simple design they are very easy to print but are known to be inefficient for work at high speeds (Apparao and Raju, 2021). This weakness has made the selection of material to print a key factor. Helical gears are similar to spur gears, but their edges are angled compared to the axis of rotation (Berger, 2015). Helical gears are ideal for transfer motion in a typical instruments setup, such as moving a stage horizontally or vertically in a microscope. Bevel gears have edges on the conical surface of the gear, which allows for transmission of motion between intersecting or non intersecting shafts for changing the direction or speed of rotation (García-García and González-Palacios, 2018). Worm gears are known for their screw-like shape and transmit motion between non-intersecting shafts that are perpendicular to each other (Berger, 2015). All of these gears can be 3D printed with high quality.

Recently Sharkey et al. (2016) used 3D printing to generate components of an open source microscope including hinges, gears, and the stage. The 3D printed microscope was found to have sub-micron scale motion over a range of 8 × 8 × 4 mm, and a drift of only 20 μm over the course of a week was observed without temperature stabilisation. Sule et al. (2019) created a hand operated, 3D printed centrufuge with two spur gears, two bevel gears, a gear crank and a test tube holder, as shown in Figure 1. Along with a 3D printed centrifuge and microfluidic system to concetrate, separate, and extrude a mixture in sample preperation, the 3D printed microscope forms a realistic analytical paltform that can address some of the point-of-care detection needs in real-world sample analysis. With the diverse types of gears and materials available for their printing, as well as the ability to quickly and inexpensive implement customizable movement, printed gears are a valuable but often overlooked use of 3D printing technology in sensing applications.

3.2 Structural components for sensing platforms

Perhaps the most popular use of 3D printing in analytical platform construction comes in the making of structural and supporting components of the instrument. These large structures form the basis of sensing platforms when integrated with purchased or fabricated optical and/or electrical components. The required print quality in these applications is generally low, meaning they are easily accessible and rapidly producible. These features leave them particularly amenable to analytical platforms that benefit from low-cost and portability. To further reduce costs, these devices are often designed to accommodate smartphones as the light source and/or detector (Quesada-Gonzalez and Merkoci, 2017). 3D printed spectrophotometers for use with smartphones have been reported for some time, but more recent work has been focused on designing platforms that are easily fabricated and operated, while also being compatible with a range of different smartphones (Bogucki et al., 2019). Works such as these are often aimed at chemical education purposes such as making analytical instrumentation accessible to a broader number of communities, including those with limited resources. Another use of 3D printed smartphone-compatible instruments involves point-of-care medical monitoring (Chan et al., 2017). Some recent examples of this implementation include colorimetric (Zhang et al., 2021b) and electrochemiluminescent (Bhaiyya et al., 2022) monitoring of blood glucose, and nanoprobe-based fluorescent detection of glutathione (Chu et al., 2020). Platforms such as these offer simple, low cost, and portable methods for individuals and healthcare providers to monitor crucial health biomarkers. Another application for this platform is rapid on-site environmental monitoring for regulators and researchers. These sensors are generally colorimetric and have been used to detect environmental contaminants such as heavy metals (Lai et al., 2022), pesticides (Su D. et al., 2021), and halocarbons (Gul et al., 2021).

In addition, a valuable but less elegant usage of 3D printing is for quickly producing housings for home-built analytical tools. Often times these housings amount to simple boxes with cut-outs to align and insert functional components. These housings are valuable components because they can be customized to the envisioned design, improve portability, and limit outside interferences such as light and dust. One example comes from the previously mentioned work by Xiao et al. (2022) which demonstrated the use of 3D printing for the housing of instrumental components for their phone based imaging SPR device (Figure 2). da Silva et al. (2020) used a 3D printed UV chamber with a smartphone detector to achieve high throughput fluorescent analysis of quinine concentration in beverages. Using a biodegradable polymer, this method represents an economically and environmentally friendly example of applications for 3D printed housings. A more complex use for 3D printed housings was demonstrated by Casto et al. (2019) who designed a dual-detector, Taylor dispersion analysis module that could be integrated with a capillary electrophoresis (CE) instrument. In a future publication by the same group, they removed the need for the CE instrument and produced a 3D printed instrument featuring a fully 3D printed eductor that allowed for highly stable pressure through the capillary (Moser et al., 2022). Even though range of potential applications for 3D printed structural components in analytical instrumentation are extremely broad, the examples presented in this section are representative of the bulk of the uses and should provide an introduction to some of their demonstrated uses.

4 3D printed optics

There are a number of in-depth reviews that focus on the additive manufacture of optical components. Berglund et al. (2022) provide an excellent overview of recent developments and future outlooks in 3D printed optics as well as practical considerations for selecting proper 3D printing method for a particular component. For information regarding specific materials, Zhang D. et al. (2021) and Blachowicz et al. (2021)

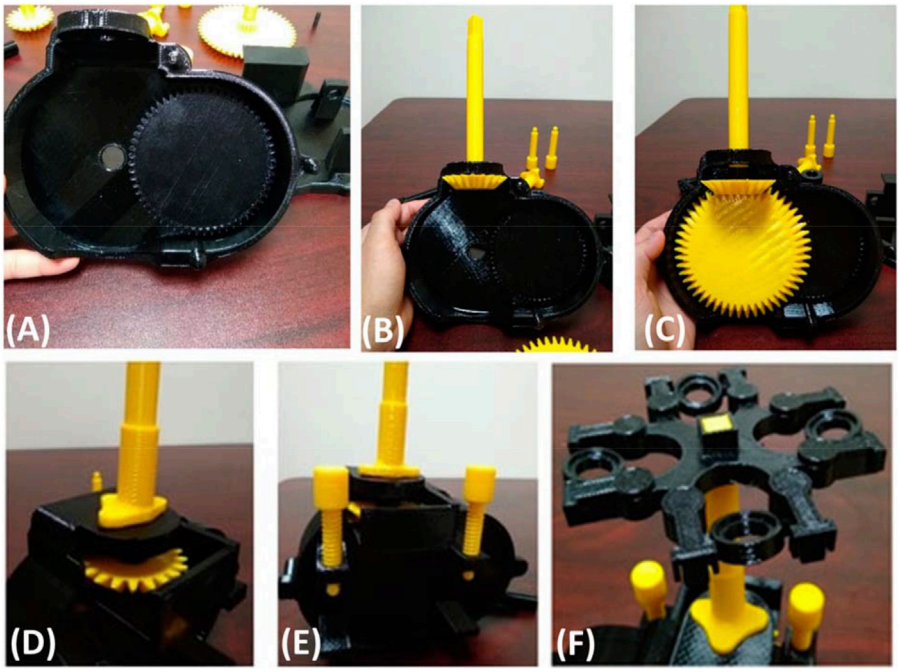

FIGURE 1
(A) Picture of 3D printed plate and printed spur gear locked in. **(B)** 3D printed bevel gear inserted into what is shown in **(A)**. **(C)** Another 3D printed spur gear inserted into the 3D printed apparatus. **(D)** Aparatus closed with all internal and external 3D printed components. **(E)** Use of 3D printed bolts to hold the two 3D printed casings covering the 3D printed gears in place. **(F)** 3D printed testube holders designed to move to allow for centrufigation through a 3D printed hand cranked system not shown. All images are adapted from Sule et al. (2019).

have published reviews on 3D printed glass and polymer optical components respectively. To set this section apart from these reviews and a host of other reviews on the subject, we will instead focus on presenting recent examples that are closely related to the integration of 3D printed optical components in analytical applications, as well as recent developments in the materials and methods aimed at platform development. Additionally, in this section we aim to provide a full picture on the field of available 3D printed optical components and some of the key applications to which they can be applied.

Optical components comprise some of the most important and difficult to produce components in analytical instrumentation. As a result, the additive manufacture of optical components for sensing has seen rapid development over the past decade, aided by the burgeoning advancement of 3D printing over the same period (Jiang et al., 2022; Bhuvanesh Kumar and Sathiya, 2021). 3D printing of optical components shares many of the general advantages conferred by additive manufacture such as heightened accessibility, reduced waste, and rapid prototyping (Lambert et al., 2018). Compared to traditional manufacture of glass optics, 3D printing allows for fine control over internal and external structures (Shu et al., 2022; Vogt and Leonhardt, 2016), as well as optical properties through the use of additives inside the deposition material (Destino et al., 2018; Aslani et al., 2023; Ali et al., 2021). In addition, the process can be completed on site in labs with limited resources. However, optical components have specific requirements and considerations when compared to other additively manufactured components. More specifically, they generally require high homogeneity, optical transparency, and refractive indices with an accompanying low surface roughness to reduce losses due to scattering. Achieving satisfactory results over the range of sensing applications to which these optics are applicable has necessitated significant research on both materials and methods.

The materials used in 3D printed optics can be broken down into two major sub-classes: glass and transparent resins/polymers. Glass is an ideal material for optics owing to its high optical transparency and refractive index, as well as its thermal and chemical stability. However, the high melting point of glass has resulted in significant difficulties in producing 3D printed glass with appropriate size, shape, porosity, structural integrity, surface roughness, and/or transparency while maintaining low cost and ease of production. As a result, 3D printing of effective glass optics has largely been restricted to micro-optical components that can reasonably be printed with high resolution methods (Nguyen et al., 2017; Luo et al., 2014; Moore et al., 2020). However, there have been some advances, particularly in regards to glass micro-optics, in the past few years that will be discussed further into this section. Transparent resin and photopolymer-based 3D printing materials, while exhibiting fewer ideal properties for optical applications, are far more compatible with available 3D printing methodologies. Examples of the effective use of these materials in optical components include waveguides (Dingeldein et al., 2013), lenses (He et al., 2018), gratings (Purtov et al., 2019), collimators (Thiele et al., 2016), and refractive elements (Xiao et al., 2016). With the rapid increase in the library of available 3D printing materials and methods, the range and quality of optical components produced may result in printed optics eventually supplanting traditional glass optics as the preferred components for analytical instrumentation.

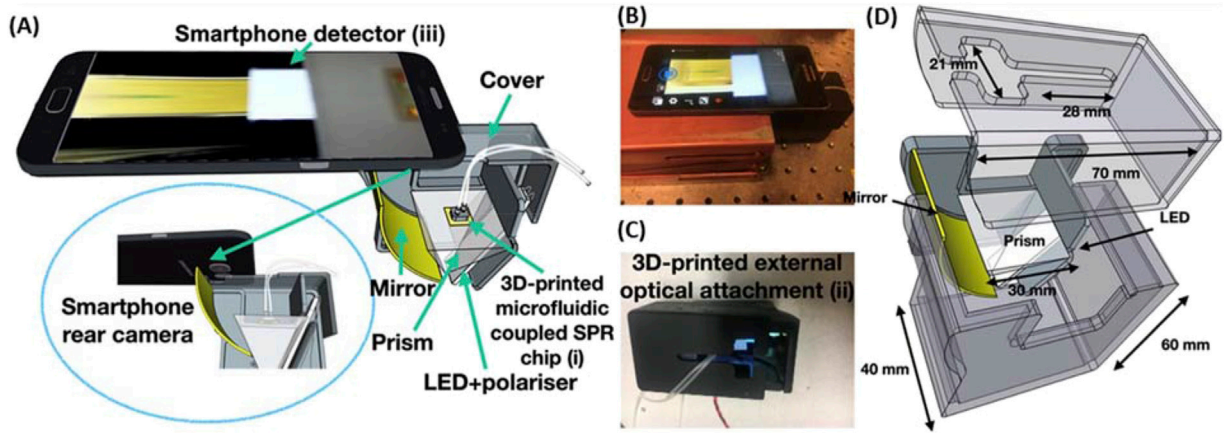

FIGURE 2
(A) Schematic of the imaging SPR smartphone system integrated with the 3D printed microfluidic system on top of an SPR chip in the Kretschmann configuration. **(B)** Image of the entire device assembled. **(C)** Image of the 3D printed structural component to house the optical attachment. **(D)** The CAD image with appropriate dimensions for the SPR-based smartphone structural attachment. Adapted from Xiao et al. (2022).

In the proceeding section we will review recent advances in this field that may contribute to this prediction becoming a reality.

4.1 Optical component developments

Due to inherent difficulties associated with 3D printing of glass optical components, the bulk of recent publications in the field remain focused on polymer-based optics. However, there are some notable recent developments to speak of. Toombs et al. (2022) recently demonstrated the high resolution 3D printing of silica glass microfluidic and micro-optical components using a photopolymer-silica nanocomposite material. The use of multi-component materials with direct laser writing (DLW) photopolymerization followed by sintering to remove the photopolymer, leaving behind nonporous glass with high optical transparency, has been in use for some time (Kotz et al., 2017; Gonzalez-Hernandez et al., 2021). However, the unique development presented in Toombs' work is the integration of a tomographic photopolymerization method, dubbed microscale computed axial lithography (micro-CAL). Instead of photopolymerizing the structure layer-by-layer as with typical SLA/DLP methods, the structures are formed within the bulk solution by projecting 2D images into the resin. Some benefits include smoother surfaces, increased mechanical strength, and more complex geometries due to the lack of need for solid supporting structures. Additionally, compared to T-PP methods, micro-CAL is capable of producing the desired component more quickly. All of these advantages are highly desirable in the design of optical components, and it can be expected that micro-CAL will see future use as a lithographic method not only for glass, but other 3D printing materials as well.

The production of high-quality 3D printed glass optics with polymerization-sintering methods has long been plagued by the issue of shrinkage with accompanying defects (bubbles, warping, etc.) that occur in the process of burning off organic material. In the aim of minimizing this issue, Hong et al. demonstrated the 3D printing single and multi-component glass micro-optics using pre-condensed liquid silica resins (LSRs) (Hong et al., 2021; Hong et al., 2022). These LSRs are synthesized by polymerization of tetramethoxysilane (TMOS) with methacryloxymethyltrimethoxysilane (MMTS), causing a high degree of crosslinking. (Figure 3A). In their first work, the authors were able to produce micro-optics and gratings with surface roughness lower than 6 nm and shrinkage of only 17%. However, it was found that the LSR used in this work containing about 6.5 mol% MMTS had insufficient mechanical stability to support large aspect ratios and more complex multi-component optical components. Increasing MMTS mol% led to a higher degree of cross-linkage resulting in improved mechanical strength, but this was accompanied by increased shrinkage due to the higher organic fraction. Selecting 15% MMTS as their most ideal material composition, Hong and colleagues were able to produce a range of complex micro-optical components boasting surface roughness's less than 6 nm (Figures 3B–E). To demonstrate a use case for this optimized strategy for glass micro-optic 3D printing, it was used to produce a high-resolution snapshot hyperspectral imaging (HSHI) system (Hong et al., 2023a). While the produced light guide arrays for the HSHI system are too limited in size and structural stability for many applications, with a printer boasting a high range-of-movement stage with appropriate precision, along with material improvements, they could see utility in a range of analytical systems.

Recent advances in the materials for 3D printed glass optics are not limited to silica glass. Hong et al. recently reported the production of large (mm-to-cm scale) 3D printed germanate glass optics using a fiber-fed printing method (Hong et al., 2023b). The production of optics-quality glass by 3D printing has primarily been limited to the micrometer regime due to the slow print speeds of high resolution methods. Germanate glass has many positive properties including high mid-IR transparency, refractive indices, chemical stability, and thermal stability. Due to these factors, it has tremendous potential for application to mid-IR sensing applications, but compared to other glass materials, it is comparatively difficult to shape, polish, and grind to appropriate

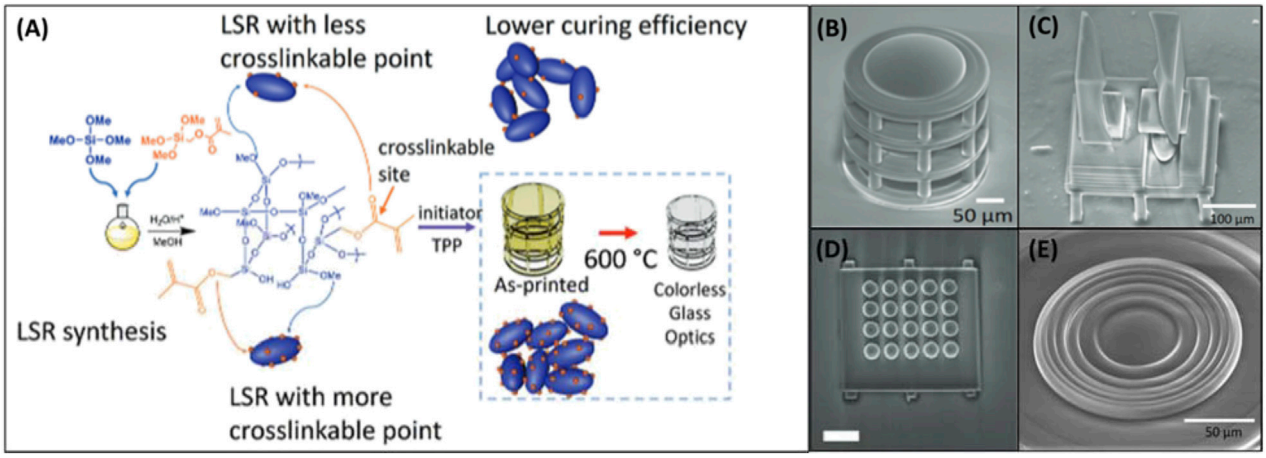

FIGURE 3
(A) Scheme for LSR synthesis and glass micro-optic fabrication. **(B)** SEM of printed micro-objective. **(C)** SEM of 3D printed Alvarez lens. **(D)** SEM of 3D printed lenslet array. **(E)** SEM of 3D printed Fresnel surface. Adapted from (Hong et al., 2022).

quality for these tasks, thereby limiting its usage (Li et al., 2009). With their optimized printing system, Hong and colleagues produced simple lenses and a multi-lens microscopy system exhibiting surface roughnesses less than 1 nm. This work represents a significant first step in not only the practicality of 3D printing optics-quality germanate glass, but glass optics with other materials as well through their optimized heating and deposition process.

As polymer-based 3D printed optics are the most practical and widely adopted in the field of additive manufacture, the number of publications reporting material and methodological developments extend beyond what can be reasonably encompassed here. Instead, we will present recent examples that are particularly notable and/or impactful and could prove valuable in the development of analytical instrumentation. Publications in this area can be divided into methodological and material developments, or both categories if the new material enables a new printing method or the production of a unique optical component. Additionally, methodological advancements include novel applications of existing 3D printing methods.

The purpose of developing new materials for 3D printing is often to improve the quality of the printed optics. However, an alternative avenue is to expand the range of possible applications through cost, accessibility, or new material properties. One of these properties that is often overlooked is material flexibility, which has particular utility for analytical instrumentation utilizing waveguides. Flexible waveguides have unique potential in analytical platforms by allowing simple and inexpensive routing of light in the system. Nseowo Udofia and Zhou (2020) recently reported the use of ballistic gel materials with a custom micro-extrusion 3D printer to produce highly soft and elastic optical components. The material was used to generate caustic patterns, beam splitters, optical encoders, and decorative waveguides with low cost, low transmission loss, and high optical transparency. Another material development that allows for unique optical application for 3D printing is the addition of fluorescent particles into the printing resin. Tai et al. (2019) integrated perovskite nanocrystals, which have broad applications in optoelectronics (Zhan et al., 2022), into polycaprolactone (PCL) as a protective and workable carrier resin. Using this material, they were able to generate low micron-sized fluorescent fibers and demonstrate tunable down-conversion of light from a blue LED to produce white light, a process that has been the subject of significant research for decades.

As with glass optics, the time and cost efficient 3D printing of high quality polymer-based optical components in the mesoscale without additional (and possibly inconsistent) polishing steps has been a difficult challenge to overcome (Bhaduri et al., 2017; Vaidya and Solgaard, 2018b). One recent attempt to address this comes from Nair et al. (2022) who modified a low-cost and commercially available LCD 3D printer with a fiber-optic taper to improve the resolution of printed components at the cost of reduced print speed (Figure 4A). The fiber-optic taper reduced print speed from 30 mm^3 s^{-1} to 0.25 mm^3 s^{-1}, but significantly reduced surface roughness from ~2 µm to tens of nanometers. It should be noted that while the print speed is significantly reduced, this method is still orders of magnitude faster than most T-PP methods. However, the acquired surface roughness remains significantly higher than what can be acquired with polished glass optics (Chada et al., 2015; Lu et al., 2019). Considering the cost, print speed, and lack of need for additional processing steps, this method may prove attractive for applications where optics of low or medium quality are acceptable. Notably, this work does not represent the technical peak of rapid 3D printing of optics, as another publication reporting a higher printing speed and lower surface roughness of ~1.35 mm^3 s^{-1} and 13.7 nm respectively (Shao et al., 2019). This was achieved with a custom projection microstereolithography (PµSL) system (Figure 4B) that was able to produce a 3 mm high lens in only 2 min. However, these printing quality improvements do come at the cost of decreased accessibility and significantly increased price of the system. However, once the printing system is in place, the bulk of components for a microscope can be produced in 50 min at a cost of only $4 as was demonstrated in a follow up study (Figure 4A). (Hai et al., 2023) When focusing on the lens specifically (Figure 4B), it was produced in only 3 min at a unit cost of ~7 cents while

boasting improved surface roughness (~7.63 nm), structural integrity, and imaging contrast when compared to commercially available lenses (Figures 4C, D). Another recent example of mm-scale 3D printed optics comes from Ristok et al. (2020) who produced lenses up to 2 mm across with optical performance and surface roughnesses (~2.9 nm) comparable to commercial glass lenses. These lenses were produced by a dip-in laser lithography (DILL) T-PP method with an objective that allows for a larger than normal writing field. With a print time of 5 h for the 1 mm lens and 23 h for the 2 mm lens, this method is much slower when compared to the previously presented examples. Nevertheless, these examples clearly demonstrate that there is no ideal method for producing optical components on the mesoscale, and it requires the user to balance quality against the competing factors of cost and print time.

Aside from waveguides and simple UV-Vis or IR lenses, 3D printing has been used for manufacturing other optical components. Sanli et al. (2022) report a custom 3D laser lithography system that allows for the production of high resolution kinoforms. A kinoform is a type of lens that allows for highly efficient focusing of x-rays. These lenses often require complex nanofabrication procedures and are dependent on small feature sizes to perform efficiently. This work demonstrates a relatively low-cost method to produce high quality optics that could be implemented in analytical systems that utilize X-rays. DLW-printed multicomponent achromat and apochromat lenses have been demonstrated that greatly reduce chromatic aberration (Schmid et al., 2021). Optical instruments using multiple wavelength sources can benefit from these lenses that ensure all wavelengths of light are efficiently focused on the same position. One particularly unique implementation of 3D printed lenses comes in the form of customizable optical tweezer arrays with dynamic control of each tweezer using a digital micromirror device (Schaffner et al., 2020). They allow for highly precise trapping and control of individual particles for a wide range of investigations relating to subjects such as biological systems, atmospheric chemistry, and dielectric particles (Gorkowski et al., 2020; Quang et al., 2018; Catala-Castro et al., 2022). The rapid design of 3D-printed optical tweezer arrays that can be customized for individual studies may prove to be an extremely valuable application for additive manufacturing moving forward.

Another advantage to the high level of control inherent to additive manufacture is the ability to produce diffractive optical elements (DOEs) that generate precise optical patterns with utility in a broad range of applications (O'Shea et al., 2003; Tang et al., 2019; Kunwar et al., 2020). Producing these components relies not only on the optimization of printing methodologies, but also the design of the DOEs through modeling. Despite the rapid prototyping ability implicit to additive manufacture, modeling an optimal design prior to production greatly minimizes tedious trial and error. Wang et al. (2020) recently developed a modeling system for the design of "near-perfect" diffractive optical elements, which utilized four key parameters of 3D printing systems–laser power, beam scan speed, hatching distance, and slicing distance–to predict print quality and correct for subwavelength morphological variations before fabrication. Their model, dubbed the lumped 3D printing TPL parametric model, was employed to produce Dammann gratings that generate arrays of light with highly uniform intensity and spacing (Figure 5A). Taking modeling a step further, 3D printed diffractive element networks designed by deep learning (Figure 5B) have recently been demonstrated to control the amplitude and phase of incoming light (Veli et al., 2021). This work proves to be highly impactful to many applications, including spectroscopy, as it lays the groundwork for the rapid design and production of elements for precise control of light. Although the networks demonstrated low power efficiency and the output pulse did not precisely match the computed models (Figure 5C), these issues could be largely remedied in the future by implementation of lower-absorption materials and improved modeling strategies. The combination of high-resolution 3D printing with advanced modelling for prototyping is a new and potentially highly impactful development for optical analytical instruments.

4.2 3D printed optic integration in sensing

3D printed materials have a history of implementation in optical sensing with some examples including Kretschmann configuration surface plasmon resonance (SPR) sensing of cholera toxin (Hinman et al., 2017), surface-enhanced infrared spectroscopy detection of PMMA (Braun and Maier, 2016), and surface layer thickness terahertz sensing (Li et al., 2017). However, as the additive manufacture of optical components is still very much in its infancy, traditionally manufactured components remain largely preferred for actual sensing applications. At this time, the startup cost of obtaining a 3D printer of appropriate quality as well as the materials and training required makes this approach less sensible for researchers who do not have particular interest in making developments in 3D printing itself. In this section, recent examples that demonstrate potential advantages to the use of 3D printed components beyond simple per-unit cost and prototyping considerations will be presented. A focus will be placed on examples where the use of additive manufacture allows for new sensing configurations and improvements instead of simply being used as replacement for traditionally manufactured components.

One of the major practical benefits of the low per-unit price of 3D printed optics is that they can be implemented into sensing units that are disposable. This is particularly beneficial in applications where the optical component is the sensing surface itself and its timely replacement improves performance as the surface becomes fouled or degraded over time. One relevant example is SPR sensing, in which the sensing surface (generally ~50 nm film of gold) can be directly deposited on the optical coupling element (prism) that can be 3D printed. Hinman et al. (2017) established a method for 3D printing and polishing of transparent prisms for SPR sensing. Lertvachirapaiboon et al. (2021) recently expanded this design by using soft lithography to imprint a grating onto one side of the prism. After depositing gold over the grating, they demonstrated the generation of two different modes of SPR coupling, occurring at visible and NIR wavelengths. The sensitivity of the instrument was also found to correspond to the absorption profile of materials deposited on the surface. In addition, it allowed rapid tuning of SPR wavelength for specific analytes. Disposable 3D printed prisms have also been integrated into single-use cultivation vessels for determining the optical density of microbial culture (Kuhnke et al., 2022). By integrating the prisms into the vessels, light is deflected 90°

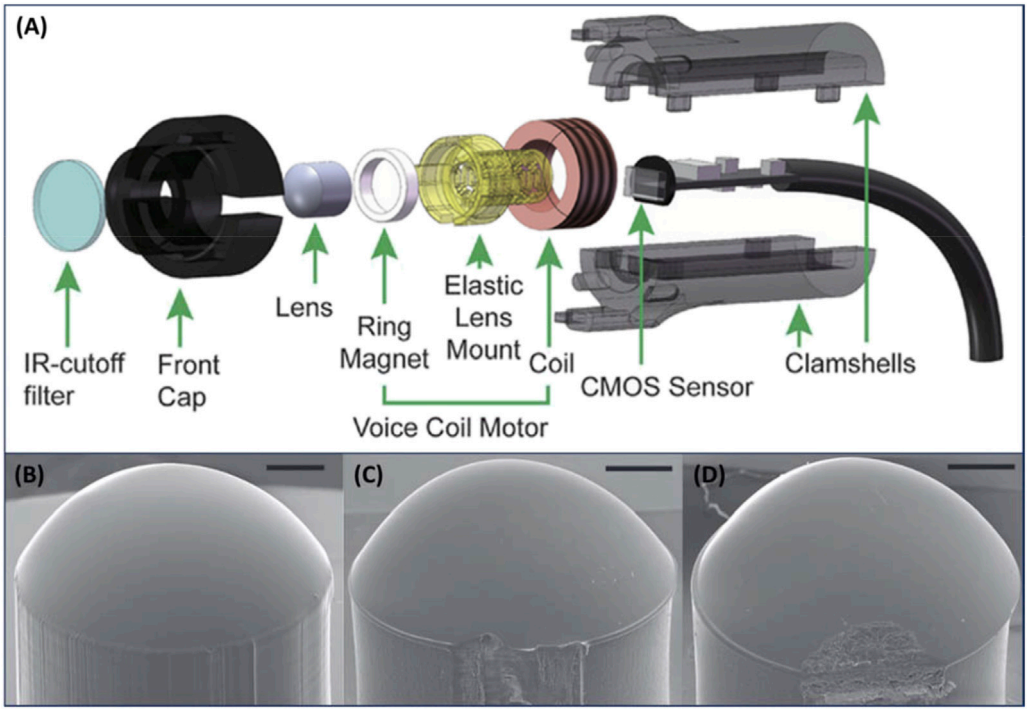

FIGURE 4
(A) Illustration of design and components used in 3D printed optical microscope. **(B)** Image of 3D printed lens aspherical lens. **(C)** Image of lens purchased from Edmund Optics (15-271). **(D)** Image of lens purchased from Thorlabs, Inc. (APL0303). Scale bars: 500 μm. Adapted from (Vogt and Leonhardt, 2016).

from the source located under the vessel and detected in the horizontal plane, thereby avoiding perturbations occurring at the liquid-air interface. With this adjustment they were able to achieve roughly 3-times the sensitivity than traditional vessels.

Waveguide based sensors are another emerging use for 3D printing technologies due to the broad range of configurations and materials that are readily accessible. Valued for their simple design and low cost, these sensors typically utilize light transmission change through the waveguide for quantification as the presence of an analyte causes alterations to the resonant modes. Analyte concentration can be determined by measuring the power/intensity change at a set wavelength or the change in the resonant wavelength. While many sensors carry this common motif, the analyte responsive materials and their implementation vary greatly. The waveguide itself can be used to sense the analyte, as reported by Swargiary et al. (2020) The "tower" waveguide was utilized as an isopropanol vapor sensor by measuring output changes as the isopropanol vapor caused swelling. Detection can also be accomplished based on interactions with the cladding material. Darder et al. (2022) reported a 3D printed fiber optic waveguide coated with a cladding composed of Nafion containing Leuco Fuchsin dyes. Formaldehyde vapor was detected based on the intensity change occurring as a result of contact with formaldehyde. The use of a 3D printed optic fiber was necessary to bring the limit of detection within the ranges as removing existing cladding from commercial fiber optics results in high brittleness and chemical instability that negatively affects sensing performance. The use of long-period fiber gratings (LFGs) by 3D printing for various sensing applications has been demonstrated. With LFGs, spaced strips of material that swell in response to an analyte are placed over a fiber optic cable, where they cause a wavelength shift due to changes in refractive index and accompanying resonance changes. This method has been employed for the detection of biologically relevant levels of glucose by DLP-based patterning of ConA and dextran containing hydrogel over a fiber optic cable (Wei et al., 2023). Glucose competes with dextran for binding to ConA, leading to swelling of the polymer, thereby causing the refractive index and resulting wavelength change that enables sensing.

5 3D printed fluidic systems

One major 3D printing application has been the development of flow systems due to the ability to rapidly prototype and adapt new flow geometries at minimal cost. As a result, 3D printed fluidic devices have been extensively reviewed in recent years (Musgrove et al., 2022; Nielsen et al., 2020). 3D printing of microfluidic systems for applications aimed at instrument design and improvement, however, is less explored. In this Review, we will report advancements that expand the capabilities of 3D printed fluidics and recent work that demonstrates the printing of fluidic systems for implementation into analytical instrumentation.

Flow systems are an integral part of many analytical instrumentations by enabling samples to be split, mixed, and separated in various ways to facilitate the sample treatment and processing necessary for detection. While 3D printing has not yet fundamentally changed the capabilities of fluidics, it has drastically improved their accessibility. This has particularly empowered

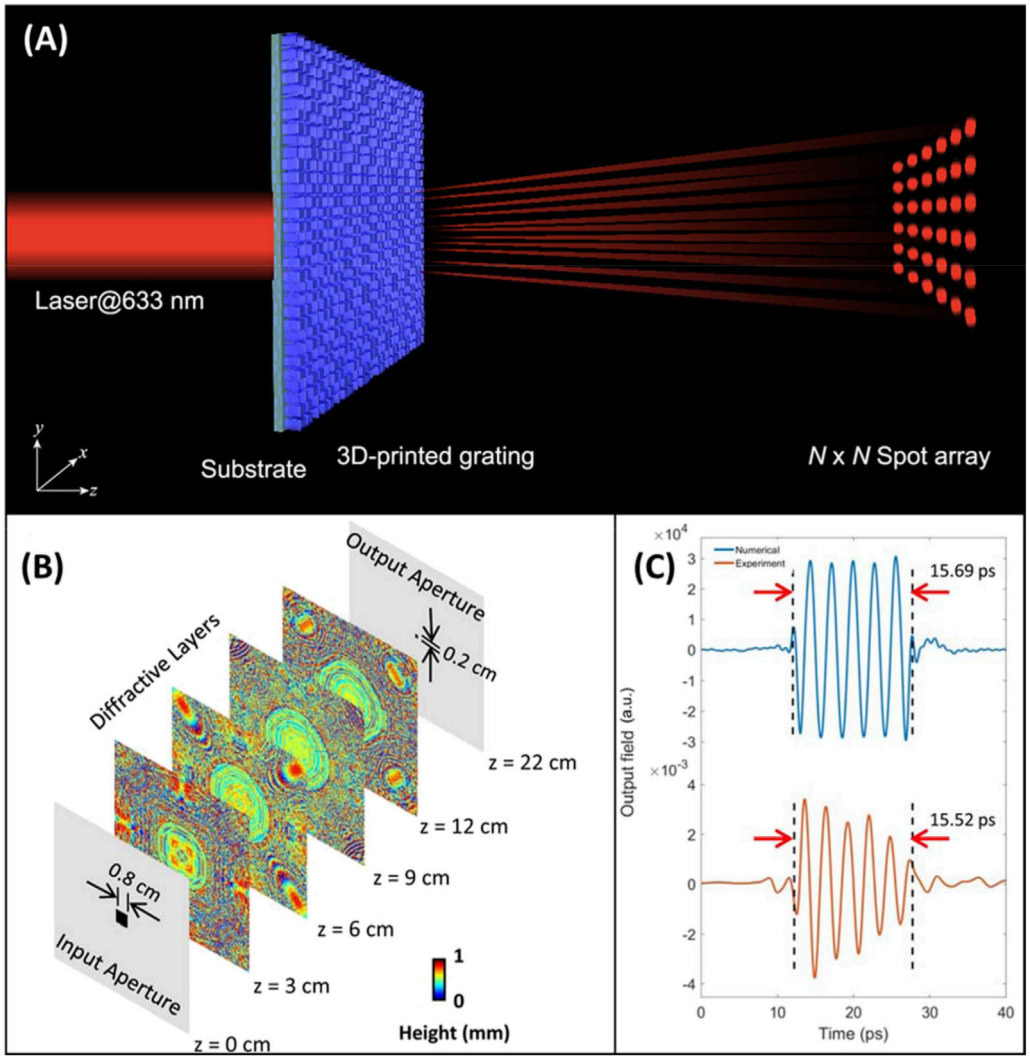

FIGURE 5
(A) Illustration of 3D printed Dammann grating generating a precise optical array pattern. Adapted from (Wang et al., 2020). **(B)** Multi-layer pulse shaping network with deep learning designed diffractive layers. **(C)** Numerical and experimental shaped output pulses from the diffractive network. Adapted from (Veli et al., 2021).

instrumentation development that was previously prohibited by the cost of precise machining. Recent advancements in printing materials and methods with improved resolution, as discussed in previous sections, have permitted 3D printers to achieve smaller channel sizes and more complex geometries that may prove to revolutionize the field of fluidics going forward.

The benefits of increased accessibility are clearly evident in the broad applications of recent 3D printed fluidic systems such as extraction, separation, sensing, and cell growth. Each of these applications relies on advancements in 3D printing technology and materials over the past few decades. These applications will be reviewed in the following sections that focus on extraction and separation techniques, microfluidic sensing applications, cell growth and sorting, as well as reaction vessels and other unique applications. Additionally, recent work with 3D printed fluidics will be discussed, along with their interfacing with 3D printed parts and applications in both benchtop and point-of-care instrumentations.

5.1 Extraction and separation

One major use for 3D printing in the field of microfluidics is to enable rapid extraction and separation of small volumes of analyte solutions. To achieve this, a small 3D printed module is implemented within the analytical platform to automate the commonly laborious steps of extraction/separation. These modules can take many different forms based on their particular use case. A vast range of designs have been reported to achieve maximal capabilities and compatibility with point-of-care sensing and instrumentation.

One area where 3D printed microfluidics have been extensively utilized is solid phase extraction (SPE) through polymerization/packing of monoliths in 3D printed fluidic channels. These SPE materials have been applied in various ways. Gupta and Paull (2021) demonstrated a microfluidic chip capable of splitting flow across 64 channels with highly uniform flow velocities that could be useful for SPE applications (Figure 6). A detachable piston shaped roof was

attached within the print that allowed sorbent to be placed in the reservoir. Extraction efficency was greatly improved with the three dimensional bifurcating flow distribution, compared to a single channel or 2D flow distributor due to the substantially higher number of channels. Furthermore, the 3D distributor did not show signs of sorbent saturation as opposed to the 2D distributor, which the authors attirbuted to more uniform distribution of flow across the whole particle bed. Alternatively, Irlam et al. (2020) tested various printing materials and commercial sorbents to develop a 3D printed housing that connects with syringes, allowing detection of various trace explosives through SPE when used in combination with liquid chromatography. 3D printed microfluidics have also been combined with antibody labeled SPE monoliths to enable immunoaffinity specific extraction (Almughamsi et al., 2022). Three antibodies for pre-term birth biomarkers were immobilized to the monolith to enable the extraction and analysis of these markers in serum. It should be noted that the formulation of these monoliths within a microfluidic device can be a difficult task. In an attempt to address this problem, Ren et al. (Belkilani et al., 2022) developed miniature 3D printed solid phase extraction cartridges that simplify the assimilation of SPE materials into the device. The use of integrated frits with porous microstructures between the support and the build materials for polyjet printing (Keshan Balavandy et al., 2021) created a channel that captures SPE materials while maintaining flow. The small tunable SPE cartridges were 3D printed with precise dimensions and connections needed for a select application. SPE materials have also been used in 3D printed centrifugation based separation devices (Zhang et al., 2019; Zhang et al., 2020c) showing excellent promise for all-in-one sample treatment, which could be interfaced with instrumentation for rapid analysis. To this end, 3D printed SPE applications have been interfaced with HPLC (Carrasco-Correa et al., 2020) and ICP-MS (Su and Lin, 2020) to enable direct analysis of extracted components.

Various non-SPE microfluidic devices have been developed for fluid mixing (Duarte et al., 2022), concentration gradient generation (Heuer et al., 2022; Zhang et al., 2021c), cellular lysis (Yang Z. et al., 2022; Nittala et al., 2023), and many other applications (Ogishi et al., 2022; Shrimal et al., 2022; Li et al., 2021; Kulkarni et al., 2023). There are several examples of the integration of these systems with analytical techniques, demonstrating their promise for use in wholly 3D printed system. Habib et al. (2022) demonstrated the combination of microfluidics techniques to enable protein purification. Yang et al. developed a 3D printed microfluidic device to lyse, mix, and separate algal cells for MALDI-MS based lipid profiling, as shown in Figure 7 (Yang Z. et al., 2022). Algal cells were introduced into an array of micropillars that caused droplet breakup and significant mass transfer between the two phases. The lipid rich organic phase was collected from an outlet in the reservoir and spotted on a MALDI-MS chip for lipidomics study. While others have reported 3D printed serpentine microfluidic channels to enable single cell separation for a subsequent analysis with pulsed electric field-induced electrospray ionization MS (Feng et al., 2022). Where cell to cell heterogeneity was analyzed by rapid separation via 3D printed microfluidics. Concentration gradients have also been produced using 3D printed microfluidic devices enabling antibiotic susceptibility testing (Heuer et al., 2022; Zhang et al., 2021c; Winkler et al., 2022), where gradient generating microfluidics formed multiple wells or growth chambers with varying concentrations allowing measurement of bacterial susceptibility to antibiotics.

Beginning with work by Fee et al. (2014), the past decade has seen significant interest in harnessing the high degree of control conferred by 3D printing to produce highly ordered and efficiently packed chromatographic columns. Approaching the theoretical limits of separation in liquid chromatography columns is not achieved under many of the prevaling industrial fabrication processes that involve randomly packing a slurry of particles into the column (Dolamore et al., 2018). While improvements in separation efficiency and speed have long been driven by reducing particle size, there is a limit that is being quickly approached, leaving packing orientation as an attractive alternative (Salmean and Dimartino, 2019). Theoretical work has long indicated that ordered particle distributions such as in the face centered cubic (FCC) orientation results in lower theoretical plate heights, and by extention, better separation efficiency (Schure et al., 2004). Unfortunately, the often competing factors of print speed, accuracy, and resolution have limited the viability of producing larger 3D printed liquid chromatography columns that can actually outperform commercial columns. To achieve pore/particle sizes of appropriately small size (<2 μm) requires the usage of high resolution methods such as T-PP, which severely limits the column sizes that can be produced. This conflict was recently demonstrated by Matheuse et al. who were able to achieve pore sizes as low as 500 nm using T-PP at the cost of a 470 h print time for a 75 μm × 15 cm column (Matheuse et al., 2022). Beyond the print speed limitations, T-PP lacks compatible resins with ideal chemical and physical properties. An example of recent work attempting to resolve the speed limitation without compromising too heavily on feature size has come from Gritti and Nawata, in which they developed a 3D printing technique that combines stereolithography and photolithography. Dubbed hybrid stereolithography, they were able to achieve resolutions as low as 20 μm with print times not exceeding a few hours (Gritti and Nawada, 2022). Unfortunately, due to the feature size and printing innacuracies, the column was not able to achieve plate heights near those of commercial columns. For a more comprehensive review on progress and challenges in 3D printed chromatography materials, readers are referred to a recent paper by Salmean and Dimartino (2019). Though they still have a long way to go, recent advances in 3D printing technology have shown promise to resolve some of these issues and improve the prospect of rapidly producable and highly customizable liquid chromatography columns.

Electrophoresis has been a highly effective separation technique for decades and the introduction of 3D printing systems provide many of the same opportunities for application to electrophoretic mobility as other separation technologies. This topic has been discussed in depth by Esene et al. (2023) but has seen some major advancements in recent years that warrant discussion. Notably 3D printed microfluidic channels can be interfaced with electrophoresis to enable separation and detection. This has been demonstrated by Selemani and Martin for various neurotransmitters, finding the ability to separate dopamine, catechol, and Dopac using a 3D printed device with integrated microwire electrodes (Selemani and Martin, 2024). A microchip electrophoresis device has also been interfaced with solid-phase extraction to enable the detection of preterm birth biomarkers (PTB)

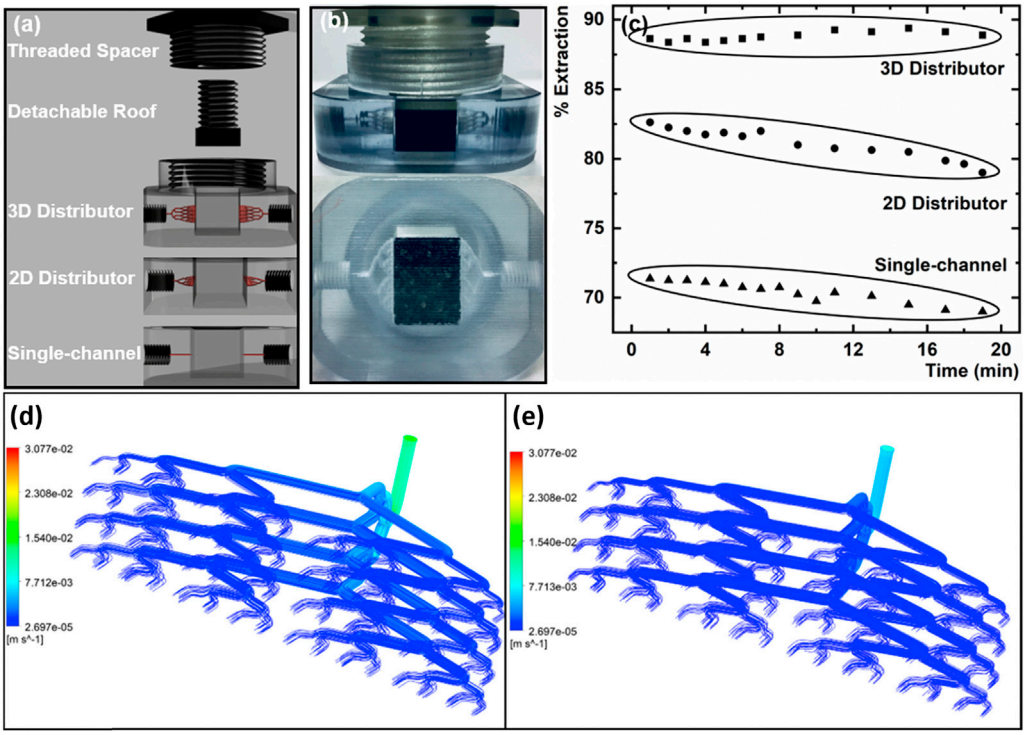

FIGURE 6
(A) Representation of the multi channeled 3D printed fluidics utilized for solid phase extraction. **(B)** Image of the 3D bifurcating distributor with activated charcoal packed in the solid phase extraction reservoir. **(C)** Resulting extraction percent based on different fluidic systems. With fluid dynamic simulations of fluid flow through the 3D flow distributor with flow rates of **(D)** 0.2 mL min^{-1} and **(E)** 0.1 mL min^{-1}. Adapted from (Gupta and Paull, 2021).

(Esene et al., 2024). They captured PTB biomarkers on an SPE monolith and then eluted them for separation via electrophoresis where four of these biomarkers were detected in the complex matrix of 50% serum. This demonstrates the potential of utilizing 3D printing to develop electrophoretic separation systems and that these systems can be interfaced with other 3D printed systems for extraction or detection.

As demonstrated above, one aspect of extraction that is necessary for analytical instrumentation but is often overlooked is the collection of biologically relevant matrices such as blood/serum (Hoffman et al., 2023), sweat (Yang P. et al., 2022), and saliva (Liao et al., 2023). Advancements in 3D printed microfluidic methodologies for simple extraction of these important biological fluids have been demonstrated in recent years, thereby providing a foundation for 3D printing devices to collect, process, and analyze blood/serum samples. For example, the extraction of blood has been enabled through printing of hollow microneedle structures that can puncture and extract blood through microfluidic channels (Cheng et al., 2023). Microfluidic systems have also been extensively employed for collection of sweat through wearable patches that collect and concentrate sweat into internal microfluidic channels (Chung-Han Wu et al., 2023; Wei et al., 2022). Saliva can be interfaced to microfluidic devices for extraction, separation, or detection through ports that accommodate insertion of commonly utilized oral swabs (Lee et al., 2020). Alternatively, 3D printed mouthguards that contains a paper microfluidic system to collect and test saliva glucose levels have been demonstrated (de Castro et al., 2019). Once collected, these fluids were subjected to further separation or immediately linked to a sensing component for analyte detection.

These examples clearly demonstrate that 3D printed fluidic systems have enabled extraction and separation techniques to be consolidated into easily fabricated devices, which have been further applied to reduce time of operation and simplify complex processes. Similarly, biological fluid extraction has been enabled through printed fluidic systems. The use of 3D printed microfluidics will likely continue to see significant growth in coming years for both separation and separation-facilitated sensing applications.

5.2 3D printed sensors

Clearly sample extraction and separation can be readily achieved within a 3D printed sensing device, and the versatility of 3D printing can further enable microfluidic channels to be modified with sensing applications in mind. This is particularly evident in recent work focused on point-of-care sensors where 3D printing can rapidly fabricate inexpensive fluidic devices for the detection of disease biomarkers. An important aspect of these devices is the introduction of capture and sensing components into the 3D printed fluidic system. Capture systems vary, but commonly rely on affinity interactions to selectively collect the target analyte, whereas the sensing itself is generally achieved through the use of electrochemical or optical methods (Muñoz and Pumera, 2020; Abdalla and Patel, 2021). A popular recent use for 3D printed microfluidics sensors has been the rapid detection of SARS-CoV-

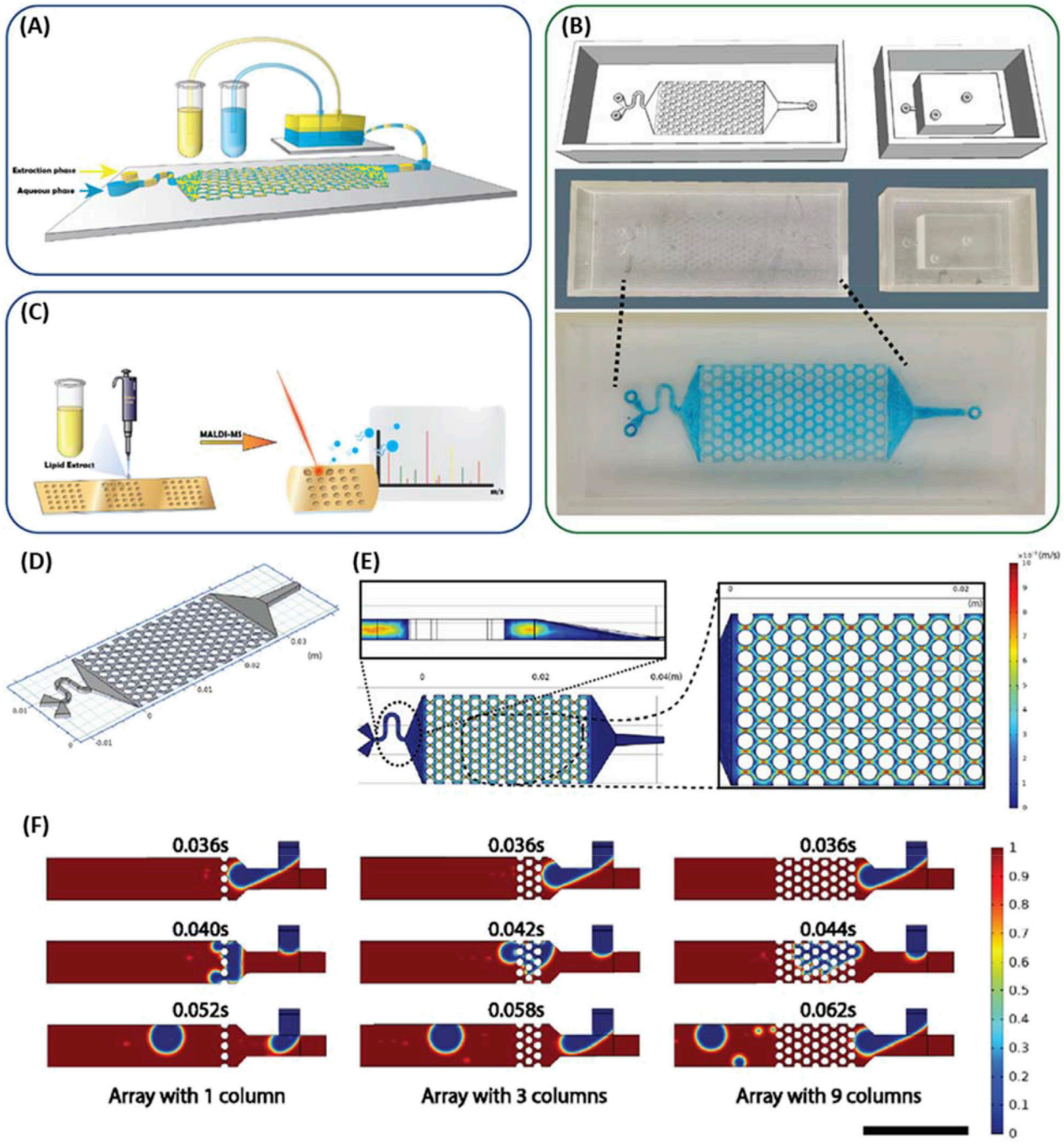

FIGURE 7
(A) Scheme of 3D printed microfluidic biochip platform for the mixing and separation of the extraction phases. **(B)** Computer generated print sketches of micromixer and reservoir, printed device with PMMA resin, and the image of the micromixer with filled dye solution in blue. **(C)** Schematic of workflow for lipid extract loading on the microarray chip for matrix assisted laser desorption ionization time of flight mass spectrometry. **(D)** Geometry of micromixer for the velocity field simulation. **(E)** Single phase velocity simulation for water in the micromixer with a focus on the velocity field plot for a sample longitudinal section and cross section. **(F)** Simulation of the droplet formation in the microfluidics' T-junction and how the droplets breakup in the microfluidic channels with varying number of columns (Bar = 500 μm). Adapted from (Yang Z. et al., 2022).

2 using both electrochemical (de Matos Morawski et al., 2023; Muhsin et al., 2023; Ali et al., 2022) and optical (Ning et al., 2023; Nguyen et al., 2022) techniques, which have been reviewed by Lin et al. (Lin et al., 2023).

For electrochemical sensing, the electrodes are typically integrated into the microfluidic channels. This can be realized in one of two ways. The first way is through implementation of conductive materials in the printing process (Ryan et al., 2022), as has been addressed in the previous section covering 3D printing materials. The other method is to integrate electrodes into the 3D printed flow channels by either inseting them after printing (Ambrosi et al., 2020; Capel et al., 2018) or by directly printing

around the electrode (Li et al., 2019; Su et al., 2022). Both methods have demonstrated promise in enabling electrochemical sensing of a plethora of analytes within 3D printed microfluidic channels. For example, recent work by Chittuam et al. (2023) demonstrated the simultaneous detection of HIV-1 and HCV based on DNA hybridization using a layered microfluidics chip with fully printed electrodes. Ferreira et al. (2021) employed 3D printing to develop an electrochemical cell compatible with various working electrodes. They also employed a 3D pen to fabricate the embedded counter and reference electrodes. Development of portable electrochemical sensors has also become feasible owing to advances in 3D printing. Vinoth et al. demonstrated a point-of-care sensor for saliva biomarkers using passive microfluidic flow, filtration, electrochemical sensors, and a PCB microcontroller, all within a hand-sized device (Vinoth et al., 2023). While electrochemical methods have seen extensive integration with microfluidics systems, other methods can also be employed in conjunction to expand the sensing capability. Sikula et al. (2023) demonstrated a 3D printed spectroelectrochemical sensor that achieves both cyclic voltammetry and UV-Vis spectroscopy. This simultaneous collection of optical and electrochemical data, and the collection of spectroscopic data through optically transparent printed components, is a unique and innovative development.

Optical sensing methodologies have also seen substantial use in the development of microfluidic sensors. This has been accentuated by utilizing smartphone cameras for data acquisition where a 3D printed system is interfaced to measure light intensity change or a colorimetric response. Xiao et al. (2022) fabricated a handheld SPR instrument enabled by smartphone imaging, with 3D printed microfluidics and a casing that holds optical components in alignment. Shang et al. (2022) developed a microfluidic sensor for *E. coli* that utilizes DNA extraction and amplification with fluorescence detection (Figure 8). The entire system was built onto a single microfluidic chip controlled by finger actuation with detection achieved by smartphone camera. Magnetic nanoparticles were used to separate the bacteria from food samples followed by nucleic acid extraction/purification and finished with recombinase polymerase amplification combined with CRISPR/Cas12a for fluorescence detection. Another reported method utilizing 3D printed finger-powered microfluidic pumps demonstrated detection of myocardial biomarkers using surface enhanced Raman spectroscopy (Liu et al., 2023). Target biomarkers were captured via a sandwich immunoassay between magnetic beads and gold nanoparticles. Magnetic separation within a 3D printed microfluidic system has also been employed to detect okadaic acid via horseradish peroxidase through catalyzed color change detected by a smartphone (Ji et al., 2023). Recently Kumar et al. (2023) developed a portable chemiluminescence-based point-of-care sensor where the fluidic components were 3D printed and interfaced with a temperature controller and smartphone, enabling sample processing and detection of alkaline phosphatase all within a handheld device.

5.3 Cell growth and sorting

Enabling studies involving cell sorting and growth are another popular avenue for the use of 3D printed fluidics. One example is 3D printing of flow chambers that allow 3D growth of cells and organoids (Zheng et al., 2021). Organ-on-a-chip platforms have been fabricated for mimicking and testing cellular systems, and these uses have been previously reviewed (Milton et al., 2023; Saorin et al., 2023). 3D printing has also been expanded to printing with cells, biomaterials, and biomolecules, as discussed in a recent review on 3D bioprinting (Vanaei et al., 2021). Clearly 3D printing technology has been instrumental in enabling rapid development of technqiues for cell-based study and systems.

Recently, 3D printing has been used to faciliate the vascularization of organoids, one of the major limitations that has plagued 3D cell culture (Salmon et al., 2022; Grebenyuk et al., 2023; Homan et al., 2019). Salmon et al. (2022) utilized small microfluidic channels adjacent to the organoid growth chamber for vascular network growth that enabled synchronization of organoids and vasculature (Figure 9). With this system, organoids, endothelial cells, and pericytes from human pluripotent stem cells (hPSC) were cultured. Flow of endothelial cells and pericytes through channels next to the organoid chamber induced vascular growth similar to naturally occurring tumor systems. Grebenyuk et al. (2023) employed a basket like grid of 3D printed microfluidic capilaries to hold and perfuse organoids as they grew. Homan et al. (2019) developed a microfluidic chamber and tested it by allowing for the maturation of organoids, which showed improved vascularization. 3D printing has been utilized to develop a microfluidic chamber for organoid growth that can be interfaced with microscopy instrumentation for imaging (Khan et al., 2021). These systems rely on continual flow from nonprinted pump systems for cell perfussion. Dhwaj et al. (2022) recently demonstrated a 3D printed impedance pump based on repeated tapping on a small portion of tubing for driving flow forward and employed it to maintin liver cell growth. The production of pumping systems for organoid growth is a promising use for 3D printing moving forward.

Another avenue where 3D printed microfluidics have found notable use is as a cheap and customizable method for cell sorting. Ding et al. (2022) developed a system composed of multiple printed units to mix, separate, and concentrate cells. To upscale the system to enable a large scale cell harvesting, Zhu et al. (2020) employed 3D printing to fabricate a system for extraction of white blood cells from whole blood. The system contained modules for blood mixing, lysis of red blood cells, and subsequent extraction of white blood cells. A few studies have also employed 3D printed microfluidics for malignant tumor cell sorting from red and white blood cells (Jiang and Xiang, 2022; Xu et al., 2022). Others have utilized 3D printed fluidics to develop an immunomagnetic platform for cell sorting based on phenotype (Philpott et al., 2022). Wang et al. (2023) developed one of these platforms to separate and analyze circulating tumor-reactive lymphocytes, and printed microfluidics were utilized for cell counting in blood cell analysis, as demonstrated by Yan et al. (2022) In this work, the change in resistance caused by each cell passing through a small hole between the electrodes is measured, thereby allowing cells to be counted.

The adaptability of 3D printing has inspired many applications where microfluidics are integrated or utilized within. The ability to fabricate any conceivable fluidic geometry with ease at low cost has allowed a plethora of different systems to be built. In addition to the applications mentioned above, there are various other topics including reaction catalysis (Pose-Boirazian et al., 2022) and drug encapsulation (Jia et al., 2022) that have been reviewed.

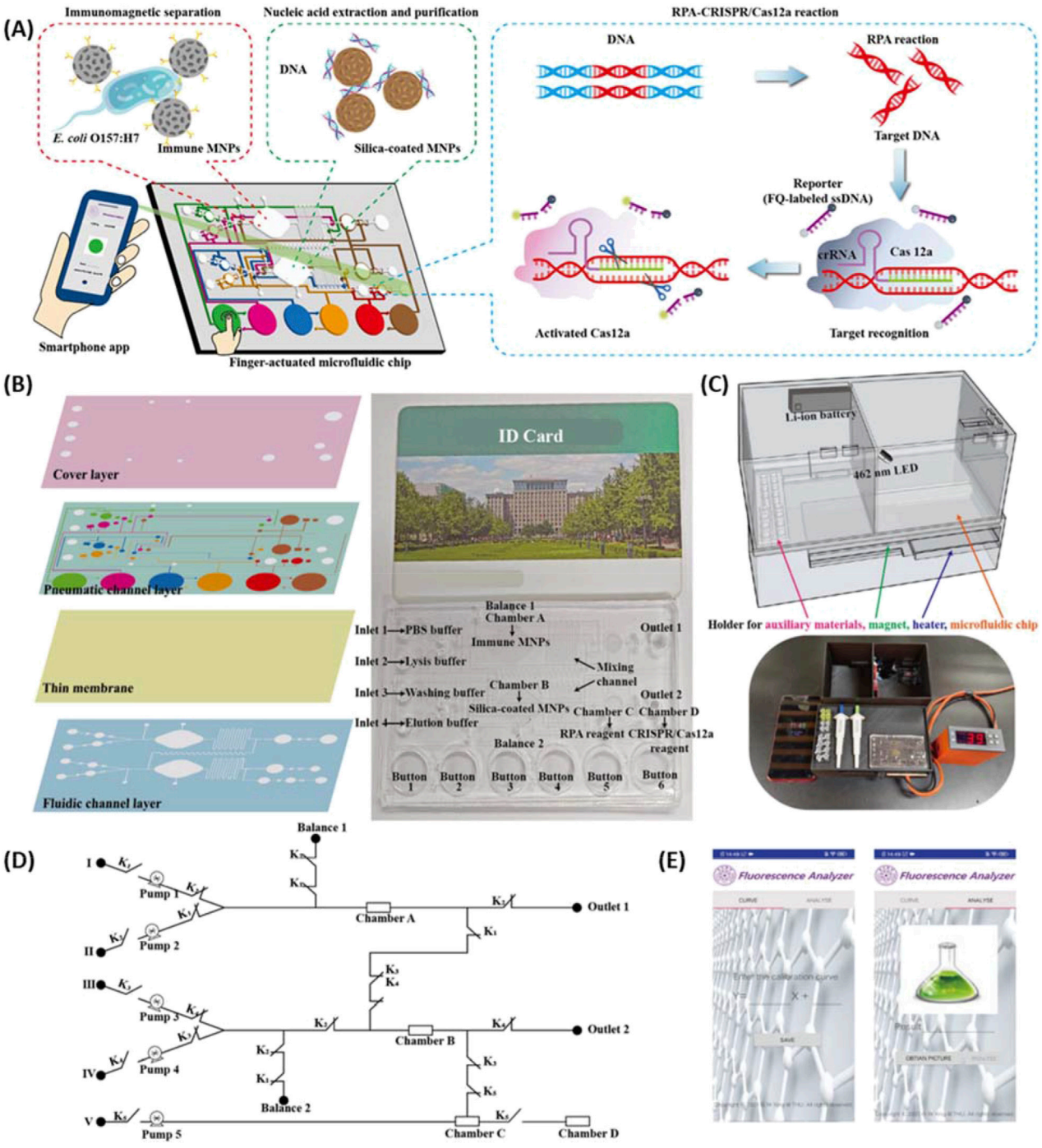

FIGURE 8
(A) Scheme of the finger actuated microfluidic chip for *E. coli* detection using RPA-CRISPR/Cas12a fluorescence collected via a smartphone app. **(B)** Design of the microfluidic chip made up of four layers (left) and image of combined microfluidic chip with id card for scale (right). **(C)** Model and image of the 3D printed device. **(D)** Circuit of the fluid control for the microfluidics. **(E)** Image of the smartphone app developed to interface with the sensor. Adapted from (Shang et al., 2022).

6 Conclusion

This review has summarized the current trends and advancements in the field of 3D printing that are closely related to the construction of analytical instrumentation. The main focus of this work is placed on recent progress in the production of 3D printed components, their implementation in sensing applications, and how 3D printing of an entire analytical instrument could be envisioned, designed, and realized. Highlighted here are the advancements in 3D printing techniques and materials, currently available and being developed, for the creation of optical, microfluidic,

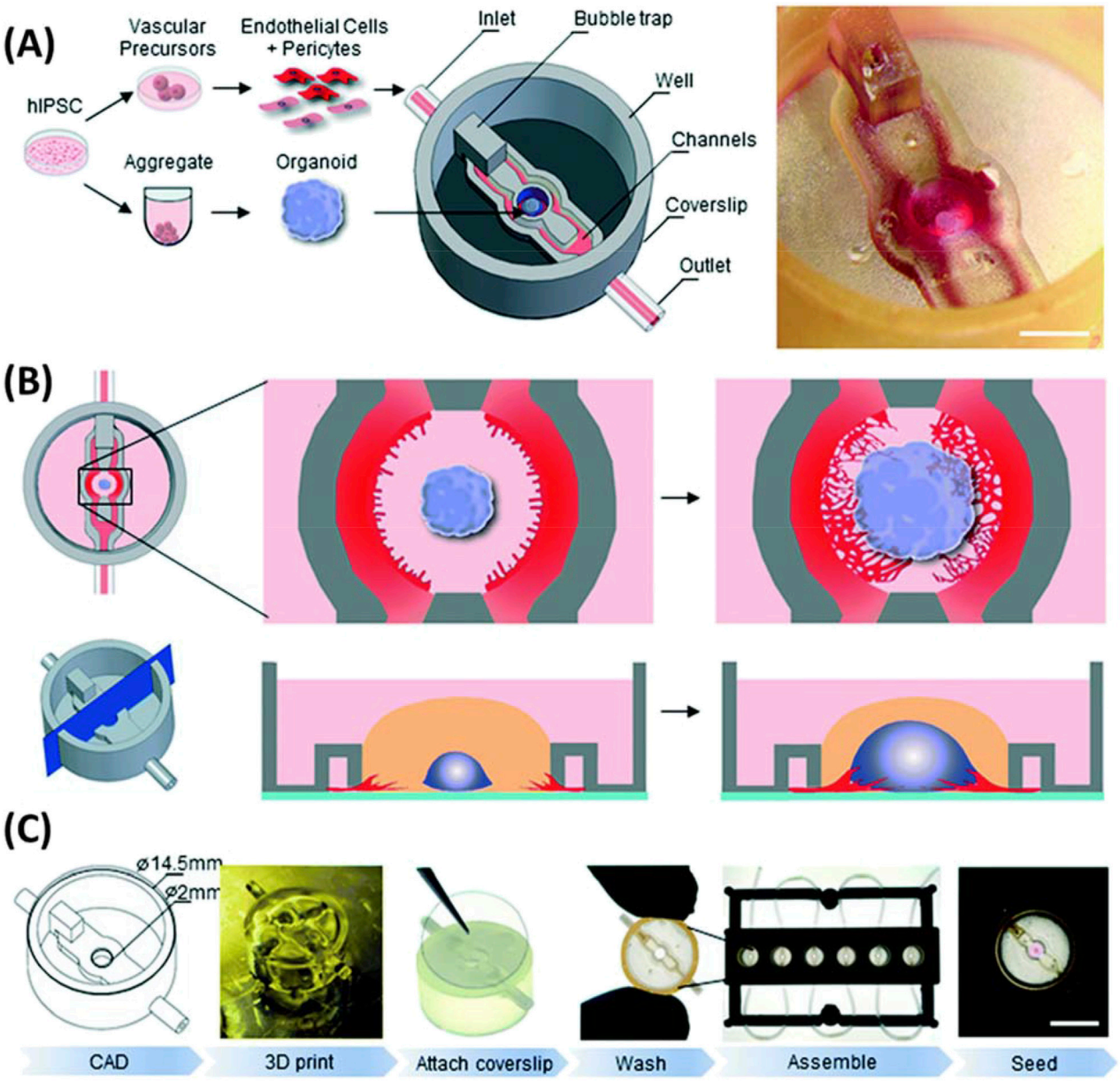

FIGURE 9
Microfluidics platform utilized for growth of vascularized organoids. **(A)** With growth of organoids and vascular precursors from the same human induced pluripotent stem cell culture and implemented into a microfluidics chip. **(B)** Allowing for vascularization to grow into the organoid from adjacent channels with endothelial cells and pericytes. **(C)** Workflow of chip fabrication and organoid seeding. Adapted from (Salmon et al., 2022).

mechanical, and structural components. 3D printing has shortened prototyping time and provided cost improvements but is still limited to a small set of feasible materials. However, this material space has significantly expanded in recent years with new printing systems and methods, an area we expect to observe continued growth in the coming years. With the capabilities of these new materials, their extension to sensing applications has become a significant trend that will be fueled by the continual introduction of new materials. The field is progressing rapidly, and it is clear that it has reached a point that one could practically 3D print all of the key components of an analytical platform, except the light or other forms of source and the electronic detector. Based on this, we expect to see 3D printing applications continue to expand. It is clear with time the 3D printers and their source materials will get progressively cheaper, continuously making 3D printing more and more accessible. Furthermore, as new methodologies are developed and implemented the resolution capabilities of 3D printing systems are bound to improve. These advancements are key to the future utilization of 3D printing in analytical instrumentation where small parts or flow channels are currently 3D printing limited. We could envision a 3D printer in nearly every academic lab in the near future due to the incredible versatility it provides in creating diverse devices

from the simplest instrument support to complex sample handling devices.

Author contributions

AM: Conceptualization, Formal Analysis, Investigation, Writing–original draft, Writing–review and editing. CE: Conceptualization, Investigation, Writing–original draft, Writing–review and editing. DS: Conceptualization, Investigation, Writing–original draft, Writing–review and editing. SV: Conceptualization, Investigation, Writing–original draft, Writing–review and editing. VH: Writing–original draft, Writing–review and editing. QC: Conceptualization, Formal Analysis, Funding acquisition, Investigation, Project administration, Supervision, Validation, Writing–original draft, Writing–review and editing.

Funding

The author(s) declare that financial support was received for the research, authorship, and/or publication of this article. We would like to acknowledge the financial support from NSF (CHE-2109042).

Conflict of interest

The authors declare that the research was conducted in the absence of any commercial or financial relationships that could be construed as a potential conflict of interest.

The author(s) declared that they were an editorial board member of Frontiers, at the time of submission. This had no impact on the peer review process and the final decision.

Generative AI statement

The author(s) declare that no Generative AI was used in the creation of this manuscript.

Publisher's note

References

Abdalla, A., and Patel, B. A. (2021). 3D printed electrochemical sensors. *Annu. Rev. Anal. Chem. (Palo Alto Calif)* 14 (1), 47–63. doi:10.1146/annurev-anchem-091120-093659

Agrawaal, H., and Thompson, J. (2021). Additive manufacturing (3D printing) for analytical chemistry. *Talanta Open* 3, 100036. doi:10.1016/j.talo.2021.100036

Ahn, D., Stevens, L. M., Zhou, K., and Page, Z. A. (2020). Rapid high-resolution visible light 3D printing. *ACS central Sci.* 6 (9), 1555–1563. doi:10.1021/acscentsci.0c00929

Al-Dulaijan, Y. A., Alsulaimi, L., Alotaibi, R., Alboainain, A., Alalawi, H., Alshehri, S., et al. (2022). Comparative evaluation of surface roughness and hardness of 3D printed resins. *Materials* 15 (19), 6822. doi:10.3390/ma15196822

Ali, M., Alam, F., Ahmed, I., AlQattan, B., Yetisen, A. K., and Butt, H. (2021). 3D printing of Fresnel lenses with wavelength selective tinted materials. *Addit. Manuf.* 47, 102281. doi:10.1016/j.addma.2021.102281

Ali, M. A., Zhang, G. F., Hu, C., Yuan, B., Jahan, S., Kitsios, G. D., et al. (2022). Ultrarapid and ultrasensitive detection of SARS-CoV-2 antibodies in COVID-19 patients via a 3D-printed nanomaterial-based biosensing platform. *J. Med. Virol.* 94 (12), 5808–5826. doi:10.1002/jmv.28075

Almughamsi, H. M., Howell, M. K., Parry, S. R., Esene, J. E., Nielsen, J. B., Nordin, G. P., et al. (2022). Immunoaffinity monoliths for multiplexed extraction of preterm birth biomarkers from human blood serum in 3D printed microfluidic devices. *Analyst* 147 (4), 734–743. doi:10.1039/d1an01365c

Ambrosi, A., and Bonanni, A. (2021). How 3D printing can boost advances in analytical and bioanalytical chemistry. *Microchim. Acta* 188. doi:10.1007/s00604-021-04901-2

Ambrosi, A., Shi, R. R. S., and Webster, R. D. (2020). 3D-printing for electrolytic processes and electrochemical flow systems. *J. Mater. Chem. A* 8 (42), 21902–21929. doi:10.1039/d0ta07939a

Amini, A., Guijt, R. M., Themelis, T., De Vos, J., and Eeltink, S. (2023). Recent developments in digital light processing 3D-printing techniques for microfluidic analytical devices. *J. Chromatogr. A* 1692, 463842. doi:10.1016/j.chroma.2023.463842

Apparao, D., and Raju, M. J. (2021). Design and analysis of spur gear manufactured by DMLS process. *Mater. Today Proc.* 46, 149–153. doi:10.1016/j.matpr.2020.07.078

Arena, M., Ambrogiani, P., Raiola, V., Bocchetto, F., Tirelli, T., and Castaldo, M. (2023). Design and qualification of an additively manufactured manifold for aircraft landing gears applications. *Aerospace* 10 (1), 69. doi:10.3390/aerospace10010069

Aslani, V., Toulouse, A., Schmid, M., Giessen, H., Haist, T., and Herkommer, A. (2023). 3D printing of colored micro-optics. *Opt. Mater. Express* 13 (5), 1372. doi:10.1364/ome.489681

Balakrishnan, H. K., Doeven, E. H., Merenda, A., Dumée, L. F., and Guijt, R. M. (2021). 3D printing for the integration of porous materials into miniaturised fluidic devices: a review. *Anal. Chim. acta* 1185, 338796. doi:10.1016/j.aca.2021.338796

Belkilani, M., Farre, C., Chevalier, Y., Minot, S., Bessueille, F., Abdelghani, A., et al. (2022). Mechanisms of influenza virus HA2 peptide interaction with liposomes studied by dual-wavelength MP-SPR. *ACS Appl. Mater. Interfaces* 14 (29), 32970–32981. doi:10.1021/acsami.2c09039

Berger, U. (2015). Aspects of accuracy and precision in the additive manufacturing of plastic gears. *Virtual Phys. Prototyp.* 10 (2), 49–57. doi:10.1080/17452759.2015.1026127

Berglund, G., Wisniowiecki, A., Gawedzinski, J., Applegate, B., and Tkaczyk, T. S. (2022). Additive manufacturing for the development of optical/photonic systems and components. *Optica* 9 (6), 623. doi:10.1364/optica.451642

Bhaduri, D., Penchev, P., Batal, A., Dimov, S., Soo, S. L., Sten, S., et al. (2017). Laser polishing of 3D printed mesoscale components. *Appl. Surf. Sci.* 405, 29–46. doi:10.1016/j.apsusc.2017.01.211

Bhaiyya, M., Pattnaik, P. K., and Goel, S. (2022). Multiplexed and simultaneous biosensing in a 3D-printed portable six-well smartphone operated electrochemiluminescence standalone point-of-care platform. *Mikrochim. Acta* 189 (2), 79. doi:10.1007/s00604-022-05200-0

Bhuvanesh Kumar, M., and Sathiya, P. (2021). Methods and materials for additive manufacturing: a critical review on advancements and challenges. *Thin-Walled Struct.* 159, 107228. doi:10.1016/j.tws.2020.107228

Bishop, G. W., Satterwhite-Warden, J. E., Kadimisetty, K., and Rusling, J. F. (2016). 3D-printed bioanalytical devices. *Nanotechnology* 27 (28), 284002. doi:10.1088/0957-4484/27/28/284002

Blachowicz, T., Ehrmann, G., and Ehrmann, A. (2021). Optical elements from 3D printed polymers. *e-Polymers* 21 (1), 549–565. doi:10.1515/epoly-2021-0061

Bogucki, R., Greggila, M., Mallory, P., Feng, J., Siman, K., Khakipoor, B., et al. (2019). A 3D-printable dual beam spectrophotometer with multiplatform smartphone adaptor. *J. Chem. Educ.* 96 (7), 1527–1531. doi:10.1021/acs.jchemed.8b00870

Braun, A., and Maier, S. A. (2016). Versatile direct laser writing lithography technique for surface enhanced infrared spectroscopy sensors. *ACS Sensors* 1 (9), 1155–1162. doi:10.1021/acssensors.6b00469

Buj-Corral, I., and Zayas-Figueras, E. E. (2023). Comparative study about dimensional accuracy and form errors of FFF printed spur gears using PLA and Nylon. *Polym. Test.* 117, 107862. doi:10.1016/j.polymertesting.2022.107862

Capel, A. J., Rimington, R. P., Lewis, M. P., and Christie, S. D. R. (2018). 3D printing for chemical, pharmaceutical and biological applications. *Nat. Rev. Chem.* 2 (12), 422–436. doi:10.1038/s41570-018-0058-y

Cardoso, R. M., Kalinke, C., Rocha, R. G., Dos Santos, P. L., Rocha, D. P., Oliveira, P. R., et al. (2020). Additive-manufactured (3D-printed) electrochemical sensors: a critical review. *Anal. Chim. acta* 1118, 73–91. doi:10.1016/j.aca.2020.03.028

Carlotti, M., and Mattoli, V. (2019). Functional materials for two-photon polymerization in microfabrication. *Small* 15 (40), 1902687. doi:10.1002/smll.201902687

Carrasco-Correa, E. J., Cocovi-Solberg, D. J., Herrero-Martínez, J. M., Simó-Alfonso, E. F., and Miró, M. (2020). 3D printed fluidic platform with *in-situ* covalently immobilized polymer monolithic column for automatic solid-phase extraction. *Anal. Chim. Acta* 1111, 40–48. doi:10.1016/j.aca.2020.03.033

Carrasco-Correa, E. J., Simó-Alfonso, E. F., Herrero-Martínez, J. M., and Miró, M. (2021). The emerging role of 3D printing in the fabrication of detection systems. *TrAC Trends Anal. Chem.* 136, 116177. doi:10.1016/j.trac.2020.116177

Casto, L. D., Do, K. B., and Baker, C. A. (2019). A miniature 3D printed LED-induced fluorescence detector for capillary electrophoresis and dual-detector taylor dispersion analysis. *Anal. Chem.* 91 (15), 9451–9457. doi:10.1021/acs.analchem.8b05824

Catala-Castro, F., Schaffer, E., and Krieg, M. (2022). Exploring cell and tissue mechanics with optical tweezers. *J. Cell Sci.* 135 (15), jcs259355. doi:10.1242/jcs.259355

Cecil, F., Guijt, R. M., Henderson, A. D., Macka, M., and Breadmore, M. C. (2020). One step multi-material 3D printing for the fabrication of a photometric detector flow cell. *Anal. Chim. Acta* 1097, 127–134. doi:10.1016/j.aca.2019.10.075

Chada, N., Sigdel, K. P., Gari, R. R. S., Matin, T. R., Randall, L. L., and King, G. M. (2015). Glass is a viable substrate for precision force microscopy of membrane proteins. *Sci. Rep.* 5, 12550. doi:10.1038/srep12550

Chan, H. N., Tan, M. J. A., and Wu, H. (2017). Point-of-care testing: applications of 3D printing. *Lab. Chip* 17 (16), 2713–2739. doi:10.1039/c7lc00397h

Chen, J.-Y., Hwang, J. V., Ao-Ieong, W. S., Lin, Y. C., Hsieh, Y. K., Cheng, Y. L., et al. (2018). Study of physical and degradation properties of 3D-printed biodegradable, photocurable copolymers, PGSA-co-PEGDA and PGSA-co-PCLDA. *Polymers* 10 (11), 1263. doi:10.3390/polym10111263

Cheng, J., Huang, J., Xiang, Q., and Dong, H. (2023). Hollow microneedle microfluidic paper-based chip for biomolecules rapid sampling and detection in interstitial fluid. *Anal. Chim. Acta* 1255, 341101. doi:10.1016/j.aca.2023.341101

Chittuam, K., Jampasa, S., Vilaivan, T., Tangkijvanich, P., Chuaypen, N., Avihingsanon, A., et al. (2023). Electrochemical capillary-driven microfluidic DNA sensor for HIV-1 and HCV coinfection analysis. *Anal. Chim. Acta* 1265, 341257. doi:10.1016/j.aca.2023.341257

Chu, S., Wang, H., Du, Y., Yang, F., Yang, L., and Jiang, C. (2020). Portable smartphone platform integrated with a nanoprobe-based fluorescent paper strip: visual monitoring of glutathione in human serum for health prognosis. *ACS Sustain. Chem. and Eng.* 8 (22), 8175–8183. doi:10.1021/acssuschemeng.0c00690

Chung-Han Wu, H. J. H. M., Paul, B., Balanay, R. K., Ray, T. R., and Ray, T. R. (2023). Skin-interfaced microfluidic systems with spatially engineered 3D fluidics for sweat capture and analysis. *Sci. Adv.* 9 (18), eadg4272. doi:10.1126/sciadv.adg4272

Darder, M. d.M., Serrano, L. A., Bedoya, M., and Orellana, G. (2022). 3D printing filaments facilitate the development of evanescent wave plastic optical fiber (POF) chemosensors. *Chemosensors* 10 (2), 61. doi:10.3390/chemosensors10020061

da Silva, E. K. N., dos Santos, V. B., Resque, I. S., Neves, C. A., Moreira, S. G., Franco, M. d. O., et al. (2020). A fluorescence digital image-based method using a 3D-printed platform and a UV-LED chamber made of polyacid lactic for quinine quantification in beverages. *Microchem. J.* 157, 104986. doi:10.1016/j.microc.2020.104986

Dawood, A., Marti Marti, B., Sauret-Jackson, V., and Darwood, A. (2015). 3D printing in dentistry. *Br. Dent. J.* 219 (11), 521–529. doi:10.1038/sj.bdj.2015.914

de Castro, L. F., de Freitas, S. V., Duarte, L. C., de Souza, J. A. C., Paixão, T. R. L. C., and Coltro, W. K. T. (2019). Salivary diagnostics on paper microfluidic devices and their use as wearable sensors for glucose monitoring. *Anal. Bioanal. Chem.* 411 (19), 4919–4928. doi:10.1007/s00216-019-01788-0

Del Rosario, M., Heil, H. S., Mendes, A., Saggiomo, V., and Henriques, R. (2022). The field guide to 3D printing in optical microscopy for life sciences. *Adv. Biol.* 6 (4), 2100994. doi:10.1002/adbi.202100994

de Matos Morawski, F., Martins, G., Ramos, M. K., Zarbin, A. J. G., Blanes, L., Bergamini, M. F., et al. (2023). A versatile 3D printed multi-electrode cell for determination of three COVID-19 biomarkers. *Anal. Chim. Acta* 1258, 341169. doi:10.1016/j.aca.2023.341169

Destino, J. F., Dudukovic, N. A., Johnson, M. A., Nguyen, D. T., Yee, T. D., Egan, G. C., et al. (2018). 3D printed optical quality silica and silica–titania glasses from sol–gel feedstocks. *Adv. Mater. Technol.* 3 (6). doi:10.1002/admt.201700323

Dhwaj, A., Roy, N., Jaiswar, A., Prabhakar, A., and Verma, D. (2022). 3D-Printed impedance micropump for continuous perfusion of the sample and nutrient medium integrated with a liver-on-chip prototype. *ACS Omega* 7 (45), 40900–40910. doi:10.1021/acsomega.2c03818

Ding, L., Razavi Bazaz, S., Asadniaye Fardjahromi, M., McKinnirey, F., Saputro, B., Banerjee, B., et al. (2022). A modular 3D printed microfluidic system: a potential solution for continuous cell harvesting in large-scale bioprocessing. *Bioresour. Bioprocess.* 9 (1), 64. doi:10.1186/s40643-022-00550-2

Dingeldein, J. C., Walczak, K. A., Swatowski, B. W., Friedrich, C. R., Middlebrook, C. T., and Roggemann, M. C. (2013). Process characterization for direct dispense fabrication of polymer optical multi-mode waveguides. *J. Micromechanics Microengineering* 23 (7), 075015. doi:10.1088/0960-1317/23/7/075015

Dizon, J. R. C., Gache, C. C. L., Cascolan, H. M. S., Cancino, L. T., and Advincula, R. C. (2021). Post-processing of 3D-printed polymers. *Technologies* 9 (3), 61. doi:10.3390/technologies9030061

Dolamore, F., Fee, C., and Dimartino, S. (2018). Modelling ordered packed beds of spheres: the importance of bed orientation and the influence of tortuosity on dispersion. *J. Chromatogr. A* 1532, 150–160. doi:10.1016/j.chroma.2017.12.004

Duarte, L. C., Pereira, I., Maciel, L. I. L., Vaz, B. G., and Coltro, W. K. T. (2022). 3D printed microfluidic mixer for real-time monitoring of organic reactions by direct infusion mass spectrometry. *Anal. Chim. Acta* 1190, 339252. doi:10.1016/j.aca.2021.339252

Erokhin, K. S., Gordeev, E. G., and Ananikov, V. P. (2019). Revealing interactions of layered polymeric materials at solid-liquid interface for building solvent compatibility charts for 3D printing applications. *Sci. Rep.* 9 (1), 20177. doi:10.1038/s41598-019-56350-w

Esene, J. E., Burningham, A. J., Tahir, A., Nordin, G. P., and Woolley, A. T. (2024). 3D printed microfluidic devices for integrated solid-phase extraction and microchip electrophoresis of preterm birth biomarkers. *Anal. Chim. Acta* 1296, 342338. doi:10.1016/j.aca.2024.342338

Esene, J. E., Nasman, P. R., Akuoko, Y., Tahir, A., and Woolley, A. T. (2023). Past, current, and future roles of 3D printing in the development of capillary electrophoresis systems. *TrAC Trends Anal. Chem.* 162, 117032. doi:10.1016/j.trac.2023.117032

Fee, C., Nawada, S., and Dimartino, S. (2014). 3D printed porous media columns with fine control of column packing morphology. *J. Chromatogr. A* 1333, 18–24. doi:10.1016/j.chroma.2014.01.043

Feng, D., Li, H., Xu, T., Zheng, F., Hu, C., Shi, X., et al. (2022). High-throughput single cell metabolomics and cellular heterogeneity exploration by inertial microfluidics coupled with pulsed electric field-induced electrospray ionization-high resolution mass spectrometry. *Anal. Chim. Acta* 1221, 340116. doi:10.1016/j.aca.2022.340116

Fernandes, Q. R., Jesus, D. P. d., and Fracassi da Silva, J. A. (2023). Simple modification to allow high-efficiency and high-resolution multi-material 3D-printing fabrication of microfluidic devices. *Lab a Chip* 23 (16), 3694–3703. doi:10.1039/d3lc00356f

Ferreira, P. A., de Oliveira, F. M., de Melo, E. I., de Carvalho, A. E., Lucca, B. G., Ferreira, V. S., et al. (2021). Multi sensor compatible 3D-printed electrochemical cell for voltammetric drug screening. *Anal. Chim. Acta* 1169, 338568. doi:10.1016/j.aca.2021.338568

Gadagi, B., and Lekurwale, R. (2021). A review on advances in 3D metal printing. *Mater. Today Proc.* 45, 277–283. doi:10.1016/j.matpr.2020.10.436

García-García, R., and González-Palacios, M. A. (2018). Method for the geometric modeling and rapid prototyping of involute bevel gears. *Int. J. Adv. Manuf. Technol.* 98 (1-4), 645–656. doi:10.1007/s00170-018-2246-9

Gastaldi, M., Cardano, F., Zanetti, M., Viscardi, G., Barolo, C., Bordiga, S., et al. (2020). Functional dyes in polymeric 3D printing: applications and perspectives. *ACS Mater. Lett.* 3 (1), 1–17. doi:10.1021/acsmaterialslett.0c00455

Gonzalez-Hernandez, D., Varapnickas, S., Merkininkaitė, G., Čiburys, A., Gailevičius, D., Šakirzanovas, S., et al. (2021). Laser 3D printing of inorganic free-form micro-optics. *Photonics* 8 (12), 577. doi:10.3390/photonics8120577

Gorkowski, K., Donahue, N. M., and Sullivan, R. C. (2020). Aerosol optical tweezers constrain the morphology evolution of liquid-liquid phase-separated atmospheric particles. *Chem* 6 (1), 204–220. doi:10.1016/j.chempr.2019.10.018

Grajewski, M., Hermann, M., Oleschuk, R. D., Verpoorte, E., and Salentijn, G. I. (2021). Leveraging 3D printing to enhance mass spectrometry: a review. *Anal. Chim. Acta* 1166, 338332. doi:10.1016/j.aca.2021.338332

Grebenyuk, S., Abdel Fattah, A. R., Kumar, M., Toprakhisar, B., Rustandi, G., Vananroye, A., et al. (2023). Large-scale perfused tissues via synthetic 3D soft microfluidics. *Nat. Commun.* 14 (1), 193. doi:10.1038/s41467-022-35619-1

Gritti, F., and Nawada, S. (2022). On the road toward highly efficient and large volume three-dimensional-printed liquid chromatography columns? *J. Sep. Sci.* 45 (17), 3232–3240. doi:10.1002/jssc.202100962

Gross, B., Lockwood, S. Y., and Spence, D. M. (2017). Recent advances in analytical chemistry by 3D printing. *Anal. Chem.* 89 (1), 57–70. doi:10.1021/acs.analchem.6b04344

Gul, I., Aer, L., Zhang, M., Jiang, H., Khan, A. A., Bilal, M., et al. (2021). Multifunctional 3D-printed platform integrated with a smartphone ambient light sensor for halocarbon contaminants monitoring. *Environ. Technol. and Innovation* 24, 101883. doi:10.1016/j.eti.2021.101883

Guo, H., Lv, R., and Bai, S. (2019). Recent advances on 3D printing graphene-based composites. *Nano Mater. Sci.* 1 (2), 101–115. doi:10.1016/j.nanoms.2019.03.003

Gupta, V., and Paull, B. (2021). PolyJet printed high aspect ratio three-dimensional bifurcating microfluidic flow distributor and its application in solid-phase extraction. *Anal. Chim. Acta* 1168, 338624. doi:10.1016/j.aca.2021.338624

Guttridge, C., Shannon, A., O'Sullivan, A., O'Sullivan, K. J., and O'Sullivan, L. W. (2022). Biocompatible 3D printing resins for medical applications: a review of marketed intended use, biocompatibility certification, and post-processing guidance. *Ann. 3D Print. Med.* 5, 100044. doi:10.1016/j.stlm.2021.100044

Habib, T., Brämer, C., Heuer, C., Ebbecke, J., Beutel, S., and Bahnemann, J. (2022). 3D-Printed microfluidic device for protein purification in batch chromatography. *Lab. Chip* 22 (5), 986–993. doi:10.1039/d1lc01127h

Hai, R., Shao, G., Ware, H. O. T., Jones, E. H., and Sun, C. (2023). 3D printing a low-cost miniature accommodating optical microscope. *Adv. Mater* 35 (20), e2208365. doi:10.1002/adma.202208365

Hartcher-O'Brien, J., Evers, J., and Tempelman, E. (2019). Surface roughness of 3D printed materials: comparing physical measurements and human perception. *Mater. Today Commun.* 19, 300–305. doi:10.1016/j.mtcomm.2019.01.008

He, Z., Lee, Y. H., Chanda, D., and Wu, S. T. (2018). Adaptive liquid crystal microlens array enabled by two-photon polymerization. *Opt. Express* 26 (16), 21184–21193. doi:10.1364/OE.26.021184

Heikkinen, I. T., Kauppinen, C., Liu, Z., Asikainen, S. M., Spoljaric, S., Seppälä, J. V., et al. (2018). Chemical compatibility of fused filament fabrication-based 3-D printed components with solutions commonly used in semiconductor wet processing. *Addit. Manuf.* 23, 99–107. doi:10.1016/j.addma.2018.07.015

Hengsteler, J., Mandal, B., van Nisselroy, C., Lau, G. P. S., Schlotter, T., Zambelli, T., et al. (2021). Bringing electrochemical three-dimensional printing to the nanoscale. *Nano Lett.* 21 (21), 9093–9101. doi:10.1021/acs.nanolett.1c02847

Heuer, C., Preuss, J. A., Buttkewitz, M., Scheper, T., Segal, E., and Bahnemann, J. (2022). A 3D-printed microfluidic gradient generator with integrated photonic silicon sensors for rapid antimicrobial susceptibility testing. *Lab. Chip* 22 (24), 4950–4961. doi:10.1039/d2lc00640e

Hinman, S. S., McKeating, K. S., and Cheng, Q. (2017). Plasmonic sensing with 3D printed optics. *Anal. Chem.* 89 (23), 12626–12630. doi:10.1021/acs.analchem.7b03967

Hoffman, M. S. F., McKeage, J. W., Xu, J., Ruddy, B. P., Nielsen, P. M. F., and Taberner, A. J. (2023). Minimally invasive capillary blood sampling methods. *Expert Rev. Med. Devices* 20 (1), 5–16. doi:10.1080/17434440.2023.2170783

Homan, K. A., Gupta, N., Kroll, K. T., Kolesky, D. B., Skylar-Scott, M., Miyoshi, T., et al. (2019). Flow-enhanced vascularization and maturation of kidney organoids *in vitro*. *Nat. Methods* 16 (3), 255–262. doi:10.1038/s41592-019-0325-y

Hong, Z., Luo, T., Jiang, S., and Liang, R. (2023b). Fiber-fed 3D printing of germanate glass optics. *Photonics* 10 (4), 378. doi:10.3390/photonics10040378

Hong, Z., Sun, Y., Ye, P., Loy, D. A., and Liang, R. (2023a). Bio-inspired compact, high-resolution snapshot hyperspectral imaging system with 3D printed glass lightguide array. *Adv. Opt. Mater.* 11 (9), 2300156. doi:10.1002/adom.202300156

Hong, Z., Ye, P., Loy, D. A., and Liang, R. (2021). Three-dimensional printing of glass micro-optics. *Optica* 8 (6), 904. doi:10.1364/optica.422955

Hong, Z., Ye, P., Loy, D. A., and Liang, R. (2022). High-precision printing of complex glass imaging optics with precondensed liquid silica resin. *Adv. Sci. (Weinh)* 9 (18), e2105595. doi:10.1002/advs.202105595

Irlam, R. C., Hughes, C., Parkin, M. C., Beardah, M. S., O'Donnell, M., Brabazon, D., et al. (2020). Trace multi-class organic explosives analysis in complex matrices enabled using LEGO®-inspired clickable 3D-printed solid phase extraction block arrays. *J. Chromatogr. A* 1629, 461506. doi:10.1016/j.chroma.2020.461506

Ji, Y., Cai, G., Liang, C., Gao, Z., Lin, W., Ming, Z., et al. (2023). A microfluidic immunosensor based on magnetic separation for rapid detection of okadaic acid in marine shellfish. *Anal. Chim. Acta* 1239, 340737. doi:10.1016/j.aca.2022.340737

Jia, F., Gao, Y., and Wang, H. (2022). Recent advances in drug delivery system fabricated by microfluidics for disease therapy. *Bioeng. (Basel)* 9 (11), 625. doi:10.3390/bioengineering9110625

Jiang, F., and Xiang, N. (2022). Integrated microfluidic handheld cell sorter for high-throughput label-free malignant tumor cell sorting. *Anal. Chem.* 94 (3), 1859–1866. doi:10.1021/acs.analchem.1c04819

Jiang, Y., Islam, M. N., He, R., Huang, X., Cao, P., Advincula, R. C., et al. (2022). Recent advances in 3D printed sensors: materials, design, and manufacturing. *Adv. Mater. Technol.* 8 (2). doi:10.1002/admt.202200492

Jonušauskas, L., Juodkazis, S., and Malinauskas, M. (2018). Optical 3D printing: bridging the gaps in the mesoscale. *J. Opt.* 20 (5), 053001. doi:10.1088/2040-8986/aab3fe

Junk, S., and Kuen, C. (2016). Review of open source and freeware CAD systems for use with 3D-printing. *Procedia CIRP* 50, 430–435. doi:10.1016/j.procir.2016.04.174

Kalinke, C., Neumsteir, N. V., Aparecido, G. d. O., Ferraz, T. V. d. B., Dos Santos, P. L., Janegitz, B. C., et al. (2020). Comparison of activation processes for 3D printed PLA-graphene electrodes: electrochemical properties and application for sensing of dopamine. *Analyst* 145 (4), 1207–1218. doi:10.1039/c9an01926j

Keshan Balavandy, S., Li, F., Macdonald, N. P., Maya, F., Townsend, A. T., Frederick, K., et al. (2021). Scalable 3D printing method for the manufacture of single-material fluidic devices with integrated filter for point of collection colourimetric analysis. *Anal. Chim. Acta* 1151, 238101. doi:10.1016/j.aca.2020.11.033

Khalfa, A. L., Becker, M. L., and Dove, A. P. (2021). Stereochemistry-controlled mechanical properties and degradation in 3D-printable photosets. *J. Am. Chem. Soc.* 143 (42), 17510–17516. doi:10.1021/jacs.1c06960

Khan, I., Prabhakar, A., Delepine, C., Tsang, H., Pham, V., and Sur, M. (2021). A low-cost 3D printed microfluidic bioreactor and imaging chamber for live-organoid imaging. *Biomicrofluidics* 15 (2), 024105. doi:10.1063/5.0041027

Khosravani, M. R., and Reinicke, T. (2020). Effects of raster layup and printing speed on strength of 3D-printed structural components. *Procedia Struct. Integr.* 28, 720–725. doi:10.1016/j.prostr.2020.10.083

Kotkar, T., Masure, P., Modake, P., Lad, C., and Patil, B. (2018). Modelling and testing of spur gear made of different 3D printed materials. *Int. JS Res. Sci. Eng.* 4, 1389–1394.

Kotz, F., Arnold, K., Bauer, W., Schild, D., Keller, N., Sachsenheimer, K., et al. (2017). Three-dimensional printing of transparent fused silica glass. *Nature* 544 (7650), 337–339. doi:10.1038/nature22061

Kruth, J.-P., Wang, X., Laoui, T., and Froyen, L. (2003). Lasers and materials in selective laser sintering. *Assem. Autom.* 23 (4), 357–371. doi:10.1108/01445150310698652

Kuhnke, L. M., Rehfeld, J. S., Ude, C., and Beutel, S. (2022). Study on the development and integration of 3D-printed optics in small-scale productions of single-use cultivation vessels. *Eng. Life Sci.* 22 (6), 440–452. doi:10.1002/elsc.202100131

Kulkarni, M. B., Velmurugan, K., Nirmal, J., and Goel, S. (2023). Development of dexamethasone loaded nanomicelles using a 3D printed microfluidic device for ocular drug delivery applications. *Sensors Actuators A Phys.*, 357. doi:10.1016/j.sna.2023.114385

Kumar, P. S., Madapusi, S., and Goel, S. (2023). 3D printed microfluidic chemiluminescence PoC device with self-powering and integrated incubating system: Validation via ALP detection on disposable μPADs. *Microchem. J.* 189, 108518. doi:10.1016/j.microc.2023.108518

Kunwar, P., Jannini, A. V. S., Xiong, Z., Ransbottom, M. J., Perkins, J. S., Henderson, J. H., et al. (2020). High-resolution 3D printing of stretchable hydrogel structures using optical projection lithography. *ACS Appl. Mater Interfaces* 12 (1), 1640–1649. doi:10.1021/acsami.9b19431

Lai, W. Q., Chang, Y. F., Chou, F. N., and Yang, D. M. (2022). Portable FRET-based biosensor device for on-site lead detection. *Biosens. (Basel)* 12 (3), 157. doi:10.3390/bios12030157

Lambert, A., Valiulis, S., and Cheng, Q. (2018). Advances in optical sensing and bioanalysis enabled by 3D printing. *ACS Sens.* 3 (12), 2475–2491. doi:10.1021/acssensors.8b01085

Layani, M., Wang, X., and Magdassi, S. (2018). Novel materials for 3D printing by photopolymerization. *Adv. Mater.* 30 (41), 1706344. doi:10.1002/adma.201706344

Lee, J.-Y., An, J., and Chua, C. K. (2017). Fundamentals and applications of 3D printing for novel materials. *Appl. Mater. today* 7, 120–133. doi:10.1016/j.apmt.2017.02.004

Lee, K., Yoon, T., Yang, H., Cha, S., Cheon, Y., Kashefi-Kheyrabadi, L., et al. (2020). All-in-one platform for salivary cotinine detection integrated with a microfluidic channel and an electrochemical biosensor. *Lab. Chip* 20 (2), 320–331. doi:10.1039/C9LC01024F

Lertvachirapaiboon, C., Baba, A., Shinbo, K., and Kato, K. (2021). Dual-mode surface plasmon resonance sensor chip using a grating 3D-printed prism. *Anal. Chim. Acta* 1147, 23–29. doi:10.1016/j.aca.2020.12.027

Li, H., Lousteau, J., Suo, R., Jiang, X., MacPherson, W. N., Bookey, H. T., et al. (2009). "Sensing properties of germanate and tellurite glass optical fibres," in *20th international conference on optical fibre sensors*. doi:10.1117/12.835317

Li, F., Macdonald, N. P., Guijt, R. M., and Breadmore, M. C. (2019). Increasing the functionalities of 3D printed microchemical devices by single material, multimaterial, and print-pause-print 3D printing. *Lab a Chip* 19 (1), 35–49. doi:10.1039/c8lc00826d

Li, J., Nallappan, K., Guerboukha, H., and Skorobogatiy, M. (2017). 3D printed hollow core terahertz Bragg waveguides with defect layers for surface sensing applications. *Opt. Express* 25 (4), 4126–4144. doi:10.1364/OE.25.004126

Li, X., He, Z., Li, C., and Li, P. (2021). One-step enzyme kinetics measurement in 3D printed microfluidics devices based on a high-performance single vibrating sharp-tip mixer. *Anal. Chim. Acta* 1172, 338677. doi:10.1016/j.aca.2021.338677

Liao, C., Chen, X., and Fu, Y. (2023). Salivary analysis: an emerging paradigm for non-invasive healthcare diagnosis and monitoring. *Interdiscip. Med.* 1. doi:10.1002/inmd.20230009

Ligon, S. C., Liska, R., Stampfl, J., Gurr, M., and Mülhaupt, R. (2017). Polymers for 3D printing and customized additive manufacturing. *Chem. Rev.* 117 (15), 10212–10290. doi:10.1021/acs.chemrev.7b00074

Lin, T., Xu, Y., Zhao, A., He, W., and Xiao, F. (2022). Flexible electrochemical sensors integrated with nanomaterials for *in situ* determination of small molecules in biological samples: a review. *Anal. Chim. Acta* 1207, 339461. doi:10.1016/j.aca.2022.339461

Lin, Z., Zou, Z., Pu, Z., Wu, M., and Zhang, Y. (2023). Application of microfluidic technologies on COVID-19 diagnosis and drug discovery. *Acta Pharm. Sin. B* 13, 2877–2896. doi:10.1016/j.apsb.2023.02.014

Liu, S., Wang, W., Xu, W., Liu, L., Zhang, W., Song, K., et al. Continuous three-dimensional printing of architected piezoelectric sensors in minutes, 2022, 9790307, doi:10.34133/2022/9790307Research, 2022.

Liu, Y., Gao, R., Zhuo, Y., Wang, Y., Jia, H., Chen, X., et al. (2023). Rapid simultaneous SERS detection of dual myocardial biomarkers on single-track finger-pump microfluidic chip. *Anal. Chim. Acta* 1239, 340673. doi:10.1016/j.aca.2022.340673

Lu, A., Jin, T., Liu, Q., Guo, Z., Qu, M., Luo, H., et al. (2019). Modeling and prediction of surface topography and surface roughness in dual-axis wheel polishing of optical glass. *Int. J. Mach. Tools Manuf.* 137, 13–29. doi:10.1016/j.ijmachtools.2018.10.001

Luo, J., Pan, H., and Kinzel, E. C. (2014). Additive manufacturing of glass. *J. Manuf. Sci. Eng.* 136 (6). doi:10.1115/1.4028531

Maines, E. M., Porwal, M. K., Ellison, C. J., and Reineke, T. M. (2021). Sustainable advances in SLA/DLP 3D printing materials and processes. *Green Chem.* 23 (18), 6863–6897. doi:10.1039/d1gc01489g

Mao, M., He, J., Li, X., Zhang, B., Lei, Q., Liu, Y., et al. (2017). The emerging frontiers and applications of high-resolution 3D printing. *Micromachines* 8 (4), 113. doi:10.3390/mi8040113

Matheuse, F., Vanmol, K., Van Erps, J., De Malsche, W., Ottevaere, H., and Desmet, G. (2022). On the potential use of two-photon polymerization to 3D print chromatographic packed bed supports. *J. Chromatogr. A* 1663, 462763. doi:10.1016/j.chroma.2021.462763

Milton, L. A., Viglione, M. S., Ong, L. J. Y., Nordin, G. P., and Toh, Y. C. (2023). Vat Photopolymerization 3D printed microfluidic devices for organ-on-a-chip applications. *Lab a Chip* 23, 3537–3560. doi:10.1039/d3lc00094j

Mohamed, O. A., Masood, S. H., and Bhowmik, J. L. (2015). Optimization of fused deposition modeling process parameters: a review of current research and future prospects. *Adv. Manuf.* 3, 42–53. doi:10.1007/s40436-014-0097-7

Moore, D. G., Barbera, L., Masania, K., and Studart, A. R. (2020). Three-dimensional printing of multicomponent glasses using phase-separating resins. *Nat. Mater* 19 (2), 212–217. doi:10.1038/s41563-019-0525-y

Moser, M. R., Smith, C. M., Gutierrez, G. G., and Baker, C. A. (2022). 3D printed instrument for taylor dispersion analysis with two-point laser-induced fluorescence detection. *Anal. Chem.* 94 (16), 6089–6096. doi:10.1021/acs.analchem.1c04566

Muhsin, S. A., He, Y., Al-Amidie, M., Sergovia, K., Abdullah, A., Wang, Y., et al. (2023). A microfluidic biosensor architecture for the rapid detection of COVID-19. *Anal. Chim. Acta* 1275, 341378. doi:10.1016/j.aca.2023.341378

Muñoz, J., and Pumera, M. (2020). 3D-printed biosensors for electrochemical and optical applications. *TrAC Trends Anal. Chem.* 128, 115933. doi:10.1016/j.trac.2020.115933

Musgrove, H. B., Catterton, M. A., and Pompano, R. R. (2022). Applied tutorial for the design and fabrication of biomicrofluidic devices by resin 3D printing. *Anal. Chim. Acta* 1209, 339842. doi:10.1016/j.aca.2022.339842

Nair, S., Trisno, J., Ruan, Q., Daqiqeh Rezaei, S., Simpson, R. E., Yang, J. K. W., et al. (2022). 3D printing mesoscale optical components with a low-cost resin printer integrated with a fiber-optic taper. *ACS Photonics* 9 (6), 2024–2031. doi:10.1021/acsphotonics.2c00125

Naz, S. A., Huynh, V. T., Doeven, E. H., Adams, S., Kouzani, A., and Guijt, R. M. (2023). Closed-loop control systems for pumps used in portable analytical systems. *J. Chromatogr. A* 1695, 463931. doi:10.1016/j.chroma.2023.463931

Ng, W. L., Lee, J. M., Zhou, M., Chen, Y. W., Lee, K. X. A., Yeong, W. Y., et al. (2020). Vat polymerization-based bioprinting—process, materials, applications and regulatory challenges. *Biofabrication* 12 (2), 022001. doi:10.1088/1758-5090/ab6034

Ngo, T. D., Kashani, A., Imbalzano, G., Nguyen, K. T., and Hui, D. (2018). Additive manufacturing (3D printing): a review of materials, methods, applications and challenges. *Compos. Part B Eng.* 143, 172–196. doi:10.1016/j.compositesb.2018.02.012

Nguyen, D. T., Meyers, C., Yee, T. D., Dudukovic, N. A., Destino, J. F., Zhu, C., et al. (2017). 3D-printed transparent glass. *Adv. Mater.* 29 (26), 1701181. doi:10.1002/adma.201701181

Nguyen, P. Q. M., Wang, M., Ann Maria, N., Li, A. Y., Tan, H. Y., Xiong, G. M., et al. (2022). Modular micro-PCR system for the onsite rapid diagnosis of COVID-19. *Microsyst. Nanoeng.* 8, 82. doi:10.1038/s41378-022-00400-3

Ni, J., Ling, H., Zhang, S., Wang, Z., Peng, Z., Benyshek, C., et al. (2019). Three-dimensional printing of metals for biomedical applications. *Mater. Today Bio* 3, 100024. doi:10.1016/j.mtbio.2019.100024

Nielsen, A. V., Beauchamp, M. J., Nordin, G. P., and Woolley, A. T. (2020). 3D printed microfluidics. *Annu. Rev. Anal. Chem. (Palo Alto Calif)* 13 (1), 45–65. doi:10.1146/annurev-anchem-091619-102649

Ning, S., Chang, H. C., Fan, K. C., Hsiao, P. Y., Feng, C., Shoemaker, D., et al. (2023). A point-of-care biosensor for rapid detection and differentiation of COVID-19 virus (SARS-CoV-2) and influenza virus using subwavelength grating micro-ring resonator. *Appl. Phys. Rev.* 10 (2), 021410. doi:10.1063/5.0146079

Nittala, P. V. K., Hohreiter, A., Rosas Linhard, E., Dohn, R., Mishra, S., Konda, A., et al. (2023). Integration of silicon chip microstructures for in-line microbial cell lysis in soft microfluidics. *Lab. Chip* 23 (9), 2327–2340. doi:10.1039/d2lc00896c

Norani, M. N. M., Abdullah, M., Abdollah, M. F. B., Amiruddin, H., Ramli, F. Z., and Tamaldin, N. (2021). Mechanical and tribological properties of FFF 3D-printed polymers: a brief review. *J. Tribol.* 29, 11–30.

Nseowo Udofia, E., and Zhou, W. (2020). 3D printed optics with a soft and stretchable optical material. *Addit. Manuf.* 31, 100912. doi:10.1016/j.addma.2019.100912

Odent, J., Wallin, T. J., Pan, W., Kruemplestaedter, K., Shepherd, R. F., and Giannelis, E. P. (2017). Highly elastic, transparent, and conductive 3D-printed ionic composite hydrogels. *Adv. Funct. Mater.* 27 (33), 1701807. doi:10.1002/adfm.201701807

Ogishi, K., Osaki, T., Morimoto, Y., and Takeuchi, S. (2022). 3D printed microfluidic devices for lipid bilayer recordings. *Lab. Chip* 22 (5), 890–898. doi:10.1039/d1lc01077h

Oladapo, B. I., Zahedi, S. A., Ismail, S. O., and Omigbodun, F. T. (2021). 3D printing of PEEK and its composite to increase biointerfaces as a biomedical material-A review. *Colloids Surfaces B Biointerfaces* 203, 111726. doi:10.1016/j.colsurfb.2021.111726

O'Shea, D. C., Suleski, T. J., Kathman, A. D., and Prather, D. W. (2003). *Diffractive optics: design, fabrication, and test*. Bellingham, WA, USA: SPIE Press, 1–260.

Pakkanen, J., Manfredi, D., Minetola, P., and Iuliano, L. (2017). About the use of recycled or biodegradable filaments for sustainability of 3D printing: state of the art and research opportunities. *Sustain. Des. Manuf. Sel. Pap. Sustain. Des. Manuf.* 4, 776–785. doi:10.1007/978-3-319-57078-5_73

Philpott, D. N., Chen, K., Atwal, R. S., Li, D., Christie, J., Sargent, E. H., et al. (2022). Ultrathroughput immunomagnetic cell sorting platform. *Lab. Chip* 22 (24), 4822–4830. doi:10.1039/d2lc00798c

Pose-Boirazian, T., Martinez-Costas, J., and Eibes, G. (2022). 3D printing: an emerging technology for biocatalyst immobilization. *Macromol. Biosci.* 22 (9), e2200110. doi:10.1002/mabi.202200110

Purtov, J., Rogin, P., Verch, A., Johansen, V. E., and Hensel, R. (2019). Nanopillar diffraction gratings by two-photon lithography. *Nanomater. (Basel)* 9 (10), 1495. doi:10.3390/nano9101495

Quan, H., Zhang, T., Xu, H., Luo, S., Nie, J., and Zhu, X. (2020). Photo-curing 3D printing technique and its challenges. *Bioact. Mater.* 5 (1), 110–115. doi:10.1016/j.bioactmat.2019.12.003

Quang, Q. H., Doan, T. T., Quoc, T. D., and Manh, T. N. (2018). Nonlinear optical tweezers for longitudinal control of dielectric particles. *Opt. Commun.* 421, 94–98. doi:10.1016/j.optcom.2018.03.068

Quesada-Gonzalez, D., and Merkoci, A. (2017). Mobile phone-based biosensing: an emerging "diagnostic and communication" technology. *Biosens. Bioelectron.* 92, 549–562. doi:10.1016/j.bios.2016.10.062

Ranjan, R., Kumar, D., Kundu, M., and Chandra Moi, S. (2022). A critical review on Classification of materials used in 3D printing process. *Mater. today Proc.* 61, 43–49. doi:10.1016/j.matpr.2022.03.308

Rett, J. P., Traore, Y. L., and Ho, E. A. (2021). Sustainable materials for fused deposition modeling 3D printing applications. *Adv. Eng. Mater.* 23 (7), 2001472. doi:10.1002/adem.202001472

Ristok, S., Thiele, S., Toulouse, A., Herkommer, A. M., and Giessen, H. (2020). Stitching-free 3D printing of millimeter-sized highly transparent spherical and aspherical optical components. *Opt. Mater. Express* 10 (10), 2370. doi:10.1364/ome.401724

Romanczuk-Ruszuk, E., Sztorch, B., Pakuła, D., Gabriel, E., Nowak, K., and Przekop, R. E. (2023). 3D printing ceramics—materials for direct extrusion process. *Ceramics* 6 (1), 364–385. doi:10.3390/ceramics6010022

Ryan, K. R., Down, M. P., Hurst, N. J., Keefe, E. M., and Banks, C. E. (2022). Additive manufacturing (3D printing) of electrically conductive polymers and polymer nanocomposites and their applications. *eScience* 2 (4), 365–381. doi:10.1016/j.esci.2022.07.003

Salmean, C., and Dimartino, S. (2019). 3D-printed stationary phases with ordered morphology: state of the art and future development in liquid chromatography. *Chromatographia* 82 (1), 443–463. doi:10.1007/s10337-018-3671-5

Salmon, I., Grebenyuk, S., Abdel Fattah, A. R., Rustandi, G., Pilkington, T., Verfaillie, C., et al. (2022). Engineering neurovascular organoids with 3D printed microfluidic chips. *Lab. Chip* 22 (8), 1615–1629. doi:10.1039/d1lc00535a

Sanli, U. T., Messer, T., Weigand, M., Lötgering, L., Schütz, G., Wegener, M., et al. (2022). High-resolution kinoform X-ray optics printed via 405 nm 3D laser lithography. *Adv. Mater. Technol.* 7 (9). doi:10.1002/admt.202101695

Saorin, G., Caligiuri, I., and Rizzolio, F. (2023). Microfluidic organoids-on-a-chip: the future of human models. *Seminars Cell and Dev. Biol.* 144, 41–54. doi:10.1016/j.semcdb.2022.10.001

Schaffner, D., Preuschoff, T., Ristok, S., Brozio, L., Schlosser, M., Giessen, H., et al. (2020). Arrays of individually controllable optical tweezers based on 3D-printed microlens arrays. *Opt. Express* 28 (6), 8640–8645. doi:10.1364/OE.386243

Schmid, M., Sterl, F., Thiele, S., Herkommer, A., and Giessen, H. (2021). 3D printed hybrid refractive/diffractive achromat and apochromat for the visible wavelength range. *Opt. Lett.* 46 (10), 2485–2488. doi:10.1364/OL.423196

Schure, M. R., Maier, R. S., Kroll, D. M., and Davis, H. T. (2004). Simulation of ordered packed beds in chromatography. *J. Chromatogr. A* 1031 (1-2), 79–86. doi:10.1016/j.chroma.2003.12.030

Selemani, M. A., and Martin, R. S. (2024). Use of 3D printing to integrate microchip electrophoresis with amperometric detection. *Anal. Bioanal. Chem.* 416 (21), 4749–4758. doi:10.1007/s00216-024-05260-6

Shafranek, R. T., Millik, S. C., Smith, P. T., Lee, C. U., Boydston, A. J., and Nelson, A. (2019). Stimuli-responsive materials in additive manufacturing. *Prog. Polym. Sci.* 93, 36–67. doi:10.1016/j.progpolymsci.2019.03.002

Shahrubudin, N., Lee, T. C., and Ramlan, R. (2019). An overview on 3D printing technology: technological, materials, and applications. *Procedia Manuf.* 35, 1286–1296. doi:10.1016/j.promfg.2019.06.089

Shang, Y., Xing, G., Liu, X., Lin, H., and Lin, J. M. (2022). Fully integrated microfluidic biosensor with finger actuation for the ultrasensitive detection of *Escherichia coli* O157: H7. *Anal. Chem.* 94 (48), 16787–16795. doi:10.1021/acs.analchem.2c03686

Shanmugam, V., Pavan, M. V., Babu, K., and Karnan, B. (2021). Fused deposition modeling based polymeric materials and their performance: a review. *Polym. Compos.* 42 (11), 5656–5677. doi:10.1002/pc.26275

Shao, G., Hai, R., and Sun, C. (2019). 3D printing customized optical lens in minutes. *Adv. Opt. Mater.* 8 (4). doi:10.1002/adom.201901646

Sharkey, J. P., Foo, D. C. W., Kabla, A., Baumberg, J. J., and Bowman, R. W. (2016). A one-piece 3D printed flexure translation stage for open-source microscopy. *Rev. Sci. Instrum.* 87 (2), 025104. doi:10.1063/1.4941068

Shrimal, P., Jadeja, G., and Patel, S. (2022). Ultrasonic enhanced emulsification process in 3D printed microfluidic device to encapsulate active pharmaceutical ingredients. *Int. J. Pharm.* 620, 121754. doi:10.1016/j.ijpharm.2022.121754

Shu, M., Wu, W., Yang, Q., Chen, J., Guo, C., and Zhang, A. (2022). Compact filters based on dual-mode gap waveguide cavities and 3D printing technology. *Microw. Opt. Technol. Lett.* 65 (3), 727–732. doi:10.1002/mop.33549

Sikula, M., Vaněčková, E., Hromadová, M., and Kolivoška, V. (2023). Spectroelectrochemical sensing of reaction intermediates and products in an affordable fully 3D printed device. *Anal. Chim. Acta* 1267, 341379. doi:10.1016/j.aca.2023.341379

Singh, S., Ramakrishna, S., and Berto, F. (2020). 3D Printing of polymer composites: a short review. *Mater. Des. Process. Commun.* 2 (2), e97. doi:10.1002/mdp2.97

Spoerk, M., Holzer, C., and Gonzalez-Gutierrez, J. (2020). Material extrusion-based additive manufacturing of polypropylene: a review on how to improve dimensional inaccuracy and warpage. *J. Appl. Polym. Sci.* 137 (12), 48545. doi:10.1002/app.48545

Sta. Agueda, J. R. H., Chen, Q., Maalihan, R. D., Ren, J., da Silva, Í. G. M., Dugos, N. P., et al. (2021). 3D printing of biomedically relevant polymer materials and biocompatibility. *MRS Commun.* 11 (2), 197–212. doi:10.1557/s43579-021-00038-8

Stefano, J. S., Guterres E Silva, L. R., Rocha, R. G., Brazaca, L. C., Richter, E. M., Abarza Muñoz, R. A., et al. (2022). New conductive filament ready-to-use for 3D-printing electrochemical (bio) sensors: towards the detection of SARS-CoV-2. *Anal. Chim. Acta* 1191, 339372. doi:10.1016/j.aca.2021.339372

Su, C.-K. (2021). Review of 3D-Printed functionalized devices for chemical and biochemical analysis. *Anal. Chim. Acta* 1158, 338348. doi:10.1016/j.aca.2021.338348

Su, C. K., and Lin, J. Y. (2020). 3D-Printed column with porous monolithic packing for online solid-phase extraction of multiple trace metals in environmental water samples. *Anal. Chem.* 92 (14), 9640–9648. doi:10.1021/acs.analchem.0c00863

Su, D., Zhao, X., Yan, X., Han, X., Zhu, Z., Wang, C., et al. (2021b). Background-free sensing platform for on-site detection of carbamate pesticide through upconversion nanoparticles-based hydrogel suit. *Biosens. Bioelectron.* 194, 113598. doi:10.1016/j.bios.2021.113598

Su, R., Park, S. H., Ouyang, X., Ahn, S. I., and McAlpine, M. C. (2022). 3D-printed flexible organic light-emitting diode displays. *Sci. Adv.* 8 (1), eabl8798. doi:10.1126/sciadv.abl8798

Su, X., Wang, T., and Guo, S. (2021a). Applications of 3D printed bone tissue engineering scaffolds in the stem cell field. *Regen. Ther.* 16, 63–72. doi:10.1016/j.reth.2021.01.007

Subramaniyan, M., Karuppan, S., Radhakrishnan, K., Rajesh Kumar, R., and Saravana Kumar, K. (2022). Investigation of wear properties of 3D-printed PLA components using sandwich structure–a review. *Mater. Today Proc.* 66, 1112–1119. doi:10.1016/j.matpr.2022.04.913

Sule, S. S., Petsiuk, A. L., and Pearce, J. M. (2019). Open source completely 3-D printable centrifuge. *Instruments* 3 (2), 30. doi:10.3390/instruments3020030

Swargiary, K., Jarutatsanangkoon, P., Suwanich, P., Jolivot, R., and Mohammed, W. S. (2020). Single-step 3D-printed integrated optical system and its implementation for a sensing application using digital light processing technology. *Appl. Opt.* 59 (1), 122–128. doi:10.1364/AO.59.000122

Tai, C. L., Hong, W., Kuo, Y., Chang, C., Niu, M., Ochathevar, M. K. P., et al. (2019). Stretchable luminescent organic-inorganic perovskite nanocrystal-polymer composites for 3D printing and white light-emitting diodes. *ACS Appl. Mater Interfaces* 11 (33), 30176–30184. doi:10.1021/acsami.9b06248

Tang, J., Ren, J., and Han, K. Y. (2019). Fluorescence imaging with tailored light. *Nanophotonics* 8 (12), 2111–2128. doi:10.1515/nanoph-2019-0227

Thiele, S., Gissibl, T., Giessen, H., and Herkommer, A. M. (2016). Ultra-compact on-chip LED collimation optics by 3D femtosecond direct laser writing. *Opt. Lett.* 41 (13), 3029–3032. doi:10.1364/OL.41.003029

Toombs, J. T., Luitz, M., Cook, C. C., Jenne, S., Rapp, B. E., Kotz-Helmer, F., et al. (2022). Volumetric additive manufacturing of silica glass with microscale computed axial lithography. *Science* 376 (6590), 308–312. doi:10.1126/science.abm6459

Tümer, E. H., and Erbil, H. Y. (2021). Extrusion-based 3D printing applications of PLA composites: a review. *Coatings* 11 (4), 390. doi:10.3390/coatings11040390

Upadhyay, R. K., Mishra, A. K., and Kumar, A. (2020). Mechanical degradation of 3D printed PLA in simulated marine environment. *Surfaces Interfaces* 21, 100778. doi:10.1016/j.surfin.2020.100778

Vaidya, N., and Solgaard, O. (2018a). 3D printed optics with nanometer scale surface roughness. *Microsystems Nanoeng.* 4 (1), 18. doi:10.1038/s41378-018-0015-4

Vaidya, N., and Solgaard, O. (2018b). 3D printed optics with nanometer scale surface roughness. *Microsyst. Nanoeng.* 4, 18. doi:10.1038/s41378-018-0015-4

Vanaei, S., Parizi, M., Salemizadehparizi, F., and Vanaei, H. (2021). An overview on materials and techniques in 3D bioprinting toward biomedical application. *Eng. Regen.* 2, 1–18. doi:10.1016/j.engreg.2020.12.001

Vasilescu, M. D. (2019). Constructiv and technological consideration on the generation of gear made by the DLP 3D-printed methode. *Mat. Plast.* 56, 440–443. doi:10.37358/mp.19.2.5203

Veli, M., Mengu, D., Yardimci, N. T., Luo, Y., Li, J., Rivenson, Y., et al. (2021). Terahertz pulse shaping using diffractive surfaces. *Nat. Commun.* 12 (1), 37. doi:10.1038/s41467-020-20268-z

Vinoth, R., Sangavi, P., Nakagawa, T., Jayaraman, M., and Vinu Mohan, A. M. (2023). All-in-one microfluidic device with an integrated porous filtration membrane for on-site detection of multiple salivary biomarkers. *Sensors Actuators B Chem.*, 379. doi:10.1016/j.snb.2022.133214

Vogt, D. W., and Leonhardt, R. (2016). 3D-Printed broadband dielectric tube terahertz waveguide with anti-reflection structure. *J. Infrared, Millim. Terahertz Waves* 37 (11), 1086–1095. doi:10.1007/s10762-016-0296-3

Wang, H., Zhang, W., and Yang, J. K. W. (2020). Toward near-perfect diffractive optical elements via nanoscale 3D printing. *ACS Nano* 14 (8), 10452–10461. doi:10.1021/acsnano.0c04313

Wang, Z., Ahmed, S., Labib, M., Wang, H., Wu, L., Bavaghar-Zaeimi, F., et al. (2023). Isolation of tumour-reactive lymphocytes from peripheral blood via microfluidic immunomagnetic cell sorting. *Nat. Biomed. Eng.* 7, 1188–1203. doi:10.1038/s41551-023-01023-3

Wei, H., Han, L., Yin, R., Yang, T., Liu, Y., Mou, C., et al. (2023). Micro-3D printed Concanavalin A hydrogel based photonic devices for high-sensitivity glucose sensing. *Sensors Actuators B Chem.*, 386. doi:10.1016/j.snb.2023.133707

Wei, L., Fang, G., Kuang, Z., Cheng, L., Wu, H., Guo, D., et al. (2022). 3D-printed low-cost fabrication and facile integration of flexible epidermal microfluidics platform. *Sensors Actuators B Chem.* 353, 131085. doi:10.1016/j.snb.2021.131085

Wei, X., Li, D., Jiang, W., Gu, Z., Wang, X., Zhang, Z., et al. (2015). 3D printable graphene composite. *Sci. Rep.* 5 (1), 11181–11187. doi:10.1038/srep11181

Wen, X., Zhang, B., Wang, W., Ye, F., Yue, S., Guo, H., et al. (2021). 3D-printed silica with nanoscale resolution. *Nat. Mater.* 20 (11), 1506–1511. doi:10.1038/s41563-021-01111-2

Winkler, S., Menke, J., Meyer, K. V., Kortmann, C., and Bahnemann, J. (2022). Automation of cell culture assays using a 3D-printed servomotor-controlled microfluidic valve system. *Lab. Chip* 22 (23), 4656–4665. doi:10.1039/d2lc00629d

Xiao, C., Eriksson, J., Suska, A., Filippini, D., and Mak, W. C. (2022). Print-and-stick unibody microfluidics coupled surface plasmon resonance (SPR) chip for smartphone imaging SPR (Smart-iSRP). *Anal. Chim. Acta* 1201, 339606. doi:10.1016/j.aca.2022.339606

Xiao, T. P., Cifci, O. S., Bhargava, S., Chen, H., Gissibl, T., Zhou, W., et al. (2016). Diffractive spectral-splitting optical element designed by adjoint-based electromagnetic optimization and fabricated by femtosecond 3D direct laser writing. *ACS Photonics* 3 (5), 886–894. doi:10.1021/acsphotonics.6b00066

Xing, J.-F., Zheng, M.-L., and Duan, X.-M. (2015). Two-photon polymerization microfabrication of hydrogels: an advanced 3D printing technology for tissue engineering and drug delivery. *Chem. Soc. Rev.* 44 (15), 5031–5039. doi:10.1039/c5cs00278h

Xu, X., Huang, X., Sun, J., Chen, J., Wu, G., Yao, Y., et al. (2022). 3D-Stacked multistage inertial microfluidic chip for high-throughput enrichment of circulating tumor cells. *Cyborg Bionic Syst.* 2022, 2022. doi:10.34133/2022/9829287

Yan, J., Wang, C., Fu, Y., Guo, J., and Guo, J. (2022). 3D printed microfluidic Coulter counter for blood cell analysis. *Analyst* 147 (14), 3225–3233. doi:10.1039/d2an00633b

Yang, P., Wei, G., Liu, A., Huo, F., and Zhang, Z. (2022b). A review of sampling, energy supply and intelligent monitoring for long-term sweat sensors. *npj Flex. Electron.* 6 (1), 33. doi:10.1038/s41528-022-00165-9

Yang, Z., Li, B., Stuart, D. D., and Cheng, Q. (2022a). Three-dimensional printed microfluidic mixer/extractor for cell lysis and lipidomic profiling by matrix-assisted laser desorption/ionization mass spectrometry. *View* 4 (1). doi:10.1002/viw.20220041

Yuk, H., Lu, B., Lin, S., Qu, K., Xu, J., Luo, J., et al. (2020). 3D printing of conducting polymers. *Nat. Commun.* 11 (1), 1604. doi:10.1038/s41467-020-15316-7

Zatopa, A., Walker, S., and Menguc, Y. (2018). Fully soft 3D-printed electroactive fluidic valve for soft hydraulic robots. *Soft Robot.* 5 (3), 258–271. doi:10.1089/soro.2017.0019

Zhan, Y., Cheng, Q., Song, Y., and Li, M. (2022). Micro-nano structure functionalized perovskite optoelectronics: from structure functionalities to device applications. *Adv. Funct. Mater.* 32 (24). doi:10.1002/adfm.202200385

Zhang, D., Liu, X., and Qiu, J. (2021a). 3D printing of glass by additive manufacturing techniques: a review. *Front. Optoelectron* 14 (3), 263–277. doi:10.1007/s12200-020-1009-z

Zhang, H., Chen, Z., Dai, J., Zhang, W., Jiang, Y., and Zhou, A. (2021b). A low-cost mobile platform for whole blood glucose monitoring using colorimetric method. *Microchem. J.* 162, 105814. doi:10.1016/j.microc.2020.105814

Zhang, H., Yao, Y., Hui, Y., Zhang, L., Zhou, N., and Ju, F. (2021c). A 3D-printed microfluidic gradient concentration chip for rapid antibiotic-susceptibility testing. *Bio-Design Manuf.* 5 (1), 210–219. doi:10.1007/s42242-021-00173-0

Zhang, Y., Xiang, J., Wang, Y., Qiao, Z., and Wang, W. (2020c). 3D printing fabrication and test of a centrifugal cartridge with an integrated gravity valve for solid phase extractions. *Sensors Actuators A Phys.*, 315. doi:10.1016/j.sna.2020.112353

Zhang, Y., Mao, K., Leigh, S., Shah, A., Chao, Z., and Ma, G. (2020b). A parametric study of 3D printed polymer gears. *Int. J. Adv. Manuf. Technol.* 107, 4481–4492. doi:10.1007/s00170-020-05270-5

Zhang, Y., Purssell, C., Mao, K., and Leigh, S. (2020a). A physical investigation of wear and thermal characteristics of 3D printed nylon spur gears. *Tribol. Int.* 141, 105953. doi:10.1016/j.triboint.2019.105953

Zhang, Y., Xiang, J., Wang, Y., Qiao, Z., and Wang, W. (2019). A 3D printed centrifugal microfluidic platform for spilled oil enrichment and detection based on solid phase extraction (SPE). *Sensors Actuators B Chem.* 296, 126603. doi:10.1016/j.snb.2019.05.080

Zheng, F., Xiao, Y., Liu, H., Fan, Y., and Dao, M. (2021). Patient-specific organoid and organ-on-a-chip: 3D cell-culture meets 3D printing and numerical simulation. *Adv. Biol. (Weinh)* 5 (6), e2000024. doi:10.1002/adbi.202000024

Zhu, S., Wu, D., Han, Y., Wang, C., Xiang, N., and Ni, Z. (2020). Inertial microfluidic cube for automatic and fast extraction of white blood cells from whole blood. *Lab. Chip* 20 (2), 244–252. doi:10.1039/c9lc00942f

Zolfagharian, A., Kouzani, A. Z., Khoo, S. Y., Moghadam, A. A. A., Gibson, I., and Kaynak, A. (2016). Evolution of 3D printed soft actuators. *Sensors Actuators A Phys.* 250, 258–272. doi:10.1016/j.sna.2016.09.028

frontiers | Frontiers in Analytical Science

TYPE Review
PUBLISHED 23 December 2024
DOI 10.3389/frans.2024.1513153

OPEN ACCESS

EDITED BY
Marianne Fillet,
University of Liège, Belgium

REVIEWED BY
Abdul Ghaffar Memon,
NED University of Engineering and Technology, Pakistan
Harnish H. Soni,
Maharaja Sayajirao University of Baroda, India

*CORRESPONDENCE
Sayan Bhattacharya,
sayan.evs@gmail.com,
sbhattacharya@nalandauniv.edu.in

RECEIVED 17 October 2024
ACCEPTED 09 December 2024
PUBLISHED 23 December 2024

CITATION
Kundu P, Dutta N and Bhattacharya S (2024) Application of microalgae in wastewater treatment with special reference to emerging contaminants: a step towards sustainability. *Front. Anal. Sci.* 4:1513153.
doi: 10.3389/frans.2024.1513153

Application of microalgae in wastewater treatment with special reference to emerging contaminants: a step towards sustainability

Pritha Kundu[1], Nalok Dutta[2] and Sayan Bhattacharya[1]*

[1]School of Ecology and Environment Studies, Nalanda University, Bihar, India, [2]Biochemical Engineering Department, University College London, London, United Kingdom

Emerging contaminants includes diverse types of synthetic or natural chemical compounds which are not detected, monitored, or controlled in the environment regularly and are released from anthropogenic activities. Substantial quantities of emerging contaminants can be found in the wastewater, originating from agro-industrial and industrial outlets, containing oil and grease, heavy metals, and harmful chemicals. Different species of microalgae can be applied in biological remediation of such contaminants in wastewater. This research emphasizes the multifaceted roles of microalgae in wastewater treatment in context of pollutants, especially the removal of emerging contaminants. A comprehensive overview of different emerging contaminant removal processes was conveyed through an in-depth examination and depiction of the uptake mechanisms employed by microalgae in wastewater treatment in this review. The final section of this review focuses on the articulation of difficulties and prospects for the future of microalgae-based wastewater treatment technology. It is subsequently established how the microalgal technologies for emerging contaminant remediation can be helpful to achieve Sustainable Development Goals (SDGs). This review establishes the connection between phytoremediation technologies with Sustainable Development, and shows how successful implementation of such technologies can lead to the remediation of emerging contaminants and effective management of wastewater.

KEYWORDS

microalgae, emerging contaminants, phycoremediation, wastewater treatment, biodegradation, sustainable development

1 Introduction

Chemicals of emerging concern and are of anthropogenic origin, found in different water bodies because of commercial, agricultural, and domestic discharges with concentrations ranging from microgram to milligram per litre are generally referred to as emerging pollutants (EPs) (Wanda et al., 2017). These pollutants can be organic or inorganic in nature. Organic pollutants include pharmaceutical ingredients, personal care products, endocrine disruptors, hormones, etc.,; heavy metals are examples of inorganic pollutants. These contaminants ultimately cause ecosystem imbalances due to their exceptionally high biological and chemical oxygen demand (BOD and COD). Excess nutrients, such as nitrogen (N) and phosphorus (P), will lead to eutrophication of

waterbodies, disrupting the health of water systems. COD, nitrogen, and phosphorus concentrations in various wastewaters were investigated (Amenorfenyo et al., 2019; Chai et al., 2021; Noorani et al., 2024). This phenomenon causes environmental concerns such as the generation of solid waste and byproducts, the emission of undesirable products into the atmosphere, the excessive growth of undesirable microbes that threaten aquatic life forms, and the deterioration of water quality, which leads to widespread health-related problems in areas close to the discharge range. The global issue of emerging pollutants (EPs) accumulated in wastewater has garnered attention. Recently, policymakers and researchers have shown interest in addressing emerging pollutants in wastewater due to their potential hazards to human health and the ecosystem. The treatment of emerging pollutants (EPs) is receiving significant attention due to the potential risks to human health and adverse effects on the environment. (Wanda et al., 2017).

The treatment of wastewater is conducted through primary, secondary, or tertiary levels, employing physical, biological, or chemical methods. Primary treatment targets the removal of easily settled materials, which could lead to operational challenges in subsequent treatment stages. On the contrary, secondary treatment involves physical or biological processes that break down the organic content in wastewater by utilizing dissolved organic matter and oxidizing essential nutrients into nitrate and orthophosphate. Consequently, secondary effluent contains elevated levels of inorganic nitrogen and phosphorus, contributing to eutrophication and posing severe threats to aquatic habitats and human health due to the release of unmanageable amount of organic compounds and heavy metals. (Gondi et al., 2022; Rathod, 2014; Shitu et al., 2024). However, tertiary treatment, which is a progressive treatment method that reduces nitrates, phosphates, and organic matter, is required to produce clean and harmless effluent that will be released into water bodies (Molazadeh et al., 2019). In tertiary treatment, denitrification involves the reduction of nitrate to nitrite, followed by the further reduction of nitrite to nitrogen gas, which is then released into the atmosphere. The inadequate performance of wastewater treatment facilities in certain countries can be attributed to design deficiencies in the water treatment process, a shortage of expertise, and insufficient financial resources. Consequently, the need for well-designed wastewater treatment methods and feasible economic approaches is becoming progressively crucial. (Farazaki and Gikas, 2019).

Conventional wastewater treatment systems focus primarily on eliminating solid suspension and reducing BOD through activated sludge. Consequently, the efficacy of traditional water treatment methods in removing micropollutants and inorganic nutrients remains suboptimal. In situations where water contains substantial quantities of additional components like heavy metals, xenobiotics, and nutrient loads, the biodegradation process, limited by the capabilities of traditional wastewater treatment methods to break down both organic and inorganic constituents, is likely to be ineffective. (Gondi et al., 2022; Wollmann et al., 2019). This phenomenon will result in a lethal environmental issue affecting the ecosystem, namely, oxygen depletion and a higher level of effluent toxicity to aquatic life (Umamaheswari and Shanthakumar, 2016). Furthermore, untreated nutrients in wastewater effluent will reduce the functionality of the disinfection stage, resulting in an increase in chlorine demand, which is harmful to the aquatic ecosystem and human health. As a result, there is a higher demand for treatment processes that can eradicate these nutrients prior to discharge (Chai et al., 2021).

According to the United Nations' Report (United Nations, 2019), only 70% of domestic and industrial wastewater undergoes treatment in high-income countries. In contrast, the situation is significantly worse in middle- and low-income countries, where only 28%–38% and 8% of wastewater, respectively, is treated. This means, globally more than 80% of all wastewater is discharged into the environment without proper treatment. Traditional wastewater treatment plants (WWTPs), however, are only capable of removing approximately 50% of pharmaceutical contaminants typically present in wastewater (World Health Organization, 2024). These facilities are, in fact, a major source of pollutant discharge into natural water bodies, as illustrated by Zhang, et al. (2017).

For example, Castiglioni et al. (2018) reported that three WWTPs in Milan managed to treat only 13% of personal care products (PCPs) present in their influent. The occurrence of various classes of emerging contaminants (ECs) in wastewater has been studied globally, revealing significant variations in their concentrations depending on geographical location (Tran, et al., 2018). Ciprofloxacin, a commonly used antibiotic, has been detected at concentrations ranging from below detection limits to 6.4 μg L^{-1} in Asia, and from <LDL to 246.1 μg L^{-1} in North America. Similarly, ibuprofen concentrations in wastewater have ranged from 34.8 to 55,975 ng L^{-1} in Asia and from 2,500 to 45,000 ng L^{-1} in North America. Table 1 summarizes concentrations of widely used antibiotics in WWTP influent and effluent across Asia, Europe, and North America.

Pharmaceuticals in drinking water can pose significant risks to the environment and wildlife. For instance, natural and synthetic hormones like progesterone have been detected in wastewater (Houtman, et al., 2018). When animals ingest such compounds, their endocrine systems may be disrupted, potentially leading to fertility issues, delayed development of reproductive organs, and damage to the kidney or liver (Fang, et al., 2021). Observed that chronic or sub-chronic exposure to 17-β-estradiol in mosquitofish altered hormonal balances and vitellogenin protein levels. The growing production of pharmaceuticals further exacerbates the issue, increasing the concentrations of these ECs in domestic wastewater. For example, India's pharmaceutical market is expanding at a rate of 10% annually, making it one of the fastest-growing globally (IQVIA, 2018). This raises concerns about the emergence of antibiotic resistance genes, which could undermine the efficacy of antibiotics. Additionally, microplastics have recently been classified as emerging contaminants.

Finally, it is important to emphasize that the "emerging" nature of these contaminants reflects the fact that many of their impacts remain insufficiently studied or understood, leaving significant gaps in our knowledge of their long-term effects.

Table 1 shows the concentration ranges of various emerging contaminants (ECs) in raw influent and treated effluent from full-scale wastewater treatment plants (WWTPs), adapted from Tran et al., 2018. Wastewater treatment technologies based on microalgae present an attractive solution due to their efficient fixation of inorganic compounds like carbon dioxide and heavy metals, and to deal with emerging contaminants (Inuwa et al., 2023). Microalgae

TABLE 1 Typical concentration ranges of various emerging contaminants (ECs) in raw influent and treated effluent from full-scale wastewater treatment plants (WWTPs). Adapted from (Tran, et al., 2018).

Emerging contaminants	Concentration (ngL^{-1})					
	Asia		Europe		North America	
	Influent	Effluent	Influent	Effluent	Influent	Effluent
Antibiotics						
Amoxicillin	<LDL–6516	<LDL–1670	<LDL	<LDL–190	Nr	<LDL
Azithromycin	1537–303,500	60–980	77–1139	38–784	61–2500	57–1300
Ceftazidime	<LDL	<LDL	–	–	–	–
Chloramphenicol	<LDL–2430	<LDL–1050	<LDL–319	<LDL	–	–
Chlortetracycline	2333–15,911	<LDL–1986	Nr	<LDL	<LDL–310	<LDL–420
Ciprofloxacin	15.5–6453	<LDL–524.1	<LDL–13,625	<LDL–5692	<LDL–246,100	<LDL–620
Clarithromycin	26–1854	4.79–637.1	0.4–647	25–359	<LDL–8000	130–7000
Clindamycin	23.8–26.6	2.94–4.2	<LDL–101	10–180	–	–
Enrofloxacin	<LDL	<LDL	<LDL–18	<LDL–636	5.9–250	3.5–270
Erythromycin Erythromycin-H_2O	111.4–403.3 226–20,600	70–186.6 194.5–14,400	<LDL–2130 24–6755	<LDL–290 15–2841	– <LDL–3900	– <LDL–838
Lincomycin	<LDL–19,401	3.92–21,278	<LDL–281	<LDL	<LDL–360	4.9–510
Meropenem	264.8–433.6	27–67.9	–	–	–	–
Minocycline	730.9–3808	<LDL	–	–	<LDL	<LDL
Ofloxacin	54.8–1274	13.3–7870	Nr	71–8637	470–1000	<LDL–506
Oxytetracycline	<LDL–30,049	<LDL–2014	<LDL–7	<LDL–5	<LDL–47,000	<LDL–4200
Sulfamethazine	<LDL–1814	<LDL–260.8	<LDL–680	<LDL	<LDL–300	<LDL–363
Sulfamethoxazole	3.0–1389	<LDL–562	<LDL–11,555	<LDL–544	<LDL–4200	<LDL–1800
Tetracycline	<LDL–12,340	<LDL–1536	<LDL–790	<LDL–850	<LDL–48,000	<LDL–3600
Trimethoprim	19.5–570	3.7–772	<LDL–4342	<LDL–3052	<LDL–6796	<LDL–37,000
Tylosin	<LDL	<LDL	<LDL	<LDL–173	<LDL–1500	21–720
Vancomycin	962–43,740	<LDL	Nr	<LDL–8514	–	–
Anticonvulsants						
Carbamazepine	<LDL–18,500	<LDL–900	<LDL–3110	<LDL–4596	<LDL–440	28–551
Gabapentin	4825.5–15,359	213–8855	6442–25,079	7651–56,810	Nr	1000 ± 900
Sulpiride	64.9–15,358.8	70.7–322.4	113–1100	110–294	Nr	33–137
Anti-itching						
Crotamiton	<LDL–1500	<LDL–1000	<LDL–140	<LDL–100	–	–
Antimicrobials						
Miconazole	<LDL–597	<LDL	<LDL–337.9	<LDL–35.7	5.2–43	1.6–27
Thiabendazole	<LDL–1.3	<LDL	–	–	6.8–220	6.2–140
Triclocarban	341.1–8880	8.4–5860	97–140	Nr	340–4644	64–617
Triclosan	1.3–2500	49.1–263.9	<LDL–5260	<LDL–430	14–6817	3.1–360
Artificial sweeteners						
Acesulfame	560–13400	5840–9147	12,000–43,000	15,000–46,000	90–2270	600–4330

(Continued on following page)

TABLE 1 (*Continued*) Typical concentration ranges of various emerging contaminants (ECs) in raw influent and treated effluent from full-scale wastewater treatment plants (WWTPs). Adapted from (Tran, et al., 2018).

Emerging contaminants	Concentration (ngL^{-1})					
	Asia		Europe		North America	
	Influent	Effluent	Influent	Effluent	Influent	Effluent
Cyclamate	<LDL–66,400	<LDL–160	10,000–65,000	<LDL–450	–	–
Saccharin	9310–389,000	<LDL–2370	7100–18,000	<LDL–1800	1860–25,100	220–700
Sucralose	1100–6520	1300–5490	2000–9100	2000–8800	17,500–46,100	18,700–48,900
β-blockers						
Atenolol	<LDL–294,700	<LDL–518.6	<LDL–33,106	<LDL–7602	500–2642	<LDL–14,200
Metoprolol	<LDL–79,500	<LDL–268	<LDL–4148	<LDL–5762	16–154	15–212
Propranolol	<LDL–9.56	<LDL–8.3	<LDL–1962	<LDL–615	–	–
Insect repellent						
N,N-diethyl-meta-toluamide (DEET)	124–2341.9	21.6–324.8	<LDL–6900	Nr	200–42,334	13–1663
Hormones						
Estrone	<LDL–132.5	<LDL–51.2	2.4–670	<LDL–95	8–52	<LDL–56
Estriol	<LDL–802	<LDL–30.2	<LDL–660	<LDL–275	<LDL–217	<LDL
17 α- ethinylestradiol	<LDL–26.1	<LDL–13.1	0.4–70	0.5–106	<LDL–242	<LDL
Lipid regulators						
Bezafibrate	16.8–159	<LDL–51.4	100–7600	<LDL–4800	–	65–359
Clofibric acid	<LDL–65	<LDL–44.9	<LDL–265.9	<LDL–91	<LDL	<LDL–44
Gemfibrozil	<LDL–453.4	<LDL–535.2	<LDL–17,055	<LDL–5233	<LDL–36,530	<LDL–1493
Nonsteroidal anti-inflammatory drugs						
Acetaminophen	67–147,700	<LDL–2568	<LDL–482,687	<LDL–24,525	21,000–500,000	<LDL–62,000
Codeine	<LDL–242	<LDL–208	150–32,295	9.7–15,593	77–5700	80–3300
Diclofenac	13–445	<LDL–69.2	<LDL–4869	<LDL–5164	140–2450	<LDL–359
Fenoprofen	<LDL–2260	<LDL–23.4	Nr	<LDL–280	<LDL	<LDL–405
Ibuprofen	34.8–55,975	<LDL–1890	<LDL–83,500	<LDL–24,600	2500–45,000	16–14,600
Indomethacin	<LDL–449.4	<LDL–61.4	<LDL–297	<LDL	<LDL–640	<LDL–507
Ketoprofen	<LDL–286	<LDL–183	<LDL–5700	<LDL–1620	60–150	40–90
Naproxen	<LDL–7762	<LDL–159	<LDL–611,000	<LDL–33,900	1700–25,000	<LDL–3500
Salicylic acid	167–16,900	<LDL–1426	<LDL–164,400	<LDL–10,100	2820–27,800	<LDL–320
Plasticizer						
Bisphenol A	55.6–5850	<LDL–123	<LDL–2376	16–1840	595–2469	2–450
Stimulant						
Caffeine	759–60,500	13–51,700	102–113,200	30–13,900	5809–82,882	<LDL–37,200
UV filters						
Octocrylene	<LDL	<LDL–153	100–1200	<LDL–300	–	–
Oxybenzone	<LDL–2616.8	<LDL–772	<LDL–7800	<LDL–700	–	–

(Continued on following page)

TABLE 1 (*Continued*) Typical concentration ranges of various emerging contaminants (ECs) in raw influent and treated effluent from full-scale wastewater treatment plants (WWTPs). Adapted from (Tran, et al., 2018).

Emerging contaminants	Concentration (ngL^{-1})					
	Asia		Europe		North America	
	Influent	Effluent	Influent	Effluent	Influent	Effluent
X-ray contrast media						
Iohexol	63.8–124,966	2100–8700	18,000 ± 2000	1200 ± 100	Nr	8623–9237
Iopromide	47.7–12,200	<LDL–7140	<LDL–7500	<LDL–9300	–	–
Iopamidol	82.8–45,611	<LDL–6520	4300 ± 900	4700 ± 1000	–	–

exhibit a notable capacity for the uptake of inorganic nutrients, requiring nitrogen and phosphorus for protein synthesis and utilizing heavy metals as micronutrients for their development. Consequently, employing microalgae as agents for bioremediation in wastewater proves effective in extracting nitrogen and phosphorus from the wastewater, maintaining dissolved oxygen levels, and contributing to the reduction of pathogens and faecal bacteria present in the wastewater. The study's findings indicate that the interaction between wastewater and microalgae resulted in a significant decrease in levels of several contaminants, especially the emerging contaminants in wastewater (Das et al., 2019; Rathod, 2014). Microalgae treatment is also a more efficient method of wastewater treatment because it can treat wastewater in a single step, as opposed to traditional wastewater treatment, which requires a number of steps to fix the carbon, nitrogen, and phosphorus ratios (C:N:P). It is also an environmentally sustainable option because it can convert carbon dioxide into chemical substances and fuel products without resulting in pollution, thereby aiding in the reduction of greenhouse gas emissions (Klinthong et al., 2015). Microalgal biomass harvested from wastewater treatment can be converted into valuable bio-based products such as health supplements, biohydrogen, bio-alcohols, and bio-hydrocarbons to offset its production costs (Koyande et al., 2019; Perez-Garcia and Bashan, 2015). Microalgae have found widespread application in wastewater treatment, with eukaryotic and prokaryotic blue-green algae being the most commonly employed species in experimental setups. The concentrations of non-renewable resource phosphorus and another essential nutrient, nitrogen, found in wastewater, are sufficient to support the cultivation of microalgae for cell growth substrates, biomass yields, and carbon neutrality. Consequently, there is a reduced reliance on freshwater and industrial nutrients typically needed for conventional biological purification, leading to a significant reduction in overall operational costs and the environmental impact of the treatment process. (Delrue et al., 2016).

This review aims to demonstrate the potential of microalgae in removal of emerging contaminants from wastewater through different treatment processes. Different sections discuss phycoremediation of wastewater in removal of several chemicals of emerging concern (ex. dyes, heavy metals, xenobiotic compounds, pesticides, pharmaceuticals, inorganic nutrients, and different microorganisms, especially the pathogens). Different mechanisms employed by microorganisms to remove the emerging contaminants (ex. biosorption, bioaccumulation, biodegradation, etc.) are explained. Also, the influences of several environmental factors (pH, temperature, light, etc.) on the actions of microalgae for wastewater treatment are discussed in this article. Finally, the advantages, limitations, and future perspectives of the microalgae-based treatment method are explained, and it is established that how these eco-friendly technologies can ensure sustainability.

2 Phycoremediation of wastewater

Microalgae, minute organisms consisting of eukaryotic cells, employ the photosynthetic process akin to that found in higher plants. The cellular structure of microalgae encompasses essential components such as cell walls, plasma membranes, cytoplasm, nuclei, and organelles. Notably, microalgae cells contain plastids housing chlorophyll, a pigment crucial for synthesizing food through photosynthesis. A distinguishing feature of microalgae is the absence of a vascular system for nutrient transport, a contrast to higher plants. This lack is compensated by the photoautotrophic nature of each microalgal cell, enabling direct absorption of nutrients without the need for an elaborate vascular network. This unique characteristic simplifies nutrient uptake processes in microalgae, setting them apart from higher plants in terms of nutrient transport strategies. (Emparan et al., 2019). Through their uptake mechanism, microalgae-based wastewater treatment is effective in removing inorganic compounds such as nitrate, phosphate, heavy metals, inorganic carbon, toxic substances (organic and inorganic), BOD, COD, and other impurities dissolved in wastewater (Borowitzka, 1998). Microalgae use photons as energy in their chloroplast cells and extract CO_2 from exhaust gases generated by combustion or bacterial respiration, as well as nutrients from wastewater, to synthesise biomass while producing oxygen. As a result, the microalgae biomass is obtained and O_2 is released into the atmosphere. The conversion of CO_2 and water into organic compounds does not require any additional energy, thereby avoiding secondary pollution. The oxygen released by microalgae is sufficient to meet bacteria's aerobic requirements for metabolising residual organic substances in treated wastewater (Chai et al., 2021).

2.1 Nutrient removal

The uptake and consumption of nitrates and phosphates by microalgae cells for growth can significantly reduce the nitrogen and

phosphorus content of wastewater and improve the quality of the wastewater discharge. The ability of different microalgae strains to remove nitrogen and phosphate was investigated (*Chlamydomonas sp., Chlorella sp., and Oocystis sp.*) by assessing NO_3^--N and PO_4^{3-}- P loss. Algae require nitrogen and phosphorus to grow (Rasoul-Amini et al., 2014). Phosphorus is required for the synthesis of nucleic acids, phospholipids, and phosphate esters in the cells, whereas nitrogen binds to proteins in the algal cell, which account for 45%–60% of the dry weight. They use nitrogen and phosphorus-containing organic compounds derived from their carbon sources. The use of those compounds by algae results in the removal of nutrients from the wastewater, a process that can last from a few hours to a few days (Kaloudas et al., 2021).

2.1.1 Phosphorus removal

Inorganic phosphorus, which can be found naturally in lipids, nucleic acids, and proteins in wastewater, is important for microalgae energy metabolism and growth. Inorganic phosphates are transported across the plasma membrane of microalgae cells. Through phosphorylation, inorganic phosphorus in the forms of mono- and dihydrogen phosphate (HPO_4^{2-} and H_2PO_4) is integrated into organic compounds such as adenosine diphosphate (ADP) in the case of algae. To produce its final product, ATP, the phosphorylation process requires energy. Energy can be obtained through the oxidation of respiratory substrates, the electron transport system of mitochondria found in eukaryotic microalgae, and light used in photosynthesis (Chai et al., 2021; Emparan et al., 2019).

2.1.2 Nitrogen removal

Organic nitrogen can enter wastewater from land where animal manure is stored or applied via sewage effluent. Organic nitrogen is a critical component of biological substances such as enzymes, peptides, proteins, chlorophylls, and energy transfer molecules like ADP and ATP. Organic nitrogen is derived from inorganic sources encompassing nitrite (NO_2^-), nitrate (NO_3^-), nitric acid (HNO_3), ammonia (NH_3), ammonium (NH_4^+), and nitrogen gas (N_2). The presence of nitrogen in wastewater is usually in the form of NH_4^+, NO_2^- and NO_3^-. Assimilation can be used by eukaryotic microalgae to convert inorganic nitrogen into organic forms. transformation mechanism that takes place across the microalgae plasma membrane is the reduction of nitrate (NO_3^-) to nitrite (NO_2^-) and to ammonium (NH_4^+) subsequently, which is then integrated into amino acids (the organic form of nitrogen). The first step in nitrate assimilation involves nitrate reductase (NR), which is the reduced form of nicotinamide adenine dinucleotide (NADH), $C_{21}H_{27}N_7O_{14}P_2$, which is found in microalgae and transfers two electrons in the reaction of converting nitrate to nitrite. Following that, ferrodoxin (Fd) from microalgae and nitrite reductase (NADPH, $C_{21}H_{29}N_7O_{17}P_3$) produced from the photosynthesis reaction involving ADP, phosphate, and NADP transfer six electrons in the reaction of reducing NO2 to NH_4+. All inorganic forms of nitrogen will be reduced to NH4+ as a result of this action within the intracellular fluid of microalgae. Finally, glutamic acids (Glu), $C_5H_9NO_4$, neuroactive amino acids found in microalgae, and adenosine triphosphate (ATP) released from phosphorylation (the process of assimilation of phosphates into organic compounds) incorporate ammonium into amino acids (glutamine) within microalgae intracellular fluid (Chai et al., 2021; Emparan et al., 2019; Kaloudas et al., 2021).

In one of the recent studies, two microalgal species (*Chlorella* sorokiniana and Selenastrum sp.) were applied for fish processing wastewater (FPWW) after fat and oil removal, with an objective of facilitating the reuse of wastewater and recovery of several nutrients. The results showed that Chlorella sorokiniana cultivated in the unfiltered FPWW displayed the highest growth and nutrient removal (Khalatbari et al., 2024).

2.2 Xenobiotic compounds removal

Microalgae play an important role in the dispersion, chemical transformation, and bioaccumulation of many toxic xenobiotic compounds. Incomplete combustion of organic materials produces polycyclic aromatic hydrocarbons (PAHs). Because they are generally persistent and highly toxic, with carcinogenic and/or teratogenic properties, they are the subject of strict control and monitoring (Torres et al., 2008). Some microalgae species have a metabolic profile that allows them to survive in PAH-contaminated environments and even assimilate and degrade these contaminants under certain conditions. These organisms can bio-transform low-molecular-weight PAHs; naphthalene can be hydroxylated to form two-ringed PAHs, while phenanthrene (tricyclic PAH) can be bio-transformed to its hydroxylated intermediates (Olmos-Espejel et al., 2012; Lei et al., 2007) tested the possibility of removing fluoranthene (1.0 mg/L), pyrene (1.0 mg/L) and a mixture of fluoranthene (0.5 mg/L) and pyrene (0.5 mg/L) using four microalgae species (*C. vulgaris, S. platydiscus, S. quadricauda, and Selenastrum capricornutum*) incubated for 7 days. *S. capricornutum* performed best, with removal efficiencies ranging from 88% to 98% for various pollutant concentrations.

Monoaromatic hydrocarbons are also known to be mutagenic and carcinogenic. The production, transportation, and storage of oil and oil products are the primary sources of contamination by these compounds. They are highly soluble in water and are strongly absorbed by the soil. When macro- and micronutrients are available at ideal environmental conditions for microalgae growth, these pollutants serve as carbon sources (Semple et al., 1999; Paixão et al., 2007) performed controlled experiments in which they exposed *T. chuii* cultures to 14 different types of gasoline at varying concentrations (0%, 4.6%, 10.0%, 22.0%, 46.0%, and 100%) for 96 and 24 h. Growth inhibition and abnormalities occurred only at concentrations greater than 50% gasoline, demonstrating significant tolerance to such monoaromatic hydrocarbon mixtures. Chlorophenols are another type of highly toxic and persistent xenobiotic with carcinogenic properties. These compounds are widely used in the manufacture of pesticides and wood preservatives (Petroutsos et al., 2008). investigated the potential of 2,4-dichlorophenol (2,4-DCP) removal using the microalgae *Tetraselmis marina* and found that the microalga could metabolise more than 1 mmol L1 2,4-DCP in a 2 L photobioreactor after 6 days of exposure to the contaminant. *Anabaena* and *Aulosira fertilissima* demonstrated remarkable abilities to bioconcentrate and degrade DDT into its two main metabolites; dichlorodiphenyldichloroethylene (DDD) and dichlorodiphenyldichloroethane (DDE) (Lal et al., 1987).

2.3 Dyes removal

Because of their high surface area and binding affinity, microalgae have been used to remove colour and vinyl sulfone dye from textile wastewater. The cell wall of microalgae is involved in dye removal mechanisms such as biosorption, electrostatic attraction, complexation, and bioconversion (Andrade et al., 2018). Dye ions adhere and accumulate on the surface of algal biopolymers, then diffuse onto the biopolymer's solid phase. Extracellular polymers with functional groups can aid in the biosorption of dye molecules onto polymer surfaces (Saha et al., 2023). *Spirogyra* biomass, a microalga species, has been demonstrated to be an effective biosorbent for reactive dye removal. *Caulerpa lentillifera* and *Caulerpa scalpelliformis* biomass can remove basic dyes via biosorption. Furthermore, *C. vulgaris* has been widely used as a biosorbent for the removal of reactive dyes like Remazol Black B (Aksu and Tezer, 2005). Microalgae disintegrate dyes into simpler compounds for bioconversion. *Chlorella vulgaris* can remove (63–69) % of the colour from mono-azo dye by converting it to aniline, as demonstrated by adding them to different concentrations of textile wastewater (Supranol Red 3BW) for a 10-day culture period. Furthermore, five microalgal strains, *A. flos aquae*, *N. elepsosporum*, *N. linkia*, *A. variabilis*, and *C. vulgaris*, were evaluated for their ability to remove red coloration from textile industrial effluent. The experiment revealed that all microalgae strains tested could remove the red dye from the treated textile wastewater effluent with varying reduction percentages. The dye was completely removed by *N. elepsosporum*, followed by *C. vulgaris* (96.16%), *A. variabilis* (88.71%), *N. linkia* (79.03%), and *A. flos aquae* (50.81%). The complexity of the textile wastewater, which contains entangled compositions of other chemicals such as heavy metals, does not appear to affect the efficacy of colour removal by microalgae (Ghazal et al., 2018; Kumar et al., 2014).

2.4 Heavy metals (HM) removal

Heavy metals are metals with atomic densities greater than 4000 kg/m^3 (Vardhan et al., 2019). HMs pollution is a major issue worldwide due to their non-biodegradable properties, abundant sources, toxicity, and accumulative behaviour. Even at low concentrations, HMs are naturally toxic and cause serious diseases in humans and animals (Edelstein and Ben-Hur, 2018). HMs are classified as radionuclides (U, Ra, Am, and Th), precious metals (Au, Pd, Pt, and Ru), and toxic metals (Cu, Cr, As, Zn, Ni, Ag, Sn, Co, and Pb). HMs enter aquatic systems through industrial discharges and agricultural runoff, in addition to naturally occurring sources (Pavithra et al., 2020). Various treatment approaches are available, with varying degrees of success, to remove HMs from the aquatic environment. In any case, these traditional treatment methods generate secondary waste while incurring high operating and maintenance costs. As a result, developing effective, environmentally friendly, and economically viable treatments is critical. Metal bioaccumulation by microalgae may be a viable method of wastewater remediation (Vardhan et al., 2019). Most metal removal techniques use algae, both dry biomass and dead forms, with adsorption as the primary removal mechanism. Microalgae can accumulate toxic heavy metal ions from aqueous solutions at concentrations on the order of 15 mg/g biomass, demonstrating that the process is competitive with other treatment methods (Abdel-Raouf et al., 2012).

Several microalgae species, including *C. vulgaris*, *Scenedesmus sp.*, *Chlorococcum sp.*, *Lyngbya spiralis*, *Tolypothirx tenuis*, *Stigonema sp.*, *Phormidium molle*, *Aphanothece halophytica*, and *Chroococcus paris*, can remove Hg (II), Cd (II), and Pb (II) (Tüzün et al., 2005). Metal absorption by microalgae occurs in two stages: first, the surface of algal cells interacts with metals via physical adsorption or ion exchange in a fast process. The following step, known as chemisorption, is slower and takes place intracellularly, and it is related to metabolic processes involving active binding groups. A cellular distribution analysis revealed that large amounts of metal ions bind to the cell wall, while an insoluble fraction accumulates intracellularly (Omar, 2002).

In a detoxification assay using *C. vulgaris* (Shen et al., 2013), investigated the mechanism of bioconversion of Cr (VI) into its less toxic form of Cr (III). Secondary alcohols were found to be primarily responsible for the reduction of Cr (VI) to Cr (III), with -NH2 and -COOH being the main functional groups associated with the biosorption and bio-fixation of these elements. Magro et al. report a chromium hexavalent (Cr VI) removal value of 60.92% when cultivating Spirulina platensis strain in a mixture of artificial medium and wastewater under controlled air, temperature, and lighting conditions.

(Chong et al., 2000) investigated the treatment of synthetic wastewater containing nickel (Ni) and zinc (Zn) using 11 microalga species with the same cell density. The *S. quadricauda* species was singled out for its ability to reduce an initial concentration of nickel (Ni) and zinc (Zn) of 30 mg/L to 0.9 mg/L. The removal of these metals reached 97% within the first 5 min, then dropped to 0.4 mg/L within the next 90 min. This efficiency can be attributed to the fact that it has a larger surface area than the other microalgae studied.

Arsenic (As) is a toxic element that can be found in nearly all terrestrial environments. The organic forms are less toxic than the inorganic forms [arsenite, As (III) and arsenate, As (V)]. Arsenic exposure through drinking water is linked to a variety of skin diseases, respiratory, neurological, cardiovascular, gastrointestinal, and urinary disorders, as well as an increased risk of high blood pressure and diabetes (Mestrot et al., 2013; Zhang et al., 2013) demonstrated that the marine microalga *Ostreococcus tauri* can convert inorganic arsenic into a less toxic organic form that can be easily incorporated into biogeochemical cycles and can promote As volatilization via the biomethylation metabolic mechanism.

2.5 Pathogens removal

Pathogen removal mechanisms of microalgae in wastewater include nutrient competition, pH and dissolved oxygen level elevation, pathogen adhesion and sedimentation, and algal toxins (Dar et al., 2019). The CO_2 assimilation in photosynthesis causes the pH value to rise during microalgae cultivation. Nitrogen absorption by microalgae raises the pH of the medium because every nitrate ion converted to ammonia produces one OH^- ion. This phenomenon will result in pathogen eradication. Because of the limited transfer of

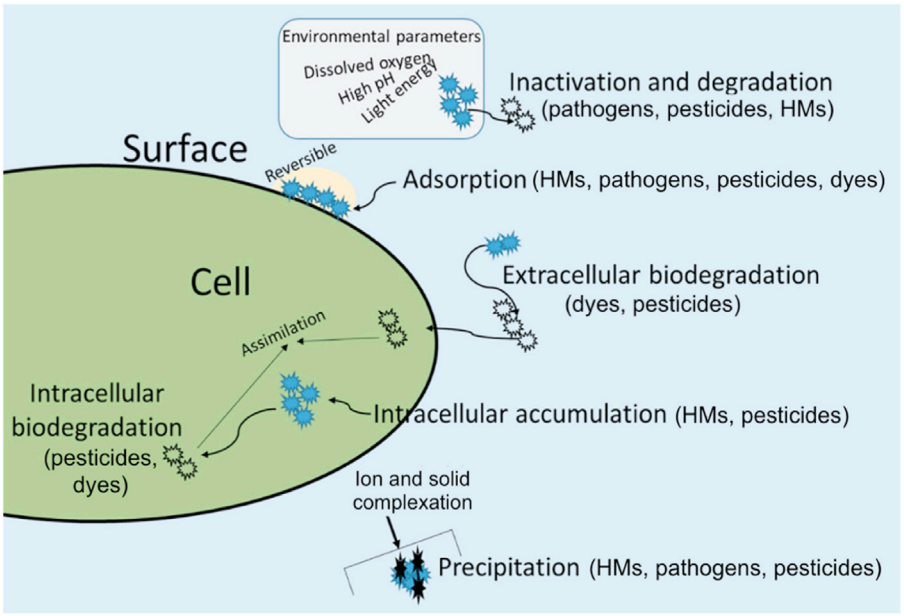

FIGURE 1
Removal mechanisms of pathogens, pesticides, dyes and heavy metals by microalgae. Reprinted with permission from Elsevier (Chai et al., 2021), licence number 5705400764493.

carbon dioxide from the atmosphere and the process of microbial oxygenation, microalgae will also raise pH levels, potentially causing pathogens to die off. Fluctuations in pH are also known to have an adverse effect on *E. coli* survival, resulting in a remarkable elimination of faecal coliforms such as *Escherichia coli*, *Enterococci*, and *Clostridium perfringens* in waterbodies (Ansa et al., 2011). Oxygenation caused by bacterial respiration in treatment ponds that contributes to algal growth has been linked to faecal bacteria annihilation due to the presence of toxic oxygen formations. Microalgae photosynthesis activity is also sufficient to raise oxygen concentrations in waterbodies to levels that are harmful to faecal bacteria. Oxygen concentrations greater than 0.5 mg/L have been linked to faecal bacteria removal (Ansa et al., 2011). The adhesion of faecal bacteria to microalgae in wastewater is critical because it ensures that bacterial cells are in close proximity when microalgae elevate pH and dissolved oxygen. Pathogens will first attach to the solid matter that will sink as sediment and deposit on the surface of microalgal cells for adhesion to occur. Following that, the polysaccharides that are available for expression by bacterial cells will form positively charged amino groups. The positively charged polymers will then neutralise the negatively charged microalgal surface, resulting in the formation of a bridge between the particles and bacterial cell adhesion to microalgae (Dar et al., 2019). Furthermore, a toxin called microcystin-LR produced by an algal strain called *Synechocystis sp.* and toxins of long-chain fatty acids produced by *C. vulgaris* under high pH conditions have been found to be toxic to pathogens and faecal bacteria (Mohamed, 2008). In another experiment, *Salmonella enterica* was found to be eliminated by a microalgae species, *Scenedesmus sp.* (Mezzari et al., 2017). The effect of elevated microalgae pH and dissolved oxygen (DO) levels on the removal and inactivation of *E. coli*, *Enterococci*, and *C. perfringens* was studied (Liu et al., 2020).

2.6 Pesticides removal

Through biosorption and biodegradation, microalgae can assimilate a wide range of organic pollutants, including pesticides, as an energy source for their growth in wastewater. Biosorption includes mechanisms of absorption, adsorption, surface complexation, ion exchange, and precipitation that occur in both living and dead cell walls. Biodegradation occurs when microalgae produce enzymes that break down the bonds in pesticide molecules. *Chlorella vulgaris* was exposed to four common fungicides, propamocarb, mandipropamid, cyprodinil, and metalaxyl, in two experiments: short-term involving biosorption (60 min) and long-term involving biodegradation (4 days) in a study conducted by (Chai et al., 2021). Another set of short and long-term experiments was carried out to determine the percentage of pesticides removed by microalgae. Chlorella vulgaris was used in the experiment, and the pesticides used were molinate, simazine, isoproturon, atrazine, propanil, carbofuran, dimethoate, pendimethalin, metoalcholar, and pyproxin. The results showed that microalgae removed more pesticides in the long-term experiment than in the short-term experiment (Hussein et al., 2016).

Removal of pathogens, pesticides, dyes and heavy metals by microalgae with associated mechanisms are shown in Figure 1.

2.7 Pharmaceuticals removal

Pharmaceutical compounds (PCs) are a broad class of chemical substances that are widely used around the world. PC residues pollute aquatic environments from agricultural operations, hospital effluents, industrial pollution, and household trash. The removal of emerging pharmaceuticals in conventional wastewater treatment plants ranges from 10% to 100%, depending on the method and the emerging

TABLE 2 Quantitative comparison between the steps of phycoremediation.

	Biosorption	Bioaccumulation, or bio-uptake	Biodegradation	Photodegradation	Hydrolysis	References
Definition	The attachment of pollutants on the surface of the microorganisms is referred to as biosorption	The accumulation of pollutants from an external environment inside the cell's cytoplasm	Biodegradation is the metabolic breakdown or degradation of pollutants	The degradation of a material due to photon exposure	The chemical breakdown of a compound due to reaction with water	Gondi et al. (2022)
pH	pH of solution strongly affects sorption capacity of heavy metals though the process can take place over wide range of pH	Significant pH can seriously affect living cells	Initial pH does influence bioremediation	The initial pH is one of the most effective parameters in photodegradation processes	Hydrolysis reaction is pH dependent at some level	Chai et al. (2021)
Cost	Usually, low. Biomass can be got from wastes	Usually high since process involves living cells that need to be supported (in case of bio-uptake)	Cost effective step	Usually, low cost. Requires high cost where artificial light is needed	In most of the cases, enzymatic hydrolysis is considered to be the most expensive operational process	Kaloudas et al. (2021)
Rate of uptake	Generally fast, few seconds for outer cell wall accumulation	Slower compared to biosorption. Intercellular uptake takes a long time	Initially slow. Later goes comparatively fast as growth of microalgae takes place simultaneously	Too much lengthy process	Begins slowly but becomes fast after sometime	Gondi et al. (2022)
Energy demand	Low	Energy is required for cell growth	Highly dependent on energy involved in breaking down contaminants	Caused by photon energy in light	Still uncleared though timed additions of fixed amounts of substrate may help in minimizing the energy required	Olawale (2021)
Regeneration and reuse	High possibility of biosorbent regeneration and reuse	Reuse is limited due to intercellular accumulation	Reuse is not possible	In most of the cases, it can be easily recovered	It is possible to reuse the free enzymes	Olawale (2021)
Temperature	Within a modest range	Inhibited by low temperature	The temperature will vary with micro-algae species. The optimal temperature range for microalgae cultures is 20°C–30°C	Within a modest range	Mostly higher temperature	Gondi et al., 2022

pollutant (Kruglova et al., 2016). Pharmaceutical compounds have measured concentrations ranging from 0.008 to 55.78 g/L, while pesticides have measured concentrations ranging from 0.01 to 8845 g/L. Some of the negative effects on aquatic organisms include behavioural changes, the accumulation of pharmaceutical and cosmetic products, reproductive damage, and the inhibition of cell proliferation (Mascolo et al., 2010). Microalgae extracellular enzymes convert certain antibiotics into less toxic or even non-toxic intermediates. Enzymes in cells then bioaccumulate and degrade these intermediates. Furthermore, the degree of biodegradability is determined by the complexity of the structures (Naghdi et al., 2018). Both ketoprofen and ibuprofen, which are both nonsteroidal anti-inflammatory drugs, are eliminated from wastewater in different ways. Ibuprofen was eliminated more efficiently than ketoprofen using vascular plants and microalgae-mediated treatment. *Chlorella sorokiniana* completely destroyed paracetamol and ibuprofen (Bai and Acharya, 2017). Adsorption, accumulation, and eventually biodegradation of various substances is facilitated by the EPS matrix. Because of the presence of carboxyl, hydroxyl, and phosphoryl functional groups, microalgae are predominantly negatively charged, which is advantageous for capturing positively charged PC molecules (Hom-Diaz et al., 2015). Many recent studies have demonstrated the rapid uptake of PCs onto the cell wall using EPS. In general, the studies suggest that PCs are eliminated through a variety of mechanisms, with bio-adsorption being the most common. Bio-adsorption contributes differently depending on the microalgae used and the micropollutant absorbed (Bai and Acharya, 2017). Study has demonstrated that *Scenedesmus dimorphus* can biodegrade about 85% of 17 a-estradiol within 7 days (Zhang et al., 2014).

2.8 Carbon dioxide fixation

Industrial effluents contain about 10%–15% CO_2, making them an excellent source of CO_2 for microalgae cultivation and a

potentially more efficient route for bio-fixation (Ji et al., 2013). Microalgae have received a lot of attention among biological CO_2 fixation technologies because they can convert CO_2 (and complementary nutrients) into biomass at much higher rates than conventional crops (Farhadian et al., 2008). Furthermore, they are a sustainable ecological alternative to CO_2 mitigation in the atmosphere. Microalgae contain approximately 50% carbon in their composition, and to produce 1 tonne of microalgae requires approximately 1.83 tonnes of CO_2. Direct use of combustion gases from chimneys in microalgae cultures reduces pre-treatment costs but requires tolerance to extreme conditions such as high CO_2 concentrations and the presence of inhibitory compounds such as NOx and SOx (Kumar et al., 2010; Cheng et al., 2006) tested different concentrations of CO_2 as the input gas when controlling CO_2 levels in a culture of *C. vulgaris* in membrane photobioreactors with a closed environment and achieved the best results for CO_2 removal at a concentration of 1.0% (Chiu et al., 2011). Investigated the growth and potential for on-site bioremediation of Chlorella sp. MTF-7, a thermotolerant and CO_2-tolerant strain. This microalga was grown in a tubular photobioreactor with an artificial directly aerated medium and an intermittent flow of steel industry combustion gas. In this cultivation, average CO_2, SO_2, and NO removal efficiencies of 60, 70, and 50%, respectively, were obtained.

2.9 Biological oxygen demand (BOD) reduction

High levels of biochemical oxygen demand can deplete the oxygen in the water, causing the fish to suffocate and creating conditions for anaerobiosis in the water. When it comes to wastewater treatment, removing biochemical oxygen demand is a primary goal. Because microalgae produce oxygen through photosynthesis, they can reduce biological oxygen demand in wastewater. The removal of phenolic compounds reduces the waterbody's biochemical oxygen demand (Kaloudas et al., 2021). Microalgae such as *Chlorella pyrenoidosa*, *Chlorella kessleri*, and *Spirulina sp*. have been shown in experimental procedures to have the ability to remove phenolic compounds from water and can be prominent species for phenol removal (Zhang C. et al., 2020). Although the removal of phenolic compounds by algae in wastewater treatment may be difficult because microalgae can only biodegrade phenol under limited carbon source conditions in which they use phenol as an alternative carbon source, wastewaters are typically rich in carbon sources for the algae to utilise, reducing the potential use of phenol compounds as an alternative energy source (Kaloudas et al., 2021).

3 Microalgal mechanisms for the removal of emerging pollutants

Pollutant removal via a microalgal-based treatment system involves a variety of reaction mechanisms. The bioremediation mechanisms of the microalgae-based treatment method for removing emerging pollutants are depicted in Figure 1. The mechanisms underlying microalgal-based EP bioremediation are described as follows, (a) During bio uptake, pollutants pass through the algal cell wall and attach to intracellular proteins in living cells and (b) in the non-living cell during bioaccumulation (c) during biosorption, pollutants are adsorbed into the algal cell wall or Extra Polymeric substances (EPS) (d) During biodegradation, complex pollutants are broken down into simpler, less toxic compounds (e) During photodegradation, they undergo exposure to direct or UV light (Gondi et al., 2022). Table 2 shows the quantitative comparison between the steps of phyco-remediation.

3.1 Biosorption

Biosorption refers to the adherence of pollutants to the surface of microorganisms. Algae has the potential to be used as a bio-sorbent. On the algal cell surface, different functional groups such as polysaccharides, lipids, and proteins serve as adsorption sites (El-Naggar et al., 2019). There are two types of biosorption; physisorption (physical biosorption) and chemisorption (chemical biosorption). Solute molecules interact with the binding sites on the sorbent surface during physical adsorption, whereas chemical bonds are formed during chemisorption. The advantages of this method include lower costs, simple processes, no sludge production, and the ability to remediate large amounts of wastewater with low pollutant concentrations (Lo et al., 2014; Olawale, 2021). Microalgae, which can produce Exopolysaccharides (EPSs), are used as surface-active agents for eliminating pollutants (primarily heavy metals). Algal biosorption is influenced by a variety of factors, including cell wall composition, which is essential for electrostatic attraction and chelation or complexation. Algal bioremediation is facilitated by functional groups on the algal cell surface, especially the carboxyl group. The interaction of positively charged pollutants and negatively charged microalgae cellular walls is involved in the biosorption mechanism. The rate of biosorption is influenced by dissolved oxygen, pollutants concentration, initial pH level, and hydraulic retention time (Gusain et al., 2020; Ma et al., 2020).

3.2 Bioaccumulation and bio-uptake

Bioaccumulation is defined as the accumulation of contaminants from the external environment within the cytoplasm of a cell. *Spirogyra*, for example, can efficiently absorb and collect contaminants inside their cells and use them to grow. *Nannochloris sp*. absorbed only 11% of sulfamethoxazole, 11% of trimethoprim, 27% of triclosan, and 13% of carbamazepine (Rezania et al., 2016). Pollutant bio-adsorption and bioaccumulation mechanisms are completely distinct. The estimation of bioaccumulation and bio-adsorption of pollutants is difficult because both processes occur in most cases in parallel. The first stage of the bioaccumulation process is bio-adsorption. Molecules must be adsorbed within the microalgal cell in order to bioaccumulate there. Pharmaceuticals (triclosan and sulfamethoxazole) have been found to bioaccumulate in microalgae, resulting in an excess of reactive oxygen species and, eventually, cell death (Bai and Acharya, 2017).

In bioaccumulation and bio-uptake, contaminants can enter algal cells through the cell wall and bind to intracellular proteins.

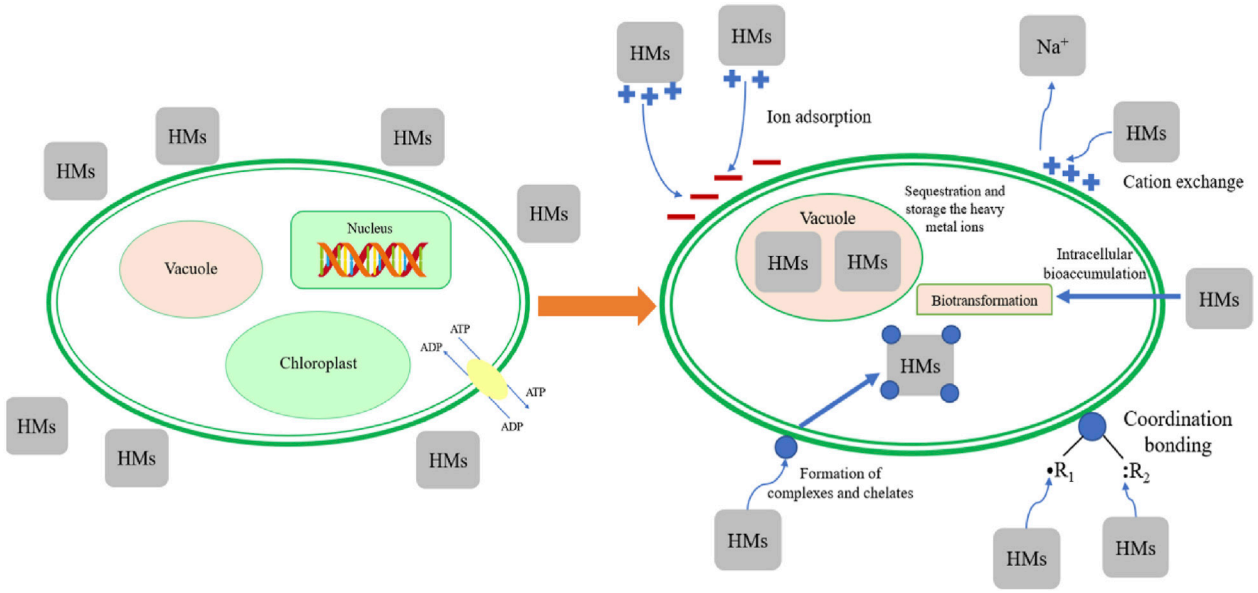

FIGURE 2
Biosorption, biodegradation and detoxification of heavy metals by microalgae. Reprinted with permission from Elsevier (Yan et al., 2022), licence number 5705480505642.

The primary distinction among bioaccumulation and bio-uptake is that bio-uptake of contaminants can only occur in living microalgae cells. The transfer of hazardous substances or pollutants from the surrounding environment into the cells is known as biological or bio-uptake. Microalgae can absorb nutrients and can be mass cultivated (Mulla et al., 2019).

3.3 Biodegradation

Enzymes catalyse the metabolic breakdown or degradation of contaminants during biodegradation. In general, microalgae degrade complex parent compounds into simpler ones. Several enzymatic processes, such as hydroxylation, glycosylation dehydrogenation, hydrogenation, and hydrolysis, may be involved (Varjani, 2017). Pollutant biodegradation by algal-bioremediation occurs in three stages, with several enzymes involved in the catalysis. The first phase of cytochrome P450 detoxification involves hydrolysis, oxidation, or reduction activities. During this phase, the addition of the hydroxyl group transforms the lipophilic molecules to hydrophilic molecules. In the second phase, compounds with electrophilic groups develop a conjugate bond with glutathione in the second phase that shields the cell from oxidative damage. A variety of enzymes (such as carboxylase, dehydrogenase, laccases, and decarboxylase) are used in the third phase. The biodegradability of compounds is determined by the complexity of their structures (Xiong et al., 2016). Compounds with a linear and unsaturated structure, as well as electron-donating groups, biodegrade faster than complex compounds with a cyclic structure, as demonstrated by *Navicula sp., C. pyrenoidosa, and S. obliquus,* which showed 95% biodegradation. Other examples include the biodegradation of levofloxacin by *C. vulgaris*. Due to the presence of few extracellular enzymes, EPS is hygroscopic, forming a matrix around the cells that aids in adsorption, accumulation, and biodegradation (Xiong et al., 2016; Posadas et al., 2014) proposed that contaminants biodegradability is affected by the C:N:P ratio of wastewater, and that the ideal C:N:P for optimum biodegradability is 100:18:2. Biodegradation, as opposed to bioaccumulation or biosorption, can reduce contaminants toxicity in algae cells, and algal biomass could be used to produce biofuels and value-added bioproducts. Biodegradation can occur in two ways; co-metabolism and metabolic biodegradation. The co-metabolism biodegradation process includes the breakdown of contaminants catalysed by enzymes, with contaminants serving as a carbon source for algae throughout metabolic biodegradation (Norvill et al., 2016).

Biosorption, biodegradation and detoxification of heavy metals by microalgae is shown in Figure 2 with possible mechanisms.

3.4 Photodegradation

Even if a pollutant cannot be bioremediated using the techniques described above, microalgae can still play an essential part in effective bioremediation via photodegradation. There are two types of photodegradation: photooxidative degradation and photolysis (Abo et al., 2016). When a pollutant interacts with oxidants like hydroxyl radicals formed as a result of photooxidation, photooxidative degradation occurs. Photolysis occurs when a pollutant absorbs light, causing a change in the pollutant's conformation and, as a result, its degradation. The photodegradation process is controlled by the physicochemical characteristics of the pollutant and wastewater, as well as the intensity and wavelength of light. The introduction of Dissolved Organic Molecules (DOM) is another method for increasing the rate of photodegradation. DOM is a class of compounds that include fulvic acids, humic acids, and hemicellulose and play an active part in enhancing photodegradation through mechanisms such as

hydroxyl radical production or redox cycling. Pollutants that absorb less light become photosensitized and transformed as a result of interactions with EOMs (Extracellular Organic Matter) and DOMs (Gondi et al., 2022). There are two types of photo-degradation; direct and indirect photo-degradation. Algal systems use algal scrubbers and turbulent mixing in both photobioreactors to increase light exposure. This process, however, is highly selective, as not all pollutants can be photodegraded (Reymann et al., 2020).

3.5 Hydrolysis

In conventional treatment processes, hydrolysis can be used to deactivate some emerging pollutants. This process is primarily determined by the pollutant structure. The disadvantage of the method is the fact that numerous emerging pollutants, particularly pharmaceuticals, can withstand hydrolysis. Hydrolysis, for example, can only be used to break down a few pharmaceuticals, such as lactam antibiotics. This process is resistant to pharmaceuticals that include sulphonamide and fluoroquinolone (Banu et al., 2020). Chemical structure, pollutant concentration, temperature, and pH are all factors that influence hydrolysis. Although information on antibiotic hydrolysis in micro-algal bioremediation is limited, the chemical reactions involved are pollutant-specific. The rate of hydrolysis in an algal pond can increase as the temperature rises (Zhang S. et al., 2020). Furthermore, because the pH of algal ponds can vary greatly, new contaminants that hydrolyse at high pH levels can breakdown significantly during the day. Emerging pollutants that were hydrolysed at neutral pH, on the other hand, may still degrade at night while the pH values return to neutral bandwidth (Gondi et al., 2022).

4 Factors affecting wastewater treatment by microalgae

The efficiency of microalgal-bioremediation processes is affected by various physicochemical factors. These factors include pH levels, redox potential, temperature, the duration and intensity of light exposure, hydraulic retention time, and the size of the adsorbent. These elements collectively play a crucial role in shaping the rate and effectiveness of microalgae-mediated bioremediation mechanisms. The pH of the environment, the redox state, and the prevailing temperature can significantly impact the metabolic activity and growth of microalgae, influencing their capacity to remediate contaminants. The duration and intensity of light exposure are essential considerations, as they directly affect photosynthesis, a key process in microalgal remediation. Hydraulic retention time, representing the duration of water within the system, and the size of the adsorbent particles also contribute to the overall efficiency of microalgal-bioremediation processes by influencing contact time and surface area availability for remediation processes.

4.1 pH

pH is a critical parameter that can influence the mechanism of microalgal bioremediation. pH also influences the ionisation states of various functional groups on the adsorbent's surface (Ummalyma et al., 2016). Any change in the optimal pH of any biological process may slow down the rate of the reaction. Because at lower pH, the algal surface becomes positively charged, reducing molecule adsorption (Chen et al., 2016). When the pH rises above the isoelectric point, the algal surface becomes negatively charged, causing absorption to increase. A pH greater than 9 has a negative impact on algal growth because the capacity for carbon dioxide absorption is significantly reduced and RuBisCO activity cannot be maintained (Sutherland et al., 2015).

4.2 Temperature

Industrial wastewater effluents, when discharged, often carry elevated temperatures, posing a risk of thermal pollution in aquatic ecosystems. Microalgae, despite having strain-specific optimal temperatures, exhibit a versatile ability to thrive across a broad temperature spectrum. This adaptability allows them to withstand and potentially mitigate the thermal impacts associated with the immediate disposal of heated industrial wastewater into aquatic habitats. In essence, while microalgae have temperature preferences, their capacity to flourish within a wide range makes them valuable in scenarios where temperature fluctuations in wastewater discharges are a concern. The optimal temperature range for commonly cultivated microalgal strains is 15°C–35°C. Once the optimal temperature is reached, biomass productivity decreases dramatically with increasing temperature (Chen et al., 2020). Temperature fluctuations are a major source of concern in microalgae cultivation facilities. Microalgal species such as *Spirulina plantesis* thrive at 35C, while *Scenedesmus* sp. thrives at varying temperatures. As a result, microalgae that can grow in wastewater at high temperatures (30°C–40°C) are critical microorganisms for algal-bioremediation of emerging pollutants (Cheah et al., 2015).

4.3 Light intensity

Algae, being phototrophic organisms, harness light energy to synthesize the essential chemical compounds necessary for their growth. The photosynthetic process, facilitated by the presence of inorganic carbon, adequate light, and suitable temperatures, enables algae to absorb nutrients vital for their development. The growth of algae is intricately linked to the availability and intensity of light, a factor that plays a pivotal role in shaping the nutrient utilization efficiency within the waterbody. The interplay of these factors underscores the complex relationship between light, photosynthesis, and nutrient dynamics, influencing the overall ecological balance of the aquatic environment. (Whitton et al., 2015). Microalgae photosynthetic systems are more productive in the blue and red regions of the spectrum, 400 and 600–700 nm, respectively, resulting in better utilisation of nitrogen and phosphorus from wastewater, with red light stimulating algal growth. Although the use of artificial light increases the cost of wastewater treatment, the technology of the light-emitting diode, which provides a longer lightbulb lifespan in combination with lower electricity consumption, makes the use of artificial light sources to enhance the photosynthetic activity of the algae and

thus enhancing nutrient uptake from the waterbody more prominent (Ibrahim et al., 2014). The best light source for algae cultivation is thought to be developed light-emitting diode technology with narrowband wavelengths. A study using *Spirulina platensis* found that red light increased the growth rate of the microalgae by 38%. Green light was used to achieve maximum productivity with *C. vulgaris* (Wang et al., 2007).

4.4 Hydraulic retention time

The efficiency of microalgae in taking up pollutants can be influenced by the hydraulic retention time. A shorter hydraulic retention time may lead to incomplete or partial removal of pollutants in certain instances. The interplay between microalgal biomass and hydraulic retention time is a critical factor influencing pollutant removal. There is an observable trend where, up to a certain threshold, the removal rate increases with higher concentrations of microalgae and longer hydraulic retention times. However, once the hydraulic retention time surpasses a certain limit, or if it is prolonged excessively, the removal efficiencies may experience a notable decrease. This highlights the importance of optimizing hydraulic retention time in conjunction with microalgal biomass for effective pollutant removal in wastewater treatment processes. (De-Bashan and Bashan, 2010).

4.5 Dose of adsorbent and particle size

The greater the permeability of the pollutant particle, the greater the absorption into the cell wall. This interaction is also affected by the pollutant's toxicity. It is due to the availability of more surface area, which increases the availability of binding sites. Nano compounds are more readily absorbed. Surface area, electrostatic capacity, and the functional groups involved in the interaction are all factors that influence algal bioremediation via adsorption (Hlongwane et al., 2019). The absorption was found to increase as the hydraulic retention time between the pollutants and the adsorbent increased (Sarkar and Dey, 2021).

5 Transformation and fate of contaminants inside the microalgal cells

Despite the benefits of the bioaccumulation process, many studies fail to consider the fate of emerging contaminants within the algal cell. There is still much debate about how to safely dispose of hazardous algal biomass after bioaccumulation (Gojkovic et al., 2019). The conversion and breakdown of complex compounds into simpler molecules is known as biodegradation or biotransformation. Compound breakdown can take place both intracellularly and extracellularly. Biodegradation has the capability to minimise the toxic effects of contaminants within algal cells and in bulk medium when compared to bio-adsorption or bioaccumulation processes. Microalgae biomass can be converted into additional value-added products. Biodegradation can take place through two main mechanisms: metabolic degradation and co-metabolism. Contaminants provides carbon to microalga throughout metabolic degradation. The degradation of contaminants in the co-metabolism process is mediated by enzymes that catalyse the substrates in the bulk medium (Tiwari et al., 2017).

Considerable research efforts have been dedicated to exploring the effectiveness of microalgal biodegradation in removing pharmaceuticals and personal care products from wastewater. This ongoing research aims to understand and optimize the capabilities of microalgae in breaking down and eliminating these contaminants, offering a potential environmentally friendly solution for wastewater treatment. The investigation focuses on the mechanisms and efficiency of microalgal biodegradation, with the goal of developing sustainable and effective methods to address the presence of pharmaceuticals and personal care products in wastewater. (Nguyen et al., 2021). Microalgal biodegradation was found to be the most effective method of removing estrogenic hormones. It was discovered that enzymes oversee biodegradation, and enzyme activation can be measured by the concentration of EC in the bulk medium. Thus, the EC threshold concentration is critical for triggering enzyme activity and microalgal biodegradation (Xiong et al., 2018). Microalgae biotransformation of these constant and robust ECs is complex. There is still substantial disagreement about the role of enzymes in the biodegradation process (Sutherland and Ralph, 2019). Further investigation into the function of enzymes and their degradation procedure in wastewater medium is required.

It is also worth noting that not all the contaminants are readily biodegradable, and some can be toxic to microalgal cells (Villar-Navarro et al., 2018). Some non-biodegradable pharmaceutical contaminants (e.g., carbamazepine) were found to be resistant to photolysis in high-rate algal ponds. It is proposed that microalgal strains can be pre-acclimated to target EC concentrations that are not toxic. This is a critical first step towards effective toxic substance remediation. Studies have shown that when microalgae are exposed to contaminants, their metabolisms and cellular processes improve. Microalgae tolerance to ECs appeared to increase in response to chronic exposure to target EC. This is because enzymatic pathways are activated to combat the toxic effects of ECs (Norvill et al., 2016; Chen et al., 2015) reported that when *C. pyrenoidosa* was pre-exposed to the antibiotic cefradine, its removal efficiency increased.

Microalgae may indirectly improve the biodegradation process through symbiotic interaction with bacteria. The synthesis of reactive oxygen species during photosynthesis was thought to be aided by photosynthetically mediated pH changes and high oxygen production. Because algal biomass is less toxic after biodegradation, it can be used for a variety of purposes, including biofuel. However, there is a chance that accumulation and sorption will leave some ECs after bioremediation (Agüera et al., 2020).

6 Advantages of microalgal-bioremediation systems for removal of emerging pollutants

Flocculation, chemical precipitation, activated charcoal, reverse osmosis, ultraviolet disinfection (UV disinfection), ultrafiltration, electro-coagulation, and ion exchange are the most common wastewater treatment methods. These approaches are not cost-effective because they necessitate a significant amount of energy and labour (Sankaran et al., 2020). Microalgal-bioremediation systems have been shown to be an effective method of

wastewater treatment. Microalgae are abundant in most environments, do not generate toxic substances, grow quickly, and have a large surface area.

- Cultivating microalgae recovers essential nutrients from wastewater and prevents eutrophication of freshwater, whereas in conventional treatments, nitrogen is removed as atmospheric nitrogen, carbon is oxidised to carbon dioxide, while phosphorus is precipitated (Nagarajan et al., 2020).
- Microalgae can withstand a variety of emerging pollutants. *Scenedesmus*, *Chlamydomonas*, and *Chlorella Sp.* were discovered to be among the most reported microalgal strains in proof-of-concept studies and are extensively studied (Wang et al., 2016).
- Microalgae play a crucial role in mitigating global warming by capturing atmospheric carbon dioxide through photosynthesis. Utilizing this natural process, microalgae absorb carbon dioxide from the atmosphere and convert it into organic compounds, thereby serving as an effective carbon sink. This carbon sequestration by microalgae helps reduce the concentration of greenhouse gases in the atmosphere, ultimately contributing to the mitigation of climate change and alleviating the severity of global warming. (Kannah et al., 2021).
- Cultivating microalgae on barren land offers a valuable opportunity to alleviate pressure on traditional agricultural land. By utilizing barren or non-arable areas, microalgae cultivation provides an alternative and sustainable approach to food and biomass production. This method not only optimizes land use but also mitigates the competition for fertile soil resources with traditional crops. Additionally, microalgae cultivation on barren land has the potential to contribute to ecosystem restoration and enhance resource efficiency in areas where conventional agriculture may be impractical or unsustainable. (Farooq et al., 2015).
- Value-added products are bioproducts that have been modified or improved as a result of a process. Possibility of producing a variety of value-added bioproducts for various industries and applications (fish feed, lipids, biofuel, sugars, bio pigments, enzymes, biofertilizers, algal plastics, and biomaterials). Furthermore, determining the protein and oil content is critical for determining what types of bioproducts can be produced (Banu et al., 2020).
- Microalgae grow at a rate that is 10–50 times faster than that of other terrestrial plants. Numerous studies have shown that cultivating microalgae is effective. Several studies have reported successful cultivation of several microalgae species for wastewater treatment, including *Chlorella, Chlamydomonas, Botryococcus, Scenedesmus, Arthrospira, and Phormidium* (Pittman et al., 2011).

7 Limitations/challenges associated with microalgae-based wastewater treatment

Traditional wastewater treatment plants (WWTPs) primarily target organic matter and nutrients but are ineffective at fully removing emerging contaminants (ECs) such as pharmaceuticals, hormones, antibiotic resistance genes (ARGs), and microplastics, with removal rates for some contaminants as low as 50% (World Health Organization, 2024; Zhang et al., 2017). Advanced methods like ozonation, reverse osmosis, and advanced oxidation processes (AOPs) offer higher efficiency but are energy-intensive, costly, and often produce harmful byproducts, such as bromates. Emerging biological approaches, including microalgae-based treatments, show promise but face challenges such as scalability, large space requirements, and the need for controlled environmental conditions. These limitations are further compounded in low- and middle-income countries, where only a small fraction of wastewater is treated due to financial and operational barriers. Additionally, there are significant gaps in understanding the long-term environmental and health impacts of ECs, as well as variability in contaminant concentrations across regions, which complicates the standardization of treatment technologies. Residual sludge management and the lack of real-world validation for many pilot-scale innovations also remain critical challenges.

The limitations of microalgae-based wastewater treatment are as follows:

- While microalgae-based wastewater treatment is geared towards efficient nitrogen and phosphorus removal, not all emerging pollutants and heavy metals can be effectively eliminated. Before integrating microalgae with wastewater treatment, the inhibition factors from the environment and wastewater itself must be considered because they have a large impact on the growth and treatment efficiency of microalgae (Chai et al., 2021).
- Significant amounts of solids suspensions and high turbidity in industrial wastewater may affect light radiation through the wastewater, thereby affecting photosynthesis and interfering with microalgae growth. As a result, an additional wastewater method with high solids removal efficiency, such as sedimentation, adsorption, coagulation, and so on, can be used to ensure high photosynthesis efficiency (Amenorfenyo et al., 2019).
- Even though the cultivation of microalgae in wastewater is simple and effective, it is not an enticing alternative wastewater treatment method in terms of cost. According to (Umamaheswari and Shanthakumar, 2016) high downstream processing costs, a small scale of production, and only selected microalgae species and cultivation modes can yield high quality biomass that can be converted into useful bioproducts all contribute to this treatment method's less profitable property. Furthermore, enclosed photobioreactors that require an artificial light source and chemical agents for sterilisation raise the overall cost of production.
- It is critical to choose the right species of microalgae for wastewater treatment. The selected microalgae species should be able to cope with variations in environmental factors due to the different physical and chemical composition of wastewater from various sources. Furthermore, the species should be able to share metabolites in order to accommodate stress and survive any attack by unwanted species as well as nutrient

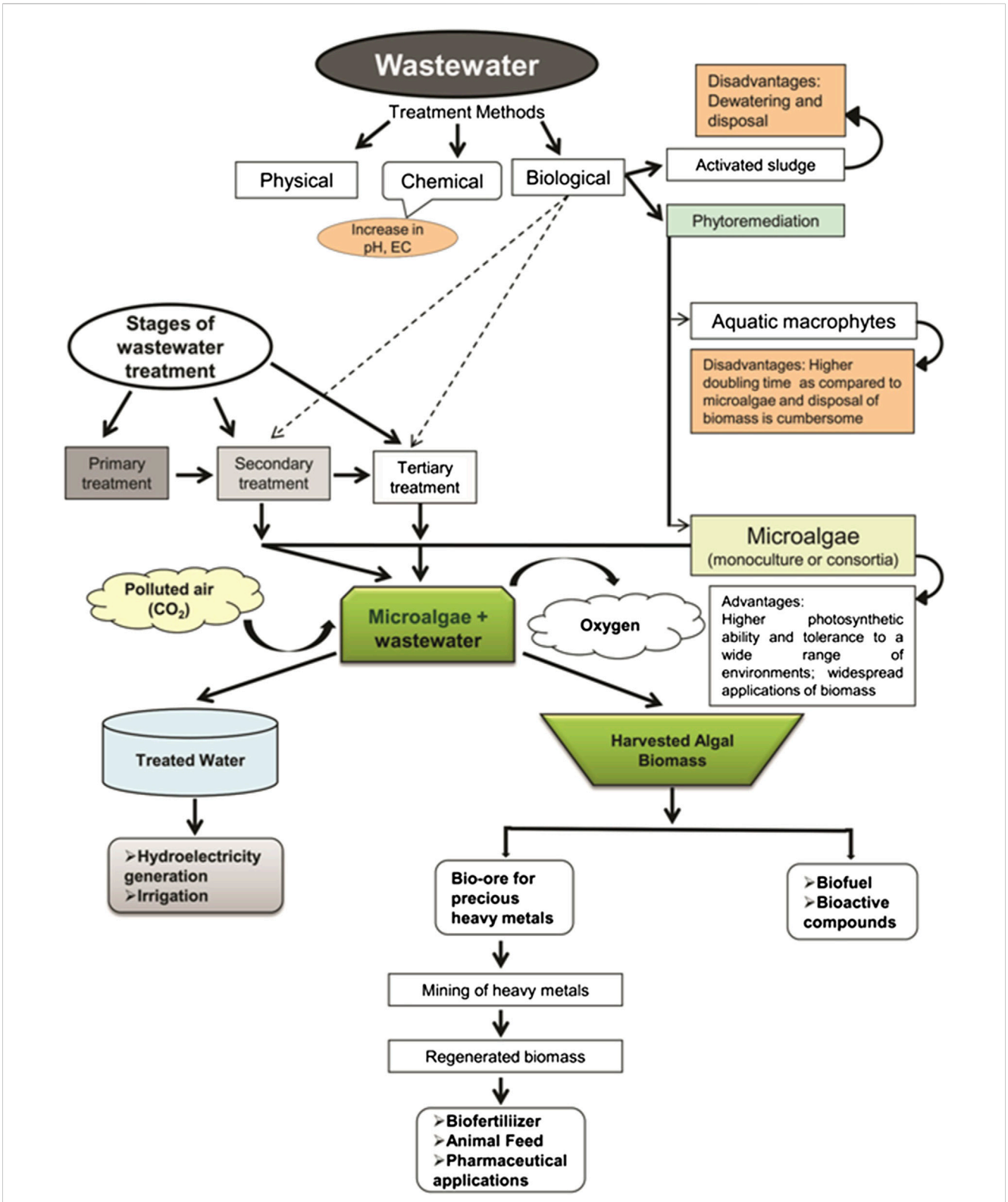

FIGURE 3
Different processes involving wastewater treatment by microalgae with their advantages and disadvantages. Reprinted with permission from Springer-Nature (Renuka et al., 2015), licence number 5705400031262.

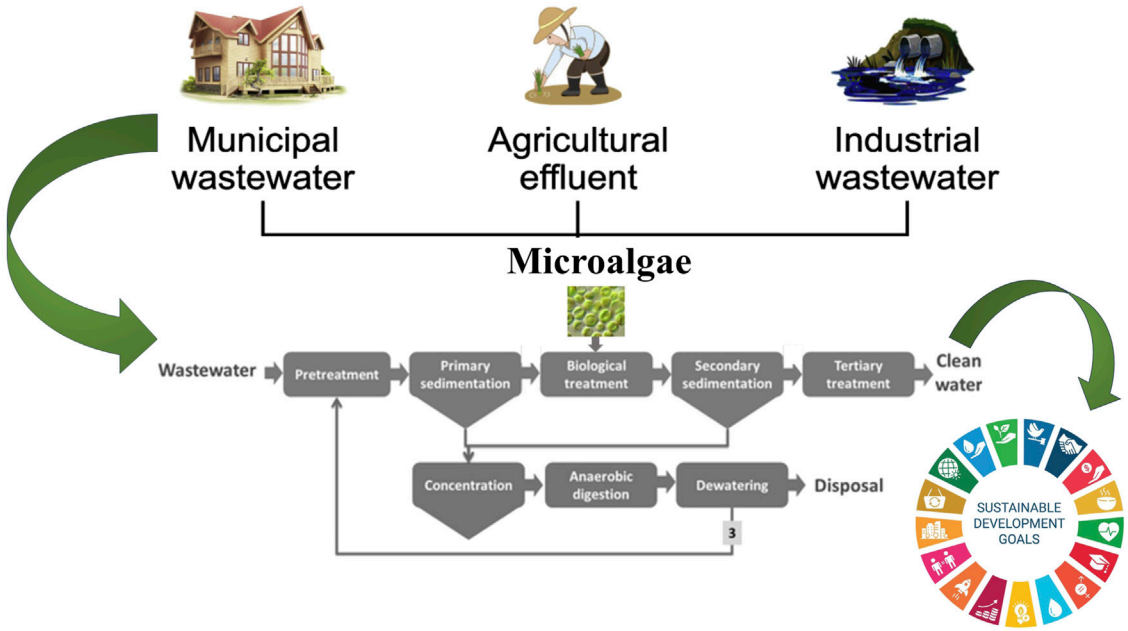

FIGURE 4
Different processes of microalgae-based wastewater system to achieve sustainable development goals.

limitations. Microalgae species that are facultative for utilising organic carbons as sole substrates and cut off any light source for cultivation are also limited for heterotrophic and mixotrophic microalgae (Amenorfenyo et al., 2019).

- Higher altitudes make it inconceivable to cultivate microalgae, which has a direct impact on algal biomass concentration. Selection and cultivation of extremophile varieties could be an option (Gondi et al., 2022). However, the effectiveness of such strains' microalgal bioremediation must also be considered.

Different processes involving wastewater treatment by microalgae with the advantages and disadvantages are summarized in Figure 3.

8 Applications of microalgae to achieve sustainable development goals (SGDs)

Goal 6 in UN Sustainable Development Goals (SDGs) aims to ensure availability and sustainable management of water and sanitation for all. Especially, target 6.a. under Goal 6 stated "By 2030, expand international cooperation and capacity-building support to developing countries in water-and sanitation-related activities and programmes, including water harvesting, desalination, water efficiency, wastewater treatment, recycling and reuse technologies" (United Nations, 2022). Target 6.3. stated "By 2030, improve water quality by reducing pollution, eliminating dumping and minimizing release of hazardous chemicals and materials, halving the proportion of untreated wastewater and substantially increasing recycling and safe reuse globally." wastewater treatment using microalgae can be one of the sustainable solutions in this regard. Advanced application of different microalgal strains in wastewater remediation can play a direct role in advancing Sustainable Development Goal 6, which aims to ensure the availability and sustainable management of clean water. The removal of emerging contaminants from wastewater can thereby mitigate the potential health risks associated with the exposure of emerging contaminants and can foster overall wellbeing.

The approaches and findings discussed in this research can be applied to real-world wastewater treatment by integrating innovative and sustainable technologies into existing systems. Upgrading conventional wastewater treatment plants (WWTPs) with advanced processes like advanced oxidation processes (AOPs), membrane bioreactors (MBRs), or activated carbon adsorption can significantly enhance the removal of emerging contaminants (ECs), such as pharmaceuticals, hormones, and microplastics. This hybrid approach closes the efficiency gap in addressing these pollutants. Additionally, nature-based solutions, such as microalgae and constructed wetlands, offer sustainable, cost-effective methods for EC removal while reducing energy consumption and generating valuable byproducts like biofuels and fertilizers, promoting a circular economy (Dutta et al., 2023).

Real-time monitoring systems can further enhance treatment effectiveness by detecting and targeting high-priority contaminants. Scaling up pilot technologies, such as microalgae-based treatments, through collaboration between academia, industry, and government can validate their practicality in diverse environments. In low- and middle-income regions, decentralized and affordable solutions like algal ponds or modular bioreactors can address infrastructure limitations, offering scalable and cost-effective alternatives.

Policy support and public awareness are crucial to the success of these innovations. Stricter regulations on EC discharges and campaigns promoting responsible pharmaceutical disposal can reduce contaminant loads in wastewater systems. Additionally,

incorporating technologies that target antibiotic residues and resistance genes can mitigate global health risks associated with antibiotic resistance. Resource recovery technologies that reclaim nutrients or water for reuse can further enhance the sustainability and economic viability of treatment systems, particularly in water-scarce areas. These strategies collectively provide practical, scalable, and eco-friendly solutions for improving wastewater treatment while safeguarding public health and ecosystems.

Large-scale algae production for wastewater treatment typically involves systems like open ponds, raceway ponds, or photobioreactors. Open or raceway ponds are cost-effective and simple to operate, while photobioreactors offer better control over environmental conditions (Qin et al., 2019), enhancing algae growth efficiency but with higher initial costs. The time required to achieve large-scale algal biomass depends on factors like species, nutrient availability, light, temperature, and system design (Pruvost et al., 2016). Sustainable approaches in developing large-scale remediation facilities can be effective in wastewater bio-treatment. In terms of cost-effectiveness, algae-based treatment can be competitive, especially when considering the co-benefits. Harvested algae can be converted into valuable byproducts like biofuels, bioplastics, animal feed, or fertilizers, generating additional revenue. The initial investment may be higher than conventional systems, but operational costs are often offset by reduced chemical usage, energy savings, and the potential for resource recovery, making algae systems increasingly viable in the long term (Dutta et al., 2023) the outline of different processes involved in microalgae-based wastewater system to achieve sustainable development goals is shown in Figure 4.

9 Recommendation and future perspectives

Several investigations have been conducted to pave the way for industrial scale microalgae application by determining the associated processes and technologies. However,

- The transition from pilot to industrial scale activities frequently exposes microalgae to unfavourable conditions, resulting in significantly lower bioproduct yields. As a result, more studies and research are needed to ensure the monetary and environmental feasibility of integrating robust microalgae cells and bioprocess engineering methods. Further genetic or metabolic engineering research should be carried out to ensure the cultivation of genome-modified microalgal cells with improved characteristics related to unfavourable environment adaptation and higher performance for removing pollutants and bioproduct yields.
- Sorting microalgal biomass from treated wastewater after bioremediation is a significant challenge, particularly in suspended cultivation. To address this, securing microalgae cultivation to a media/supporter may be used, ensuring the separation process more accessible and decreasing hydraulic retention time.
- Only a few studies have been completed, so cost-effectiveness studies of microalgae-based wastewater treatment and assessments to traditional methods must be investigated. The lack of basic design and operation guidelines for microalgae-based wastewater treatment, on the other hand, encourages researchers to investigate harder to provide basic guidance and recommendations for enhancing the resilience and flexibility of microalgal strains to deal with different types of wastewaters.
- More research on incorporating microalgae into the biological treatment process, as well as a thorough understanding of the relationships between microalgae and existing bacteria in wastewater, is required.
- Before introducing microalgae, it is recommended to regulate the influents with adequate input and/or pretreat. Furthermore, the wide variety of nutrients and their strength in wastewater necessitate several pretreatments in order to produce an ideal balance of nutrients for the microalgae. In such cases, researchers should use optimised mixtures of multiple wastewater sources as a single, well-balanced nutrient media for microalgae.
- Assessing wastewater from industries and microalgae cultivation modes may differ depending on geographical zone due to variations in sunlight availability and temperature. As a result, colder zones should concentrate on photobioreactor-based microalgae cultivation with the goal of producing high-value-added products from microalgae grown on wastewater.
- The microalgae-based wastewater treatment processes and overall method monitoring (e.g., pH, temperature, microalgae cell conditions, BOD, and DO) are complicated operations that necessitate the development of innovative technologies such as online monitoring and remote control.

10 Conclusion

The bioremediation capabilities of microalgae in wastewater have been demonstrated and confirmed by recent and available literature studies. Microalgae are promising possibility for carbon capture technology because they have been shown to be effective at removing heavy metals and nutrients from various types of wastewaters. Microalgae have an accurately high potential to remove newly emerging contaminants. However, each species of microalgae has distinctive traits and the capacity to eliminate different kinds of contaminants. Because different types of microalgae have different inherent abilities, particularly nutrient uptake, tolerance for harsh or extreme environmental conditions, and competitive potential relative to native organisms, the response and development of different types of microalgae in wastewater also varies. The ultimate objective of wastewater treatment is to reduce the biochemical oxygen demand as well as organic, inorganic, and synthetic elements like high levels of ammonium, bicarbonate, phosphate, potassium, sulphur, heavy metals, dyes, pesticides, pharmaceuticals, and a wide range of pathogenic bacteria. Phyco-remediation, or the bioremediation of wastewater using algal species, can remove biological and chemical compounds using microalgae. High concentrations of nutrients found in domestic, industrial, and agricultural wastewaters encourage the growth of microalgae, reducing or even eliminating the need for supplemental feeding. After the consumption of heavy metals or toxic substances, algae do

not cause secondary pollution. Even dead algal biomass can eliminate heavy metals from wastewaters through the biosorption process, though this method is less efficient than using live algae cells. Utilising algae to treat wastewater is a key component of new technologies. Molecular techniques are also used to develop novel algal strains with improved phyco-remediation capabilities. In order to increase the viability and compatibility of microalgae cultivated at full scale, more research is needed to examine the industrial scale of microalgae and the improvement of bioproduct quality. For the future advancement of microalgal technology, numerous experiments evaluating the removal effectiveness of a wide range of heavy metal ions by various microalgal strains either individually or in combination should be carried out. To increase the opportunities for the application of microalgal treatment in wastewater plants, more research on the integration of current treatment systems and microalgal treatment needs to be conducted and reported.

Author contributions

PK: Writing–original draft. ND: Writing–original draft, Writing–review and editing. SB: Conceptualization, Supervision, Validation, Writing–original draft, Writing–review and editing.

Funding

The author(s) declare that no financial support was received for the research, authorship, and/or publication of this article.

Conflict of interest

The authors declare that the research was conducted in the absence of any commercial or financial relationships that could be construed as a potential conflict of interest.

Generative AI statement

The author(s) declare that no Generative AI was used in the creation of this manuscript.

Publisher's note

References

Abdel-Raouf, N., Al-Homaidan, A., and Ibraheem, I. (2012). Microalgae and wastewater treatment. *Saudi J. Biol. Sci.* 19, 257–275. doi:10.1016/j.sjbs.2012.04.005

Abo, R., Kummer, N.-A., and Merkel, B. J. (2016). Optimized photodegradation of Bisphenol A in water using ZnO, TiO 2 and SnO 2 photocatalysts under UV radiation as a decontamination procedure. *Drink. Water Eng. Sci.* 9, 27–35. doi:10.5194/dwes-9-27-2016

Agüera, A., Plaza-Bolaños, P., and Fernández, F. A. (2020) "Removal of contaminants of emerging concern by microalgae-based wastewater treatments and related analytical techniques," in *Current developments in biotechnology and bioengineering*. Elsevier, 503–525.

Aksu, Z., and Tezer, S. (2005). Biosorption of reactive dyes on the green alga Chlorella vulgaris. *Process Biochem.* 40, 1347–1361. doi:10.1016/j.procbio.2004.06.007

Amenorfenyo, D. K., Huang, X., Zhang, Y., Zeng, Q., Zhang, N., Ren, J., et al. (2019). Microalgae brewery wastewater treatment: potentials, benefits and the challenges. *Int. J. Environ. Res. public health* 16, 1910. doi:10.3390/ijerph16111910

Andrade, C., Andrade, L., Dias, M., Nascimento, C., and Mendes, M. (2018). Microalgae for bioremediation of textile wastewater. An overview. *MOJ Food Process Technol.* 6, 432–433. doi:10.15406/mojfpt.2018.06.00200

Ansa, E., Lubberding, H. J., Ampofo, J., and Gijzen, H. (2011). The role of algae in the removal of Escherichia coli in a tropical eutrophic lake. *Ecol. Eng.* 37, 317–324. doi:10.1016/j.ecoleng.2010.11.023

Bai, X., and Acharya, K. (2017). Algae-mediated removal of selected pharmaceutical and personal care products (PPCPs) from Lake Mead water. *Sci. Total Environ.* 581, 734–740. doi:10.1016/j.scitotenv.2016.12.192

Banu, J. R., Kannah, R. Y., Kavitha, S., Ashikvivek, A., Bhosale, R. R., and Kumar, G. (2020). Cost effective biomethanation via surfactant coupled ultrasonic liquefaction of mixed microalgal biomass harvested from open raceway pond. *Bioresour. Technol.* 304, 123021. doi:10.1016/j.biortech.2020.123021

Borowitzka, M. A. (1998). Limits to growth. *Wastewater Treat. algae*, 203–226. doi:10.1007/978-3-662-10863-5_12

Castiglioni, S., Davoli, E., Riva, F., Palmiotto, M., Camporini, P., Manenti, A., et al. (2018). Mass balance of emerging contaminants in the water cycle of a highly urbanized and industrialized area of Italy. *Water Res.* 131, 287–298. doi:10.1016/j.watres.2017.12.047

Chai, W. S., Tan, W. G., Munawaroh, H. S. H., Gupta, V. K., Ho, S.-H., and Show, P. L. (2021). Multifaceted roles of microalgae in the application of wastewater biotreatment: a review. *Environ. Pollut.* 269, 116236. doi:10.1016/j.envpol.2020.116236

Cheah, W. Y., Show, P. L., Chang, J.-S., Ling, T. C., and Juan, J. C. (2015). Biosequestration of atmospheric CO2 and flue gas-containing CO2 by microalgae. *Bioresour. Technol.* 184, 190–201. doi:10.1016/j.biortech.2014.11.026

Cheirsilp, B., Maneechote, W., Srinuanpan, S., and Angelidaki, I. (2023). Microalgae as Tools for bio-circular-green economy: zero-waste approaches for sustainable production and biorefineries of microalgal biomass. *Bioresour. Technol.* 387, 129620. doi:10.1016/j.biortech.2023.129620

Chen, J., Zheng, F., and Guo, R. (2015). Algal feedback and removal efficiency in a sequencing batch reactor algae process (SBAR) to treat the antibiotic cefradine. *PLoS One* 10, e0133273. doi:10.1371/journal.pone.0133273

Chen, R., Liu, Y., and Liao, W. (2016). Using an environmentally friendly process combining electrocoagulation and algal cultivation to treat high-strength wastewater. *Algal Res.* 16, 330–337. doi:10.1016/j.algal.2016.03.032

Chen, Z., Shao, S., He, Y., Luo, Q., Zheng, M., Zheng, M., et al. (2020). Nutrients removal from piggery wastewater coupled to lipid production by a newly isolated self-flocculating microalga Desmodesmus sp. PW1. *Bioresour. Technol.* 302, 122806. doi:10.1016/j.biortech.2020.122806

Cheng, L., Zhang, L., Chen, H., and Gao, C. (2006). Carbon dioxide removal from air by microalgae cultured in a membrane-photobioreactor. *Sep. Purif. Technol.* 50, 324–329. doi:10.1016/j.seppur.2005.12.006

Chiu, S.-Y., Kao, C.-Y., Huang, T.-T., Lin, C.-J., Ong, S.-C., Chen, C.-D., et al. (2011). Microalgal biomass production and on-site bioremediation of carbon dioxide, nitrogen oxide and sulfur dioxide from flue gas using Chlorella sp. cultures. *Bioresour. Technol.* 102, 9135–9142. doi:10.1016/j.biortech.2011.06.091

Chong, A., Wong, Y., and Tam, N. (2000). Performance of different microalgal species in removing nickel and zinc from industrial wastewater. *Chemosphere* 41, 251–257. doi:10.1016/s0045-6535(99)00418-x

Dar, R. A., Sharma, N., Kaur, K., and Phutela, U. G. (2019). Feasibility of microalgal technologies in pathogen removal from wastewater. *Appl. Microalgae Wastewater Treat. Domest. Industrial Wastewater Treat.* 1, 237–268. doi:10.1007/978-3-030-13913-1_12

Das, A., Adhikari, S., and Kundu, P. (2019). Bioremediation of wastewater using microalgae. *Environ. Biotechnol. soil wastewater Implic. Ecosyst.*, 55–60. doi:10.1007/978-981-13-6846-2_8

De-Bashan, L. E., and Bashan, Y. (2010). Immobilized microalgae for removing pollutants: review of practical aspects. *Bioresour. Technol.* 101, 1611–1627. doi:10.1016/j.biortech.2009.09.043

Delrue, F., Álvarez-Díaz, P. D., Fon-Sing, S., Fleury, G., and Sassi, J.-F. (2016). The environmental biorefinery: using microalgae to remediate wastewater, a win-win paradigm. *Energies* 9, 132. doi:10.3390/en9030132

Dutta, N., Kundu, P., Lee, J. T. E., and Bhattacharya, S. (2023). Implementation and optimization of algal biomass in value-added products recovery: a step towards algae-based green economy. *Hydrobiolog* 2, 326–346. doi:10.3390/hydrobiology2020021

Edelstein, M., and Ben-Hur, M. (2018). Heavy metals and metalloids: sources, risks and strategies to reduce their accumulation in horticultural crops. *Sci. Hortic.* 234, 431–444. doi:10.1016/j.scienta.2017.12.039

El-Naggar, N. E.-A., Hamouda, R. A., Rabei, N. H., Mousa, I. E., and Abdel-Hamid, M. S. (2019). Phytoremediation of lithium ions from aqueous solutions using free and immobilized freshwater green alga Oocystis solitaria: mathematical modeling for bioprocess optimization. *Environ. Sci. Pollut. Res.* 26, 19335–19351. doi:10.1007/s11356-019-05214-x

Emparan, Q., Harun, R., and Danquah, M. (2019). Role of phycoremediation for nutrient removal from wastewaters: a review. *Appl. Ecol. and Environ. Res.* 17, 889–915. doi:10.15666/aeer/1701_889915

Fang, G. Z., Huang, G. Y., Ying, G. G., Qiu, S. Q., Shi, W. J., Xie, L., et al. (2021). Endocrine disrupting effects of binary mixtures of 17β-estradiol and testosterone in adult female western mosquitofish (*Gambusia affinis*). *Ecotoxicol. Environ. Saf.* 208, 111566. doi:10.1016/j.ecoenv.2020.111566

Farazaki, M., and Gikas, P. (2019). Nitrification-denitrification of municipal wastewater without recirculation, using encapsulated microorganisms. *J. Environ. Manag.* 242, 258–265. doi:10.1016/j.jenvman.2019.04.054

Farhadian, M., Vachelard, C., Duchez, D., and Larroche, C. (2008). *In situ* bioremediation of monoaromatic pollutants in groundwater: a review. *Bioresour. Technol.* 99, 5296–5308. doi:10.1016/j.biortech.2007.10.025

Farooq, W., Suh, W. I., Park, M. S., and Yang, J.-W. (2015). Water use and its recycling in microalgae cultivation for biofuel application. *Bioresour. Technol.* 184, 73–81. doi:10.1016/j.biortech.2014.10.140

Ghazal, F., Mahdy, E., El-Fattah, M., El-Sadany, A., Elg, Y., and Doha, N. (2018). The use of microalgae in bioremediation of the textile wastewater effluent. *Nat. Sci.* 16, 98–104.

Gojkovic, Z., Lindberg, R. H., Tysklind, M., and Funk, C. (2019). Northern green algae have the capacity to remove active pharmaceutical ingredients. *Ecotoxicol. Environ. Saf.* 170, 644–656. doi:10.1016/j.ecoenv.2018.12.032

Gondi, R., Kavitha, S., Kannah, R. Y., Karthikeyan, O. P., Kumar, G., Tyagi, V. K., et al. (2022). Algal-based system for removal of emerging pollutants from wastewater: a review. *Bioresour. Technol.* 344, 126245. doi:10.1016/j.biortech.2021.126245

Gusain, R., Kumar, N., and Ray, S. S. (2020). Recent advances in carbon nanomaterial-based adsorbents for water purification. *Coord. Chem. Rev.* 405, 213111. doi:10.1016/j.ccr.2019.213111

Hlongwane, G. N., Sekoai, P. T., Meyyappan, M., and Moothi, K. (2019). Simultaneous removal of pollutants from water using nanoparticles: a shift from single pollutant control to multiple pollutant control. *Sci. Total Environ.* 656, 808–833. doi:10.1016/j.scitotenv.2018.11.257

Hom-Diaz, A., Llorca, M., Rodríguez-Mozaz, S., Vicent, T., Barceló, D., and Blánquez, P. (2015). Microalgae cultivation on wastewater digestate: β-estradiol and 17α-ethynylestradiol degradation and transformation products identification. *J. Environ. Manag.* 155, 106–113. doi:10.1016/j.jenvman.2015.03.003

Houtman, C. J., Ten Broek, R., and Brouwer, A. (2018). Steroid hormonal bioactivities, culprit natural and synthetic hormones and other emerging contaminants in waste water measured using bioassays and UPLC-tQ-MS. *Sci. Total Environ.* 630, 1492–1501. doi:10.1016/j.scitotenv.2018.02.273

Hussein, M., Abdullah, A., Eladal, E., and El-Din, N. B. (2016). Phytoremediation of some pesticides by microchlorophyte alga, Chlorella Sp. *J. Fertil. Pestic.* 7, 2. doi:10.4172/2471-2728.1000173

Ibrahim, M. A., MacAdam, J., Autin, O., and Jefferson, B. (2014). Evaluating the impact of LED bulb development on the economic viability of ultraviolet technology for disinfection. *Environ. Technol.* 35, 400–406. doi:10.1080/09593330.2013.829858

Inuwa, A. B., Pervez, ·.A., Nazir, ·.R., and Huang, B. (2023). Microalgae-based wastewater treatment system: current state, antibiotic resistant bacteria and antibiotic resistance genes reduction potentials. *Int. J. Environ. Sci. Technol.* 20, 14053–14072. doi:10.1007/s13762-023-05069-3

IQVIA (2018). Winning the Indian pharmaceutical market. Available at: https://www.iqvia.com/locations/india/library/white-papers/winning-in-the-indian-pharmaceutical-market (accessed on November 24, 2024).

Ji, M.-K., Abou-Shanab, R. A., Kim, S.-H., Salama, E.-S., Lee, S.-H., Kabra, A. N., et al. (2013). Cultivation of microalgae species in tertiary municipal wastewater supplemented with CO2 for nutrient removal and biomass production. *Ecol. Eng.* 58, 142–148. doi:10.1016/j.ecoleng.2013.06.020

Kaloudas, D., Pavlova, N., and Penchovsky, R. (2021). Phytoremediation of wastewater by microalgae: a review. *Environ. Chem. Lett.* 19, 2905–2920. doi:10.1007/s10311-021-01203-0

Kannah, R. Y., Kavitha, S., Karthikeyan, O. P., Rene, E. R., Kumar, G., and Banu, J. R. (2021). A review on anaerobic digestion of energy and cost effective microalgae pretreatment for biogas production. *Bioresour. Technol.* 332, 125055. doi:10.1016/j.biortech.2021.125055

Khalatbari, S., Sotaniemi, V., Suokas, M., Taipale, S., and Leiviskä, T. (2024). Microalgae technology for polishing chemically-treated fish processing waste water. *Groundw. Sustain. Dev.* 24, 101074. doi:10.1016/j.gsd.2023.101074

Klinthong, W., Yang, Y.-H., Huang, C.-H., and Tan, C.-S. (2015). A review: microalgae and their applications in CO2 capture and renewable energy. *Aerosol Air Qual. Res.* 15, 712–742. doi:10.4209/aaqr.2014.11.0299

Koyande, A. K., Chew, K. W., Rambabu, K., Tao, Y., Chu, D.-T., and Show, P.-L. (2019). Microalgae: a potential alternative to health supplementation for humans. *Food Sci. Hum. Wellness* 8, 16–24. doi:10.1016/j.fshw.2019.03.001

Kruglova, A., Kråkström, M., Riska, M., Mikola, A., Rantanen, P., Vahala, R., et al. (2016). Comparative study of emerging micropollutants removal by aerobic activated sludge of large laboratory-scale membrane bioreactors and sequencing batch reactors under low-temperature conditions. *Bioresour. Technol.* 214, 81–88. doi:10.1016/j.biortech.2016.04.037

Kumar, A., Ergas, S., Yuan, X., Sahu, A., Zhang, Q., Dewulf, J., et al. (2010). Enhanced CO2 fixation and biofuel production via microalgae: recent developments and future directions. *Trends Biotechnol.* 28, 371–380. doi:10.1016/j.tibtech.2010.04.004

Kumar, S. D., Santhanam, P., Nandakumar, R., Anath, S., Prasath, B. B., Devi, A. S., et al. (2014). Preliminary study on the dye removal efficacy of immobilized marine and freshwater microalgal beads from textile wastewater. *Afr. J. Biotechnol.* 13, 2288–2294. doi:10.5897/ajb2013.13242

Lal, S., Lal, R., and Saxena, D. (1987). Bioconcentration and metabolism of DDT, fenitrothion and chlorpyrifos by the blue-green algae Anabaena sp. and Aulosira fertilissima. *Environ. Pollut.* 46, 187–196. doi:10.1016/0269-7491(87)90076-5

Lei, A.-P., Hu, Z.-L., Wong, Y.-S., and Tam, N. F.-Y. (2007). Removal of fluoranthene and pyrene by different microalgal species. *Bioresour. Technol.* 98, 273–280. doi:10.1016/j.biortech.2006.01.012

Liu, L., Hall, G., and Champagne, P. (2020). The role of algae in the removal and inactivation of pathogenic indicator organisms in wastewater stabilization pond systems. *Algal Res.* 46, 101777. doi:10.1016/j.algal.2019.101777

Lo, Y.-C., Cheng, C.-L., Han, Y.-L., Chen, B.-Y., and Chang, J.-S. (2014). Recovery of high-value metals from geothermal sites by biosorption and bioaccumulation. *Bioresour. Technol.* 160, 182–190. doi:10.1016/j.biortech.2014.02.008

Ma, Y., Shen, Y., and Liu, Y. (2020). State of the art of straw treatment technology: challenges and solutions forward. *Bioresour. Technol.* 313, 123656. doi:10.1016/j.biortech.2020.123656

Mascolo, G., Balest, L., Cassano, D., Laera, G., Lopez, A., Pollice, A., et al. (2010). Biodegradability of pharmaceutical industrial wastewater and formation of recalcitrant organic compounds during aerobic biological treatment. *Bioresour. Technol.* 101, 2585–2591. doi:10.1016/j.biortech.2009.10.057

Mestrot, A., Xie, W.-Y., Xue, X., and Zhu, Y.-G. (2013). Arsenic volatilization in model anaerobic biogas digesters. *Appl. Geochem.* 33, 294–297. doi:10.1016/j.apgeochem.2013.02.023

Mezzari, M., Prandini, J., Kich, J. D., and Silva, M. (2017). Elimination of antibiotic multi-resistant *Salmonella typhimurium* from swine wastewater by microalgae-induced antibacterial mechanisms. *J. Bioremediat. Biodegr.* 8, 379.

Mohamed, Z. A. (2008). Polysaccharides as a protective response against microcystin-induced oxidative stress in Chlorella vulgaris and Scenedesmus quadricauda and their possible significance in the aquatic ecosystem. *Ecotoxicology* 17, 504–516. doi:10.1007/s10646-008-0204-2

Molazadeh, M., Ahmadzadeh, H., Pourianfar, H. R., Lyon, S., and Rampelotto, P. H. (2019). The use of microalgae for coupling wastewater treatment with CO2 biofixation. *Front. Bioeng. Biotechnol.* 7, 42. doi:10.3389/fbioe.2019.00042

Mulla, S. I., Bharagava, R. N., Belhaj, D., Ameen, F., Saratale, G. D., Gupta, S. K., et al. (2019). A review of micropollutant removal by microalgae. *Appl. Microalgae Wastewater Treat. Domest. Industrial Wastewater Treat.* 1, 41–55. doi:10.1007/978-3-030-13913-1_3

Nagarajan, D., Lee, D.-J., Chen, C.-Y., and Chang, J.-S. (2020). Resource recovery from wastewaters using microalgae-based approaches: a circular bioeconomy perspective. *Bioresour. Technol.* 302, 122817. doi:10.1016/j.biortech.2020.122817

Naghdi, M., Taheran, M., Brar, S. K., Kermanshahi-Pour, A., Verma, M., and Surampalli, R. Y. (2018). Removal of pharmaceutical compounds in water and wastewater using fungal oxidoreductase enzymes. *Environ. Pollut.* 234, 190–213. doi:10.1016/j.envpol.2017.11.060

Nguyen, H. T., Yoon, Y., Ngo, H. H., and Jang, A. (2021). The application of microalgae in removing organic micropollutants in wastewater. *Crit. Rev. Environ. Sci. Technol.* 51, 1187–1220. doi:10.1080/10643389.2020.1753633

Noorani, KRPM, Flora, G., Surendarnath, S., Mary Stephy, G., Amesho, K. T. T., Chinglenthoiba, C., et al. (2024). Recent advances in remediation strategies for mitigating the impacts of emerging pollutants in water and ensuring environmental sustainability. *J. Environ. Manage* 351, 119674. doi:10.1016/j.jenvman.2023.119674

Norvill, Z. N., Shilton, A., and Guieysse, B. (2016). Emerging contaminant degradation and removal in algal wastewater treatment ponds: identifying the research gaps. *J. Hazard. Mater.* 313, 291–309. doi:10.1016/j.jhazmat.2016.03.085

Olawale, S. A. (2021). Biosorption of heavy metals from aqueous solutions: an insight and review. *Arch. Ind. Eng.* 3, 1–31.

Olmos-Espejel, J. J., de Llasera, M. P. G., and Velasco-Cruz, M. (2012). Extraction and analysis of polycyclic aromatic hydrocarbons and benzo [a] pyrene metabolites in microalgae cultures by off-line/on-line methodology based on matrix solid-phase

dispersion, solid-phase extraction and high-performance liquid chromatography. *J. Chromatogr. A* 1262, 138–147. doi:10.1016/j.chroma.2012.09.015

Omar, H. H. (2002). Bioremoval of zinc ions by Scenedesmus obliquus and Scenedesmus quadricauda and its effect on growth and metabolism. *Int. Biodeterior. and Biodegrad.* 50, 95–100. doi:10.1016/s0964-8305(02)00048-3

Paixão, J. F., Nascimento, I. A., Pereira, S. A., Leite, M., Carvalho, G. C., Silveira, J., et al. (2007). Estimating the gasoline components and formulations toxicity to microalgae (Tetraselmis chuii) and oyster (Crassostrea rhizophorae) embryos: an approach to minimize environmental pollution risk. *Environ. Res.* 103, 365–374. doi:10.1016/j.envres.2006.06.015

Pavithra, K. G., Kumar, P. S., Jaikumar, V., Vardhan, K. H., and SundarRajan, P. (2020). Microalgae for biofuel production and removal of heavy metals: a review. *Environ. Chem. Lett.* 18, 1905–1923. doi:10.1007/s10311-020-01046-1

Perez-Garcia, O., and Bashan, Y. (2015). Microalgal heterotrophic and mixotrophic culturing for bio-refining: from metabolic routes to techno-economics. *Algal Biorefineries Volume 2 Prod. Refin. Des.*, 61–131. doi:10.1007/978-3-319-20200-6_3

Petroutsos, D., Katapodis, P., Samiotaki, M., Panayotou, G., and Kekos, D. (2008). Detoxification of 2, 4-dichlorophenol by the marine microalga Tetraselmis marina. *Phytochemistry* 69, 707–714. doi:10.1016/j.phytochem.2007.09.002

Pittman, J. K., Dean, A. P., and Osundeko, O. (2011). The potential of sustainable algal biofuel production using wastewater resources. *Bioresour. Technol.* 102, 17–25. doi:10.1016/j.biortech.2010.06.035

Posadas, E., Bochon, S., Coca, M., García-González, M., García-Encina, P., and Muñoz, R. (2014). Microalgae-based agro-industrial wastewater treatment: a preliminary screening of biodegradability. *J. Appl. Phycol.* 26, 2335–2345. doi:10.1007/s10811-014-0263-0

Pruvost, J., Cornet, J. F., and Pilon, L. (2016). "Large-scale production of algal biomass: photobioreactors," in *Algae biotechnology*. Editors F. Bux, and Y. Chisti (Cham: Green Energy and Technology. Springer).

Qin, L., Alam, M. A., and Wang, Z. (2019). "Open pond culture systems and photobioreactors for microalgal biofuel production," in *Microalgae biotechnology for development of biofuel and wastewater treatment*. Editors M. Alam, and Z. Wang (Singapore: Springer).

Rasoul-Amini, S., Montazeri-Najafabady, N., Shaker, S., Safari, A., Kazemi, A., Mousavi, P., et al. (2014). Removal of nitrogen and phosphorus from wastewater using microalgae free cells in bath culture system. *Biocatal. Agric. Biotechnol.* 3, 126–131. doi:10.1016/j.bcab.2013.09.003

Rathod, H. (2014) "Algae based wastewater treatment," in *A seminar report of master of technology in civil engineering*. Uttarakhand, India: Roorkee.

Renuka, N., Sood, A., Prasanna, R., and Ahluwalia, A. S. (2015). Phycoremediation of wastewaters: a synergistic approach using microalgae for bioremediation and biomass generation. *Int. J. Environ. Sci. Technol.* 12, 1443–1460. doi:10.1007/s13762-014-0700-2

Reymann, T., Kerner, M., and Kümmerer, K. (2020). Assessment of the biotic and abiotic elimination processes of five micropollutants during cultivation of the green microalgae Acutodesmus obliquus. *Bioresour. Technol. Rep.* 11, 100512. doi:10.1016/j.biteb.2020.100512

Rezania, S., Taib, S. M., Din, M. F. M., Dahalan, F. A., and Kamyab, H. (2016). Comprehensive review on phytotechnology: heavy metals removal by diverse aquatic plants species from wastewater. *J. Hazard. Mater.* 318, 587–599. doi:10.1016/j.jhazmat.2016.07.053

Saha, I., Datta, S., and Biswas, D. (2023). Mechanistic approach on comparative biosorption of dyes by extracellular polymer of Ochrobactrum pseudintermedium C1 utilizing waste mineral lubricating oil. *Bioremedia. Journal.* 28 (3), 266–285. doi:10.1080/10889868.2023.2269220

Sankaran, R., Cruz, R. A. P., Pakalapati, H., Show, P. L., Ling, T. C., Chen, W.-H., et al. (2020). Recent advances in the pretreatment of microalgal and lignocellulosic biomass: a comprehensive review. *Bioresour. Technol.* 298, 122476. doi:10.1016/j.biortech.2019.122476

Sarkar, P., and Dey, A. (2021). Phycoremediation–an emerging technique for dye abatement: an overview. *Process Saf. Environ. Prot.* 147, 214–225. doi:10.1016/j.psep.2020.09.031

Semple, K. T., Cain, R. B., and Schmidt, S. (1999). Biodegradation of aromatic compounds by microalgae. *FEMS Microbiol. Lett.* 170, 291–300. doi:10.1016/s0378-1097(98)00544-8

Shen, Q.-H., Zhi, T.-T., Cheng, L.-H., Xu, X.-H., and Chen, H.-L. (2013). Hexavalent chromium detoxification by nonliving Chlorella vulgaris cultivated under tuned conditions. *Chem. Eng. J.* 228, 993–1002. doi:10.1016/j.cej.2013.05.074

Shitu, A., Tadda, M. A., Zhao, J., Danhassan, U. A., Ye, Z., Liu, D., et al. (2024). Review of recent advances in utilising aquaculture wastewater for algae cultivation and microalgae-based bioproduct recovery. *Environ. Geochem Health* 46 (12), 485. doi:10.1007/s10653-024-02286-8

Sutherland, D. L., Howard-Williams, C., Turnbull, M. H., Broady, P. A., and Craggs, R. J. (2015). Enhancing microalgal photosynthesis and productivity in wastewater treatment high rate algal ponds for biofuel production. *Bioresour. Technol.* 184, 222–229. doi:10.1016/j.biortech.2014.10.074

Sutherland, D. L., and Ralph, P. J. (2019). Microalgal bioremediation of emerging contaminants-Opportunities and challenges. *Water Res.* 164, 114921. doi:10.1016/j.watres.2019.114921

Tiwari, B., Sellamuthu, B., Ouarda, Y., Drogui, P., Tyagi, R. D., and Buelna, G. (2017). Review on fate and mechanism of removal of pharmaceutical pollutants from wastewater using biological approach. *Bioresour. Technol.* 224, 1–12. doi:10.1016/j.biortech.2016.11.042

Torres, M. A., Barros, M. P., Campos, S. C., Pinto, E., Rajamani, S., Sayre, R. T., et al. (2008). Biochemical biomarkers in algae and marine pollution: a review. *Ecotoxicol. Environ. Saf.* 71, 1–15. doi:10.1016/j.ecoenv.2008.05.009

Tran, N. H., Reinhard, M., and Gin, K. Y. (2018). Occurrence and fate of emerging contaminants in municipal wastewater treatment plants from different geographical regions-a review. *Water Res.* 133, 182–207. doi:10.1016/j.watres.2017.12.029

Tüzün, İ., Bayramoğlu, G., Yalçın, E., Başaran, G., Celik, G., and Arıca, M. Y. (2005). Equilibrium and kinetic studies on biosorption of Hg (II), Cd (II) and Pb (II) ions onto microalgae Chlamydomonas reinhardtii. *J. Environ. Manag.* 77, 85–92. doi:10.1016/j.jenvman.2005.01.028

Umamaheswari, J., and Shanthakumar, S. (2016). Efficacy of microalgae for industrial wastewater treatment: a review on operating conditions, treatment efficiency and biomass productivity. *Rev. Environ. Sci. bio/technology* 15, 265–284. doi:10.1007/s11157-016-9397-7

Ummalyma, S. B., Mathew, A. K., Pandey, A., and Sukumaran, R. K. (2016). Harvesting of microalgal biomass: efficient method for flocculation through pH modulation. *Bioresour. Technol.* 213, 216–221. doi:10.1016/j.biortech.2016.03.114

United Nations (2019). *The united Nations world water development report 2023: partnerships and cooperation for water*. Paris: UNESCO.

United Nations (2022). Sustainable development goals. Available at: https://sdgs.un.org/goals August 17, 2022).

Vardhan, K. H., Kumar, P. S., and Panda, R. C. (2019). A review on heavy metal pollution, toxicity and remedial measures: current trends and future perspectives. *J. Mol. Liq.* 290, 111197. doi:10.1016/j.molliq.2019.111197

Varjani, S. J. (2017). Microbial degradation of petroleum hydrocarbons. *Bioresour. Technol.* 223, 277–286. doi:10.1016/j.biortech.2016.10.037

Villar-Navarro, E., Baena-Nogueras, R. M., Paniw, M., Perales, J. A., and Lara-Martín, P. A. (2018). Removal of pharmaceuticals in urban wastewater: high rate algae pond (HRAP) based technologies as an alternative to activated sludge based processes. *Water Res.* 139, 19–29. doi:10.1016/j.watres.2018.03.072

Wanda, E. M., Nyoni, H., Mamba, B. B., and Msagati, T. A. (2017). Occurrence of emerging micropollutants in water systems in gauteng, mpumalanga, and North west provinces, South Africa. *Int. J. Environ. Res. public health* 14, 79. doi:10.3390/ijerph14010079

Wang, C.-Y., Fu, C.-C., and Liu, Y.-C. (2007). Effects of using light-emitting diodes on the cultivation of Spirulina platensis. *Biochem. Eng. J.* 37, 21–25. doi:10.1016/j.bej.2007.03.004

Wang, Y., Ho, S.-H., Cheng, C.-L., Guo, W.-Q., Nagarajan, D., Ren, N.-Q., et al. (2016). Perspectives on the feasibility of using microalgae for industrial wastewater treatment. *Bioresour. Technol.* 222, 485–497. doi:10.1016/j.biortech.2016.09.106

Whitton, R., Ometto, F., Pidou, M., Jarvis, P., Villa, R., and Jefferson, B. (2015). Microalgae for municipal wastewater nutrient remediation: mechanisms, reactors and outlook for tertiary treatment. *Environ. Technol. Rev.* 4, 133–148. doi:10.1080/21622515.2015.1105308

Wollmann, F., Dietze, S., Ackermann, J. U., Bley, T., Walther, T., Steingroewer, J., et al. (2019). Microalgae wastewater treatment: biological and technological approaches. *Eng. Life Sci.* 19, 860–871. doi:10.1002/elsc.201900071

World Health Organization (2024). Water, sanitation and hygiene (WASH). Available at: https://www.who.int/health-topics/water-sanitation-and-hygiene-wash#tab=tab_1 (accessed on December 6, 2024).

Xiong, J.-Q., Kurade, M. B., Abou-Shanab, R. A., Ji, M.-K., Choi, J., Kim, J. O., et al. (2016). Biodegradation of carbamazepine using freshwater microalgae Chlamydomonas mexicana and Scenedesmus obliquus and the determination of its metabolic fate. *Bioresour. Technol.* 205, 183–190. doi:10.1016/j.biortech.2016.01.038

Xiong, J.-Q., Kurade, M. B., and Jeon, B.-H. (2018). Can microalgae remove pharmaceutical contaminants from water? *Trends Biotechnol.* 36, 30–44. doi:10.1016/j.tibtech.2017.09.003

Zhang, C., Wang, X., Ma, Z., Luan, Z., Wang, Y., Wang, Z., et al. (2020a). Removal of phenolic substances from wastewater by algae. A review. *Environ. Chem. Lett.* 18, 377–392. doi:10.1007/s10311-019-00953-2

Zhang, S., Xiao, J., Wang, G., and Chen, G. (2020b). Enzymatic hydrolysis of lignin by ligninolytic enzymes and analysis of the hydrolyzed lignin products. *Bioresour. Technol.* 304, 122975. doi:10.1016/j.biortech.2020.122975

Zhang, S.-Y., Sun, G.-X., Yin, X.-X., Rensing, C., and Zhu, Y.-G. (2013). Biomethylation and volatilization of arsenic by the marine microalgae Ostreococcus tauri. *Chemosphere* 93, 47–53. doi:10.1016/j.chemosphere.2013.04.063

Zhang, X., Zhao, H., Du, J., Qu, Y., Shen, C., Tan, F., et al. (2017). Occurrence, removal, and risk assessment of antibiotics in 12 wastewater treatment plants from Dalian, China. *Environ. Sci. Pollut. Res. Int.* 24 (19), 16478–16487. doi:10.1007/s11356-017-9296-7

Zhang, Y., Habteselassie, M. Y., Resurreccion, E. P., Mantripragada, V., Peng, S., Bauer, S., et al. (2014). Evaluating removal of steroid estrogens by a model alga as a possible sustainability benefit of hypothetical integrated algae cultivation and wastewater treatment systems. *ACS Sustain. Chem. and Eng.* 2, 2544–2553. doi:10.1021/sc5004538

frontiers | Frontiers in Analytical Science

TYPE Perspective
PUBLISHED 03 January 2025
DOI 10.3389/frans.2024.1512573

OPEN ACCESS

EDITED BY
Makusu Tsutsui,
Osaka University, Japan

REVIEWED BY
Liam McDonnell,
Fondazione Pisana per la Scienza Onlus, Italy

*CORRESPONDENCE
Ernesto S. Nakayasu,
ernesto.nakayasu@pnnl.gov

RECEIVED 16 October 2024
ACCEPTED 06 December 2024
PUBLISHED 03 January 2025

CITATION
You Y, Many G and Nakayasu ES (2025) Protein carbamylation and proteomics: from artifacts to elucidation of biological functions.
Front. Anal. Sci. 4:1512573.
doi: 10.3389/frans.2024.1512573

Protein carbamylation and proteomics: from artifacts to elucidation of biological functions

Youngki You, Gina Many and Ernesto S. Nakayasu*

Biological Sciences Division, Pacific Northwest National Laboratory, Richland, WA, United States

Lysine carbamylation is a non-enzymatic protein post-translational modification (PTM) that plays important roles in regulating enzymatic activity and the pathogenesis of diseases such as atherosclerosis, rheumatoid arthritis, and uremia. The progress of understanding the roles of carbamylation in biological systems has been delayed due to lack of systematic assays to study its functions. To aggravate this scenario, carbamylation is a major artifact in proteomics analysis given that urea, which is used during sample preparation, induces carbamylation. In addition, anti-acetyllysine antibodies co-purify carbamylated and acetylated peptides. In a recent paper, we leveraged co-purification with anti-acetyllysine antibodies to develop a method for analyzing carbamylated proteomes. In this perspective article, we discuss how this method may be applied to characterize the physiological functions of carbamylation in humans and other biological models, as well as the utility of establishing novel disease biomarkers.

KEYWORDS

carbamylation, post-translational modification, proteomics, function, disease

1 Introduction

Post-translational modifications (PTMs) of proteins expand the repertoire properties of the 21 genetically coded amino acids. These modifications are critical for regulating protein function, activity, localization, interaction, and turnover. To date, there are over 400 known PTMs (Li et al., 2022), but most of the knowledge is concentrated around a few modifications, such as phosphorylation, glycosylation, acetylation, and ubiquitination. Carbamylation is a PTM that occurs via nonenzymatic modification of the amine groups of protein N-terminus or lysine side chains. Lysine carbamylation has been identified as an important regulator of disease development and thus serves as a biomarker. Mechanistically, carbamylation regulates protein/enzyme activity, gene expression, cell signaling and metabolism (Figure 1A). Mass spectrometry-based proteomic analysis provides an instrumental resource for discovering novel roles of protein PTMs, including carbamylation in biological systems. However, protein carbamylation is a major artifact in proteomics sample preparation, representing a major challenge. In this perspective article, we describe recent developments in proteomics analysis of protein carbamylation as well as opportunities and needs to advance the field.

10.3389/frans.2024.1512573

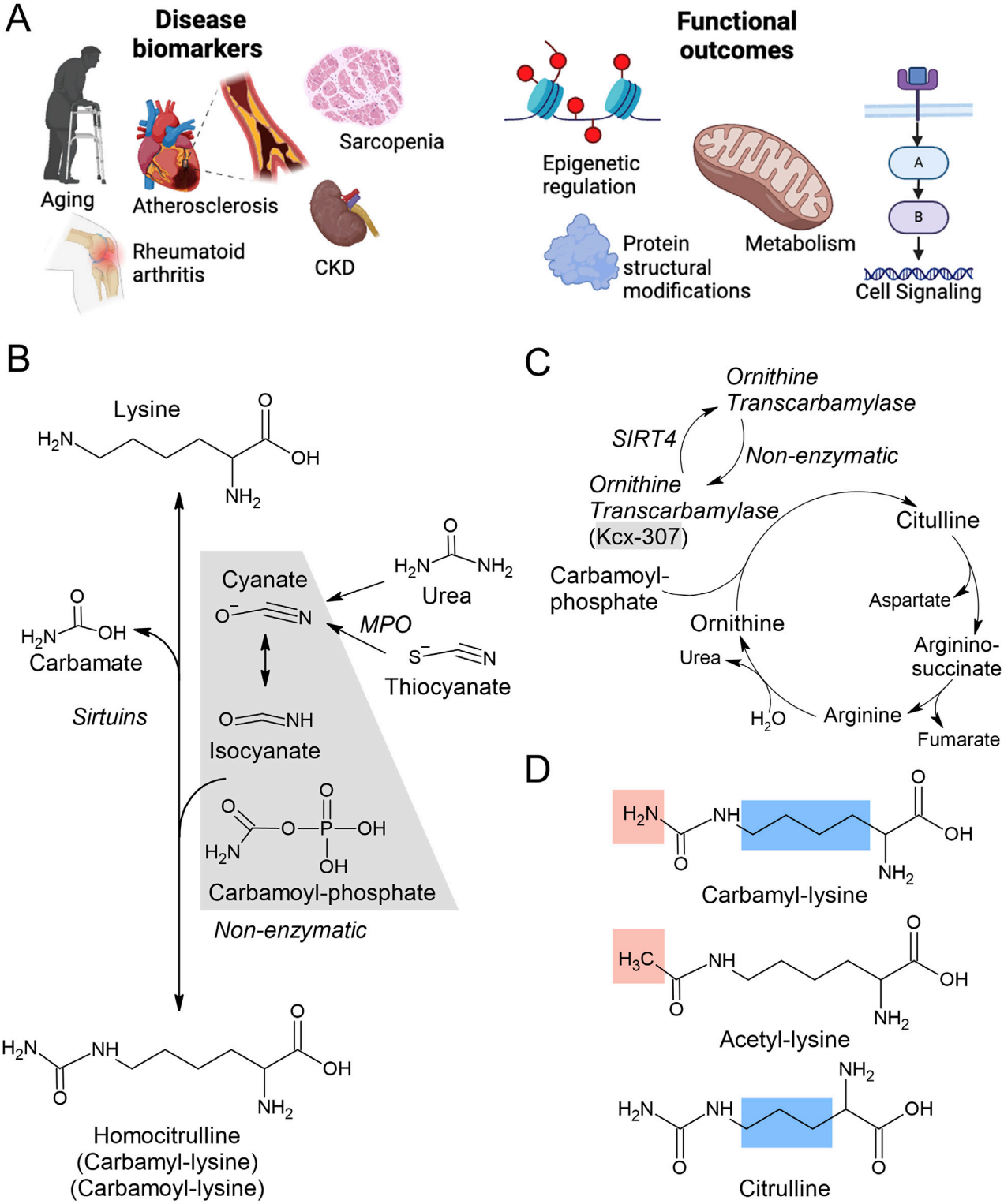

FIGURE 1
Lysine carbamylation. **(A)** Biological functions of protein carbamylation. **(B)** Mechanism of protein carbamylation and decarbamylation. MPO; Myeloperoxidase. **(C)** A role of carbamylation on ornithine transcarbamylase in the urea cycle. Kcx-307; carbamylated lysine-307 **(D)** Structure of carbamyl-lysine and related molecules. The structural differences are highlighted by the colors.

2 Mechanism of protein carbamylation and de-carbamylation

The current mechanisms for known to induce lysine carbamylation are non-enzymatic reaction of cyanate, isocyanate or carbamoyl-phosphate that adds a carbamoyl moiety ($-CONH_2$) forming $N^{\varepsilon'}$-carbamyl-lysine (also known as carbamoyl-lysine or homocitrulline) (Figure 1B). Cyanate and isocyanate are formed by upstream degradation of urea or by oxidation of thiocyanate by myeloperoxidase (MPO) (Figure 1B) (Verbrugge et al., 2015). In the case of carbamoyl-phosphate, this is a natural metabolite of the organism, being an intermediate of the urea cycle and the *de novo* pyrimidine biosynthesis pathway (Joshi et al., 2015; Matsumoto et al., 2019; Chen et al., 2023). Carbamylation activates ornithine transcarbamylase (Hu et al., 2023), the first step of the urea cycle, by transferring the carbamyl moiety from carbamoyl phosphate to ornithine to produce citrulline (Figure 1C). Citrulline is converted to arginine by argininosuccinate lyase, which is consequently cleaved by arginase to release urea and recycle ornithine (Figure 1C) (Matsumoto et al., 2019). The released urea is excreted into urine to detoxify the body from nitrogen (Matsumoto et al., 2019). This mechanism is regulated by sirtuins, specifically, SIRT4 (Hu et al., 2023). SIRT4 removes carbamylation from ornithine transcarbamylase, reducing its activity (Figure 1C) (Hu et al., 2023). However, in amino acid excess (the main source of nitrogen in the body), SIRT4 expression is downregulated to increase urea production and excretion (Hu et al., 2023). In humans, the sirtuin family comprises of 7 enzymes that cleave multiple acyl groups from lysine residues, including acetylation, lactylation, and malonylation (Bheda et al., 2016). Therefore, it is possible that other members of this family also have decarbamylase activity. Sirtuins are part of a much larger group of proteins named histone deacetylases (HDACs) (Park and Kim, 2020); yet the decarbamylase activity of other HDACs has not been investigated. Therefore, the current literature suggests that lysine carbamylation occurs through non-enzymatic mechanisms, while its removal being catalyzed by enzymes, such as SIRT4. However, it is possible that other enzymes, particularly within HDAC families, may also exhibit decarbamylase activity.

3 From *in vitro* artifact to opportunities to study functions of carbamylation

The use of various buffers, detergents, and salts for efficient cell lysis and protein extraction is fundamental in proteomics. Urea, a common denaturing agent, was first used in protein denaturation in the early 20th century (Mirsky and Pauling, 1936) and has been used for proteomics since the 1990s (Henzel et al., 1993; Shevchenko et al., 1996). Urea effectively denatures and solubilizes proteins; however, it also induces carbamylation, an artifact that can mislead protein analysis results. Carbamylation occurs when urea decomposes into cyanate in aqueous solutions, which then reacts with N-terminal amino groups and the side chains of lysines (Figure 1B) (Marier and Rose, 1964; Kollipara and Zahedi, 2013). This artifact not only alters carbamylation levels in target proteins but also disrupts quantitative chemical labeling (e.g., tandem mass tags), blocks trypsin digestion, and modifies peptide charge, mass, and retention time (Stanfill et al., 2018). Moreover, artifactual carbamylated peptides negatively affect the enrichment of lysine-acetylated peptides during immuno-purification by competing for binding with anti-acetylated lysine antibodies. This cross-reaction is due to the structural similarities between carbamyl- and acetyl-lysines (Figure 1D) (Martinez-Val et al., 2017). Several strategies can mitigate artifact carbamylation, such as adjusting temperature, pH, urea concentration, and incubation time. Freshly prepared urea and room temperature sample preparation significantly reduces carbamylation since urea decomposes faster into cyanate at higher temperatures (Wisniewski et al., 2009). Detergents like sodium deoxycholate (SDC) can be used as an alternative to urea to avoid protein carbamylation. SDC improves protein denaturation and solubilization, increasing the number of detected proteins and enhancing spectra quality (Lau and Othman, 2019; Lin et al., 2008; Masuda et al., 2008; León et al., 2013; Shahinuzzaman et al., 2020). Using SDC limits carbamylation to endogenous levels, with studies showing over a 67% reduction in carbamylated lysine residues compared to urea-based buffers (Martinez-Val et al., 2017; Lau and Othman, 2019). Recently, we used SDC to avoid artifactual carbamylation and leveraged the copurification of carbamylated peptides using anti-acetylated lysine antibodies (You et al., 2023). We tested the approach to study the role of carbamylation in inflammation using a macrophage cell line treated with bacterial lipopolysaccharide (LPS). Quantitative analysis revealed 2,378 endogenously carbamylated peptides, 360 of which were regulated by LPS. Functional-enrichment analysis indicates that these proteins are involved in diverse cellular processes from metabolism to signaling pathways. We also found that carbamylation regulates ubiquitination machinery (You et al., 2023). Overall, the use of non-carbamylating denaturing agents, such as SDC, prevents the formation of artifactual carbamylation and the use of anti-acetyl-lysine antibodies enables a comprehensive analysis of the carbamylated proteome. This opens opportunities to discover new roles for protein carbamylation, evidenced by our discovery of carbamylation regulation of ubiquitination machinery.

4 Role of protein carbamylation in regulating enzymatic activity

As mentioned above for ornithine transcarbamylase, lysine carbamylation is a regulator of enzymatic activity. Carbamylation is also a component of enzyme catalytic sites. For instance, ureases bear a carbamylated lysine along with multiple histidines, and an aspartate in their catalytic site, which coordinate two metal ions (Proshlyakov et al., 2021). Most of the known ureases have two nickel ions but others have two iron ions, which induce the cleave and release of ammonia from urea (Figure 2A) (Proshlyakov et al., 2021). Similarly, most of the members of the cyclic amidohydrolase family have a carbamylated lysine in their catalytic site that coordinates metal ion binding (Guan et al., 2021; Huang, 2020; Huang et al., 2023). This family includes allantoinase, dihydroorotase, dihydropyrimidinase, hydantoinase, and imidase (Figure 2B) (Guan et al., 2021; Huang, 2020; Huang et al., 2023). For instance, in the case of *Escherichia coli* allantoinase,

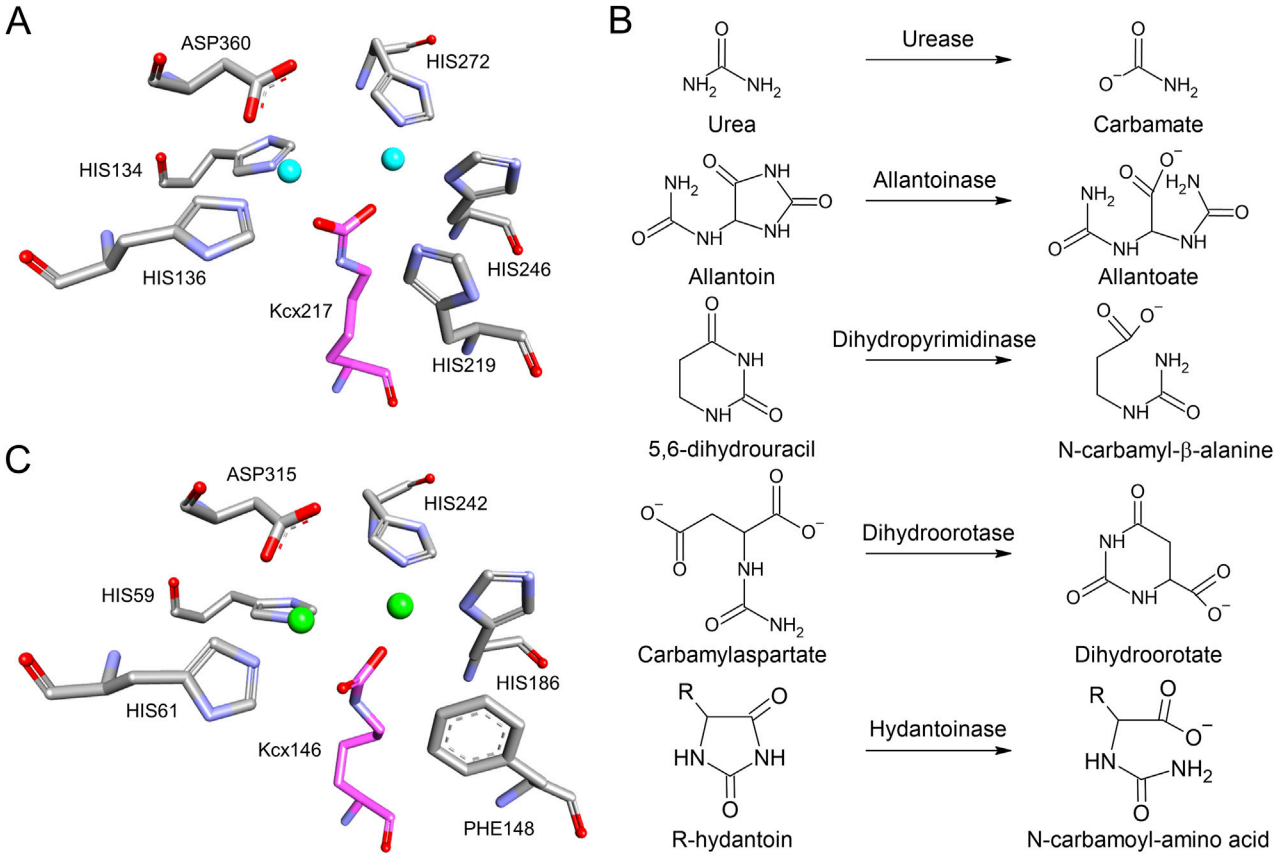

FIGURE 2
Carbamylated lysine in enzyme catalytic sites. **(A)** The catalytic site of urease from *K. aerogenes* (PDB 1FWJ). Nikel ions are presented by cyan spheres. **(B)** Substrates and products of urease and the cyclic amidohydrolase family, which have carbamylated lysine in their catalytic sites. **(C)** The catalytic site of *E. coli* allantoinase (PDB 8HFD). Zinc ions are presented by green spheres. Carbamyl-lysine is colored by magenta.

the catalytic site is composed of four histidines, one aspartate and one carbamylated lysine that coordinate two zinc ions (Figure 2C) (Huang et al., 2023). Therefore, lysine carbamylation is an important structural component of the catalytic site of the cyclic amidohydrolase family, helping in their activity of opening or closing the rings of their substrates (Guan et al., 2021; Huang, 2020; Huang et al., 2023). It might not be a coincidence that the cyclic aminohydrolases have similar mechanism than urease, their substrates are all ureides (Figure 2B). It is possible that elevated urea concentrations induce carbamylation, leading to the activation of these enzymes.

Another mechanism by which carbamylation regulates enzymatic activity is by modifying substrates and preventing them to be used or recognized by the enzymes. For example, carbamylation of ubiquitin blocks the formation of polyubiquitin chains (Pawloski et al., 2022). This can have detrimental effects on cells, as polyubiquitination regulates a variety of cellular processes, including targeting proteins for degradation in the proteasome. Indeed, carbamylated proteins are not degraded in the proteasome and accumulate in cells (Desmons et al., 2019). Carbamylation also affects the de-polymerization of polyubiquitin chains (You et al., 2023). We have recently shown that carbamylation of M1-linked diubiquitin blocks it from being cleaved by the deubiquitinase OTULIN (You et al., 2023). In summary, carbamylation has important roles in regulating enzymatic activity. The advances in carbamylated proteomics analysis will enable to further study the role of carbamylation in other enzymes and proteins with other functions.

5 Protein carbamylation as biomarker and mechanistic transducer of diseases

In vivo carbamylation can be mediated by myeloperoxidase, a critical inducer of neutrophile extracellular trap (NET) formation, and by urea-derived cyanate (Figure 1B). MPO-mediated protein carbamylation is implicated in the pathogenesis of numerous diseases such as atherosclerosis, rheumatoid arthritis, periodontitis, and chronic kidney disease (Wang et al., 2007; Shi et al., 2011; Gorisse et al., 2016). MPO-induced carbamylation of lipoproteins is implicated in the pathogenesis of atherosclerosis (Wang et al., 2007). MPO is enriched in atherosclerotic lesions (Hazen, 2004) and has been shown to carbamylate low-density lipoprotein (LDL) and cardioprotective high density lipoprotein (HDL), resulting in proatherosclerotic conversion of HDL (Denimal, 2023). Carbamylated HDL is elevated in both type 1

(T1D) and type 2 diabetes (T2D), where it correlates to patient cardiovascular risk in T2D and glycemic control in T1D (Denimal, 2023). Carbamylated LDL is also elevated in T2D prior to kidney dysfunction, where it has been shown to directly induce epithelial cell death, suggestive of a central role of carbamylation in the concurrent pathogenesis of T2D, atherosclerosis, and chronic kidney disease (Shiu et al., 2014; Ok et al., 2005). Carbamylated LDL promotes thrombus formation, oxidative stress, and endothelial nitric oxide synthase uncoupling (Denimal, 2023). Smoking promotes MPO-mediated carbamylation and is thought to be a critical mediator of smoking-induced atherosclerosis (Wang et al., 2007). Given de-carbamylation is dependent on enzyme availability and often modifies proteins with long half-lives, including extracellular matrix proteins, carbamylation has been proposed as a biomarker of aging as its tissue accumulation is inversely associated with lifespan (Gorisse et al., 2016). Such associations of this PTM with the pathogenesis of numerous diseases make the development of methods to study carbamylation critical. While we have outlined several lines of evidence, suggesting the overall biological significance of carbamylation, further developments enabling high throughput analysis of global protein carbamylation is needed to characterize its biological significance, regulation, and function.

Given anti-citrullinated protein antibodies (ACPAs) are well-established biomarkers of rheumatoid arthritis (RA), antibodies to other PTMs, such as carbamylated proteins have also been explored as disease biomarkers. Citrullination and carbamylation result in the structurally similar PTMs citrulline and carbamyl-lysine, respectively (Figure 1D). While less well-explored, anti-carbamylated protein (anti-CarP) antibodies are detected in nearly half of patients with RA and may serve as useful biomarkers to predict both preclinical disease and disease progression to bone erosion (Shi et al., 2011; O'Neil et al., 2020). Such PTMs accumulate over time and are especially long-lived in the joint given the slow turnover of extracellular matrix proteins in the articular cartilage of synovial joints. In transgenic mice overexpressing the humanized RA MHC II HLADRB1* 04:01, NETs externalize carbamylated peptides and induce anti-carbamylated antibody responses (O'Neil et al., 2020). However, protein carbamylation in the inflamed human joint has not been thoroughly investigated (McHugh, 2023). Several other studies have suggested a role of carbamylated proteins in autoimmunity. *Ex vivo* cell culture models have shown that carbamylation of vimentin induces T-cell reactivity as indicated by IFNγ production (Choudhury et al., 2023). Carbamylated aldolase and cytokeratin display increased MHC I binding affinity compared to non-modified proteins (Shah et al., 2023). It appears that not all individuals with RA that are ACPA-positive display anti-CarP antibodies. In systemic lupus erythematosus (SLE), anti-CarP antibodies correlate with markers of systemic inflammation and arthralgia (Li et al., 2020). A consequence of many autoimmune diseases includes progressive aging phenotypes, such as early-onset of age-related muscle wasting (sarcopenia) and cardiometabolic disease, both of which target striated muscle. However, the mechanisms leading to such phenotypes are mainly described as chronic inflammation-related and lack well-defined targets aside from anti-inflammatory therapeutics primarily targeting direct disease activity (Casanova-Vallve et al., 2020; Mehta et al., 2023). Tissue-specific neutrophil activation and NET formation are implicated in cardiovascular and sarcopenic phenotypes that are increased in autoimmune diseases (Ma, 2021; Nie et al., 2024). For example, skeletal muscle IL-8 abundance, an activator of neutrophil NET formation, correlates to disease activity in RA patients (Huffman et al., 2017). In patients with heart failure with dilated cardiomyopathy, cardiac NET abundance correlates with cardiac dysfunction and clinical outcomes (Ichimura et al., 2024). Together, these data suggest a potential role of carbamylation in mediating the pathogenesis and severity of both cardiometabolic and autoimmune disease phenotypes and highlight the vast clinical utility of studying protein carbamylation as a molecular regulator and target in human diseases.

6 Future directions

6.1 Technical needs

Co-purification of acetylated and carbamylated peptides with anti-acetyl-lysine antibodies facilitated our method development for analyzing carbamylated proteomes (You et al., 2023). This method also provides a future opportunity to integrate multiple PTMs in proteomic analyses as carbamylation and acetylation data can be obtained simultaneously. However, the similar masses of lysine acetylation (+42.0103 Da) and carbamylation (+43.00543 Da) represents a challenge for reliable peptide identification. This is especially relevant when comparing carbamylation to the ^{13}C isotope of acetylation +43.0137 Da, only an 8 mDa difference. Isotopic correction, mass recalibration, and narrow mass error tolerances during peptide identification can reduce misidentification (You et al., 2023). To improve identification reliability, peptides can be validated by the presence of characteristic fragments in the tandem mass spectrum. For instance, the fragmentation of acetyl-lysines generates a fragment at m/z 126.1 (Nakayasu et al., 2014). This fragment is present in 98% of the acetylated peptide tandem mass spectra (Trelle and Jensen, 2008), but absent in tandem mass spectra of carbamylated peptides (Guo et al., 2018). A diagnostic fragment for carbamylation has not been described yet, but as more data becomes available, it opens the opportunity of performing systematic studies on the fragmentation patterns (Geiszler et al., 2023). This can improve the annotation of spectra from carbamylated peptides.

The development of specific affinity purification methods for carbamylated peptides provides the opportunity to reduce misidentification and may even improve proteome coverage as the sample complexity would be reduced. This is a challenging issue because the antibodies should have a broad specificity to enrich carbamylated peptides, but at the same time should distinguish carbamylation from acetylation and citrullination. We have previously tested one anti-carbamylation antibody conjugated to agarose beads (Cayman), but it was not ideal for proteomics analysis and only yielded identification of 128 carbamylated peptides (unpublished observations). Another point to consider is that carbamylated antibodies display significant cross-reactivity with citrullinated peptides. For instance, Sahlström et al. tested 12 anti-citrullination monoclonal antibodies and observed half

(6) to display significant cross-reactivity to protein carbamylation (Sahlstrom et al., 2020). Therefore, there is a need to systematically test anti-carbamylation antibody specificity and performance to develop proteomics assays.

As mentioned above, the method developed for analyzing carbamylation has already enabled the discovery of new functions for this PTM. However, there are remaining technical needs for the development of reliable carbamylated peptide identification and enrichment methods.

6.2 Metabolic regulation and cell signaling

Increasing carbamylated proteome coverage will open opportunities to study the role of this PTM in metabolic regulation and cell signaling. The current literature demonstrates that carbamylation regulates nitrogen metabolism, including the urea cycle and metabolism of ureides. The fact that carbamylation is non-enzymatic, makes us believe that it may result in lysine modifications in catalytic or co-factor-binding sites of enzymes. Such modifications could then activate the enzymes, such as ureases and cyclic amidohydrolases, or inhibit enzymes that require the free primary amine groups of the lysine residues. We have identified similar mechanism in which acetylation modifies and subsequently inhibits enzymes involved in the central carbon metabolism in bacteria (Nakayasu et al., 2017).

Similar to acetylation, carbamylation is implicated in many cell-signaling processes as well. For instance, recognition of carbamylated TLR5 by anti-carbamylated protein autoantibodies induces receptor activation and pro-inflammatory signaling. Another example is the suppression of mTOR signaling by carbamylation (Wang et al., 2019). In chronic kidney disease, high urea levels are associated with depression by inducing the carbamylation of mTOR, which leads to loss of neuronal synapses (Wang et al., 2019). In-depth carbamylated proteome analysis integrated with other PTMs will be instrumental for determining new roles for carbamylation in cell signaling. A multi-PTM approach facilitates comprehensive characterization of differential pathway regulation by different PTMs. Our current method analyzes carbamylation and acetylation simultaneously, and additional PTMs can be easily obtained by sequential purification on the same sample, spurring additional mechanistic insight. In our previous work, we combined carbamylation, acetylation, and phosphorylation to identify a function of carbamylation in regulating ubiquitination machinery (You et al., 2023). In addition to multi-omics integration, structural analysis is instrumental for identifying important carbamylated modification sites. Modifications on catalytic or cofactor-binding sites, as well in interacting regions and activation loops on proteins can provide key functional information for PTMs. We have used such approach to study the role of PTMs in bacteria and to discover how carbamylation on ubiquitin regulates the activity of the deubiquitinase OTULIN (You et al., 2023; Nakayasu et al., 2017; Feid et al., 2022; Walukiewicz et al., 2024). In summary, we believe that analysis of carbamylated proteomes integrated with other omics and structural analyses will have major impact in discovery new roles for carbamylation in regulating the cell metabolism and signaling.

6.3 Gene expression regulation

Histones are among the most carbamylated proteins. In neutrophils, MPO produces cyanate that induces histone carbamylation (O'Neil et al., 2020). Histone carbamylation is also induced by carbamoyl-phosphate produced by carbamoyl-phosphate synthase located in the nucleus of the cell (Joshi et al., 2015). Similar to acetylation, carbamylation also promotes transcriptional activation (Joshi et al., 2015). However, it is not known whether acetylation and carbamylation share the same transcription regulators or how the dynamics between these two modifications regulate transcription. Similar to how mass spectrometry contributes to understanding the role of acetylation and other PTMs on histones, it will likely provide insight into the functional role of carbamylation on gene regulation. Mass spectrometry analysis of carbamylated histone proteins can provide a detailed view of the functional role of PTMs in disease pathogenesis and treatment. The combination of these PTM signatures with chromatin immunoprecipitation with sequencing (ChIP-seq), assay for transposase-accessible chromatin with sequencing (ATAC-seq), and RNA sequencing should illustrate transcriptional network regulation by carbamylation. In addition, affinity purification-mass spectrometry (AP-MS) can be used to discover factors that bind to carbamylated proteins, facilitating the identification of transcription factors that are regulated by carbamylation. Furthermore, mass spectrometry can be used to discover decarbamylases, which may play a role in downregulating gene expression. Overall, mass spectrometry will be instrumental in determining the roles of carbamylation in the regulation of gene expression.

6.4 Biomarkers

Current and future advances in protein carbamylation analysis mass spectrometry will also have an impact on biomarker discovery and validation. As discussed above, carbamylation is involved in a variety of conditions, making carbamylated proteins promising biomarkers. In biomarker studies, it is often crucial to prepare and analyze hundreds to thousands of samples. A recently developed automated platform to enrich for acetylated peptides can be applied to carbamylation analysis in the future (Gritsenko et al., 2024). This automated enrichment platform with the increased speed of the new generations of LC-MS, allows for the analysis of dozens to hundreds of samples a day. Therefore, the current technology is ready for carrying out large scale biomarker studies of protein carbamylation.

7 Conclusion

Lysine carbamylation has a variety of roles in human physiology and disease pathogenesis. However, progress in comprehensively understanding the role and mechanisms of protein carbamylation in health and disease has been slow given it is a major artifact in proteomic analyses. Development of workflows to perform carbamylation/acetylation proteomics opens many opportunities to study the roles of carbamylation in health and in disease.

Further optimization of proteomic analyses along with multi-PTM integration will further advance our understanding of the functional role of protein carbamylation.

Data availability statement

The original contributions presented in the study are included in the article/supplementary material, further inquiries can be directed to the corresponding author.

Author contributions

YY: Conceptualization, Visualization, Writing–original draft, Writing–review and editing. GM: Conceptualization, Visualization, Writing–original draft, Writing–review and editing. EN: Conceptualization, Funding acquisition, Visualization, Writing–original draft, Writing–review and editing.

Funding

The author(s) declare that financial support was received for the research, authorship, and/or publication of this article. This work was supported by the Catalyst Award from the Human Islet Research Network (HIRN) (to EN) (via U24 DK104162) and by National Institutes of Health, National Institute of Diabetes and Digestive and Kidney Diseases (NIDDK) grants R01 DK138335 (to EN) and U01 DK127505 (to EN).

Conflict of interest

The authors declare that the research was conducted in the absence of any commercial or financial relationships that could be construed as a potential conflict of interest.

The author(s) declared that they were an editorial board member of Frontiers, at the time of submission. This had no impact on the peer review process and the final decision.

Generative AI statement

The authors declare that no Generative AI was used in the creation of this manuscript.

Publisher's note

References

Bheda, P., Jing, H., Wolberger, C., and Lin, H. (2016). The substrate specificity of sirtuins. *Annu. Rev. Biochem.* 85, 405–429. doi:10.1146/annurev-biochem-060815-014537

Casanova-Vallve, N., Constantin-Teodosiu, D., Filer, A., Hardy, R. S., Greenhaff, P. L., and Chapman, V. (2020). Skeletal muscle dysregulation in rheumatoid arthritis: metabolic and molecular markers in a rodent model and patients. *PLoS One* 15, e0235702. doi:10.1371/journal.pone.0235702

Chen, J., Yang, S., Li, Y., Ziwen, X., Zhang, P., Song, Q., et al. (2023). *De novo* nucleotide biosynthetic pathway and cancer. *Genes Dis.* 10, 2331–2338. doi:10.1016/j.gendis.2022.04.018

Choudhury, R. H., Daniels, I., Vaghela, P., Atabani, S., Kirk, T., Symonds, P., et al. (2023). Immune responses to citrullinated and homocitrullinated peptides in healthy donors are not restricted to the HLA SE shared allele and can be selected into the memory pool. *Immunology* 169, 467–486. doi:10.1111/imm.13645

Denimal, D. (2023). Carbamylated lipoproteins in diabetes. *World J. Diabetes* 14, 159–169. doi:10.4239/wjd.v14.i3.159

Desmons, A., Okwieka, A., Doue, M., Gorisse, L., Vuiblet, V., Pietrement, C., et al. (2019). Proteasome-dependent degradation of intracellular carbamylated proteins. *Aging (Albany NY)* 11, 3624–3638. doi:10.18632/aging.102002

Feid, S. C., Walukiewicz, H. E., Wang, X., Nakayasu, E. S., Rao, C. V., and Wolfe, A. J. (2022). Regulation of translation by lysine acetylation in *Escherichia coli*. *mBio* 13, e0122422. doi:10.1128/mbio.01224-22

Geiszler, D. J., Polasky, D. A., Yu, F., and Nesvizhskii, A. I. (2023). Detecting diagnostic features in MS/MS spectra of post-translationally modified peptides. *Nat. Commun.* 14, 4132. doi:10.1038/s41467-023-39828-0

Gorisse, L., Pietrement, C., Vuiblet, V., Schmelzer, C. E., Kohler, M., Duca, L., et al. (2016). Protein carbamylation is a hallmark of aging. *Proc. Natl. Acad. Sci. U. S. A.* 113, 1191–1196. doi:10.1073/pnas.1517096113

Gritsenko, M. A., Tsai, C. F., Kim, H., and Liu, T. (2024). Automated immunoprecipitation workflow for comprehensive acetylome analysis. *Methods Mol. Biol.* 2823, 173–191. doi:10.1007/978-1-0716-3922-1_12

Guan, H. H., Huang, Y. H., Lin, E. S., Chen, C. J., and Huang, C. Y. (2021). Structural analysis of *Saccharomyces cerevisiae* dihydroorotase reveals molecular insights into the tetramerization mechanism. *Molecules* 26, 7249. doi:10.3390/molecules26237249

Guo, C., Guo, X., Zhao, L., Chen, D., Wang, J., and Sun, J. (2018). Optimization of carbamylation conditions and study on the effects on the product ions of carbamylation and dual modification of the peptide by Q-TOF MS. *Eur. J. Mass Spectrom.* 24, 384–396. doi:10.1177/1469066718788665

Hazen, S. L. (2004). Myeloperoxidase and plaque vulnerability. *Arterioscler. Thromb. Vasc. Biol.* 24, 1143–1146. doi:10.1161/01.ATV.0000135267.82813.52

Henzel, W. J., Billeci, T. M., Stults, J. T., Wong, S. C., Grimley, C., and Watanabe, C. (1993). Identifying proteins from two-dimensional gels by molecular mass searching of peptide fragments in protein sequence databases. *Proc. Natl. Acad. Sci. U. S. A.* 90, 5011–5015. doi:10.1073/pnas.90.11.5011

Hu, S. H., Feng, Y. Y., Yang, Y. X., Ma, H. D., Zhou, S. X., Qiao, Y. N., et al. (2023). Amino acids downregulate SIRT4 to detoxify ammonia through the urea cycle. *Nat. Metab.* 5, 626–641. doi:10.1038/s42255-023-00784-0

Huang, C. Y. (2020). Structure, catalytic mechanism, posttranslational lysine carbamylation, and inhibition of dihydropyrimidinases. *Adv. Protein Chem. Struct. Biol.* 122, 63–96. doi:10.1016/bs.apcsb.2020.05.002

Huang, Y. H., Yang, P. C., Lin, E. S., Ho, Y. Y., Peng, W. F., Lu, H. P., et al. (2023). Crystal structure of allantoinase from *Escherichia coli* BL21: a molecular insight into a role of the active site loops in catalysis. *Molecules* 28, 827. doi:10.3390/molecules28020827

Huffman, K. M., Jessee, R., Andonian, B., Davis, B. N., Narowski, R., Huebner, J. L., et al. (2017). Molecular alterations in skeletal muscle in rheumatoid arthritis are related to disease activity, physical inactivity, and disability. *Arthritis Res. Ther.* 19, 12. doi:10.1186/s13075-016-1215-7

Ichimura, S., Misaka, T., Ogawara, R., Tomita, Y., Anzai, F., Sato, Y., et al. (2024). Neutrophil extracellular traps in myocardial tissue drive cardiac dysfunction and adverse outcomes in patients with heart failure with dilated cardiomyopathy. *Circ. Heart Fail* 17, e011057. doi:10.1161/CIRCHEARTFAILURE.123.011057

Joshi, A. D., Mustafa, M. G., Lichti, C. F., and Elferink, C. J. (2015). Homocitrullination is a novel histone H1 epigenetic mark dependent on aryl hydrocarbon receptor recruitment of carbamoyl phosphate synthase 1. *J. Biol. Chem.* 290, 27767–27778. doi:10.1074/jbc.M115.678144

Kollipara, L., and Zahedi, R. P. (2013). Protein carbamylation: *in vivo* modification or *in vitro* artefact? *Proteomics* 13, 941–944. doi:10.1002/pmic.201200452

Lau, B. Y. C., and Othman, A. (2019). Evaluation of sodium deoxycholate as solubilization buffer for oil palm proteomics analysis. *PLOS ONE* 14, e0221052. doi:10.1371/journal.pone.0221052

León, I. R., Schwämmle, V., Jensen, O. N., and Sprenger, R. R. (2013). Quantitative assessment of in-solution digestion efficiency identifies optimal protocols for unbiased protein analysis. *Mol. and Cell. Proteomics* 12, 2992–3005. doi:10.1074/mcp.M112.025585

Li, Y., Jia, R., Liu, Y., Tang, S., Ma, X., Shi, L., et al. (2020). Antibodies against carbamylated vimentin exist in systemic lupus erythematosus and correlate with disease activity. *Lupus* 29, 239–247. doi:10.1177/0961203319897127

Li, Z. Y., Li, S. F., Luo, M. Q., Jhong, J. H., Li, W. S., Yao, L. T., et al. (2022). dbPTM in 2022: an updated database for exploring regulatory networks and functional associations of protein post-translational modifications. *Nucleic Acids Res.* 50, D471–D479. doi:10.1093/nar/gkab1017

Lin, Y., Zhou, J., Bi, D., Chen, P., Wang, X. C., and Liang, S. P. (2008). Sodium-deoxycholate-assisted tryptic digestion and identification of proteolytically resistant proteins. *Anal. Biochem.* 377, 259–266. doi:10.1016/j.ab.2008.03.009

Ma, Y. (2021). Role of neutrophils in cardiac injury and repair following myocardial infarction. *Cells* 10, 1676. doi:10.3390/cells10071676

Marier, J. R., and Rose, D. (1964). Determination of cyanate, and a study of its accumulation in aqueous solutions of urea. *Anal. Biochem.* 7, 304–314. doi:10.1016/0003-2697(64)90135-6

Martinez-Val, A., Garcia, F., Ximénez-Embún, P., Martínez Teresa-Calleja, A., Ibarz, N., Ruppen, I., et al. (2017). Urea artifacts interfere with immuno-purification of lysine acetylation. *J. Proteome Res.* 16, 1061–1068. doi:10.1021/acs.jproteome.6b00463

Masuda, T., Tomita, M., and Ishihama, Y. (2008). Phase transfer surfactant-aided trypsin digestion for membrane proteome analysis. *J. Proteome Res.* 7, 731–740. doi:10.1021/pr700658q

Matsumoto, S., Haberle, J., Kido, J., Mitsubuchi, H., Endo, F., and Nakamura, K. (2019). Urea cycle disorders-update. *J. Hum. Genet.* 64, 833–847. doi:10.1038/s10038-019-0614-4

McHugh, J. (2023). Carbamylated NETs promote bone erosion in RA. *Nat. Rev. Rheumatol.* 19, 193. doi:10.1038/s41584-023-00938-0

Mehta, P. K., Levit, R. D., Wood, M. J., Aggarwal, N., O'Donoghue, M. L., Lim, S. S., et al. (2023). Chronic rheumatologic disorders and cardiovascular disease risk in women. *Am. Heart J. Plus* 27, 100267. doi:10.1016/j.ahjo.2023.100267

Mirsky, A. E., and Pauling, L. (1936). On the structure of native, denatured, and coagulated proteins. *Proc. Natl. Acad. Sci.* 22, 439–447. doi:10.1073/pnas.22.7.439

Nakayasu, E. S., Burnet, M. C., Walukiewicz, H. E., Wilkins, C. S., Shukla, A. K., Brooks, S., et al. (2017). Ancient regulatory role of lysine acetylation in central metabolism. *mBio* 8, e01894. doi:10.1128/mBio.01894-17

Nakayasu, E. S., Wu, S., Sydor, M. A., Shukla, A. K., Weitz, K. K., Moore, R. J., et al. (2014). A method to determine lysine acetylation stoichiometries. *Int. J. Proteomics* 2014, 730725. doi:10.1155/2014/730725

Nie, H., Liu, Y., Zeng, X., and Chen, M. (2024). Neutrophil-to-lymphocyte ratio is associated with sarcopenia risk in overweight maintenance hemodialysis patients. *Sci. Rep.* 14, 3669. doi:10.1038/s41598-024-54056-2

Ok, E., Basnakian, A. G., Apostolov, E. O., Barri, Y. M., and Shah, S. V. (2005). Carbamylated low-density lipoprotein induces death of endothelial cells: a link to atherosclerosis in patients with kidney disease. *Kidney Int.* 68, 173–178. doi:10.1111/j.1523-1755.2005.00391.x

O'Neil, L. J., Barrera-Vargas, A., Sandoval-Heglund, D., Merayo-Chalico, J., Aguirre-Aguilar, E., Aponte, A. M., et al. (2020). Neutrophil-mediated carbamylation promotes articular damage in rheumatoid arthritis. *Sci. Adv.* 6, eabd2688. doi:10.1126/sciadv.abd2688

Park, S. Y., and Kim, J. S. (2020). A short guide to histone deacetylases including recent progress on class II enzymes. *Exp. Mol. Med.* 52, 204–212. doi:10.1038/s12276-020-0382-4

Pawloski, W., Komiyama, T., Kougentakis, C., Majumdar, A., and Fushman, D. (2022). Site-specific detection and characterization of ubiquitin carbamylation. *Biochemistry* 61, 712–721. doi:10.1021/acs.biochem.2c00085

Proshlyakov, D. A., Farrugia, M. A., Proshlyakov, Y. D., and Hausinger, R. P. (2021). Iron-Containing ureases. *Coord. Chem. Rev.* 448, 214190. doi:10.1016/j.ccr.2021.214190

Sahlstrom, P., Hansson, M., Steen, J., Amara, K., Titcombe, P. J., Forsstrom, B., et al. (2020). Different hierarchies of anti-modified protein autoantibody reactivities in rheumatoid arthritis. *Arthritis Rheumatol.* 72, 1643–1657. doi:10.1002/art.41385

Shah, S., Cook, K. W., Symonds, P., Weisser, J., Skinner, A., Al Omari, A., et al. (2023). Vaccination with post-translational modified, homocitrullinated peptides induces CD8 T-cell responses that mediate antitumor immunity. *J. Immunother. Cancer* 11, e006966. doi:10.1136/jitc-2023-006966

Shahinuzzaman, A. D. A., Chakrabarty, J. K., Fang, Z. X., Smith, D., Kamal, A. M., and Chowdhury, S. M. (2020). Improved in-solution trypsin digestion method for methanol-chloroform precipitated cellular proteomics sample. *J. Sep. Sci.* 43, 2125–2132. doi:10.1002/jssc.201901273

Shevchenko, A., Wilm, M., Vorm, O., and Mann, M. (1996). Mass spectrometric sequencing of proteins silver-stained polyacrylamide gels. *Anal. Chem.* 68, 850–858. doi:10.1021/ac950914h

Shi, J., Knevel, R., Suwannalai, P., van der Linden, M. P., Janssen, G. M., van Veelen, P. A., et al. (2011). Autoantibodies recognizing carbamylated proteins are present in sera of patients with rheumatoid arthritis and predict joint damage. *Proc. Natl. Acad. Sci. U. S. A.* 108, 17372–17377. doi:10.1073/pnas.1114465108

Shiu, S. W., Xiao, S. M., Wong, Y., Chow, W. S., Lam, K. S., and Tan, K. C. (2014). Carbamylation of LDL and its relationship with myeloperoxidase in type 2 diabetes mellitus. *Clin. Sci. (Lond)* 126, 175–181. doi:10.1042/CS20130369

Stanfill, B. A., Nakayasu, E. S., Bramer, L. M., Thompson, A. M., Ansong, C. K., Clauss, T. R., et al. (2018). Quality control analysis in real-time (QC-ART): a tool for real-time quality control assessment of mass spectrometry-based proteomics data. *Mol. Cell Proteomics* 17, 1824–1836. doi:10.1074/mcp.RA118.000648

Trelle, M. B., and Jensen, O. N. (2008). Utility of immonium ions for assignment of epsilon-N-acetyllysine-containing peptides by tandem mass spectrometry. *Anal. Chem.* 80, 3422–3430. doi:10.1021/ac800005n

Verbrugge, F. H., Tang, W. H., and Hazen, S. L. (2015). Protein carbamylation and cardiovascular disease. *Kidney Int.* 88, 474–478. doi:10.1038/ki.2015.166

Walukiewicz, H. E., Farris, Y., Burnet, M. C., Feid, S. C., You, Y., Kim, H., et al. (2024). Ancient regulatory role of lysine acetylation in central metabolism. *mBio* 8, e01894. doi:10.1128/mBio.01894-17

Wang, H., Huang, B., Wang, W., Li, J., Chen, Y., Flynn, T., et al. (2019). High urea induces depression and LTP impairment through mTOR signalling suppression caused by carbamylation. *EBioMedicine* 48, 478–490. doi:10.1016/j.ebiom.2019.09.049

Wang, Z., Nicholls, S. J., Rodriguez, E. R., Kummu, O., Horkko, S., Barnard, J., et al. (2007). Protein carbamylation links inflammation, smoking, uremia and atherogenesis. *Nat. Med.* 13, 1176–1184. doi:10.1038/nm1637

Wisniewski, J. R., Zougman, A., Nagaraj, N., and Mann, M. (2009). Universal sample preparation method for proteome analysis. *Nat. Methods* 6, 359–362. doi:10.1038/nmeth.1322

You, Y., Tsai, C. F., Patel, R., Sarkar, S., Clair, G., Zhou, M., et al. (2023). Analysis of a macrophage carbamylated proteome reveals a function in post-translational modification crosstalk. *Cell Commun. Signal* 21, 241. doi:10.1186/s12964-023-01257-3

frontiers | Frontiers in Analytical Science

TYPE Review
PUBLISHED 22 January 2025
DOI 10.3389/frans.2025.1510588

OPEN ACCESS

EDITED BY
Jason Cheng,
University of California, Riverside, United States

REVIEWED BY
Shekappa Lamani,
Rani Channamma University, Belagavi, India
Marius Koch,
Solvias AG, Switzerland

*CORRESPONDENCE
Anisha Anand,
anishaanand84@gmail.com

†These authors have contributed equally to this work

RECEIVED 13 October 2024
ACCEPTED 03 January 2025
PUBLISHED 22 January 2025

CITATION
Chu H-W, Demissie GG, Huang C-C and Anand A (2025) Protein-templated metal nanoclusters for chemical sensing.
Front. Anal. Sci. 5:1510588.
doi: 10.3389/frans.2025.1510588

Protein-templated metal nanoclusters for chemical sensing

Han-Wei Chu[1†], Girum Getachew Demissie[1†], Chih-Ching Huang[2] and Anisha Anand[3*]

[1]Department of Biomedical Sciences, College of Medicine, Chang Gung University, Taoyuan, Taiwan, [2]Department of Bioscience and Biotechnology, National Taiwan Ocean University, Keelung, Taiwan, [3]Department of Biomedical Engineering, Chang Gung University, Taoyuan, Taiwan

Metal nanoclusters (MNCs) possess unique optical properties, discrete energy levels, biocompatibility and photostability, making them pivotal photoluminescent probes in chemical sensing. While substantial work has addressed the synthesis, theoretical studies and applications of gold-, copper-, and silver-based MNCs, this review introduces fresh perspectives on how the nature and concentration of templates—particularly protein molecules—affect the optical properties, stability and sensing capabilities of MNCs. We delve into the merits of using protein templates for creating highly stable MNCs with tunable photoluminescence (PL), providing a detailed comparison with non-protein based systems. This review also unveils recent advancements in the photophysical characteristics and chemical sensing applications of protein-templated MNCs, setting it apart from previous reviews by focusing on cutting-edge innovations in template influence. Challenges and future prospects for protein-templated MNCs in chemical sensing are highlighted, marking critical pathways for upcoming research. This work not only integrates current knowledge but also identifies gaps and opportunities not covered extensively in earlier reviews, such as the nuanced effects of template variation on MNCs' functional properties.

KEYWORDS

metal nanoclusters, protein templates, precise control, tunable PL, chemical sensing

1 Introduction

Over the past decades, metal nanoclusters (MNCs) have captured significant interest across various scientific and technological disciplines due to their remarkable opto-electronic properties, high electron mobility, extended photoluminescence (PL) lifetimes and considerable diffusion lengths (Zare et al., 2021; Qiao et al., 2021; Jin et al., 2020; Lin et al., 2022; Wei et al., 2022). These clusters are characterized by a core-shell structure, with metal at the core and stabilizing ligands forming a protective shell that interacts covalently with the metal surface (Chen T. et al., 2022; Yang et al., 2020; Xiao et al., 2021; Lin et al., 2021a; Hu et al., 2022; Mathew et al., 2023). MNCs are crafted using diverse metal ions to create ligand-protected, quantum-sized clusters with cores smaller than 2 nm, exhibiting unique photophysical traits (Wei et al., 2022; Paulrajpillai et al., 2012; Thakran et al., 2021). The high surface-to-volume ratio (molecular-like) and quantum confinement effects endow MNCs with exceptional optical properties and catalytic activities (Li X. et al., 2021; Ebina et al., 2020; Kang and Zhu, 2019; Wang C C et al., 2016). The physicochemical properties of MNCs are intricately linked to the nature of the metal core and surface ligand chemistry, along with other environmental factors such as temperature, solvent and pH (Romeo et al., 2021; Qian et al., 2022; Chakraborty and Mukherjee, 2022). Crucially, the size of the metal

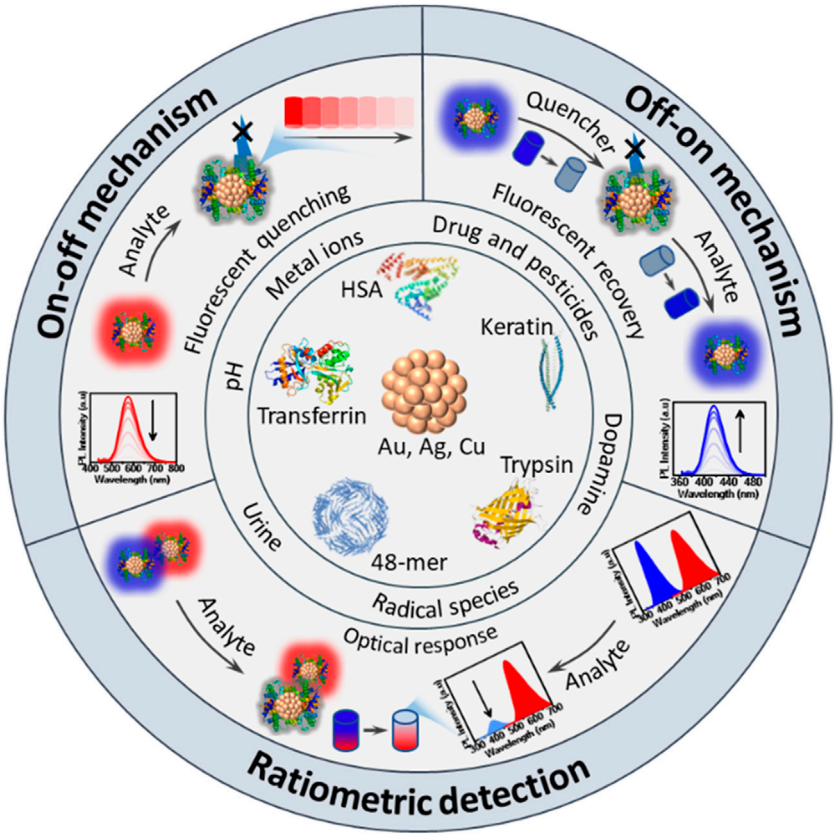

GRAPHICAL ABSTRACT

core and the chemistry of the surface ligands play pivotal roles in defining the PL properties and catalytic capabilities of MNCs. By varying the particle size, one can tune these PL properties due to the quantum confinement effect, potentially altering their characteristics and enhancing their performance across various applications. Particularly, the use of photoluminescent MNCs in chemical sensing is driven by their notable PL properties and prolonged PL lifetimes (Lin et al., 2022; Thakran et al., 2021; Lin et al., 2024).

MNC-based sensors fabricated from metals such as gold (Au), copper (Cu), silver (Ag) and platinum (Pt) have been widely recognized as excellent probes for photoluminescent sensing applications (Lin et al., 2021b; Shen et al., 2021; Fereja et al., 2021; Liu et al., 2020; Chang et al., 2021; Chen X. et al., 2020; Yen et al., 2022; Yu et al., 2017; Tseng et al., 2018; Jin et al., 2019). Numerous studies have investigated the role of surface ligands and ligand-metal interfaces in the performance of MNC-based chemical sensors (Matus and Häkkinen, 2023; Aparna et al., 2022; Nasrollahpour et al., 2023). Surface ligands play a critical role in enhancing the stability and selectivity of the sensors. Functional moieties on these surface ligand molecules form either strong covalent bonds or matrix encapsulations with the metal core, contributing to the sensor's long-term stability and improved selectivity toward specific substrates. Moreover, the surface chemistry of these ligands is essential for regulating the interaction between the analyte and the metal core, which directly influences the PL properties and sensitivity of the sensors. The ligands can also act as templates, promoting the nucleation and growth of the nanoclusters. In particular, recent advancements have shown that incorporating polymeric or protein-based ligands into the sensor design can lead to enhanced performance, such as increased luminescence and improved dispersibility in aqueous media (Chen et al., 2023; Aires et al., 2018). Additionally, the quantum confinement effects, which arise due to the extremely small size of the metal cores (less than 2 nm), allow MNCs to exhibit unique optical properties, such as size-tunable PL. This tunability is highly desirable for applications in chemical sensing, where precise detection of specific analytes is crucial. For instance, by manipulating the core size or changing the surface ligands, researchers can fine-tune the emission spectra and sensitivity of these sensors for various applications. These combined factors make MNC-based sensors particularly useful for real-time detection of trace analytes in complex environments (Lin et al., 2022; Chen et al., 2019; Xu et al., 2019), opening up further applications in environmental monitoring, biomedical diagnostics and industrial sensing technologies.

The vast advantages offered by functional MNCs in chemical sensing are evident from the significant rise in research publications over the past two decades, underscoring the growing importance of this field (Figure 1). This paper provides a thorough and comprehensive review of MNC-based sensors, with particular emphasis on protein-templated MNCs for chemical sensing applications. The review begins by offering foundational insights into the structural composition and physicochemical properties of

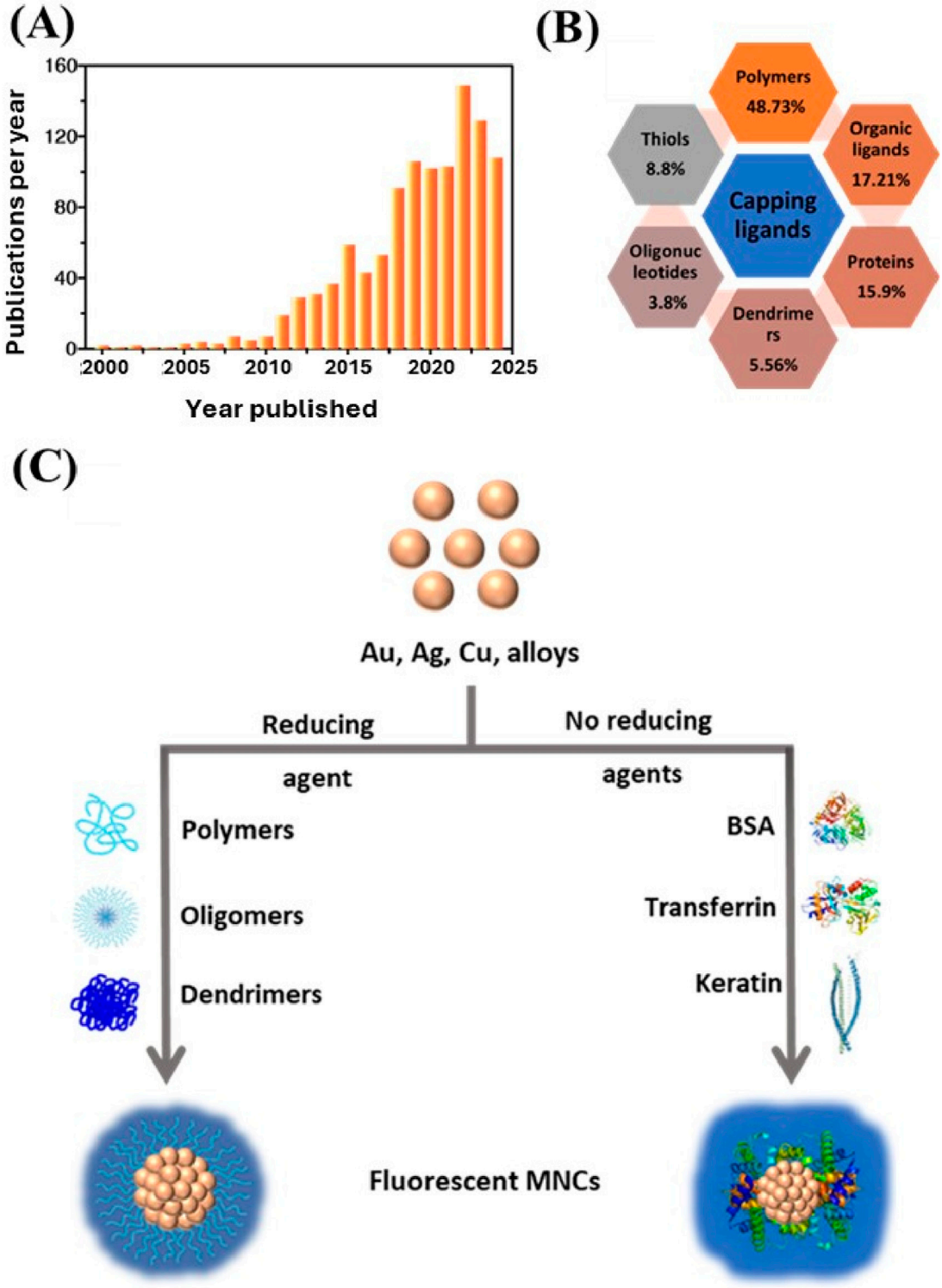

FIGURE 1
Overview of MNCs-based sensors research trends. **(A)** Exponential growth in publications on MNCs-based sensors over the last two decades, demonstrating increasing research interest, based on Scopus search data. **(B)** Various types of surface ligands utilized in MNCs preparation, illustrating diversity in chemical functionalization. **(C)** Diagram of factors influencing the physicochemical properties of MNCs, emphasizing the role of size, surface chemistry and environmental conditions.

MNCs, exploring how these properties influence their function as sensors. Furthermore, it delves into the critical factors affecting the performance of MNC-based sensors, including the impact of metal core size, surface stabilizers and the morphology of the nanoclusters. These factors play a key role in determining the sensitivity, selectivity and efficiency of the sensors. The review also provides

an in-depth comparison of the advantages of using protein templates over polymer and organic ligand templates in the synthesis of MNCs. Protein templates offer superior stability, biocompatibility and functional versatility, making them highly attractive for creating efficient chemical sensors. In addition to reviewing recent advancements in the application of MNCs in chemical sensing, this review offers an extensive analysis of the current literature, providing critical insights into the state of the field. Finally, we discuss the existing challenges and limitations in the development of MNC-based sensors, such as the need for more versatile templates and improved stability under harsh conditions. The review also highlights future research directions, including the potential for expanding the use of MNCs in various sensing applications and the development of more sophisticated synthesis techniques to enhance their performance.

2 Factors effecting the properties of MNCs

The properties of MNCs are significantly influenced by several factors, including the synthesis method, the size and type of metal core, and the nature of the surface ligands. Bottom-up synthesis strategies are widely used for fabricating luminescent MNCs. This approach involves the reduction of metal ions to their zero-valent state in the presence of surface-stabilizing ligands. The resulting nanoclusters possess highly active metal cores with large surface areas, but these bare surfaces can be fragile, making them prone to undesirable side reactions, self-aggregation and structural deformation (Fang et al., 2015). To overcome these challenges, the surface of the metal core must be stabilized through the incorporation of encapsulating agents, which prevent further aggregation and enhance the stability of the nanoclusters.

The physicochemical properties and sensing performance of MNCs, particularly those templated with proteins, are predominantly regulated by the size and type of metal core as well as the surface ligands that protect the core (Tan et al., 2023). The metal core size directly impacts quantum confinement effects, which are responsible for the unique optical and electronic properties of MNCs (Nasrollahpour et al., 2023). Smaller metal cores lead to more pronounced quantum effects, resulting in size-tunable PL, which is a critical feature in chemical sensing applications. The type of metal and alloy also plays a vital role in determining the PL and catalytic activity of the nanoclusters, with Au, Ag, Cu, and Pt being the most commonly used metals due to their favorable optical and chemical properties.

Surface ligands, on the other hand, play a crucial role in stabilizing the metal core and defining the overall characteristics of the MNCs. They form protective layers around the core, preventing its aggregation and modulating the electronic properties by influencing the energy levels involved in PL (Tan et al., 2023). Ligands also offer functionalization possibilities, enabling the MNCs to interact selectively with specific analytes, which is essential for developing highly sensitive and selective chemical sensors. In the case of protein-templated MNCs, the three-dimensional structure of proteins offers numerous functional groups (e.g., amines, thiols, carboxylates) that can bind strongly to metal ions, promoting the nucleation and growth of the nanoclusters. These proteins not only stabilize the MNCs but also improve their dispersibility in aqueous environments, enhance their biocompatibility and, in some cases, act as reducing agents. This combination of factors contributes to the high stability, tunable PL and excellent sensing capabilities of protein-templated MNCs.

2.1 Metal cores

The properties of the metal core play a fundamental role in determining the PL characteristics of MNCs. The primary source of PL in MNCs is the interband transitions between the occupied d-orbitals and the Fermi level of the metal atoms in the core (Chen P.-C. et al., 2016). These transitions are heavily influenced by the size and type of metal core, which directly impact the optical properties of the nanoclusters. The López-Quintela group demonstrated this through theoretical calculations on copper nanoclusters (Cu NCs), showing that as the size of the copper core increases from Cu_5 to Cu_{20}, the PL peaks shift to longer wavelengths (Vilar-Vidal et al., 2012). This size-dependent shift is attributed to the quantum confinement effect, which becomes more pronounced as the size of the metal core decreases.

The quantum confinement effect is a critical phenomenon in MNCs, where the energy levels are discrete due to the small size of the clusters, leading to tunable PL properties. The Jellium model is often applied to describe the relationship between the number of metal atoms in the clusters and the emission spectra, providing a theoretical framework to calculate the metal core size based on PL measurements (Sinha-Roy et al., 2023; Aikens and Jarrold, 2023). This model explains how the dynamic polarizability of d-electrons affects the dielectric function of the nanocluster due to size-dependent surface imperfections. As a result, the plasmon energy becomes size-dependent, meaning that the reduced d-electron shielding and lower electron density at the metal core's surface layer significantly influence the physicochemical properties of MNCs.

Beyond size, the type of metal used in the core also plays a pivotal role in determining the PL properties of MNCs. Different metals exhibit unique optical and electronic properties, which can be fine-tuned to suit specific applications. Research by Chang's group further highlighted the importance of metal type in PL behavior by studying three distinct types of MNCs: BSA/TSA-Au NCs, BSA/TSA-Ag NCs and BSA/TSA-Cu NCs (Nain et al., 2020). By using an excitation wavelength of 350 nm, they observed distinct PL emission spectra at 700, 624 and 430 nm for Au, Ag and Cu NCs, respectively. These findings underscore the significant impact that both metal type and core size have on the optical characteristics of MNCs.

Moreover, atomically precise MNCs, which have an exact number of metal atoms, offer highly controlled and tunable PL properties (Liu Z. et al., 2024; Xu et al., 2020; Lipok et al., 2023; Li Y. et al., 2021). This precision allows for the fine-tuning of the nanoclusters' light absorption efficiency and emission wavelengths, making them highly versatile for applications such as chemical sensing, bioimaging and catalysis. Atomically precise gold nanoclusters (Au NCs) have shown tunable PL from visible to near-infrared (NIR-I and NIR-II) regions (Liu Z. et al., 2024). By manipulating the size, structure and composition of the Au NCs, researchers have been able to achieve emissions spanning from the

visible spectrum (around 500 nm) to the NIR-II region (up to 1700 nm). This tunability has been facilitated by techniques such as heterometal doping, surface motif rigidification and core phonon engineering, which improve PL quantum yields. When different number of Ag atoms are introduced into the Au_{25} rod, the structure remains intact, but the electronic properties, specifically the HOMO-LUMO energy gap, are altered (Wang et al., 2014). This doping increases the HOMO-LUMO gap, particularly because Ag atoms have higher energy orbitals than Au. The replacement of Au atoms with Ag, starting with the vertex and waist Au atoms, significantly boosts the quantum yield (QY) of PL, with QY values of 8% for pure Au_{25}, 29% for $Ag_{13}Au_{12}$ and 56% for $Ag_{12}Au_{13}$. The enhancement in PL is attributed to the larger energy gap between the ground (S0) and excited (T1) states, which suppresses non-radiative processes and increases radiative efficiency (Mitsui et al., 2022). Despite the small differences in the HOMO-LUMO gap between Au_{25} and Ag-doped clusters, other factors beyond just the energy gap seem to contribute to the significant increase in PL efficiency, warranting further research. Heteroatom doping in Ag and Cu NCs also impacts both radiative and non-radiative processes (Song et al., 2021; Brocha Silalahi et al., 2021; Kang et al., 2016), but more investigation is needed to fully understand the mechanisms behind the improved PL. In summary, the size, type, alloy composition and structural arrangement of the metal core are critical factors that govern the photophysical properties of MNCs. Careful manipulation of these parameters allows for precise control over their optical and electronic behavior. This tunability is key to customizing MNCs for a wide range of applications, including chemical sensing, optical devices and biomedicine.

2.2 Ligands and surface states

Recent studies have moved beyond the traditional quantum confinement view of MNCs, recognizing them as molecular-like entities where surface ligands and states profoundly influence PL properties (Matus and Häkkinen, 2023; Zhang B. et al., 2021; Hossain et al., 2020). Surface ligands, including thiolates, phosphines and biopolymers, not only stabilize the MNCs but also crucially modulate their electronic structures, affecting the energy levels involved in PL processes (Yuan et al., 2020; Häkkinen, 2012; Jin, 2015). The interplay between the metal core and these ligands is pivotal in determining the overall optical behavior of the clusters, where each ligand type brings a distinct influence on stability, optical properties and functional capabilities of MNC sensors.

MNCs typically possess a core-shell structure, featuring an inner metal kernel and outer metal-ligand motifs. These surface metal-ligand motifs are crucial to the PL properties of MNCs, where restricting intramolecular motions has been identified as an effective method to minimize energy loss from photoexcited states via non-radiative relaxation, thus enhancing emission efficiency (Liu Z. et al., 2024). Various methods have been developed to impede these intramolecular motions, thereby inducing rigidity in the surface motifs (Kolay et al., 2022). These include bonding strategies that involve bulky group bonding and other interactions such as hydrogen bonds, dipolar, van der Waals, or electrostatic interactions, which rigidify the metal-ligand shell, enhancing the PL intensity. For instance, bonding between $Au_{22}(SG)_{18}$ clusters (where, SG = glutathione) and bulky tetraoctylammonium cations has demonstrated significant PL enhancements by making the Au(I)-thiolate shell rigid (Pyo et al., 2015). Furthermore, bis-Schiff base linkages formed between dialdehydes such as 2,6-pyridinedicarboxaldehyde and amino functionalities on Au_{22}(SG) 18 induce cross-linking of Au(I)-SG motifs, leading to significant reductions in non-radiative decay rates and remarkable increase in PL intensity (Pyo et al., 2015).

Other strategies include host–guest interactions, aggregation-induced emission (AIE) and self-locking effects (Guo et al., 2022; Luo et al., 2012). The host–guest self-assembly involves encapsulating smaller molecules within larger host structures, significantly influencing the rigidity of the metal-thiolate shell and promoting radiative decay while suppressing non-radiative processes (Guo et al., 2022). Additionally, the aggregation-induced emission mechanism illustrates how non-luminescent oligomeric Au(I)-thiolate complexes become luminescent upon aggregation (Luo et al., 2012). The self-locking effect utilizes specific surface motifs formed into elongated or interlocked arrangements, reducing non-radiative decay pathways and effectively increasing the quantum yield of radiative decay (Luo et al., 2012). This collective array of strategies highlights a profound and evolving understanding of surface motif rigidification and its pivotal role in enhancing the PL properties of Au NCs.

Traditionally, MNCs have been stabilized by monolayers of small molecules like thiolates and phosphines. However, the shift towards using larger ligands such as polymers, nucleic acids and proteins in the synthesis of MNCs is due to their ability to offer a greater number of functional groups, enabling more versatile and robust interactions with the metal core (van de Looij et al., 2021). This approach not only enhances the stability of the nanoclusters but also allows for the fine-tuning of their optical properties through specific ligand-metal interactions, which is essential for applications that require precise photoluminescent efficiency and specificity. Moreover, larger biomolecules like proteins and nucleic acids introduce biocompatibility, making MNCs particularly suitable for biomedical applications, including drug delivery, bioimaging and biosensing (Zare et al., 2021). The use of polymeric ligands improves the dispersibility of MNCs in various solvents, a crucial attribute for applications in heterogeneous environments where uniform dispersion is necessary. Additionally, the structural diversity and tunable characteristics of these larger ligands permit the design of MNCs with tailored functionalities. These engineered nanoclusters can respond to environmental stimuli or interact specifically with target molecules, thereby broadening their utility across a spectrum of sensing and catalytic applications.

2.2.1 Polymer as template

Polymers have proven to be versatile scaffolding materials for the synthesis and stabilization of MNCs (Qiao et al., 2021; Casteleiro et al., 2021). By varying the polymer templates used in synthesis, researchers can effectively control the size, shape and optical properties of the resulting nanoclusters. This approach has proven effective for a variety of metals, including Au, Ag and Cu, demonstrating the flexibility of polymer-based synthesis. Encapsulation of MNCs within polymers helps prevent

degradation of the nanoclusters during harsh synthesis processes, offering improved stability and functionality in various environments. A wide array of polymers has been employed in this capacity, ranging from naturally derived chitosan to synthetic polyacrylamide, each offering specific benefits depending on the application. *In situ* synthesis during encapsulation often enhances the properties of the nanoclusters, overcoming their inherent instability and offering better protection against aggregation and oxidation during reactions (Casteleiro et al., 2021). Synthetic polymers like poly (methacrylic acid) (PMAA) and poly (vinyl pyrrolidone) (PVP) have shown significant promise in the synthesis of fluorescent MNCs, thanks to their abundant carboxylic and amine groups (Casteleiro et al., 2021). These functional groups interact with metal ions, acting as both a reducing and stabilizing agent. The PL of these nanoclusters can be further tuned by altering polymer properties such as molecular weight, crosslinking density and hydrophobicity.

One of the most exciting applications of polymer-encapsulated nanoclusters is in biomedical fields such as bioimaging and drug delivery. Chitosan, a biodegradable polymer known for its non-toxicity and biocompatibility, has been extensively studied as a vehicle for nanocluster encapsulation (Duan et al., 2018). Its amine groups not only assist in the stabilization of the clusters but also enhance cellular uptake, making chitosan-Au NC composites particularly suitable for *in vivo* applications. Studies have shown that encapsulation within chitosan nanogels significantly increases the PL of Au NCs, allowing for better imaging capabilities under physiological conditions (Wang et al., 2023). In addition to improving imaging, encapsulated Au NCs can be functionalized with various targeting ligands or drugs, making them a powerful tool for theranostics, where diagnostic imaging and therapeutic delivery are combined in a single nanomaterial.

Beyond biomedical applications, encapsulated MNCs have also demonstrated significant utility in catalysis. The interaction between the polymer matrix and the MNCs can modulate the catalytic activity, enhancing reaction specificity and efficiency (Koga et al., 2016). For instance, polystyrene (PS)-encapsulated Au NCs have been shown to be effective catalysts for oxidation reactions, such as the aerobic oxidation of alcohols and boronic acids (Miyamura et al., 2014). The ability of the polymer to control access to the Au NC surface, combined with its inherent chemical stability, makes these nanocomposites promising candidates for industrial-scale catalysis. Furthermore, encapsulation helps prevent aggregation, which is a common issue with unprotected MNCs, ensuring prolonged catalytic activity across multiple reaction cycles.

For chemosensors, Chang's research group has developed several sensors using polymers as template. For example, Lin et al. developed polydiallyldimethylammonium (PDDA)-templated GSH-Au NCs (GSH = glutathione) for the sensing of sulfides (Lin et al., 2021a). Upon excitation at 365 nm, PDDA/GSH-Au NCs exhibited two distinct PL peaks at 620 and 690 nm, corresponding to GSH-Au and PDDA/GSH-Au NCs, respectively. The formation of Au_2S-induced PL quenching in the PDDA/GSH-Au NCs, enabled the detection of sulfide with a linear range of 1–10 μM and a low detection limit of 0.32 μM. Similarly, a polymer-supported Cu NCs using polystyrene sulfonate (PSS) and penicillamine (PA) for hydrogen sulfide detection using a similar method has been reported (Chen P.-C. et al., 2016). By altering the ratio of PSS during the synthesis, size-tunable PSS-PA-Cu NCs were produced in the range of 173 nm to 5.5 μm. The extent of polymer aggregation on the surface of Cu NCs resulted in the formation of layers that enhanced the dispersibility and stability of the NCs compared to the PA-Cu NCs. The luminescence intensity of as-prepared PSS-PA-Cu NCs becomes higher when increasing PSS ratio to 0.1 wt% and declines with further increasing concentration of PSS. Compared to PA-Cu NCs, smaller-sized PSS-PA-Cu NCs were obtained via metal-thiol interaction with high aqueous dispersibility and luminescence. Hydrodynamic size and zeta potential measurements support the size- and charge-tunability of PSS-PA-Cu NCs in the presence of various modifications of PSS. At 0.05 wt% and 0.1 wt% of PSS concentration, the particle growth is suppressed, resulting in PSS-PA-Cu NCs with a particle diameter of 173 nm. The maximum particle diameter obtained in this report is nearly 5.5 μm in the absence of PSS, indicating that PSS introduction caused size-tunable PSS-PA-Cu NCs. The PL stability of PSS-PA-Cu NCs improved as compared to PA-Cu NCs owing to the ultra-thin coating of PSS on the surface of Cu NCs.

2.2.2 DNA as template

DNA, akin to polymers, functions as an exceptional template for the formation of MNCs, particularly silver nanoclusters (Ag NCs) (Yang et al., 2023). These DNA-templated Ag NCs exhibit unique structural, electronic and photophysical properties, all of which are influenced by the sequence and conformation of the DNA template. This programmable nature of DNA provides an unprecedented ability to fine-tune the properties of nanoclusters by altering parameters such as sequence length, base composition and secondary structures. Consequently, DNA-templated MNCs have found numerous applications in fields like chemical and biomolecular sensing, bioimaging, theranostics and nanophotonics (Xu et al., 2021). The integration of DNA as a template in nanocluster synthesis is driven by its versatility, biocompatibility and molecular programmability, rendering these nanostructures highly promising for advanced technological applications.

The use of DNA as a template for metal nanocluster formation relies on the electrostatic interactions and coordination chemistry between metal ions and the nucleobases of DNA. Each base within a DNA strand offers specific binding sites for metal ions: adenine (A) and cytosine (C) are rich in nitrogen and can form coordination bonds with metal ions, while guanine (G) and thymine (T) offer additional pathways for interaction due to their specific electronic configurations (Song et al., 2019). These interactions facilitate the nucleation and growth of metal nanoclusters along the DNA strand, with the final size, shape and electronic structure of the MNCs being dependent on the sequence and conformation of the DNA template. An excellent example of this phenomenon is the synthesis of silver nanoclusters using polycytosine (poly-C) sequences (O'Neill et al., 2009). Poly-C DNA strands have been shown to preferentially bind silver ions due to their affinity for nitrogenous bases, promoting the formation of highly fluorescent Ag NCs. Furthermore, by varying the length of the poly-C sequence, researchers have been able to precisely control the size of the resulting Ag NCs, with longer sequences producing larger clusters and shorter sequences yielding smaller, more fluorescent nanoclusters (O'Neill et al., 2009). These DNA-templated Ag NCs exhibit excellent stability

in aqueous environments and show a rich variety of fluorescence properties, which can be harnessed for sensing and imaging applications.

One of the most intriguing aspects of DNA-templated nanoclusters is their tunable fluorescence, which can be tailored by modifying the DNA sequence used as a template. This tunability arises because different sequences provide unique spatial arrangements for the nucleation of metal atoms, which in turn affect the electronic structure and energy states of the resulting MNCs (New et al., 2016). For example, Ag NCs templated by guanine-rich DNA sequences often exhibit fluorescence that spans the visible to near-infrared regions (Wen et al., 2020). Moreover, a notable study demonstrated the formation of highly fluorescent DNA-templated Ag NCs using a hairpin DNA structure (O'Neill et al., 2009). The researchers found that altering the base sequences in the stem-loop structure of the hairpin significantly impacted the emission properties of the resulting nanoclusters. Shorter hairpins tended to produce blue-emitting clusters, while longer hairpins favored red or near-infrared emissions. This flexibility allows for the design of highly specific fluorophores that can be used in multiplexed bioimaging or sensing systems, where different emission wavelengths are needed for distinguishing between multiple targets. In addition, specific DNA sequences can induce the self-assembly of nanoclusters into highly organized structures, further enhancing their optical properties. In one example, a Y-shaped DNA scaffold was used to template the formation of Ag NCs that exhibited superior photostability and enhanced fluorescence due to the ordered arrangement of the clusters (Yang et al., 2022). Moreover, by incorporating specific functional groups or sequences into the DNA template, researchers can fine-tune the interaction between the metal atoms and the DNA, resulting in clusters with tailored properties. For example, thiolated DNA (DNA-SH) has been used to template Ag NCs, where the sulfur-containing thiol groups provide additional binding sites for silver ions, stabilizing the nanocluster and enhancing its fluorescence (Zhang et al., 2018). This approach has been particularly effective in preventing the oxidation of Ag NCs, which is a common issue in the synthesis of silver-based nanostructures.

Moreover, the versatility of DNA templates extends beyond Ag to other metals, including Au and Cu, which further expands the potential applications of DNA-templated MNCs (Wang et al., 2019; Li P. et al., 2023; Zhang et al., 2019). Au NCs, for instance, have been synthesized using DNA templates and have exhibited tunable fluorescence similar to Ag NCs (Wang et al., 2019). These Au NCs, due to their excellent photostability and biocompatibility, are particularly well-suited for bioimaging applications. DNA-templated Au NCs could be used for cellular imaging, where their NIR emission enabled deep tissue penetration, making them highly effective for non-invasive imaging techniques. The potential of DNA-templated MNCs extends beyond Ag NCs and Au NCs to bimetallic clusters, which combine the properties of two different metals to create nanostructures with enhanced functionality (Zaleska-Medynska et al., 2016). Bimetallic clusters, such as Au-Ag or Au-Cu, have been templated using DNA to create nanoclusters with unique optical and catalytic properties (Sun et al., 2019; Pei et al., 2024). For instance, DNA-templated Au-Ag nanoclusters have been shown to exhibit enhanced catalytic activity for the reduction of 4-nitrophenol, a model reaction commonly used to test the catalytic efficiency of metal nanoparticles (Zhou et al., 2019).

DNA-templated MNCs have shown remarkable potential in the development of chemical and biomolecular sensors, owing to their tunable fluorescence, high sensitivity and selective binding capabilities. These properties are particularly advantageous in biosensing, where the detection of specific analytes such as metal ions, nucleic acids and proteins is of paramount importance (Song et al., 2019; Tang et al., 2024; Yang et al., 2023). For instance, DNA-templated Ag NCs have been successfully employed as highly sensitive probes for the detection of metal ions, such as mercury (Hg^{2+}) and copper (Cu^{2+}) (Song et al., 2019; Li and Wei, 2017). In a typical sensing mechanism, the presence of the target metal ion induces a conformational change in the DNA template, which in turn alters the fluorescence of the bound nanocluster (Chen Y.-C et al., 2016). For example, a study demonstrated the use of DNA-templated Ag NCs to detect Hg^{2+} ions in water samples with a detection limit as low as parts-per-billion (ppb). The binding of Hg^{2+} to thymine-rich regions of the DNA scaffold led to quenching of the fluorescence signal, enabling highly sensitive and selective detection (Guo et al., 2021).

2.2.3 Protein as template

Protein-templated metal nanoclusters (MNCs) have emerged as ideal candidates for various nanotechnology applications due to their bioavailability, biocompatibility, ease of functionalization and ability to form stable, water-soluble complexes (Guo et al., 2021; López-Domene et al., 2023; Lettieri et al., 2021; Suo et al., 2019). These advantages, coupled with the unique properties conferred by proteins, have positioned protein-templated MNCs as highly attractive for use in chemical sensing, bioimaging, catalysis and theranostics (Duan et al., 2018). Unlike other surface capping agents, such as synthetic polymers or small molecules, the inherent three-dimensional structure of proteins offers an abundance of functional groups (e.g., amines, thiols, carboxylates) that facilitate the binding of metal ions and promote the nucleation and growth of MNCs (Zare et al., 2021; Chakraborty and Parak, 2019; Yu et al., 2020; Cheng et al., 2023). This enables precise control over the size, structure and photophysical properties of the resulting nanoclusters.

The ability of proteins to act as templates for MNC formation is due to their intricate folded structures, which provide binding sites that stabilize the metal cores and prevent undesirable aggregation (Qiao et al., 2021; Kailasa et al., 2021). For example, bovine serum albumin (BSA), a commonly used protein template, has been shown to stabilize Au NCs through strong interaction between its cysteine residues and the gold atoms (Xie et al., 2009). This results in Au NCs with enhanced PL properties, which are critical for applications in bioimaging. Research has shown that protein-templated Au NCs can exhibit size-tunable fluorescence, with emission wavelengths ranging from the visible to the near-infrared region, depending on the specific protein used and its interaction with the gold atoms (Tan et al., 2023).

The PL of protein-templated MNCs is largely determined by the interaction between the metal atoms and the protein's functional groups (Qiao et al., 2022; Voet and Tame, 2017; Czyżowska et al., 2021; Yarramala et al., 2017). The sulfur-containing thiol groups of cysteine residues, in particular, play a crucial role in the formation of

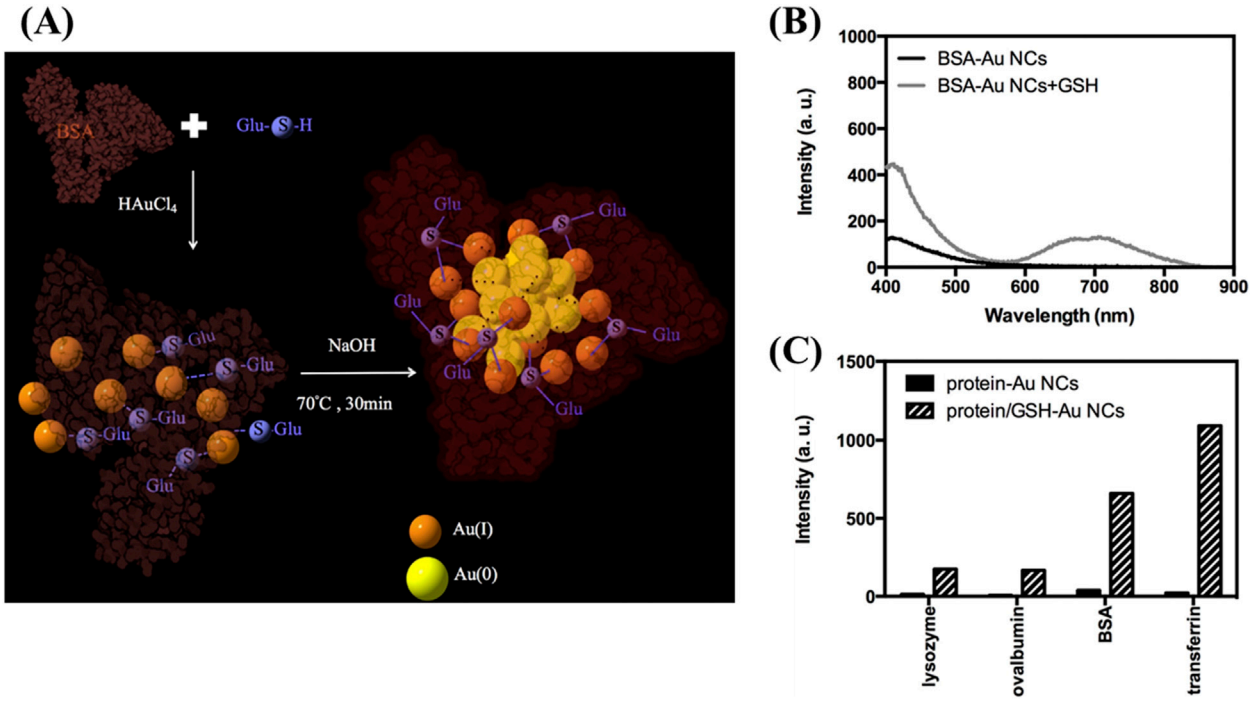

FIGURE 2
Preparation and photoluminescence of protein/GSH-Au NCs. **(A)** Schematic diagram illustrating the synthesis of BSA/GSH-Au NCs. **(B)** Photoluminescence spectra of BSA-Au NCs prepared from 2 mM Au^{3+} and 30 μM BSA at 70 °C for 30 min (black curve) and a mixture of as-formed BSA-Au NCs with 3 mM GSH reacted at the same conditions (gray curve). **(C)** PL intensities at 650 nm of various protein-Au NCs and protein/GSH-Au NCs under excitation at 330 nm; concentrations are maintained at 30 μM for proteins and 3 mM for GSH. Reproduced from Wu et al. (2017). Copyright 2017, Elsevier.

Au-S bonds, which contribute to the stability and PL properties of the nanoclusters. For instance, studies by Chang's group demonstrated that the cysteine content of the protein template can significantly influence the PL intensity of Au NCs (Wu et al., 2017). By manipulating the cysteine content or adding exogenous thiol compounds such as glutathione (GSH), it is possible to reduce the amount of protein required for nanocluster synthesis while still maintaining high PL yields (Figure 2).

The influence of cysteine residues on the formation of protein-based Au NCs was further validated by Chen's group through detailed mass spectrometry analysis (Hsu et al., 2019). Their investigation revealed that gold atoms preferentially bind to cysteine sites and selectively attach to disulfide groups within the protein structure. The primary capping sites for red-emitting Au NCs were identified as C75–C91/C90–C101 in domain IA, C315–C360/C359–C368 in domain IIB and C513–C558/C557–C566 in domain IIIB. Peptides containing oxidized cysteines, such as sulfinic or cysteic acids, were found to be the main reducing agents, predominantly located outside the core regions of the protein. This observation suggests that the oxidation-induced cleavage of disulfide bonds, coupled with accompanying conformational changes in the protein facilitated the subsequent nucleation and growth of nanoclusters near intact disulfide pairs.

The versatility of protein templates extends to their ability to form nanoclusters with metals other than Au, such as Ag and Cu. For instance, Ag NCs templated by BSA have been shown to exhibit strong PL and excellent colloidal stability, making them suitable for use in sensing and bioimaging applications (Sarkar et al., 2023). Similarly, Cu NCs have been templated using proteins such as lysozyme and hemoglobin (Sebastian et al., 2023), which provide a biocompatible scaffold that enhances the stability and functionality of the Cu NCs in aqueous environments.

A key advantage of using proteins as templates for MNC synthesis is their ability to act as reducing agents in addition to providing structural stability. This dual functionality simplifies the synthesis process by eliminating the need for external reducing agents, which are typically required in other MNC synthesis methods. For example, Yarramala et al. successfully synthesized size-controllable Au NCs using bovine apo-α-lactalbumin (apo-α-LA), a protein with specific binding sites for calcium and lanthanum ions (Yarramala et al., 2017). Apo-α-LA interacts with Au^{3+} ions, facilitating both the formation of Au_{10} clusters and the reduction of Au^{3+} to the Au^0 state. The protein effectively inhibits excessive particle growth, yielding Au NCs of varying sizes, including Au_{10}, Au_9, Au_8, Au_7 and Au_6. The presence of apo-α-LA significantly enhances the surface stability and luminescence properties of the Au NCs, making the protein a crucial factor in maintaining their structural and optical integrity (Figure 3).

Other studies have explored the use of different proteins as templates for MNC synthesis, each offering unique advantages based on their size, amino acid composition and structural properties. Bao's group, for instance, demonstrated that the size of the protein template and its amino acid content, particularly the balance of

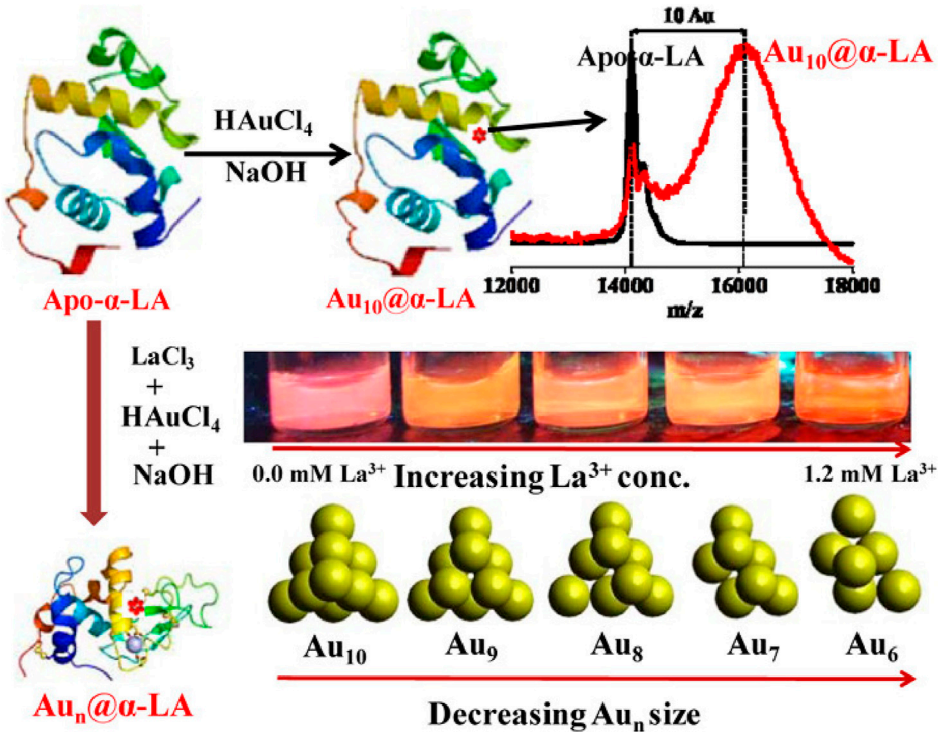

FIGURE 3
Size-controllabled synthesis of Au NCs using bovine apo-α-lactalbumin. Reproduced from Yarramala et al. (2017). Copyright 2017, ACS Publications.

amine and tyrosine/tryptophan residues, play a crucial role in the formation and stabilization of Au NCs (Xu et al., 2014). Their study revealed that smaller proteins with fewer cysteine residues tend to produce Au NCs with a blue shift in fluorescence emission and shorter fluorescent lifetimes. This suggests that amino acids other than cysteine, such as tryptophan, may also contribute to the stabilization and optical properties of the nanoclusters.

In addition to the well-documented use of BSA, other proteins such as chicken egg white (CEW) protein and hemoglobin have been successfully employed as templates for MNC synthesis (Zare et al., 2021; Akyüz et al., 2020; Cun et al., 2023). Apak's group, for example, synthesized Au NCs with high PL properties using CEW protein as both a protecting and reducing agent. The resulting Au NCs exhibited a broad emission peak at 640 nm, with excellent stability and biocompatibility, making them ideal candidates for biosensing and imaging applications (Akyüz et al., 2020).

In summary, protein-templated MNCs represent a versatile and highly effective platform for the synthesis of stable, biocompatible and functional nanoclusters. The unique properties of proteins, including their abundance of functional groups and ability to act as both stabilizers and reducing agents, make them ideal candidates for templating MNCs. The tunable optical properties, excellent colloidal stability and biocompatibility of protein-templated MNCs have enabled their widespread use in applications such as sensing, bioimaging, catalysis and theranostics. As research continues to explore new protein templates and synthesis strategies, the potential of protein-templated MNCs is likely to expand further, offering exciting opportunities for the development of advanced nanomaterials for a wide range of scientific and technological applications.

3 Protein-templated MNCs as PL probe

3.1 On-off sensors

In signal-off biosensing strategies involving protein-templated MNCs, the PL of the NCs is quenched in the presence of specific analytes. This quenching effect can occur via two primary mechanisms (Panthi and Park, 2022; Tan et al., 2023). First, the analyte may interact directly with the protein, disrupting its protective function and exposing the metal core. In the second mechanism, the analyte binds to the metal core itself, causing structural changes that reduce the PL intensity. In both cases, the reduction in PL is proportional to the concentration of the analyte, forming the basis for signal-off biosensing.

The protein structure plays a critical role in this process due to its numerous functional groups, such as carboxyl, amine and sulfhydryl groups, which are readily available to bind quenching agents. Metal ions are the most commonly used quenchers, given their strong affinity for the functional groups on the protein surface. Proteins such as BSA, lysozyme and hemoglobin are frequently used as templates because they provide a robust scaffold for the formation of MNCs and offer a rich array of functional groups that can bind analytes. For instance, lysozyme-templated Ag NCs have been employed to detect glutathione, where the binding of glutathione leads to a reduction in fluorescence (Sam et al., 2024). This

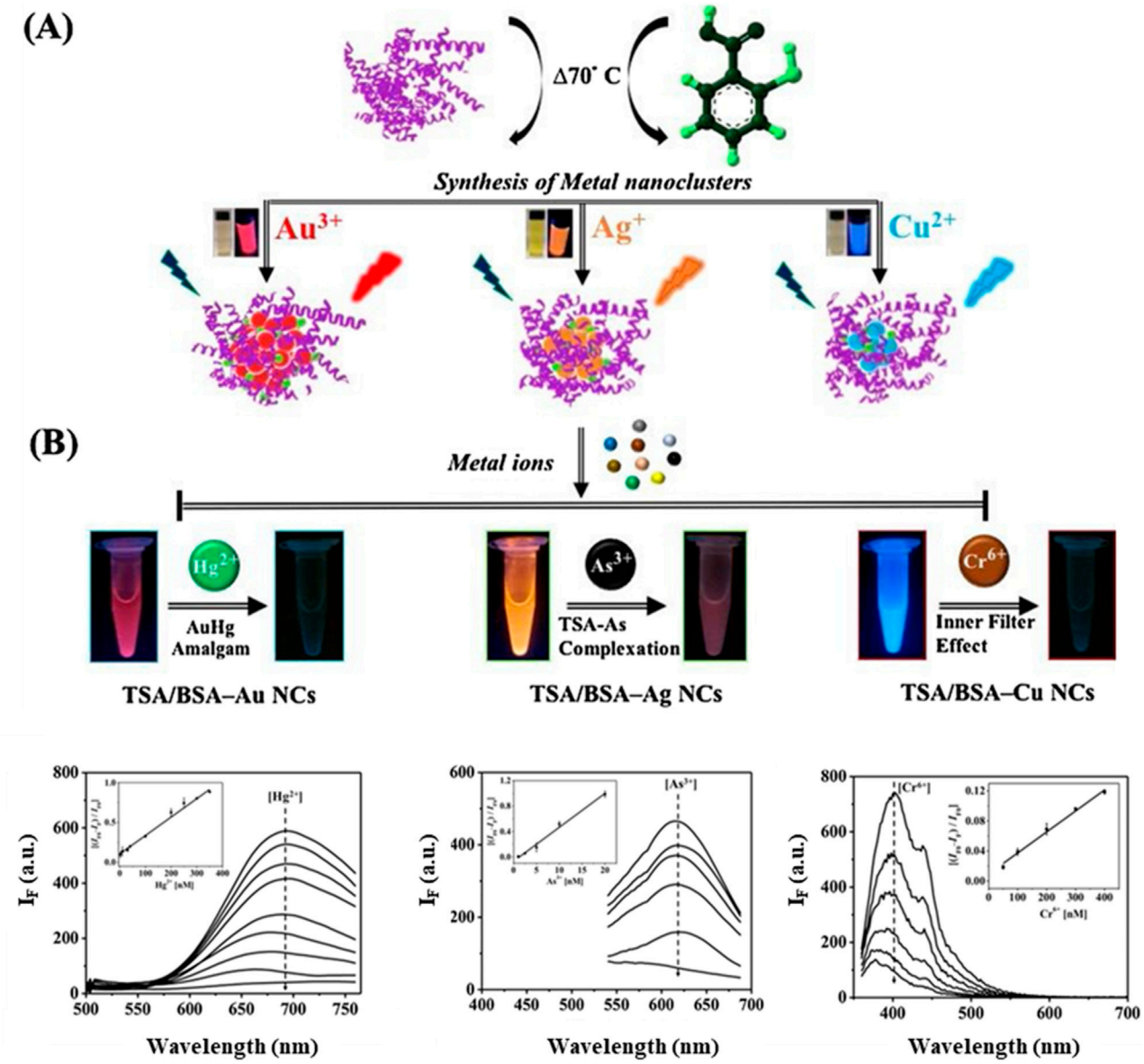

FIGURE 4
Synthesis and applications of TSA/BSA-Stabilized MNCs. **(A)** Schematic representation of the synthesis process for TSA/BSA-stabilized metal nanoclusters (MNCs). **(B)** Applications of these MNCs for the selective detection of heavy metal ions, including Hg^{2+}, As^{3+} and Cr^{6+}. Reproduced from Nain et al. (2020). Copyright 2020, Elsevier.

interaction between the analyte and the protein-templated MNCs is highly specific, enabling selective detection of target analytes in complex biological samples. For example, BSA-templated Au NCs have been shown to exhibit significant quenching in the presence of Hg^{2+} ions, which bind to cysteine residues and disrupt the Au-S bonds that stabilize the nanoclusters (Chen et al., 2013). This results in a loss of fluorescence, allowing for highly sensitive detection of mercury. Furthermore, Nain et al. has synthesized various Au, Ag and Cu NCs protected by BSA and thiosalicylic acid (TSA), each exhibiting PL emissions at wavelengths of 700, 624 and 430 nm, respectively (Nain et al., 2020). These NCs enable the sensitive detection of Hg^{2+}, arsenic (As^{3+}) and Cr^{6+} ions by utilizing PL quenching, achieving a low detection limit in the nanomolar range (Figure 4).

In addition to their use in detecting metal ions, protein-templated MNCs have been applied to the detection of small molecules and biomolecules. For example, BSA-templated Au NCs have been used to detect GSH (Wong et al., 2021), a key antioxidant in biological systems. The interaction between GSH and the metal core of the Au NCs disrupts the PL emission, providing a simple and effective method for GSH quantification. In another study, Chang's group presents a dual-emission BSA-Au NC probe for the detection and quantification of cathinone analogues, in aqueous solutions. Upon interaction with cathinone drugs, the PL of the BSA-Au NCs in the 650 nm range was quenched while the 460 nm PL remained unaffected causing a color shift from red to dark blue, allowing for detection limits as low as 0.14 mM and a PL color-change threshold of 10.0 mM for 4-chloromethcathinone

(Yen et al., 2019). These examples highlight the versatility of protein-templated MNCs in signal-off biosensing, offering a wide range of applications from environmental monitoring to biomedical diagnostics.

In summary, the signal-off biosensing strategy utilizing protein-templated MNCs relies on the interaction between the analyte and the metal core or protein scaffold, leading to a measurable reduction in PL. The abundance of functional groups on protein templates makes them ideal for binding quenching agents, particularly metal ions and the inherent stability and biocompatibility of proteins enhance the performance of these biosensors. As research into protein-templated MNCs continues to advance, new opportunities for improving sensitivity, selectivity and application diversity will emerge, solidifying their role in biosensing technologies for environmental and biomedical applications.

3.2 Off-on sensors

Off-on sensors represent a sophisticated and versatile approach in the design of biosensors based on MNCs. In this strategy, the PL of the MNCs is initially quenched through interaction with a quenching mediator. The introduction of the target analyte subsequently triggers a competitive interaction, where the quenching mediator binds preferentially to the analyte rather than the MNCs (Duan et al., 2018; Zhu et al., 2019; Dong et al., 2021). This competitive binding results in the restoration of the PL signal, which had initially been suppressed. This off-on approach has become a highly valuable tool in biosensing due to its sensitivity and the ease with which PL changes can be monitored, offering significant promise for detecting biomolecules, metal ions and other relevant analytes.

In a typical off-on sensor, the initial quenching phase is achieved by introducing a quenching mediator, such as metal ions or other small molecules, that interacts with the metal core or functional groups on the MNCs. For example, BSA-Au NCs have been used extensively in such sensors, where quenching agents such as Fe^{3+} or Cu^{2+} ions are employed (Duan et al., 2018; Zhu et al., 2019). These metal ions bind to the sulfur atoms of the BSA-Au NCs, forming non-radiative complexes that effectively dampen the PL. Once the target analyte is introduced, it displaces the quenching agent, restoring the PL. The restoration of the fluorescence serves as a signal that the analyte has successfully been detected. This mechanism provides a clear and direct means of detecting the presence of specific targets, making it highly effective for applications in biomedical diagnostics and environmental monitoring.

One of the key advantages of the off-on strategy is its ability to achieve highly sensitive detection limits. For instance, Ding et al. demonstrated an innovative approach using BSA-Au NCs coated on nanopipettes for the detection of bio-thiols such as cysteine (Ding et al., 2020). The nanopipettes provide a confined space that enhances the interaction between the target analyte and the nanoclusters. In this system, the PL of the BSA-Au NCs is initially quenched, but the presence of cysteine reverses the quenching, restoring the fluorescence. This method achieved a remarkable detection limit of 1 fM (fM) and a dynamic range of 0.001–1 pM (pM), highlighting the sensitivity of the system. The combination of electrochemical and fluorometric detection in this method further enhanced its versatility, allowing for more precise monitoring of analytes in complex biological environments.

Another compelling example of the off-on strategy is found in the work of Deng et al., who developed BSA/3-mercaptopropionic acid (MPA) co-modified Au NCs for the detection of pyrophosphate (PPi) (Deng et al., 2020). In this system, Fe^{3+} ions act as quenching mediators, suppressing the PL of the BSA-MPA Au NCs. The introduction of PPi results in the chelation of Fe^{3+} ions, effectively removing them from the MNCs and restoring the PL signal. This off-on sensor was further employed to detect alkaline phosphatase (ALP) activity in human osteosarcoma cells. The competitive interaction between Fe^{3+} ions and PPi allowed for a highly sensitive detection of ALP, with a linear detection range of 0.8–16 UL^{-1} and a detection limit of 0.78 UL^{-1}. This system demonstrates the potential of off-on sensors to be used in real-world biological applications, where detecting enzyme activity in cells can be crucial for diagnosing and monitoring diseases.

In summary, off-on sensors based on MNCs represent a highly versatile and sensitive approach for detecting a wide range of analytes, from metal ions to small biomolecules. The use of a quenching mediator that can be displaced by the target analyte allows for the restoration of the PL signal, providing a clear and measurable readout. The adaptability of this approach, combined with its ability to integrate multiple detection modalities and perform multiplexed detection, makes off-on sensors a powerful tool for biosensing and diagnostics. As research continues to refine the design of MNCs and quenching mediators, off-on sensors are likely to play an increasingly important role in fields such as environmental monitoring, medical diagnostics and point-of-care testing.

3.3 Ratiometric sensors

Ratiometric detection is a more advanced and reliable technique compared to traditional single-wavelength methods, particularly in the field of sensing using MNCs. In ratiometric detection, PL intensities at two distinct wavelengths are measured and the ratio of these intensities is used as the primary readout. This ratio provides an internal reference that helps mitigate potential environmental variations, such as fluctuations in light intensity, probe concentration, or surrounding conditions, which can otherwise affect the accuracy of single-wavelength measurements. This approach is particularly advantageous in enhancing the sensitivity and accuracy of the probe for quantification purposes. By comparing the PL intensities at two wavelengths, it becomes easier to detect even small changes in analyte concentration with higher precision.

Ratiometric detection has been successfully applied in various MNC-based sensing platforms. For instance, in the detection of heavy metal ions like Hg^{2+}, ratiometric sensors utilizing Au and Ag NCs can measure the intensity changes at two wavelengths corresponding to the nanoclusters' emission and the analyte-induced spectral shift (Li et al., 2019). This dual-wavelength comparison enhances the accuracy of detecting small concentrations of Hg^{2+}, even in complex biological or environmental samples, where matrix effects might otherwise interfere with single-wavelength readings.

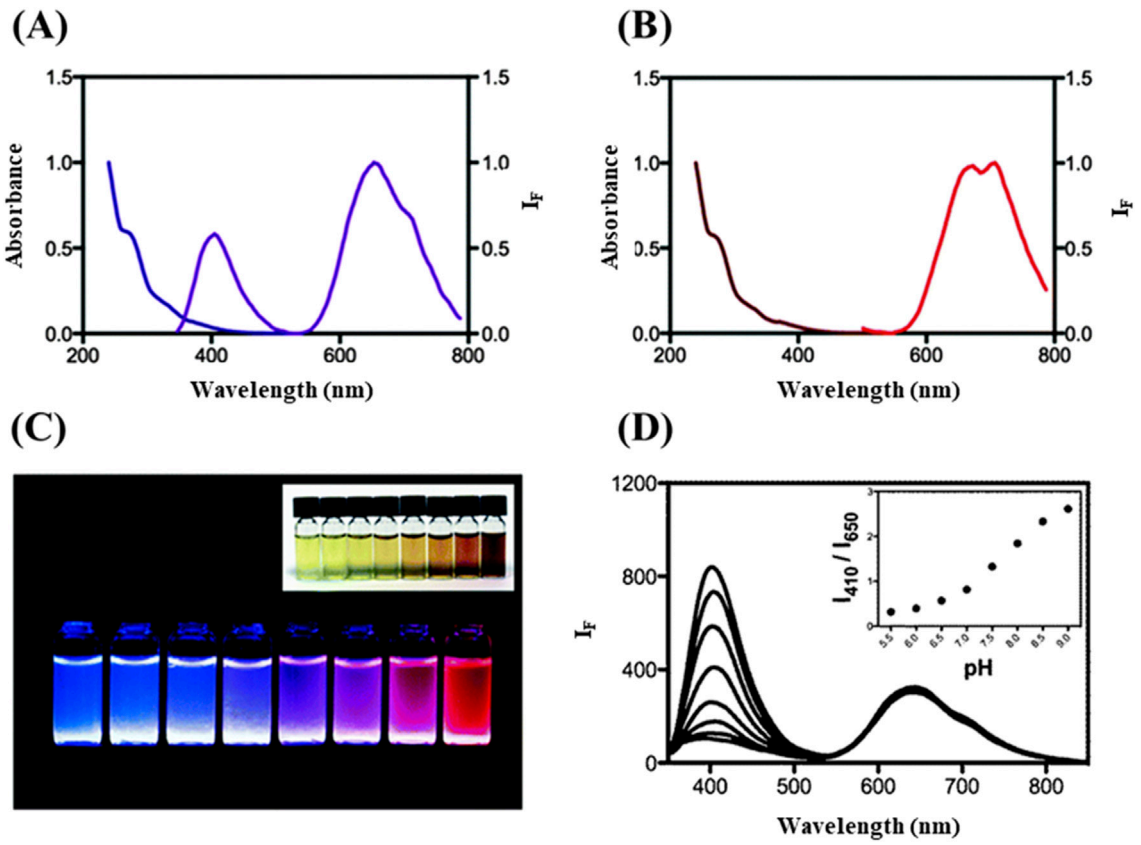

FIGURE 5
Spectroscopic analysis of BSA-Ce/Au NCs and its application for pH monitoring. **(A)** Absorption and PL spectra of BSA–Ce/Au nanoclusters. **(B)** Spectra for BSA-Au nanoclusters. **(C)** Photographic representation of photoluminescent solutions of BSA with Ce(IV) and Au(III) across different molar ratios; BSA concentration is maintained at 0.76 mM, with Ce(IV)/Au(III) ratios ranging from 1,000/0 to 0/10. **(D)** PL responses of BSA–Ce/Au NCs in 20 mM phosphate buffer across pH values from 5.5 to 9.0, with inset showing PL intensity ratios at 410 and 650 nm across these pH values. Reproduced from Chen et al. (2014). Copyright 2014, Royal Society of Chemistry.

The introduction of additional metal ions can be used to provide additional fluorophores that provide PL at different wavelengths. For example, Chang's group developed a one-pot synthesis of photoluminescent BSA-stabilized Ce/Au NCs, which were used as ratiometric pH probes (Figure 5) (Chen et al., 2014). These nanoclusters exhibited dual-emission properties, with distinct PL intensities at two wavelengths that varied depending on the pH of the solution. One emission at ca. 650 nm remained relatively constant, serving as an internal reference, while another emission intensity at ca. 410 nm shifted in response to changes in pH. This ratiometric approach allowed for precise and accurate measurement of pH levels across a wide range, making the BSA–Ce/Au nanoclusters highly effective for biological and environmental sensing applications. The internal referencing provided by the ratiometric system enhanced the reliability of pH measurements compared to traditional single-wavelength methods, where environmental fluctuations could lead to inaccurate readings. BSA–Ce/Au NCs can also be used for the detection of cyanide ions (CN^-). As the concentration of CN^- increased, the PL intensity of the BSA–Ce/Au NCs at 658 nm gradually decreased due to the dissolution of the Au NCs, while the intensity at 410 nm increased. This dual response enabled the detection of CN^- with a detection limit as low as 50 nM and a linear detection range from 0.1 to 15 μM (Wang C W et al., 2016). Similarly, Li et al. incorporated Eu^{3+} ions into BSA-Au NCs and applied for the detection of dipicolinic acid (DPA) with a low detection limit of 0.8 μM (Li X. et al., 2021). This was also applied in the detection of DPA released during the germination of *Bacillus subtilis* spores.

Xiao et al. developed two types of PL emitting BSA-Au NCs by synthesizing them at different pH levels, which allowed for distinct emission profiles (Xiao et al., 2020). These two types of Au NCs were subsequently combined into a single thin film using a layer-by-layer (LBL) assembly technique. The resulting thin film exhibited dual PL peaks when excited at 372 nm, corresponding to blue emission at 443 nm and red emission at 622 nm from the two Au NC types, respectively. This ratiometric system enabled highly sensitive detection of bilirubin, where the interaction of bilirubin with the Au NCs caused differential quenching of the two emission peaks. This differential quenching allowed for ratiometric detection of bilirubin with a limit of detection (LOD) of 8.90 nM in serum samples, demonstrating the effectiveness of ratiometric sensing for biological applications.

Similarly, Wu et al. utilized BSA-Au NCs in combination with BSPOTPE, an AIE active molecule, as detection and reference probes, respectively, for glucose sensing in a GOx detection system (Wu et al., 2020) (Figure 6). In this system, the H_2O_2

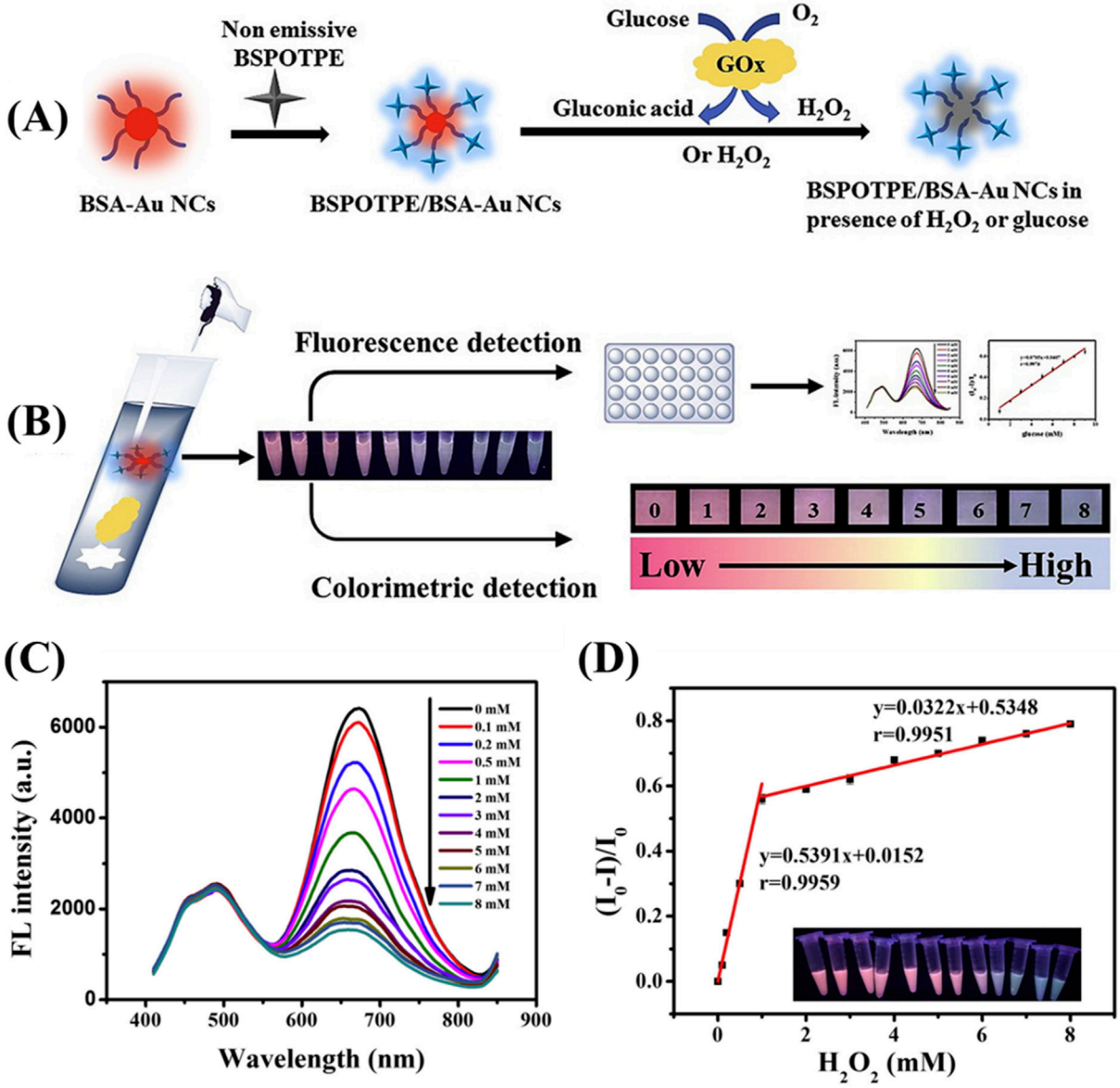

FIGURE 6
BSPOTPE/BSA-AuNCs as ratiometric fluorescence probe **(A)** Schematic representation of the synthesis process and detection mechanism of BSPOTPE/BSA-AuNCs. **(B)** Application of the BSPOTPE/BSA-AuNCs ratiometric fluorescence probe for glucose detection. **(C)** Fluorescence spectra of BSPOTPE/BSA-AuNCs in the presence of varying concentrations of H_2O_2 (0–8 mM). **(D)** Calibration plot of relative fluorescence intensity change $(I_0–I)/I_0$ as a function of H_2O_2 concentration, with two linear ranges: 0–1 mM and 1–8 mM. Reproduced from Wu et al. (2020). Copyright 2020, Elsevier.

produced by the enzymatic reaction of glucose with GOx induced the oxidation of the Au NCs, resulting in a decrease in their PL intensity. However, BSPOTPE, which remains photoluminescent, served as a stable reference probe, allowing for accurate ratiometric detection of glucose. This system achieved glucose detection down to 1 mM under UV light, demonstrating the potential of combining BSA-Au NCs with AIE-active molecules for sensitive and reliable biosensing.

The ratiometric sensors are particularly advantageous in complex biological and environmental samples, where fluctuations in external factors such as light intensity, probe concentration and environmental conditions can otherwise compromise the accuracy of single-wavelength measurements. By using ratiometric sensing, these variations are effectively minimized, leading to more precise and reproducible results. Furthermore, the ability to integrate ratiometric detection into multiplexed sensor systems enhances their utility for simultaneous detection of multiple targets, further expanding their applicability in point-of-care testing and real-time monitoring. Looking forward, the continued refinement of nanomaterials and the development of innovative ratiometric sensor designs, such as dual-emission nanoclusters and integration with AIE molecules, offer exciting opportunities for even greater sensitivity, selectivity and functional flexibility. As the field progresses, ratiometric sensors are poised to play an increasingly vital role in precision diagnostics, environmental sensing and a wide array of applications where robust and reliable detection is essential.

3.4 MNCs-based composite sensors

Recent efforts have been made to enhance the PL sensing capabilities of MNCs by incorporating non-metallic elements into their structure. These non-metallic elements, such as carbon, nitrogen, phosphorus and sulfur offer unique electronic and chemical properties that can improve the PL efficiency and sensing performance of MNCs. These attempts to integrate non-metallic elements not only improve the optical performance of MNCs but also open new avenues for developing multifunctional sensors with superior selectivity and responsiveness. Materials such as metal-organic framework (MOF), carbon nanomaterials and porous silica have been introduced into the MNCs to form a new kind of sensing probe. For instance, Khataee et al. reported dual emissive PL probe fabricated by encapsulating both Au NCs and Cu NCs into zeolitic imidazolate framework-8 (ZIF-8) and the obtained composite (AuCu NCs@MOF) was utilized for ratiometric determination of tetracycline (Tcy) antibiotic (Khataee et al., 2020). The logarithm of the PL ratio against the concentration of Tcy exhibited a linear range from 20 to 650 nM with a detection limit of 4.8 nM. The probe was applied for Tcy quantification in milk samples with superior results. Kong et al. designed a novel dual-emission reverse change ratio PL nanoplatform for fluorimetric and colorimetric sensing of heparin (Hep) and chondroitin sulfate (CS) based on green emissive terbium metal-organic framework (Tb MOF) and red emissive BSA@Au NCs (Kong et al., 2022).

In collaboration with Chang's research group, Chen's team developed a handheld pathogen sensor using a paper-based analytical device (μPAD) for rapid and sensitive pathogen detection (Yuan et al., 2022). This detection system utilizes graphene quantum dots (GQDs) and Au NCs, which are conjugated with antibodies to produce a colorimetric signal in the presence of pathogenic antigens. The sensor exhibited excellent performance, with linear detection ranges for protein A and exotoxin A between 0.3 and 30 ng/mL and detection limits of 0.2 ng/mL and 0.1 ng/mL, respectively. Additionally, Hu et al. designed a ratiometric detection system employing Au NCs as the probe and vesicle carbon dots (VCDs) as the internal standard (Figure 7) (Hu et al., 2022). This configuration confines Au NCs, enzymes and analytes within VCDs to increase local concentrations and improve assay sensitivity. In this study, cholesterol oxidase (ChOX) was used as a model enzyme for cholesterol quantification. The H_2O_2 produced through the enzymatic reaction caused PL quenching of the Au NCs (emission at 670 nm), while the VCDs (emission at 400 nm) remained unaffected. This ratiometric PL method enabled the detection of H_2O_2 within a range of 1–100 μM, with a detection limit of 0.673 μM and cholesterol concentrations ranging from 5 to 100 μM, with a detection limit of 2.8 μM, making it suitable for evaluating cholesterol levels in human serum samples.

The nanocomposite (BCD@SiO_2@Au NCs) served as a ratiometric photoluminescent sensor for the selective detection of Gram-negative bacteria, exploiting the copper-homeostasis mechanism inherent to these bacteria (Figure 8). The sensor's principle of detection relies on the quenching effect of Cu^{2+} on Au NCs and the concurrent reduction of Cu^{2+} by Gram-negative bacteria, demonstrating strong selectivity (Fu et al., 2022). In a related research by Zhang et al., a ratiometric photoluminescent probe (CQDs-Au NCs) was developed by combining amidated carbon quantum dots (CQDs) with BSA-coated Au NCs. This probe displayed dual emission peaks at 446 nm and 670 nm, producing purple PL upon excitation at 397 nm. The probe's effectiveness is attributed to the quenching of this purple PL by dopamine (DA), which occurs via electron transfer from the CQDs to DA, inhibiting the Förster resonance energy transfer (FRET) between CQDs and Au NCs. This ratiometric probe selectively detects DA, with a detection limit of 2.66 nM and a linear response spanning several concentration ranges: 2.66 nM–0.18 mM, 0.511–3.79 mM and 4.87–13.1 mM (Zhang Y et al., 2021).

Looking forward, future directions for MNC-based composite sensors will likely focus on the continued development of hybrid systems that leverage the unique properties of both MNCs and functional materials. One promising area is the exploration of novel MOFs and carbon-based nanomaterials that can further enhance the stability and PL efficiency of MNCs, particularly in challenging environments such as highly acidic or oxidative conditions. Additionally, the incorporation of responsive materials, such as stimuli-sensitive polymers or smart hydrogels, could lead to the creation of dynamic sensing platforms capable of adapting to real-time changes in their environment.

4 Summary and prospects

MNCs have seen significant advancements over the past decades and have become integral to various *in vitro* and *in vivo* detection applications. Protein-templated MNCs have facilitated the synthesis of nanoclusters with precise atomic numbers, ultra-small sizes and low toxicity, enabling their use in a wide range of sensing platforms. These include the detection of small molecules, metal ions and biological species, as well as *in vivo* imaging. One of the most promising developments in this field is the rise of MNC-based ratiometric sensing, which provides greater accuracy compared to traditional on-off or off-on sensing mechanisms. Additionally, the integration of composite materials into MNC platforms has further enhanced the sensitivity and accuracy of these sensors, making them more effective for real-world applications.

Despite these advancements, several challenges and limitations still exist in the development of MNCs, particularly in their broader adoption in environmental, clinical and industrial settings. One of the primary challenges is the limited variety of protein templates available for MNC synthesis. While proteins such as BSA have been widely used, the diversity of templates is still lacking, limiting the potential to create MNCs with tailored properties. Moreover, the use of functional proteins like antibodies or enzymes as templates is not well-established, partly because their biological activity is often compromised during synthesis. This functional loss, coupled with the high cost of functional proteins, remains a significant barrier to their widespread application. Though the use of GSH has been shown to reduce the required concentration of protein for cluster formation, the cost of biologically significant proteins is still prohibitive for large-scale use.

Another limitation is the narrow range of metal cores used in MNCs, with most research focusing on Au, Ag and Cu. While other

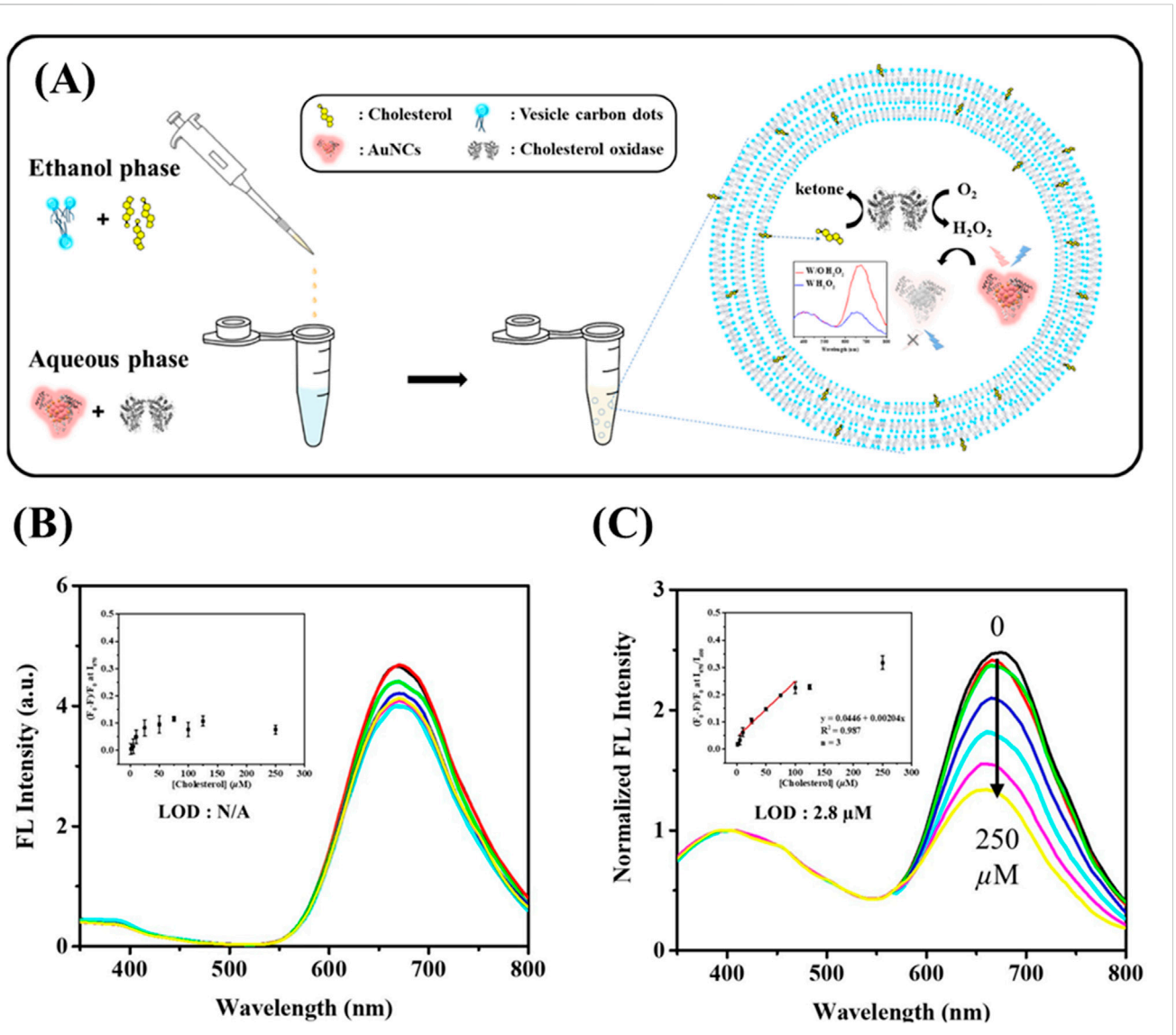

FIGURE 7
Cholesterol detection using BSA-Au NC/VCD nanocomposites. **(A)** Schematic illustration of the sensing system for detecting cholesterol using PL. PL emission spectra of **(B)** GSH/BSA-stabilized Au NCs and **(C)** GSH/BSA-Au NCs encapsulated in vesicle-like carbon dots (VCDs) in aqueous solution, upon addition of various concentrations of cholesterol (from top to bottom: 0, 1, 5, 25, 50, 125, 250 μM), excited at 320 nm. Inset shows the Stern–Volmer plot illustrating the quenching effect of cholesterol on PL intensity. Reproduced from Hu et al. (2022), licensed under CC BY.

metals, such as cadmium (Cd) and palladium (Pd), have been explored, their lower PL efficiency and stability compared to Au, Ag and Cu restrict their applicability. To address this, future research could explore alloying metals or incorporating other metal ions to improve PL properties and extend MNC functionality. Expanding the range of metal cores will be crucial for developing MNCs that exhibit dual-emission properties and broader spectral responses, which are highly desirable for multiplexed sensing and imaging applications.

A pressing challenge is the development of MNCs with PL in the NIR range, particularly in the NIR-II window (1000–1700 nm), which is optimal for deep tissue imaging due to its minimal light scattering and absorption in biological tissues. Currently, protein-templated MNCs lack consistent methods for synthesizing NIR-II emitting nanoclusters, which limits their use in advanced applications such as deep tumor imaging and precision chemical sensing. Incorporating thiolated ligands or other functional groups into MNCs could be a viable strategy to achieve tunable NIR-II luminescence. Achieving efficient PL in the NIR-II range remains a critical goal for researchers, as this would greatly expand the utility of MNCs in biomedical diagnostics and therapeutic applications.

Future research directions should focus on addressing these limitations and exploring new strategies for MNC synthesis and functionalization. Developing more diverse protein templates, exploring alternative metal cores and achieving tunable NIR-II PL are key areas that will drive the next wave of innovation in MNC-based sensing. Advances in materials science, such as the integration of NCs with stimuli-responsive materials, could lead to

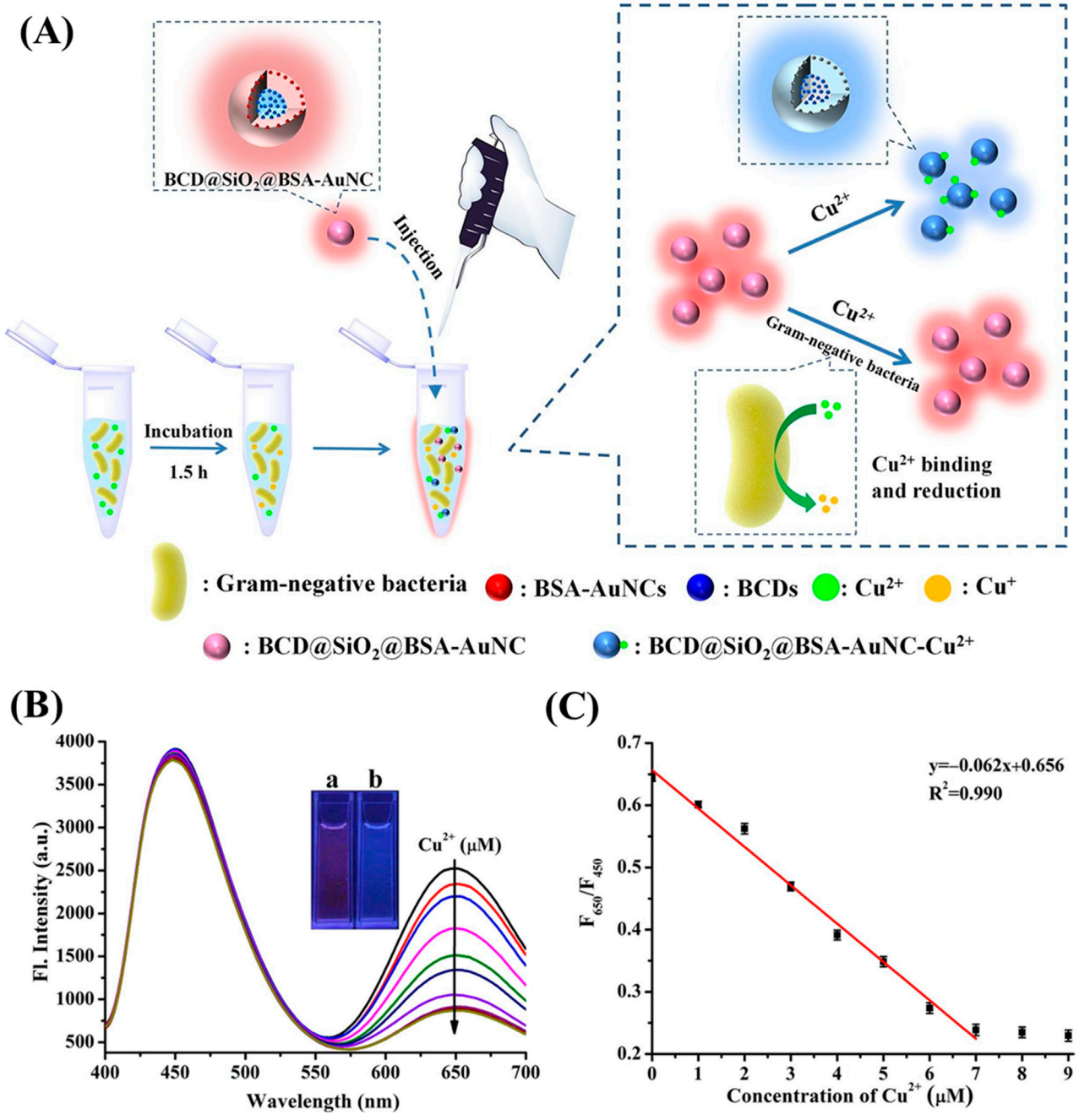

FIGURE 8
BCD@SiO_2@BSA-AuNC-based ratiometric fluorescent sensor. **(A)** Schematic illustration of the ratiometric fluorescent sensor based on BCD@SiO_2@BSA-AuNCs for the detection of Gram-negative bacteria. **(B)** Fluorescence spectra of BCD@SiO_2@BSA-AuNC at λ_{ex} = 370 nm on exposure to various concentrations of Cu^{2+} from 0 to 7.0 × 10^{-6} M. **(C)** Calibration curve of the fluorescence intensity ratio (F_{650}/F_{450}) as a function of Cu^{2+} concentration in carbonate buffer (10 mM, pH 11.0). The inset is the photos of BCD@SiO_2@BSA-AuNC **(A)** and Cu^{2+} (7.0 × 10^{-6} M) + BCD@SiO_2@BSA-AuNC **(B)** under the irradiation of a 365 nm UV lamp. Reproduced from Fu et al. (2022). Copyright 2022, Elsevier.

highly dynamic and adaptable sensors for real-time monitoring in complex biological environments. Moreover, incorporating machine learning and artificial intelligence into sensor design and data interpretation may open new frontiers in the precision and efficiency of MNC-based diagnostics.

In conclusion, while MNCs have demonstrated great promise in sensing, there are still significant challenges to overcome to fully realize their potential. With continued advancements in MNC design, synthesis techniques, and functionalization strategies, MNCs are poised to become central to future innovations in biosensing, early disease detection, environmental monitoring and therapeutic applications. The development of NIR-II emitting MNCs, in particular, will likely revolutionize deep-tissue imaging and disease treatment,

positioning MNCs as pivotal tools in next-generation sensing and biomedical technologies.

Author contributions

H-WC: Writing–original draft, Writing–review and editing. GD: Writing–original draft. C-CH: Writing–review and editing. AA: Writing–original draft, Writing–review and editing.

Funding

The author(s) declare that financial support was received for the research, authorship, and/or publication of this article. We are grateful to the National Science and Technology Council (NSTC) of Taiwan for providing financial support for this study under contracts NSTC 112-2811-B-182-022 and NSTC113-2622-E-182-004, Chang Gung Memorial Hospital, Linkou under Contract No. CMRPD1N0271, Chang Gung University under Contract No. UMRPD1N0051 and UMRPD1N0141.

Conflict of interest

The authors declare that the research was conducted in the absence of any commercial or financial relationships that could be construed as a potential conflict of interest.

Generative AI statement

The author(s) declare that no Generative AI was used in the creation of this manuscript.

Publisher's note

References

Aikens, C. M., and Jarrold, C. C. (2023). Virtual issue on experiment–theory synergies in the study of metal and metal-containing clusters. *J. Phys. Chem. A* 127, 3–5. doi:10.1021/acs.jpca.2c08524

Aires, A., Lopez-Martinez, E., and Cortajarena, A. L. (2018). Sensors based on metal nanoclusters stabilized on designed proteins. *Biosensors* 8, 110. doi:10.3390/bios8040110

Akyüz, E., Şen, F. B., Bener, M., Başkan, K. S., and Apak, R. (2020). A novel gold nanocluster–based fluorometric biosensor for measuring prooxidant activity with a large Stokes shift. *Talanta* 208, 120425. doi:10.1016/j.talanta.2019.120425

Aparna, A., Sreehari, H., Chandran, A., Anjali, K. P., Alex, A. M., Anuvinda, P., et al. (2022). Ligand-protected nanoclusters and their role in agriculture, sensingand allied applications. *Talanta* 239, 123134. doi:10.1016/j.talanta.2021.123134

Brocha Silalahi, R. P., Chiu, T.-H., Kao, J.-H., Wu, C.-Y., Yin, C.-W., Liu, Y.-C., et al. (2021). Reactivities of interstitial hydrides in a Cu11 template: en route to bimetallic clusters. *Inorg. Chem.* 60, 10799–10807. doi:10.1021/acs.inorgchem.1c01489

Casteleiro, B., Martinho, J. M. G., and Farinha, J. P. S. (2021). Encapsulation of gold nanoclusters: stabilization and more. *Nanoscale* 13, 17199–17217. doi:10.1039/D1NR04939A

Chakraborty, I., and Parak, W. J. (2019). Protein-induced shape control of noble metal nanoparticles. *Adv. Mat. Interfaces* 6, 1801407. doi:10.1002/admi.201801407

Chakraborty, S., and Mukherjee, S. (2022). Effects of protecting groups on luminescent metal nanoclusters: spectroscopic signatures and applications. *Chem. Commun.* 58, 29–47. doi:10.1039/D1CC05396E

Chang, X., Gao, P., Li, Q., Liu, H., Hou, H., Wu, S., et al. (2021). Fluorescent papain-encapsulated platinum nanoclusters for sensing lysozyme in biofluid and gram-positive bacterial identification. *Sens. Actuators B Chem.* 345, 130363. doi:10.1016/j.snb.2021.130363

Chen, M., Ning, Z., Ge, X., Yang, E., Sun, Q., Yin, F., et al. (2023). Ligands engineering of gold nanoclusters with enhanced photoluminescence for deceptive information encryption and glutathione detection. *Biosens. Bioelectron.* 219, 114805. doi:10.1016/j.bios.2022.114805

Chen, P.-C., Chiang, C.-K., and Chang, H.-T. (2013). Synthesis of fluorescent BSA–Au NCs for the detection of Hg^{2+} ions. *J. Nanopart. Res.* 15, 1336. doi:10.1007/s11051-012-1336-0

Chen, P.-C., Li, Y.-C., Ma, J.-Y., Huang, J.-Y., Chen, C.-F., and Chang, H.-T. (2016). Size-tunable copper nanocluster aggregates and their application in hydrogen sulfide sensing on paper-based devices. *Sci. Rep.* 6, 24882. doi:10.1038/srep24882

Chen, T., Lin, H., Cao, Y., Yao, Q., and Xie, J. (2022). Interactions of metal nanoclusters with light: fundamentals and applications. *Adv. Mat.* 34, 2103918. doi:10.1002/adma.202103918

Chen, X., Wang, T., Le, W., Huang, X., Gao, M., Chen, Q., et al. (2020). Smart sorting of tumor phenotype with versatile fluorescent Ag nanoclusters by sensing specific reactive oxygen species. *Theranostics* 10, 3430–3450. doi:10.7150/thno.38422

Chen, Y.-C., Wang, C.-W., Lee, J. D., Chen, P.-C., and Chang, H.-T. (2016). Control of the fluorescence of DNA-templated silver nanoclusters by adenosine triphosphate and mercury(II). *J. Chin. Chem. Soc.* 64, 8–16. doi:10.1002/jccs.201600246

Chen, Y.-N., Chen, P.-C., Wang, C.-W., Lin, Y.-S., Ou, C.-M., Ho, L.-C., et al. (2014). One-pot synthesis of fluorescent BSA–Ce/Au nanoclusters as ratiometric pH probes. *Chem. Commun.* 50, 8571–8574. doi:10.1039/C4CC03949A

Chen, Y.-W., Periasamy, A. P., Chen, C.-F., and Chang, H.-T. (2019). Quantification of glucose via *in situ* growth of Cu2O/Ag nanoparticles. *Sens. Actuators B* 285, 224–231. doi:10.1016/j.snb.2019.01.050

Cheng, Y., Zhao, Y., Yuan, H., Zhou, H., Xu, J., Chen, X., et al. (2023). Bovine serum albumin protected Cd8 nanoclusters as efficient two-photon absorbers for near-infrared excited fluorescence imaging of intracellular pH. *Sens. Actuators B* 394, 134427. doi:10.1016/j.snb.2023.134427

Cun, X., Jansman, M. M. T., Liu, X., Boureau, V., Thulstrup, P. W., and Hosta-Rigau, L. (2023). Hemoglobin-stabilized gold nanoclusters displaying oxygen transport ability, self-antioxidation, auto-fluorescence propertiesand long-term storage potential. *RSC Adv.* 13, 15540–15553. doi:10.1039/D3RA00689A

Czyżowska, A., Barbasz, A., Szyk-Warszyńska, L., Oćwieja, M., Csapó, E., and Ungor, D. (2021). The surface-dependent biological effect of protein-gold nanoclusters on human immune system mimetic cells. *Colloids Surf. A* 620, 126569. doi:10.1016/j.colsurfa.2021.126569

Deng, H.-H., Deng, Q., Li, K.-L., Zhuang, Q.-Q., Zhuang, Y.-B., Peng, H.-P., et al. (2020). Fluorescent gold nanocluster-based sensor for detection of alkaline phosphatase in human osteosarcoma cells. *Spectrochim. Acta A Mol. Biomol. Spectrosc.* 229, 117875. doi:10.1016/j.saa.2019.117875

Ding, S., Liu, C., Fu, D., Shi, G., and Zhu, A. (2020). Coordination of ligand-protected metal nanoclusters and glass nanopipettes: conversion of a liquid-phase fluorometric assay into an enhanced nanopore analysis. *Anal. Chem.* 93, 1779–1785. doi:10.1021/acs.analchem.0c04620

Dong, W., Yu, J., Gong, X., Liang, W., Fan, L., and Dong, C. (2021). A turn-off-on near-infrared photoluminescence sensor for sequential detection of Fe^{3+} and ascorbic acid based on glutathione-capped gold nanoclusters. *Spectrochimica Acta Part A Mol. Biomol. Spectrosc.* 247, 119085. doi:10.1016/j.saa.2020.119085

Duan, Y., Duan, R., Liu, R., Guan, M., Chen, W., Ma, J., et al. (2018). Chitosan-stabilized self-assembled fluorescent gold nanoclusters for cell imaging and biodistribution *in vivo*. *ACS Biomater. Sci. Eng.* 4, 1055–1063. doi:10.1021/acsbiomaterials.7b00975

Ebina, A., Hossain, S., Horihata, H., Ozaki, S., Kato, S., Kawawaki, T., et al. (2020). One-two-and three-dimensional self-assembly of atomically precise metal nanoclusters. *Nanomaterials* 10, 1105. doi:10.3390/nano10061105

Fang, J., Li, J., Zhang, B., Yuan, X., Asakura, H., Tanaka, T., et al. (2015). The support effect on the size and catalytic activity of thiolated Au_{25} nanoclusters as precatalysts. *Nanoscale* 7, 6325–6333. doi:10.1039/c5nr00549c

Fereja, S. L., Li, P., Guo, J., Fang, Z., Zhang, Z., Zhuang, Z., et al. (2021). Silver-enhanced fluorescence of bimetallic Au/Ag nanoclusters as ultrasensitive sensing probe for the detection of folic acid. *Talanta* 233, 122469. doi:10.1016/j.talanta.2021.122469

Fu, L., Chen, Q., and Jia, L. (2022). Carbon dots and gold nanoclusters assisted construction of a ratiometric fluorescent biosensor for detection of Gram-negative bacteria. *Food Chem.* 374, 131750. doi:10.1016/j.foodchem.2021.131750

Guo, Y., Amunyela, H. T., Cheng, Y., Xie, Y., Yu, H., Yao, W., et al. (2021). Natural protein-templated fluorescent gold nanoclusters: syntheses and applications. *Food Chem.* 335, 127657. doi:10.1016/j.foodchem.2020.127657

Guo, Y., Han, Y., and Chen, C. (2022). Chiral nanocluster complexes formed by host–guest interaction between enantiomeric 2,6-helic[6]arenes and silver cluster Ag20: emission enhancement and chirality transfer. *Molecules* 27, 3932. doi:10.3390/molecules27123932

Häkkinen, H. (2012). The gold–sulfur interface at the nanoscale. *Nat. Chem.* 4, 443–455. doi:10.1038/nchem.1352

Hossain, S., Imai, Y., Motohashi, Y., Chen, Z., Suzuki, D., Suzuki, T., et al. (2020). Understanding and designing one-dimensional assemblies of ligand-protected metal nanoclusters. *Mat. Horiz.* 7, 796–803. doi:10.1039/C9MH01691K

Hsu, Y.-C., Hung, M.-J., Chen, Y.-A., Wang, T.-F., Ou, Y.-R., and Chen, S.-H. (2019). Identifying reducing and capping sites of protein-encapsulated gold nanoclusters. *Molecules* 24, 1630. doi:10.3390/molecules24081630

Hu, S.-R., Yang, C.-R., Huang, Y.-F., Huang, C.-C., Chen, Y.-L., and Chang, H.-T. (2022). Ratiometric fluorescence probe of vesicle-like carbon dots and gold clusters for quantitation of cholesterol. *Chemosensors* 10, 160. doi:10.3390/chemosensors10050160

Jin, L., Shi, L., Shi, W., Meng, Z., Shang, L., and Shen, Y. (2019). Fluorescence lifetime-based pH sensing by platinum nanoclusters. *Analyst* 144, 3533–3538. doi:10.1039/C9AN00061E

Jin, R. (2015). Atomically precise metal nanoclusters: stable sizes and optical properties. *Nanoscale* 7, 1549–1565. doi:10.1039/C4NR05794E

Jin, R., Li, G., Sharma, S., Li, Y., and Du, X. (2020). Toward active-site tailoring in heterogeneous catalysis by atomically precise metal nanoclusters with crystallographic structures. *Chem. Rev.* 121, 567–648. doi:10.1021/acs.chemrev.0c00495

Kailasa, S. K., Borse, S., Koduru, J. R., and Murthy, Z. (2021). Biomolecules as promising ligands in the synthesis of metal nanoclusters: sensing, bioimaging and catalytic applications. *Trac. Trends Environ. Anal. Chem.* 32, e00140. doi:10.1016/j.teac.2021.e00140

Kang, X., Wang, S., Song, Y., Jin, S., Sun, G., Yu, H., et al. (2016). Bimetallic Au2Cu6 nanoclusters: strong luminescence induced by the aggregation of copper(I) complexes with gold(0) species. *Angew. Chem. Int. Ed.* 55, 3611–3614. doi:10.1002/anie.201600241

Kang, X., and Zhu, M. (2019). Metal nanoclusters stabilized by selenol ligands. *Small* 15, 1902703. doi:10.1002/smll.201902703

Khataee, A., Jalili, R., Dastborhan, M., Karimi, A., and Azar, A. E. F. (2020). Ratiometric visual detection of tetracycline residues in milk by framework-enhanced fluorescence of gold and copper nanoclusters. *Spectrochim. Acta A Mol. Biomol. Spectrosc.* 242, 118715. doi:10.1016/j.saa.2020.118715

Koga, H., Sakata, K., Ato, Y., Hayashi, A., Tada, K., and Okumura, M. (2016). Advances in polymer-stabilized Au nano-cluster catalysis: interplay of theoretical calculations and experiments. *Chin. J. Catal.* 37, 1588–1593. doi:10.1016/S1872-2067(16)62463-4

Kolay, S., Bain, D., Maity, S., Devi, A., Patra, A., and Antoine, R. (2022). Self-assembled metal nanoclusters: driving forces and structural correlation with optical properties. *Nanomaterials* 12, 544. doi:10.3390/nano12030544

Kong, X.-J., Tian, J.-X., Fang, Y.-Z., Chen, T.-L., Yu, R., He, J.-Y., et al. (2022). Terbium metal-organic framework/bovine serum albumin capped gold nanoclusters-based dual-emission reverse change ratio fluorescence nanoplatform for fluorimetric and colorimetric sensing of heparin and chondroitin sulfate. *Sens. Actuators B Chem.* 356, 131331. doi:10.1016/j.snb.2021.131331

Lettieri, M., Palladino, P., Scarano, S., and Minunni, M. (2021). Protein-templated copper nanoclusters for fluorimetric determination of human serum albumin. *Microchim. Acta* 188, 116–119. doi:10.1007/s00604-021-04764-7

Li, C., and Wei, C. (2017). DNA-templated silver nanocluster as a label-free fluorescent probe for the highly sensitive and selective detection of mercury ions. *Sens. Actuators B Chem.* 242, 563–568. doi:10.1016/j.snb.2016.11.091

Li, J.-J., Qiao, D., Zhao, J., Weng, G.-J., Zhu, J., and Zhao, J.-W. (2019). Ratiometric fluorescence detection of Hg^{2+} and Fe^{3+} based on BSA-protected Au/Ag nanoclusters and His-stabilized Au nanoclusters. *Methods Appl. Fluoresc.* 7, 045001. doi:10.1088/2050-6120/ab34be

Li, P., Xie, Z., Zhuang, L., Deng, L., and Huang, J. (2023). DNA-templated copper nanocluster: a robust and universal fluorescence switch for bleomycin assay. *Int. J. Biol. Macromol.* 234, 123756. doi:10.1016/j.ijbiomac.2023.123756

Li, X., Luo, J., Jiang, X., Yang, M., and Rasooly, A. (2021). Gold nanocluster-europium (III) ratiometric fluorescence assay for dipicolinic acid. *Microchim. Acta* 188, 26–28. doi:10.1007/s00604-020-04667-z

Li, Y., Zhou, M., and Jin, R. (2021). Programmable metal nanoclusters with atomic precision. *Adv. Mat.* 33, 2006591. doi:10.1002/adma.202006591

Lin, H., Song, X., Huang Chai, O. J., Yao, Q., Yang, H., and Xie, J. (2024). Photoluminescent characterization of metal nanoclusters: basic parameters, methodsand applications. *Adv. Mater* 36, 2401002. doi:10.1002/adma.202401002

Lin, Y.-F., Yang, C.-R., Huang, Y.-F., and Chang, H.-T. (2022). Fluorescent carbon dots and noble metal nanoclusters for sensing applications: minireview. *J. Chin. Chem. Soc.* 69, 1200–1209. doi:10.1002/jccs.202200150

Lin, Y.-S., Chuang, L.-W., Wu, B.-Y., Lin, Y.-H., and Chang, H.-T. (2021a). Polymer/glutathione Au nanoclusters for detection of sulfides. *Sens. Actuators B* 333, 129356. doi:10.1016/j.snb.2020.129356

Lin, Y.-S., Lin, Y.-F., Nain, A., Huang, Y.-F., and Chang, H.-T. (2021b). A critical review of copper nanoclusters for monitoring of water quality. *Sens. Actuators Rep.* 3, 100026. doi:10.1016/j.snr.2021.100026

Lipok, M., Obstarczyk, P., Parzyszek, S., Wang, Y., Bagiński, M., Bürgi, T., et al. (2023). Circularly polarized luminescence from atomically precise gold nanoclusters helically assembled by liquid-crystal template. *Adv. Opt. Mat.* 11, 2201984. doi:10.1002/adom.202201984

Liu, R., Duan, S., Bao, L., Wu, Z., Zhou, J., and Yu, R. (2020). Photonic crystal enhanced gold-silver nanoclusters photoluminescent sensor for Hg^{2+} ion. *Anal. Chim. Acta* 1114, 50–57. doi:10.1016/j.aca.2020.04.011

Liu, Z., Luo, L., and Jin, R. (2024). Visible to NIR-II photoluminescence of atomically precise gold nanoclusters. *Angew. Chem. Int. Ed.* 36, 2309073. doi:10.1002/adma.202309073

López-Domene, R., Vázquez-Díaz, S., Modin, E., Beloqui, A., and Cortajarena, A. L. (2023). An emerging nanozyme class for à la carte enzymatic-like activities based on protein-metal nanocluster hybrids. *Adv. Funct. Mat.* 33, 2301131. doi:10.1002/adfm.202301131

Luo, Z., Yuan, X., Yu, Y., Zhang, Q., Leong, D. T., Lee, J. Y., et al. (2012). From aggregation-induced emission of Au(I)–thiolate complexes to ultrabright Au(0)@Au(I)–thiolate core–shell nanoclusters. *J. Am. Chem. Soc.* 134, 16662–16670. doi:10.1021/ja306199p

Mathew, M. S., Krishnan, G., Mathews, A. A., Sunil, K., Mathew, L., Antoine, R., et al. (2023). Recent progress on ligand-protected metal nanoclusters in photocatalysis. *Nanomaterials* 13, 1874. doi:10.3390/nano13121874

Matus, M. F., and Häkkinen, H. (2023). Understanding ligand-protected noble metal nanoclusters at work. *Nat. Rev. Mat.* 8, 372–389. doi:10.1038/s41578-023-00537-1

Mitsui, M., Arima, D., Kobayashi, Y., Lee, E., and Niihori, Y. (2022). On the origin of photoluminescence enhancement in biicosahedral Ag_xAu_{25-x} nanoclusters (x = 0–13) and their application to triplet–triplet annihilation photon upconversion. *Adv. Opt. Mat.* 10, 2200864. doi:10.1002/adom.202200864

Miyamura, H., Yasukawa, T., and Kobayashi, S. (2014). Preparation of polymer incarcerated gold nanocluster catalysts (PI-Au) and their application to aerobic oxidation reactions of boronic acids, alcoholsand silyl enol ethers. *Tetrahedron* 70, 6039–6049. doi:10.1016/j.tet.2014.05.014

Nain, A., Tseng, Y.-T., Lin, Y.-S., Wei, S.-C., Mandal, R. P., Unnikrishnan, B., et al. (2020). Tuning the photoluminescence of metal nanoclusters for selective detection of multiple heavy metal ions. *Sens. Actuators B* 321, 128539. doi:10.1016/j.snb.2020.128539

Nasrollahpour, H., Jurado Sánchez, B., Sillanpää, M., and Moradi, R. (2023). Metal nanoclusters in point-of-care sensing and biosensing applications. *ACS Appl. Nano Mat.* 6, 12609–12672. doi:10.1021/acsanm.3c01569

New, S. Y., Lee, S. T., and Su, X. D. (2016). DNA-templated silver nanoclusters: structural correlation and fluorescence modulation. *Nanoscale* 8, 17729–17746. doi:10.1039/C6NR05872H

O'Neill, P. R., Velazquez, L. R., Dunn, D. G., Gwinn, E. G., and Fygenson, D. K. (2009). Hairpins with poly-C loops stabilize four types of fluorescent Agn. *J. Phys. Chem. C* 113, 4229–4233. doi:10.1021/jp809274m

Panthi, G., and Park, M. (2022). Synthesis of metal nanoclusters and their application in Hg^{2+} ions detection: a review. *J. Hazard. Mat.* 424, 127565. doi:10.1016/j.jhazmat.2021.127565

Paulrajpillai, L. X., Chaudhari, K., Baksi, A., and Pradeep, T. (2012). Protein-protected luminescent noble metal quantum clusters: an emerging trend in atomic cluster nanoscience. *Nano Rev.* 3, 14767. doi:10.3402/nano.v3i0.14767

Pei, G. X., Zhang, L., and Sun, X. (2024). Recent advances of bimetallic nanoclusters with atomic precision for catalytic applications. *Coord. Chem. Rev.* 506, 215692. doi:10.1016/j.ccr.2024.215692

Pyo, K., Thanthirige, V. D., Kwak, K., Pandurangan, P., Ramakrishna, G., and Lee, D. (2015). Ultrabright luminescence from gold nanoclusters: rigidifying the Au(I)-thiolate shell. *J. Am. Chem. Soc.* 137, 8244–8250. doi:10.1021/jacs.5b04210

Qian, S., Wang, Z., Zuo, Z., Wang, X., Wang, Q., and Yuan, X. (2022). Engineering luminescent metal nanoclusters for sensing applications. *Coord. Chem. Rev.* 451, 214268. doi:10.1016/j.ccr.2021.214268

Qiao, Z., Yan, Y., and Bi, S. (2022). Three-dimensional DNA structures *in situ* decorated with metal nanoclusters for dual-mode biosensing of glucose. *Sens. Actuators B* 352, 131073. doi:10.1016/j.snb.2021.131073

Qiao, Z., Zhang, J., Hai, X., Yan, Y., Song, W., and Bi, S. (2021). Recent advances in templated synthesis of metal nanoclusters and their applications in biosensing,

bioimaging and theranostics. *Biosens. Bioelectron.* 176, 112898. doi:10.1016/j.bios.2020.112898

Romeo, M. V., Lopez-Martinez, E., Berganza-Granda, J., Goni-de-Cerio, F., and Cortajarena, A. L. (2021). Biomarker sensing platforms based on fluorescent metal nanoclusters. *Nanoscale Adv.* 3, 1331–1341. doi:10.1039/D0NA00796J

Sam, S., Swathy, S., and Kumar, K. G. (2024). Lysozyme functionalized silver nanoclusters as a dual channel optical sensor for the effective determination of glutathione. *Talanta* 277, 126326. doi:10.1016/j.talanta.2024.126326

Sarkar, P., Nandi, N., Barnwal, N., and Sahu, K. (2023). BSA-capped dual-emissive silver nanoclusters for detection of IO_4^- and Cu^{2+} ions. *ACS Appl. Nano Mat.* 6, 15851–15859. doi:10.1021/acsanm.3c02752

Sebastian, A., Aarya, Sarangi, B. R., and Sen Mojumdar, S. (2023). Lysozyme protected copper nano-cluster: a photo-switch for the selective sensing of Fe^{2+}. *J. Photochem. Photobiol. A Chem.* 436, 114378. doi:10.1016/j.jphotochem.2022.114378

Shen, J., Xiao, Q., Sun, P., Feng, J., Xin, X., Yu, Y., et al. (2021). Self-assembled chiral phosphorescent microflowers from Au nanoclusters with dual-mode pH sensing and information encryption. *ACS Nano* 15, 4947–4955. doi:10.1021/acsnano.0c09766

Sinha-Roy, R., García-González, P., López-Lozano, X., and Weissker, H.-C. (2023). Visualizing screening in noble-metal clusters: static vs. dynamic. *Phys. Chem. Chem. Phys.* 25, 2075–2083. doi:10.1039/D2CP04316E

Song, C., Xu, J., Chen, Y., Zhang, L., Lu, Y., and Qing, Z. (2019). DNA-templated fluorescent nanoclusters for metal ions detection. *Molecules* 24, 4189. doi:10.3390/molecules24224189

Song, Y., Li, Y., Zhou, M., Liu, X., Li, H., Wang, H., et al. (2021). Ultrabright Au@Cu14 nanoclusters: 71.3% phosphorescence quantum yield in non-degassed solution at room temperature. *Sci. Adv.* 7, eabd2091. doi:10.1126/sciadv.abd2091

Sun, H., Qing, T., He, X., Shangguan, J., Jia, R., Bu, H., et al. (2019). Rapid synthesis of Au/Ag bimetallic nanoclusters with highly biochemical stability and its applications for temperature and ratiometric pH sensing. *Anal. Chim. Acta* 1070, 88–96. doi:10.1016/j.aca.2019.04.029

Suo, Z., Hou, X., Hu, Z., Liu, Y., Xing, F., and Feng, L. (2019). Fibrinogen-templated gold nanoclusters for fluorometric determination of cysteine and mercury (II). *Microchim. Acta* 186, 799–9. doi:10.1007/s00604-019-3919-2

Tan, S. C. L., He, Z., Wang, G., Yu, Y., and Yang, L. (2023). Protein-templated metal nanoclusters: molecular-like hybrids for biosensing, diagnosticsand pharmaceutics. *Molecules* 28, 5531. doi:10.3390/molecules28145531

Tang, X., Lu, M., Wang, J., Man, S., Peng, W., and Ma, L. (2024). Recent advances of DNA-templated metal nanoclusters for food safety detection: from synthesis, applications, challengesand beyond. *J. Agric. Food Chem.* 72, 5542–5554. doi:10.1021/acs.jafc.3c09621

Thakran, A., Nain, A., Kataria, M., Paul Inbaraj, C. R., Lin, H.-Y., Lin, H.-I., et al. (2021). Highly efficient photodetection in metal nanocluster/graphene heterojunctions. *ACS Photonics* 8, 2955–2965. doi:10.1021/acsphotonics.1c00885

Tseng, Y.-T., Chang, H.-Y., Harroun, S. G., Wu, C.-W., Wei, S.-C., Yuan, Z., et al. (2018). Self-assembled chiral gold supramolecules with efficient laser absorption for enantiospecific recognition of carnitine. *Anal. Chem.* 90, 7283–7291. doi:10.1021/acs.analchem.8b00490

van de Looij, S. M., Hebels, E. R., Viola, M., Hembury, M., Oliveira, S., and Vermonden, T. (2021). Gold nanoclusters: imaging, therapyand theranostic roles in biomedical applications. *Bioconjugate Chem.* 33, 4–23. doi:10.1021/acs.bioconjchem.1c00475

Vilar-Vidal, N., Rivas, J., and Lopez-Quintela, M. A. (2012). Size dependent catalytic activity of reusable subnanometer copper (0) clusters. *ACS Catal.* 2, 1693–1697. doi:10.1021/cs300355n

Voet, A. R., and Tame, J. R. (2017). Protein-templated synthesis of metal-based nanomaterials. *Curr. Opin. Biotechnol.* 46, 14–19. doi:10.1016/j.copbio.2016.10.015

Wang, C. C., Wu, S. M., Li, H. W., and Chang, H. T. (2016). Biomedical applications of DNA-conjugated gold nanoparticles. *ChemBioChem* 17, 1052–1062. doi:10.1002/cbic.201600014

Wang, C.-W., Chen, Y.-N., Wu, B.-Y., Lee, C.-K., Chen, Y.-C., Huang, Y.-H., et al. (2016). Sensitive detection of cyanide using bovine serum albumin-stabilized cerium/gold nanoclusters. *Anal. Bioanal. Chem.* 408, 287–294. doi:10.1007/s00216-015-9104-5

Wang, H.-B., Bai, H.-Y., Dong, G.-L., and Liu, Y.-M. (2019). DNA-templated Au nanoclusters coupled with proximity-dependent hybridization and guanine-rich DNA induced quenching: a sensitive fluorescent biosensing platform for DNA detection. *Nanoscale Adv.* 1, 1482–1488. doi:10.1039/C8NA00278A

Wang, M., Li, H., Wang, Y., Hu, X., Fang, S., Ma, H., et al. (2023). Spatial confinement-enhanced electrochemiluminescence of gold nanoclusters in chitosan nanogels and its application for ultrasensitive detection of aflatoxin B1. *J. Electroanal. Chem.* 943, 117595. doi:10.1016/j.jelechem.2023.117595

Wang, S., Meng, X., Das, A., Li, T., Song, Y., Cao, T., et al. (2014). A 200-fold quantum yield boost in the photoluminescence of silver-doped AgxAu25-x nanoclusters: the 13th silver atom matters. *Angew. Chem. Int. Ed.* 53, 2376–2380. doi:10.1002/anie.201307480

Wei, S., Li, Y., Liang, H., Yen, Y., Lin, Y., and Chang, H. (2022). Photoluminescent carbon nanomaterials for sensing of illicit drugs: focus. *Anal. Sci.* 38, 247–260. doi:10.2116/analsci.21SAR06

Wen, Q.-L., Peng, J., Liu, A.-Y., Hu, Y.-L., Wang, J., Ling, J., et al. (2020). Fluorescent silver nanoclusters stabilized in guanine-enhanced DNA hybridization for recognizing different small biological molecules. *J. Lumin.* 221, 117038. doi:10.1016/j.jlumin.2020.117038

Wong, X. Y., Quesada-González, D., Manickam, S., New, S. Y., Muthoosamy, K., and Merkoçi, A. (2021). Integrating gold nanoclusters, folic acidand reduced graphene oxide for nanosensing of glutathione based on "turn-off" fluorescence. *Sci. Rep.* 11, 2375. doi:10.1038/s41598-021-81677-8

Wu, B.-Y., Wang, C.-W., Chen, P.-C., and Chang, H.-T. (2017). Glutathione assisted preparation of gold nanoclusters using minimum amount of protein. *Sens. Actuators B Chem.* 238, 1258–1265. doi:10.1016/j.snb.2016.09.071

Wu, X., Wu, P., Gu, M., and Xue, J. (2020). Ratiometric fluorescent probe based on AuNCs induced AIE for quantification and visual sensing of glucose. *Anal. Chim. Acta* 1104, 140–146. doi:10.1016/j.aca.2020.01.004

Xiao, W., Zhi, D., Pan, Q., Liang, Y., Zhou, F., and Chen, Z. (2020). A ratiometric bilirubin sensor based on a fluorescent gold nanocluster film with dual emissions. *Anal. Methods* 12, 5691–5698. doi:10.1039/D0AY01781G

Xiao, Y., Wu, Z., Yao, Q., and Xie, J. (2021). Luminescent metal nanoclusters: biosensing strategies and bioimaging applications. *Aggregate* 2, 114–132. doi:10.1002/agt2.11

Xie, J., Zheng, Y., and Ying, J. Y. (2009). Protein-directed synthesis of highly fluorescent gold nanoclusters. *J. Am. Chem. Soc.* 131, 888–889. doi:10.1021/ja806804u

Xu, D., Lin, Q., and Chang, H.-T. (2019). Chiral Ag and Au nanomaterials based optical approaches for analytical applications. *Part. Part. Syst. Charact.* 36, 1800552. doi:10.1002/ppsc.201800552

Xu, F., Qing, T., and Qing, Z. (2021). DNA-coded metal nano-fluorophores: preparation, properties and applications in biosensing and bioimaging. *Nano Today* 36, 101021. doi:10.1016/j.nantod.2020.101021

Xu, M.-M., Jia, T.-T., Li, B., Ma, W., Chen, X., Zhao, X., et al. (2020). Tuning the properties of atomically precise gold nanoclusters for biolabeling and drug delivery. *Chem. Commun.* 56, 8766–8769. doi:10.1039/D0CC03498C

Xu, Y., Sherwood, J., Qin, Y., Crowley, D., Bonizzoni, M., and Bao, Y. (2014). The role of protein characteristics in the formation and fluorescence of Au nanoclusters. *Nanoscale* 6, 1515–1524. doi:10.1039/C3NR06040C

Yang, C., Deng, H., He, J., Zhang, X., Gao, J., Shang, X., et al. (2022). Amplifiable ratiometric fluorescence biosensing of nanosilver multiclusters populated in three-way-junction DNA branches. *Biosens. Bioelectron.* 199, 113871. doi:10.1016/j.bios.2021.113871

Yang, M., Zhu, L., Yang, W., and Xu, W. (2023). Nucleic acid-templated silver nanoclusters: a review of structures, propertiesand biosensing applications. *Coord. Chem. Rev.* 491, 215247. doi:10.1016/j.ccr.2023.215247

Yang, T.-Q., Peng, B., Shan, B.-Q., Zong, Y.-X., Jiang, J.-G., Wu, P., et al. (2020). Origin of the photoluminescence of metal nanoclusters: from metal-centered emission to ligand-centered emission. *Nanomaterials* 10, 261. doi:10.3390/nano10020261

Yarramala, D. S., Baksi, A., Pradeep, T., and Rao, C. P. (2017). Green synthesis of protein-protected photoluminescent gold nanoclusters (AuNCs): reducing the size of AuNCs by partially occupying the Ca^{2+} site by La^{3+} in apo-α-lactalbumin. *ACS Sustain. Chem. Eng.* 5, 6064–6069. doi:10.1021/acssuschemeng.7b00958

Yen, Y.-T., Chen, T.-Y., Chen, C.-Y., Chang, C.-L., Chyueh, S.-C., and Chang, H.-T. (2019). A photoluminescent colorimetric probe of bovine serum albumin-stabilized gold nanoclusters for new psychoactive substances: cathinone drugs in seized street samples. *Sensors* 19, 3554. doi:10.3390/s19163554

Yen, Y.-T., Lin, Y.-S., Chang, Y.-J., Li, M.-T., Chyueh, S.-C., and Chang, H.-T. (2022). Nanomaterial-based sensor arrays with deep learning for screening of illicit drugs. *Adv. Mat. Technol.* 7, 2200243. doi:10.1002/admt.202200243

Yu, Q., Gao, P., Zhang, K. Y., Tong, X., Yang, H., Liu, S., et al. (2017). Luminescent gold nanocluster-based sensing platform for accurate H_2S detection *in vitro* and *in vivo* with improved anti-interference. *Light Sci. Appl.* 6, e17107. doi:10.1038/lsa.2017.107

Yu, Y., Di Lee, W., and Tan, Y. N. (2020). Protein-protected gold/silver alloy nanoclusters in metal-enhanced singlet oxygen generation and their correlation with photoluminescence. *Mat. Sci. Eng. C* 109, 110525. doi:10.1016/j.msec.2019.110525

Yuan, H., Lin, J.-H., Dong, Z.-S., Chen, W.-T., Chan, Y. K., Yeh, Y.-C., et al. (2022). Detection of pathogens using graphene quantum dots and gold nanoclusters on paper-based analytical devices. *Sens. Actuators B Chem.* 363, 131824. doi:10.1016/j.snb.2022.131824

Yuan, X., Chng, L. L., Yang, J., and Ying, J. Y. (2020). Miscible-solvent-assisted two-phase synthesis of monolayer-ligand-protected metal nanoclusters with various sizes. *Adv. Mat.* 32, 1906063. doi:10.1002/adma.201906063

Zaleska-Medynska, A., Marchelek, M., Diak, M., and Grabowska, E. (2016). Noble metal-based bimetallic nanoparticles: the effect of the structure on the optical, catalyticand photocatalytic properties. *Adv. Colloid Interface Sci.* 229, 80–107. doi:10.1016/j.cis.2015.12.008

Zare, I., Chevrier, D. M., Cifuentes-Rius, A., Moradi, N., Xianyu, Y., Ghosh, S., et al. (2021). Protein-protected metal nanoclusters as diagnostic and therapeutic platforms for biomedical applications. *Mat. Today* 66, 159–193. doi:10.1016/j.mattod.2020.10.027

Zhang, B., Chen, J., Cao, Y., Chai, O. J. H., and Xie, J. (2021). Ligand design in ligand-protected gold nanoclusters. *Small* 17, 2004381. doi:10.1002/smll.202004381

Zhang, X., Qian, Y., Ma, X., Xia, M., Li, S., and Zhang, Y. (2018). Thiolated DNA-templated silver nanoclusters with strong fluorescence emission and a long shelf-life. *Nanoscale* 10, 76–81. doi:10.1039/C7NR06358J

Zhang, Y., Xu, H., Yang, Y., Zhu, F., Pu, Y., You, X., et al. (2021). Efficient fluorescence resonance energy transfer-based ratiometric fluorescent probe for detection of dopamine using a dual-emission carbon dot-gold nanocluster nanohybrid. *J. Photochem. Photobiol. A Chem.* 411, 113195. doi:10.1016/j.jphotochem.2021.113195

Zhang, Z., Liu, T., Wang, S., Ma, J., Zhou, T., Wang, F., et al. (2019). DNA-templated gold nanocluster as a novel fluorometric sensor for glutathione determination. *J. Photochem. Photobiol. A Chem.* 370, 89–93. doi:10.1016/j.jphotochem.2018.10.021

Zhou, W., Fang, Y., Ren, J., and Dong, S. (2019). DNA-templated silver and silver-based bimetallic clusters with remarkable and sequence-related catalytic activity toward 4-nitrophenol reduction. *Chem. Commun.* 55, 373–376. doi:10.1039/C8CC08810A

Zhu, Y., Li, W., Ju, C., Gong, X., Song, W., Zhao, Y., et al. (2019). Selective detection of glutathione based on the recovered fluorescence of BSA-AuNCs/Cu^{2+} system. *Micro and Nano Lett.* 14, 952–956. doi:10.1049/mnl.2018.5772

frontiers | Frontiers in Analytical Science

TYPE Original Research
PUBLISHED 19 February 2025
DOI 10.3389/frans.2025.1533486

OPEN ACCESS

EDITED BY
Marianne Fillet,
University of Liège, Belgium

REVIEWED BY
Qingchun Lan,
Fudan University, China
Kumar Katragunta,
University of Mississippi, United States

*CORRESPONDENCE
Jianping Chen,
lycjp@126.com
Jihang Chen,
chenjihang@cuhk.edu.cn

†These authors have contributed equally to this work

RECEIVED 24 November 2024
ACCEPTED 10 January 2025
PUBLISHED 19 February 2025

CITATION
Cheng J, Meng X, Fang D, Zhu Y, Liu Z, Li X, Jie K, Huang S, Li H, Zhang S, Chen J and Chen J (2025) The chemicalome profiling of Zishen Yuzhen Pill *in vivo* and its promoting effect on osteogenic differentiation of MC3T3-E1 cells. *Front. Anal. Sci.* 5:1533486.
doi: 10.3389/frans.2025.1533486

The chemicalome profiling of Zishen Yuzhen Pill *in vivo* and its promoting effect on osteogenic differentiation of MC3T3-E1 cells

Juanjuan Cheng[1†], Xinyue Meng[2†], Daozheng Fang[2], Yong Zhu[2], Zhihao Liu[2], Xinyue Li[2], Ke Jie[3,4,5], Shiying Huang[1], Huilin Li[1], Shangbin Zhang[1], Jihang Chen[2*] and Jianping Chen[1*]

[1]Shenzhen Key Laboratory of Hospital Chinese Medicine Preparation, Shenzhen Traditional Chinese Medicine Hospital, The Fourth Clinical Medical College of Guangzhou University of Chinese Medicine, Shenzhen, China, [2]Shenzhen Key Laboratory of Steroid Drug Discovery and Development, School of Medicine, The Chinese University of Hong Kong, Shenzhen, China, [3]The Eighth Clinical Medical College of Guangzhou University of Chinese Medicine, Foshan, China, [4]Foshan Hospital of Traditional Chinese Medicine, Foshan, China, [5]Guangzhou University of Chinese Medicine, Guangzhou, China

Zishen Yuzhen Pill (ZYP) is a Chinese herbal product developed by Shenzhen TCM Hospital, which have been frequently used to treat osteoporosis (OP). This study aimed to determine the major chemical components of ZYP and its prototype compounds and metabolites in rat biological samples, as well as explore the potential effect of ZYP-containing serum in MC3T3-E1 cells. UPLC-Q/TOF-MS was used to identify the chemical components. Then, ZYP was orally administered to rat, and samples of plasma, urine, feces, bile, and tissue were collected to identify prototype compounds and metabolites. The viability of MC3T3-E1 cells was evaluated using the CCK-8 method after treatment with various concentrations (2%, 4%, and 8%) of ZYP-containing serum. Following treatment of MC3T3-E1 cells with ZYP-containing serum, the activity of alkaline phosphatase (ALP) and Alizarin red S (ARS) were measured, and the levels of Runx2, Opn, Opg and Osterix were quantified using the qPCR and Western blot analysis. And cells were collected for RNA-seq analysis. Results indicated that a total 152 compounds were identified in ZYP, including flavonoids, iridoid, lignans, triterpene saponins, etc. Furthermore, we detected a total of 70 prototype components and 99 metabolites distributed in different tissues. In addition, ZYP-containing serum observably promoted osteogenesis by increasing ALP and ARS activities, as well as up-regulating the expression of Runx2, Opn, Opg and Osterix in MC3T3-E1 cells. RNA-seq results indicated that the beneficial effects may be related to the upregulation of mitochondrial oxidative

Abbreviations: ABR, Achyranthis Bidentatae Radix; ALP, alkaline phosphatase; AR, Astragali Radix; BP, biological process; CC, cellular component; CR Codonopsis Radix; DR, Drynariae Rhizoma; ECL, enhanced chemiluminescence; EF, Epimedii Folium; FBS, fetal bovine serum; MF, molecular function; NRR, Notoginseng Radix Et Rhizoma; OD, Os Draconis; OP, osteoporosis; PBS, phosphate-buffered saline; OS, Oyster Shell; PR, Polygonati Rhizoma; Q/TOF-MS, quadrupole time-of-flight mass spectrometry; RR, Rehmanniae Radix; SCF, Schisandrae Chinensis Fructus; TCM, Traditional Chinese medicine; TP, Tortoise Plastron; TS, Turtle Shell; UPLC, ultra-high performance liquid chromatography; ZYP, Zishen Yuzhen Pill.

phosphorylation. This work provided further support for the traditional application of ZYP in the treatment of OP. And this study can promote the further pharmacokinetic and pharmacological evaluation of ZYP.

KEYWORDS

Zishen Yuzhen Pill, UPLC-QTOF/MS, chemical characterization, osteoporosis, MC3T3-E1 cells

1 Introduction

Osteoporosis (OP) is defined by the World Health Organization (WHO) as "a chronic systemic bone disease." The main characteristic of this disease is the loss of bone mass and destruction of the microstructure of bone tissue, eventually leading to increased bone fragility and fracture (Liu et al., 2019). OP is a major cause of fractures and can lead to persistent pain and serious injury in patients. Approximately 200 million people worldwide suffer from OP, causing around 8.9 million fractures annually. The medical cost of surgery-related fractures in China alone is predicted to reach $25.4 billion by 2050, nearly a 30-fold increase from 2010 (Si et al., 2015). There is no doubt that the prevention and treatment of OP is a public health challenge faced by the entire human population. Despite significant progress in the prevention and treatment of OP, current therapies have major limitations and adverse effects. Newly developed drugs are often expensive, limiting their widespread clinical use (Clynes et al., 2020). Additionally, adverse drug reactions, such as gastrointestinal issues, can affect patient compliance (Iolascon et al., 2020). Therefore, it is urgent to explore more effective and safer therapeutic drugs to overcome the treatment deadlock.

Traditional Chinese medicine (TCM) has been recognized as an integral part of modern medicine, serving as a vital resource of natural medicines and playing a significant role in the treatment of OP. The distinctive characteristic of TCM preparations is the use of multiple herbs, which contain numerous active ingredients that work synergistically on various targets to treat diseases, thereby enhancing the therapeutic effects and minimizing toxicity. In the theoretical system of traditional Chinese medicine (TCM), OP is called "*Gu Wei,*" which refers to the bone loss caused by kidney deficiency. Zishen Yuzhen Pill (ZYP), formerly known as Zishen Jiangtang Pill, is a Chinese herbal product developed by Professor Li Huilin of Shenzhen TCM Hospital, which has controllable quality, convenient administration, exact curative effect and independent intellectual property rights. It consists of 14 herbs, including Astragali Radix (AR), Achyranthis Bidentatae Radix (ABR), Codonopsis Radix (CR), Rehmanniae Radix (RR), Drynariae Rhizoma (DR), Schisandrae Chinensis Fructus (SCF), Epimedii Folium (EF), Polygonati Rhizoma (PR), Notoginseng Radix Et Rhizoma (NRR), Tortoise Plastron (TP), Turtle Shell (TS), Os Draconis (OD) and Oyster Shell (OS) (Li et al., 2018). Based on the theory of "kidney dominating bone," this prescription selects the products filled with lean marrow, which has the effect of tonifying Qi and nourishing Yin, nourishing the kidneys and strengthen bones. For over 20 years, it has a solid therapeutic foundation in clinical use to maintain blood glucose level and bone density. Previous studies indicated that ZYP can effectively improve abnormal bone metabolism in rat (Chu et al., 2021; Li et al., 2018). Moreover, ZYP also inhibited the adipocytes differentiate of mouse bone marrow mesenchymal stem cells, upregulation of RUNX2 and BMP-2 genes promotes osteogenic differentiation of BMSCs, and exerts multi-target anti-OP effects (Guo et al., 2011). However, a detailed analysis of the chemical composition of an ZYP remain unclear. In addition, the potential effect of ZYP on osteogenic differentiation in MC3T3-E1 cells is unknown. Therefore, it is crucial to systematically elucidate the chemical compositions and metabolite profiles of ZYP, particularly the qualitative identification and dynamic changes in the effective compounds *in vivo*. It is very important for us to better understand the bioactive ingredients responsible for the pharmacological effect of ZYP and provide a scientific basis for elucidating the substance basis of its therapeutic effect on OP.

Up to date, many modern analytical techniques have been used to explore the chemical composition of TCM. And with the application of mass spectrometers with high resolution, high sensitivity, and high mass accuracy, the identification level of various compounds of TCM has been greatly improved. It is well known that the use of ultra-high performance liquid chromatography (UPLC) for rapid separation of complex compounds in traditional Chinese medicine, and the use of quadrupole time-of-flight mass spectrometry (Q/TOF-MS) to obtain accurate structural characterization. The UPLC-QTOF/MS analytical method can help to fully explore the bioactive components, metabolites, and metabolic pathways of the TCM formulations after absorption by the human body (Ren et al., 2022; Yuan et al., 2024). The results will provide a powerful approach for the analysis of TCM or biological samples and deepen our understanding of the therapeutic effects of herbal preparations (Liu et al., 2017; Mi et al., 2019; Xiao et al., 2018). The major herb SCF in the formulation has been identified with 43 compounds by UPLC-QTOF/MS (Mu et al., 2022). There are still significant gaps in the understanding of ZYP bioactive components and *in vivo* metabolic pathways, especially its role in specific tissues. Therefore, it is important to establish a reliable methodology to overcome these problems.

In this study, we aim to analyze the chemical compounds of ZYP and the metabolic profile of the serum via UPLC-Q/TOF-MS. And the prototype compounds and potential metabolites identified were assessed using a semiquantitative method to investigate the potential therapeutic compounds of ZYP. Moreover, we also evaluate the effect of ZYP on MC3T3-E1 cell to provide new evidence for the anti-OP effect of ZYP.

2 Materials and methods

2.1 Chemicals and reagents

ZYP were obtained from the Pharmacy Department of Shenzhen TCM Hospital [Approval number: Guangdong Pharmaceutical Preparation Z20070083]. Its specific formula composition and preparation method refer to our previous

reports (Chen et al., 2019). Formic acid (FA), methanol (HPLC grade), and acetonitrile (HPLC grade) were purchased from Thermo Fisher Scientific (Waltham, MA, United States). Ultrapure deionized water was obtained from a Unique-R20 water-purification system (Xiamen, China). MC3T3-E1 cells were purchased from Procell Life Science and Technology Company (Cat# CL-0378, Wuhan, China). Ultrapure deionized water was obtained from a Unique-R20 water-purification system (Xiamen, China).

β-glycerophosphate sodium (#G9422), ascorbic acid (#A4403) and dexamethasone (#D4902) were purchased from Sigma-Aldrich (St. Louis, MO, United States). α-MEM media, fetal bovine serum (FBS) and phosphate-buffered saline (PBS) were purchased from Gibco (Grand Island, NY, United States). The Cell Counting Kit-8 (CCK-8, #C0037), alkaline phosphatase (ALP, #P0321) color development kit, Alizarin red S staining kit (ARS, #c0148), RNAeasy™ Animal RNA Isolation Kit (Beyotime, #R0027) and horseradish peroxidase (HRP)- conjugated goat anti-rabbit or goat anti-mouse antibody (#A0208 or #A0216), BeyoECL plus kit (#P0018) were obtained from Beyotime Biotechnology Co., (Jiangsu, China). Runx2 (#ab192256) and Osterix (#ab209484) primary antibody was purchased from Abcam (Cambridge, United Kingdom). Osteoprotegerin (OPG, #41289) primary antibodies was purchased from Signalway Antibody (CA, United States). Osteopontin (OPN, #22952) primary antibody was purchased from Proteintech company (Rosemont, IL, United States). β-actin (#3700) antibody was obtained from Cell Signaling Technology (Danvers, MA, United States). The PrimerScript RT reagent kit and SYBR qPCR Master Mix Kit were purchased from Vazyme (Biotech Co., Ltd., Nanjing, China).

2.2 Phytochemical analysis by UPLC-QTOF-MS

Phytochemical compounds were analyzed using Waters Acquity HSS T3 column (2.1 × 150 mm, 1.8 μm, Waters corporation, MA, United States) system. The mobile phase was a mixture of 0.1% formic acid in water (A) and acetonitrile (B), with an optimized gradient elution as follows: 0–5 min, 3%–8% B; 5–11 min, 8%–30% B; 11–20 min, 30%–80% B; 20–21 min, 80%–95% B; 21–27 min, 95%–95%. The injection volume was 2 μL, the column temperature was 35°C and flow rate was set at 0.30 mL/min. The MS analysis was performed using an X500B Q-TOF mass spectrometer (AB Sciex, Foster City, CA, United States). The MS data parameters were set as follows: the instrument was operated in positive (5.5 kV) or negative (−4.5 kV) ion mode, the full MS scan range was *m/z* 100–1,250. Then, some chemical components were identified by comparing with standard reference and an internal database (LibraryView). Others were identified by literature and online databases, such as MetaScope, ChemSpider and Progenesis QI software.

2.3 Animal

Specific pathogen-free male Sprague Dawley rats (SD, weighing 190–210 g) were provided by Beijing Vital River Laboratory Animal Technology Co., Ltd. The rats were housed in an animal facility with a standard 12 h light/dark cycle under constant temperature conditions and with free access to food and water. The experimental procedures were conducted in accordance with the Ethics Committees of the Chinese University of Hong Kong (Shenzhen, license number: CUHKSZ-AE2023014).

2.4 Rat treatment and sample collection

After 1 week of adaptive feeding, all rats were randomly divided into three groups: a control group for collecting blank bio-samples, ZYP -treated group (1.62 g/kg) for collecting plasma, urine, feces, and tissues, and ZYP -treated group (1.62 g/kg) for collecting bile. Rats in the control group were given normal saline by intragastric administration.

In different groups, blood samples were collected at 5, 15, 30, 60, 120, 240, 360, 480 and 600 min after intragastric administration and placed into heparin anticoagulant tubes. The tubes were then centrifuged at 4,500 rpm for 5 min to obtain plasma samples, which were combined for each time point and stored at −80°C until further analysis. Feces, urine and bile acid samples were collected from 0–600 min after administration, and collected every 120 min. After taking the above samples, rats were killed and the tissues were collected.

2.5 Sample preparation

After mixing 60 μL plasma (600 μL in total) at each time point, 1.8 mL ice acetonitrile was added. The sample was swirled for 2 min and centrifuged (at 13,000 rpm, 10 min, 4°C). Next, 400 μL of the supernatant was removed, and dry with nitrogen. The sample was redissolved with 200 μL 50% acetonitrile, centrifuged for 10 min at 13,000 rpm. 2 μL of the supernatant was analyzed by LC-MS.

A 0.3 g aliquot of tissue or feces sample were mixed with 1 mL methanol and homogenized six times for 30 s each time. The homogenate was centrifuged at 13,000 rpm for 10 min at 4°C. Next, 200 μL tissue supernatant dry with nitrogen. Redissolved with 200 μL 50% acetonitrile, centrifuged for 10 min at 13,000 rpm, which were then absorbed 2 μL supernatant to LC-MS.

Appropriate amount of urine/bile was centrifuged, centrifuged at 4,000 rpm for 10 min. Then, 1 mL of the supernatant was added to the activated C18 solid phase extraction column, washed with 1 mL of pure water, and then eluted with 1 mL of methanol. Finally, the eluent is collected. The MS/MS spectrum, Human Metabolome Database, METLIN database and literature data were used to identify metabolites.

2.6 Preparation of drug-containing serum

The prescribed dosage for ZYP was set at 18 g/d. Based on the dose equivalency conversion formula between humans and rat presented in the "Pharmacological Experimental Methodology," a dosage of 1.62 g/kg for ZYP was determined. Ten SD rats were administered with ZYP (0.81 g/kg) via intragastric administration twice a day to gain ZYP-containing serum, while another ten rats were treated with normal saline (10 mL/kg) to gain control serum. After treatment for 3 days, blood samples were collected and then subjected to centrifugation at 3,000 rpm for 10 min at 4°C. Finally, the collected supernatant was inactivated at 56°C for 30 min, sterilized through a 0.22 μm filter, and stored at −80°C for further use.

2.7 Cell culture

MC3T3-E1 cells were cultured in α-MEM supplemented with 10% FBS and 1% PS (100 U/mL penicillin and 100 μg/mL streptomycin) at 37°C, 5% CO_2. Subculturing of the cells was performed when they reached 80% confluence, and the medium was refreshed every 2 days. For induction of MC3T3-E1 osteogenic differentiation, the medium was added with 10 mM β-glycerophosphate sodium, 50 μg/L ascorbic acid and 100 μM dexamethasone. ALP staining was performed after 7 days of osteogenic differentiation. The medium was changed every 2 days.

2.8 Cell viability analysis and treatment

CCK-8 solution was used for the assessment of cell vitality following the instructions. 2×10^3 cells/well was maintained for the seeding of MC3T3-E1 cells in a 96-well plate for 24 h. Then, the cells were treated with different concentrations of drug-containing serum for 48 h. Cells were divided into the following groups: (1) Control group, (2) ZYP-treated group with 2%, 4% and 8% drug-containing serum, (3) Blank group with 8% control serum. After that, the working solution containing 10% CCK-8 reagent was added to each well and incubated for 1 h. The absorbance was measured at 450 nm with a multifunctional microplate reader.

2.9 ALP and ARS staining

After inducing osteogenic differentiation for 7 days or 21 days, the ALP and ARS staining in different treatment groups were performed according to the manufacturer's instructions of the corresponding assay kit. Briefly, the cells were fixed with 4% paraformaldehyde for 30 min. Then, cells were incubated with staining solution at room temperature for 18 h. After incubation, the cells were washed with PBS, and the stained cells were observed under a microscope immediately.

2.10 qRT-PCR

Total RNA was isolated from MC3T3-E1 cells using RNAeasy™ Animal RNA Isolation Kit. Then, RNA was utilized to synthesize cDNA following the manufacturer's guide. The result of qRT-PCR was analyzed by CFX 96 system (Version 3.1, Bio-Rad Corporation, CA, United States) by using SYBR qPCR Master Mix Kit. The gene expression level was calculated based on the $2^{-\triangle\triangle Ct}$ method and *β-actin* was used as a housekeeping gene. The primer sequences were listed in Table 1.

TABLE 1 Primer sequences.

Gene		Sequence (5′ to 3′)
Mouse-Runx2	Forward	ACTTCGTCAGCATCCTATCAGTTCC
	Reverse	CGTCAGCGTCAACACCATCATTC
Mouse-Opn	Forward	AAGAGCGGTGAGTCTAAGGAGTCC
	Reverse	TGGCTGCCCTTTCCGTTGTTG
Mouse-Opg	Forward	CCCTTGCCCTGACCACTCTTATAC
	Reverse	CCCTTCCTCACACTCACACACTC
Mouse-Osterix	Forward	TCGTCTGACTGCCTGCCTAGTG
	Reverse	CTGCGTGGATGCCTGCCTTG
Mouse-β-actin	Forward	CTGAGAGGGAAATCGTGCGTGAC
	Reverse	ACCGCTCGTTGCCAATAGTGATG

2.11 Western blot

In brief, cells were lysed in RIPA with 1% PMSF for 25 min, and then centrifuged at 12,000 rpm for 15 min at 4°C. Following that, equal protein (20 μg) was separated using 10% SDS-PAGE and blotted to a PVDF membrane. After transfer, the membrane was blocked with 5% skimmed milk for 1 h and then the following diluted primary antibodies were added at 4°C overnight: anti-Runx2 (1:1,000), anti-OPN (1:2,000), anti-OPG (1:1,000), anti-Osterix (1:1,000), anti-β-actin (1:1,000). Thereafter, the membranes were then incubated with HRP-conjugated goat anti-rabbit or anti-mouse antibody (1:5,000) at room temperature for 50 min. Finally, the chemiluminescence of target protein bands were performed with the enhanced chemiluminescence (ECL) detection system (ProteinSimple, San Jose, CA, United States).

2.12 RNA-sequencing

After induction of osteoblast differentiation for 2 days, total RNA from MC3T3-E1 cells was extracted by utilizing Trizol reagent. The RNA-sequencing analysis was conducted and analyzed. Briefly, the extracted RNA was evaluated for quality and integrity, and library preparation was conducted. Differential expression analysis between two groups was performed by employing the DESeq2 R package. Genes with FDR <0.05 and $|\log2(\text{foldchange})| \geq 1$ found by DESeq2 were regarded as differentially expressed genes (DEGs). KOBAS software was employed to test the statistical enrichment of DEGs in KEGG pathways.

2.13 Statistical analysis

All values are expressed as mean ± SD (standard deviation). Statistical difference was evaluated using one-way analysis of variance (ANOVA) followed by Tukey's test (GraphPad Pro Prism 8.0, San Diego, CA). $P < 0.05$ was considered statistically significant.

3 Results

3.1 Identification the main constituents of ZYP by UPLC-QTOF-MS/MS

As shown in Figures 1A, B, there was the representative base peak chromatogram (BPC) of ZYP in the positive and negative-ion scan. Based on the structural analysis and identification strategy of UPLC-QTOF/MS, the unknown components were classified

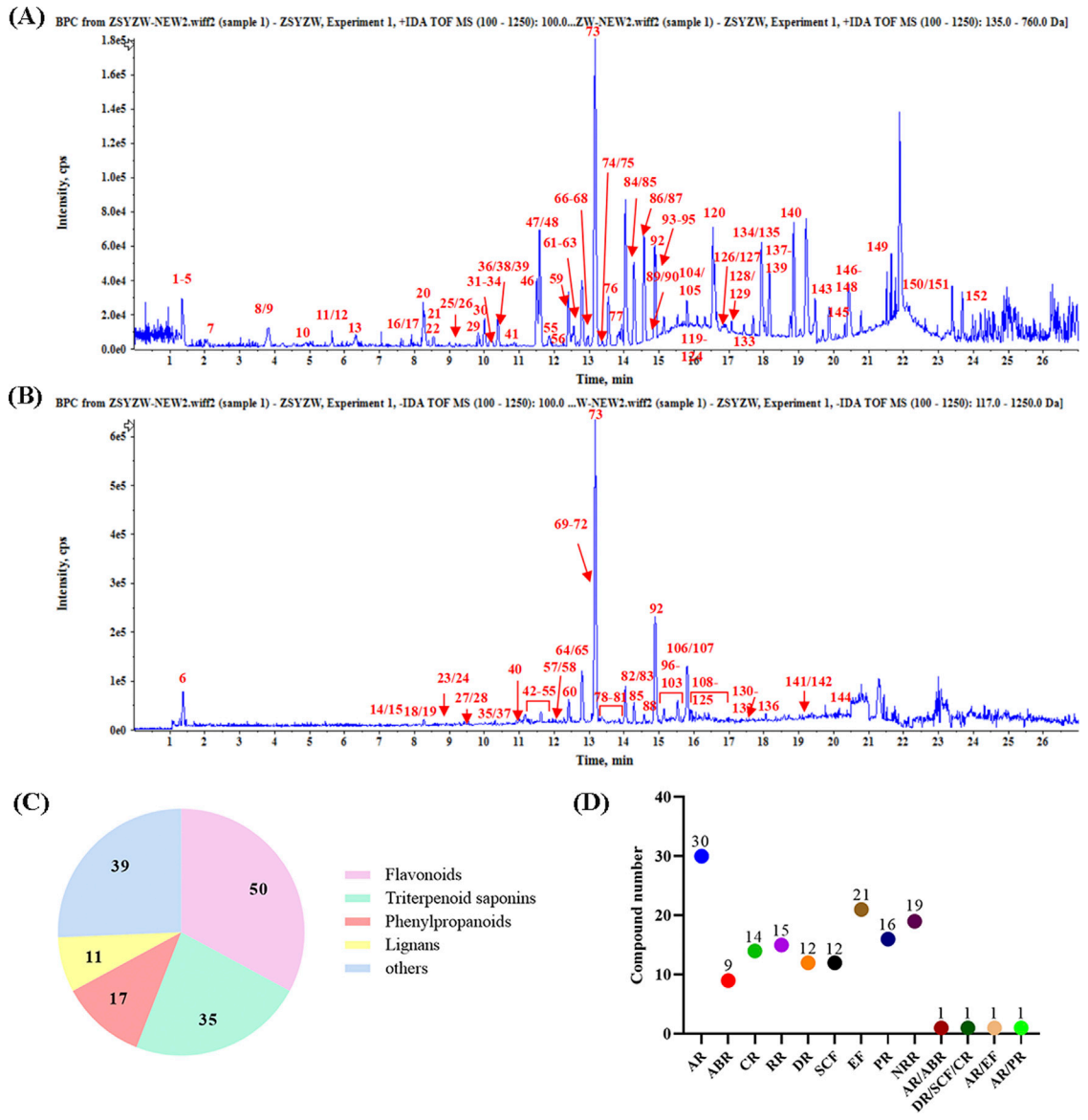

FIGURE 1
Base peak chromatogram (BPC) of ZYP. **(A)** Positive-ion scan. **(B)** Negative-ion scan. **(C)** Structural classification of compounds contained in ZYP. **(D)** The number of chemical components for each herb.

according to the fragmenting rules and diagnostic ions of different structural types of components. A total of 152 compounds were firstly tentatively identified from identified in ZYP, including 50 flavonoids, 35 triterpenoid saponins, 17 phenylpropanoids, 11 lignans, and 14 others (Figure 1C). The herbs and the number of their components are further summarized in Figure 1D (AR 30, ABR 9, CR 14, RR 15, DR 12, SCF 12, EF 21, PR 16, NRR 19, AR/ABR 1, DR/SCF/CR 1, AR/EF 1, and AR/PR 1). The details of these compounds were listed in Supplementary Table S1.

Subsequently, fifteen chemical components were accurately identified in CR, including amino acids, nucleosides, alkaloids, and glycosides, such as codonopsis. RR also contains fifteen chemical components, with characteristic components including iridoid, phenylpropanoid, and polysaccharides. DR was found to be rich in thirteen compounds, including flavonoids and phenylpropanoids, with naringin as its representative component. Seventeen compounds were identified in PR, with main components being flavonoids such as puerarin and luteolin. Results showed that AR was rich in thirty-three compounds, mainly flavonoids like mullein isoflavones and triterpenoid saponins such as astragalus saponins. Ten compounds were identified from ABR, mainly steroids and saponins. A total of nineteen compounds were identified in NRR, characterized by triterpenoid saponins, especially ginsenosides. Thirteen compounds were identified from SCF, with lignans as the characteristic components. A total of twenty-two flavonoids, such as icariin, were identified as the characteristic components of EF. The representative structures of each herb are depicted in Figure 2.

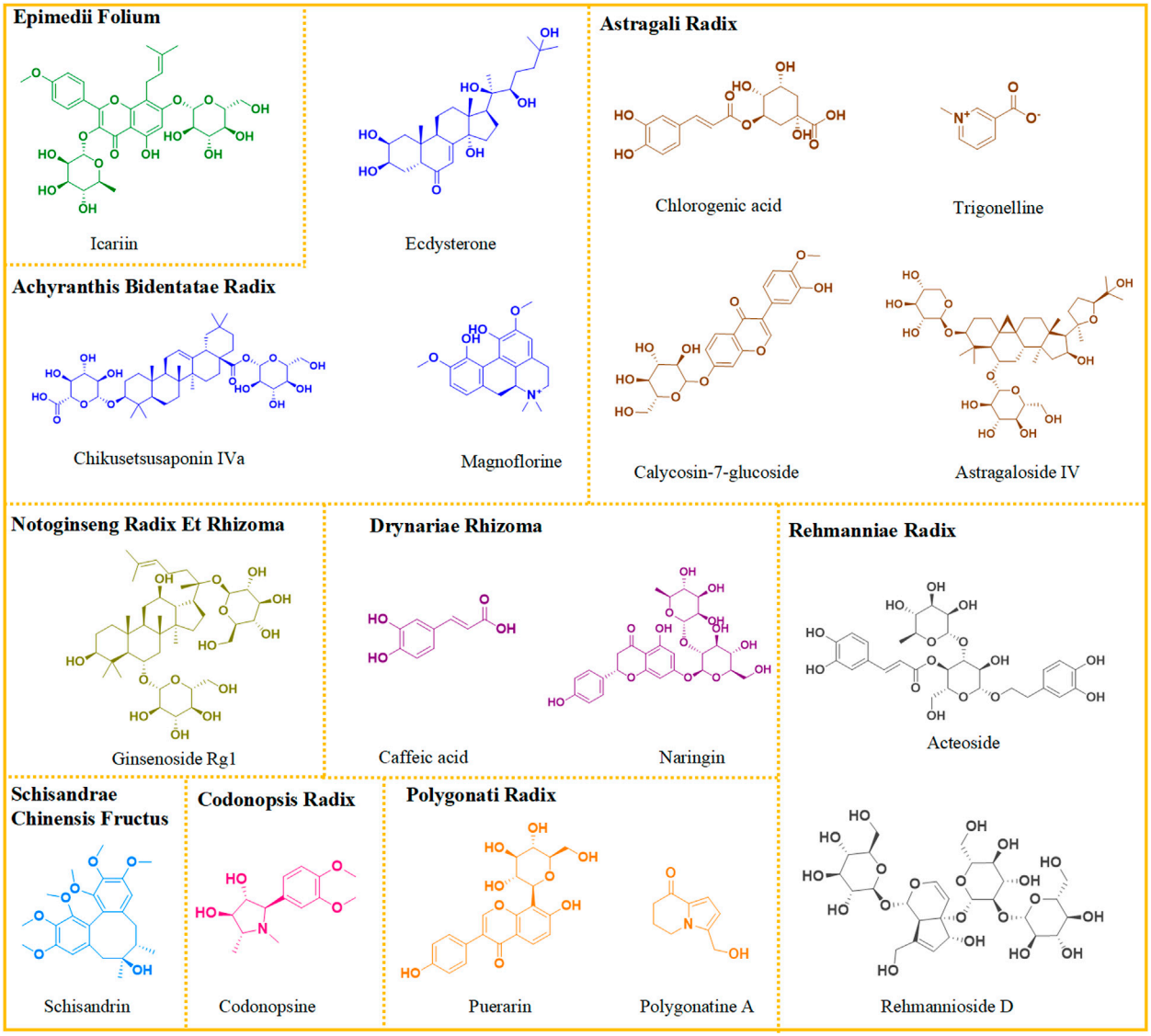

FIGURE 2
Representative chemical structures of each medicine in ZYP.

3.2 The mass spectrometry of characteristic compounds

According to the typical characteristic compounds, the secondary fragmentation and cracking behavior presented by secondary mass spectra were analyzed.

3.2.1 Alkaloid

Trigonelline, codonopsine, polygonatine and magnoflorine belong to categories of pyridine alkaloids, pyrrolidine alkaloids, indole alkaloids, and isoquinoline alkaloids, respectively. Alkaloids generally exhibit a good response in the positive ion mode, and the fragmentation typically occurs at the N-C junction. For example, the molecular ion peak of Magnoflorine in the mass spectrum is $[M]^+$ m/z 342.1699. In the secondary mass spectrum, the fragments m/z 299–297 are produced by cleavage at the N-heterocyclic site, and the fragment m/z 265 is formed by the further loss of CH_2O. Additional removal of CO generates the fragment m/z 237, and the fragment m/z 58 corresponds to the N-heterocyclic fragment $C_3H_8N^+$. The fragmentation pattern and secondary spectra are shown in Figure 3A.

3.2.2 Phenylpropanoids compounds

Phenylpropanoid compounds have the structural characteristics of C6-C3. Chlorogenic acid serves as an example to explain its fragmentation pattern. As shown in Figure 3B, the fragments are mainly formed by the cleavage of caffeoyl and quinic acid. The parent ion of chlorogenic acid is $[M-H]^-$ *m/z* 353.0879/$[M+H]^+$ *m/z* 355.1028. In the positive ion mode, the loss of one caffeoyl group produces the ion m/z 191. The continued removal of the caffeoyl group results in m/z 191, or the removal of the quinic acid part produces the ion m/z 179. Further removal of a CO_2 molecule generates the ion m/z 135.

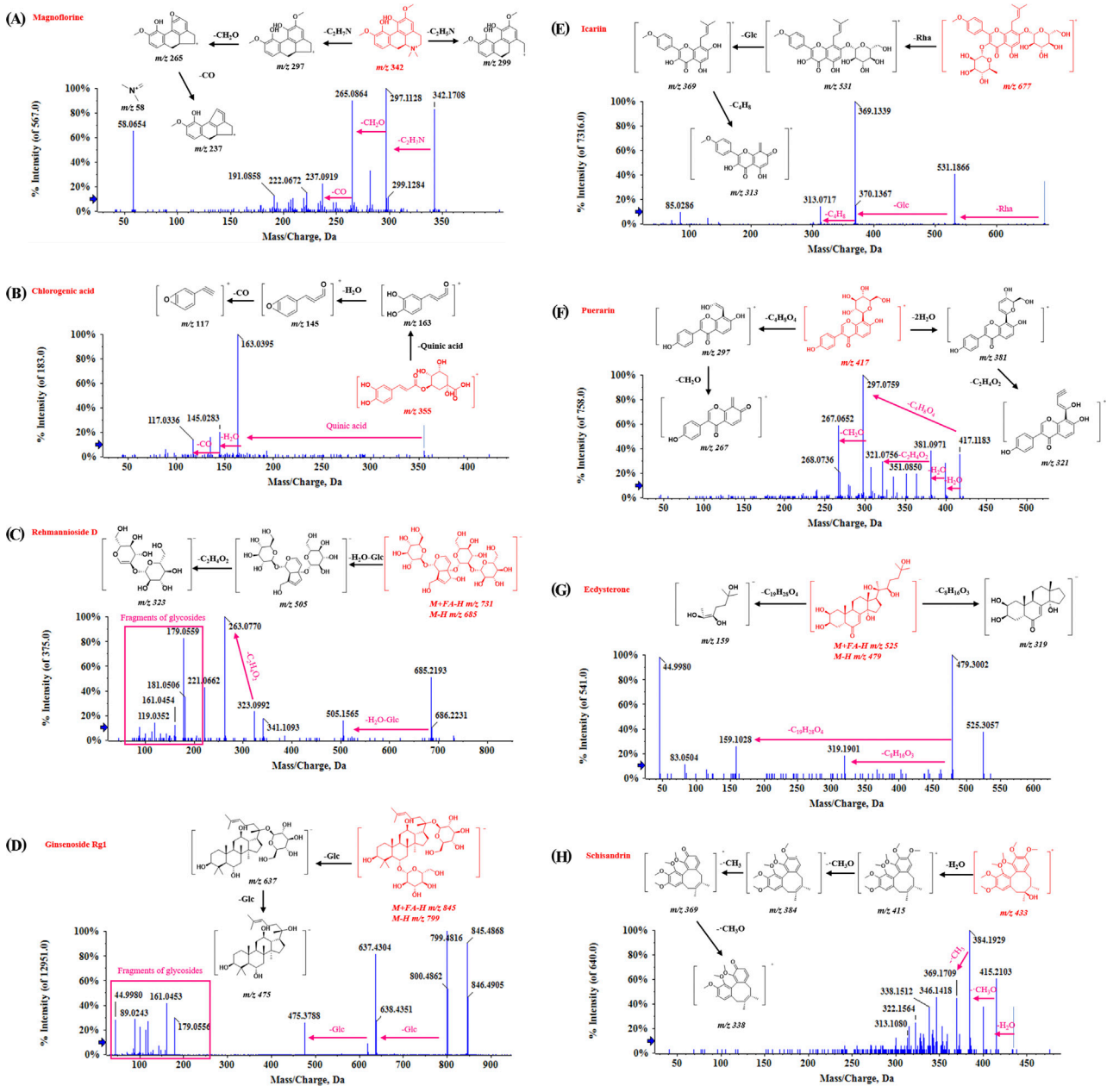

FIGURE 3
The mass spectrometry of characteristic compounds in ZYP. **(A)** Magnoflorine. **(B)** Chlorogenic acid. **(C)** Rehmannioside D. **(D)** Ginsenoside Rg1. **(E)** Icariin. **(F)** Puerarin. **(G)** Ecdysterone. **(H)** Schisandrin.

3.2.3 Iridoid terpenoids compounds

The iridoid terpenoids identified in the compound were derived from RR. Take Rehmannioside D, a characteristic compound in RR as an example, the parent ion was $[M+FA-H]^-$ *m/z* 731.2252, and $[M-H]^-$ *m/z* 685 could be observed in the secondary mass spectrometry. The loss of one molecule of water and one molecule of glucose produces a fragment at m/z 505. The disaccharide part generates fragments at *m/z* 323, and the neutral loss of $C_2H_4O_2$ results in fragments at *m/z* 263. In addition, fragments produced by the cleavage of other sugar residues, such as *m/z* 179 and 119, can be observed. The fragmentation pattern and secondary spectra are shown in Figure 3C.

3.2.4 Triterpenoid saponins compounds

Triterpenoid saponins are abundant in ZYP, as well as in NRR, AR, and ABR. The fragmentation patterns of saponins are consistent, with sequential glycoside cleavage commonly observed in secondary mass spectrometry. For example, the Ginsenoside Rg1, the parent ion has $[M+FA-H]^-$ at *m/z* of 845.4899. Its secondary mass spectrometry shows $[M-H]^-$ at m/z 799, with fragments at m/z 637 and m/z 475 resulting from the sequential removal of two glucose molecules (162 Da each). In addition, fragments at m/z 619 are produced by dehydration of hydroxyl groups on aglycones, and fragments at m/z 179, 161, 119, and 89 are generated from sugar residues. The fragmentation patterns and secondary spectra are illustrated in Figure 3D.

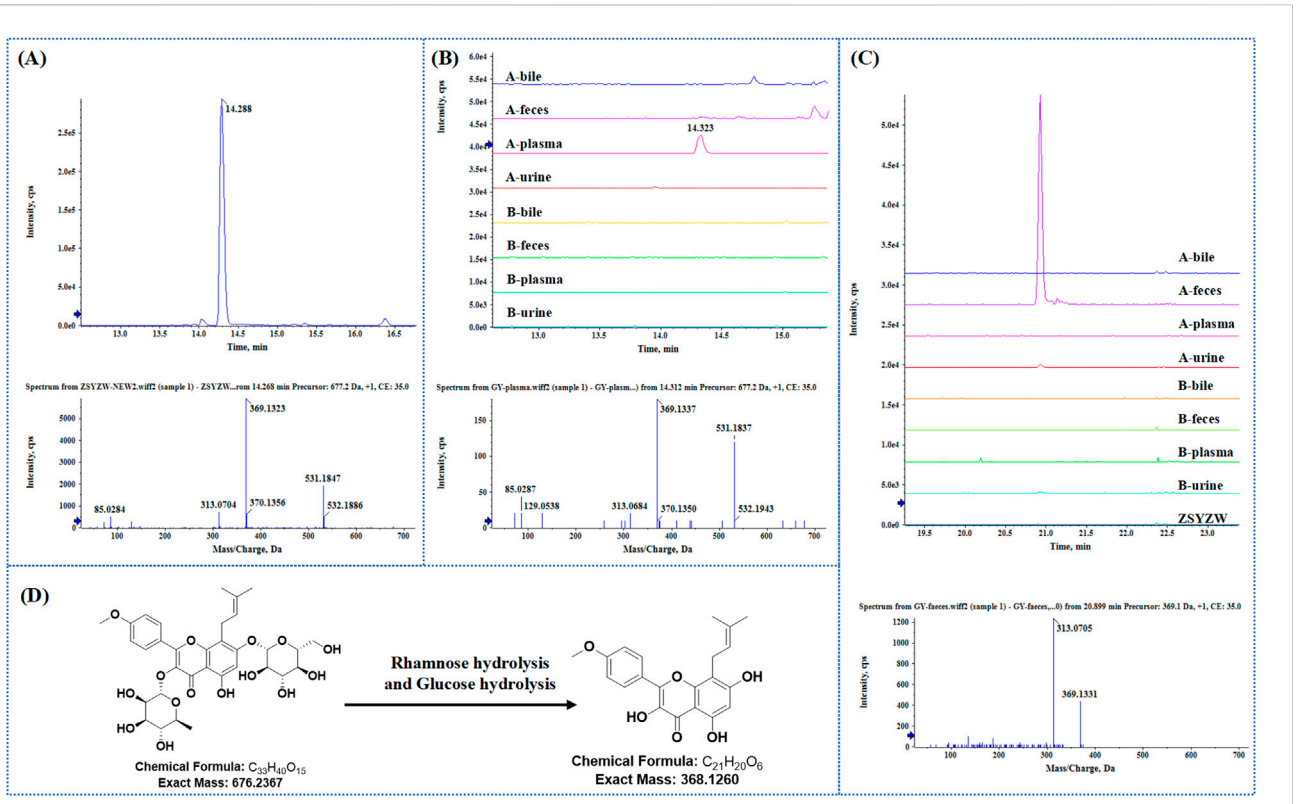

FIGURE 4
NO.85 Icariin was taken as an example to identify the prototype and metabolite in bio-samples. **(A)** Extraction ion flow and secondary mass spectrometry of Icariin in ZYP. **(B)** The superposition of Icariin in each biological sample extraction ion flow diagram and secondary mass spectrometry of administered plasma. **(C)** The superposition of M69 in ZYP and various biological samples extracted ion flow diagram and secondary mass spectrometry in the administered feces. **(D)** Examples of Icariin-M69 structural formulas and biotransformation pathways.

3.2.5 Flavonoids compounds

There are many kinds of flavonoids in ZYP, primarily derived from licorice. Flavonoids can be categorized based on their aglycones into flavanones, flavonoids, and flavonols. They can also be commonly substituted by oxosides, carbosides, and glucuronides, depending on the glycoside types. Regardless of the flavonoid type, desugar cleavage is common (e.g., oxoside losses of 162 Da, 146 Da, 176 Da, and carboside losses of 30 Da, 60 Da, 120 Da). Additionally, retro-Diels-Alder (RDA) cleavage occurs on aglycones. Icariin and Puerarin were used to illustrate the regularity of flavonoid cleavage in our results. Icariin, a flavonoside, shows distinct daughter ion peaks at m/z 531 and m/z 369 following the loss of −Rha (147 Da) and −Glc (162 Da). Icariin also forms a fragment at m/z 313 after the A-ring side chain is removed. Puerarin, a flavonoid glycoside, exhibits dehydration peaks and characteristic neutral losses of glycosides in secondary mass spectrometry. The fragmentation patterns and secondary spectra are shown in Figures 3E, F.

3.2.6 Steroid compounds

The steroids identified in ZYP are mainly derived from ABR, with ecdysterone being the characteristic component. Ecdysterone shows responses in both positive and negative ion modes. In its secondary mass spectrometry, numerous dehydration peaks are observed, such as m/z 445 and m/z 427. In the negative ion mode, the fragments m/z 319 and m/z 159 produced by the cracking of the group at position 17 can be very clearly observed. The fragmentation patterns are illustrated in Figure 3G.

3.2.7 Lignans compounds

The lignans identified in ZYP are primarily derived from SCF. For instance, in Schisandrin, the loss of methyl and methoxy groups from the benzene ring is common in secondary fragments. The fragmentation patterns are illustrated in Figure 3H.

3.3 Basic characterization of chemical substances in ZYP within biological samples of rats

Based on the chemical characterization of ZYP, the MS^2 fragments and retention time were used to analyze its components in plasma, urine, feces, and bile. Icariin (**85**) was selected as an example. As shown in Figure 4A, the extracted ion chromatogram (XIC) and secondary spectrum of icariin (RT 14.29 min, $[M+FA-H]^-$ *m/z* 721.2343 $[M+H]^+$ *m/z* 677.2435) in the extraction solution revealed characteristic fragments at m/z 531, 369, and 313. Figure 4B shows the superimposed XIC of Icariin in bile, feces, plasma, and urine from both administered and blank groups. The results indicated that Icariin responded only in the administered plasma at the corresponding retention time (with no response in blank samples), and the primary ppm met the requirements (<10 ppm). The secondary spectra were highly similar to those of Icariin in the extraction solution, with consistent secondary fragments (m/z 531, 369, 313), indicating

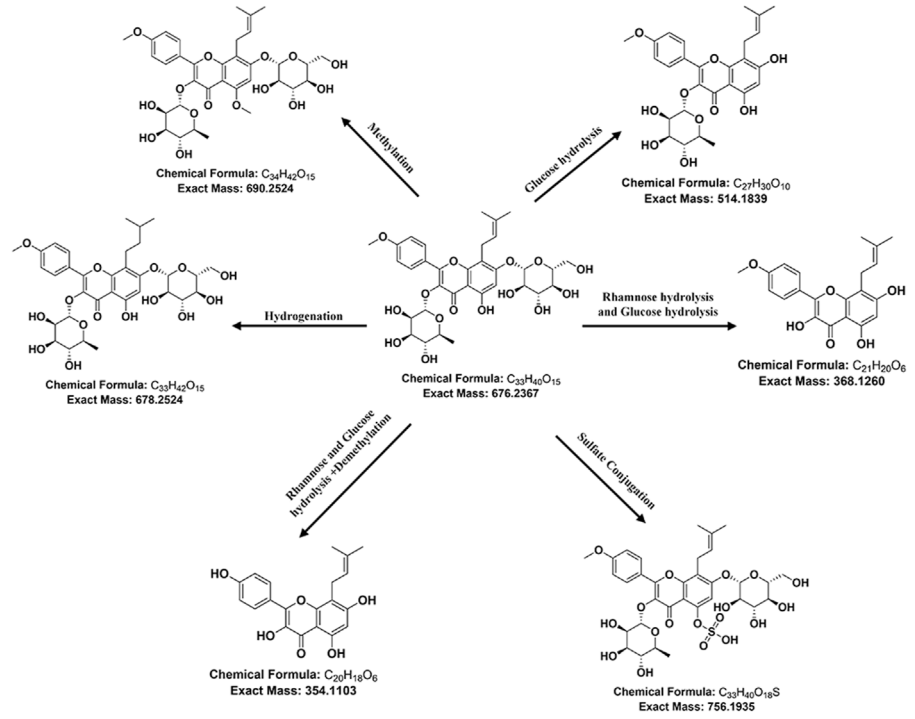

FIGURE 5
Icariin-related metabolite correlation diagram.

that Icariin can be absorbed into the blood and remain in the body to exert its effects.

Based on the phase I and phase II metabolism patterns and the similarity of the secondary mass spectrum profiles, metabolite libraries distinct from the prototype components can be quickly screened from the matrix. These metabolites are then automatically matched with the prototype components to assist in their identification and annotation. For example, the mass deviation between Icariin and M69 (m/z 369.1331, RT 20.93 min) was Δm = 308.1107, consistent with the molecular weight loss of Rhamnose and Glucose. This biological transformation pathway conforms to "Rhamnose hydrolysis and Glucose hydrolysis." The XIC superposition of M69 in each sample, as shown in Figure 4C, indicated a weak response in urine, but its chromatogram m/z was 369.1513 with ppm >10. The secondary profile of M69 in administered feces was similar to Icariin, with consistent fragments, including m/z 369 and m/z 313, indicating that M69 is a metabolite of Icariin. Additionally, M69's response in stool suggests it may be metabolized by intestinal flora. Figure 4D shows the structural formula of Icariin-M69. Following this principle, a total of six metabolites were matched to Icariin, and their structural association diagrams are presented in Figure 5.

3.4 Tissue distribution of prototypes and metabolites in ZYP

A total of 110, 65, 63, 59, 27 compounds were extracted from feces, plasma, urine, intestine and colon, respectively. And 70 compounds were detected in other tissues (Figure 6A). In detail, 70 prototype compounds were extracted from plasma, urine, feces, or bile (Figure 6B). Among them, 41 were detected in plasma, 25 in urine, 48 in feces, and 1 in bile. Further analysis of these prototype compounds revealed a total of 99 matched metabolites, with 24 detectable in plasma, 38 in urine, 62 in feces, and 3 in bile (Figure 6C). The tissue distribution of these compounds indicated that both prototypes and metabolites could be detected in various tissues, particularly in the intestines, the primary organ for digestion and absorption. Specifically, 18 prototypes and 9 metabolites were detected in the colon, while 36 prototypes and 23 metabolites were detected in the small intestine. These findings suggest that ZYP's impact on overall host metabolism, through regulation of intestinal flora, may be a significant mechanism of action. The detailed distribution of prototypes and metabolites is presented in Supplementary Tables S2, S3, respectively.

Figure 7 illustrates the association network between the prototypes and their related metabolites. Metabolites detected in feces may be processed by intestinal flora, while those metabolized by the liver are detectable in bile, plasma, and urine. Detailed biotransformation and annotation of prototype and metabolite components are provided in Supplementary Table S4.

3.5 Effects of ZYP-containing serum on cell viability and osteogenic capability in MC3T3-E1 cells

Figure 8A is a simple cell study protocols. As shown in Figure 8B, ZYP-containing serum (2%, 4%, and 8%) and 8% blank serum exerted

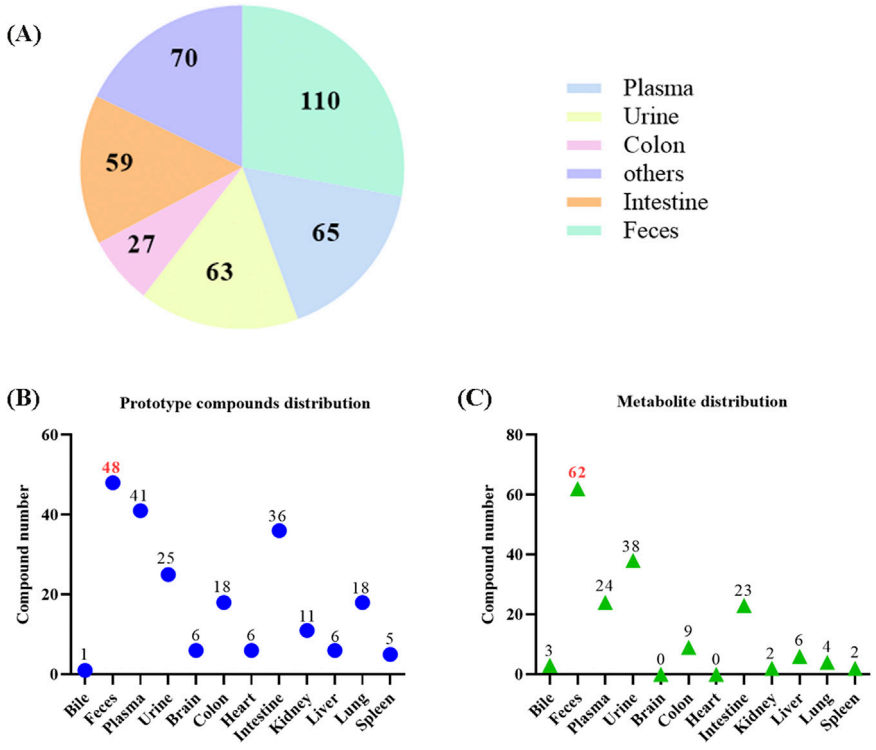

FIGURE 6
Tissue distribution of prototypes and metabolites in ZYP. **(A)** The number of components for each tissue. **(B)** The number of prototype compounds in different tissues. **(C)** The number of metabolite distribution in different tissues.

no obvious effect on the viability of MC3T3-E1 cells. In addition, we performed ALP staining to assess the osteogenic differentiation ability of MC3T3-E1 cells. Although the positive rate of ALP and ARS staining in 8% blank serum treated samples was similar to that of the control samples, our results showed that ZYP-containing serum treatment resulted in a higher rate of positive ALP and ARS staining in MC3T3-E1 cells compared to the control group (Figures 8C, D).

3.6 Effect of ZYP-containing serum on the expression levels of osteogenic differentiation-related proteins in MC3T3-E1 cells

The results revealed that the addition of 8% blank serum to MC3T3-E1 cells did not yield any noticeable differences in the mRNA and protein levels of Runx2, Opn, Opg and Osterix when compared with the control group. Conversely, the mRNA and protein levels of Runx2, Opn, Opg and Osterix were elevated by ZYP-containing serum at concentrations of 2%, 4%, and 8% in MC3T3-E1 cells when compared with the blank group (as depicted in Figure 9). Taken together, these findings suggest the role of ZYP-containing serum promotes the levels of osteogenic differentiation-related proteins in MC3T3-E1 cells.

3.7 ZYP-containing serum upregulate oxidative phosphorylation in the process of osteogenic differentiation in MC3T3-E1 cells

To elucidate the potential mechanism underlying the impact of ZYP-containing serum in promoting the osteogenic differentiation, RNA-seq analysis was further conducted. A total of 5,249 DEGs with 2,700 upregulated and 2,549 downregulated genes were confirmed between MC3T3-E1 treated with or without ZYP-containing serum (Figure 10A). Moreover, the heat map suggested that a set of genes (Cox5a, Cox7a2, Cox7c, Ndufa2, Ndufs8, Atp5g3, Atp5o, Atp5d, Ndufb5, Ndufa9, Ndufa12, Uqcrh, Ndufb7, Ndufb8, Ppa1, Ndufb10 and Ndufab1) of MC3T3-E1 were upregulated by ZYP-containing serum (Figure 10B).

The top 20 enriched KEGG pathways and GO terms (biological process (BP), cellular component (CC), molecular function (MF)) were shown in Figure 11. The results suggested that ZYP-containing serum significantly promoted osteogenic differentiation may be closely related to the upregulation of mitochondrial oxidative phosphorylation.

4 Discussion

OP is recognized as a serious public health problem worldwide. At present, the researchers are working to identify products with

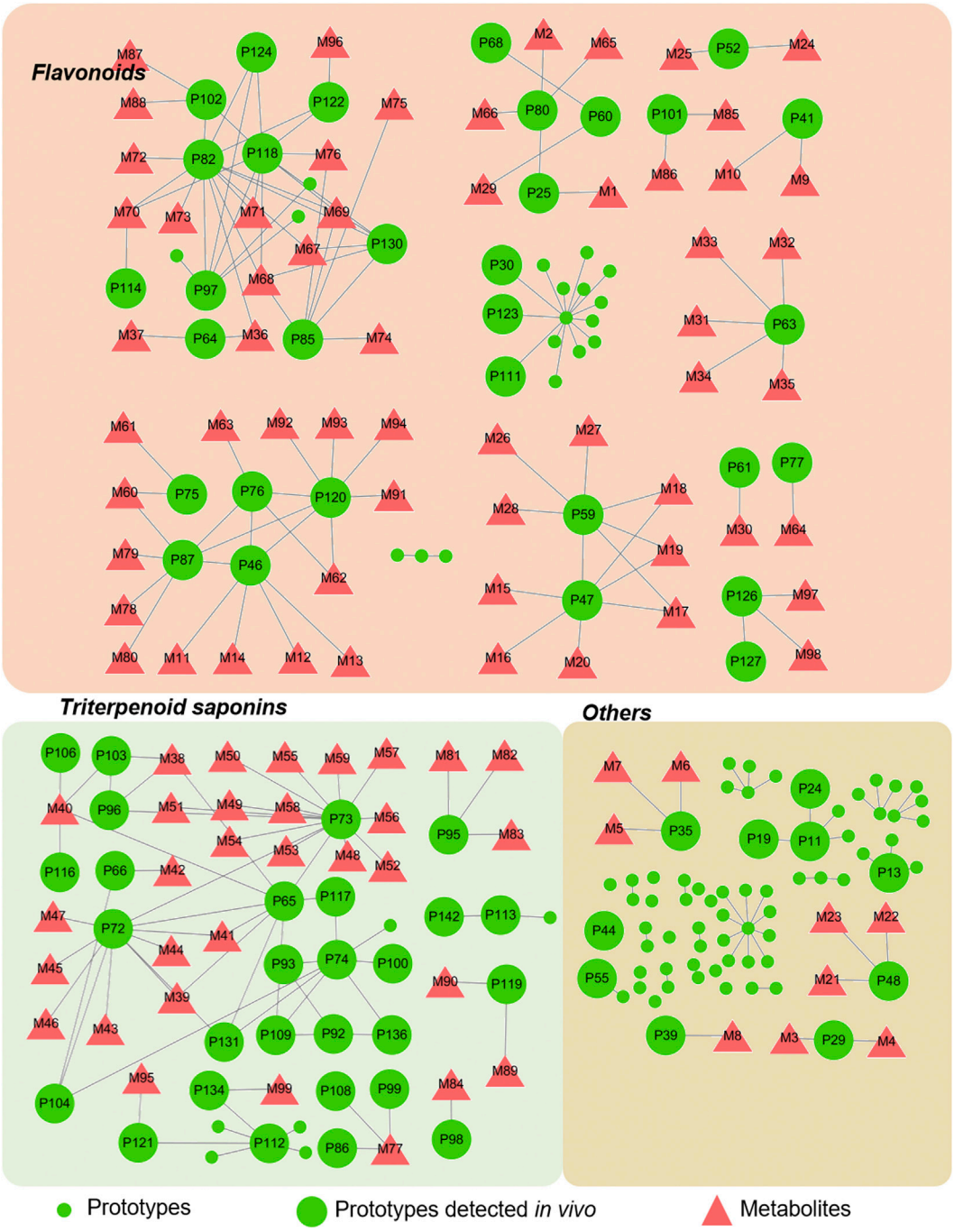

FIGURE 7
Correlation between prototype and metabolites.

reduced osteoclast absorption activity, namely anti-bone absorbents (Vasikaran et al., 2011). Clinically, estrogen, bisphosphonates, and other selective estrogen receptor modulators are widely used for the treatment of OP (Cosman et al., 2014). Unfortunately, these agents can produce some adverse effects, such as gastrointestinal distress, as well as osteonecrosis of jaw (Christenson et al., 2012; Weinstein, 2012; Otto et al., 2011). Natural products, especially the Chinese herbal medicine, offer a promising alternative treatment for maintaining bone health and preventing metabolic bone diseases (Putnam et al., 2007; An et al., 2016). ZYP is a TCM compound developed by Shenzhen TCM Hospital and widely used in the treatment of OP.

In this study, a high-sensitivity and high-resolution UPLC-QTOF-MS/MS method was used to determine the material basis of ZYP. To the best of our knowledge, this is the first comprehensive characterization of the chemical composition of ZYP. Through comparison with standards and literature references, 152 chemical compounds in ZYP were tentatively identified,

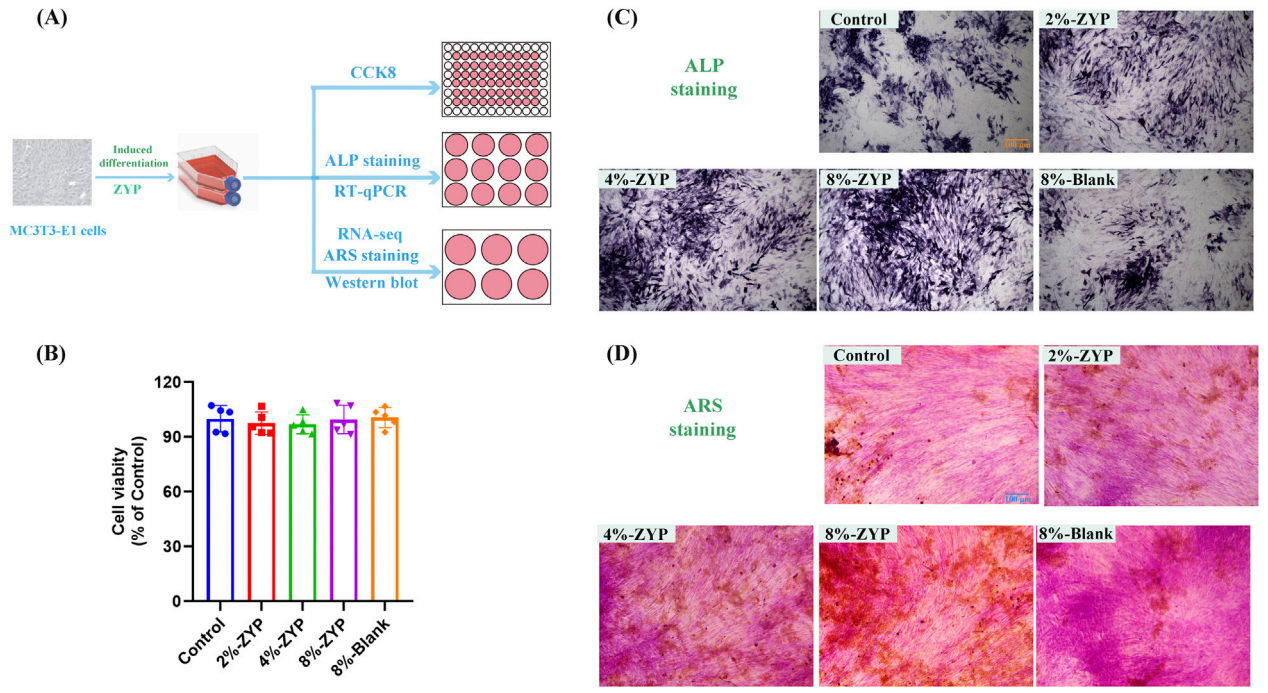

FIGURE 8
ZYP-containing serum improves osteogenic capability in differentially treated group. **(A)** Cell study protocols. **(B)** Cell viability of ZYP-containing serum in MC3T3-E1 cells. **(C)** Representative images showing ALP staining on the 7th day. **(D)** Representative images showing ARS staining on the 21st day.

including flavonoids, iridoids, lignans, triterpene saponins, and others. The composition of ZYP is complex, and after oral administration, these compounds are transformed within the organism, making the composition of exogenous small molecule compounds even more complicated.

Our results indicated the presence of a total of 70 prototype compounds of ZYP in plasma, urine, feces, and bile. Further analysis of these prototypes revealed 99 metabolites. To investigate the *in vivo* process of ZYP further, a tissue distribution study was performed. The results revealed that the compounds in ZYP had a wide distribution throughout the body. Notably, the tissue distribution showed that both prototypes and metabolites could be detected in various tissues, especially in the colon and intestine, which are crucial organs for digestion and absorption. Specifically, 27 compounds were detected in the colon, and 59 compounds were detected in the intestine. These results clearly indicated that intestinal flora may be one of the important pathways through which ZYP exerts its pharmacological effects.

It has been reported that many compounds found in the colon and intestine could ameliorate osteoporosis. For instance, **39** Magnoflorine has been shown to promote new osteoid formation and help restore the integrity of trabecular bone microstructures of the spinal canal, thus preventing the progression of osteoarthritis (Cai et al., 2018). Various flavonoid compounds, such as **52** Hyperoside (Chen et al., 2018; An et al., 2023), **59** Naringin (Wang et al., 2022; Li et al., 2014), **122** Sagittatoside B (Song et al., 2023), **124** 2-O-Rhamnosylicariside II (Zhao et al., 2016) and **130** Baohuoside I (Ma et al., 2022) could ameliorate development of osteoporosis through different mechanisms, including regulation of miR-19a-5p/IL-17A axis, inhibition of the TRAF-6 mediated RANKL/RANK/NF-kB pathway, elevation of the OPG/RANKL ratio, suppression of the JAK2/STAT3 pathway, regulation of immune functions and antioxidant activity. Additionally, triterpenoid saponins, such as **65** Notoginsenoside R1 (Wang et al., 2015; Li et al., 2021), **72** Ginsenoside Re (Kim et al., 2016; Park et al., 2016), **73** Ginsenoside Rg1 (Jiang et al., 2024; Chen et al., 2022), **92** Ginsenoside Rb1 (Cheng et al., 2012; Zhang et al., 2022; Ding et al., 2023), **100** Ginsenoside Rg2 (Lee et al., 2023), **113** Chikusetsusaponin Iva (Tao et al., 2019), **119** Soyasaponin Bb (Kim et al., 2019), **121** Astragaloside II (Kong et al., 2012) and **136** Ginsenoside Rg3 (Zhang et al., 2020; Song et al., 2020) have demonstrated therapeutic effects in improving osteoporosis. These findings provided theoretical support for the prevention and treatment of osteoporosis by ZYP.

MC3T3-E1 cells are derived from mouse embryonic osteoblast precursor cells. An osteogenic induction medium can promote the osteogenic differentiation of MC3T3-E1. Our results revealed that ZYP-containing serum significantly accelerates this process. ALP activity is the most widely recognized biochemical index of osteoblastic activity (Vimalraj, 2020), as it is atypical protein product of osteoblast phenotype and osteoblast differentiation. Runx2 plays a pivotal role in promoting osteogenesis by initiating the expression of osteogenic-specific matrix proteins, such as ALP and OCN (de Farias et al., 2023). OPN, a "bone-bridging" protein abundant in mineralized tissues, has long been involved in bone remodeling (Denhardt and Noda, 1998). Osterix is an osteoblast-specific transcription factor essential for cell differentiation, and its knockout results in an osteoporotic

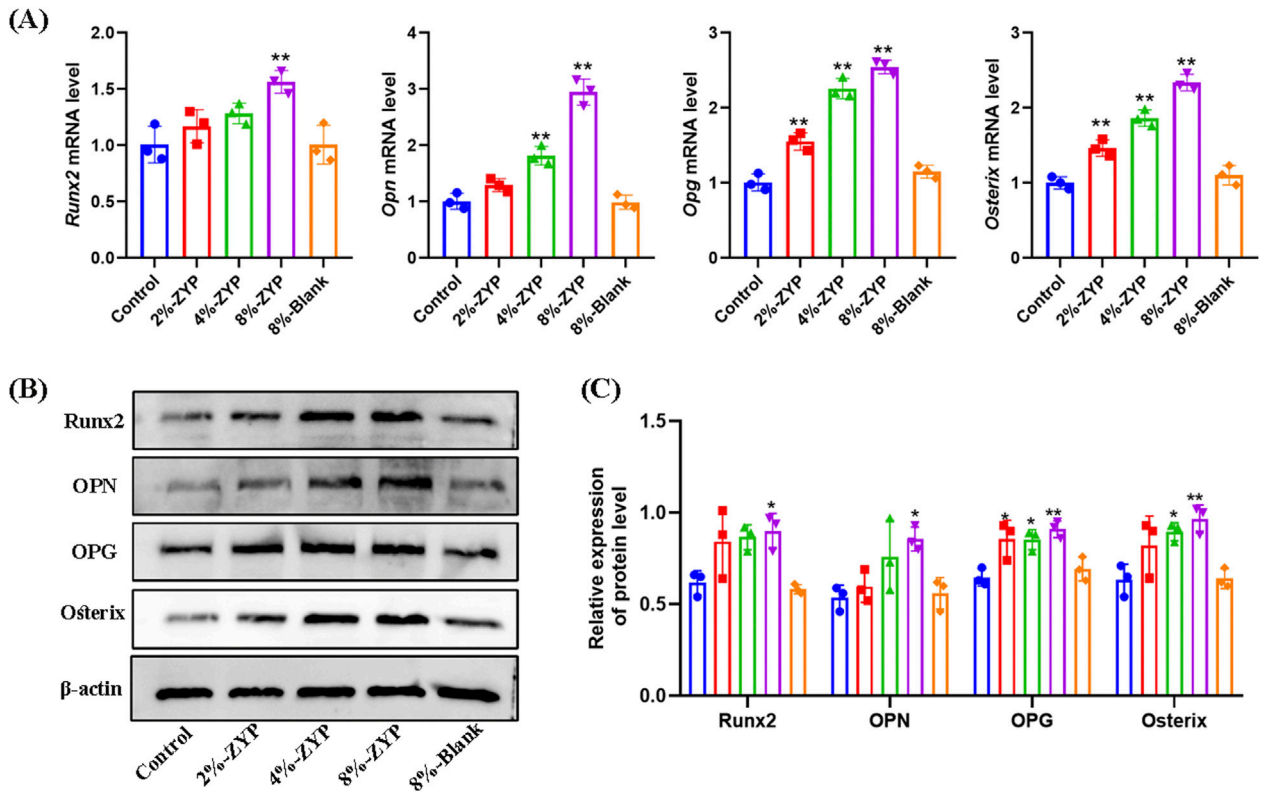

FIGURE 9
Effect of ZYP-containing serum on the expression profiles of osteogenesis associated proteins in MC3T3-E1 cells. **(A)** The mRNA expression of *Runx2*, *Opn*, *Opg* and *Osterix*. **(B)** Representative Western blotting images of Runx2, Opn, Opg and Osterix in different treatment groups. **(C)** Quantitative analysis of Runx2, Opn, Opg and Osterix protein expression levels. $*p < 0.05$, $**p < 0.01$ vs. Control group.

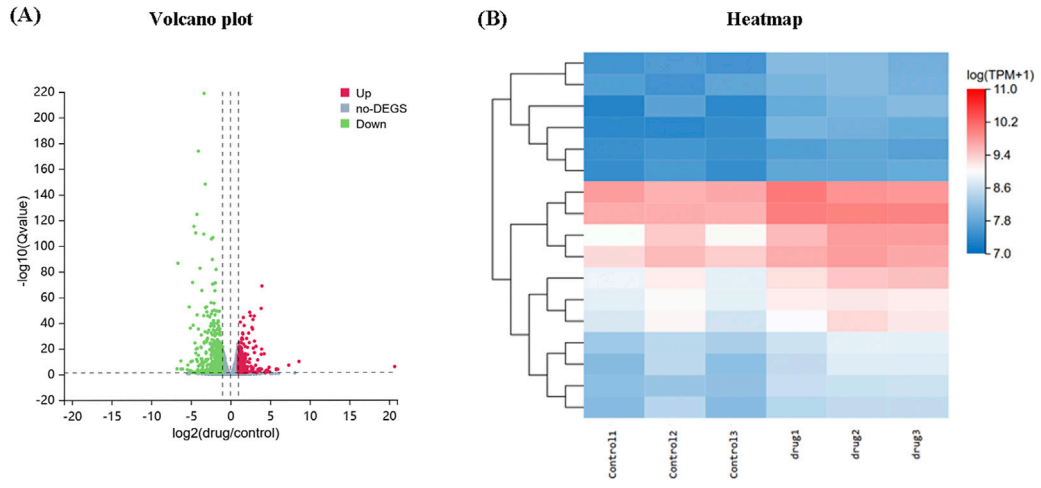

FIGURE 10
(A) Volcano plots of RNA-seq. **(B)** Heatmap of RNA-seq.

phenotype in bone growth due to reduced osteoblast function during bone formation (Sinha and Zhou, 2013; Baek et al., 2009). OPG, a potent osteoclast activation inhibitor, decreases the bone resorption capacity of osteoclasts and plays a regulatory role in bone mineral density (Lacey et al., 2000). These bone formation markers reflect the osteogenic ability of MC3T3-E1 cells.

Our present results indicated that ZYP-containing serum treatment resulted in a higher rate of positive ALP staining in

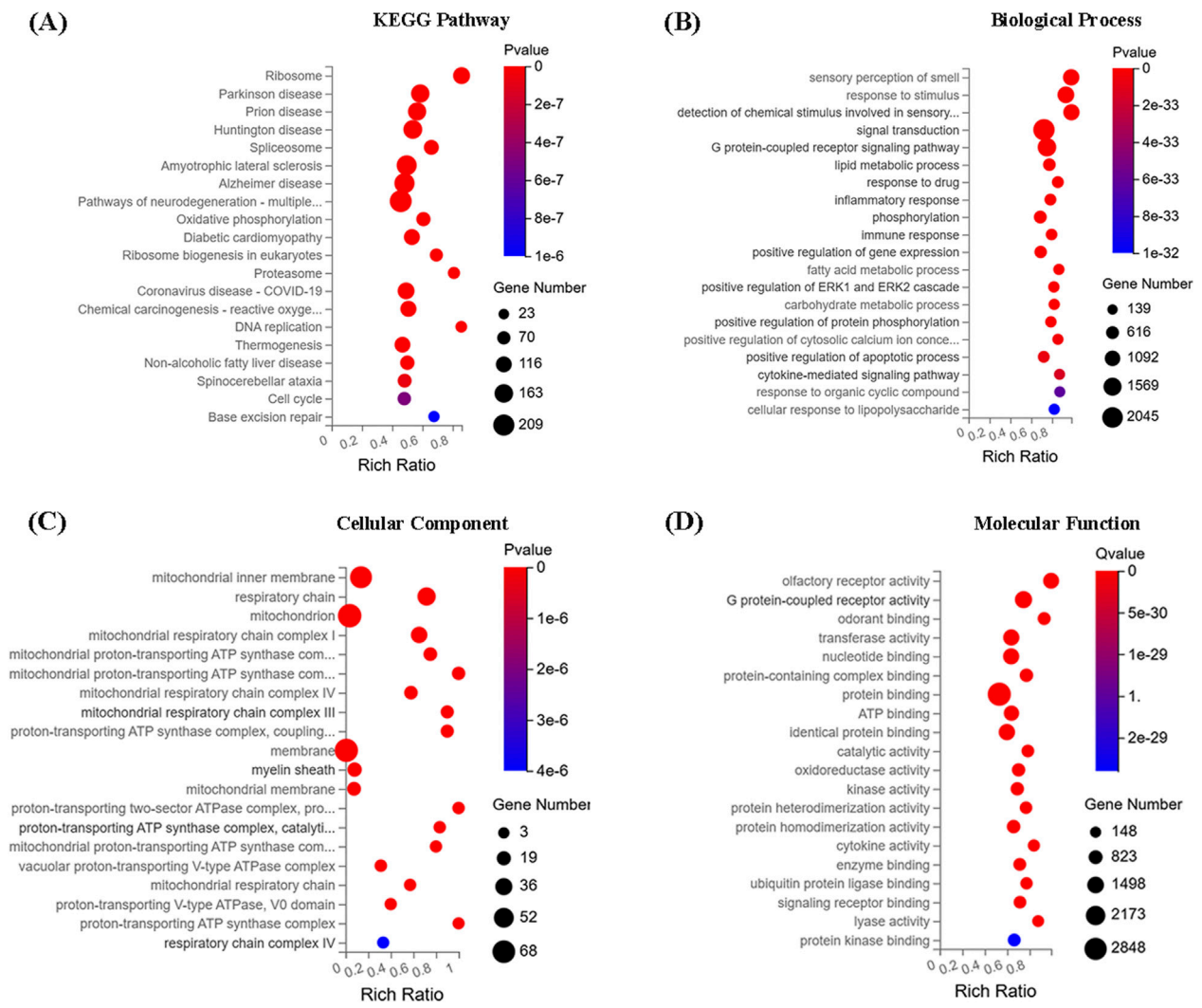

FIGURE 11
RNA-seq results. **(A)** KEGG function enrichment analysis. **(B)** GO function enrichment-biology process. **(C)** GO function enrichment-cell component. **(D)** GO function enrichment-molecular function.

MC3T3-E1 cells compared to the control group. The expression of Runx2, OPN, Osterix and OPG increased when MC3T3-E1 cells were treated with ZYP-containing serum, which suggested that ZYP-containing serum was actively involved in the early osteogenic differentiation and the late bone mineralization of osteoblasts. The mechanism may be related to the upregulation of mitochondrial oxidative phosphorylation, as indicated by RNA-seq analysis. Therefore, further investigation into the effect of this drug on the process of mitochondrial oxidative phosphorylation is necessary. In addition, the chemical composition of ZYP remains unclear.

The present study is the first to identify the chemical components in ZYP, which was important to determine whether prototypical compounds or metabolites involved in specific diseases. In addition, our results also indicated that ZYP-containing serum prominently promoted the osteogenic differentiation of MC3T3-E1. However, more efforts are merited to investigate the underlying mechanism and potential benefit of ZYP.

5 Conclusion

To summarize, UPLC-Q/TOF-MS was first applied for the characterization of the chemical compound of ZYP. Subsequently, prototype compounds and metabolites were identified after gavage of ZYP in rats. Moreover, the multi-compound pharmacokinetics strategy combined with semi-quantitative methods presented the dynamic changes in the prototypical compounds and metabolites *in vivo* by UPLC-Q/TOF-MS. This work provided a dependable and appropriate strategy for the screening and discovery of potentially bioactive ingredients that promote the pharmacological effects of TCM, laying a foundation for further in-depth studies on the bioactive ingredients of ZYP. In addition, the current study demonstrated ZYP-containing serum prominently promoted the osteogenic differentiation of MC3T3-E1. The possible mechanism may be related to the upregulation of mitochondrial oxidative phosphorylation.

Data availability statement

The datasets presented in this study can be found in online repositories. The names of the repository/repositories and accession number(s) can be found in the article/Supplementary Material.

Ethics statement

The animal study was approved by the Chinese University of Hong Kong. The study was conducted in accordance with the local legislation and institutional requirements.

Author contributions

JC: Conceptualization, Data curation, Formal Analysis, Investigation, Methodology, Project administration, Software, Writing–original draft. XM: Data curation, Investigation, Software, Writing–original draft. DF: Investigation, Project administration, Software, Writing–original draft. YZ: Investigation, Project administration, Software, Writing–original draft. ZL: Investigation, Methodology, Writing–original draft. XL: Investigation, Methodology, Writing–original draft. KJ: Investigation, Methodology, Writing–original draft. SH: Methodology, Visualization, Writing–original draft. HL: Conceptualization, Project administration, Writing–original draft. SZ: Conceptualization, Project administration, Writing–review and editing. JHC: Formal Analysis, Investigation, Project administration, Writing–review and editing. JPC: Conceptualization, Funding acquisition, Writing–review and editing.

Funding

The author(s) declare that financial support was received for the research, authorship, and/or publication of this article. This research was supported by the Sanming Project of Medicine in Shenzhen (SZZYSM202111002), Shenzhen Medical Research Fund (B2302008), Shenzhen Science and Technology Program (JSGG20210802093208023, JCYJ20220818103402006, JCYJ20210324140204011 and ZDSYS201606081515458), Foundation of Guangdong Provincial Key Laboratory of Functional Substances in Medicinal Edible Resources and Healthcare Products (No. GPKLFSHP202101), and Traditional Chinese Medicine Bureau of Guangdong Province (20231286).

Conflict of interest

The authors declare that the research was conducted in the absence of any commercial or financial relationships that could be construed as a potential conflict of interest.

Generative AI statement

The author(s) declare that no Generative AI was used in the creation of this manuscript.

Publisher's note

Supplementary material

The Supplementary Material for this article can be found online at: https://www.frontiersin.org/articles/10.3389/frans.2025.1533486/full#supplementary-material

References

An, H., Chu, C., Zhang, Z., Zhang, Y., Wei, R., Wang, B., et al. (2023). Hyperoside alleviates postmenopausal osteoporosis via regulating miR-19a-5p/IL-17A axis. *Am. J. Reprod. Immunol.* 90 (1), e13709. doi:10.1111/aji.13709

An, J., Yang, H., Zhang, Q., Liu, C., Zhao, J., Zhang, L., et al. (2016). Natural products for treatment of osteoporosis: the effects and mechanisms on promoting osteoblast-mediated bone formation. *Life Sci.* 147, 46–58. doi:10.1016/j.lfs.2016.01.024

Baek, W. Y., Lee, M. A., Jung, J. W., Kim, S. Y., Akiyama, H., de Crombrugghe, B., et al. (2009). Positive regulation of adult bone formation by osteoblast-specific transcription factor osterix. *J. Bone. Min. Res.* 24 (6), 1055–1065. doi:10.1359/jbmr.081248

Cai, Z., Feng, Y., Li, C., Yang, K., Sun, T., Xu, L., et al. (2018). Magnoflorine with hyaluronic acid gel promotes subchondral bone regeneration and attenuates cartilage degeneration in early osteoarthritis. *Bone* 116, 266–278. doi:10.1016/j.bone.2018.08.015

Chen, J., Zheng, L., Hu, Z., Wang, F., Huang, S., Li, Z., et al. (2019). Metabolomics reveals effect of Zishen Jiangtang Pill, a Chinese Herbal product on high-fat diet-induced type 2 diabetes mellitus in mice. *Front. Pharmacol.* 10, 256. doi:10.3389/fphar.2019.00256

Chen, W., Jin, X., Wang, T., Bai, R., Shi, J., Jiang, Y., et al. (2022). Ginsenoside Rg1 interferes with the progression of diabetic osteoporosis by promoting type H angiogenesis modulating vasculogenic and osteogenic coupling. *Front. Pharmacol.* 13, 1010937. doi:10.3389/fphar.2022.1010937

Chen, Y., Dai, F., He, Y., Chen, Q., Xia, Q., Cheng, G., et al. (2018). Beneficial effects of hyperoside on bone metabolism in ovariectomized mice. *Biomed. Pharmacother.* 107, 1175–1182. doi:10.1016/j.biopha.2018.08.069

Cheng, B., Li, J., Du, J., Lv, X., Weng, L., and Ling, C. (2012). Ginsenoside Rb1 inhibits osteoclastogenesis by modulating NF-κB and MAPKs pathways. *Food. Chem. Toxicol.* 50 (5), 1610–1615. doi:10.1016/j.fct.2012.02.019

Christenson, E. S., Jiang, X., Kagan, R., and Schnatz, P. (2012). Osteoporosis management in post-menopausal women. *Minerva Ginecol.* 64 (3), 181–194.

Chu, S., Liu, D., Zhao, H., Shao, M., Liu, X., Qu, X., et al. (2021). Effects and mechanism of zishen Jiangtang Pill on diabetic osteoporosis rats based on proteomic analysis. *Evidence-based complementary Altern. Med. eCAM* 2021, 7383062. doi:10.1155/2021/7383062

Clynes, M. A., Harvey, N. C., Curtis, E. M., Fuggle, N. R., Dennison, E. M., and Cooper, C. (2020). The epidemiology of osteoporosis. *Br. Med. Bull.* 133 (1), 105–117. doi:10.1093/bmb/ldaa005

Cosman, F., de Beur, S. J., Leboff, M. S., Lewiecki, E. M., Tanner, B., Randall, S., et al. (2014). Clinician's guide to prevention and treatment of osteoporosis. *Osteoporos. Int.* 25 (10), 2359–2381. doi:10.1007/s00198-014-2794-2

de Farias, C. S., Garcez, A. S., Teixeira, L. N., and Suzuki, S. S. (2023). *In vitro* effects of photobiomodulation on cell migration and gene expression of ALP, COL-1, RUNX-2, and osterix in cementoblasts. *Lasers Med. Sci.* 38 (1), 121. doi:10.1007/s10103-023-03775-5

Denhardt, D. T., and Noda, M. (1998). Osteopontin expression and function: role in bone remodeling. *Cell. Biochem.* 72 (S30-31), 92–102. doi:10.1002/(SICI)1097-4644(1998)72:30/31+<92::AID-JCB13>3.0.CO;2-A

Ding, L., Gao, Z., Wu, S., Chen, C., Liu, Y., Wang, M., et al. (2023). Ginsenoside compound-K attenuates OVX-induced osteoporosis via the suppression of RANKL-induced osteoclastogenesis and oxidative stress. *Nat. Product. Bioprospecting.* 13 (1), 49. doi:10.1007/s13659-023-00405-z

Guo, B., Liu, Z., Zeng, B., Ling, Y., Xiao, Y., Chen, Z., et al. (2011). Efect of Zishen Jiangtang Pills on adipogenic diferentiation of mice MSC and its mechanisms. *China Pharm.* 22 (11), 985–987. (Chinese).

Iolascon, G., Moretti, A., Toro, G., Gimigliano, F., Liguori, S., and Paoletta, M. (2020). Pharmacological therapy of osteoporosis: what's new? *Clin. Interv. Aging.* 15, 485–491. doi:10.2147/CIA.S242038

Jiang, Z., Deng, L., Li, M., Alonge, E., Wang, Y., and Wang, Y. (2024). Ginsenoside Rg1 modulates PI3K/AKT pathway for enhanced osteogenesis via GPER. *Phytomedicine* 124, 155284. doi:10.1016/j.phymed.2023.155284

Kim, H. M., Kim, D. H., Han, H. J., Park, C. M., Ganipisetti, S. R., Valan, A. M., et al. (2016). Ginsenoside Re promotes osteoblast differentiation in mouse osteoblast precursor MC3T3-E1 cells and a zebrafish model. *Molecules* 22 (1), 42. doi:10.3390/molecules22010042

Kim, S. H., Yuk, H. J., Ryu, H. W., Oh, S. R., Song, D. Y., Lee, K. S., et al. (2019). Biofunctional soyasaponin Bb in peanut (*Arachis hypogaea* L.) sprouts enhances bone morphogenetic protein-2-dependent osteogenic differentiation via activation of runt-related transcription factor 2 in C2C12 cells. *Phytother. Res.* 33 (5), 1490–1500. doi:10.1002/ptr.6341

Kong, X. H., Niu, Y. B., Song, X. M., Zhao, D. D., Wang, J., Wu, X. L., et al. (2012). Astragaloside II induces osteogenic activities of osteoblasts through the bone morphogenetic protein-2/MAPK and Smad1/5/8 pathways. *Int. J. Mol. Med.* 29 (6), 1090–1098. doi:10.3892/ijmm.2012.941

Lacey, D. L., Tan, H. L., Lu, J., Kaufman, S., Van, G., Qiu, W., et al. (2000). Osteoprotegerin ligand modulates murine osteoclast survival *in vitro* and *in vivo*. *Am. J. Pathol.* 157 (2), 435–448. doi:10.1016/S0002-9440(10)64556-7

Lee, S. H., Park, S. Y., Kim, J. H., Kim, N., and Lee, J. (2023). Ginsenoside Rg2 inhibits osteoclastogenesis by downregulating the NFATc1, c-Fos, and MAPK pathways. *BMB Rep.* 56 (10), 551–556. doi:10.5483/BMBRep.2023-0100

Li, F., Sun, X., Ma, J., Ma, X., Zhao, B., Zhang, Y., et al. (2014). Naringin prevents ovariectomy-induced osteoporosis and promotes osteoclasts apoptosis through the mitochondria-mediated apoptosis pathway. *Biochem. Biophys. Res. Commun.* 452 (3), 629–635. doi:10.1016/j.bbrc.2014.08.117

Li, H., Chu, S., Zhao, H., Liu, D., Liu, X., Qu, X., et al. (2018). Effect of zishen Jiangtang Pill, a Chinese herbal product, on rats with diabetic osteoporosis. *Evidence-based complementary Altern. Med. eCAM* 2018, 7201914. doi:10.1155/2018/7201914

Li, X., Lin, H., Zhang, X., Jaspers, R. T., Yu, Q., Ji, Y., et al. (2021). Notoginsenoside R1 attenuates oxidative stress-induced osteoblast dysfunction through JNK signalling pathway. *J. Cell. Mol. Med.* 25 (24), 11278–11289. doi:10.1111/jcmm.17054

Liu, J., Curtis, E. M., Cooper, C., and Harvey, N. C. (2019). State of the art in osteoporosis risk assessment and treatment. *J. Endocrinol. Invest.* 42 (10), 1149–1164. doi:10.1007/s40618-019-01041-6

Liu, K., Song, Y., Liu, Y., Peng, M., Li, H., Li, X., et al. (2017). An integrated strategy using UPLC-QTOF-MS(E) and UPLC-QTOF-MRM (enhanced target) for pharmacokinetics study of wine processed Schisandra Chinensis fructus in rats. *J. Pharm. Biomed. Anal.* 139, 165–178. doi:10.1016/j.jpba.2017.02.043

Ma, M., Fan, A. Y., Liu, Z., Yang, L. Q., Huang, J. M., Pang, Z. Y., et al. (2022). Baohuoside I inhibits osteoclastogenesis and protects against ovariectomy-induced bone loss. *Front. Pharmacol.* 13, 874952. doi:10.3389/fphar.2022.874952

Mi, N., Cheng, T., Li, H., Yang, P., Mu, X., Wang, X., et al. (2019). Metabolite profiling of traditional Chinese medicine formula Dan Zhi Tablet: an integrated strategy based on UPLC-QTOF/MS combined with multivariate statistical analysis. *J. Pharm. Biomed. Anal.* 164, 70–85. doi:10.1016/j.jpba.2018.10.024

Mu, X., Liu, J., Li, B., Wei, X., Qi, Y., Zhang, B., et al. (2022). A comparative study on chemical characteristics, antioxidant, and hepatoprotective activity from different parts of Schisandrae Chinensis Fructus. *J. Food Process. Preserv.* 46 (11). doi:10.1111/jfpp.16990

Otto, S., Abu-Id, M. H., Fedele, S., Warnke, P. H., Becker, S. T., Kolk, A., et al. (2011). Osteoporosis and bisphosphonates-related osteonecrosis of the jaw: not just a sporadic coincidence-a multi-centre study. *J. Craniomaxillofac. Surg.* 39 (4), 272–277. doi:10.1016/j.jcms.2010.05.009

Park, C. M., Kim, H. M., Kim, D. H., Han, H. J., Noh, H., Jang, J. H., et al. (2016). Ginseno*side re* inhibits osteoclast differentiation in mouse bone marrow-derived macrophages and zebrafish scale model. *Mol. Cells.* 39 (12), 855–861. doi:10.14348/molcells.2016.0111

Putnam, S. E., Scutt, A. M., Bicknell, K., Priestley, C. M., and Williamson, E. M. (2007). Natural products as alternative treatments for metabolic bone disorders and for maintenance of bone health. *Phytother. Res.* 21 (2), 99–112. doi:10.1002/ptr.2030

Ren, S. M., Zhang, Q. Z., Jiang, M., Chen, M. L., Xu, X. J., Wang, D. M., et al. (2022). Systematic characterization of the metabolites of defatted walnut powder extract *in vivo* and screening of the mechanisms against NAFLD by UPLC-Q-Exactive Orbitrap MS combined with network pharmacology. *J. Ethnopharmacol.* 285, 114870. doi:10.1016/j.jep.2021.114870

Si, L., Winzenberg, T. M., Jiang, Q., Chen, M., and Palmer, A. J. (2015). Projection of osteoporosis-related fractures and costs in China: 2010-2050. *Osteoporos. Int.* 26 (7), 1929–1937. doi:10.1007/s00198-015-3093-2

Sinha, K. M., and Zhou, X. (2013). Genetic and molecular control of osterix in skeletal formation. *J. Cell. Biochem.* 114 (5), 975–984. doi:10.1002/jcb.24439

Song, L., Zhou, Y., Qu, L., Wang, D., Diao, X., Zhang, X., et al. (2023). Exploring effects and mechanism of ingredients of herba epimedii on osteogenesis and osteoclastogenesis *in vitro*. *Comb. Chem. and High Throughput Screen* 27, 2824–2837. doi:10.2174/0113862073243559231023065934

Song, M., Jia, F., Cao, Z., Zhang, H., Liu, M., and Gao, L. (2020). Ginsenoside Rg3 attenuates aluminum-induced osteoporosis through regulation of oxidative stress and bone metabolism in rats. *Biol. Trace Elem. Res.* 198 (2), 557–566. doi:10.1007/s12011-020-02089-9

Tao, Y., Huang, S., Yan, J., and Cai, B. (2019). Determination of major components from Radix Achyranthes bidentate using ultra highperformance liquid chromatography with triple quadrupole tandem mass spectrometry and an evaluation of their anti-osteoporosis effect *in vitro*. *J. Sep. Sci.* 42 (13), 2214–2221. doi:10.1002/jssc.201900146

Vasikaran, S., Eastell, R., Bruyere, O., Foldes, A. J., Garnero, P., Griesmacher, A., et al. (2011). Markers of bone turnover for the prediction of fracture risk and monitoring of osteoporosis treatment: a need for international reference standards. *Osteoporos. Int.* 22 (2), 391–420. doi:10.1007/s00198-010-1501-1

Vimalraj, S. (2020). Alkaline phosphatase: structure, expression and its function in bone mineralization. *Gene* 754, 144855. doi:10.1016/j.gene.2020.144855

Wang, T., Wan, D., Shao, L., Dai, J., and Jiang, C. (2015). Notoginsenoside R1 stimulates osteogenic function in primary osteoblasts via estrogen receptor signaling. *Biochem. Biophys. Res. Commun.* 466 (2), 232–239. doi:10.1016/j.bbrc.2015.09.014

Wang, W., Mao, J., Chen, Y., Zuo, J., Chen, L., Li, Y., et al. (2022). Naringin promotes osteogenesis and ameliorates osteoporosis development by targeting JAK2/STAT3 signalling. *Clin. Exp. Pharmacol. Physiol.* 49 (1), 113–121. doi:10.1111/1440-1681.13591

Weinstein, R. S. (2012). Glucocorticoid-induced osteoporosis and osteonecrosis. *Endocrinol. Metab. Clin. North. Am.* 41 (3), 595–611. doi:10.1016/j.ecl.2012.04.004

Xiao, J., Song, N., Lu, T., Pan, Y., Song, J., Chen, G., et al. (2018). Rapid characterization of TCM Qianjinteng by UPLC-QTOF-MS and its application in the evaluation of three species of Stephania. *J. Pharm. Biomed. Anal.* 156, 284–296. doi:10.1016/j.jpba.2018.04.044

Yuan, S., Chen, J., Cao, Y., Zhao, H., Lin, S., Xiong, J., et al. (2024). Investigation of bioactive components and metabolic pathways of Zhen-Wu-tang in rat plasma and renal tissue by UPLC-Q-TOF/MS. *Phytochem. Anal.* doi:10.1002/pca.3455

Zhang, D., Du, J., Yu, M., and Suo, L. (2022). Ginsenoside Rb1 prevents osteoporosis via the AHR/PRELP/NF-κB signaling axis. *Phytomedicine* 104, 154205. doi:10.1016/j.phymed.2022.154205

Zhang, X., Huang, F., Chen, X., Wu, X., and Zhu, J. (2020). Ginsenoside Rg3 attenuates ovariectomy-induced osteoporosis via AMPK/mTOR signaling pathway. *Drug Dev. Res.* 81 (7), 875–884. doi:10.1002/ddr.21705

Zhao, B. J., Wang, J., Song, J., Wang, C. F., Gu, J. F., Yuan, J. R., et al. (2016). Beneficial effects of a flavonoid fraction of herba epimedii on bone metabolism in ovariectomized rats. *Planta Med.* 82 (4), 322–329. doi:10.1055/s-0035-1558294

frontiers | Frontiers in Analytical Science

TYPE Original Research
PUBLISHED 27 February 2025
DOI 10.3389/frans.2025.1527110

OPEN ACCESS

EDITED BY
Elefteria Psillakis,
Technical University of Crete, Greece

REVIEWED BY
Alessandra Cincinelli,
University of Florence, Italy
Ashok K. Shakya,
Al-Ahliyya Amman University, Jordan

*CORRESPONDENCE
Marianela Savio,
msavio@exactas.unlpam.edu.ar

RECEIVED 12 November 2024
ACCEPTED 03 February 2025
PUBLISHED 27 February 2025

CITATION
Cora Jofre F, Barros AI, Nóbrega JA and Savio M (2025) Multi-energy calibration in plasma emission spectrometry: elemental analysis of animal feeds.
Front. Anal. Sci. 5:1527110.
doi: 10.3389/frans.2025.1527110

Multi-energy calibration in plasma emission spectrometry: elemental analysis of animal feeds

Florencia Cora Jofre[1,2], Ariane I. Barros[3], Joaquim A. Nóbrega[4] and Marianela Savio[1,2]*

[1]Facultad Ciencias Exactas y Naturales, Universidad Nacional de La Pampa (UNLPam), Santa Rosa, La Pampa, Argentina, [2]Instituto de Ciencias de la Tierra y Ambientales de La Pampa (Consejo Nacional de Investigaciones Científicas y Técnicas - Universidad Nacional de La Pampa), INCITAP, Mendoza, Argentina, [3]Study Group on Soil Residues and Organic Matter, Department of Rural and Soil Engineering, Faculty of Agronomy and Zootechnics, Federal University of Mato Grosso, Mato Grosso, Brazil, [4]Group for Applied Instrumental Analysis, Department of Chemistry, Federal University of São Carlos, São Carlos, Brazil

This study evaluates the effectiveness of Multi-Energy Calibration (MEC) for multielemental analysis in animal feeds using plasma-based optical emission spectrometry (ICP-OES and MIP-OES). The aim was to improve accuracy in detecting essential minerals by overcoming matrix interferences that affect instrumental techniques. Swine feed samples from different growth stages were analyzed, focusing on essential minerals for animal health and productivity, such as Ca, Co, Cu, Fe, K, Mg, Mn, Na, P, and Zn. The MEC strategy utilizes multiple wavelengths per element, reducing calibration complexity and enhancing accuracy by using only two calibration solutions per sample. Results demonstrate that MEC improves recoveries (80%–105%) when compared to traditional external calibration (EC). The limits of quantification (LOQs) ranged from 0.09 mg kg^{-1} for Mn to 31 mg kg^{-1} for Ca and Na using MEC-ICP-OES, and from 0.08 mg kg^{-1} for Mn to 354 mg kg^{-1} for P using MEC-MIP-OES. For EC, they ranged from 0.4 mg kg^{-1} for Co to 195 mg kg^{-1} for K with ICP-OES and from 2.0 mg kg^{-1} for Mg to 607 mg kg^{-1} for Fe with MIP-OES. MEC provides high precision and matrix-matching capabilities. This makes MEC a reliable method for complex feed matrices, supporting more accurate feed formulations to ensure optimal livestock nutrition.

KEYWORDS

multi-energy calibration, animal feed, multielemental determination, ICP-OES, MIP-OES

1 Introduction

The rapid growth of the global population, projected to reach nearly 10 billion by 2050, is driving a significant increase in food demand, emphasizing the need for sustainable agricultural practices (Beily et al., 2011). In alignment with the Sustainable Development Goals (SDGs), which focus on eradicating hunger, achieving food security, improving nutrition, and promoting sustainable agriculture, many countries are adopting tailored strategies to boost food production (SDGs, 2024). One major area of focus is livestock production, where confined animal systems have become prevalent, increasing the demand for nutritionally balanced feed supplements (McDowell, 1992). These supplements must provide adequate concentrations of essential nutrients such as proteins, vitamins, and minerals to ensure animal health and productivity (Solà-Oriol and Gasa, 2017; Shurson et al., 2011; Spears and Weiss, 2008). The mineral content of feed is critical, as both

deficiencies and excesses can lead to diseases, affecting not only animal wellbeing but also the quality of animal-derived food products consumed by humans (Patience, 1996; Novo et al., 2018).

Swine production offers advantages such as high efficiency in converting plant protein into animal protein, adaptability to thermal variations, and shorter production cycles compared to other livestock (Spears and Weiss, 2008). Efficient feed management, accounting for about 70% of production costs, is essential for profitability, particularly as pigs require specific nutrients at different life stages, from reproduction to growth. Therefore, the accurate measurement of essential minerals like calcium (Ca), chlorine (Cl), cobalt (Co), copper (Cu), iodine (I), iron (Fe), magnesium (Mg), manganese (Mn), phosphorus (P), potassium (K), selenium (Se), sodium (Na), sulfur (S), zinc (Zn), among others, in animal feed is crucial for ensuring optimal growth and productivity (National Research Council, 2012).

The complexity of agro-food matrices, which include pastures, grains, and rations, implies challenges for analytical techniques used in trace element determination. Sample preparation is a critical step, as it can introduce errors, with residual organic carbon and suspended solids potentially causing spectral and non-spectral interferences (Analytical Methods Committee, 2013). In recent years, different sample treatments employing microwave, infrared and/or ultrasound radiations have been proposed to improve the analyte extraction (Matusiewicz, 2017; Nóbrega et al., 2012; Jofre and Savio, 2024). Additionally, calibration is a crucial aspect of analytical procedures, as it ensures the accurate translation of signal intensities into analyte concentrations. Traditional methods like external calibration (EC) are widely used for simple matrices, but for complex matrices, alternatives like internal standardization (IS) and standard additions (SA) are often necessary to correct for interferences (Carter et al., 2018; Barros, Pinheiro, and Nóbrega, 2019; Donati and Amais, 2019).

To address conventional methods limitations, a novel calibration technique known as Multi-Energy Calibration (MEC) has been developed (Virgilio et al., 2017). When applying MEC to plasma emission spectrometry, multiple emission lines (wavelengths) for each element are measured simultaneously for calibration, instead of relying on a single emission line. Since inductively coupled plasma optical emission spectrometry (ICP-OES) and microwave induced plasma optical emission spectrometry (MIP-OES) plasmas can reach high temperatures (*ca.* 10,000 K and *ca.* 5,000K, respectively), they effectively atomize, excite, and ionize many elements, generating multiple characteristic atomic and ionic emission lines. MEC takes advantage of this fact, offering several significant advantages that make it a powerful calibration strategy in plasma emission spectrometry. By utilizing multiple wavelengths, it mitigates interferences through the identification and elimination of affected wavelengths. A fundamental advantage of the MEC strategy is its ability to facilitate the visual identification of emission lines impacted by interferences, which appear as outliers on the calibration plot (Carter et al., 2018). This method is highly efficient, requiring only two calibration solutions per sample, thereby streamlining the analytical process and reducing both time and resource demands. Furthermore, its compatibility with existing instrumentation ensures that no modifications are necessary, making MEC a straightforward and adaptable technique for diverse analytical applications (Virgilio et al., 2020).

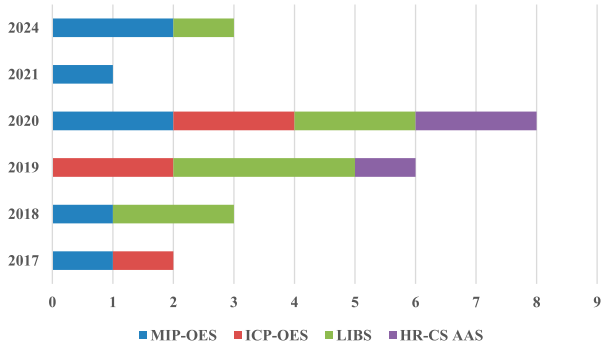

FIGURE 1
Distribution of MEC publications with MIP-OES, ICP-OES, LIBS, and HR-CS AAS from 2017 to 2024.

As shown in Figure 1, laser-induced breakdown spectroscopy (LIBS) demonstrates the highest number of publications, particularly in 2020, while MIP-OES and ICP-OES show a more consistent distribution across the years. (Santos et al., 2024; Carneiro and Dias, 2021; Virgilio et al., 2020; Pereira et al., 2020; Cruz et al., 2024; Li et al., 2020; Garde et al., 2020; Cruz et al., 2020; Gonçalves et al., 2019; Higuera, Silva, and Nogueira, 2019; Barros, Pinheiro, and Nóbrega, 2019; Machado et al., 2018; Virgilio et al., 2017; Castro, Babos, and Pereira-Filho, 2020; Carvalho et al., 2019; Vieira et al., 2019; Augusto et al., 2018; Babos et al., 2019; Babos et al., 2018; Fortunato et al., 2019; Soares, Donati, and Rocha, 2022). Notably, no MEC-related publications associated with these techniques are reported for the years 2022 and 2023 Comparative studies between ICP-OES and MIP-OES are limited to publications from 2017 to 2020, highlighting the need for additional research to provide comprehensive comparative data on these two techniques. As demonstrated in prior studies (Santos et al., 2024; Pereira et al., 2020; Machado et al., 2018; Gonçalves et al., 2019; Higuera, Silva, and Nogueira, 2019; Carter et al., 2018), MEC has proven particularly effective for complex matrices such as food, beverages, and biological samples, among others. Its versatility and robust performance in identifying interferences and delivering accurate results position MEC as a significant advancement in plasma spectrometry calibration strategies.

This study aims to evaluate the potential of MEC as a matrix-matching calibration strategy for the determination of minerals such as Ca, Co, Cu, Fe, K, Mg, Mn, Na, P, and Zn in animal feed samples using ICP-OES and MIP-OES; ensuring reliable quantification of mineral content. Additionally, the study seeks to assess the nutritional value of the feed, as this information is critical for formulating balanced rations that directly impact pig growth and development.

2 Materials and methods

2.1 Sampling and sample preservation

Thirteen swine feed samples covering different physiological stages in pork life were obtained from a local farm in La Pampa,

10.3389/frans.2025.1527110

TABLE 1 Operating conditions for ICP-OES and MIP-OES determinations, including selected wavelength lines (discarded wavelengths are indicated in bold).

Instrumental parameter	Operating condition	
	ICP-OES	MIP-OES
Radio frequency applied power [kW]	1.2	1.0
Plasma gas flow rate [L min^{-1}]	12	20
Auxiliary gas flow rate [L min^{-1}]	1	1
Nebulization gas flow rate [L min^{-1}]	0.70	1.0
Peristaltic pump speed [rpm]	12	15
View	axial	radial
Stabilization time [s]	15	15
Integration time [s]	3	3
Nebulizer	concentric	concentric
Nebulization chamber	cyclonic, double path	Single Pass
Replicates	3	3
Analyte	Wavelength [nm]*	
Ca	**183.801**; **184.006**; 315.887; 317.933; 318.128; **370.603**; **373.690**; 393.366; 396.847; 422.673; 431.865	393.366; **396.847**; **422.673**; **430.253**; **445.478**; **616.217**
Co	195.742; 228.616; 230.786; **231.160**; **235.342**; 237.862; 238.892	**240.725**; **340.512**; 341.234; **345.351**; **350.228**; **350.631**
Cu	**204.379**; **211.209**; **213.598**; 214.897; **217.894**; **219.958**; **221.810**; **224.700**; **324.754**; **327.396**	**216.510**; **217.895**; **223.008**; **324.754**; **327.395**; **510.554**
Fe	**218.719**; **233.280**; **234.349**; **238.204**; **239.562**; **240.488**; **259.837**; **259.940**; **261.187**; **271.441**; **273.074**; **274.932**; **322.775**; **371.994**	**259.940**; **358.119**; 371.993; **373.486**; **373.713**; **385.991**
K	**404.414**; **404.721**; **766.490**; **769.896**	344.738; **404.414**; **404.721**; 693.877; **766.491**; **769.897**
Mg	**202.582**; 279.079; **279.553**; 279.806; **280.270**; **285.213**	279.553; **280.271**; 285.213; 383.230; **383.829**; **517.268**; **518.360**
Mn	**191.510**; **257.610**; **259.373**; 260.589; **279.482**; **293.930**; **294.920**; **348.291**; 403.076; **403.307**	257.610; **259.372**; 279.482; **403.076**; **403.307**; **403.449**
Na	330.237; 330.298; 568.820; **588.995**; **589.592**; **818.326**	330.237; 330.298; **568.263**; **568.820**; 588.995; **589.592**
P	**177.495**; 178.284; **178.766**; **185.891**; **185.942**; **213.618**; 214.914	213.618; **214.915**; **253.560**; **255.326**; 764.934
Zn	**202.548**; **206.200**; **213.856**; **328.233**; **330.259**; **334.502**; **472.216**; 481.053	202.548; **206.200**; **213.857**; 328.233; **472.215**; **481.053**

* Emission lines employed for MEC calibration are listed in bold.

Argentina. The following different growth stages were considered: Growth stages I (3–5 kg), II (5–10 kg), III (10–20 kg), and IV (20–50 kg); Development phases I (20–50 kg), II (20–50 kg) and III (50–80 kg); Completion phase I (20–50 kg), II (50–80 kg) and III (50–80 kg); Bristle (80–120 kg); Bristle in gestation; and Bristle in lactation. All samples were gathered into polyethylene bags and stored in a dry and dark place. The samples were then pulverized using cryogenic milling equipment (model MA 775, Marconi, Piracicaba, SP, Brazil).

2.2 Sample preparation

Samples for ICP-OES determination were prepared according to the method proposed by Savio et al. (2019), using an UltraWAVE™ microwave oven with a single reaction chamber design (SRC, Milestone, Sorisole, Italy) (Nóbrega et al., 2012). For MIP-OES determination, samples were prepared following the method by Cora Jofre et al., using an infrared radiation digestion prototype (IRAD) (Jofre et al., 2020).

2.3 Instrumentation

Multielemental determinations were carried out by ICP-OES iCAP 7,000 from Thermo with dual view configuration (Thermo Fisher Scientific, Madison, WI, United States) and by MIP-OES, Agilent model MP AES 4210, operating in conventional conditions as shown in Table 1. Argon (99.999%, White Martins-Praxair) was used in all measurements.

2.4 Reagents, standards, and solutions

2.4.1 For MEC-ICP-OES determination

All reagents were of analytical grade, and all solutions were prepared using distilled-deionized water. A Millipore ultrapure water system (Millipore, Billerica, MA, United States) was utilized, which generates ultrapure deionized water (resistivity ≥18.2 MΩ cm). Concentrated HNO_3 (Merck, Darmstadt, Germany) was obtained using a sub-boiling device (Milestone). Concentrated hydrogen peroxide (30% w w^{-1}), Labsynth, Diadema, SP, Brazil) was also employed.

Standard solutions for MEC experiments were prepared by diluting of 1,000 mg L^{-1} solution of Ca, Co, Cu, Fe, K, Mg, Mn, Na, P, and Zn (Qhemis, São Paulo, SP, Brasil; Titrisol-Merck, Darmstadt, Germany and Fluka, Buchs St. Gallen, Switzerland) in 0.14 mol L^{-1} HNO_3 solution. To assess the accuracy of the method, two reference materials (RM-Agro E3001a - Bovine Liver and MRC20 - Corn grain) and a proficiency test material "animal mineral supplement" (SM18-03) produced by EMBRAPA Pecuária Sudeste (São Carlos, SP, Brazil), were used.

2.4.2 For MEC-MIP-OES determination

All solutions were prepared using ultrapure water sourced from a Millipore® ultrapure water system (Mili-Q) as described previously. For sample digestion, nitric acid (HNO_3, 65% w w^{-1}, MERCK) was purified using a Berghoff® sub-boiling mineral acid distillation system to produce ultrapure, metal-free acid. Hydrogen peroxide (H_2O_2, 30% w w^{-1}, SIGMA-ALDRICH) was also utilized. Standard solutions were prepared by diluting individual 1,000 mg L^{-1} stock solutions of Ca, Co, Cu, Fe, K, Mg, Mn, Na, P, and Zn (Sigma-Aldrich) for MEC analytical calibration. The proposed method was validated using the same reference materials as Section 2.4.1.

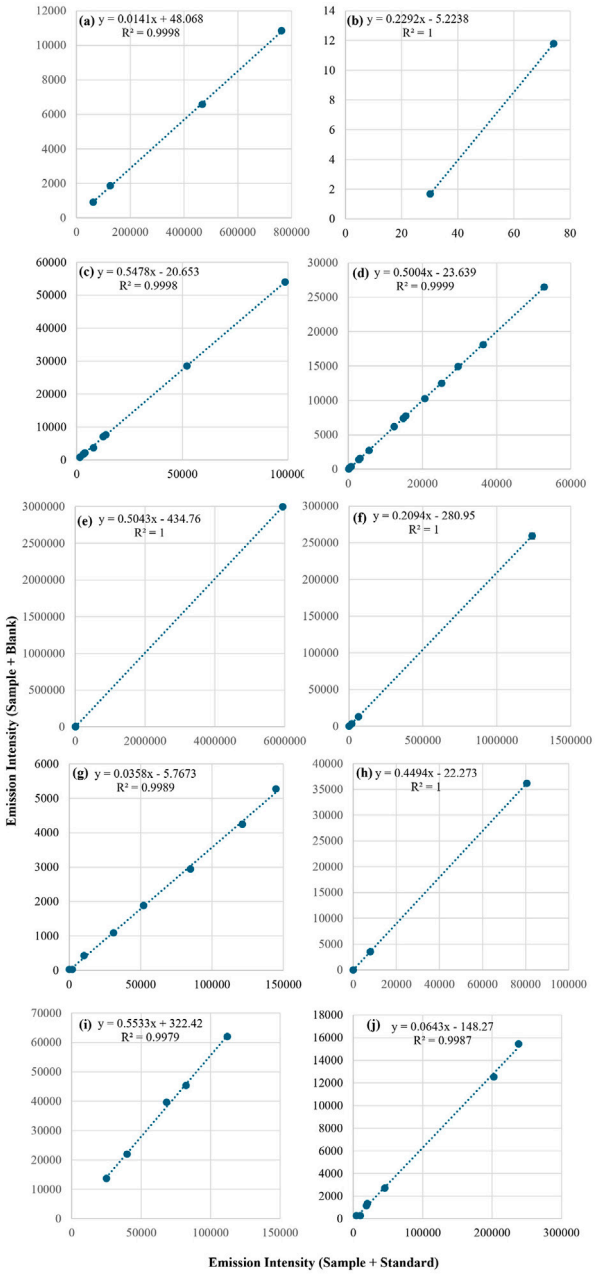

FIGURE 2
Multi-energy calibration curves for **(A)** Ca, **(B)** Co, **(C)** Cu, **(D)** Fe, **(E)** K, **(F)** Mg, **(G)** Mn, **(H)** Na, **(I)** P and **(J)** Zn determined in RM-Agro E3001a - Bovine Liver by ICP-OES.

2.5 Preparation of solutions and calculations for MEC experiments

For preparing the calibration curves based on MEC strategy two solutions per sample and a mixing proportion of 1:1 (v v^{-1}) were adopted. The solution 1 (S1) was comprised of 50% (v v^{-1}) of the digested sample and 50% (v v^{-1}) of the standard solutions containing all analytes (Ca, Co, Cu, Fe, K, Mg, Mn, Na, P, and Zn) at varying concentrations (C_std) determined according to the expected analyte concentrations in the samples, as outlined by Carter et al. (Carter et al., 2018). Solution 2 (S2) consisted of 50% (v v^{-1}) of the digested sample and 50% (v v^{-1}) of an analytical blank solution (Virgilio et al., 2017; Machado et al., 2018). For the construction of MEC calibration curve, emission intensities at multiple wavelengths were recorded for each analyte, where the signals for S1 and S2 are plotted on the x and y-axes, respectively, resulting in a straight line. Once the MEC calibration curves were established, the concentration of each analyte was calculated using the following Equation 1 proposed by Virgilio et al. (2017):

$$C(A)_{Sm} = \frac{slope \times C_{Std}}{(1 - slope)} \quad (1)$$

All experiments were carried out in triplicate, and the results were expressed as the mean of the measurements ± a confidence interval (α = 0.05).

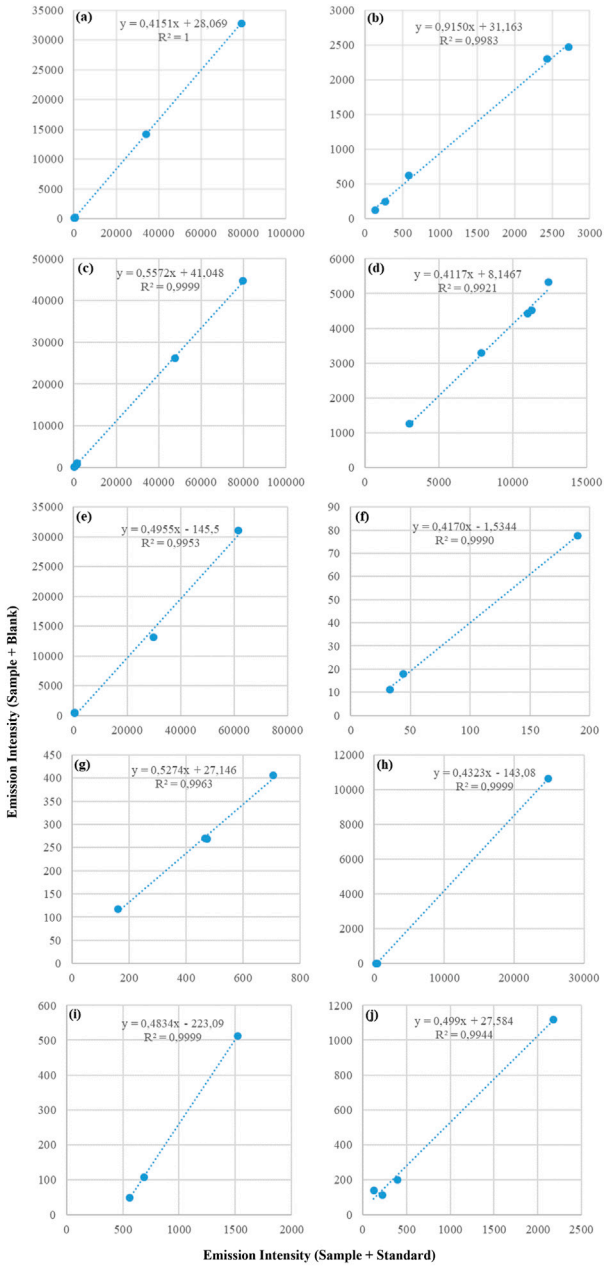

FIGURE 3
Multi-energy calibration curves for **(A)** Ca, **(B)** Co, **(C)** Cu, **(D)** Fe, **(E)** K, **(F)** Mg, **(G)** Mn, **(H)** Na, **(I)** P and **(J)** Zn determined in RM-Agro E3001a - Bovine Liver by MIP-OES.

2.6 Statistical analysis

Microsoft Office Professional Plus Excel™ was utilized for all computations, including calibrations, performance metrics, recovery analyses, correlation assessments, comparisons, and associated statistical tests.

For MEC, the calculation of limits of detection (LODs) and quantification (LOQs) were made following error propagation approach, employing the concentration of the standard solution (C_std), the standard deviation of the slope (S_slope), and the slope itself, as described by Virgilio et al. (2020). The following Equations 2, 3 were applied:

$$LOD = 3^{*}\left(\frac{C_{std}{}^{*}S_{slope}}{(1-slope)^{2}}\right) \quad (2)$$

$$LOQ = 10^{*}\left(\frac{C_{std}{}^{*}S_{slope}}{(1-slope)^{2}}\right) \quad (3)$$

3 Results and discussion

3.1 Multi-energy calibration strategy optimization

For the MEC method, optimal analytical lines were selected based on their sensitivity and interference absence. Each one, presented in Table 1, was used to obtain the calibration curve. Lines that deviate from the expected calibration model, indicated as outliers, were systematically excluded (emission lines employed for MEC calibration are listed in Table 1 in bold).

In the present study, the MEC strategy was applied to multielement determinations using both ICP-OES and MIP-OES. Signals from S1 (x-axis) and S2 (y-axis) were used to construct the MEC plots (Virgilio et al., 2017; Machado et al., 2018). Figures 2, 3 display the calibration curves for the 10 analytes determined by ICP-OES and MIP-OES using MEC, based on the reference material RM-Agro E3001a (Bovine Liver). Supplementary Tables S1, 2 show the average intensities (n = 3) and SD used for MEC-ICP-OES and MEC-MIP-OES curves construction. Similarly, Supplementary Figures S1, 2, exhibit the calibration curves for the 10 analytes measured by ICP-OES and MIP-OES using MEC, based on Corn Grain reference material. The slopes and R^2 values are compared in Table 2 and Supplementary Table S3 for 10 analytes across different sample types (e.g., maize, bovine liver, and animal mineral supplement), using both MEC-ICP-OES and MEC-MIP-OES. The calibration plots linearity was evaluated, and curves with emission lines that exhibited R^2 values above 0.9692 for ICP-OES and 0.9025 for MIP-OES were retained for further analysis (Table 2 and Supplementary Table S3), where a R^2 near 1.000 suggests that the selected wavelengths are likely free from interferences (Pereira et al., 2020). The slopes of the calibration curves were carefully assessed to ensure all angular coefficients fell within the acceptable range (0.1 < slope <0.9), as slopes outside this range could indicate potential inaccuracies (Virgilio et al., 2020).

Slope values for ICP-OES falls outside the recommended range, particularly in bovine liver where it could be seen a lower range for Ca, Mn and Zn (between 0.0141 (Ca) and 0.0643 (Zn)), while for Co, Cu, Fe, K, Mg, Na and P the range was 0.2292 (Co) and 0.5533 (P); in the case of maize 0.0084 (Ca) and 0.045 (Na) for Ca, Cu, Mn, Na and Zn, while for Fe, K, Mg and P the range was 0.1037 (Fe) and 0.243 (P). MIP-OES has slope values in the range between 0.4117 (Fe) and 0.5572 (Cu) and Co showing a value close to 0.9150, for bovine liver (Table 2). Whereas for corn grains, the lowest slope corresponds to Ca (0.1866) and the highest to Na (0.5649). According to Santos et al. and Virgilio et al., this discrepancy in slopes could be due to an imbalance between the analyte concentrations in the calibration solutions (C_std) and the sample (C_sam) (Santos et al., 2024;

TABLE 2 Slopes and R^2 values comparison for the 10 analytes analyzed across MEC-ICP-OES and MEC-MIP-OES techniques in RM-Agro E3001a - Bovine Liver and MRC20-Corn grain.

Analytes	MEC- ICP-OES				MEC- MIP-OES			
	RM-agro E3001a (Bovine Liver)		MRC20 (corn Grain)		RM-agro E3001a (Bovine Liver)		MRC20 (corn Grain)	
	Slope	R^2	Slope	R^2	Slope	R^2	Slope	R^2
Ca	0.0141	0.9998	**0.0084**	0.9857	0.4151	1.000	0.1866	1.000
Co	0.2292	1.000	-	-	0.9150	0.9983	-	-
Cu	0.5478	0.9998	**0.0117**	0.9939	0.5572	0.9999	0.3398	0.9660
Fe	0.5004	0.9990	0.1037	0.9998	0.4117	0.9921	0.5521	0.9894
K	0.5043	1.000	0.2236	1.000	0.4955	0.9953	0.4638	1.000
Mg	0.2094	1.000	0.3575	1.000	0.4170	0.9990	0.4423	0.9993
Mn	**0.0358**	0.9989	**0.0301**	0.9994	0.5274	0.9963	0.5011	0.9991
Na	0.4494	1.000	**0.0450**	1.000	0.4323	0.9999	0.5649	1.000
P	0.5533	0.9979	0.2430	0.9991	0.4834	0.9999	0.4477	0.9025
Zn	**0.0643**	0.9987	**0.0114**	0.9970	0.4990	0.9944	0.5182	0.9984

Virgilio et al., 2020). This mismatch between the standard and sample concentrations can lead to slope values outside the ideal range. Therefore, adjusting the concentrations of the calibration solutions to be closer to those of the sample, would help to better align the slopes with the optimal range (Santos et al., 2024). As was discussed above, some ICP-OES calibration slopes fall outside the recommended range; however, MEC still maintains high recovery rates (Table 3), demonstrating that it can handle non-ideal slope values while preserving accuracy. To assess the concentration mismatch in the reference material, a proficiency test material, "Animal Mineral Supplements" (SM18-03), was analyzed. As shown in Supplementary Table S3 and Supplementary Figure S3, the slopes for elements Ca, Co, Cu, Fe, K, Mg, Mn, Na, P, and Zn ranged from 0.2221 (P) to 0.9907 (Ca). Thus, it is evident that the use of multiple wavelengths for calibration compensates for spectral and matrix interferences.

3.2 MEC vs. EC recoveries

The traditional EC and MEC methods accuracy was evaluated by analysis of the reference material RM-Agro E3001a (Bovine Liver). The concentrations of Ca, Co, Cu, Fe, K, Mg, Mn, Na, P, and Zn determined using EC by ICP-OES and MIP-OES; and MEC by ICP-OES and MIP-OES are presented in Table 3. The concentrations for MEC were calculated according to Section 2.5; Equation 1. For ICP-OES analysis, recoveries ranged from 80% to 104% for EC (Fe, Mg, and Zn did not reach 80% recovery), and from 82% to 105% for MEC. For MIP-OES, recoveries ranged from 82% to 120% for EC (Zn did not reach 80% recovery), and from 80% to 102% for MEC. In both MEC-ICP-OES and MEC-MIP-OES, Ca recoveries are nearly identical, approaching 80%. As could be seen, MEC showed similar recovery improvements in both ICP-OES and MIP-OES, with quantitative recoveries, indicating that it provides a reliable calibration for both plasma techniques. Although concentration imbalance can influence the slope, MEC, however, is less dependent on slope values because it relies on multiple calibration points derived from different energy transitions. This means that even if the slope is slightly outside range (0.1–0.9), MEC can still produce accurate results, as observed with elements like Ca, Cu, Mn, Na, and Zn. Quantitative recoveries indicate that MEC effectively mitigates matrix effects, which might otherwise skew results in complex samples like bovine liver. This is especially evident where MEC provides significantly better recoveries compared to EC (e.g., Zn in ICP-OES and MIP-OES). Additionally, Supplementary Table S4 compares analytes recoveries in reference material MRC20-Maize grain by ICP-OES and MIP-OES using MEC.

To continue comparing the results of MEC with EC calibration for ICP-OES and MIP-OES, key figures of merit such as LOD, LOQ, and precision (%Relative Standard Deviation (RSD)) were evaluated.

3.3 Analytical performance

LOD and LOQ calculated according to IUPAC guidelines may not be fully appropriated for the MEC calibration method, as they mainly consider deviations in blank measurements as the primary error source (Virgilio et al., 2020). In contrast, for multi-signal calibration methods like MEC, it is essential to incorporate errors arising from both the slope and the intercept, as multiple calibration plots are generated based on the number of replicates (Section 2.6; Equations 2, 3).

The analytical performance results are shown in Table 4. The developed procedure achieved LOQs ranging from 0.4 mg kg^{-1} for Co to 195 mg kg^{-1} for K by EC-ICP-OES and 0.09 mg kg^{-1} for Mn to 31 mg kg^{-1} for Ca and Na by MEC-ICP-OES; and 2.0 mg kg^{-1} for Mg to 607 mg kg^{-1} for Fe by EC-MIP-OES and 0.08 mg kg^{-1} for Mn to 354 mg kg^{-1} for P by MEC-MIP-OES. Consistently with Alencar et al. and Gonçalvez et al. MEC can often yield LODs an order of

TABLE 3 Comparative concentration results (mean ± confidence interval; n = 3 replicates) and recovery percentages (%) for the determination of Ca, Co, Cu, Fe, K, Mg, Mn, Na, P, and Zn (mg kg^{-1}) in the reference material RM-Agro E3001a - Bovine Liver, using EC and MEC calibrations with ICP-OES and MIP-OES.

Analytes	RM-agro E3001a - Bovine Liver								
	Certified value [mg kg^{-1}]	ICP-OES				MIP-OES			
		EC		MEC		EC		MEC	
		Found concentration [mg kg^{-1}]	Recovery [%]	Found concentration [mg kg^{-1}]	Recovery [%]	Found concentration [mg kg^{-1}]	Recovery [%]	Found concentration [mg kg^{-1}]	Recovery [%]
Ca	182 ± 12	190 ± 10	104	143 ± 1	79	218 ± 35	120	141 ± 3	78
Co	0.3 ± 0.1	0.3 ± 0.1	93	0.3 ± 0.1	97	0.3 ± 0.1	102	0.4 ± 0.1	102
Cu	233 ± 6	202 ± 37	87	244 ± 11	105	201 ± 1	82	238 ± 28	102
Fe	200 ± 30	141 ± 49	71	196 ± 4	98	231 ± 2	115	163 ± 1	81
K	11,330 ± 910	10,100 ± 200	89	10,149 ± 200	90	10,448 ± 240	92	11,198 ± 144	99
Mg	773 ± 95	500 ± 100	65	660 ± 16	85	661 ± 6	86	789 ± 36	102
Mn	8 ± 1	7 ± 1	88	8 ± 1	100	9 ± 1	108	8 ± 1	101
Na	2,631 ± 72	2,300 ± 400	87	2,395 ± 169	91	2,579 ± 513	98	2,164 ± 46	82
P	15,650 ± 1,280	12,500 ± 700	80	12,809 ± 264	82	13,306 ± 27	85	12,975 ± 1744	83
Zn	176 ± 7	137 ± 29	78	172 ± 1	98	125 ± 1	71	140 ± 7	80

10.3389/frans.2025.1527110

TABLE 4 Analytical figures of merits for EC and MEC, by ICP-OES and MIP-OES.

Analytes	ICP-OES						MIP-OES					
	EC			MEC			EC			MEC		
	LOD [mg kg^{-1}]	LOQ [mg kg^{-1}]	RSD [%]	LOD [mg kg^{-1}]	LOQ [mg kg^{-1}]	RSD [%]	LOD [mg kg^{-1}]	LOQ [mg kg^{-1}]	RSD [%]	LOD [mg kg^{-1}]	LOQ [mg kg^{-1}]	RSD [%]
Ca	16	53	2.6	9	31	3.5	1.9	5.7	2.7	0.08	0.28	0.6
Co	0.12	0.40	2.2	0.50	1.6	8.8	3.3	9.9	0.7	68	227	1.2
Cu	0.15	0.49	4.5	0.20	0.70	7.7	2.6	7.9	8	0.05	0.16	0.7
Fe	1	2	3.5	0.10	0.50	2.3	200	607	5.2	1.0	3.3	0.7
K	58	195	3.9	1.5	4.8	4.2	4.3	11	2.3	0.30	0.99	0.4
Mg	5	17	2.9	0.70	2.2	4.5	0.67	2.0	4.8	0.03	0.11	0.8
Mn	0.18	0.59	5.3	0.03	0.09	4.7	2.8	8.5	3	0.02	0.08	1.1
Na	14	47	3.2	9	31	5.3	3.9	11.7	6.5	32	107	0.1
P	22	75	4.2	8	28	2.6	156	474	2.6	106	354	5.0
Zn	0.32	1.08	5.7	0.30	0.90	1.2	7.8	23	2.1	0.40	1.40	1.2

TABLE 5 Comparison of LODs achieved with MEC using ICP-OES and MIP-OES.

LOD [µg L^{-1}]										Technique	References
Ca	Co	Cu	Fe	K	Mg	Mn	Na	P	Zn		
1	1	1	15	4	0.5	0.3	0.5	1,610	6	MIP-OES	this work
0.08*	68*	0.05*	1*	0.30*	0.03*	0.02*	*32	106*	0.4*		
200	10	4	3	29	14	1	188	167	5	ICP-OES	
9*	0.50*	0.20*	0.10*	1.5*	0.70*	0.03*	9	8	0.30		
11.88*	-	-	-	2.35*	2.57*	3.05*	5.78*	-	-	MIP-OES	Santos et al. (2024)
50	-	-	-	9	59	-	131	-	-	MIP-OES	Cruz et al. (2024)
-	-	1.3	-	-	-	0.15	-	-	3.1	MIP-OES	Carneiro and Dias (2021)
-	-	1	-	-	-	-	-	-	-	ICP-OES	Virgilio et al. (2020)
0.6*	-	0.1*	-	1.5*	0.06*	0.02*	-	-	0.03*	ICP-OES	Pereira et al. (2020)
20	-	10	1	100	2	-	200	50	60	ICP-OES	Higuera et al. (2019)
6*	-	3*	0.3*	0.4*	0.7*	-	0.6*	0.1*	19*		
-	-	1	-	-	-	-	-	-	-	ICP-OES	Gonçalves et al. (2019)
15	2.9	5.7	-	70	43	-	120	-	9.8	ICP-OES	Barros, Pinheiro, and Nóbrega (2019)
-	-	2	-	-	-	-	-	-	-	MIP-OES	Virgilio et al. (2017)
-	-	0.7	-	-	-	0.8	-	-	-	ICP-OES	

*[µg g^{-1}].

magnitude lower than EC calibration (Alencar et al., 2019; Gonçalves et al., 2019). As it could be seen in Table 4, MEC achieves lower LOQs compared to EC, except for Co and Na in MIP-OES, and for Co in ICP-OES; while Cu, Na and Zn have the same order of magnitude in ICP. This is primarily because MEC can leverage multiple wavelengths (or energy levels) for calibration, increasing signal-to-noise ratios and enhancing sensitivity. In contrast, EC relies on single wavelengths for each analyte, which may limit sensitivity. EC methods could suffer from higher background noise in complex matrices, making LOQs typically higher than those observed with MEC, especially in the lower plasma temperature, where reductions of up to two orders of

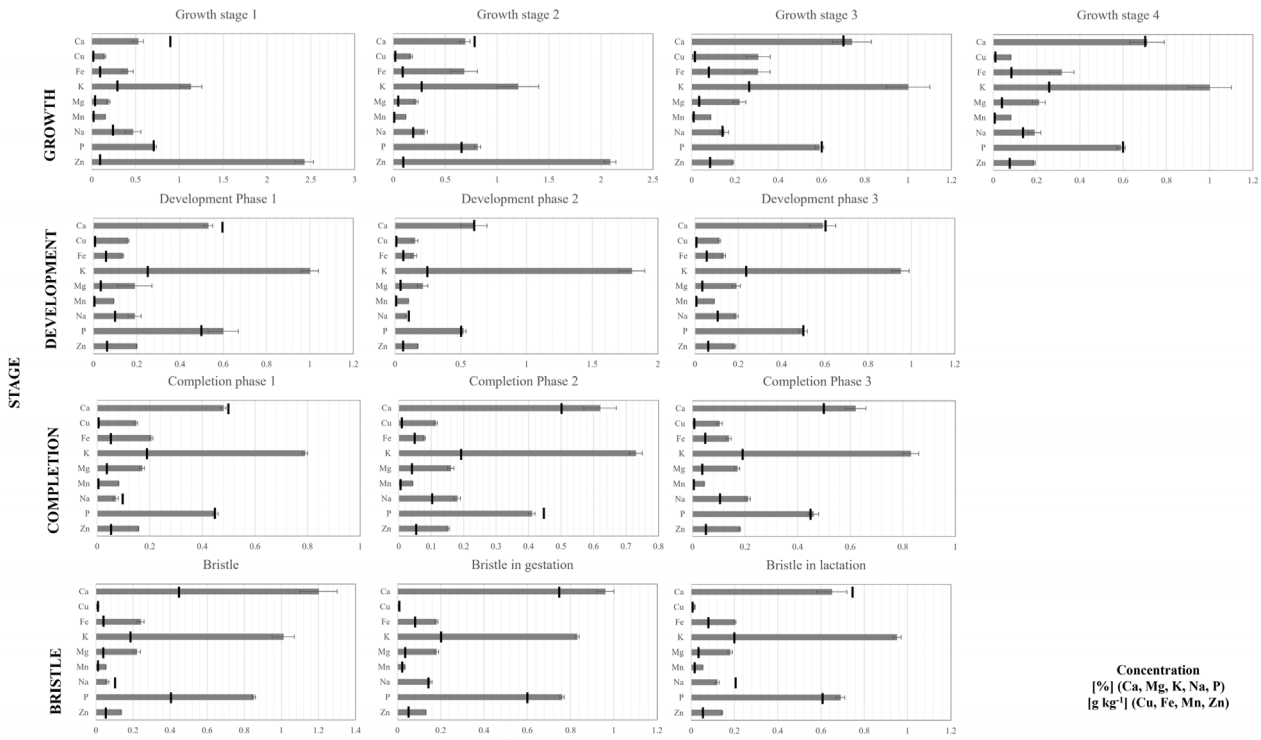

FIGURE 4
Determination of Ca, Co, Cu, Fe, K, Mg, Mn, Na, P, and Zn by MEC-MIP-OES and MEC-ICP-OES in different categories of animal feed samples. Results are reported as mean ± confidence interval (n = 3). Dietary mineral requirements for growing pigs, gestating sows, and lactating sows, as specified by National Research Council (2011), are indicated by a black line in the graph for reference.

magnitude can be observed in MIP-OES (Ca, Cu, Fe, Mg, and Mn) (Alencar et al., 2019; Oliveira et al., 2018).

As shown in Table 5, the use of MEC as a methodology in this study resulted in exceptional LODs for several elements. The best LODs for Ca, Cu, K, and Mg were achieved in this work using MEC-MIP-OES, demonstrating its capability to enhance sensitivity for these elements. For Co, the LODs reported by Barros et al., 2019 for a urine matrix were lower than those obtained in this study, highlighting that matrix effects can influence LODs even when using advanced calibration methods like MEC.

The LODs for Cu obtained in this study are consistent with those reported in the literature, falling within the same order of magnitude, showcasing MEC's reliability in achieving comparable performance. For Fe, while Higuera et al., 2019 reported the lowest LODs in μg L^{-1} for a meat matrix using ICP-OES, the best LODs expressed in μg g^{-1} were obtained in this study when MEC-ICP-OES was employed, underscoring the robustness of MEC for solid sample matrices. Similarly, for Mn, the LODs achieved using both MEC-MIP-OES and MEC-ICP-OES are similar to those reported by Pereira et al., 2020, further supporting MEC's effectiveness across techniques.

A particularly noteworthy result was observed for Na, where the MEC-MIP-OES methodology yielded LODs that were four orders of magnitude lower than those reported in other studies, demonstrating a significant improvement in sensitivity. In contrast, for P, the LODs obtained using MEC in this study were four (ICP-OES) and five (MIP-OES) orders of magnitude higher than those reported by Higuera et al., 2019, suggesting potential challenges in achieving optimal sensitivity for this element under the tested conditions.

Finally, for Zn, the LODs achieved in this study are of the same order of magnitude as those reported by Carneiro and Dias 2021 for MIP-OES and Barros et al., 2019 for ICP-OES, with the best sensitivity observed in Carneiro and Dias' study. These findings highlight MEC's significant advantages in improving sensitivity and addressing matrix effects while indicating opportunities for refinement in certain cases. Overall, MEC demonstrates its utility as a powerful calibration strategy for improving the detection of multiple elements in complex matrices.

In all cases, the MEC precision, expressed as %RSD, was better than 8.8% in ICP-OES and 1.2% in MIP-OES. For ICP-OES, only Fe, Mn, P and Zn exhibited lower RSD in MEC compared to EC. MEC-MIP-OES consistently demonstrated lower RSD for all analytes, indicating more precise measurements.

MEC demonstrated enhanced accuracy over EC, largely due to its matrix-matching capabilities, which provided higher trueness and precision. Analytes such as Co, Fe, Na, and P are more effectively determined by MEC-ICP-OES, while Ca, Cu, K, and Mg are better suited to MEC-MIP-OES, but both instrumental techniques led to accurate results for all analytes. Manganese and Zn show comparable performance with both methods.

3.4 Analytical application for animal feed quality assurance

The MEC method was applied to analyze animal feed samples and assess the mineral nutritional composition of the feed. This data is essential for formulating balanced rations and could directly influence pig growth.

The excesses or deficiencies of minerals such as Ca, Co, Cu, Fe, K, Mg, Mn, Na, P, and Zn can lead to nutritional imbalances in swine, affecting their health and productivity (McDowell, 1992; Patience, 1996; Fabà et al., 2019). To address this, the developed MEC-ICP-OES and MEC-MIP-OES procedure was applied to determine these essential mineral nutrients in pig feed samples (Figure 4).

The mineral concentrations obtained were then compared to the dietary mineral requirements for different physiological stages of swine (marked by a black line in Figure 4), including growing pigs, gestating sows, and lactating sows, as defined by the Nutrient Requirements of Swine (National Research Council, 2012) (Figure 4). The comparison revealed that most physiological stage samples did not meet the required nutritional levels exceeding the recommended values. However, certain minerals, such as Ca, Na, and P, in a few samples were nearly aligned with NRC guidelines. Given the variability in nutrient requirements based on numerous factors, it is essential for feed suppliers to enhance their ability to accurately define and evaluate feed ingredients. This necessitates continuous reevaluation of feed formulations to ensure they meet the minimum nutritional requirements for animals. Increased emphasis on quality control is critical to ensure accurate feed formulations for supporting optimal growth and health in swine.

3.5 Conclusion

MEC strategy has demonstrated robust and consistent performance for ICP-OES and MIP-OES. The results confirm that MEC is an effective calibration method for rapid, accurate multielement analysis with optical plasma techniques, reliably quantifying essential elements like Ca, Co, Cu, Fe, K, Mg, Mn, Na, P, and Zn with accurate recoveries.

This approach excels at matrix-matching in complex samples, such as biological tissues and animal feeds, offering a flexible solution that does not require instrument modifications. For laboratories already using ICP-OES or MIP-OES, MEC is an easy-to-implement enhancement to the existing instrument, reducing the need for labor-intensive matrix-matching standards and improving calibration efficiency. By optimizing the calibration process, MEC can significantly increase sample throughput and reduce analysis time.

While MEC presents clear advantages for multielement determination, some challenges remain. For instance, all calculations could be easier performed if proper data treatment was implemented in the built-in software that controls modern instruments. As an additional bonus, emission lines affected by interferences are easily spotted in the analytical calibration curve because they do not follow the expected linear response with analyte concentration. In this sense, if analytical chemistry can be seen as a science to generate chemical information about samples, MEC is a powerful ally because it allows bettering exploiting multiple analytical signals typically obtained when applying instrumental analysis.

In the context of nutritional research, such as in animal feed analysis, MEC can support improved efficiency in swine production by enabling precise mineral analysis. This is highly beneficial for producers, as reliable analytical data allow for precise feed formulation, leading to cost savings and optimized nutrition. Quality control in agri-foods, facilitated by MEC, is thus essential for ensuring that feed formulations meet nutritional standards, ultimately benefiting both suppliers and producers.

Data availability statement

The original contributions presented in the study are included in the article/Supplementary Material, further inquiries can be directed to the corresponding author.

Author contributions

FC: Conceptualization, Investigation, Validation, Writing–original draft, Writing–review and editing, Data curation, Formal Analysis. AB: Writing–review and editing, Methodology, Supervision. JN: Supervision, Writing–review and editing, Funding acquisition. MS: Supervision, Writing–review and editing, Conceptualization, Investigation, Validation, Writing–original draft.

Funding

The author(s) declare that financial support was received for the research, authorship, and/or publication of this article. This work was financially supported by the Special fund for Universidad Nacional de La Pampa. This study was financed in part by Conselho Nacional de Desenvolvimento Científico e Tecnológico (CNPq – grants 303107/2013-8, 307452/2023-9 and 428558/2018-6); Coordenação de Aperfeiçoamento de Pessoal de Nível Superior Brasil (CAPES) – Finance Code 001; Instituto Nacional de Ciências e Tecnologias Analíticas Avançadas – CNPq, Grant No. 573894/2008-6 and FAPESP and Grant No. 2014/50951-4.

Acknowledgments

The authors are grateful to the Consejo Nacional de Investigaciones Científicas y Tecnicas (CONICET), Agencia Nacional de Promoción Científica y Tecnológica (ANPCYT) and Universidad Nacional de La Pampa; Conselho Nacional de Desenvolvimento Científico e Tecnológico (CNPq), and Coordenação de Aperfeiçoamento de Pessoal de Nível Superior (CAPES/PNPD – Graduate Program in Chemistry, Federal University of São Carlos). We also acknowledge the technical support provided by Analítica (São Paulo, SP, Brazil), Milestone (Sorisole, BG, Italy) and Thermo Scientific. The authors also would like to express their gratitude to the Instituto Nacional de Ciências e Tecnologias Analíticas Avançadas (INCTAA), Instituto Nacional de

Tecnología Agropecuaria (INTA) and to swines' producers that kindly provided samples.

Conflict of interest

The authors declare that the research was conducted in the absence of any commercial or financial relationships that could be construed as a potential conflict of interest.

Generative AI statement

The author(s) declare that no Generative AI was used in the creation of this manuscript.

Publisher's note

Supplementary material

The Supplementary Material for this article can be found online at: https://www.frontiersin.org/articles/10.3389/frans.2025.1527110/full#supplementary-material

References

Alencar, M. C., Gonçalves, D. A., Nicolodelli, G., Oliveira, S. L., Donati, G. L., and Caires, A. R. L. (2019). Evaluating the applicability of multi-energy calibration as an alternative method for quantitative molecular spectroscopy analysis. *Spectrochimica Acta - Part A Mol. Biomol. Spectrosc.* 221 (October), 117221. doi:10.1016/j.saa.2019.117221

Augusto, A., Castro, J., Sperança, M., and Pereira, E. (2018). Combination of multi-energy calibration (MEC) and laser-induced breakdown spectroscopy (LIBS) for dietary supplements analysis and determination of Ca, Mg and K. *J. Braz. Chem. Soc.* doi:10.21577/0103-5053.20180211

Analytical Methods Committee (2013). "What Causes most errors in chemical analysis?". *Anal. Methods* 5 (12), 2914–2915. doi:10.1039/C3AY90035E

Babos, D. V., Barros, A. I., Nóbrega, J. A., and Pereira-Filho, E. R. (2019). Calibration strategies to overcome matrix effects in laser-induced breakdown spectroscopy: direct calcium and phosphorus determination in solid mineral supplements. *Spectrochim. Acta Part B At. Spectrosc.* 155 (1), 90–98. doi:10.1016/j.sab.2019.03.010

Babos, D. V., Virgilio, A., Costa, V. C., Donati, G. L., and Pereira-Filho, E. R. (2018). Multi-energy calibration (MEC) applied to laser-induced breakdown spectroscopy (LIBS). *J. Anal. Atomic Spectrom.* 33 (10), 1753–1762. doi:10.1039/C8JA00109J

Barros, A. I., Pinheiro, F. C., and Nóbrega, J. A. (2019). Calibration strategies to correct for matrix effects in direct analysis of urine by ICP OES: internal standardization and multi-energy calibration. *Anal. Methods* 11 (27), 3401–3409. doi:10.1039/C9AY00907H

Beily, M. E., Brunori, J., Campagna, D. A., Cottura, G., Crespo, D., and Denegri, G. D. (2011). "Buenas Prácticas Pecuarias (BPP) para la producción y comercialización porcina familiar," in *Instituto Nacional de Tecnología Agropecuaria; Organización de las Naciones Unidas para la Agricultura y la Alimentación* 277. Available at: https://www.fao.org/3/i2094s/i2094s.pdf.

Carneiro, C. N., and Dias, F. de S. (2021). Multiple response optimization of ultrasound-assisted procedure for multi-element determination in Brazilian wine samples by microwave-induced plasma optical emission spectrometry. *Microchem. J.* 171 (December), 106857. doi:10.1016/j.microc.2021.106857

Carter, J. A., Barros, A. I., Nóbrega, J. A., and Donati, G. L. (2018). Traditional calibration methods in atomic spectrometry and new calibration strategies for inductively coupled plasma mass spectrometry. *Front. Chem.* 6 (November), 504. doi:10.3389/fchem.2018.00504

Carvalho, A. A. C., Cozer, L. A., Luz, M. S., Nunes, L. C., Rocha, F. R. P., and Nomura, C. S. (2019). Multi-energy calibration and sample fusion as alternatives for quantitative analysis of high silicon content samples by laser-induced breakdown spectrometry. *J. Anal. Atomic Spectrom.* 34 (8), 1701–1707. doi:10.1039/C9JA00149B

Castro, J. P., Babos, D. V., and Pereira-Filho, E. R. (2020). Calibration strategies for the direct determination of rare Earth elements in hard disk magnets using laser-induced breakdown spectroscopy. *Talanta* 208 (February), 120443. doi:10.1016/j.talanta.2019.120443

Cruz, E., Lizeth, T., Guerrero Esperanza, M., Wrobel, K., Yanez Barrientos, E., Aguilar, F. J. A., et al. (2020). Determination of major and minor elements in Mexican red wines by microwave-induced plasma optical emission spectrometry, evaluating different calibration methods and exploring potential of the obtained data in the assessment of wine provenance. *Spectrochim. Acta Part B At. Spectrosc.* 164 (February), 105754. doi:10.1016/j.sab.2019.105754

Cruz, E., Lizeth, T., Wrobel, K., Barrientos, E. Y., Escobosa, A. R. C., Garay-Sevilla, Ma E., et al. (2024). Determination of sodium, potassium, calcium and magnesium in urine, using microwave plasma - atomic emission spectrometry and multi-energy calibration. *J. Mexican Chem. Soc.* 68 (1), 18–28. doi:10.29356/jmcs.v68i1.1906

Donati, G. L., and Amais, R. S. (2019). Fundamentals and new approaches to calibration in atomic spectrometry. *J. Anal. Atomic Spectrom.* 34 (12), 2353–2369. doi:10.1039/C9JA00273A

Fabà, L., Gasa, J., Tokach, M. D., Font-i-Furnols, M., Vilarrasa, E., and Solà-Oriol, D. (2019). Effects of additional organic micro-minerals and methionine on carcass composition, gait score, bone characteristics, and osteochondrosis in replacement gilts of different growth rate. *Animal Feed Sci. Technol.* 256 (September), 114262. doi:10.1016/j.anifeedsci.2019.114262

Fortunato, F. M., Catelani, T. A., Pomares-Alfonso, M. S., and Pereira-Filho, E. R. (2019). Application of multi-energy calibration for determination of chromium and nickel in nickeliferous ores by laser-induced breakdown spectroscopy. *Anal. Sci.* 35 (2), 165–168. doi:10.2116/analsci.18P286

Garde, R., Nakadi, F. V., García-Ruiz, E., and Resano, M. (2020). Introducing multi-energy ratios as an alternative to multi-energy calibration for Br determination *via* high-resolution continuum source graphite furnace molecular absorption spectrometry. A case study. *J. Anal. Atomic Spectrom.* 35 (11), 2606–2619. doi:10.1039/D0JA00359J

Gonçalves, D. A., Domingos de Souza, I., Rosa, A. C. G., Melo, E. S. P., Goncalves, A. M. B., de Oliveira, L. C. S., et al. (2019). Multi-wavelength calibration: determination of trace toxic elements in medicine plants by ICP OES. *Microchem. J.* 146 (May), 381–386. doi:10.1016/j.microc.2019.01.021

Higuera, J. M., Silva, A. B. S., and Nogueira, A. R. A. (2019). Multi-energy calibration: a practical method for determination of macro and micro nutrients in meat by ICP OES. *J. Braz. Chem. Soc.* 30 (12), 2575–2581. doi:10.21577/0103-5053.20190171

Jofre, C., Florencia, D. N. L., and Savio, M. (2020). An eco-friendly infrared method for rapid soil sample preparation for multielemental determination by microwave induced plasma atomic emission spectrometry. *Microchem. J.* 159 (December), 105448. doi:10.1016/j.microc.2020.105448

Jofre, F. C., and Savio, M. (2024). Infrared radiation: a sustainable and promising sample preparation alternative for inorganic analysis. *TrAC Trends Anal. Chem.* 170 (1), 117469. doi:10.1016/j.trac.2023.117469

Li, X., Zhao, T., Zhong, Q., Nie, S., Xiao, H., Zhao, S., et al. (2020). Iterative multi-energy calibration and its application in online alloy smelting process monitoring using laser-induced breakdown spectroscopy. *J. Anal. Atomic Spectrom.* 35 (10), 2171–2178. doi:10.1039/D0JA00247J

Machado, R. C., Silva, A. B. S., Donati, G. L., and Nogueira, A. R. A. (2018). Multi-energy calibration as a strategy for elemental analysis of fertilizers by microwave-induced plasma optical emission spectrometry. *J. Anal. Atomic Spectrom.* 33 (7), 1168–1172. doi:10.1039/c8ja00077h

Matusiewicz, H. (2017). Sample preparation for inorganic trace element analysis. *Phys. Sci. Rev.* 2 (5). doi:10.1515/psr-2017-8001

McDowell, L. R. (1992). *Minerals in animal and human nutrition: comparative aspects to human nutrition animal feeding and nutrition*. Elsevier Science.

Nóbrega, J. A., Pirola, C., Fialho, L. L., Rota, G., de Campos Jordão, C. E. K. M. A., and Pollo, F. (2012). Microwave-assisted digestion of organic samples: how simple can it become? *Talanta* 98 (August), 272–276. doi:10.1016/j.talanta.2012.06.079

National Research Council (2012). *Nutrient requirements of Swine: Eleventh revised edition*. Washington, DC: The National Academies Press. doi:10.17226/13298

Novo, D. L. R., Pereira, R. M., Costa, V. C., Hartwig, C. A., and Mesko, M. F. (2018). A novel and eco-friendly analytical method for phosphorus and sulfur determination in animal feed. *Food Chem.* 246 (April), 422–427. doi:10.1016/j.foodchem.2017.11.036

Oliveira, A. F., Gonzalez, M. H., and Nogueira, A. R. A. (2018). Use of multiple lines for improving accuracy, minimizing systematic errors from spectral interferences, and reducing matrix effects in MIP OES measurements. *Microchem. J.* 143 (December), 326–330. doi:10.1016/j.microc.2018.08.032

Patience, J. F. (1996). Precision in swine feeding programs: an integrated approach. *Animal Feed Sci. Technol.* 59 (1–3), 137–145. doi:10.1016/0377-8401(95)00894-2

Pereira, H. S., Nogueira da Silva, K. R., Melo, E. S. de P., Aragão do Nascimento, V., and Raposo, J. L. (2020). Multi-energy calibration: an easy strategy for fast and accurate determination of macro- and micro-nutrients in biomass waste samples by ICP OES. *J. Anal. Atomic Spectrom.* 35 (8), 1558–1565. doi:10.1039/D0JA00189A

Santos, T. S., Arruda dos Santos, E., Victor Soares de Araújo, J., Jadán-Piedra, C., Jorgensen Cassella, R., Duyck, C., et al. (2024). Multi-energy calibration and induced plasma optical emission spectrometry (MEC-MIP OES) as an alternative method for the multi-elemental determination of essential elements in cocoa. *J. Food Compos. Analysis* 136 (1), 106798. doi:10.1016/j.jfca.2024.106798

Savio, M., Fialho, L. L., and Nóbrega, J. A. (2019). Greening microwave-assisted acid digestion of animal feed samples. *Anal. Methods* 11 (46), 5857–5863. doi:10.1039/C9AY01586H

SDGs (2024). Sustainable development Goals. Available at: https://www.Un.Org/Sustainabledevelopment/.

Shurson, G. C., Salzer, T. M., Koehler, D. D., and Whitney, M. H. (2011). Effect of metal specific amino acid complexes and inorganic trace minerals on vitamin stability in premixes. *Animal Feed Sci. Technol.* 163 (2–4), 200–206. doi:10.1016/j.anifeedsci.2010.11.001

Soares, S., Donati, G. L., and Rocha, F. R. P. (2022). Digital-image photometry with multi-energy calibration. *Microchem. J.* 182 (November), 107938. doi:10.1016/j.microc.2022.107938

Solà-Oriol, D., and Gasa, J. (2017). Feeding strategies in pig production: sows and their piglets. *Animal Feed Sci. Technol.* 233 (November), 34–52. doi:10.1016/j.anifeedsci.2016.07.018

Spears, J. W., and Weiss, W. P. (2008). Role of antioxidants and trace elements in health and immunity of transition dairy cows. *Veterinary J.* 176 (1), 70–76. doi:10.1016/j.tvjl.2007.12.015

Vieira, A. L., Gonçalves, D. A., Virgilio, A., Ferreira, E. C., Jones, B. T., Donati, G. L., et al. (2019). Multi-energy calibration for the determination of non-metals by high-resolution continuum source molecular absorption spectrometry. *J. Anal. Atomic Spectrom.* 34 (5), 972–978. doi:10.1039/C9JA00006B

Virgilio, A., Gonçalves, D. A., McSweeney, T., Gomes Neto, J. A., Nóbrega, J. A., and Donati, G. L. (2017). Multi-energy calibration applied to atomic spectrometry. *Anal. Chim. Acta* 982 (August), 31–36. doi:10.1016/j.aca.2017.06.040

Virgilio, A., Silva, A. B. S., Nogueira, A. R. A., Nóbrega, J. A., and Donati, G. L. (2020). Calculating limits of detection and defining working ranges for multi-signal calibration methods. *J. Anal. Atomic Spectrom.* 35 (8), 1614–1620. doi:10.1039/D0JA00212G

Frontiers in
Analytical Science

Explores techniques for analyzing chemicals and biochemical systems

Highlights techniques for detecting, analyzing and monitoring chemical/biochemical systems across fields including medical sciences, environmental studies and forensics.

Discover the latest Research Topics

See more →

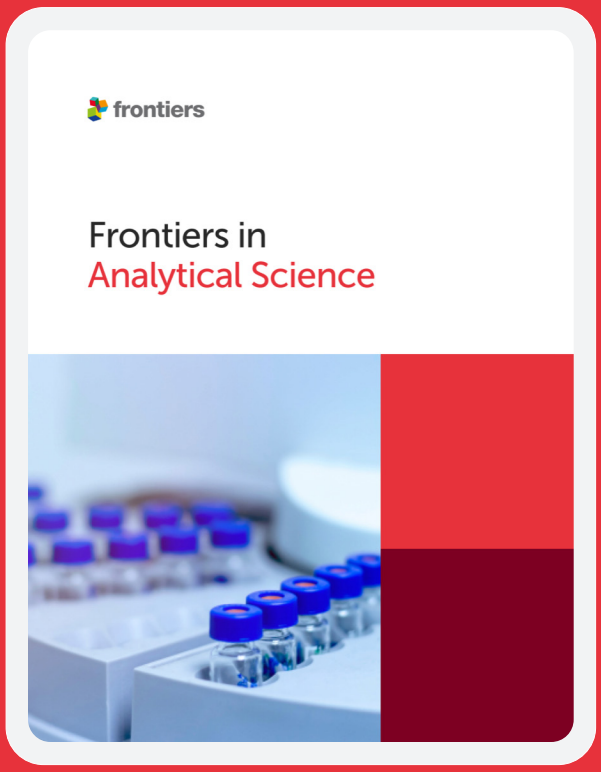

Frontiers

Avenue du Tribunal-Fédéral 34
1005 Lausanne, Switzerland
frontiersin.org

Contact us

+41 (0)21 510 17 00
frontiersin.org/about/contact